Historic, Archive Document

Do not assume content reflects current
scientific knowledge, policies, or practices.

USDA

Experimental and Numerical Investigations of Floating Breakwater Performance

by Yavuz Ozeren, Daniel Wren, and Carlos Alonso

United States
Department of
Agriculture

NATIONAL
AGRICULTURAL
LIBRARY

Advancing Access to
Global Information for
Agriculture

ACKNOWLEDGMENTS

ABSTRACT

Floating breakwaters are commonly used to protect small marinas and for shoreline erosion control in coastal areas. They are efficient wave attenuation structures for relatively short waves and shallow water depths. The main objective of the current study is to investigate the hydrodynamic interaction of small scale waves with floating breakwaters, experimentally and numerically. The breakwater models considered here are single or multiple cylindrical sections with different mooring configurations.

For the model studies a wave flume with a flap-type wave generator and a progressive wave absorber was designed, constructed, and used to investigate the wave transmission characteristics of multiple breakwater configurations for regular waves in deep and transitional water depths. The test results show that wave attenuation is achieved by different mechanisms depending on the wave characteristics and breakwater configuration. When the models were fully restrained, the primary mechanism reducing the transmission coefficient was reflection. Hence, the efficiency of the floating breakwater is strongly dependent on the draft and the freeboard of the breakwater. For partially restrained models, dissipation also becomes significant and therefore efficiency can be increased by increasing the damping characteristics of the breakwater. It was also observed that horizontal restraint is superior to vertical restraint in terms of improving breakwater efficiency.

A floating breakwater made of polyethylene irrigation tubing was designed through a laboratory model study and subjected to a short-term prototype-scale field test. In the field test, wave amplitudes were reduced by an average of approximately 60%. It is concluded from both the model and the field studies that cylindrical pipes can be used effectively as floating breakwaters for small lakes and reservoirs.

A two-dimensional vertical numerical wave tank was designed using a commercially available CFD software package, to further investigate the interaction of the waves with cylindrical floating breakwaters. A new method to generate waves by using a mass source function was developed and coded into the numerical model of the CFD software package. This source function allowed wave generation without blocking the reflected waves. The new wave generation method was tested with linear monochromatic waves and irregular waves. The results were compared with analytical solutions and experimental data. It is shown that the new method can successfully be used to generate a wide range of deep and intermediate wave conditions in numerical wave tanks. The numerical wave tank was used to examine the effect of overtopping and breakwater restraint for a wide range of wave parameters and breakwater configurations. The results are validated with the experimental measurements using far field transmission and reflection properties. The results of prototype-scale numerical simulations were compared with the field data. It is shown that modified numerical model can efficiently be used to simulate the interaction of linear monochromatic and irregular waves with floating breakwaters. Moreover, it is shown that the numerical model results compare well with the results of laboratory experiments even in case of overtopping.

TABLE OF CONTENTS

LIST OF SYMBOLS

c_o	wave propagation speed for deepwater conditions
c	wave propagation speed (celerity)
C_G	wave group velocity
d	horizontal length scale of the breakwater
E	total energy in a wave per unit width of crest
E_i	total incident wave energy
E_k	total dissipated wave energy
E_k	kinetic energy in a wave per unit width of crest
E_p	potential energy in a wave per unit width of crest
E_r	total reflected wave energy
E_t	total transmitted wave energy
Fr	Froude number
g	gravitational acceleration
h	water depth
H	wave height
H_i	incident wave height
H_{max}	maximum wave amplitude in an envelope of waves
H_{min}	minimum wave amplitude in an envelope of waves
H_r	reflected wave height
H_t	reflected wave height
K	pressure response factor
k	wave number
L	wavelength
L_0	wavelength for deepwater conditions
N_L	length scale ratio
N_T	time scale ratio
P	mean power
p	pressure intensity
Re	Reynolds number

R_{xy}	cross-correlation function
S	stroke of the paddle
t	time
T	wave period
u	horizontal component of the velocity vector
w	vertical component of the velocity vector
x	horizontal distance, in the direction of wave propagation
z_d	draft of the breakwater
z	vertical distance, the origin is at the mean water level
ε	horizontal displacement from the mean
ϕ	velocity potential
γ_w	unit weight of water
κ_r	reflection coefficient
ξ	vertical displacement from the mean
κ_t	transmission coefficient
η	vertical displacement of water surface from mean water level at $z = 0$
ω	wave angular frequency
ε_p	two-dimensional porosity of the mesh
ε_v	volumetric porosity
μ	dynamic viscosity of water
ρ_ω	mass density of water

I. INTRODUCTION

Floating breakwaters are a common method for the protection of small marinas and for shoreline erosion control (McCartney, 1985). The maximum kinetic energy concentration of waves is near the surface, where the floating breakwaters can best serve to reflect or dissipate the energy (Dean and Ursell, 1959). In spite of the large amount of work that has been done on coastal applications, a specific design for low-cost shore protection in small reservoirs was in need of development when the current work began. Relatively short fetch length (approximately 400-800 meters) available for wave generation and the relatively short wave periods (about 1.5 seconds) make floating breakwaters a viable option for levee protection (Werner, 1988).

Levee erosion by waves is controlled by wave properties and bank materials. Because of the wide range of soil types in levee embankments, the current study focused on reducing wave energy, which, for any soil type or levee configuration, should decrease erosion. Lower amplitude, less energetic, waves have been shown to cause less erosion than higher amplitude waves (CERC, 2006). The results from this study show that breakwater effectiveness improves as wave height relative to breakwater diameter decreases. Therefore, protecting the shoreline from large amplitude waves will also protect it from lower amplitude waves.

The main goal of this line of work is to investigate the effectiveness of floating breakwaters based on laboratory model study, field verification, and numerical simulations. A specific objective is to provide an inexpensive breakwater design of floating breakwaters for levee protection in small lakes and reservoirs based on physical modeling and field verification that can be implemented by landowners using commonly available materials. For this reason, a design that utilizes cylindrical pipe sections was sought, with plans to use inexpensive polyethylene irrigation tubing for the final field implementation.

Chapter II contains a review of relevant literature. The theoretical foundations of linear wave theory and floating breakwaters are described in Chapter III. Chapter IV presents technical details of the experimental methodology and equipment, and Chapter V contains the results of the experimental work. Chapter VI reports results from field trials and gives guidance on breakwater design. Chapter VII describes the theory and approximations behind the numerical solution technique. Chapter VIII presents the results of the model scale and prototype scale numerical simulations. Chapter IX contains a brief summary and conclusions. Appendices A contain detailed information related to techniques for collecting analysis of laboratory wave data. The ranges of parameters of the laboratory experiments are listed in Appendix B. Appendix C presents additional plots of the experimental results. The sensitivity analysis and selection of the mesh size are discussed in Appendix D. In Appendix E, the treatment of the open boundary is

explained. Appendix F presents the validation and verification of the numerical wave generation method. Appendix G introduces a simple approach to predict waves in small reservoirs. In Appendix H, the effect of reflected waves from the wave absorber at the end of the wave tank.

II. LITERATURE REVIEW

2.1.   Introduction

The main purpose of a breakwater is to protect the shoreline against wave action. Breakwaters can be constructed as fixed or mobile structures. The most common fixed breakwaters are rubble-mound breakwaters. Although they provide good protection from waves, they are relatively less feasible due to economical and environmental concerns (Hales, 1981).

A floating breakwater is a relatively cost effective way of providing wave protection to reduce wave energy to acceptable levels. It is not as efficient as the fixed breakwaters like rubble mound structures. But they are advantageous with their lower construction cost with shorter construction time at locations where the wave conditions are not severe and the water level is relatively high. Floating breakwaters can accommodate the depth changes easily and can be utilized for seasonal protection. They have relatively less effect on the marine environment and can be applicable at sites with poor foundation conditions.

Floating breakwaters can be classified according to their functionality and geometric configuration. When the functional aspects of the floating breakwater are considered, the transmitted wave energy is primarily reduced by reflection and dissipation. The attenuation of the incident wave height might be mainly by either one of the two mechanisms or a combination of them, depending on the nature of the waves and the type of the floating structure. Wave reflection can be described approximately by linear theory but energy dissipation involves viscous dissipation, nonlinear wave breaking and turbulence. Therefore, numerical approximations and empirical relations are widely used to model the complete phenomena.

Two types of mooring are typically used to restrain the breakwater motions; either piles or mooring lines. Piles have the advantage of restricting the horizontal motions. In some cases the roll motions are also considerably restricted. Restraining the floating breakwater considerably reduces the transmitted wave amplitude but increases loads on the piles and should be avoided in relatively deep water or poor foundation conditions. Mooring lines have lower cost compared to the pile systems, in deepwater. Moreover, certain mooring systems relax the restraining of the floating structure which also reduces the mooring forces. Wear problems at the points of contact with the piles is also a significant disadvantage for pile restrained breakwaters (Davidson, 1971). The choice of the breakwater design depends primarily on local wave and foundation conditions, the availability of construction materials, and functional aspects.

The most common parameter to characterize the floating breakwater performance is the transmission coefficient designated by κ_t, which is the ratio of the transmitted wave height, H_t, to the incident wave height, H_i. This coefficient is defined for regular monochromatic wave conditions; however the field wave conditions are often highly irregular. A similar definition used for the reflection coefficient, κ_r, as the ratio of the reflected wave height to the incident wave height. For irregular waves the transmission coefficient can be modified as the ratio of transmitted wave height squared, H_t^2 to the incident wave height squared, H_i^2 to reflect the energy transmission rate instead of wave height transmission rate. Alternatively, it can be defined as the ratio of the 0th moment (area) of the transmitted wave energy spectrum to the 0th moment of the incident wave spectrum which gives the transmission rate of the significant wave height (Akari, 1978). The transmitted wave energy is a combination of the portion of the energy that is passed through, under or over the structure if it were fixed and the portion of the energy generated by the motions of the floating breakwater itself. Waves generated by the motion of the structure may or may not be in phase with the incident wave field (Richey and Nece, 1974). Two other important dimensionless parameters considered in the design of the floating breakwater are the width to wavelength ratio (relative width) and the draft to wavelength ratio (relative draft). Selection of the parameters depends on the desired attenuation mechanism of the breakwater and the geometry of the floating structure. Increasing any of the two parameters will improve wave attenuation characteristic of the breakwater.

Although floating breakwaters have proven to be effective wave-attenuation devices, they must be designed carefully to survive extreme wave conditions (Isaacson, 1993). Floating breakwaters are mobile systems that are subjected to fluctuating loads and fatigue stresses. Also, the uncertainties in the applied loads may require design choices that increase the overall cost. The wave transmission is reduced by constraining the movements of the structure. However, the loading on the mooring system and the anchor system and the connection units between separate sections of the breakwater require durability with minimum structural complexity. The design of a floating breakwater should be simple, durable and should require minimum maintenance (Hales, 1981).

2.2.   History

The first record about a floating structure as a breakwater dates back to the early 19th century. In 1811 General Bentham, the Civil Architect and Principle Surveyor of the Royal Navy of Great Britain, proposed a breakwater model for the British fleet at Plymouth. The Breakwater would consist of triangular sections of floating wooded frames moored with iron chain. The project cost was about one-tenth the cost of the rubble and granite mound structure which was finally adopted. The idea was rejected due to the concerns about its effectiveness during severe storms (Readshaw, 1981).

4

In 1841, Captain Taylor of the Royal Navy proposed using floating sections framed timber moored to piles with a draft of 5 m in a lecture to the British Association for the Advancement of Science. He proposed to tar the timber frames or replace them periodically for maintenance (Readshaw, 1981).

In 1842, Reid's floating breakwater system was published in the Civil Engineers and Architects Journal. This breakwater system consisted of a sloping ramp supported by a timber frame (Figure 2.1a). The frame was made of 65 cm square timber sections reinforced with iron plates. The ramp was made of timber with a slope of 35 degrees downward and a vertical depth of 4.6 m. The length of each frame was 18 m. The structure was moored with iron chain (WCHL, 1981).

In 1905 J. Joly presented two floating breakwater concepts to the Royal Dublin Society for the harbours of Arklow and Wicklaw on the east coast of Ireland. The idea was to increase the inertia of the structure by the added mass of the water trapped within the walls of the structure (Figure 2.1b). The solution to the mooring problem was to construct a structure large enough that it did not respond to the incident waves. There is no record of any of the above floating breakwater modes ever being built (Readshaw, 1981).

A 120 m long rectangular concrete floating breakwater was actually constructed for a small crafts harbor at Lysekil, Sweden in 1941. The performance was satisfactory during its service (WCHL, 1981).

(a)   (b)   (c)
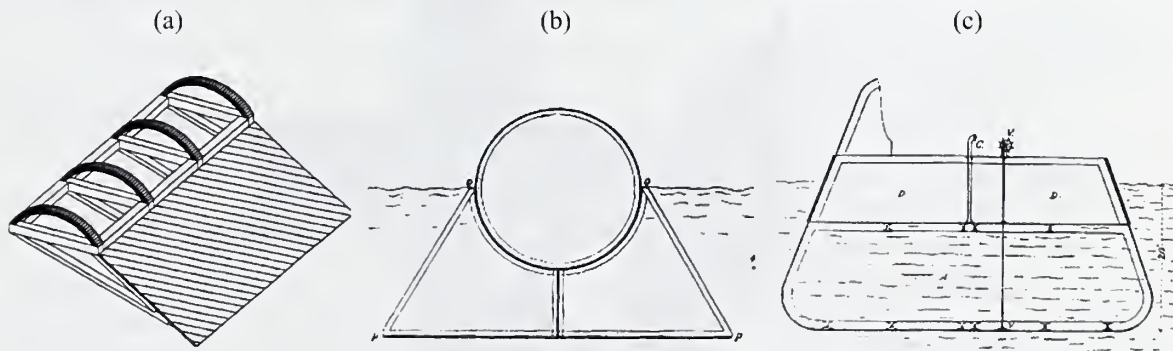
Figure 2.1 (a) Reid's floating breakwater, (Morey, 1998). (b) Joly's floating breakwater. The original illustrations are from Joly J. "On Floating Breakwaters", Royal Dublin Society, Scientific Proceedings, 1905 (Readshaw, 1981)

(a)

(b)

(c)
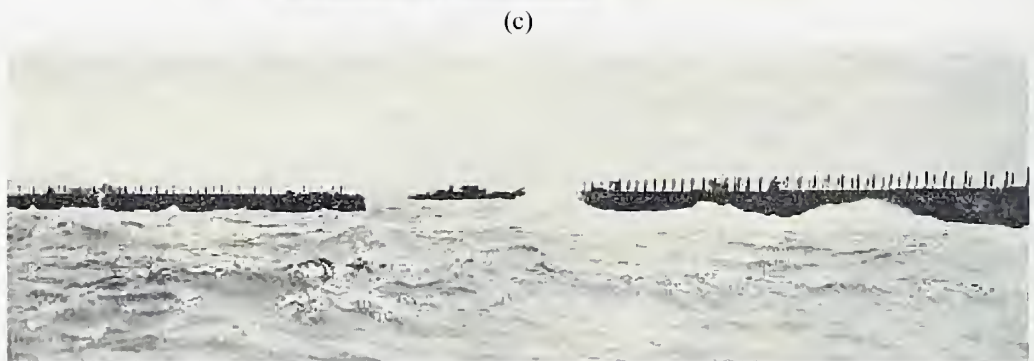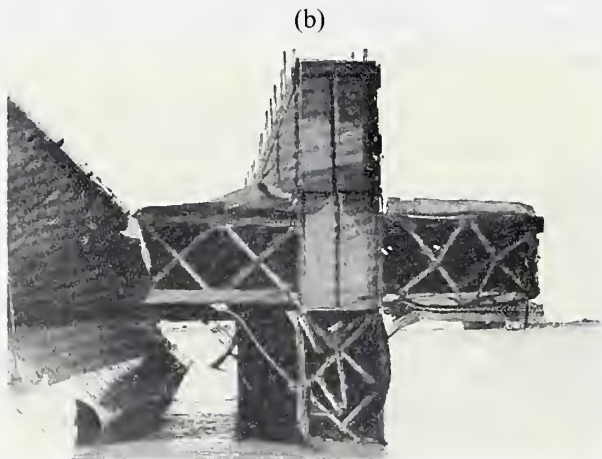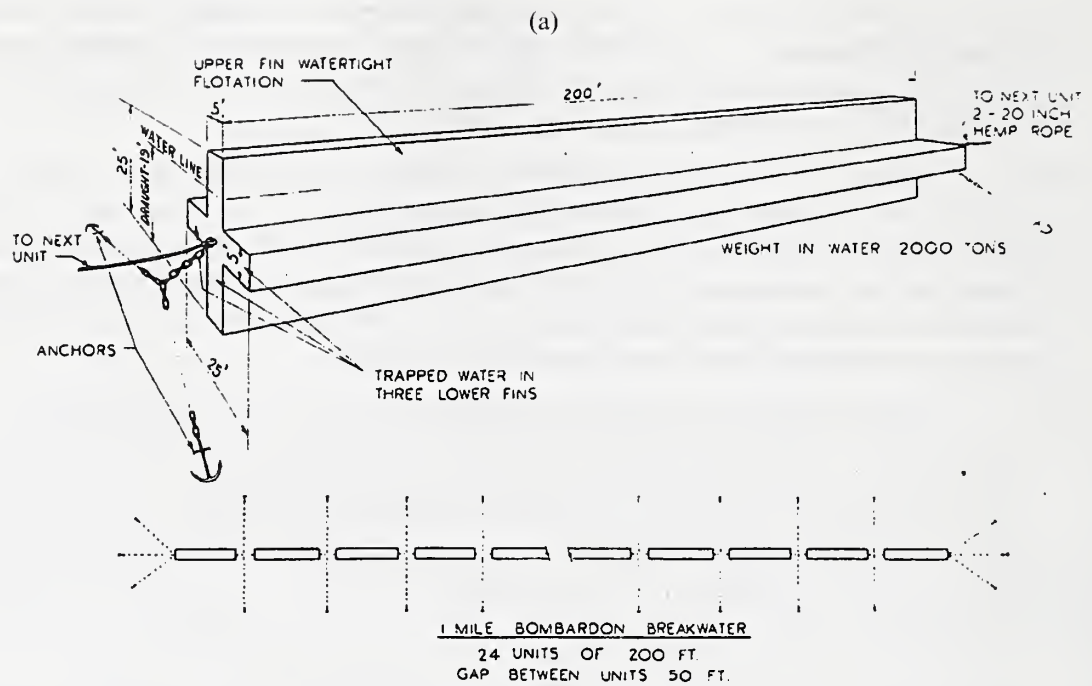
Figure 2.2. The Bombardon breakwater (Lochner et al. 1948).

6

There were no significant efforts on floating breakwaters until the Normandy Invasion of World War II in 1944. The Royal Navy in cooperation with The British Army, designed and built a floating breakwater, named the "Bombardon" breakwater. The Bombardon breakwater is one of the structural elements designed for one of the "Mulberry" harbors along the coast of France. This structure consisted of 61 m long, cross-shaped, steel pontoons. The dimensions of the cross were 7.6 x 7.6 m and the arms were 1.5 m thick. The units were bolted together with steel plates with a gap 15.2 m between each unit. The total length of the breakwater was about 3 km. The breakwaters were constructed in two lines with a 244 m gap in between them (Figures 2.2a, 2.2b and 2.2c).

The design wave height was 3.3 m and wave period was 5.6 s for an expected water depth 12.8 m. The Bombardon breakwater was successful during the invasion for 12 days with a reduction in wave height was as high as 50%. However, the structure was destroyed by a 40-year storm that generated wave heights of 4.6 m and wave periods of 8 s in a water depth of 22 m on the 19th of June, 1944. (Hales, 1981, WCHL, 1981 and Readshaw, 1981, Tsinker, 1995, Lochner et al. 1948)

In 1957 the US Naval Civil Engineering Laboratory began to explore the existing knowledge of transportable units that could serve as breakwaters. The results were summarized in a technical report in 1961 A continuation of this report in 1971 included a survey of the concepts for transportable breakwaters and about 60 of them were pronounced as floating breakwaters (Richey and Nece, 1974).

Between 1963 and 1968 Public Works Canada developed the A-frame breakwater and installed them in Ontario and British Columbia. Meanwhile concrete pontoon breakwaters were constructed in Japan and Norway (Richey and Nece, 1974)..

A large variety of different floating breakwater configurations were developed, tested and some of them were constructed after 1970. Floating breakwaters constructed with used and surplus tires were deployed in United States at different locations. A pontoon breakwater was deployed in Alaska. The Japanese Floating Breakwater Association developed floating breakwaters for small craft harbors. The Scripps Institute of Oceanography and the State of California developed the tethered float breakwater (WCHL, 1981).

The first conference on floating breakwaters was held at the University of Rhode Island in 1974 (Kowalski, 1974). The second conference on floating breakwaters was held in 1981 at the University of Washington in Seattle (Adee and Richey, 1981).

Hales (1981) made a literature survey on the state-of-the-art of floating breakwaters which was published by the U.S. Army Corps of Engineers in 1981. The study provided extensive information about the description and classification of floating breakwater configurations. The Western Canadian Hydraulics Laboratory (WCHL, 1981) conducted another detailed literature review on the description and classification of the previous investigations about floating breakwaters. Other surveys on the design of floating

breakwaters are Richey and Nece, (1974), McLaren (1981), McCartney (1985), Werner (1988) and Isaacson (1993).

Earlier work on the design of floating breakwaters can be grouped into three categories: simple analytical models, hydraulic model studies, and numerical studies. The variables used within the reviewed articles are modified to match the notation of the current study for the sake of consistency.

2.3. Simple Analytical Models

There are several analytical studies performed to determine the wave attenuation characteristics for different geometric shapes. The main goal of most of the studies is to obtain a rough estimate for transmission coefficient of the breakwater. The flow is assumed to be inviscid, irrotational and harmonic so that velocity potential exists and hence, the energy dissipation is neglected. Therefore, the relation between the transmission and reflection coefficient is:

$$\kappa_t^2 + \kappa_r^2 = 1 \tag{2.1}$$

The derivation of this relation will be discussed in Chapter II. Usually the problem is treated as a boundary value problem such that the normal velocities on the boundary of the float are assumed to be zero.

2.3.1. Rigidly Moored Breakwaters

A further simplification is to assume the floating body is rigidly held such that it does not move and generate waves. Therefore, it is also assumed that transmission and reflection coefficients strongly depend of the draft, z_d, of the breakwater.

Dean (1945) calculated the coefficients of reflection and transmission for a thin vertical plane, the top edge of which extending to a depth, z_d, below the mean water surface. It was proven that to obtain a significant reflection the breakwater should extend to a small distance below the mean water level (Figure 2.4a). The transmission coefficient is given as

$$\kappa_t = \frac{M + I_2}{\sqrt{I_1^2 + (M + I_2)^2}} \tag{1.2}$$

where I_1, I_2 and M are integral expressions. For the values of $z_d \dfrac{2\pi}{L_0}$ less the 0.25, Dean (1945) approximated these coefficients as,

$$I_1 = \log\left(\frac{L_0}{\pi z_d}\right) - 0.577 \text{ and } M + I_2 = \pi \tag{1.3}$$

8

Ursell (1947) developed a theory for the two-dimensional reflection and transmission of surface waves with a fixed vertical plane extending from the water surface to some depth, z_d (Figure 2.4b). The transmission coefficient is given by

$$\kappa_t = \frac{K_1\left(z_d \frac{2\pi}{L_0}\right)}{\sqrt{\pi^2 I_1^2\left(z_d \frac{2\pi}{L_0}\right) + K_1^2\left(z_d \frac{2\pi}{L_0}\right)}} \qquad (2.4)$$

where I_1 and K_1 are the modified Bessel functions of the first and second kind, respectively. The transmission and reflection coefficients defined by Equation 2.4 together with the Equation 2.1 are plotted against the independent variable, $z_d \frac{2\pi}{L_0}$ in Figure 2.3. The theory was in agreement with the experimental studies.

Wiegel (1960) considered the wave power transmission instead of wave height transmission for the breakwater model which consists of a thin rigid barrier extending from the water surface to some distance below the water surface. He also included the effect of finite water depth. According to this analysis the power transmitted between the bottom and the depth z_d/d below the mean water level for small amplitude waves is,

$$\frac{P_T}{P_I} = \frac{\dfrac{4\pi(z_d + h)/L}{\sinh(4\pi h / L)} + \dfrac{\sinh 4\pi(z_d + h)/L}{\sinh(4\pi h / L)}}{1 + \dfrac{4\pi h / L}{\sinh(4\pi h / L)}} \qquad (2.5)$$
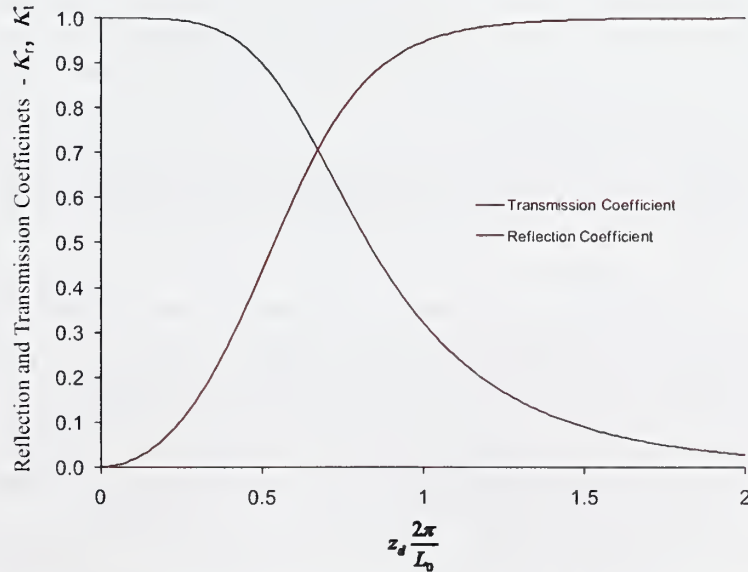
Figure 2.3 The transmission and reflection coefficients for a fixed rigid plate in deepwater (Ursell, 1947)

9
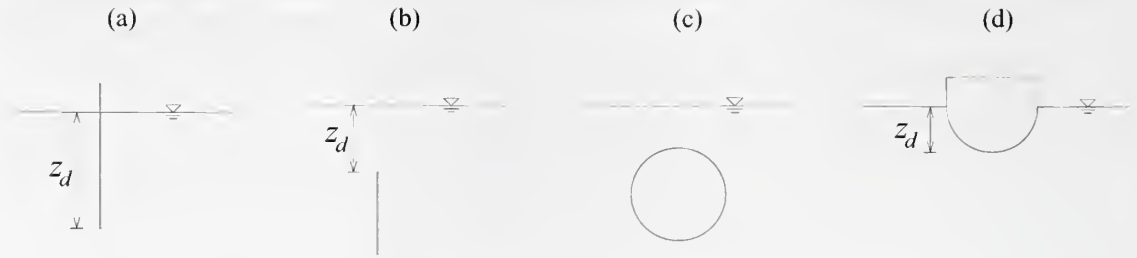
Figure 2.4 Barrier models of (a) Dean (1945), (b) Ursell (1947) and Wiegel (1960), (c) Dean and Ursell 1959, and (d) Dean (1948).

The transmission coefficient is the square root of the power transmission given by

$$\kappa_t = \sqrt{\frac{P_T}{P_I}} \qquad (2.6)$$

Wiegel (1960), using experimental results, demonstrated that this theory can be useful for deepwater conditions.

Macagno (1953) analyzed a rigid rectangular structure of finite width, height and draft fixed near the surface of the water with a finite depth subjected to incident waves of length L. It was assumed that the waves never overtop the structure. The transmission coefficient was given as

$$\kappa_t = \frac{1}{\sqrt{1 + \left[\dfrac{\pi d \sinh(\dfrac{h}{L})}{L \cosh\left(2\pi \dfrac{(h-d)}{L}\right)}\right]^2}} \qquad (1.7)$$

Dean (1948) investigated the case of a fully submerged circular cylinder fixed at an arbitrary distance below a train of deepwater waves (Figure 2.4c). The result of this analysis indicates the coefficient of reflection from the surface of the cylinder is zero; the transmitted wave height is equal to the incident wave height. The only effect of the cylinder at a great distance is a phase difference between incident and transmitted waves.

Dean and Ursell (1959) developed a theory considering a semi-immersed circular cylinder fixed in a train of surface waves with its axis parallel to the crests of deepwater waves (Figure 2.4d). The velocity potential was solved to obtain reflection and transmission coefficients and the two force components. The solution was in the form of an infinite series and approximated by a set of 20 equations.

10
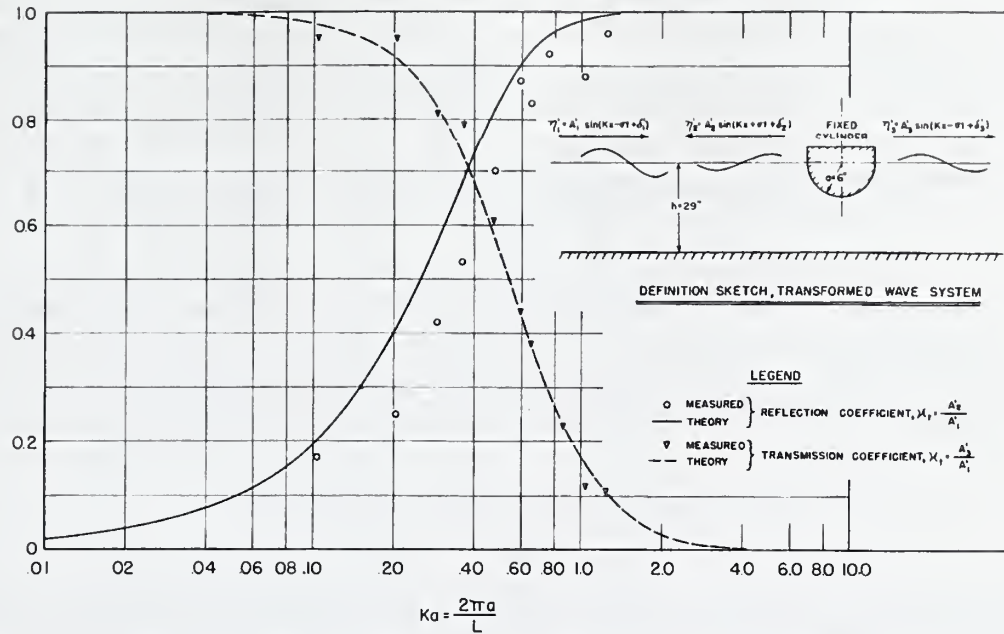
Figure 2.5 Comparison of measured and theoretical reflection and transmission coefficients (After Dean and Ursell 1959). x-axis is equivalent to the parameter $z_d \dfrac{2\pi}{L_0}$.

Dean and Ursell (1959) also compared the results with laboratory tests (Figure 2.5). The experiments were conducted in a 30.5 m wave flume with a cross-section of 76 cm wide and 91 cm deep. The water depth was 73.7 cm and the diameter of the cylindrical sections was between 15 and 30 cm. The wave height was between 0.34 cm and 2.58 cm and the wave period was between 0.64 and 3.5 s. Although the theory was based on the deepwater assumption only a small portion of the experimented waves were within the conventional deepwater range. However there was a reasonable agreement between the theory and the experiments. They also conducted experiments to determine the shallow water effect with 15 cm cylinder at an additional water depth of 30.5 cm. It was stated that the reflection coefficient increased about 30% for shallow water waves.

2.3.2. Dynamic Models

The goal of a theoretical model for the dynamic behavior of a floating breakwater is to estimate the transmitted and reflected wave properties, motions of the breakwater and wave forces on the breakwater and the mooring lines. Although there exist a large volume of publications dealing with floating breakwaters there exist few simple analytical models that describe various breakwater characteristics such as mass, draft, mooring stiffness on the performance of the breakwater. The response of a floating body to waves is analogous to the response of a linearly damped spring-mass system with one degree of freedom excited by a harmonic force. The details of this approach are given in Chapter III.

11

The earliest studies for the theoretical prediction of floating breakwater performance refer to the techniques developed in ship-motion theory. The hydrodynamic equations are formulated in terms of a boundary value problem for the velocity potential. The solution of the hydrodynamic equations of the boundary value problem is difficult because of the nonlinear free surface boundary condition. Therefore, the solution is usually approximated by linearizing this condition by restricting application to small amplitude waves and small amplitude motion response of the breakwater.

Carr (1951) developed an expression for the transmission coefficient for a rectangular cross-section freely floating and moored breakwater. The solution was made for shallow water waves hence the pressure distribution was hydrostatic. Assuming linear damping only the sideway component of the motion the transmission coefficient and using the equation of conservation of energy the transmission coefficient is given as

$$\kappa_t = \frac{1}{\sqrt{1 + \left(\frac{\pi W}{\gamma_w L h}\right)^2 \left(\left(\frac{T}{T_s}\right)^2 - 1\right)^2}} \tag{2.8}$$

where W is the weight of the breakwater per unit length, γ_w is the specific weight of water and T_s is the sideways period of the breakwater. Note that the transmission coefficient is equal to unity for $T = T_s$ and reflection coefficient zero while the measurements indicate that reflection coefficient increases as the wave period gets close to the natural period of the floating system.

Harleman and Shapiro (1961) considered the forced oscillations of fixed and submerged moored objects below the train of waves. They replaced the nonlinear damping term with a linear damping term to approximate the solution. The theory is applicable for any submerged object if the forces for the fixed case are known. They also conducted experiments for a moored sphere and for a platform supported by moored buoyant components. There was good agreement between the theory and the experiments (Ippen, 1966).

Adee and Martin (1974) developed a theoretical two-dimensional linear model for a floating breakwater subjected to deepwater waves by making use of the ship motion theory for heave, sway and roll motions. According to the model, a part of the incident wave energy is used for the exciting motions of the breakwater. The incident wave together with the generated waves by the oscillations of the body are reflected, dissipated and transmitted. The linearized solution in separated into two parts; (a) solution of the waves diffracted by a rigidly restrained structure and (b) solution of the equation of motion in still water. The effectiveness of the model was determined by comparing the theoretical model with the physical model experiments of Nece and Richey (1972). The prediction was in good agreement with the model studies (Figure 2.6). Note that the theory predicts the 100% transmission for the relative width, d/L, values less than 0.1. The sudden drop in transmission coefficient around d/L of 0.2 is due to the cancellation of the waves generated by sway and heave motions.
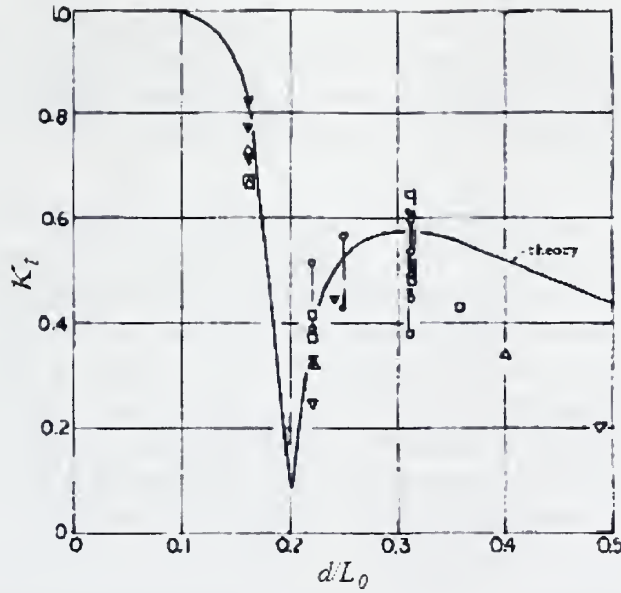
Figure 2.6 The transmission coefficient vs. relative with, d/L compared with the experimental result of Nece and Richey, (1972), for the water depth, $h = 75$ cm and different wave steepness between 0.01 and 0.08, (Adee and Martin, 1974). The original parameters are modified to match the notation of the current document.

Stiassnie (1980) developed an analytical model for vertical thin plate, whose lower edge extending to depth z_d below the mean water level and subjected to monochromatic, linear, deepwater waves. The plate is anchored at a depth b with cables which are represented by a linear spring having spring constant k per unit breadth. The incident waves are partially reflected and partially transmitted beneath the breakwater. The periodic motion of the plate driven by incident waves generated waves in both directions. Plate velocities are set as the boundary condition on the plate. The results were in terms of transmission coefficient, plate displacements in heave and roll and anchoring forces as functions of plate geometry and incident wave parameters. Unlike the other studies, the width to wavelength ratio, d/L_0 is used to adjust the mass per unit breadth since the solution is for a zero thickness plate.

The effect of mass on the transmission coefficient was determined for the free breakwater ($k = 0$) and varying the relative width (or the mass parameter), d/L_0. Figure 2.7 shows the variation of transmission coefficient as a function of relative draft for selected values of relative width compared with the fixed plate. It was concluded that a large mass is required to reach the efficiency of the fixed plate.

The relative stiffness were examined by setting the width, d equal to zero and the mooring point of the plate was selected as the mean water level so that b is equal to zero. In Figure 2.8 the variation of the transmission coefficient as a function of relative draft is plotted for three different stiffness parameters, (a) week spring, $k / \rho_w g L_o = 0.01$, (b) medium spring, $k / \rho_w g L_o = 1$, (c) strong spring, $k / \rho_w g L_o = 100$. The weak spring gives

similar results to the results of the free breakwater except for a narrow region where the plate resonates with the waves. The behavior of the breakwater with the strong spring is close to that of the fixed plate. According to Stiassnie (1980), the performance of the breakwater with no mooring is better than the breakwater moored with a medium strength spring.

Dimmer et. al. (1992) developed an analytical solution for the two-dimensional linearized problem of a box-type floating breakwater. The breakwater was free to move in heave, sway and roll. The solution domain was divided into two regions: (a) the area beneath the breakwater and (b) the remaining area. The velocity potential was divided into four parts: time independent potential due to scattering of the incident wave by a fixed body and radiated potentials caused by sway, heave and roll oscillations of the floating body. The flows caused by sway and roll are asymmetric while the flow generated by heave is symmetric. The free-body responses are found from the equations of motion of the floating breakwater. The full linearized problem was solved by eigenfunction matching method.

The analytical model was compared with a numerical solution that was developed to approximate the solution beneath the breakwater. The results of Dimmer et. al. (1992) for sway compared very good, the heave results compared good and the results associated with the roll motions were moderately good with acceptable error. According to Dimmer et. al. (1992), a substantial part of the water depth has to be blocked to achieve a higher transmission ratio. They concluded that a stiff mooring system would generate large forces on the floating body. Therefore, a flexible mooring is a practical solution for relatively large floating structures.
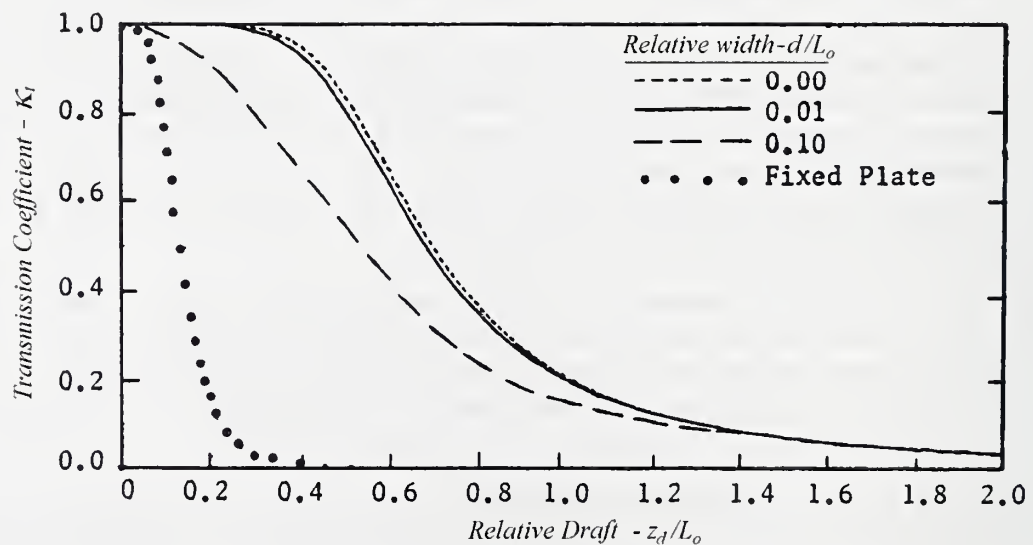
Figure 2.7 The influence of the mass parameter on the transmission coefficient, κ_t for $k = 0$ (Adopted from Hales, 1981).
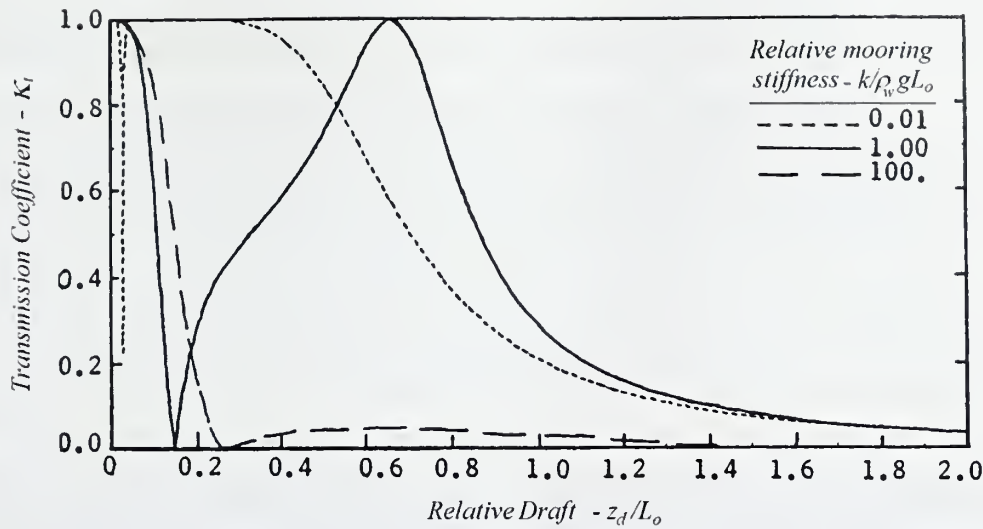
Figure 2.8 The influence of the relative mooring stiffness, $k / \rho_w g L_o$, on the transmission coefficient, κ_t for $d = 0$ (Adopted from Hales, 1981).

2.4. Physical Model and Prototype Studies

The most reliable information on breakwater efficiency can be obtained by laboratory model and field studies. The results of model studies are used to determine the effectiveness of the breakwater and sometimes the associated mooring forces. Experiments are usually conducted with regular monochromatic waves (Tsinker, 1995). There are also a few studies performed in irregular wave conditions which better reflect real wave conditions.

Published model studies usually compare breakwater parameters such as b/L to transmission and reflection coefficients where b is the beam with of the breakwater measured in the direction of the incident wave, and L is the incident wavelength. In some cases data are presented in terms of wave steepness H/L and relative draft h/L where H is the wave height and h is the water depth.

Some of the physical model studies and various prototype installations were summarized in the review by WCHL (1981). The following types of the breakwater were used in harbors or marinas: A-frame, caisson, pontoon, and floating tire. Hales (1981) sorted floating breakwater types according to the geometric configuration and functional similarities: pontoons, sloping float, scrap tire, A-frame, threaded float, porous walled, pneumatic, hydraulic, flexible-membrane, and turbulence generator. McCartney (1985) classified breakwaters in four general categories: box, pontoon, tire mat, and threaded float. Werner (1988) also classified the breakwaters according to their shape and function similar to the previous classifications as: pontoons (hollow or Styrofoam filled), Oak

Harbor catamaran, log boom or circular tube, and A-frame. Mani (1991) examined floating breakwaters in three different categories: pontoon, mat type, and tethered.

Pontoon and box breakwaters are usually simple prismatic structures. Inertia, radius of gyration, and draft are important parameters for breakwater performance. The box breakwaters are usually constructed out of reinforced concrete modules. The modules have either flexible or rigid connections between them. Pontoon breakwaters, also called Alaska or ladder, are operated in manner similar to the box breakwaters. The design of pontoons requires large mass and small internal elastic response to achieve a larger natural period with respect to the waves. This necessitates the bulk of the breakwater to be below the water surface (Wiegel, 1964). Ofuya (1968) experimentally investigated the efficiency of single and double pontoon breakwaters which were moored by a single mooring line (Figure 2.10a). The structures were efficient for a wide range of waves and the attenuation was mainly mass dependent. Davidson (1971) conducted two-dimensional model tests to obtain wave attenuation characteristics and mooring forces for a catamaran (twin-pontoon) breakwater (Figure 2.9b). Davidson (1971) tested both chain mooring and pile mooring systems (Figure 2.10). He proposed that transmission coefficient changes more with wave period than water depth.

Floating tire breakwaters are essentially a mat composed of a large number of tires floating near the surface of water. Tire mat breakwaters are advantageous with their low cost, ease of implementation, and lower reflected waves but they have limited design life and poor buoyancy. Marine growth and silt accumulation can cause the breakwater to sink. Different assembly configurations have been developed since the 1960s to efficiently form bundles of tires for floating breakwaters. Wave-Maze, Goodyear, and Wave-Guard have been extensively tested at the model and prototype scale.

Harms (1979) presented design curves for the Goodyear floating breakwater based on laboratory experiments. The results indicated that the reduction in energy transmission is due more to dissipation more than reflection. He also stated that the Froude similarity criterion is valid for practical purposes since the Reynolds number was very high. A semi-empirical relationship was developed to predict wave transmission coefficient.

$$K_t = \exp\left(0.84\frac{C_d / P}{L / b}\right)$$
(1.9)

where, C_d is the drag coefficient and P is the volumetric porosity of the breakwater. Bishop (1985) presented the wave transmission characteristics of the La Salle Park Marina Goodyear floating tire breakwater. Incident and transmitted waves and mooring forces were measured between 1981 and 1982. The results were in close agreement with the earlier model tests. An application of Goodyear floating tire breakwater is shown in Figure 2.11.
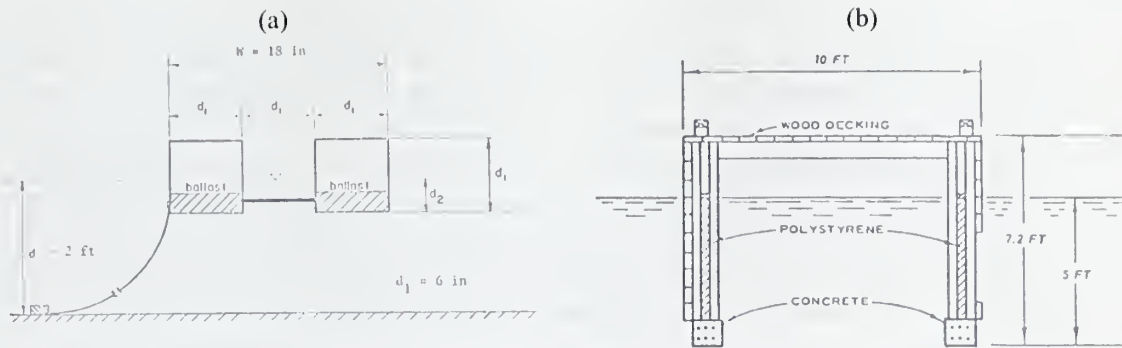
Figure 2.9 (a) Double pontoon breakwater (Ofuya, 1968) and (b) catamaran breakwater (Davidson, 1971).
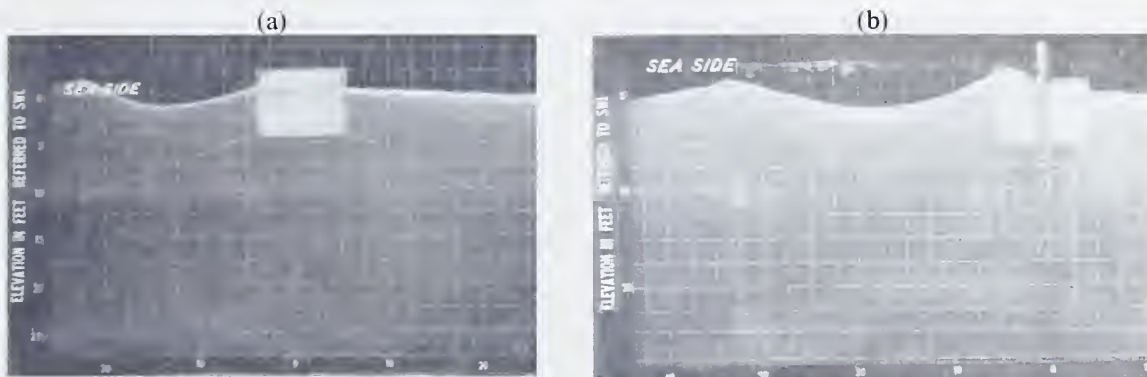
Figure 2.10 Two-dimensional model test of a catamaran type breakwater with (a) chain mooring and (b) pile mooring systems (Davidson, 1971).
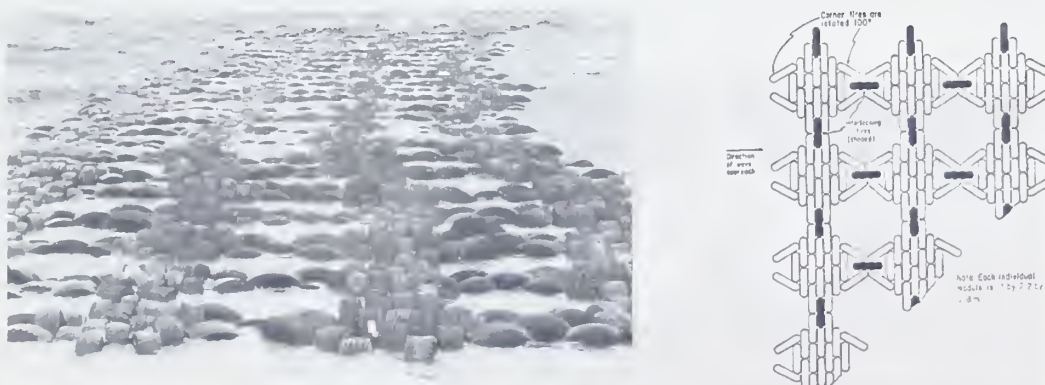
Figure 2.11 Prototype installation of the Goodyear scrap-tire floating breakwater (Hales, 1981).

Sundar et al. (2003) studied the hydrodynamic performance of a floating pipe breakwater model. The model was a horizontal array of pipes with their axes aligned perpendicular to the direction of wave propagation and with a spacing of one pile diameter between them. The breakwater was moored by a slack mooring to the bottom. It was concluded that the breakwaters with higher mass moment of inertia are more efficient in wave attenuation.

Hegde et al. (2007) conducted experiments to study the performance of a horizontal, multilayer, moored floating pipe breakwater. The breakwater model was three layers of PVC pipes aligned horizontally. The top and bottom layer of the pipes were perpendicular to the wave propagation direction and the pipes forming the middle layer were aligned parallel to the direction of wave propagation. The spacing in between the pipes was 5 times the pipe diameter for each layer. It was shown that wave attenuation increased with increasing wave steepness. Hegde et al. (2007) also compared their results with the empirical relationship developed by Harms (1979). The results were in good agreement for the tested wave steepness of $H/L = 0.04$.

Jackson (1964) conducted experimental studies with twin log floating breakwaters (Figure 2.12). The tests were conducted in a 36 m long 1.5 m wide flume at a water depth of 1.2 m. The waves were generated by a plunger type wave generator. Incident and transmitted wave heights were measured to determine the effect of angle of wave attack, water depth, log diameter, log spacing and wave period on wave attenuation. It was observed that the transmission coefficient for the experiments with 90° angle of wave attack was significantly less than the experiments with 45° angle of wave attack for longer waves. The spacing between the logs did not significantly influence effectiveness. It was concluded that wave attenuation with a twin log breakwater is primarily controlled by draft and wavelength. The results of these experiments are plotted in Figure 2.13.

Ofuya (1968) investigated experimentally a similar design which uses two cylinders filled with water to adjust the submergence. The primary wave attenuation mechanism was reflection and dissipation of the wave energy in between the cylinders. Ofuya (1968) concluded that twin-cylinder breakwater was less efficient for longer waves since the reflection and dissipations are reduced. For the experiments where relative depths, kh were greater than 4.8 the transmission coefficients were less than 0.5 (Figure 2.14).

Figure 2.12 (a) Two-dimensional model investigation of a twin-log floating breakwater (Jackson, 1964). (b) Definition sketch of the two-dimensional twin-cylinder floating breakwater (Ofuya, 1968)
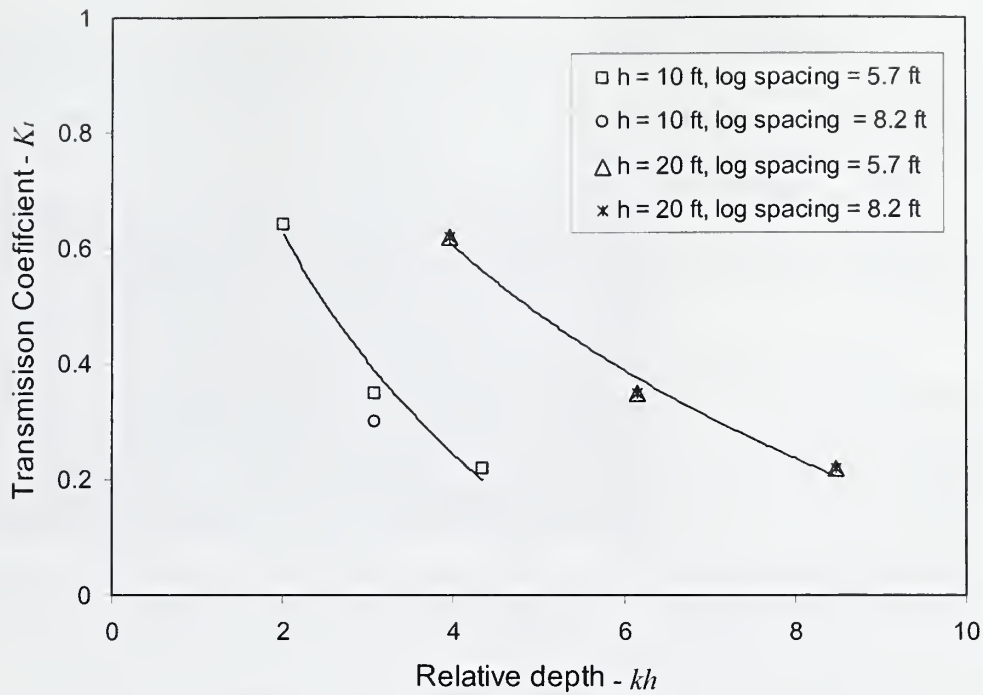
Figure 2.13 Twin log floating breakwater tests for 45° angle of attack at h= 10 ft and 20 ft, z_d/d = 0.86, d = 4ft and log spacing 5.7 ft and 8.2 ft (Jackson, 1964).
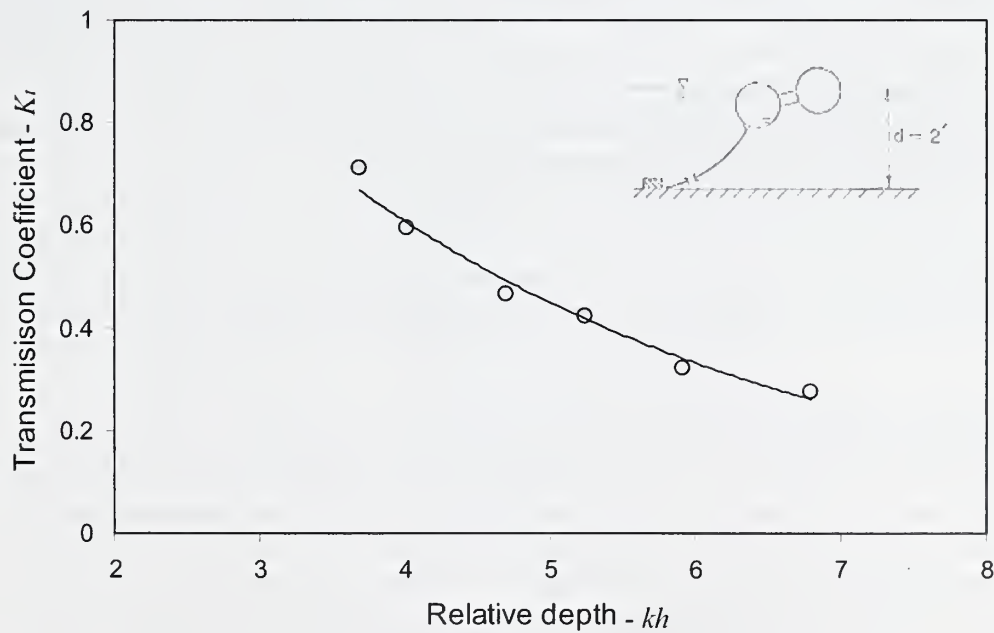
Figure 2.14 Effect of relative depth on transmission coefficient for twin cylinder floating breakwater for incident wave steepness, $H/L \cong 0.06$ (Ofuya, 1968)

19

The A-frame breakwater is constructed of two buoyant cylinders connected to a vertical panel. The structure is held in place by a mooring line connected to the bottom as shown in Figure 2.15. The energy reduction mainly depends on the mass and radius of gyration of the breakwater. WCHL (1966) and Ofuya (1968) conducted a wide range of experiments to estimate the efficiency of A-frame breakwater. The effects of wave steepness, width of the breakwater relative to the wavelength, and relative depth on transmission coefficient were investigated in these studies. It was indicated that transmitted wave height depends significantly on the draft of the breakwater (Ofuya, 1968).

Mani (1991) and Murali and Mani (1997) experimentally investigated the performance of a Y-frame breakwater. The floating breakwater was an assembly of a trapezoidal cross-section float and a row of pipes vertically attached to the bottom of the float. Murali and Mani (1997) conducted experiments including wave and currents. The proposed breakwater models were capable of reducing the transmission coefficients below 0.5 for a range of relative widths, b/L between 0.14 to 0.6 for relative drafts, $z_d/h =$ 0.46. They stated that stiffness of the mooring lines does not influence the performance but use of adequate stiffness is essential. The transmission coefficient increased by about 30% for the experiments with currents.

The tethered floating breakwater is composed of a large number of very buoyant floats (Figure 2.16). The size of each component and the spacing in between them is usually on the order of wave height (Seymour and Isaacs, 1974). The primary wave attenuation mechanism is dissipation due to turbulence around the components. At resonant wave periods the amplitude of the motion reached its maximum value, increasing the relative velocities around the components and hence inducing additional turbulent dissipation. Seymour and Isaacs (1974) developed a theoretical model to predict the wave attenuation of a particular array configuration and conducted laboratory flume experiments to validate the proposed model.
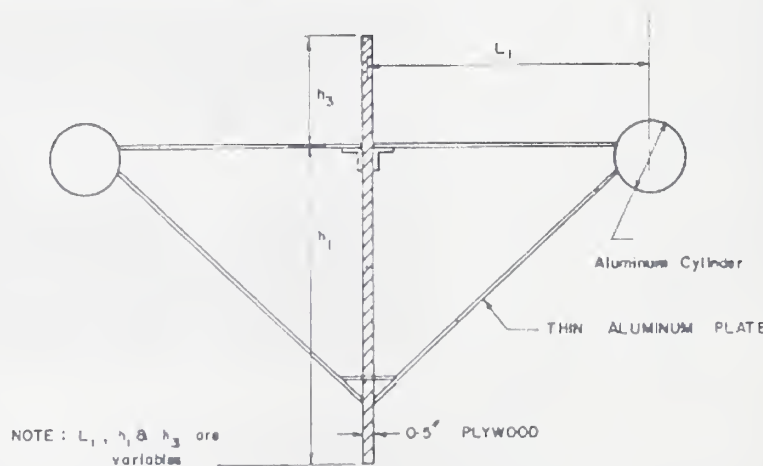
Figure 2.15 Definition sketch of an A-frame breakwater (Hales, 1981).
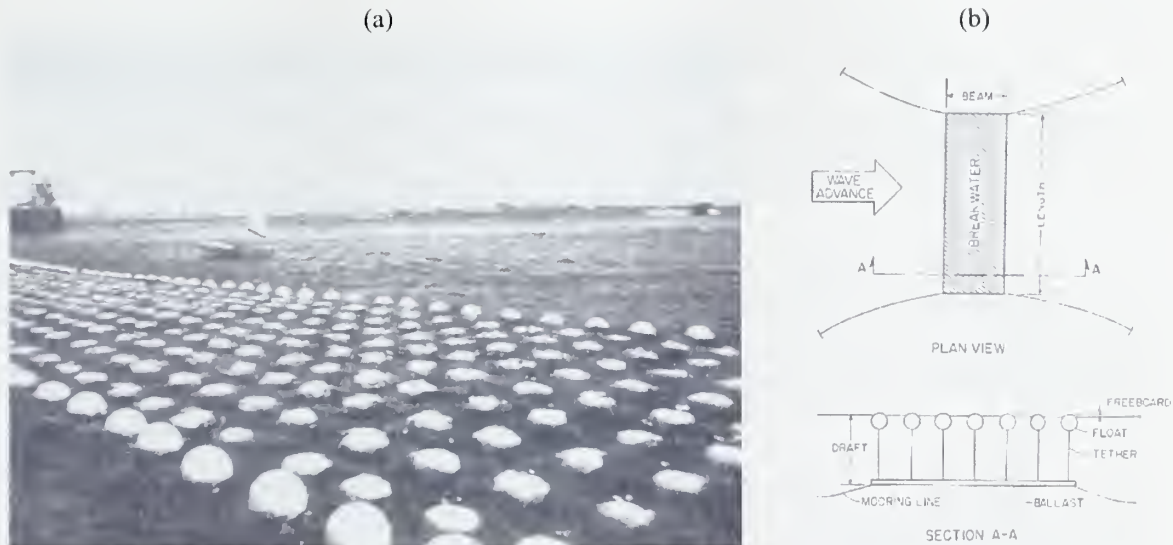
Figure 2.16 (a) Prototype tests of a tethered-float breakwater with spherical floats of 1 foot diameter, San Diego Bay, California (1975, photo by Scripps Institute of Oceanography, form Hales, 1981) (b) Definition sketch of a tethered-float breakwater (Hales, 1981).

In addition to their geometrical and functional classification, floating breakwaters can differ according to their mooring arrangements. Flexible mooring lines (chain wire or rope) and piles have been tested at the model and prototype scale. The restraint provided by the piles is significantly greater than that of mooring lines; however, piles must withstand larger loads than mooring lines. Piles are feasible in shallow sites and require suitable bottom material (McCartney, 1985).

Kim et al (1994) and Isaacson et al. (1998) investigated the performance of pile-restrained breakwaters numerically and experimentally. Kim et al. (1994) used a numerical model based on potential flow theory to examine the behavior of rectangular floating units supported by four vertical piles at the corners. They also conducted experiments to investigate the wave transmission and reflection characteristics, floating body motion, and loads on the piles. The experiments were conducted in a 27 m long, 1.5m wide wave flume with a water depth of 0.5 m. with regular and irregular wave conditions. The wave heights were kept small to avoid overtopping.

Isaacson et al. (1998) studied wave propagation past a pile-restrained floating breakwater both experimentally and numerically. The numerical model was based on two-dimensional linear wave diffraction/radiation theory. An empirical damping ratio was included to account for the friction effect with the piles. Experiments were conducted in a 20 m by 0.62 m wave flume. A rectangular breakwater model was tested during the experiments. The model was held in place by pairs of vertical piles. Wave height was small enough to avoid overtopping. The comparison of the numerical model was in good agreement with the experimental results (Figure 2.17).

21
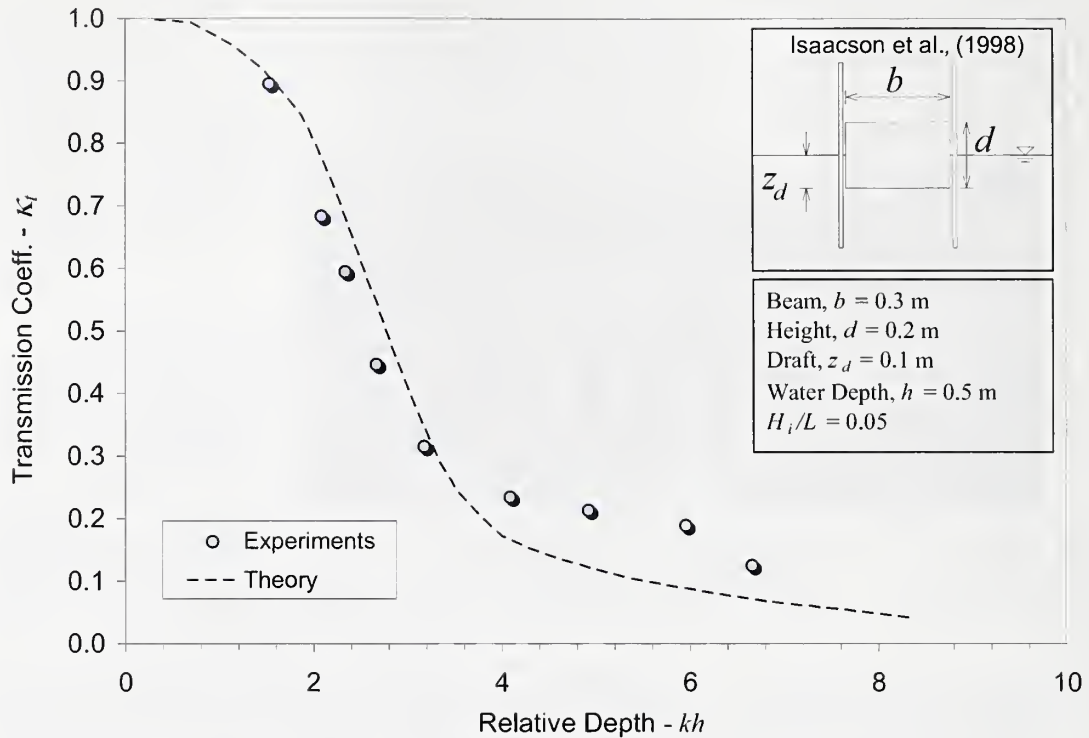
Figure 2.17 Transmission coefficients of a pile restrained floating breakwater (Isaacson, 1998).

Flexible mooring lines are constructed by connecting a series of anchors to hold the structure in position and restrict its motion. Anchors are broadly classified according to method of lateral resistance as drag embedment, dead weight, and direct embedment. The operation of these systems relies on the shear stress and the cohesive stress between the anchoring component and the soil as well as the weight of the anchor. Synthetics (i.e. nylon, Dacron and Kevlar), wire rope, and chains are commonly used as mooring line. Clump weights and tires are used to reduce the impact loads on the anchors (McCartney, 1985 and Werner, 1988).

2.5. Numerical Models

There have been various numerical studies developed to evaluate the interaction of the wave filed with a floating body. Most of the earlier studies are based on potential flow theory which assumes irrotational flow (Williams, 1991 and Sen, 1993). Moreover, the motions of the floating object are assumed to be small to linearize the boundary conditions on the surface of the body. Recent studies include wave breaking, fluid solid coupling and turbulence, however; a complete analysis of the waves in the vicinity of the

breakwater including overtopping has not been established (Kawasaki, 1999, Mizutani, 2004, and Koftis, 2006). Some of these studies are presented in the following text.

Kawasaki (1999) proposed a two-diemsional vertical numerical wave model which combined the Volume of Fluid (VOF) method with a wave generation source. The open boundary was treated with an added dissipation zone. The numerical model was validated with the conducted experiments.

Koutandos et.al. 2004 developed a finite-difference numerical model to investigate hydrodynamic behavior and efficiency of and vertical forces acting on fixed and heave motion of rectangular floating breakwater. Wave propagation model was based on Boussinesq type equations. The waves were in the range of shallow and intermediate. Pressure field is determined by Laplace equation.

Rahman et. al. (2006) developed a two-dimensional vertical numerical model to estimate the dynamics of a pontoon type moored submerged breakwater under the action of waves. VOF method was used for free surface tracking (Hirt and Nichols, 1981). The waves were generated by a mass source (Lin and Liu, 1999). The numerical model was verified with the experimental studies. It was shown that, the model was capable of simulating the water surface profiles, water particle velocities and the wave forces acting on the body for both fixed and moored floating breakwater models.

Koftis et. al. (2006) investigated the wave interaction with fixed rectangular floating breakwater numerically using two-dimensional vertical Reynolds-averaged Navier-Stokes equations. VOF method was used for free surface treatment. The results of the numerical model were in good agreement with the large scale experimental data.

In many water wave problems the wave conditions within the main fluid body can be described by the linear wave theory. The theory assumes a unidirectional, periodic, small amplitude wave train and sinusoidal free surface profile. Linear wave theory can be used to define the design wave conditions with reasonable accuracy (Isaacson, 1994). The basic assumptions and derivations of the relevant equations of this theory are described in Section 3.1. In Section 3.2 the energy content of a single wave is presented. In nature, the waves are highly irregular and random. Yet, these waves can be approximated by superposing a series of linear monochromatic waves. The fundamentals of random wave data analysis are given in Section 3.3. The interaction of the floating bodies and waves is discussed in Sections 3.4 and 3.5.

3.1.   Linear Wave Theory Formulation

Small Amplitude wave theory or linear wave theory can be described as "a first approximation to the complete theoretical behavior of the wave motion" (Ippen, 1966). Although there are limitations, the theory gives reasonable approximations to a wide range of wave parameters (CERC, 2006). This theory is presented on the monograph published by Ippen (1966), Dean and Dalrymple (1991), Wiegel (1964) and CERC (2006).

The linear wave theory is developed by solving the velocity potential and solution of Laplace and Bernoulli equations together with the appropriate boundary conditions. The x-z coordinate system for a simple progressive wave is defined in Figure 3.1 where L is the wavelength, H is the wave height, $\eta(x,t)$ is the vertical component of the water surface displacement and h is the water depth.
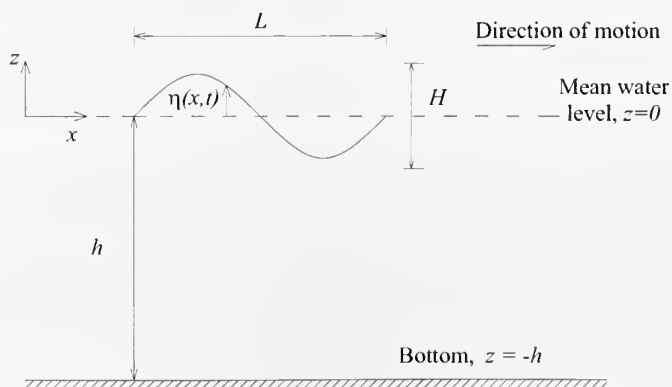
Figure 3.1. Definition sketch for small amplitude wave theory.

The surface waves in nature propagate in a viscous fluid on an irregular bottom of varying permeability. However, the viscous effects are usually concentrated in the boundary layer between the fluid and the solid surfaces. The rest of the water body is nearly irrotational. Water can also be assumed incompressible in most practical cases. A velocity potential exists for an irrotational flow and incompressible fluid. Two-dimensional velocity potential $\phi(x, z, t)$ on an x-z plane can be defined by:

$$u = -\frac{\partial \phi}{\partial x} \text{ and } w = -\frac{\partial \phi}{\partial z} \tag{3.1}$$

where u and w are horizontal and vertical components of the velocity vector $\mathbf{v}$.

For incompressible two-dimensional motion, the continuity equation in Cartesian coordinates is:

$$\frac{\partial u}{\partial x} + \frac{\partial w}{\partial z} = 0 \tag{3.2}$$

Combining Equations (3.1) and (3.2) leads to the divergence of a gradient which is called the Laplace Equation and written as:

$$\nabla \cdot \mathbf{v} = \nabla^2 \phi = 0 \tag{3.3}$$

The solutions of this Equation, $\phi(x, z, t)$, are harmonic functions. If the bottom is assumed to be impervious the bottom boundary condition is:

$$w = -\frac{\partial \phi}{\partial z} = 0 \text{ on } z = -h \tag{3.4}$$

The second-order differential equation, (3.3) should be satisfied in the region $-h \leq z \leq \eta$ and $-\infty \leq x \leq \infty$. The integrated equation of motion or the unsteady Bernoulli equation can be written in terms of the velocity potential and with the assumption of irrotational flow and incompressible fluid as follows:

$$-\frac{\partial \phi}{\partial t} + \frac{p}{\rho} + gz = c(t) \tag{3.5}$$

Here, p is the pressure, g is the gravitational acceleration, ρ is the mass density of water, c (t) is the Bernoilli term which is constant for steady flows. Second-order terms, u^2 and w^2 are neglected for the derivation of Equation 3.5 given that the velocity components u and w are assumed to be small for small amplitude wave motion. The boundary condition to be satisfied at the surface $z = \eta(x, t)$ is obtained from the integrated equation of motion taking the pressure on this surface to be zero.

$$\eta(x, t) = \frac{1}{g} \left[\frac{\partial \phi}{\partial t} \right]_{z=\eta} \tag{3.6}$$

For small amplitude waves Equation 3.6 can be linearized as,

$$\eta(x,t) = \frac{1}{g}\left[\frac{\partial\phi}{\partial t}\right]_{z=0} \tag{3.6b}$$

Since the waves are periodic in space and time, the lateral boundaries are treated with the periodic condition by:

$$\phi(x,z,t) = \phi(x+L,z,t) \text{ and } \phi(x,z,t) = \phi(x,z,t+T) \tag{3.7}$$

The boundary value problem defined above is solved by separation of variables. One solution of this differential equation yields

$$\phi = \frac{gH}{2\sigma}\frac{\cosh[k(h+z)]}{\cosh(kh)}\sin(kx - \omega t) \tag{3.8}$$

Accordingly, the equation of the water surface as a function of time t and horizontal distance x is

$$\eta = \frac{H}{2}\cos(kx - \omega t) \tag{3.9}$$

In Equation 3.8 and 3.9, the wave number k and wave angular frequency, ω are defined as:

$$k = \frac{2\pi}{L} \text{ and} \tag{3.10a}$$

$$\omega = \frac{2\pi}{T} \tag{3.10b}$$

The particle velocity components can also be obtained as:

$$u = \frac{H}{2}\omega\frac{\cosh[k(h+z)]}{\sinh(kh)}\cos(kx - \omega t) \tag{3.11a}$$

$$w = \frac{H}{2}\omega\frac{\sinh[k(h+z)]}{\sinh(kh)}\sin(kx - \omega t) \tag{3.11b}$$

The most fundamental description of a simple sinusoidal oscillating wave is by its length L, height H, period T and water depth h. The speed at which the waves propagate is the wave celerity, c. The wave celerity is related to the wave period and the wavelength by

$$c = \frac{L}{T} \tag{3.12}$$

According to linear wave theory, the wavelength, L as a function of the wave period T and water depth h is given by the dispersion relation which is written as:

$$L = \frac{gT^2}{2\pi}\tanh(kh) \text{ or } \omega^2 = gk\tanh(kh) \tag{3.13}$$

For large values of kh, $\tanh(kh)$ approaches unity. If the relative depth $\dfrac{h}{L}$ is greater than 0.5, the waves are classified as deep water and for most practical purposes this is sufficient to assume $\tanh(kh) = 1$, linearizing Equation 3.13 to the following:

$$L_o = \frac{gT^2}{2\pi}$$
(3.14)

The subscript "$_o$" stands for deepwater conditions. The classification of the waves according to the relative depth and some wave characteristics according to this classification is given in Table 3.1. The only wave characteristic which does not change with water depth is the wave period and therefore it is convenient to use T as a reference parameter.

Equations 3.11a and 3.11b express velocity components within a wave at any depth, z. For a given depth, z, the velocity components are harmonic in both space and time. The velocities decay exponentially along the z axis and if the vertical distance from the mean water level is greater than $L/2$ the velocities become negligible. The velocity of a fluid particle at a certain position in space will continuously change due to local and convective accelerations. Convective accelerations can be neglected since the wave amplitude and displacements are small.

Displacements of a particle from its mean position are derived as follows:

$$\frac{\xi^2}{A^2} + \frac{\varepsilon^2}{B^2} = 1$$
(3.15)

where ξ and ε are horizontal and vertical displacements from the mean positions, respectively and,

$$A = \frac{H}{2}\frac{\cosh[k(h+z)]}{\sinh(kh)} \quad \text{and} \quad B = \frac{H}{2}\frac{\sinh[k(h+z)]}{\sinh(kh)}$$
(3.16)

Table 3.1. Summary of wave characteristics for linear wave theory.

	Shallow water	Transitional water	Deep water
Relative Depth	$\dfrac{h}{L} < \dfrac{1}{20}$	$\dfrac{1}{20} < \dfrac{h}{L} < \dfrac{1}{2}$	$\dfrac{h}{L} > \dfrac{1}{2}$
	$kh < \dfrac{\pi}{10}$	$\dfrac{\pi}{10} < kh < \pi$	$kh > \pi$
Wave celerity C	$\sqrt{gh}$	$\sqrt{\dfrac{g}{k}\tanh(kh)}$	$\sqrt{\dfrac{g}{k_o}} = \dfrac{gT}{2\pi}$
Wavelength L	$T\sqrt{gh}$	$\dfrac{gT^2}{2\pi}\tanh(kh)$	$\dfrac{gT^2}{2\pi}$
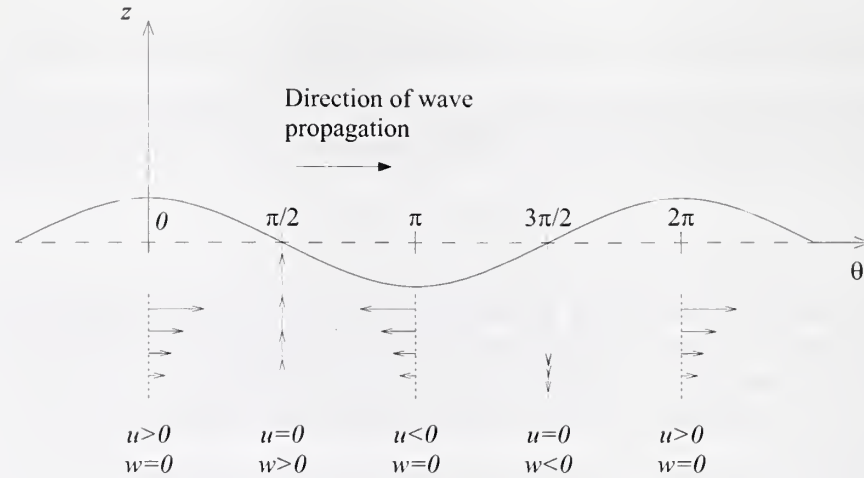
Figure 3.2 Velocity vectors at different phases.
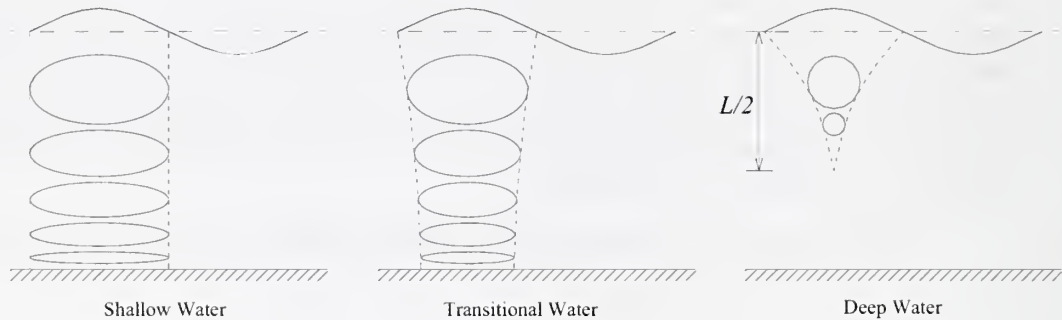
Figure 3.3 Schematic representation of water particle trajectories.

Equation 3.15 is an equation for an ellipse. The water particles move in closed orbits and each particle returns to its original position at every wave cycle. At the surface the vertical displacement is equal to the wave amplitude. For shallow water the horizontal displacement becomes nearly constant from the surface to the bottom. On the other hand, in deepwater conditions, the trajectories are circular but the radius decays exponentially along the z axis. The particle trajectories for different relative depths are presented schematically in Figures 3.2 and 3.3.

The subsurface pressure of a progressive wave can be obtained by substituting equations 3.8 and 3.9 into the linearized equation of motion for irrotational flow and incompressible fluid (Equation 3.5).

$$\frac{p}{\gamma} = \eta \frac{\cosh k(h+z)}{\cosh kh} - z \tag{3.17}$$

where γ is the unit weight of water. Note that z is negative downwards form the mean water level. The ratio $\dfrac{\cosh k(h+z)}{\cosh kh}$ is known as the "pressure response factor K". In

Equation 3.18, the elevation head z is associated with the hydrostatic pressure distribution or static pressure and the first term ηK is the head associated with the dynamic pressure. It is positive under the wave crest and negative under the wave trough.

3.2. Energy Considerations

The total energy of a wave per unit crest width is the sum of its kinetic and potential energies.

The kinetic energy in a wave per unit width of crest can be obtained by integrating the kinetic energy in a fluid element of size $dxdz$ which is given as:

$$E_k = \int_0^L \int_{-h}^{\eta \approx 0} \frac{\gamma}{2g}(u^2 + w^2)dxdz \tag{3.18}$$

where u and v are given by Equations 3.11 and 3.12. Solution of the above equation gives,

$$E_k = \frac{\gamma_w H^2 L}{16} \tag{3.19}$$

And, the total potential energy in a wave per unit crest is:

$$E_p = \int_0^L \int_0^{\eta} \gamma z dxdz \tag{3.20}$$

where $\gamma z dxdz$ is the potential energy in a fluid element displaced a distance z from the mean water level. The solution of the Equation 3.20 yields,

$$E_p = \frac{\gamma_w H^2 L}{16} \tag{3.21}$$

The total energy in a wave per unit width of crest is the sum of kinetic and potential energies which is written as:

$$E = E_P + E_K = \frac{\gamma_w H^2 L}{8} = \gamma L \frac{a^2}{2} \tag{3.22}$$

where a is the amplitude of the wave.

Power can be calculated from the product of the force acting on a vertical plane in the fluid and the velocity of the flow across that plane where the force is the product of the pressure and the area of the plane. The first approximation for the mean power per unit width of the wave crest is:

29

$$P = \frac{1}{T} \int_0^T \int_{-h}^{\eta \approx 0} (p + \rho gz)u\,dt\,dw \tag{3.23}$$

Substituting Equation 3.18 into 3.26 and integrating Equation 3.26, the mean power is:

$$P = \frac{E}{T}\frac{C_G}{C} \tag{3.24}$$

where C_G is the wave group velocity which is the time rate of propagation of the wave train. The wave train can be defined as an infinite series of disturbances such as superposition of waves of different periods or it can be defined as a finite number of consecutive waves propagating in an undisturbed fluid. In order for a wave to propagate in an undisturbed fluid it must do work on the fluid. Therefore, P is actually the average rate at which work is done over one wave period T. Equation 3.27 is essentially correct for the case of waves generated at one end of a wave tank and transmitted energy absorbed at the other end. Moreover, each successive wave generated in an undisturbed fluid has less energy than the preceding wave by a constant factor, $\dfrac{C_G}{C}$, for a certain depth. This results in a continuous variation in the amplitude starting from zero at the leading edge (Figure 3.4) and the energy is transported in the direction of phase propagation with the group velocity.

The ratio of group velocity to phase velocity is derived by superposing an infinite number of disturbances:

$$\frac{C_G}{C} = \frac{1}{2}\left(1 + \frac{2kh}{\sinh 2kh}\right) \tag{3.25}$$

this ratio can be approximated as $\dfrac{C_G}{C} = \dfrac{1}{2}$ for deep water conditions and $\dfrac{C_G}{C} = 1$ for shallow water waves.
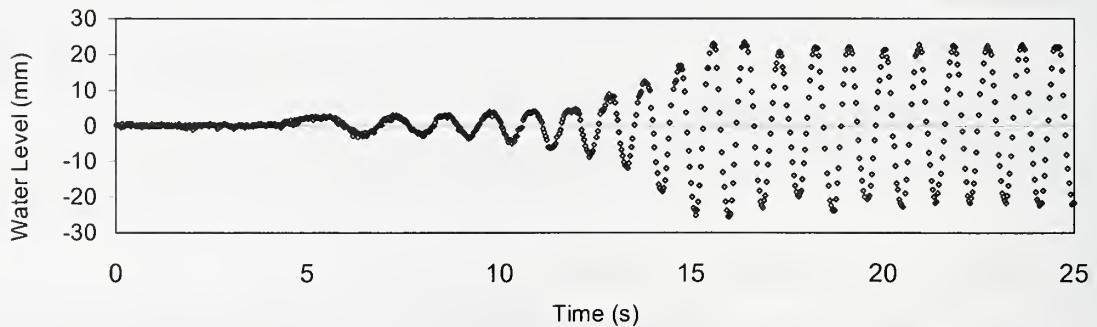
Figure 3.4 Energy propagation by waves on a previously undisturbed fluid. The data were obtained at the wave flume at the NSL for $T = 0.9$ s, $H = 50$ mm and $h = 445.6$ mm.

For linear wave theory to be valid, the steepness of the waves should be small and $\frac{L^2 H}{2d^3}$ must be small. The limiting value for $\frac{L^2 H}{2d^3}$ was stated by Longuet–Higgins (1969) as follows (Wiegel, 1964):

$$\frac{L^2 H}{2h^3} << \frac{16\pi^2}{3} .$$ (3.26)

To explain the concept of breaking of the waves the equations related with the wave phenomena should be improved extending the theory to finite amplitude waves. For any water depth and wave period there is an upper stable limit for wave height. According to the Stokes criterion if the velocity of the water particle at the crest is higher than the celerity of the wave, it will "topple over". Miche (1944) gives the limiting value for steepness as:

$$\left(\frac{H}{L}\right)_{max} = 0.142 \tanh \frac{2\pi h}{L}$$ (3.27)

Again, this equation can be simplified as $\left(\frac{H_0}{L_0}\right)_{max} = 0.142$ for deep water conditions.

3.3. Irregular Waves

The waves in nature are usually generated by winds blowing over the water surface. If the generated waves are still under the action of the winds that create them they are called 'wind waves' or 'sea'. The waves propagating free of the storm are called 'swell'. The waves discussed in the previous sections are considered as 'regular' or 'monochromatic' waves. Regular waves are expressed with constant quantities of height, period and phase. However, wind generated waves do not have a permanent wave form. The actual water surface is a combination of different waves of varying heights, periods and direction (CERC, 2006). The water surface profile is rather irregular and random in space and time (Figure 3.10).Therefore, irregular waves are described with statistical terms instead of deterministic quantities. The condition of the water surface being a stochastic field is called 'sea state'.

The recorded time series of surface elevations of irregular waves can be studied by either time-domain (wave train) or frequency domain (spectral) analysis. Time-domain analysis requires defining individual waves in a time series recording of the water surface at a fixed station. Then the wave height and period of each wave are determined.

3.3.1. Time domain analysis: Zero-Crossing Method

In this method individual waves are defined between two successive points where the water surface crosses zero line or mean water level (Figure 3.7). The profile can cross

the zero line either with a positive slope or a negative slope. If it crosses with a positive slope it is referred as up-crossing and if the slope is negative then it is called down-crossing. Although both down-crossing and up-crossing methods yield similar results, the down-crossing method is recommended by IAHR/PIANC (1986) due to the definition of wave height.

The individual wave heights are defined as the difference between the highest and lowest values of water surface readings between two zero down-crossing points and wave periods are the time span between two successive zero down-crossings. The local peak values are discarded in this analysis. The wave statistical parameters to define the sea state are obtained by processing all the individual waves in a wave record. The wave record should include several hundred individual waves to ensure statistical accuracy.

For most practical purposes it is common to neglect very small waves and measure the highest waves. It is found that wave heights estimated by visual observations correspond to the average of the highest 30 percent of the waves. The most frequently used parameter obtained by this approach is "significant wave height", (H_s) which is defined as the average of the highest one-third waves in a wave record.

$$H_s = \frac{1}{N/3} \sum_{i=1}^{N/3} H_i \qquad (H_n < H_{n-1} < \ldots < H_1) \qquad (3.28)$$

where N is the number of individual waves in the record ranked highest to lowest H_i and i is the rank number. Similarly, $H_{1/10}$ is the average height of the highest 10% waves which is given as,

$$H_{1/10} = \frac{1}{N/10} \sum_{i=1}^{N/10} H_i \qquad (H_n < H_{n-1} < \ldots < H_1) \qquad (3.29)$$

For structures subjected to wave forces, maximum wave height (H_{max}), defined as the height of the highest wave in the wave record, is also important and can be selected as the design wave.
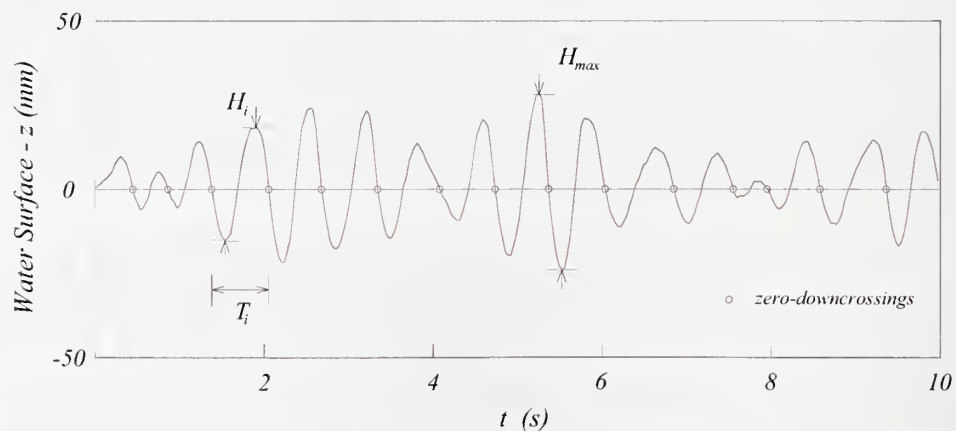
Figure 3.5 Definition sketch for zero-downcrossing method ($h=466$ mm, $H_s=40$mm, $T_p=0.65$ s).

Root-mean-square and mean wave heights are computed as follows:

$$H_{rms} = \sqrt{\frac{1}{N}\sum_{i=1}^{N} H_i^2} \quad \text{and} \quad \overline{H} = \frac{1}{N}\sum_{i=1}^{N} H_i \tag{3.30}$$

The average period of the highest one-third of the waves is called "Significant wave period" or "significant period"

$$T_s = \frac{1}{N/3}\sum_{i=1}^{N/3} T_i \qquad (T_n < T_{n-1} < \ldots < T_1) \tag{3.31}$$

The mean period of the waves can be obtained either by dividing the length of the record by the number of the waves in the record or simply averaging the periods of the individual waves. The first method gives slightly larger values since $T_w > \sum_{i=1}^{N} T_i$. The second method is used to avoid this error and the mean wave period is obtained as,

$$\overline{T} = \frac{1}{N}\sum_{i=1}^{N} T_i \tag{3.32}$$

It has been proven that individual wave heights follow the Rayleigh distribution assuming the random water surface elevation follows a Gaussian distribution (Longuet-Higgins, 1952). It is called the "narrow-band condition" when the wave energy is concentrated in a very narrow range of wave periods. Theoretical values obtained from the Rayleigh distribution are generally in agreement with a narrow-banded sea. Yet, shallow-water waves differ from the Rayleigh distribution due to wave breaking and bathymetric effects. Since the individual wave heights are considered as a statistical variable they can be represented by a histogram.
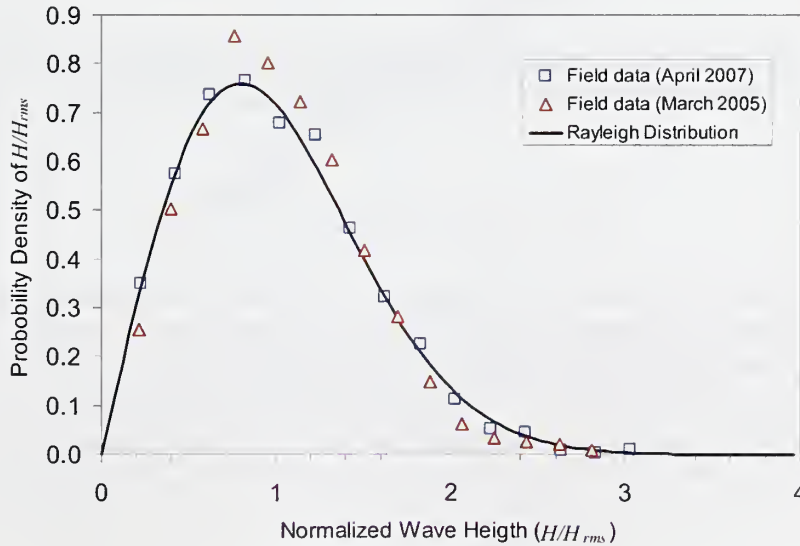
Figure 3.6 Normalized wave height histogram with Rayleigh distribution. The data contains several hundred waves recorded in Carlisle Arkansas in March 2005 and April, 2007.

Figure 3.8 presents the histogram of wave heights recorded in an irrigation pond Carlisle Arkansas in March 2005 and April, 2007. The measured wave heights have been normalized with root-mean-square wave height and compared to the Rayleigh distribution. Details of the study will be discussed in Chapter III. The probability density function for the Rayleigh distribution is given by;

$$p(H/H_{rms}) = \frac{\pi}{2}\exp\left[-\frac{\pi}{4}(H/H_{rms})^2\right]$$ (3.33)

3.3.2. Frequency Domain Analysis

Irregular waves from water surface recordings can be considered as a combination of a series of regular waves with different periods (or frequencies) and a certain amount of energy is transmitted by each component. Spectral analysis determines the distribution of the energy for each wave frequency by transforming the wave record from the time domain to the frequency domain. This is usually done by the Fast Fourier Transform (FFT) technique.

The variance of the a water surface elevation around the mean water level can be written as

$$\sigma^2 = \frac{1}{T}\int_0^T \eta^2(t)dt = \frac{1}{2}a^2$$ (3.34)

where σ^2 is the variance T is the wave period, a is the wave amplitude and $\eta(t)$ is the time series of the water surface elevation. Recalling the energy Equation 3.35, the energy and the variance of the wave field is related with

$$E = \gamma_w L \sigma^2$$ (3.36)

The time series of the surface elevation of an irregular wave can be written as the infinite sum of sinusoidal waves of amplitude a, angular frequency ω and phase δ as follows

$$\eta(t) = \sum_{i=1}^{\infty} a_i \cos(\omega_i t + \delta_i)$$ (3.37)

The distribution of variance with frequency is usually designated by $S(f)$, f being the wave frequency, assuming that the functions is continuous is frequency domain. Due to the above relation between variance and wave energy, $S(f)$ is called "wave energy spectral density" or simply the "wave spectrum". From Equations 3.45 and 3.47, the variance of the random signal around the mean water level becomes

$$\sigma^2 = \sum_{i=1}^{\infty} \frac{a_i^2}{2} = \int_0^{\infty} S(f_i)df$$ (3.38)

The above equation yields the area under the wave spectrum which is referred as the zero-th moment of the spectrum and designated by m_o. Likewise, the i-th moment of the continuous spectrum is obtained by,

$$m_i = \int_0^\infty f^i S(f) df \qquad (3.39)$$

If the wave heights of the random sea follow the Rayleigh distribution the significant wave height can be approximated by the standard deviation (square root of the variance of the signal) (Longuet-Higgins, 1952).

$$H_{mo} = 4\sqrt{m_o} \qquad (3.40)$$

This approximation requires the spectrum to be narrow-banded to satisfy the Rayleigh distribution. H_{m0} is usually about 5% greater than H_s (Longuet-Higgins 1980). Figure 3.9 is a comparison of the waves heights computed by using the two different methods discussed above. The data were obtained from two wave gauges located 9.6 m and 13.9 m away from the flap type wave generator in the 19 m wave flume at the National Sedimentation Laboratory. The peak periods range between 0.6 to 1.2 seconds at two different water depths, $h = 466$ mm and 367 mm. It can be seen from Figure 3.9 that H_{mo} is about 4% greater then the H_s.
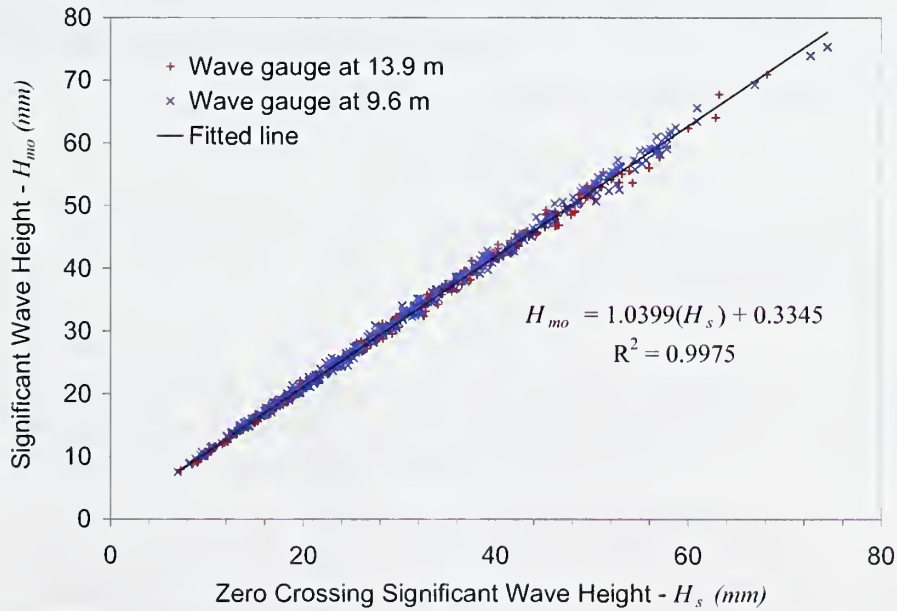
Figure 3.7 Comparison of H_s and H_{mo}. The data is obtained at stations 9.6 m and 13.9 m of the 18 m irregular wave flume at the National Sedimentation Laboratory. JONSWAP spectrum was used to generate the waves.

35

The frequency corresponding to the maximum value of the wave spectrum is defined as the "peak frequency".

$$f_p = f\big|_{S_{\max}(f)} \tag{3.41}$$

Peak period is the inverse of peak frequency:

$$T_p = \frac{1}{f_p} \tag{3.42}$$

The mean period T_m, and the mean spectral period T_z are also used in spectral analysis and can be calculated in terms of spectral moments by

$$T_m = \frac{m_0}{m_1} \quad \text{and} \tag{3.43}$$

$$T_z = \sqrt{\frac{m_0}{m_2}} \tag{3.44}$$

where m_o, m_1 and m_2 are the 0th, first and second moments of the wave spectrum, respectively. T_m and T_z each represent the typical period of the waves in the spectrum while T_p represents the periods of the higher waves.

Two other parameters are also used to define the width of the wave spectra. The spectral width parameter v_w and spectral bandwidth ε_w defined by Longuet-Higgins (1952) is obtained from the moments as follows

$$v_w = \sqrt{\frac{m_0 m_2}{m_1^2} - 1} \quad \text{and} \tag{3.45}$$

$$\varepsilon_w = \sqrt{1 - \frac{m_2^2}{m_0 m_4}} \tag{3.46}$$

where m_4 is the fourth moment of the wave spectrum. With the same m_o a wider spectrum gives larger values of higher order moments. Spectral width and spectral bandwidth range between 0 and 1. For a narrow banded spectrum both have to be close to 0.

The Joint North Sea Wave Project (JONSWAP) was started in 1967 to investigate the growth of waves under fetch-limited conditions and wave transformation from sea to shallower water area. It is actually a five-parameter spectrum with three parameters usually held constant. The parameterized JONSWAP spectrum is expressed in terms of H_{mo} and T_p as

$$S(f) = \alpha H_{mo}^2 f_p^4 f^{-5} \gamma^\beta \exp\left[-\frac{5}{4}\left(\frac{f_p}{f}\right)^4\right]$$

$$\alpha \approx \frac{0.0624}{0.230 + 0.0336\gamma - \left(\dfrac{0.185}{1.9 + \gamma}\right)}$$

$$\beta = \exp\left[-\frac{(f - f_p)^2}{2\sigma_J^2 f_p^2} \right] \tag{3.47}$$

$$\sigma_J \approx 0.07 \quad f \le f_p$$

$$\sigma_J \approx 0.09 \quad f \ge f_p$$

$$1 \le \gamma \le 7$$

γ is the peak enhancement coefficient which controls the sharpness of the spectral peak. The mean value is 3.3.

3.3.3. Random Wave Simulation

A time series wave signal can be generated by using a known energy spectrum. Using the wave spectrum for simulating random waves is known as the "deterministic spectral amplitude method" or the "random phase method". In this method the wave spectrum $S(f)$ is divided into N number of frequency bands with a bandwidth of Δf as shown in Figure 3.8. The random signal defined by Equation 3.47 is approximated by linear combination of N sinusoidal waves as

$$\eta(t) \cong \sum_{i=1}^{N} a_i \cos(\omega_i t + \delta_i) \tag{3.48}$$
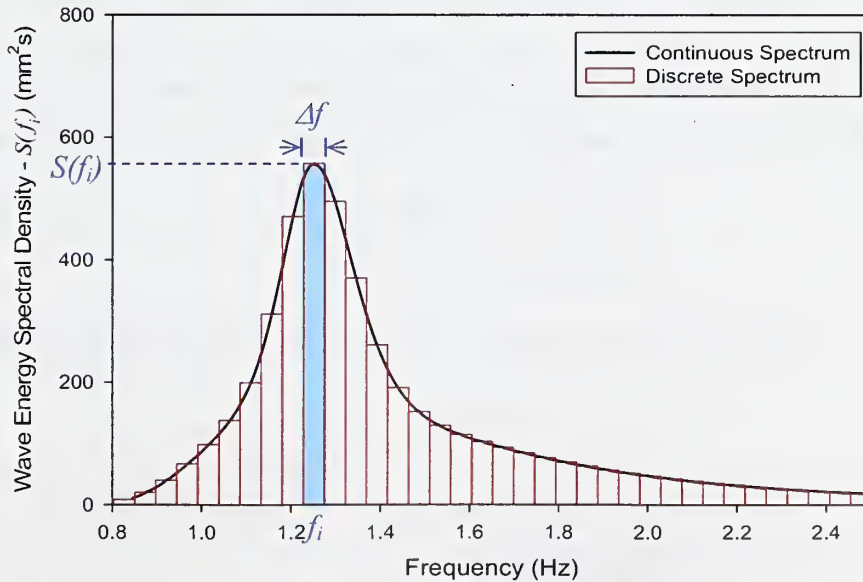
Figure 3.8 Continuous and discrete wave energy spectra. (JONSWAP $H_{mo} = 60$ mm, $T_p = 0.8$ s.)

Similarly, equation 2.49 becomes

$$m_j \cong \sum_{i=1}^{N} f_i^{\,j} S(f_i) \Delta f \tag{3.49}$$

The first moment can be approximated by using Equations 3.48 and 3.59;

$$m_0 \cong \sum_{i=1}^{N} S(f_i) \Delta f = \sum_{i=1}^{N} \frac{a_i^2}{2} \tag{3.50}$$

The wave spectrum keeps the information of frequency (and therefore T and L) and the energy density associated with each wave component but the phase information is lost. Since the surface elevation signal of the irregular waves is random, this information can be recovered by assigning a random phase to each wave component.

The amplitude (hence the wave height) of each component can be obtained by rearranging Equation 3.60

$$a_i = \frac{H_i}{2} = \sqrt{2S(f_i) \Delta f} \tag{3.51}$$

Wave angular frequency is calculated from

$$\omega_i = 2\pi f \tag{3.52}$$

and the phase angle is

$$\delta_i = 2\pi r_N \tag{3.53}$$

The phase angle of each wave is assign to a random number r_N ($0 \le r_N \le 1$). The time series wave signal can be constructed by substituting Equations 3.60, 3.61 and 3.62 into 3.48. The discrete spectrum is defined between the frequencies f_{start} and f_{stop}. The cutoff frequencies f_{start} and f_{stop} to start and stop the discrete spectrum can be defined as

$$S(f_{start}) \le p_{cutoff} S(f_p) \tag{3.54a}$$

$$S(f_{stop}) \le p_{cutoff} S(f_p) \tag{3.54b}$$

where p_{cutoff} a small number. Therefore, the frequency bandwidth is

$$\Delta f = \frac{f_{start} - f_{stop}}{N} \tag{3.55}$$

N should be large enough and p_{cutoff} should be small enough to correctly represent the continuous spectrum (e.g. $N=100$, $p_{cutoff} = 0.01$).

3.4.   Floating Breakwaters

Floating breakwaters interfere with the incident waves to reduce the transmitted wave energy by reflecting and dissipating some portion of the incoming wave energy. Therefore, the main objective for the design of a floating breakwater is to reduce the amplitude of the transmitted waves. The term floating does not refer to a freely floating structure. The restraint of the structure may vary from freely floating to a rigidly fixed case. The breakwater will occupy only a small portion of the depth of water generally near the water surface. In order to have an idea about where to locate the breakwater along the depth, the kinetic energy distribution within a wave should be considered. The percent kinetic energy above any depth or at any z is given by:

$$\text{Percent kinetic energy} = 1 - \frac{\sinh 2k(h-z)}{\sinh 2kh} \times 100\% \tag{3.56}$$

This relation is plotted in Figure 3.5 as a function z/h for the relative depths $h/L = 0.5$ and $h/L = 0.05$.

Floating breakwaters are considered as effective wave breaking structures for shorter waves for the reason that most of the kinetic energy is concentrated close to the surface of the fluid, particularly for deepwater waves. As it can be seen from Figure 3.5, in deepwater conditions, an object occupying only a small relative portion of the depth (say 10%) could interact with a significant portion of the kinetic energy (about 50%).
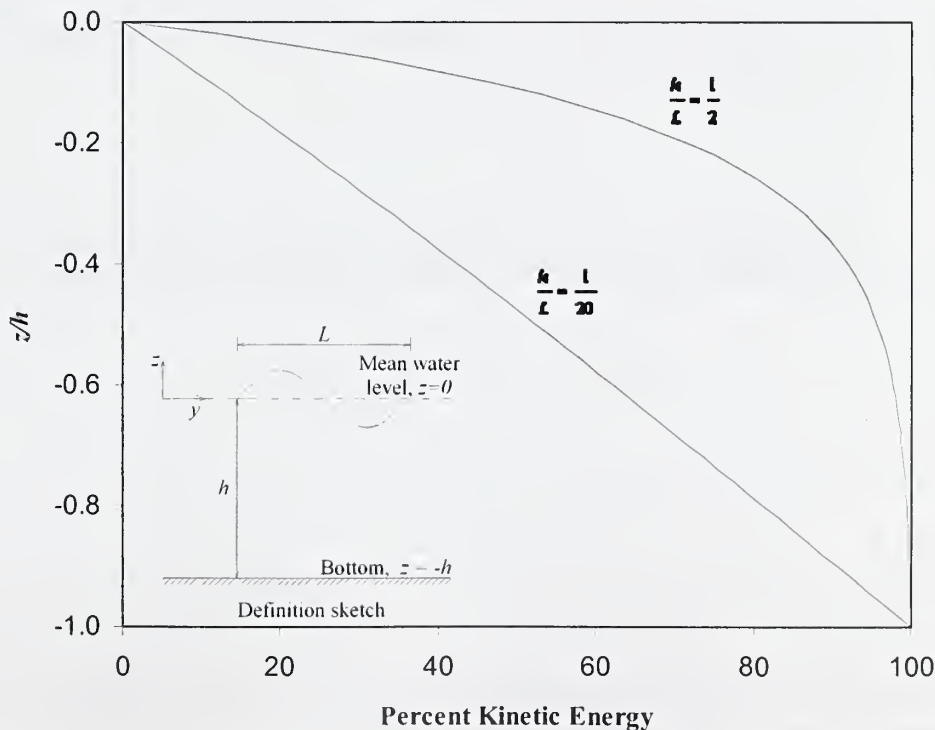
Figure 3.9. Concentration of percent kinetic energy above elevation z/h.

39

The interaction of the floating breakwater of an arbitrary shape will result in a portion of the wave energy being reflected from the absorber as a reflected wave train and a portion of the energy being transmitted through and under the breakwater as a transmitted wave train. This interaction will also cause some force components on the absorber. The energy balance equation for the physical process when a wave passes a floating breakwater can be stated as:

$$E_i = E_t + E_r + E_l \tag{3.57}$$

where E_i is the total incident wave energy, E_r is the total reflected wave energy, E_t is the total transmitted wave energy and E_l is the total dissipated wave energy.

From Equation 3.25 E_i E_t and E_r can be obtained as:

$$E_i = \frac{\gamma_w H_i^2 L}{8} \tag{3.58a}$$

$$E_r = \frac{\gamma_w H_r^2 L}{8} \tag{3.58b}$$

$$E_t = \frac{\gamma_w H_t^2 L}{8}. \tag{3.58c}$$

If losses are linked to an equivalent wave height, H_l, of the same wave period, then the total dissipated wave energy is:

$$E_l = \frac{\gamma_w H_l^2 L}{8} \tag{3.58d}$$

Substituting the Equations 3.58a, 3.58b, 3.58c and 3.58d into Equation 3.57 and with some simplifications the energy balance equation can be written as:

$$\left(\frac{H_r}{H_i}\right)^2 + \left(\frac{H_t}{H_i}\right)^2 + \left(\frac{H_l}{H_i}\right)^2 = 1 \tag{3.59}$$

or,

$$\kappa_r^2 + \kappa_t^2 + \kappa_l^2 = 1 \tag{3.60}$$

where κ_r is the reflection coefficient, κ_t is the transmission coefficient and κ_l is the loss coefficient. For an effective design of a breakwater, the transmission coefficient should be as small as possible by either making the reflection or dissipation coefficient large. It is usually undesirable to increase the reflection coefficient too much to avoid large standing waves on the offshore side of the breakwater. Throughout the theoretical analysis of the problem the floating objects are assumed to be placed in a train of small

amplitude waves and the flow is assumed to be irrotational. Therefore, the theory cannot account for any energy losses that would occur in a real system. However, it can be assumed that a progressive wave system exists far enough from the absorber including incident, reflected and transmitted wave components.

For the case with no transmission ($\kappa_t = 0$) and in the absence of dissipation, the reflected wave must have the same height with the incident wave ($\kappa_t = 1$). Due to the linearity of the Laplace operator the velocity potential of the two wave system can be obtained by summing the potentials of individual waves.

$$\phi_s = \phi_i + \phi_r \tag{3.61}$$

Using some trigonometric identities and the wave period T being an invariant quantity, the equation describing the free surface can be obtained as

$$\eta(x,t) = H \cos(kx)\sin(\omega t) \tag{3.62}$$

Equation 3.30 is the product of two functions such that one of them has no time variable and the other has no space variable. Therefore, the water level η will be zero everywhere at certain times and at some points for all times. This condition is called a "standing wave".
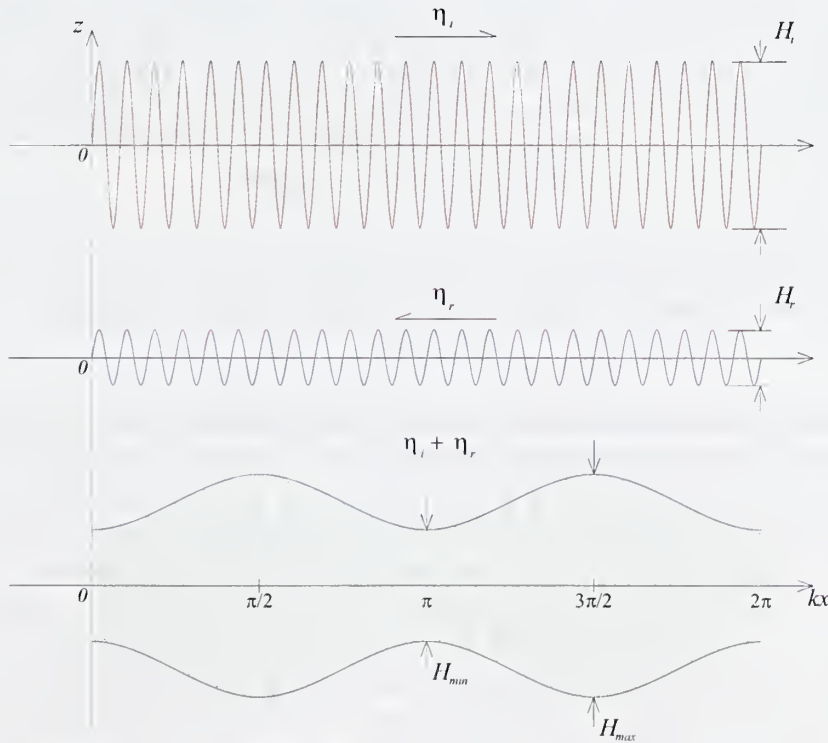
Figure 3.10. Definition sketch of incident waves (top), reflected waves (middle) and wave envelopes (bottom).

41

An incomplete reflection ($\kappa_r < 1$) from an obstacle, will form a partial standing wave and the resulting envelope of the wave amplitudes will have points of maximum and minimum amplitude (Figure 3.10). The reflection produces a stationary spatial envelope of wave heights H_{max} and H_{min}, given by:

$$H_{max} = H_i + H_r, \quad \text{the quasi-antinodes} \tag{3.63}$$

$$H_{min} = H_i - H_r, \quad \text{the quasi-nodes} \tag{3.64}$$

The reflection coefficient κ_r can be rewritten in terms of this spatial envelope:

$$\kappa_r = \frac{H_{max} - H_{min}}{H_{max} + H_{min}}. \tag{3.65}$$

3.5. Dynamics of Floating Bodies

An important parameter related to a floating body with some degrees of freedom is the natural period of the dynamic structure. When the natural period of the floating system is low with respect to the incident wave period the system can be considered as rigidly restrained (Hales, 1981). For a floating object, if the period of the wave motion approaches to the natural period of the object, the displacements can be amplified due to resonance. In the following text an estimate for the natural frequency will be derived for a circular floating rigid object assuming small amplitude oscillations and neglecting nonlinear forces due to virtual mass and irregular geometry. Also, two-way interaction of the object with the generated waves will be neglected.

The small amplitude oscillation of a floating object with a single degree of freedom can be approximated by a forced spring-dashpot system as in Figure 3.11. This arrangement is characterized by the following differential equation;

$$m\ddot{z} + c\dot{z} + kz = F(t) \tag{3.66}$$

where m is the mass of the floating body, x is the displacement, c is the linear damping coefficient, k is the spring constant and F(t) is the external force applied to the system.
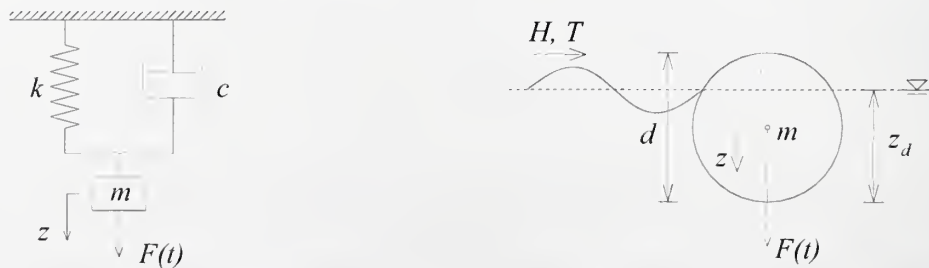
Figure 3.11 Definition sketch of the spring-dashpot model and the floating circular cylinder.

The solution of the homogenous part of Equation 10 yields

$$z = e^{-\zeta \omega_n t} A \cos(\omega t + \phi)$$ (3.67)

where,

$\omega = \omega_n \sqrt{1 - \zeta^2}$ is the damped natural angular frequency of the system, (3.68a)

$\zeta = \dfrac{c}{2m\omega_n}$ is the dimensionless damping factor and (3.68b)

$\omega_n = \sqrt{\dfrac{k}{m}}$ is the undamped natural angular frequency. (3.68c)

ϕ is the phase angle between the input and the output functions and A is a function of velocity. Note that damped natural frequency is always less than the undamped natural frequency.

The spring constant or the stiffness can be estimated from the force-displacement relationship given by Hooke's Law,

$$F_r(t) = -kz(t)$$ (3.69)

The damping coefficient c is a function of dynamic viscosity of water. If the floating body is in a wave train with a wave period T, the external force F can be defined by a periodic function in time as $F(t) = F_0 \cos(\omega_f t)$. The steady state (particular) solution of Equation 3.69 with the external force yields;

$$z(t) = z_o \sin(\omega t + \phi)$$ (3.70)

where,

$$z_0 = \frac{F_o / k}{\sqrt{\left(1 - \omega^2 / \omega^2_n\right)^2 + \left(\zeta \omega^2 / \omega^2_n\right)^2}} \quad \text{and} \quad \phi = \tan^{-1} \frac{-2\zeta \omega / \omega_n}{1 - \omega^2 / \omega_n^2}$$ (3.71)

In Figure 3.12 the dimensionless maximum displacement of the mass is plotted against dimensionless frequency. When there is no damping the amplitude goes to infinity at the resonance frequency. As the damping factor increases the resonance frequency gets smaller values and the amplitude at this frequency becomes finite values. The phase difference approaches 90° near the resonance frequency. At frequencies smaller than the resonance frequency, the output amplitude gets closer to the input amplitude and phase difference drops to zero. At frequencies higher than the resonance frequency the output amplitude approaches zero and the phase difference between external force and output displacement becomes nearly 180°. For a circular cylinder floating in calm water, the restoring force $F_r(t)$ due to the disturbance, $z(t)$ is equal to the weight of the displaced water if all the other unsteady forces are neglected as illustrated in Figure 3.13.

43
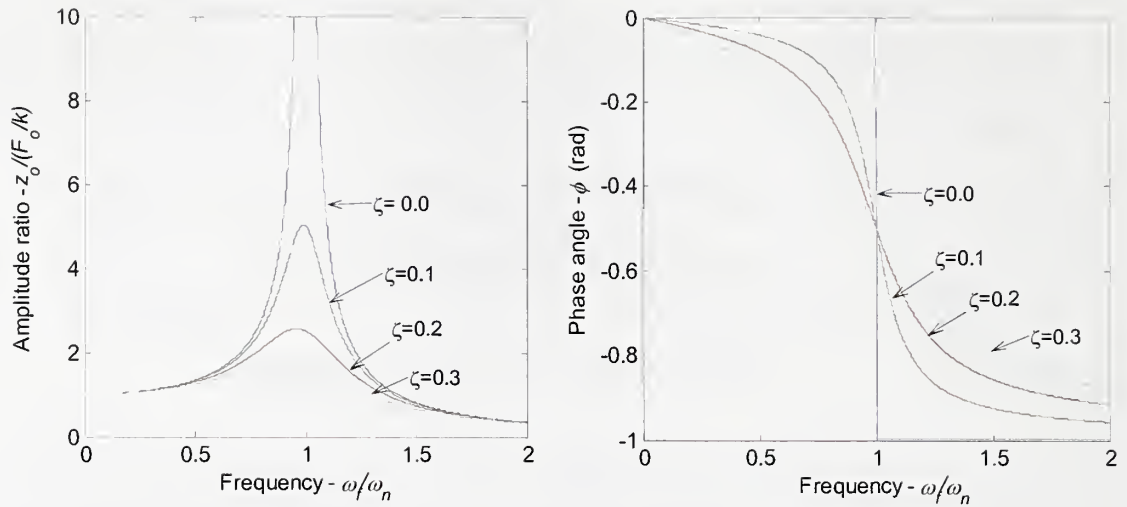
Figure 3.12 Response characteristics of a single degree of freedom system.
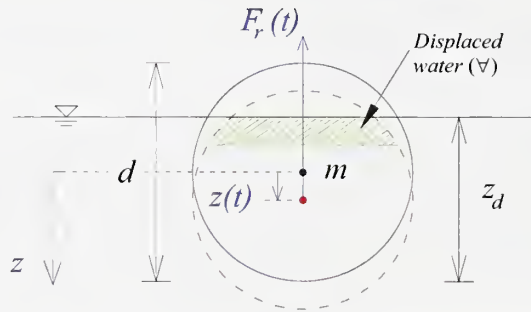
Figure 3.13 Illustration of a disturbed floating circular cylinder in calm water.

The exact equation for the volume $\forall(t)$ per unit breakwater width is

$$
\forall(t) = d^2 \left[\cos^{-1}\left(1 - \frac{2(z_d + z(t))}{d} \right) - \cos^{-1}\left(1 - \frac{2z_d}{d} \right) \right]
$$
$$
+ \left[(z_d + z(t))^2 \left(1 - \frac{d}{2(z_d + z(t))} \right) \sqrt{ \frac{d}{z_d + z(t)} - 1 } - z_d^2 \left(1 - \frac{d}{2z_d} \right) \sqrt{ \frac{d}{z_d} - 1 } \right]
$$

(3. 72)

and the restoring force per unit width of cylinder is

$$
F_r(t) = \forall(t)\gamma_w
$$

(3.73)

where γ_w is the specific gravity of water. Since the volume is nonlinearly related to the displacement, the stiffness k is also a function of displacement. Therefore, the linear spring approximation does not hold. Nevertheless, an approximate volume can be obtained by linearizing Equation 3.72 with the assumption of a small disturbance. The

simplest relation is obtained by replacing the shaded area in Figure 3.13 by a rectangular region. In this case the volume per unit width reduces to:

$$\forall(t) = z(t)\left[2z_d\sqrt{\frac{d}{z_d} - 1}\right]$$ (3.74)

Validity of this assumption depends on the amount of draft and amplitude of the oscillation. As illustrated in Figure 3.14, for $z/d = 0.1$ Equation 3.74 can be use up to $z_d/d = 0.9$ with less the 10% error.

Combining Equations 3.69, 3.73 and 3.74, an approximate stiffness, k can be obtained as;

$$k = 2\gamma_w z_d \sqrt{\frac{d}{z_d} - 1}$$ (3.75)

Substituting in Equation 3.68c, undamped natural angular frequency can be obtained as:

$$\omega_n = \sqrt{\frac{2\gamma_w z_d}{m} \sqrt{\frac{d}{z_d} - 1}}$$ (3.76)

It must be realized that m here is the mass per unit width of breakwater. The damped natural angular frequency from Equation 3.68a and 3.68c can be written as;

$$\omega_d = \sqrt{\left(\frac{2\gamma_w z_d}{m}\sqrt{\frac{d}{z_d} - 1}\right) - \left(\frac{c}{2m}\right)^2}$$ (3.77)

Recalling the relation $T = \dfrac{2\pi}{\omega}$, the natural period of the undamped oscillations is written as

$$T_n = \frac{2\pi}{\sqrt{\frac{2\gamma_w z_d}{m}\sqrt{\frac{d}{z_d} - 1}}}$$ (3.78)

Note that for a floating object the weight is related to the submerged volume, $\forall_o$ by,

$$W = mg = \gamma_w \forall_o$$ (3.79)

45
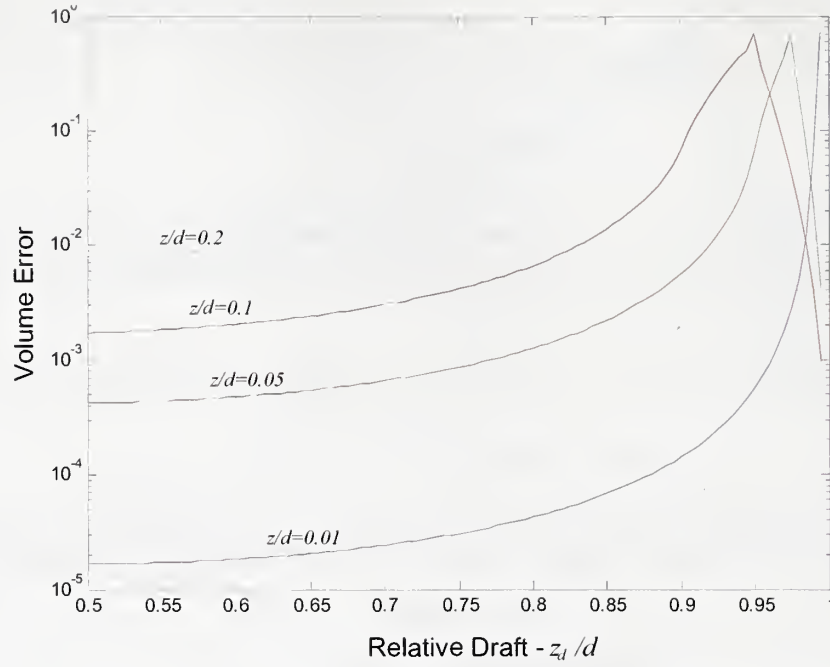
Figure 3.14 The variation of error due to the linearization of the displaced volume of a disturbed circular cylinder (Volume Error $= \left| \left(\forall_{exact} - \forall_{approximate} \right) / \forall_{exact} \right|$).

Therefore, Equation 3.78 becomes

$$T_n = \frac{2\pi}{\sqrt{\frac{2gz_d}{\forall_o}} \sqrt{\frac{d}{z_d} - 1}}$$

(3. 80)

where

$$\forall_o = d^2 \cos^{-1}\left(1 - \frac{2z_d}{d}\right) + z_d{}^2\left(1 - \frac{d}{2z_d}\right)\sqrt{\frac{d}{z_d} - 1}$$

(3. 81)

When the circular cylinder is close to the water surface the restoring force approaches zero and therefore, the natural period of the cylinder approaches infinity. It should be noted that the approximate volume is always larger than the exact volume, leading to overestimation of the restoring force $F_r(t)$. Therefore, the period estimated with Equations 3.80 is always smaller than the actual value and the error increases as z_d/d gets closer to one. For an almost submerged circular cylinder ($z_d / d \approx 1$) Figure 3.14 can be used to estimate the natural period for small oscillations. If a cylinder is almost submerged in its undisturbed state then it might be completely submerged at certain phases of its oscillation and the restoring force stays constant until it is lifted back to the water surface. This delays oscillations and increases the natural period.
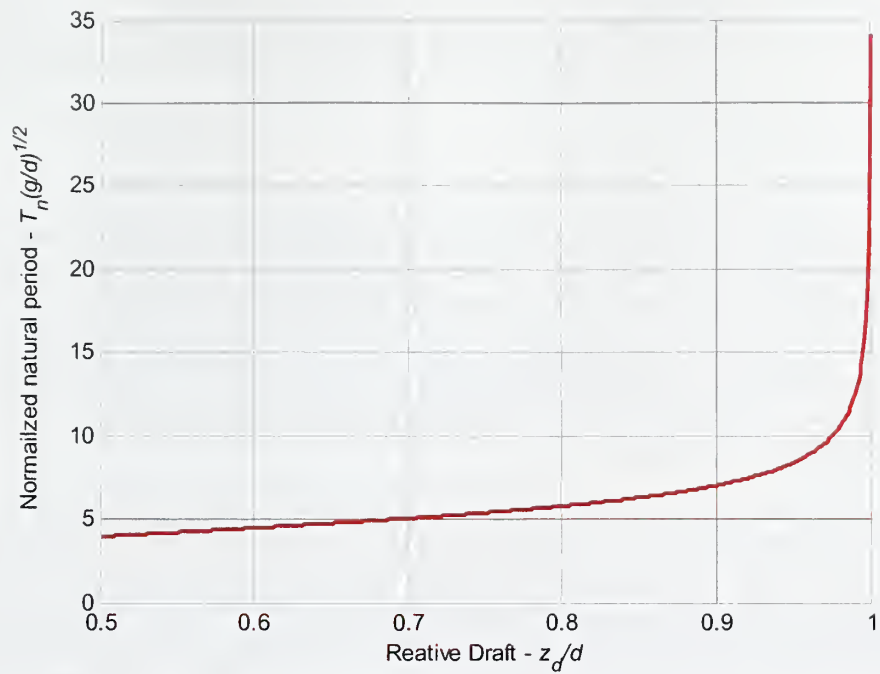
Figure 3.15 Dimensionless draft versus natural period of the cylindrical breakwater for small oscillations.

47

One way of obtaining reliable information about the performance of a floating breakwater structure is through physical model studies. A physical model can be constructed without invoking the assumptions that were made during the derivation of the analytical model. In the controlled laboratory environment experimental parameters can be controlled and the repeatability can be ensured, which is usually very difficult in the field. However, it is important to correctly scale the model by selecting proper dimensionless quantities.

2D wave tanks are commonly used in the literature to minimize the construction cost and further restrict the number of variables in the experiments with floating breakwaters. The directional effects of the waves are ignored which is the most important drawback of 2D wave tanks. The experiments are usually conducted with regular monochromatic waves as discussed in Chapter II although, there are a few studies performed in irregular wave conditions.

Based on the wave characteristics measured in an irrigation pond near Lonoke, Arkansas, a wave tank with a computer-controlled, flap-type wave generator and wire-mesh wave absorber was designed and constructed at the Hydraulics Laboratory of the USDA National Sedimentation Laboratory. The dimensional analysis and scaling requirements of the physical model are explained in Section 4.1 and 4.2. The design considerations and construction details of the wave tank, wave generator and the wave absorber are presented in the following sections.

4.1.   Dimensional Analysis

A simple model for a fixed rigid and partially submerged object interacting with linear monochromatic waves with associated terms is given in Figure 4.1.
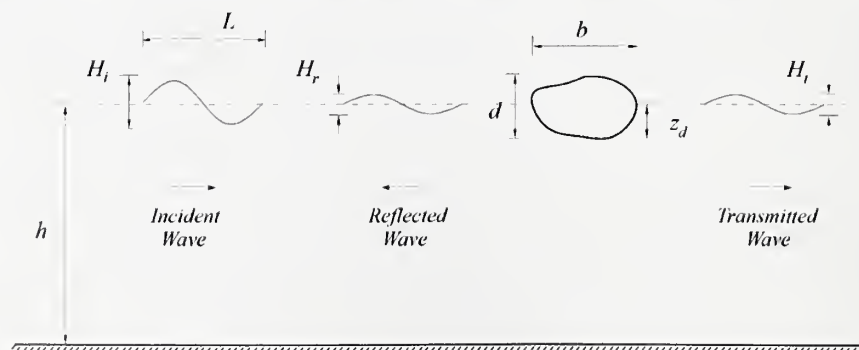
Figure 4.1 Definition of terms associated with the design problem.

The most significant parameters for the model described in Figure 4.1 and their dimensions in terms of fundamental units are listed below:

T	wave period [T]
L	wavelength [T]
h	water depth [L]
H_i	incident wave height [L]
H_r	reflected wave height [L]
H_t	transmitted wave height [L]
z_d	draft of the breakwater [L]
d	vertical length scale of the breakwater [L]
b	horizontal length scale of the breakwater [L]
ρ_ω	mass density of water [ML^{-3}]
μ	dynamic viscosity of water [ML^{-1} T^{-1}]
u	characteristic velocity of water [LT^{-1}]
g	gravitational acceleration [LT^{-2}]

As the length scale and time scale of the waves are related with the dispersion relation, we can discard one of the variables in dimensional analysis. L is selected to be the length scale.

Assuming that the remaining list contains all the important parameters for the fixed object, we can describe the phenomenon by the functional relationship:

$$f(H_i, H_r, H_t, L, h, z_d, d, b, \rho, \mu, u, g) = 0 \qquad (4.1)$$

The current study focuses on floating breakwaters as the floating object. Since the objective of a breakwater is to reduce the wave height, the primary dependent variable is the transmitted wave height, H_t. The first three parameters can be combined to get the transmission and reflection coefficients, $\kappa_t = \dfrac{H_t}{H_i}$ and $\kappa_r = \dfrac{H_r}{H_i}$.

The incident wave height, H_i, is divided by L, to get $\dfrac{H_i}{L}$, the incident wave steepness. Another common dimensionless product to describe the waves is the relative depth which can be written as $\dfrac{h}{L}$ or kh where k is the wave number defined by Equation 3.10a.

It can be assumed that the characteristic length scale of the breakwater is of the order of the wavelength scale rather than the water depth considering the type of the waves is primarily within deepwater range. The depth of submergence of the breakwater is the primary dimension in energy considerations for a fixed breakwater. Therefore, the

49

next dimensionless parameter is selected as $\frac{z_d}{L}$. The remaining parameters related with

the breakwater geometry are selected as draft ratio, $\frac{z_d}{d}$ and the aspect ratio $\frac{b}{d}$.

The remaining parameters are combined to get the Reynolds number

$(\mathbf{Re} = \frac{\rho_w u h}{\mu})$ and Froude number, $(\mathbf{Fr} = \frac{u}{\sqrt{gh}})$.

With the relations introduced above, one of the possible combinations of the parameters as a complete set of dimensionless products is obtained as follows;

$$F\left(\kappa_t, \kappa_r, \frac{H_i}{L}, \frac{h}{L}, \frac{z_d}{L}, \frac{z_d}{d}, \frac{b}{d}, \mathbf{Re}, \mathbf{Fr}\right) = 0 \qquad (4.2)$$

For small amplitude waves the velocities are usually small sufficiently far from the object. Therefore, the Froude and Reynolds Numbers can be considered constant. For

the case of a single circular cylinder the aspect ratio, $\frac{b}{d}$ becomes unity and can be

excluded. Equation 4.2 can be rearranged in terms of dependent variables as follows;

$$\kappa_t, \kappa_r = F'\left(\frac{H_i}{L}, kh, \frac{z_d}{L}, \frac{z_d}{d}\right) \qquad (4.3)$$

Equation 4.3 contains dimensionless parameters with length scales which are more readily interpretable in terms of physical parameters.

If the same object is floating with three degrees of freedom some additional parameters are also become significant to represent the dynamic behavior of the breakwater. These parameters can be listed as follows:

m	Mass of the floating object [M]
I_{yy}	Mass moment of inertia of floating object about y [ML^{-3}]
ξ_x	Amplitude of the horizontal displacement (sway) [L]
ξ_z	Amplitude of the vertical displacement (heave) [L]
ω_y	Angular velocity in y-direction (roll velocity) [L]
$(F_x)_{max}$	Maximum horizontal force [MLT^{-2}]
$(F_z)_{max}$	Maximum vertical force [MLT^{-2}]
$(T_y)_{max}$	Maximum torque [ML^{2}T^{-2}]
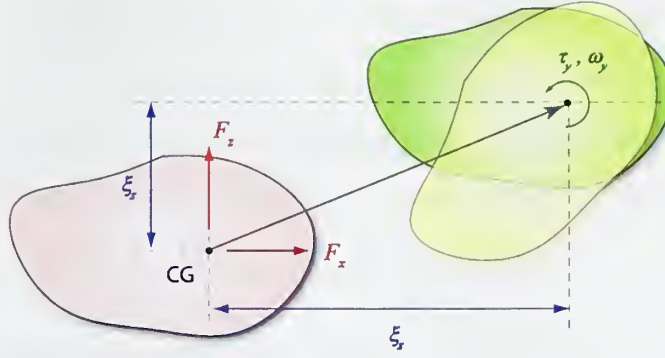
Figure 4.2 Definition of terms for the dynamic system.

For a dynamic breakwater functional relationship similar to Equation 4.1 can be obtained as follows:

$$f\left(H_i, H_r, H_t, L, h, z_d, d, b, \xi_x, \xi_z, \omega_y, (F_x)_{max}, (F_z)_{max}, (T_y)_{max}, m, I_y, \rho, \mu, u, g\right) = 0 \quad (4.4)$$

The above functional relationship can be put into a dimensionless form including the dimensionless groups in Equation 4.2 as:

$$G\left(\kappa_t, \kappa_r, \frac{H_i}{L}, \frac{h}{L}, \frac{z_d}{L}, \frac{z_d}{d}, \frac{b}{d}, \varepsilon_x, \varepsilon_z, \frac{\omega_y}{\omega}, f_x, f_z, \tau_y, m', I', \mathbf{Re}, \mathbf{Fr}\right) = 0 \quad (4.5)$$

The new dimensionless parameters introduces in Equation 4.5 are defined as follows:

$\varepsilon_x = \dfrac{\xi_x}{H_i}$ and $\varepsilon_z = \dfrac{\xi_z}{H_i}$ are the dimensionless rigid body displacements in the

horizontal and vertical directions. Here, it is assumed that the transmitted and reflected wave heights have less influence on breakwater motions compared to the incident wave height.

$f_x = \dfrac{(F_x)_{max}}{\gamma z_d b}$ and $f_z = \dfrac{(F_z)_{max}}{\gamma z_d b}$ are the dimensionless force components per unit

width (in the y-direction) of the structure in x- and z-directions where $\gamma = \rho g$ is the specific weight of water,

$\tau_y = \dfrac{(T_y)_{max}}{\gamma z_d b^2}$ is the dimensionless torque in the y-direction,

$m' = \dfrac{m}{\rho z_d b}$ and $I' = \dfrac{I_y}{\rho d^2 b^2}$ are the dimensionless mass and y-mass moment of

inertia.

51

The primary dependent variables in the dynamic analysis of the floating breakwater are the displacement components, ε_x and ε_z, angular velocity, $\dfrac{\omega_y}{\omega}$, and the force components f_x, f_z and τ_y. Upon elimination of the dimensionless parameters in a similar fashion to the fixed case, and writing in terms of dependent variables:

$$\varepsilon_x, \varepsilon_z, \frac{\omega_y}{\omega}, f_x, f_z, \tau_y = G\left(\frac{H_i}{L}, \frac{h}{L}, \frac{z_d}{L}, \frac{z_d}{d}, m', I'\right) \tag{4.6}$$

If the structure is free to move in the z-direction, the mass has to be changed to increase the draft ratio of the breakwater. In other words, the draft is a function of mass:

$$\frac{z_d}{d} = f(m') \tag{4.7}$$

Thus, one of these terms can be eliminated which reduces the equation to the following form:

$$\varepsilon_x, \varepsilon_z, \frac{\omega_y}{\omega}, f_x, f_z, \tau_y = G'\left(\frac{H_i}{L}, \frac{h}{L}, \frac{z_d}{L}, \frac{z_d}{d}, I'\right) \tag{4.8}$$

In the case of a moored breakwater, the mooring-line length and stiffness are also effective on breakwater characteristics. These parameters will be discussed separately in the text.

4.2.   Scaling requirements

The dimensions of the floating breakwater are scaled according to the Froude criterion. The floating structure should be geometrically scaled with correct weight and mass distribution so that the model has correct buoyancy and moment of inertia. This requires the model be geometrically undistorted (Hughes, 1993).

The Froude similarity criterion is given by

$$N_T = \sqrt{N_L} \tag{4.9}$$

where N_T is the time scale ratio which is the ratio of the time scale of the prototype to the corresponding time scale of the model and N_L is the length scale ratio which is the ratio of the length scale of the prototype to the length scale of the model. For our case these values are given by:

$$N_T = \left(\frac{T_p}{T_m}\right), \quad N_L = \left(\frac{L_p}{L_m}\right) \tag{4.10}$$

Therefore,

$$\left(\frac{L}{T^2}\right)_p = \left(\frac{L}{T^2}\right)_m \tag{4.11}$$

This condition is already satisfied with linear wave theory. The remaining scale requirements come from dimensional analysis.

$$\left(\frac{H_i}{L}\right)_p = \left(\frac{H_i}{L}\right)_m \tag{4.12}$$

$$\left(\frac{h}{L}\right)_p = \left(\frac{h}{L}\right)_m \tag{4.13}$$

$$\left(\frac{z}{L}\right)_p = \left(\frac{z}{L}\right)_m \tag{4.14}$$

where the subscripts p and m represent prototype and model, respectively.

The scaling relationship for the wave forces on a two-dimensional floating breakwater structure is given by;

$$\frac{F_p}{F_m} = \frac{W_p}{W_m} = \left(\frac{\gamma_p}{\gamma_m}\right) = \left(\frac{l_p}{l_m}\right)^3 \tag{4.15}$$

where F is the net force acting on the breakwater and W is the weight of the structure, γ is the specific weight of the structure or the fluid an l is the characteristic length.

Although the validity of the conventional classification of waves according to the relative depth is not well defined for use with a floating wave absorber, it is known that reflection and transmission coefficients do not strongly depend on the depth except for in the presence of very shallow water waves (Dean and Ursell, 1959). For the sake of simplicity and to extend the range of the dimensionless ratios, the relative depth was excluded during the scaling of the experimental setup. Instead, the scaling was made by selecting the size of the model then adjusting the wave parameters so that deepwater conditions were satisfied. Thereafter, the data are extended to transitional water depths.

From the data analysis, the ranges for the prototype and model parameters based on the scaling requirements are summarized in Table 4.1. The associated dimensionless parameters are given in Table 4.2. T is the peak period, and H_i is the significant wave height for the prototype.

Table 4.1. The prototype and model parameters based on the scaling requirements.

Parameters	Prototype	Model
Wave period - T (s)	1.0 – 1.7	0.5 – 1.0
Wave height - H_i (m)	0.10 – 0.25	0.02 – 0.06
Water depth - h (m)	2.5	0.30 – 0.45

Table 4.2. The prototype and model parameters based on the scaling requirements.

Parameters		Range
Incident wave steepness	$\dfrac{H_i}{L}$	$0.01 - 0.1$
Relative depth	kh	$1.9 - 7.5$

4.3.   Wave Tank

The 19 m long wave tank has a rectangular cross-section and is 55 cm wide and 60 cm deep. The definition sketch of the wave tank is given in Figure 4.3. A detailed drawing with important dimensions is presented in Figure 4.4. A flap type wave generator is located 127 cm from one end of the tank. At the other end of the tank there is a progressive wave absorber made of layers of expanded aluminum sheet. The effective length of the tank from the paddle to the toe of the absorber is 15.3 m. The sides and bottom of the tank are constructed with marine plywood and coated with epoxy based waterproofing paint (Figure 4.3). The test section is located 12 m away from the paddle. The sidewalls are made of clear polycarbonate along the test section.

The space behind the paddle is also filled with aluminum wool and scratch pipes to absorb the generated waves. On each side of the model, level sensors are mounted to record the wave height. The gauge on the offshore side of the test section is attached to a linear actuator to scan the standing wave envelope. The gauge on the onshore side of the model is fixed and records transmitted wave heights. The motion of the wave generator and moving gauge are computer-controlled. The position data of the paddle, the moving gauge, and the wave height data from the two level sensors are logged by the same computer.
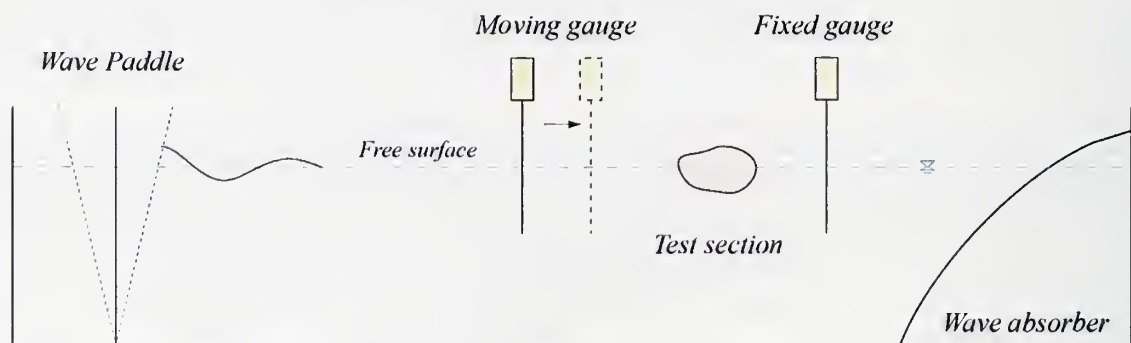
Figure 4.3 Definition sketch of the wave tank.
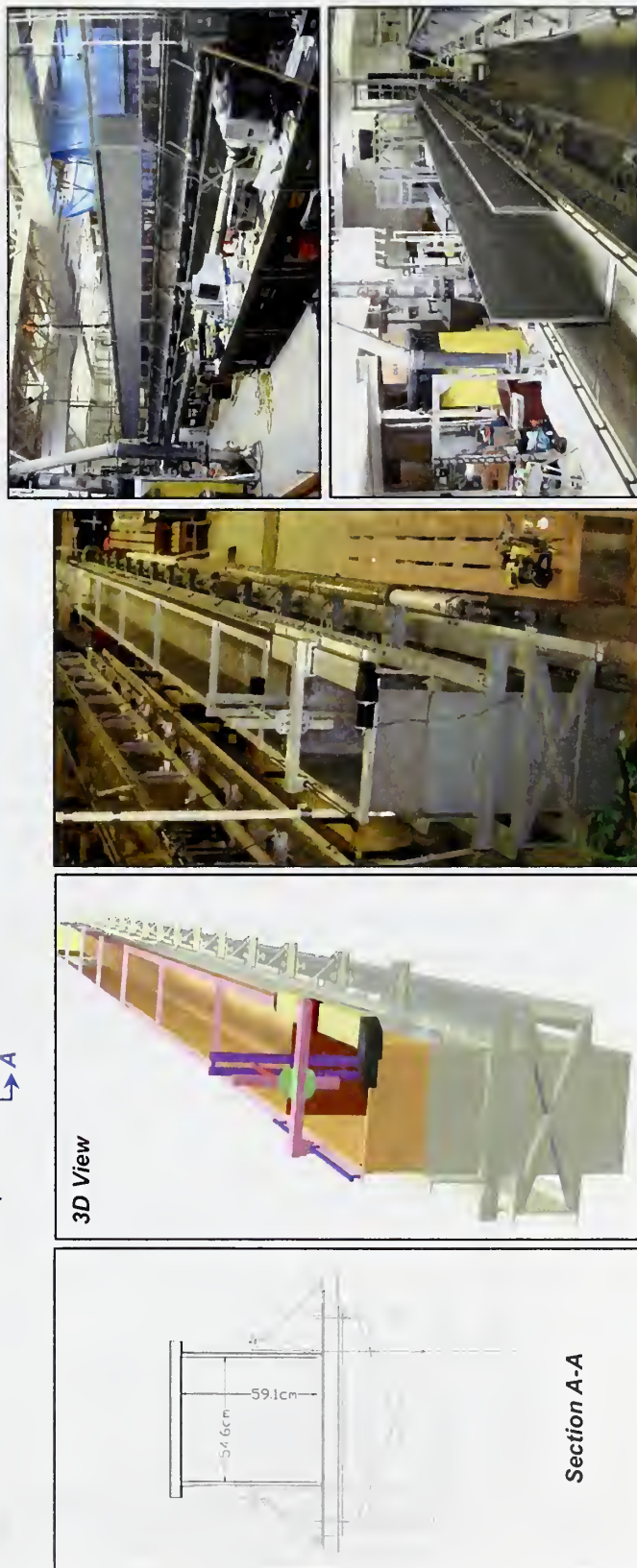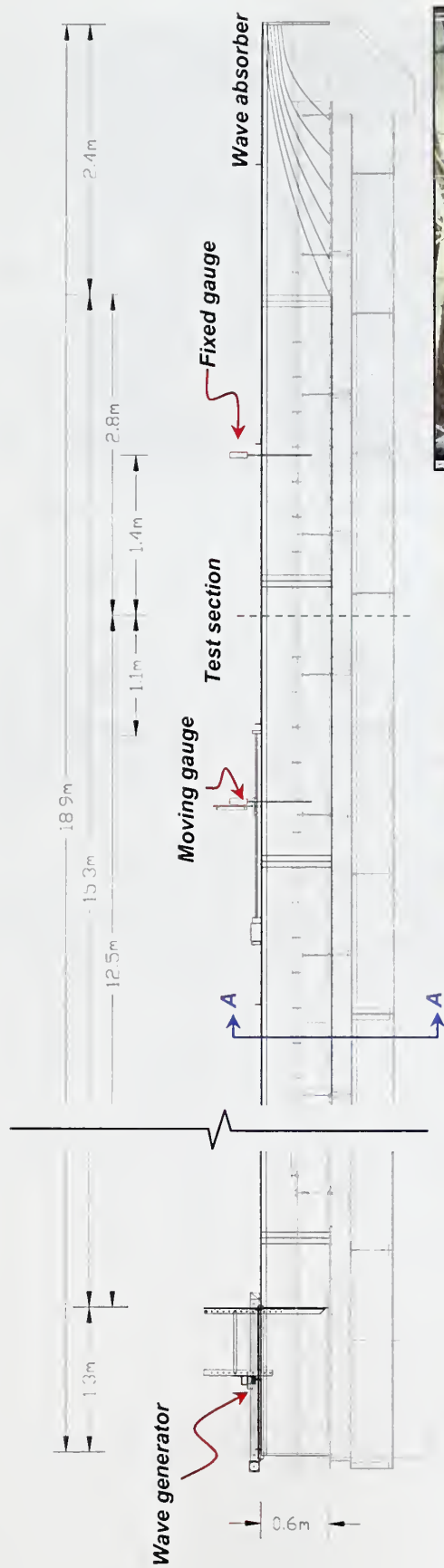
Figure 4.4 Scaled drawings of the wave tank with the wave generator and the absorber. Pictures show construction stages of the wave tank

4.3.1. Free Oscillations

An important problem related with the wave tank design is the free oscillations of the water within the tank. If the period of these oscillations gets closer to the wave period the minor disturbances can be magnified and add up additional noise into the results. The period of these oscillations can be estimated in terms of tank dimensions. A standing wave with a wavelength $2l$ will travel with a propagation speed of $\sqrt{gh}$ in the x and y directions. The natural period can be estimated from $\frac{l_x}{T_{nx}} = \sqrt{gh}$ and $\frac{l_y}{T_{ny}} = \sqrt{gh}$, where l_x and l_y are the length and width of the tank and, T_{nx} and T_{ny} are the longitudinal and lateral natural periods. The experiments were conducted at a water depth of 0.466 m. The corresponding natural period of the wave tank in the longitudinal direction was 15.6 s and in the cross-sectional direction, it was 0.51 s. The latter value is critical since it is close to the experimental range for wave period.

4.4.   Level Sensors

The Ocean Sensor systems Wave Staff was used to measure the temporal water level variation on both sides of the model (Figures 4.5 and 4.6). The Wave Staff is a capacitance type level sensor with a staff length of 50 cm and has a data sampling rate of 30Hz. The operation voltage is 5.5-40 Volts. The accuracy within 20-80% of full length is 1.25 mm. The data between the device and the computer is exchanged through an RS-232 connection.

A computer code was developed in National Instruments LabVIEW 7.1 to communicate with both of the devices and store the water depth and sensor position data. The level counts are later converted into water heights. The sensors were calibrated using a vernier scaled point gauge. The calibration curves are given in Figure 4.7.
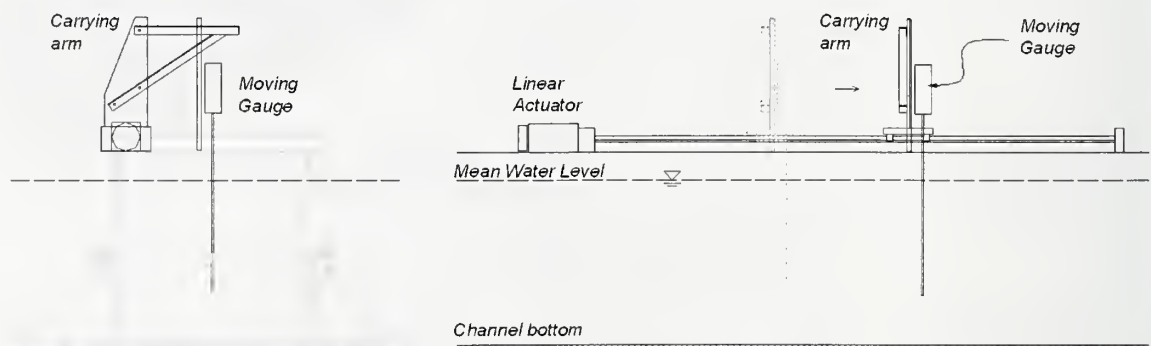
Figure 4.5 Scaled drawing of the moving gauge connection to the Linear Actuator.
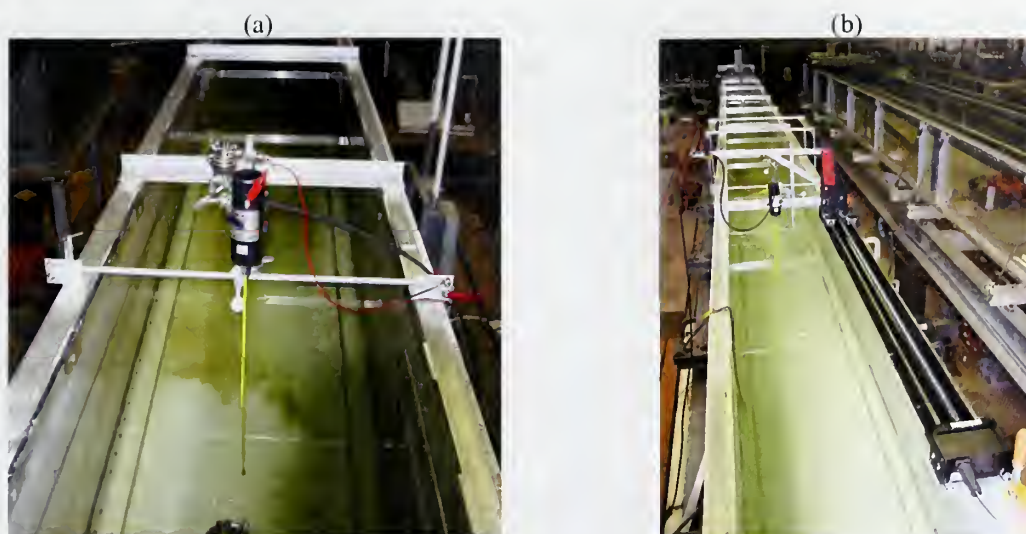
Figure 4.6 Level sensors mounted on the tank. (a) Fixed gauge and (b) moving gauge.
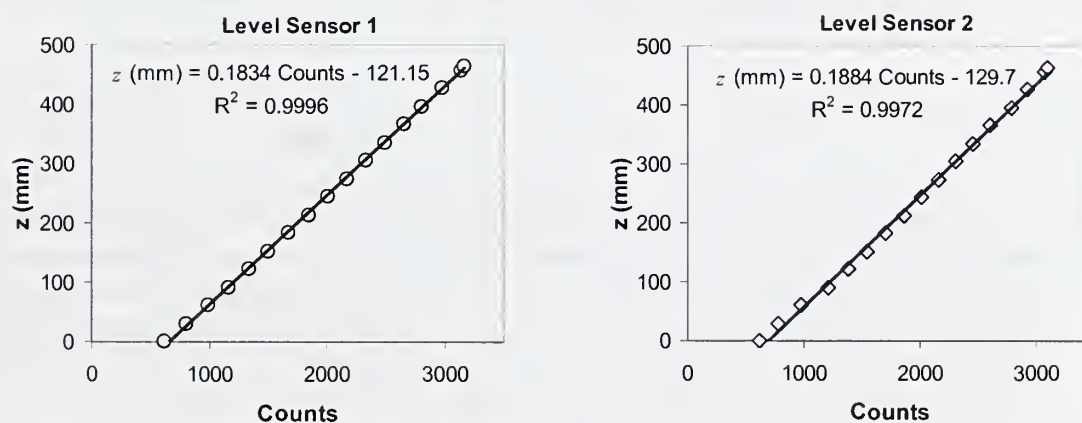
Figure 4.7 Calibration curves for the level sensors.
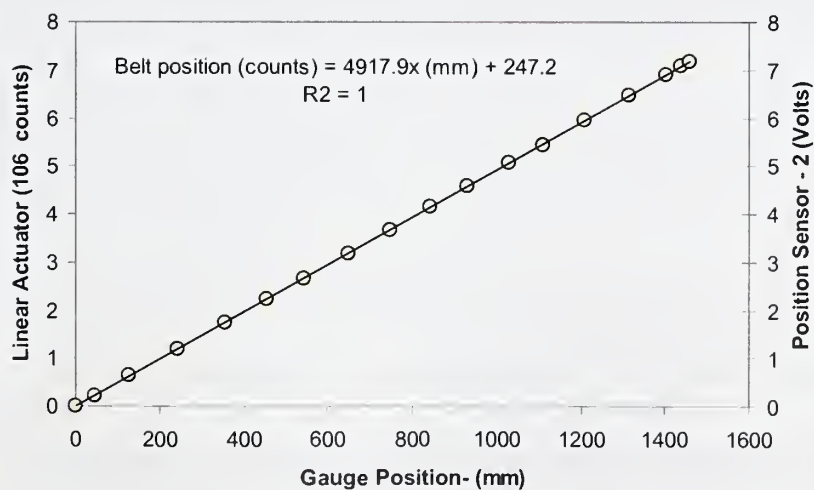
Figure 4.8 Calibration curve for the linear actuator and the position sensor.

57

As explained in Chapter III, the wave gauge on the upstream side of the model has to move along the tank to record the standing waves due to the interaction of the reflected waves from the test section with the incident waves. Therefore, the level sensor in front of the test section is attached to a linear actuator to scan the water surface. The scan length of the actuator is 147 cm. Figure 4.6 is a scaled drawing of the moving gauge. The calibration curve for the actuator is given in Figure 4.8. Its motion begins when the reflected waves from the model travel back to the moving gauge. The motion continues until the reflected waves reach to the paddle and return back to the moving gauge. The gauge moves in the same direction as the incident waves with a constant speed within this period. The wave group speed and the arrival times of the wave train to the gauges and the model are computed according to linear wave theory. For the solution of the dispersion relation (Equation 2.13) an iterative procedure is utilized for each set of experiments. Longer waves are scanned along the full length of the actuator. For the waves with shorter wavelengths compared to the length of the actuator only a few envelopes are scanned within the same period to reduce the speed and increase the resolution of the data. The programming details of the moving gauge are explained in more detail in Appendix A.

4.5.   Wave Generator

Waves in nature are commonly generated by winds blowing over the water surface. Although there are examples of small-scale wind-generated wave tanks, this method is not commonly used since the tank should be closed and sufficiently long to generate the desired waves (Hughes, 1993). The waves can also be generated with a moving wave board with a known period and stroke (Dean and Dalrymple, 1991). Although this is a very simplified approximation of the field conditions, the results were in reasonably good agreement with linear wave theory. There are a lot of studies in coastal engineering that successfully use moving boards for wave generation (Huges, 1993). Two of these models are presented in Figure 4.9 where S is defined as the stroke.
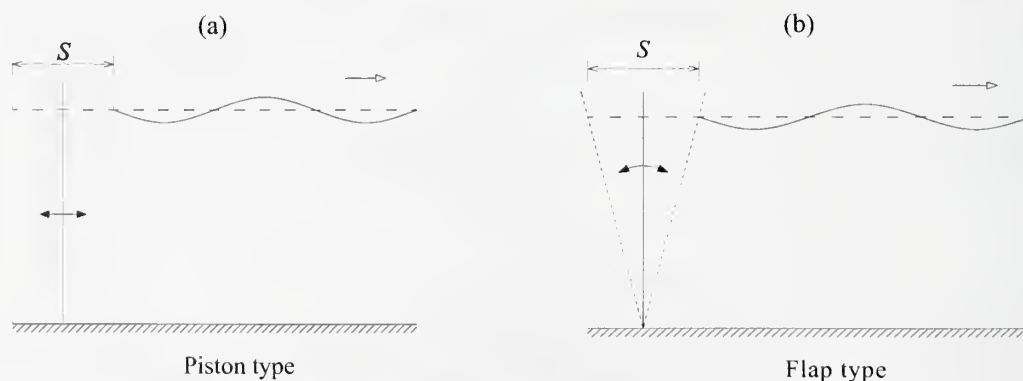
Figure 4.9 Two-dimensional wave generators: (a) Piston type, (b) Flap-type.

The same boundary value problem for two-dimensional waves propagating in an incompressible irrotational fluid defined in Chapter III is used to derive the wavemaker equations. Only the lateral boundary conditions differ from the wave propagation solution. On the open end the waves propagate outward by radiation condition. The kinematic condition should be satisfied along the wavemaker boundary. This boundary condition can be derived from the function that defines the boundary, which is written as:

$$x(t) = \frac{S(z)}{2} \sin \omega t \qquad (4.16)$$

where $S(z)$ is the stroke of the paddle. If the governing two-dimensional equations are solved with first order boundary conditions, the ratio of wave height to stroke, S, can be found as:

$$\text{Piston type,} \qquad \frac{H}{S} = \frac{4 \sinh^2 kh}{\sinh 2kh + 2kh} \qquad (4.17)$$

$$\text{Flap type,} \qquad \frac{H}{S} = \frac{4 \sinh kh}{\sinh 2kh + 2kh} \left(\sinh kh + \frac{1 - \cosh kh}{kh} \right) \qquad (4.18)$$

where k is the wave number (Eq. 4.2). The Equations 4.17 and 4.18 are plotted in Figure 4.10. It can be seen from the figures that in deep water, for the same wave height it is easier to generate waves with a flap-type generator, whereas the piston type is more efficient in shallow water. Also, it should be noted that more power is needed to generate waves with a piston type wave maker at the same depth. Therefore, it is more reasonable to use a flap-type wave generator for the current model studies where the waves are mostly within the deepwater range.
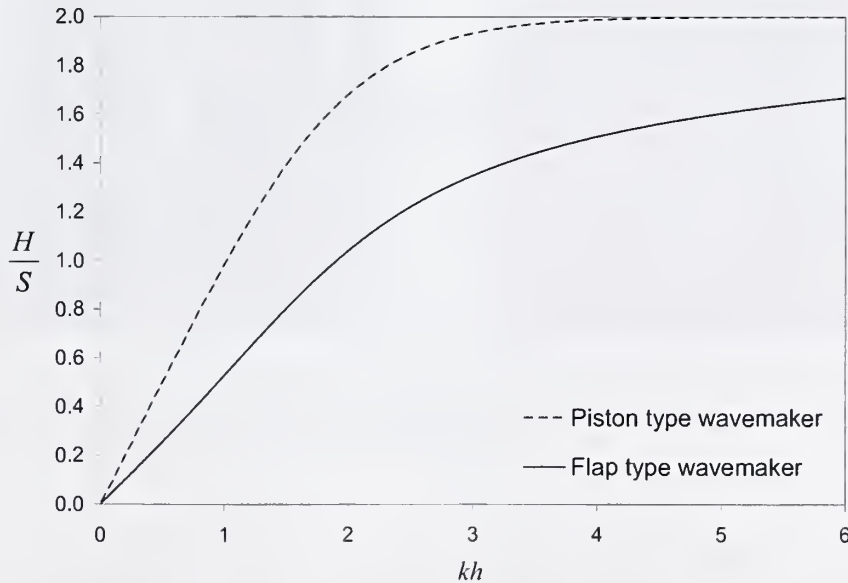
Figure 4.10 Wave height to stroke ratios versus relative depths for piston and flap-type wave makers.

4.5.1. Design Considerations for the Wave Generator

Based on the given scaling requirements given in Section 4.2 and the theory discussed in Section 4.3.2, a moving board wave generator was designed and constructed at the National Sedimentation Laboratory. Since we are considering mostly deepwater waves, as discussed in the previous section a flap-type wave generator would be more appropriate for the model studies (Figure 4.11 and 4.12). An electromechanical positioner was used to control the sinusoidal motion of the paddle. The motor of the positioner was connected to a Parker 6K4 4-axis controller (Figure 4.13c). Communication between the controller and the computer was provided by an Ethernet connection. The Parker motion control programming language was used with a Windows-based programming tool called Motion Planner to write a code that produced a sinusoidal motion profile. The paddle was made of an aluminum sheet hinged to the bottom of the tank 1.4m away form one end. It was connected to the positioner with an aluminum rod.

The operation of the belt drive was tested for different frequencies and amplitudes to obtain an operation curve. A safety line keeping all the data inside the operation window is plotted using a curve fitted to the test data. Theoretical limits of acceleration and velocity were obtained based on this safety line and the corresponding frequency vs. belt motion amplitude curves are plotted for those limiting velocity and acceleration values. Since the belt drive is connected with a different moment arm to the paddle, there is a separate limiting curve corresponding to a particular connection arrangement which is presented in Figure 4.14. The area between the maximum stroke, frequency limit, and limiting curve is the operation area for the wave generator.
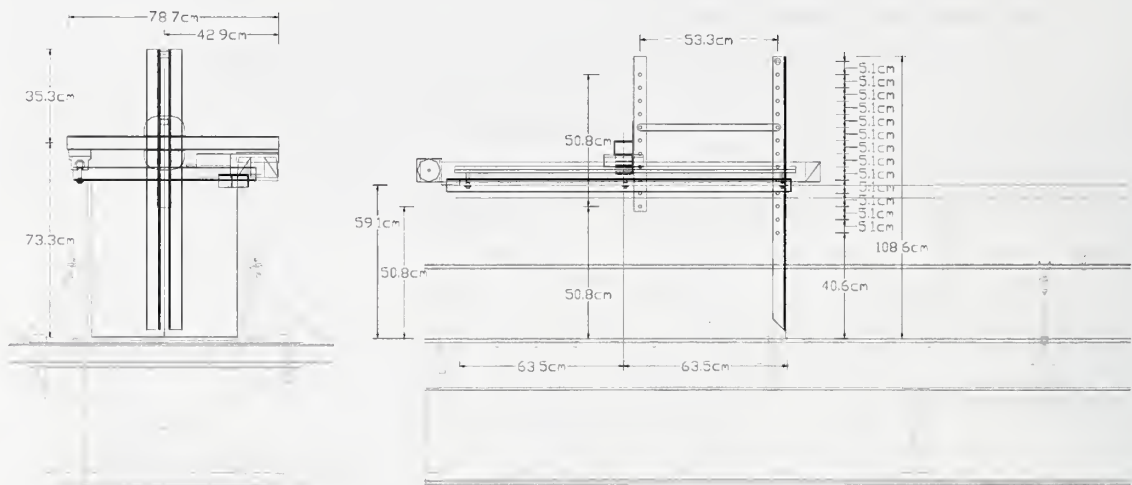
Figure 4.11 Scaled drawings for flap-type wave generator.
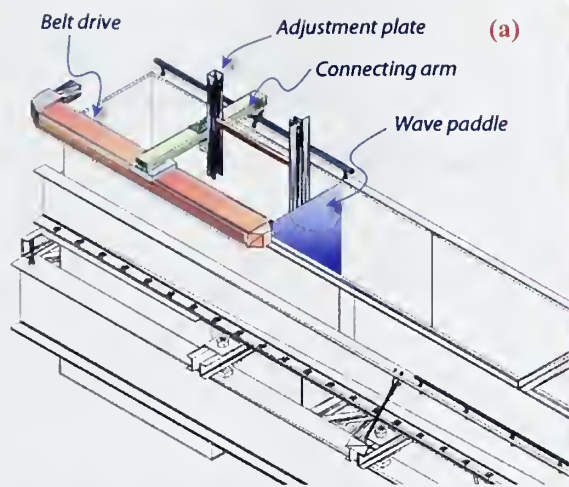
Figure 4.12 (a) The scaled view of the flap-type wave generator driven the belt drive with definition terms and (b) a picture of the wave generator after construction.
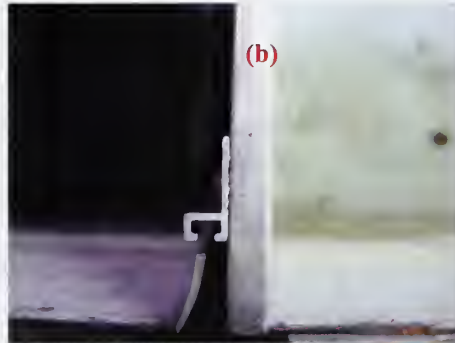
Figure 4.13 (a) The energy dissipator behind the wave paddle was improved by adding pipe sections and more aluminum wool and, (b) the sides of the paddle were sealed to cut the leakage to the front (c). Parker's 6K4 4-Axis Servo/Stepper Controller.
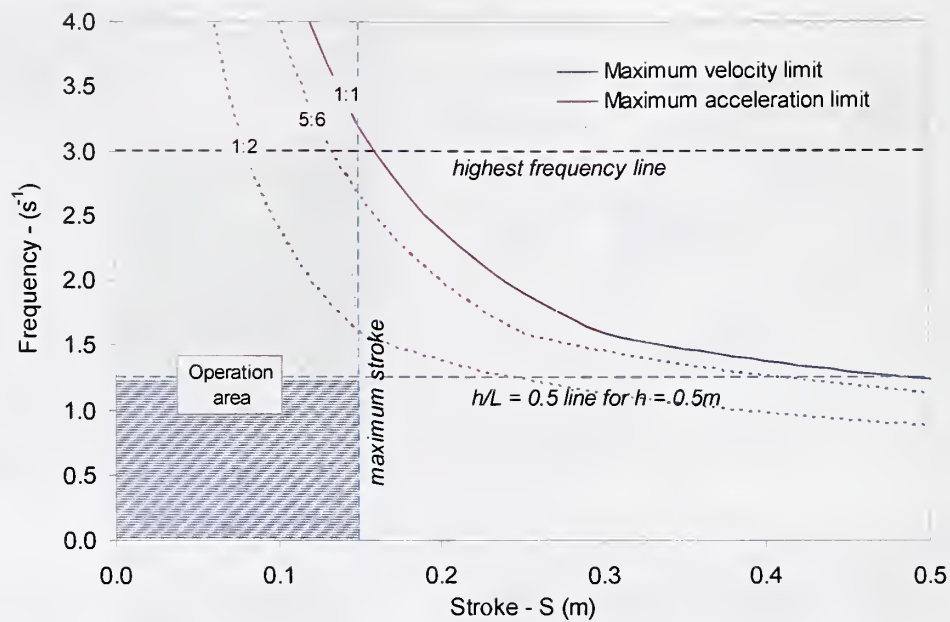
Figure 4.14 Operation curve of the Belt Drive and design curve of the wave generator.

The motion generated by the belt drive was recorded by a position sensor and compared with a theoretical sine curve. The belt drive motion matches the sine path well, confirming that the motion profile is appropriate for wave generation. The minor fluctuations in the velocity and acceleration curves are due to noise in the analog recording of the motion sensor. The calibration curves of the wave generator are given in Figure 4.15. In Figure 4.16 two examples of the recorded paddle motion are given. The paddle amplitude is divided by the stroke to get the dimensionless amplitude. The x-axis represents the phase of the motion. As clearly shown in all of the comparative figures, the wave generator produces the desired wave signal. Most of the spread in Figure 4.16 is due to the noise created by the analog position sensor connected to the paddle.

To test the efficiency of the wave generator, a set of experiments was performed just after the construction of the wave tank in February, 2006. A second set of tests was carried out after the completion of the breakwater model studies in July 2007. Each set of experiments was repeated three times to reduce the uncertainties (Table 4.3).

Table 4.3. Test conditions for the wave generator calibration

Water depth	Gauge location (distance from the paddle)	Wave height	Wave period	Incident wave steepness	Relative depth	Stroke ratio
h (mm)	xg (m)	H (mm)	T (s)	$\dfrac{H_i}{L}$	kh	$\dfrac{H}{S}$
367	2.5	14 – 76	0.5 – 1.5	0.01 – 0.1	0.9 – 5.9	0.58 – 1.6
422	2.5	14 – 76	0.5 – 1.5	0.01 – 0.1	1.0 – 6.8	0.51 – 1.7
466	2.5	14 – 76	0.5 – 1.5	0.01 – 0.1	1.1 – 13	0.55 – 1.8
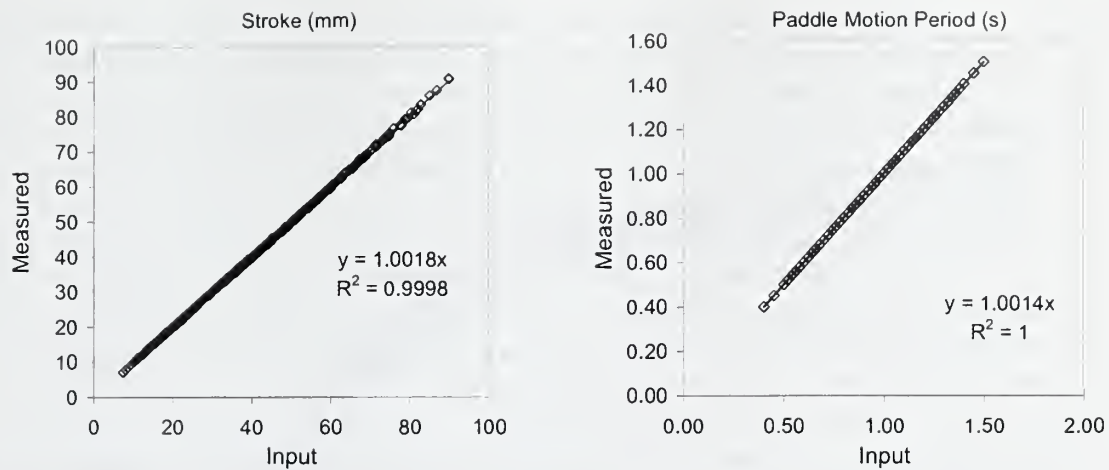
Figure 4.15 Calibration curves of the wave generator.
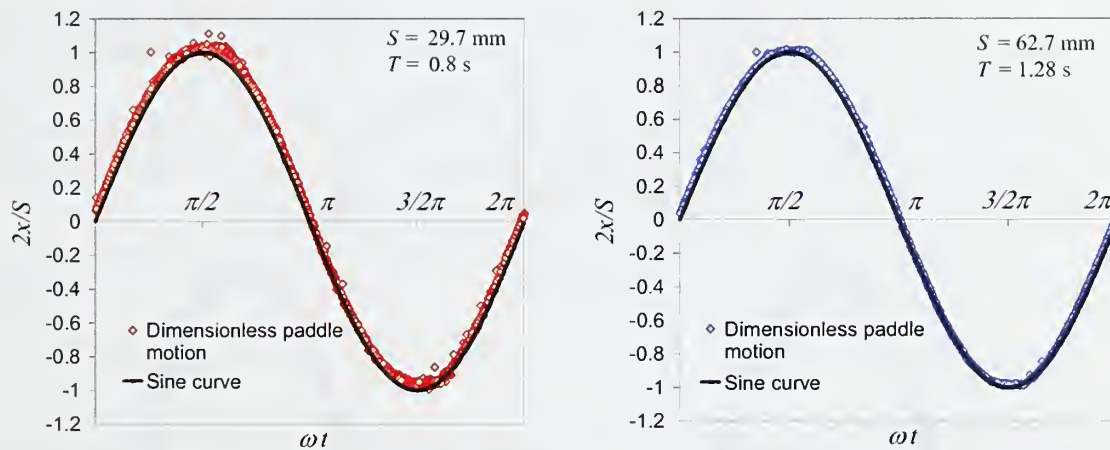
Figure 4.16 Frequency (a) and stroke response (b) of the wave generator (July, 2007).

It was observed that the motions of the water body behind the paddle influenced the generated waves in the tank. Depending on the wave period the energy transmitted around the sides of the paddle either increased or reduced the wave height at the measuring location. To test this effect, a separate set of experiments was performed. This time, the sides of the paddle were sealed with vinyl and more dissipators were added behind the paddle (Figure 4.13a). The experiments were run for the same water depths as the previous case with no sealing. The stroke and motion period response of the wave paddle are shown in Figure 4.17.

In Figure 4.17 the dimensionless water surface elevation is compared with a sine curve for two different periods. The steepness H/L for both of the data was 0.04. It can be seen that the generated wave heights are slightly less than the desired values for $T = 0.54s$. As mentioned earlier, the measured wave height was used during the experiments and therefore this effect is not reflected in the test results. Still, none of the problems discussed are significant enough to create out of the range values for most of the model studies.

The relation between the relative depth and the wave height to paddle stroke ratio was obtained experimentally and compared with first order wave maker theory in Figure 4.18 at three different water depths. It is proven that small amplitude waves within the transition and deepwater range are in good agreement with the first order flap wave maker equation (Equation 4.18). The data are less dispersed compared to the previous tests, but there is still a spread for higher frequencies. The averaged data for both with the paddle side gaps sealed and unsealed for a water depth of 466 mm is presented in Figure 4.19. The periodic deviation from theory is eliminated when the side gaps of the paddle are closed. However, the deviation from the theory is not too high for either of the cases. Also, the measured wave heights were used instead of the input wave height throughout the model studies, making it plausible to neglect the effect of the side gaps of the paddle. In Figure 4.20 the wave height to stroke ratio is plotted for different wave steepnesses at a water depth of 466 mm. It can be seen that the wave generation is not greatly affected by wave steepness.

Also, from all comparative figures it can be seen that for larger values of kh the data becomes more scattered. This can be explained by the fact that when the period of the generated waves gets closer to the lateral natural period of the tank, which was 0.51 seconds for $h = 466\ mm$ the wave patterns become irregular. Moreover, the wave heights measured are relatively lower for higher frequencies then nominal values, possibly because of side friction along the channel and viscous dissipation.
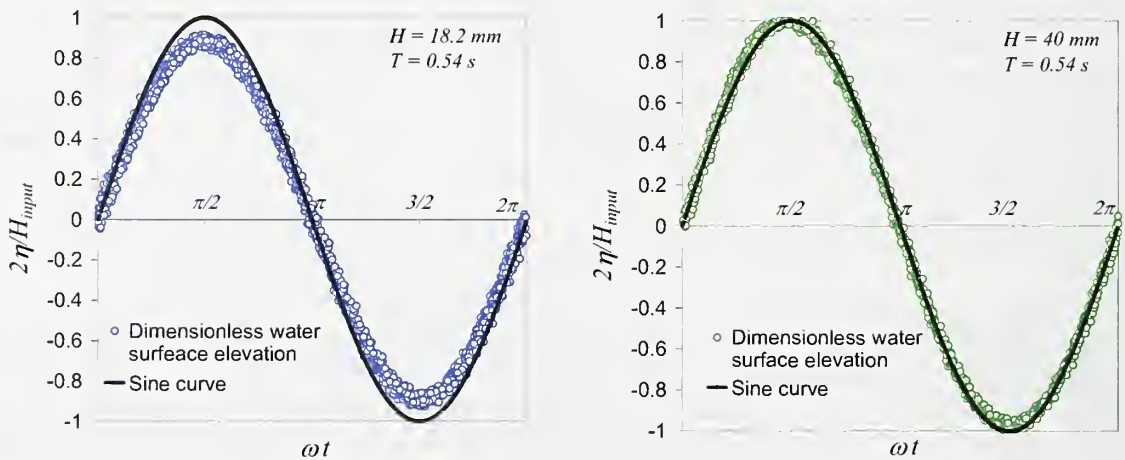
Figure 4.17 Dimensionless water surface elevations at 4 m away from the wave generator compared with the analytical solutions.
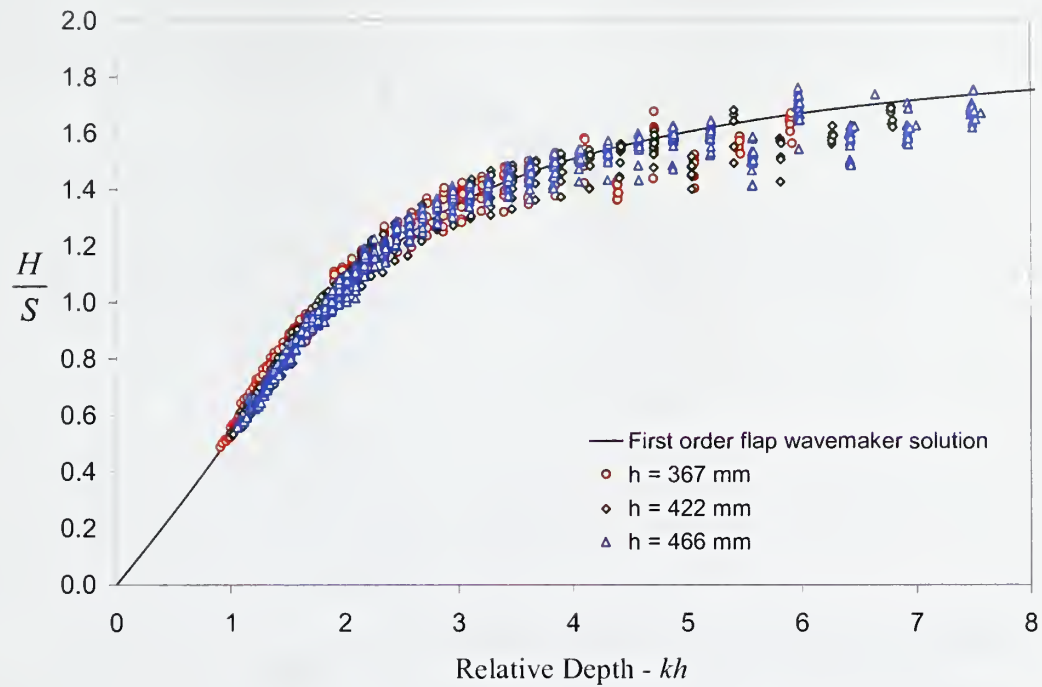
Figure 4.18 Comparison of the experiments with side gaps of the paddle sealed.
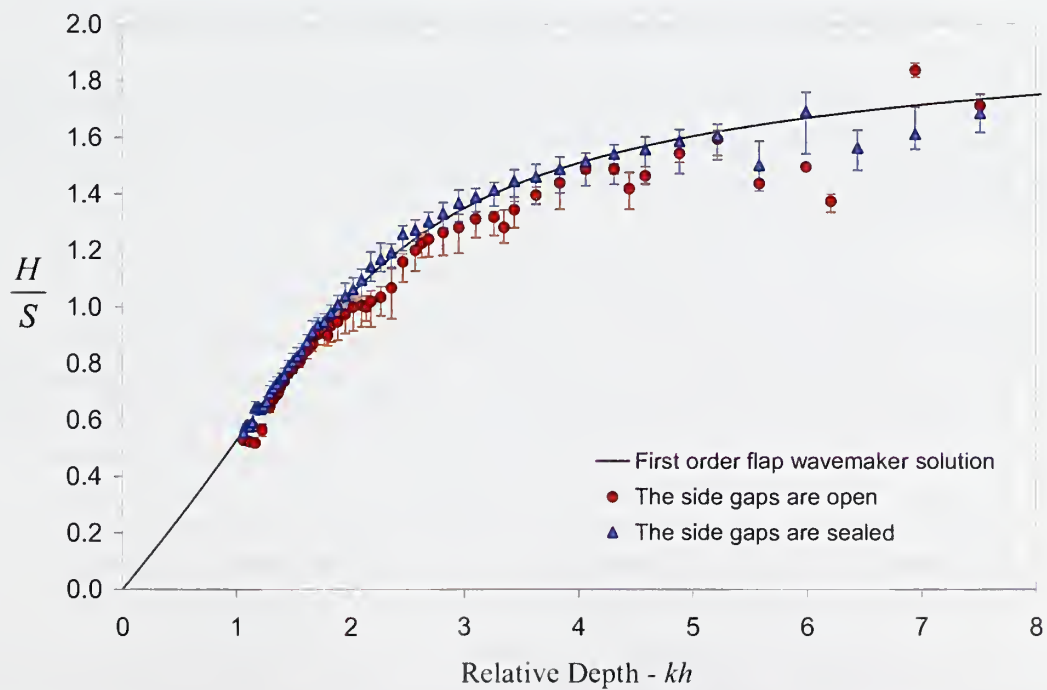
Figure 4.19 Comparison of the experiments with side gaps of the paddle are open versus sealed.
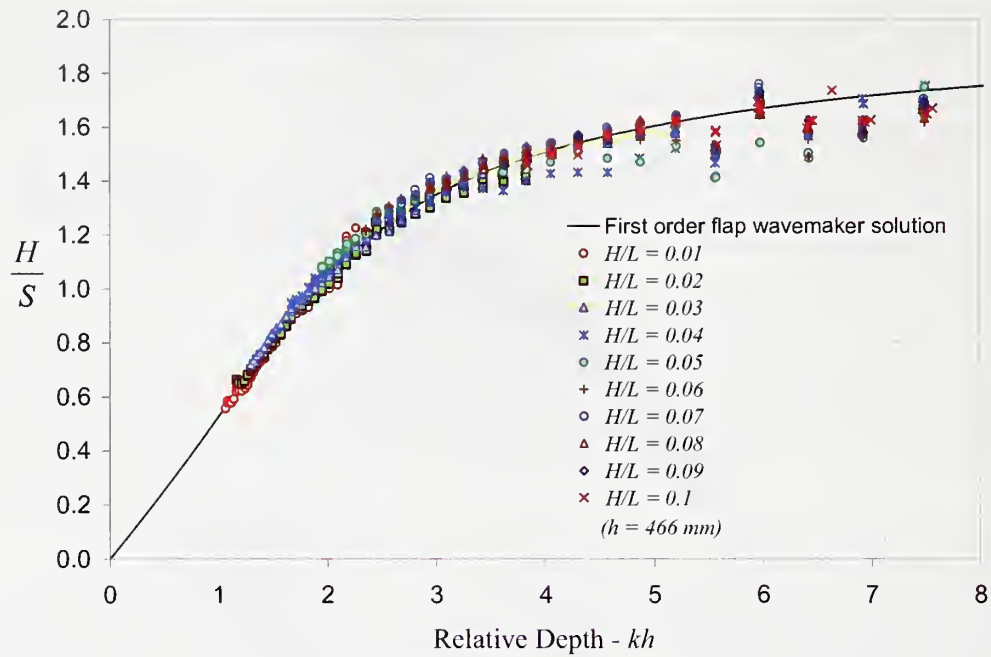
Figure 4.20 Effect of wave steepness on generated waves.

4.6.   Wave Absorber

One of the major problems of physical model studies is reflection from the boundaries. The back wall, side walls and even the wave paddle itself reflect the waves back and forward until all the energy is completely dissipated. This will result in an irregular and complex wave pattern, which makes it difficult to control the model parameters. A wave absorber was used to minimize the effect of reflected waves from the back wall of the wave tank.

There are two major methods that have been used in physical models to eliminate wave reflection: active and passive absorption methods. Active absorbing method is not widely used due to high costs. One common type of active absorber is a wave board moving with the incoming waves so that the waves act as if they pass through the boundary (Dean and Dalrymple, 1991). The most common passive wave absorbers, generally a beach of constant mild slope, less than 1:10, is constructed using sand, gravel or stones. These wave absorbers are designed for an effective reflection less than 10%. The use of a mild slope consumes a considerable length of the tank, creating a problem for limited tank lengths. Increasing the roughness of the surface or using porous materials with different geometric arrangements may help to reduce the length of the absorber.

An analytical solution for the reflection coefficient for the reflection from a smooth, mild and constant slope beach is given by Miche (1944) (Goda and Ippen, 1963). The two assumptions of Miche's analysis are: waves less than a critical steepness are

reflected completely from an impermeable constant slope beach and for wave steepness larger than the critical value the reflection coefficient decreases with increasing steepness. He developed an analytical formula for the critical deepwater standing wave steepness for a small slope β which is defined as:

$$\left(\frac{H_0}{L_0}\right)_{crit} = \left[\frac{2\beta}{\pi}\right]^{1/2} \frac{\sin^2 \beta}{\pi} \tag{4.19}$$

where β is in radians and the subscript "$_0$" indicates deepwater conditions. The reflection coefficient, deepwater wave steepness and the beach slope are related by:

$$\kappa_r = \begin{cases} 1 & for \quad \dfrac{H_0}{L_0} \leq \left(\dfrac{H_0}{L_0}\right)_{crit} \\[2em] \dfrac{\left(\dfrac{H_0}{L_0}\right)_{crit}}{\dfrac{H_0}{L_0}} & for \quad \dfrac{H_0}{L_0} > \left(\dfrac{H_0}{L_0}\right)_{crit} \end{cases} \tag{4.20}$$

According to the above relation (Equation 4.20), waves steeper than the critical steepness are partially reflected with a reflection coefficient κ_r. To account for the permeability and roughness, Miche (1944) defined a coefficient which was assumed to be independent of beach slope. This coefficient might vary between 0.68 and 1.0 for rough and smooth impermeable barriers and 0.32 is given for rubble mound beach.

Straub et. al (1956) also experimentally showed that for the same absorber length, the permeable absorbers are considerably more efficient than the impermeable ones. For higher values of wave steepness, the reflection coefficients of impermeable and inclined permeable absorbers become closer. For slopes greater then 15°, wire mesh absorbers have noticeably higher efficiency then crushed rock absorbers (Figure 4.21). The length of the absorbers should not be less than roughly half of the wavelength.

Wave reflection from a parabolic beach is less than the reflection from a plane beach with the same length. Although the amount of reflection depends on the absorber length some reflection will occur even when the absorber is very long (Lean,1967 and Madsen, 1983). An estimated reflection coefficient is given by Lean (1967) as:

$$\kappa_r \underset{l \to \infty}{\approx} \frac{fT}{8\pi} \tag{4.21}$$

where l is the absorber length, f is a friction factor which is a function of water depth, resistance coefficient of the absorber, and local wave particle velocity. The efficiency is further increased by increasing the roughness and using porous materials (Straub et. al. 1956, Lean, 1967, Ouellet and Datta 1986, Mani, 1986 and Sulisz, 2003. Also, fibrous material such as aluminum wool, rubberized hair and polyurethane foam reduce the reflections considerably Keulegan (1972).
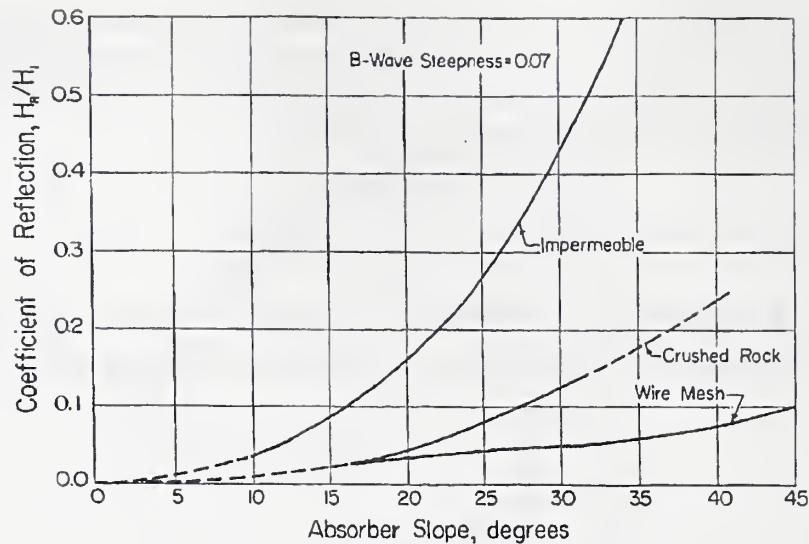
Figure 4.21. Comparison of impermeable crushed rock and wire mesh absorbers (Straub et. al., 1956).

Progressive wave absorbers are utilized to spread the wave energy dissipation along the absorber length. When the waves are transmitted from one medium to another with different properties, there will always be some reflection in response. The idea for an optimum wave progressive absorber is to minimize the overall reflection from the system Le Mehaute (1972). For larger waves the absorber will act as a solid wall while the smaller waves will penetrate freely into the absorber to be reflected from the impervious vertical wall at the end of the absorber. Therefore, higher porosities are more efficient for steeper waves whereas low porosities are efficient for milder waves (Twu and Lin 1991). The maximum absorption will occur for an intermediate height for a specific porosity and grain size. Similarly, greater friction will result in reflection from the front face with no penetration whereas zero friction will cause reflection from the back wall (Madsen, 1983). To increase the efficiency of the absorber, the porosity may be reduced successively along the absorber (Twu and Lin 1991).

4.6.1. Design Considerations for the Wave Absorber

A permeable sloping beach with parabolic cross-section was designed to dissipate the wave energy at the end of the tank. For the optimum design of an absorber with a limited length and for a wide range of water depths, different mechanisms discussed in the previous section must be combined properly. The energy dissipation rate along the absorber length should be distributed such that the reflection is minimized. Reflection occurs in two ways: the reflection from the solid portion of the porous material and the reflection from the back. The primary dissipation mechanisms for the current wave absorber design are turbulence created by breaking of the waves and frictional loss in the boundary layer. The former results on a sloping beach and the latter is achieved by a porous absorber.

Figure 4.22 Expanded metal and aluminum wool used for the absorber.
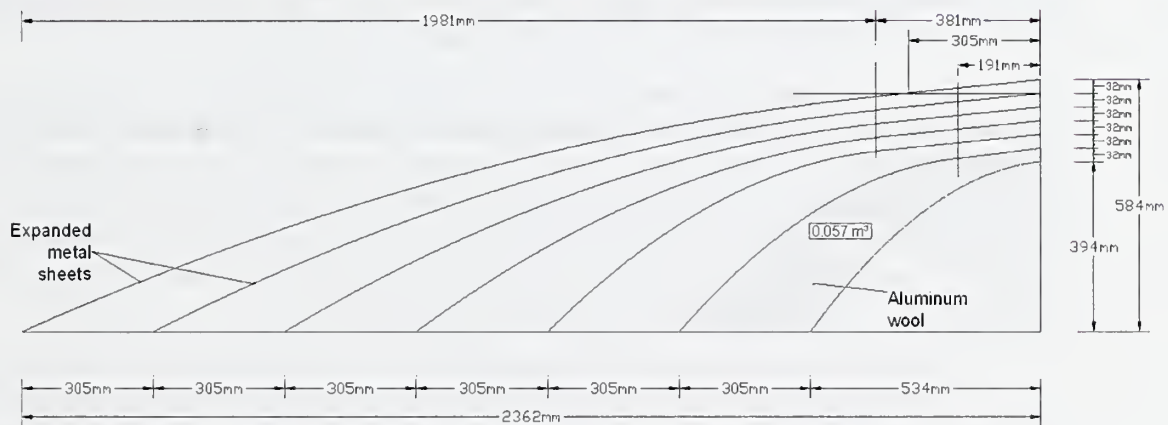
Figure 4.23 Design parameters and the final dimensions of the wave absorber.

The length of the wave absorber is 93" and the height is 23" from the bottom of the tank. The absorber is made of 7 layers. The top 6 layers are made of expended aluminum sheets and the bottom layer is made of solid aluminum sheet. The space between the bottom two layers is filled with aluminum wool. The arrangement is shown in Figures 4.22 and 4.23.

The mesh size of the expanded metal was selected to be much smaller than the minimum wave height to reduce the size of the eddies. The areal porosity, ε_p, of the mesh was:

69

$$\varepsilon_p = \frac{\text{projected area of the openings}}{\text{total area}} = 0.65 \tag{4.22}$$

Volumetric porosity, ε_v, is:

$$\varepsilon_v = 1 - \frac{\text{bulk density}}{\text{solid density of aluminum alloy 3003 (0.099lb/in}^3)} = 0.86 \tag{4.23}$$

where the bulk density is:

$$\text{bulk density} = \frac{\text{weight}}{\text{total volume}} \tag{4.24}$$

The absorber was tested for different wave heights, periods, and water depths to cover the range of variables given in Tables 4.1 and 4.2. The reflection coefficients of the absorber are plotted in Figure 4.24. It can be seen that the reflection coefficient is less than 10% for almost all of the data points. The results were also compared with the experiments conducted by Straub et. al., 1956, in Figure 4.24. There is good agreement between the two data sets for the proposed range of wave properties. The dashed line is plotted according to Miche's theory given in Equations 4.19 and 4.20 for a plane beach with the same length (24.6% slope). The reflection coefficient is plotted for different wave steepness in Figure 4.25. The reflections depend on incident wave steepness such that for steeper waves the reflection coefficient is lower. There is an oscillating pattern in Figure 4.25 for different relative depths independent of steepness.

Another important property of the absorber is the dependency of the absorber on the water depth. Since the porosity of the absorber changes with the water depth, the reflection coefficient might also change for different depths. It can be concluded from Figures 4.26 that there is no significant dependency of the reflected wave height on the water level in the tank. The absorber is more efficient for lower depth as expected, but it is still efficient for higher water levels within the design depth range. For higher values of relative depth, kh, the reflection coefficient greater than 10%.

In Figure 2.27, the wave height measured at 2.5 m away from the wave generator and the wave height extracted from the envelope is compared. It is shown that the heights computed with the envelope maximum and minimum heights gives reasonable results and can be used for the further experiments.
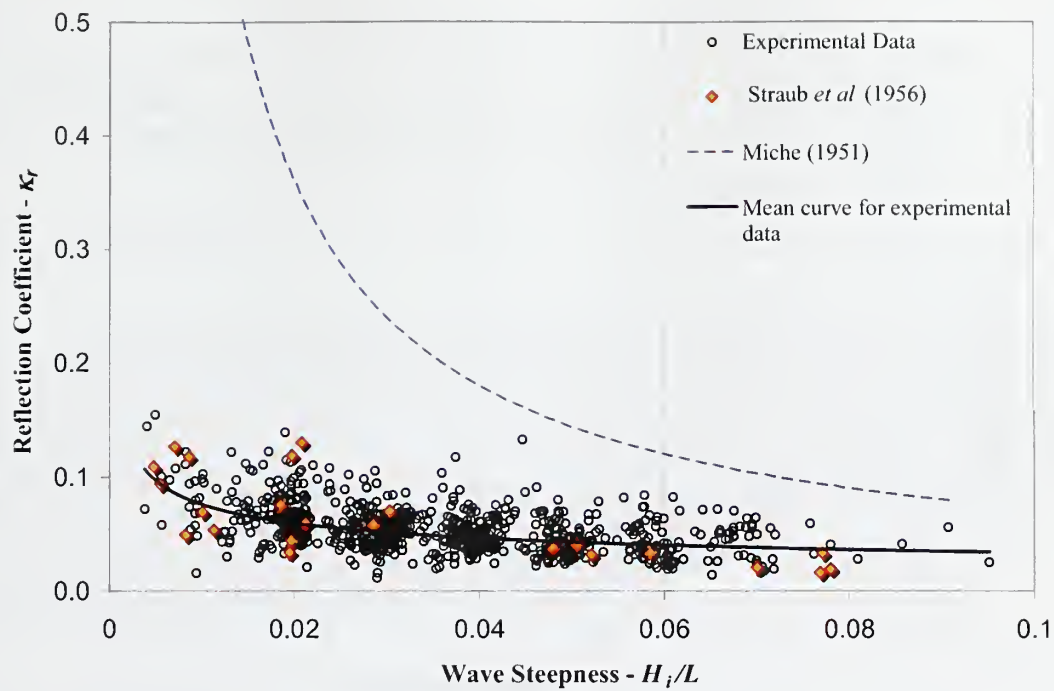
Figure 4.24 Comparison of the current data with the data from Straub *et al*, 1956.
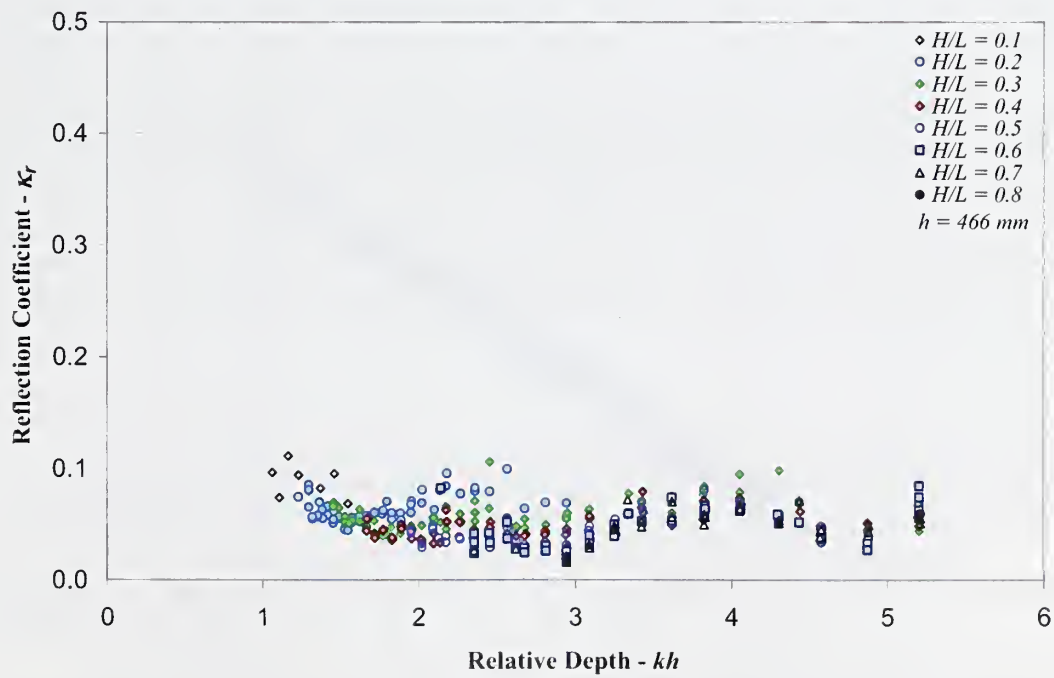
Figure 4.25 Effect of relative depth on reflection coefficient for different wave steepness.
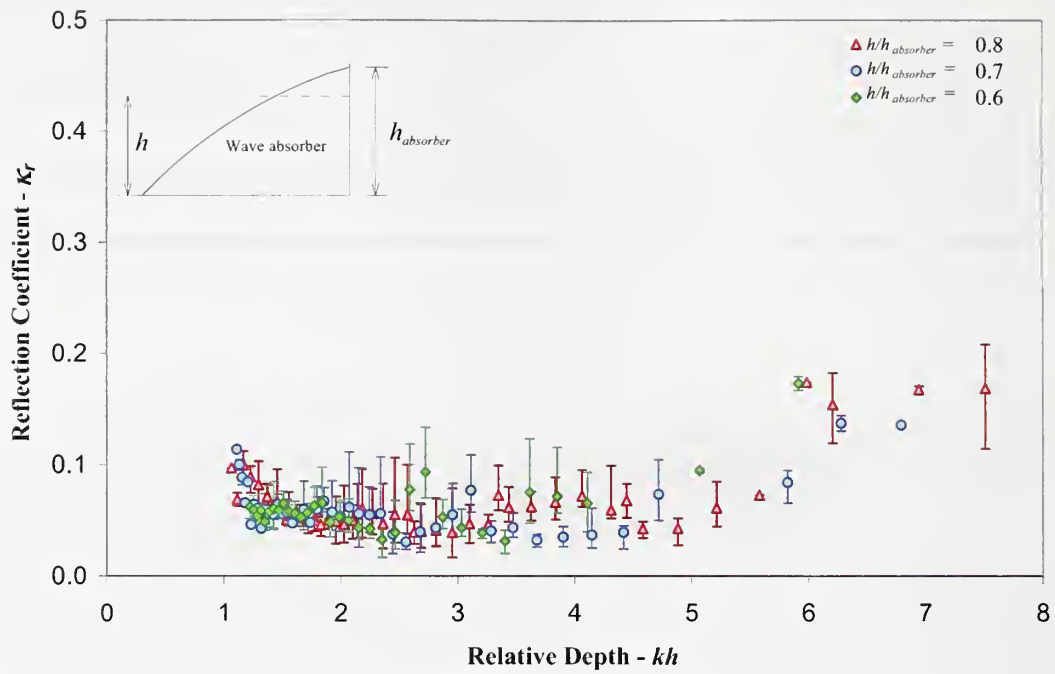
Figure 4.26. Variation of the reflection coefficient for different depth ratios of the absorber.
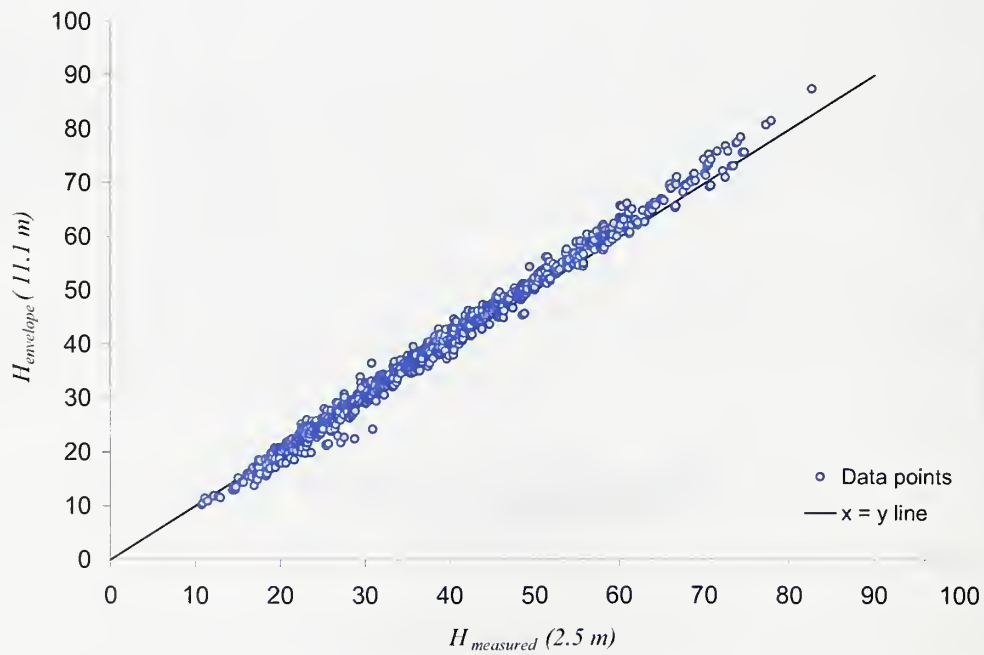
Figure 4.27 The comparison of the gencrated wave heights at 2.5 m with the wave heights calculated at 11.1 m from the standing wave envelope.

V. EXPERIMENTAL RESULTS

5.1. Introduction

The breakwater models were tested in the wave tank at the NSL with different constraints. The design considerations and construction details of the wave tank were given in Chapter IV. In this chapter, the conducted experiments with the breakwater models and their results will be introduced. Experimental procedures are described in Section 5.1. In Section 5.2 the tested models are described with their construction details. The limitation of the experimental setup is discussed in Section 5.3. The general experimental procedure is given in Section 5.4. The results of the experiments are presented and discussed in Section 5.6.

5.2. Description of the Physical Models

PVC pipes of various diameters were used to construct the model breakwater to be tested in the wave tank. The density of the PVC pipe was 1.41×10^3 kg/m³. The bulk densities are discussed separately for each model. The composite breakwater models are constructed by connecting two or more pipe sections together. The conducted experiments are classified according to the restraining properties of these breakwater models. If the breakwater model is constrained completely it is referred to as "fixed", if it is moored to the bottom of the flume with a single cable it is called "bottom moored", if it is restrained with a horizontal arm hinged to the sides of the flume then it is referred to as "arm-restrained" and if the model is restrained with two vertical pipes on each side then it is called "pile-restrained". These models are described separately in the following sections.

5.2.1. Fixed Models

The breakwater models in this group of experiments are completely restrained with no motion allowed. The ends of the pipes were sealed with rubber to exclude water and facilitate positioning in the wave channel. The widths of the pipes were matched to the width of the flume to hold them in place with only side friction during the experiments. The axis of the cylindrical pipes was adjusted perpendicular to the direction of the incoming waves.

To extend the range of parameters three different sizes of models were used. The diameters of single pipe models were 114 mm, 60.2 mm and 48.5 mm. To construct multiple pipe models 60.2 mm 48.5 mm and 33.4 mm diameter pipes were bundled together. The pipes were taped at their ends to keep them together.
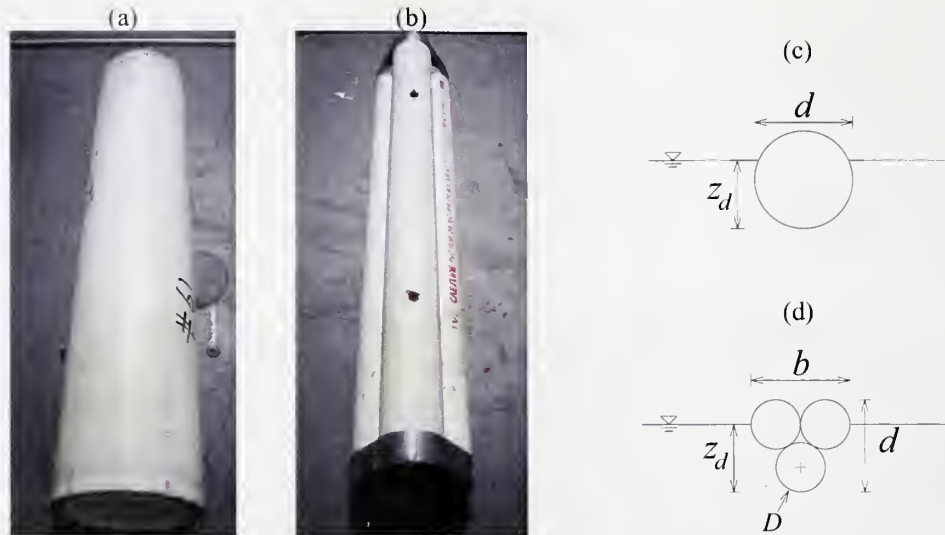
Figure 5.1. Model breakwaters: (a) single pipe with a diameter of 114.6 mm, and (b) a bundle of pipes with diameters of 97 mm each. (c) Definition sketch of single pipe models and (d) bundle of pipes.

The single pipes were immersed 50%, 70% and 100% of their diameter into the water. The bundled modes were tested for only 70% submergence. The pictures and definition sketches of two fixed modes are given in Figure 5.1. The dimensions and the ranges of some parameters of the fixed models are given in Table B.1.

5.2.2. Bottom Moored Models

The pipes in this set of experiments are tethered with a mooring line to the bottom of the wave tank. Pipes with the same diameters as in fixed model experiments were used for both single and multiple pipe bottom-moored models. The ends of the pipes were sealed with rubber to avoid water entering the pipes. The axis of the cylinders was aligned perpendicular to the incident wave direction. Braided microfilament fishing line was used as the mooring cable. The breakwater stayed on the water surface because of buoyancy, and the draft was adjusted by changing the tension in the mooring line. The breakwater was restrained on the axis coinciding with the mooring line. Two mooring cables were connected at a distance of one fourth of the length of the pipes from both ends and attached to the flume bottom.
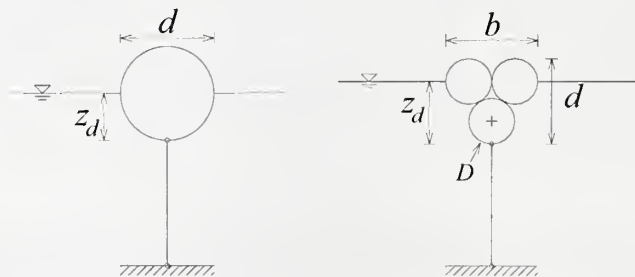
Figure 5.2 The configuration of the bottom moored breakwater models.

74

The pipes were slightly shorter than the channel width to avoid side friction. The gap between each side of the breakwater and the flume sidewall was 5 mm. A definition sketch is given in Figure 5.2. For small displacements compared to the length of the mooring cable, it can be assumed that the cylinder was restrained in the vertical axis and free to move along the horizontal axis. Rotation was partially restrained by the buoyancy. Three-dimensional motions of the model were neglected. The ranges of the experimental variables for different sizes and arrangements are given in Table B.2.

5.2.3. Arm-Restrained Models

In this configuration, the pipes were constrained horizontally with an arm attached to the sides of the flume with a hinge (Figure 5.3). The pipes were connected to the arm at two points along the axis of the pipe with fixed joints restricting the rotation of the pipe. The length of the arm was 125 cm from the pivot to the pipe, and the distance between the two restraining arms was 22 cm. Since the arm length was much larger then the wave height the models can be assumed to be fixed along the horizontal axis. Similar to the bottom moored models, the pipes were water-proof providing sufficient buoyancy to float over the water surface.

The submerged draft of the pipe is adjusted by adding weight on the holding arm. Two different diameters of pipes were used to cover the range of dimensionless parameters. The list of parameters for these models are presented in Table B.3.
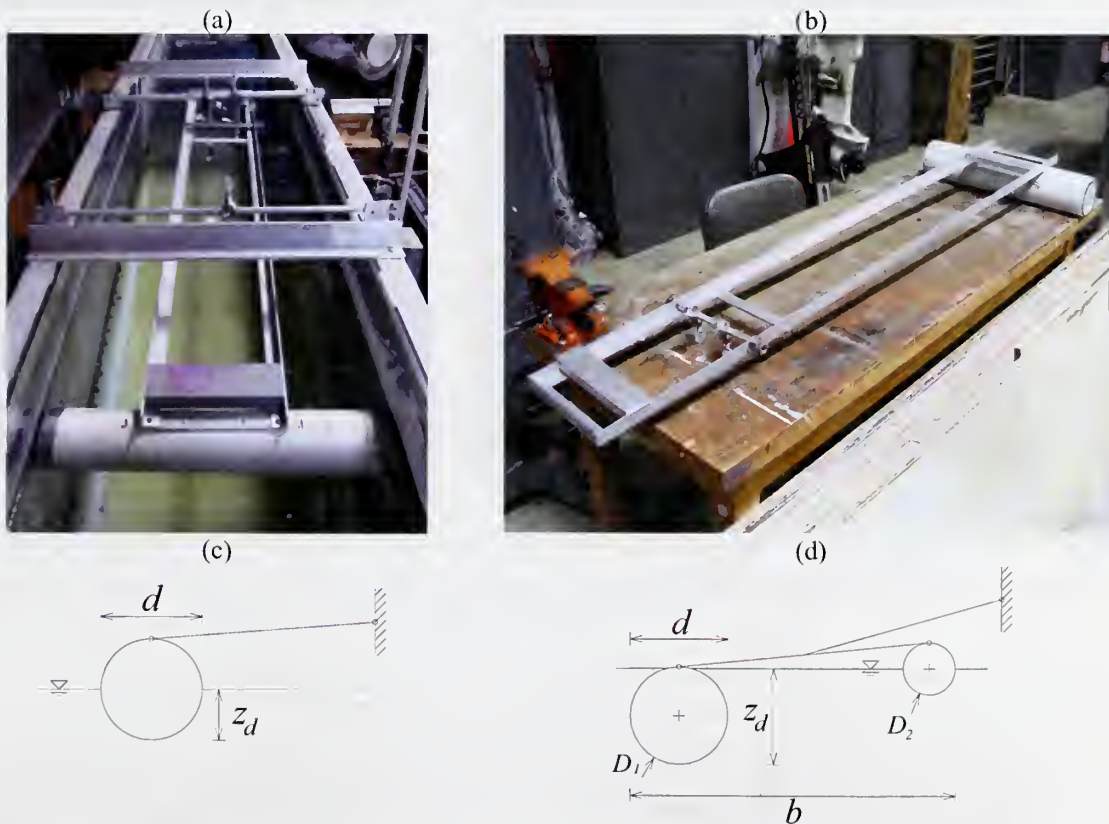
Figure 5.3. The configuration of the arm-restrained breakwater model.

5.2.4. Pile-Restrained Models

Pile-restrained breakwater models were constrained by two vertical piles on each end of the breakwater to maintain the model's position. The piles were made of aluminum rods clamped to the sides of the flume. The spacing between the flume and the piles was 1 cm. The density of the model was adjusted using Styrofoam caps at both ends. The remaining gap inside was filled with water to increase the inertia.
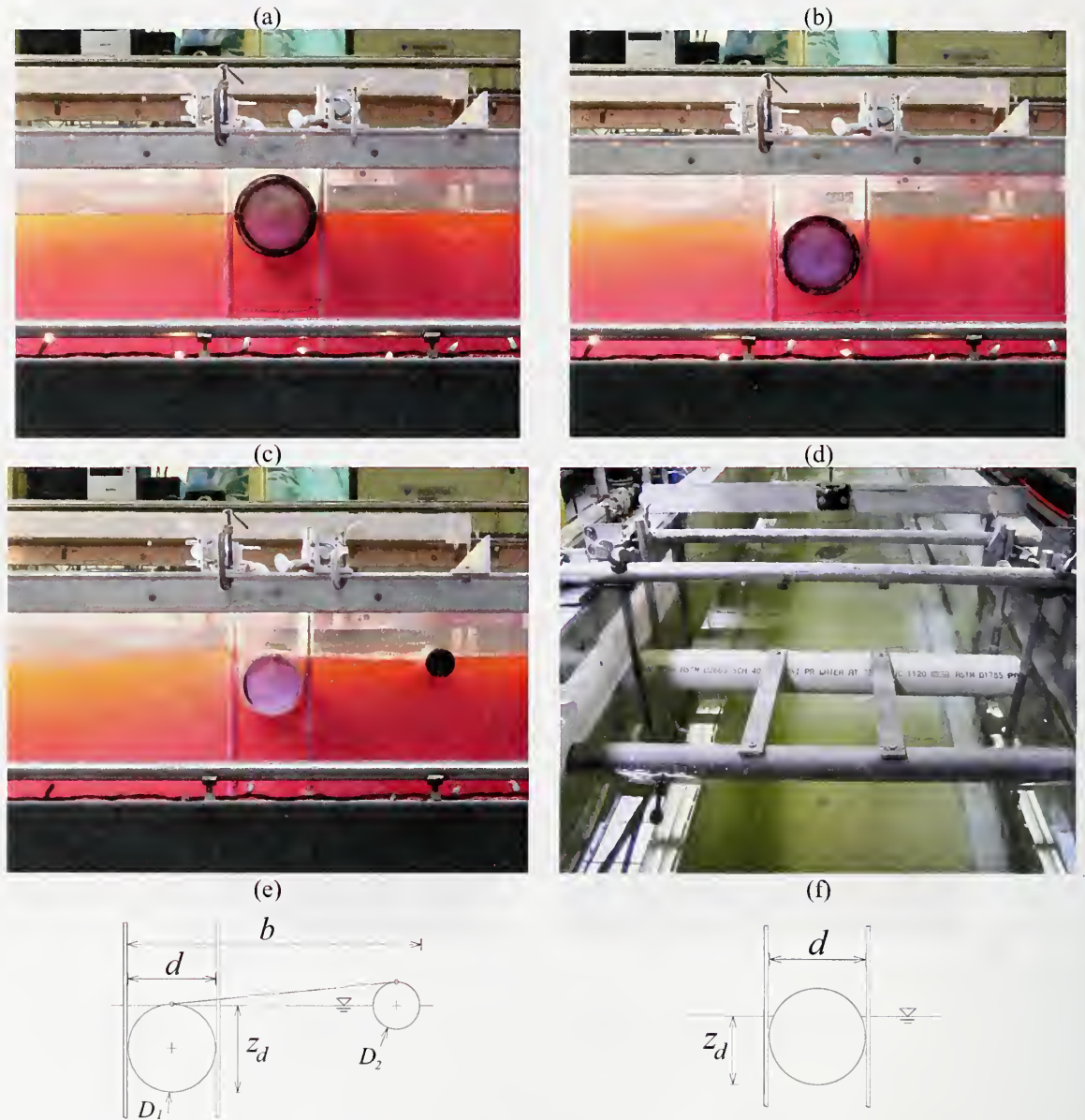
Figure 5.4. The general configurations of pile-restrained breakwaters (a and f) half-submerged single pipe, (b) fully restrained single pipe (d = 114.6 mm) and (c, d and e) the configuration of pile-restrained breakwater with two pipes (d =300 mm, D_1 = 89 mm and D_2 = 42mm)

The circular pipe sections were completely restrained in the horizontal direction, but they were free to move vertically and roll. The ranges of experimental parameters are presented in Table B.2 for each pile-restrained breakwater configuration. The general view of the single pipe configuration is given in Figure 5.4.

The composite model was built by connecting two pipes with two aluminum plates attached at the top of the pipe sections (Figure 5.35b). The submergence of each pipe was adjusted separately. Only the first pipe was restrained between the piles. The rigid connection between two pipes prevented the horizontal movement of the second pipe and rolling motion of both pipes. The gap in between two pipes provided a confined region for the overtopped waves to dissipate. The ranges of parameters and model configurations are presented in Table B.4.

5.3. Limitations of the Setup and Uncertainties

The current wave tank setup is limited to a certain range of wave heights and periods. The results of the experiments are influenced by the characteristics of the flume itself, the wave generator, the wave absorber, the water level sensors and the method of data analysis. Beyond certain limits, these can have a significant effect on experimental results.

As discussed earlier, when the wave frequency is close to the natural frequency of the flume in the lateral direction, there may be an influence on the data due to amplified secondary waves. For water depth of 466 mm the lateral natural frequency is estimated around 0.51 s. This corresponds to a relative depth of kh=7.2 (Figure 4.2). The longitudinal natural period is far out of the range of the experiments (15.6 s). The natural oscillations of the water body behind the paddle have a minor influence on the created waves along the flume due to the energy transferred around the sides of the paddle. The wave generator is limited by the acceleration and velocity of the belt drive. Therefore, all the experiments are kept within the operation area shown in Figure 4.16.

The water level sensors used during the experiments have an accuracy of 1.25 mm and 30Hz resolution. The surface tension might become significant for small wave heights. During the dynamic interaction between the gauge and the wave, the water surface will rise and fall periodically. The contact angle for a rising water surface is assumed to be zero. When the water surface starts to fall there will be a delay due to the molecular attraction between the water molecules and the Wave Staff. This can alter the results of experiments with small wave heights.

The reflected waves from the wave absorber interact with the transmitted waves to form standing waves. Since the wave gauge has a fixed location at the down-wave side of the model, the measured transmitted wave height shows deviations that depend on the wave period. This effect can be neglected if the reflection coefficient is less than 10%. Since transmitted wave height is expected to be low for an efficient model, the reflected waves from the wave absorber become insignificant for the range of interest. The

reflection from the wave absorber tends to increase when the wave steepness, *H/L*, is lower than 0.01. Likewise, when the relative depth is greater than 6, the reflection coefficient suddenly increases. The influence of the reflected waves from wave absorber on the recorded data is discussed in Appendix H.

Transmitted wave height is obtained by averaging the wave heights recorded between the arrival of the waves and the end of the data recording. The method of analysis is discussed in detail in Appendix A. Incident and reflected wave heights are extracted from the standing waves (envelops) by locating the nodes and anti-nodes. Therefore, the results are highly influenced by the shape of the envelopes and hence the reflection patterns. Since the recording time is limited by the wave celerity, for low frequency waves the number of waves in an envelope is less and the accuracy decreases. For higher wave steepness, the breaking limit of the waves should be considered. In addition, when the wave period is closer to 0.51 s, the envelope shape becomes irregular for most of the wave heights. This problem becomes more significant in dynamic models due to the additional disturbances created by the model itself.

5.4. Experimental Procedure

The experiments were conducted in the 19 m long wave tank at the USDA-ARS National Sedimentation Laboratory for regular waves and, in deep and transitional water depths. The design and construction details of the wave tank were presented in Chapter IV. The complete list of conducted experiments is given in Tables B.1 through B.4 for the tested models.

The interaction of the waves with the models to be tested will result in some of the waves being transmitted through the model and some of them reflected back. Each set of experiment had to be stopped before the re-reflected wave from the wave generator reached to the offshore water level sensor. In order to maximize the amount of data used to calculate transmitted and reflected wave properties, the distance between the wave paddle and the model should be as large as possible. Yet, the model should be far enough from the absorber and the fixed gauge to reduce the effect of local disturbances. Local disturbances are negligible beyond a distance of 3*h*, where *h* is the water depth (Ippen, 1966). Therefore, the model was installed at a distance of 12.4 m from the wave generator, allowing enough space to take measurements on both sides of the model. The initial position for the moving gauge was 9.6 m and the final position was at most 11 m from the paddle. The fixed gauge was installed 13.8 m from the wave paddle. Both of the level sensors were positioned so that the midpoint of the staff was at the mean water level. The water depth was measured before starting each experiment with a vernier scale point gauge. The water depth, connection point of the belt drive to the paddle, and gauge and test section locations with respect to the paddle were not normally altered, but could be changed if necessary.

A computer program was written in Labview to conduct multiple experiments and store the data. The tasks of the computer program for a single experiment can be summarized as follows. At the beginning of each experiment the program checks the water surface through two level sensors and keeps the system in idle until the water surface becomes still. The wave generation and data acquisition starts automatically when the standard deviation of the water surface fluctuations is below a threshold value. The offshore gauge moves at a certain speed to scan the envelope of reflected and transmitted waves. The wave generation and data acquisition stops automatically at the end of the available time which is calculated according to the wave conditions. The program stores the collected data and waits on idle for the next experiment. The water surface elevation on both sides of the breakwater model, paddle position and moving gauge position time series data was recorded and stored together with water depth and some model parameters into an ASCII file. The details of the computer program are explained in Appendix A. Two sample photos of the experiments with fixed pipes are shown in Figure 5.5. A sample of recorded data is presented in Figure 5.5. Figure 5.6a is the paddle displacement measured by a position sensor during the recording period. Figure 5.6b is the position of the moving gauge with respect to the end of the linear actuator carrying the gauge. Figures 5.6c and 5.6d is show the water level recorded at the moving and fixed gauges.
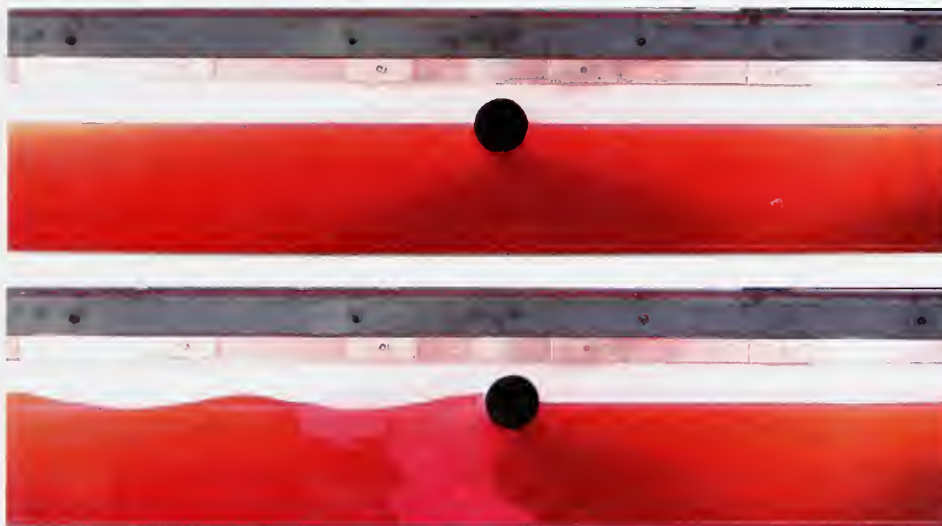
Figure 5.5. Experiments with fixed pipes for $h = 446.5$ mm, $H = 20$ mm, $T = 0.65$ s, $d = 48.5$ mm and $z/d = 0.5$ (Model # 41).
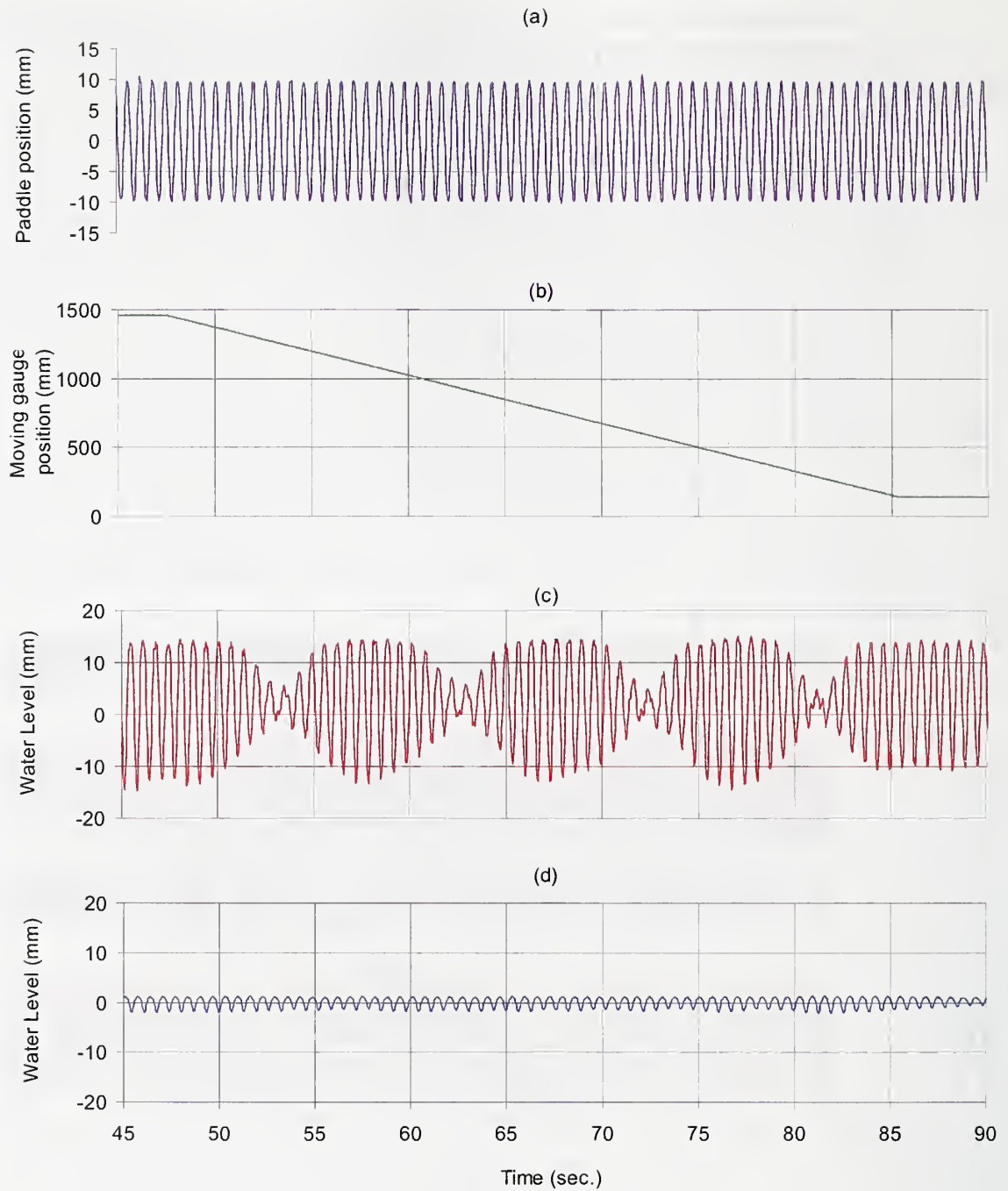
Figure 5.6. Sample recorded data for $h = 446.5$ mm, $H = 20$ mm, $T = 0.65$ sec. and $d = 114.6$ mm. (a) Paddle position, (b) moving gauge position relative to the position sensor, (c) water level from the moving gauge and (d) water level from the fixed gauge.

The data for each set of experiments was analyzed by a computer code developed in LabVIEW. A Bandpass Butterworth filter was used to remove unwanted frequency

components due to the local disturbances and noise in the recorded signal. Transmitted and envelope wave periods were obtained by using frequency domain analysis. The wave period for the envelope was corrected with the speed of the moving gauge. The amplitudes were calculated by locating the peaks of the time series data for each wave. The height of each wave was obtained by calculating the difference between a successive pair of positive and negative amplitudes. The steady portion of the wave height time series signal was then cropped an averaged to get the transmitted wave height. The maximum and minimum amplitudes of the wave envelope were computed similarly. The reflection and transmission coefficients were obtained using the theory discussed earlier in Section 3.3. The details of the data analysis can be found in Appendix A.

5.5.   Repeatability

The experiments were repeated several times to quantify the uncertainties. Some of the reasons for these uncertainties are discussed in Section 5.4. The bulk results of the experiments repeated at different dates are compared for some of the fixed and pile-restrained models. The comparison plots can be found in Appendix C (Figures C.19 through C.24). The experiments were repeated for other configurations as well, but they are not included in this section. The plots presented in Section 5.6.1 and 5.6.3 includes the data of all runs rather than the mean values.

The following conclusions can be made from the comparison of the results from the data collected during different runs:

— Transmission coefficients consistently led to similar results for different runs. The reflection coefficients are more scattered especially at higher wave frequencies. This range corresponds to periods around 0.5 – 0.6 s, which is close to the longitudinal natural frequency of the wave tank. Most of the experiments were conducted at constant wave steepness, H/L and by changing the wave period. This means the wave height was also reduced at wave periods around this range. Due to the limitations of the instruments, small disturbances become significant as the waves become smaller. Hence the data for the lower steepness waves show a wider band of scatter compared to the data of the steeper waves.

— The reflection coefficient is higher at lower wave periods in all of the experiments. The standing wave on the offshore side of the breakwater gets steeper when the reflection increases. The wave breaking and turbulence increase the perturbations of the recorded wave envelope and therefore more error is introduced during the reflection and transmission coefficient calculation.

— In experiments with partially restrained models, secondary waves are generated by the model and superimposed on the transmitted wave train. Yet, the transmission coefficient is calculated by averaging the zero crossing wave

81

height, assuming the transmitted wave is monochromatic and steady. This assumption also increases the uncertainty in the results.

— On the other end of the experimental range, when the waves are longer, the results are influenced mostly due to the gaps beside the wave paddle. The transmission and reflection coefficients at this end fluctuate around a monotonic trend regardless of the model. The details of the formation of these fluctuations are discussed in Appendix H.

5.6.   Results and Discussions

The primary parameter to characterize floating breakwater performance is the transmission coefficient, κ_t as described in the dimensional analysis given in Chapter IV. The other independent variable, the reflection coefficient κ_r, is also considered to identify the breakwater performance. The amount of transmission depends on the breakwater configuration and wave characteristics. The key parameters related with the breakwater are the relative submergence, z_d/d, the geometry of the breakwater, and the method of restraint. The most important wave characteristics are the wave steepness, H_i/L, and the relative depth kh. The data presented in the following sections are organized by these key parameters. For the case of partially restrained models the forces on the breakwater model and the resulting displacements are characterized by the mass and inertia in addition to the geometry and the wave properties. Nevertheless, these parameters are not measured during the model studies and only their effects on the transmission characteristics will be discussed here.

5.6.1. Relative Draft

The first group of plots compares the relative draft, z_d / L, which characterizes the relative size of the breakwater, with the transmission and reflection coefficients. In Figure 5.7, the reflection and transmission coefficients are plotted against the relative draft of the breakwater models of different diameters. The results are also compared with the theory and laboratory work presented in Dean and Ursell (1959) which was earlier introduced in Chapter II. It can be clearly seen that there is a good match between the two experimental works as well as the theory. In the current work, there is relatively less transmission and more reflection. Also, the complete data for the current work is shifted on the x-axis when compared with Dean and Ursell (1959).

The main reason for these differences is that the waves are relatively steeper in the current study compared to Dean and Ursell (1959). The ranges of wave steepness (H/L) values in Dean's study are on the order of 10^{-3} while it is 10^{-2} for the current work. Milder waves have smaller amplitudes for the same wave frequency. Moreover, the relative depth, kh, in Dean and Ursell's experiments is between 0.5 and 6 which is mostly in the transitional range. Hence, more energy is transmitted to the other side under the breakwater compared to the current study and for the same reason there is less reflection.
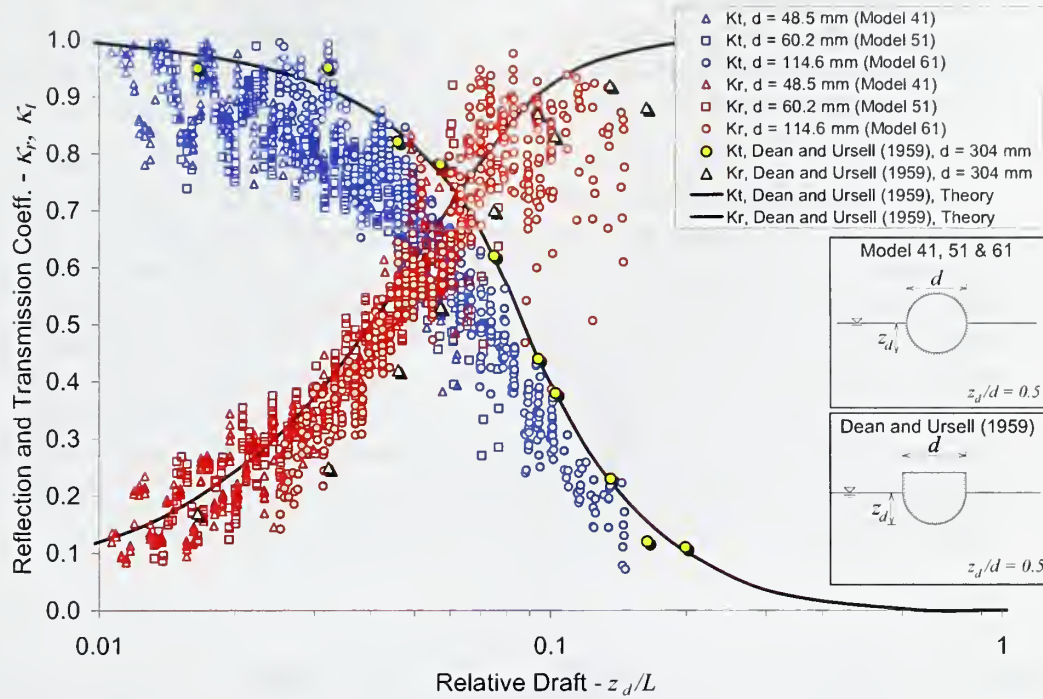
Figure 5.7 Comparison of the experimental data with the theory and experiments by Dean and Ursell, 1959. The dimensionless independent variable Ka ($Ka = 2\pi\, cylinder\, radius / wave\, length$) in Dean and Ursell is modified to match the non-dimensional parameter z_d/L.

Also note that the theory is based on the semi-immersed half cylinder while current experiments are made for a complete cylinder immersed halfway into the water. Therefore, for this study, the reflection is not from a vertical rigid wall. It is from a round surface above the mean water level which may create phase differences along a vertical axis. This minor effect causes irregularities in the standing wave pattern for steeper waves, which affecting the estimation of incident and reflected wave heights.

In Figure 5.8 the transmission and reflection coefficients are plotted against the relative draft, z_d/L, for different sizes of pipes with a submergence ratio z_d/d of 1. The scattering of the data is mostly due to the overtopping waves. The part of the absorber below the mean water level is higher for the same size of half-submerged pipe. However, more energy is transmitted over the breakwater due to overtopping. The overtopped waves cause turbulence on the onshore side of the model and increase the scattering of the transmitted wave signal. There is no significant dependency on the size of the pipe but the data are relatively more scattered for smaller pipe diameters. The reflection coefficient is less than 0.5 for most of the data. This indicates that the energy that is not transmitted is mostly dissipated rather than reflected.

A set of experiments was carried out for a submergence ratio, $z_d/d = 0.7$ with a single pipe diameter of 114.6 mm. The results showed that the reduction in transmitted energy is mostly by reflection. A group of pipes were bundled together to have the same draft and tested to compare with single pipes (Figure 5.1b). Figure 5.9 shows the effect of relative draft on reflection and transmission coefficients for different sizes of bundles.

In general, it can be concluded form all the comparative figures that for larger values of relative draft there is relatively less transmission and high reflection which is in agreement with the energy distribution concept discussed in Section 3.2. Shorter waves at this range start breaking and give rise to scattering in the reflection coefficient. Partially restrained models have similar results compared to the fixed models in terms of relative draft. A major difference between the fixed and partially restrained modes is that the trends of the data for different pipe size tend to separate at higher relative draft. The smaller size pipe sections had higher bulk densities than the larger pipes resulting in lower natural frequencies. Hence, the transmission coefficient is less for smaller pipes even though the other dimensionless coefficients were kept constant. The effect of different geometric configurations will be addressed in Section 5.6.4.
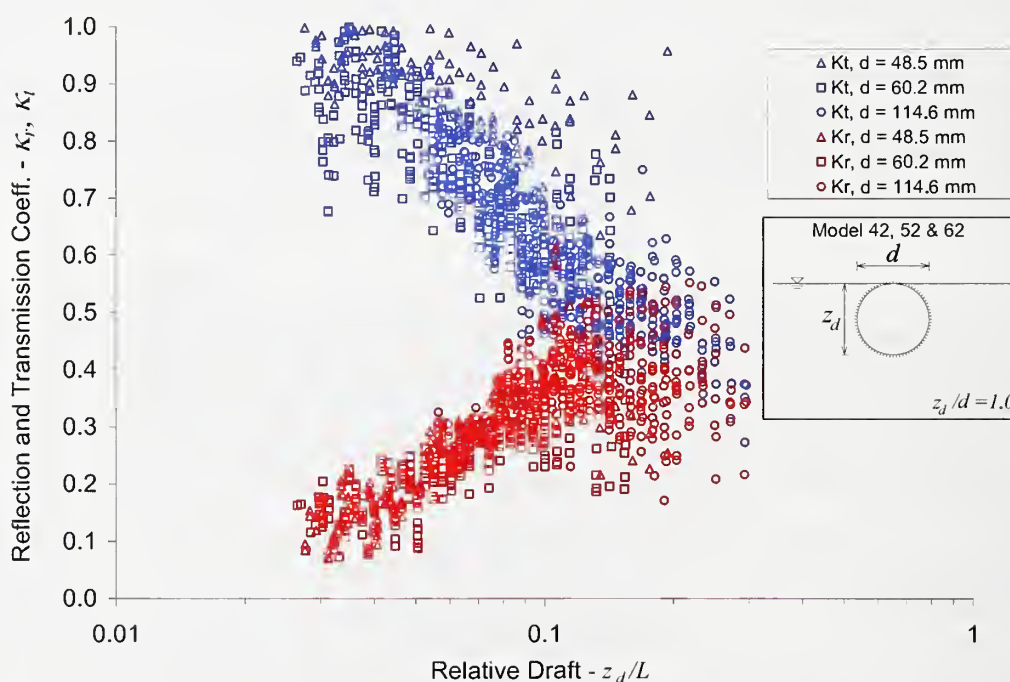
Figure 5.8. Reflection and transmission coefficients of fully submerged fixed single pipe with different diameters.
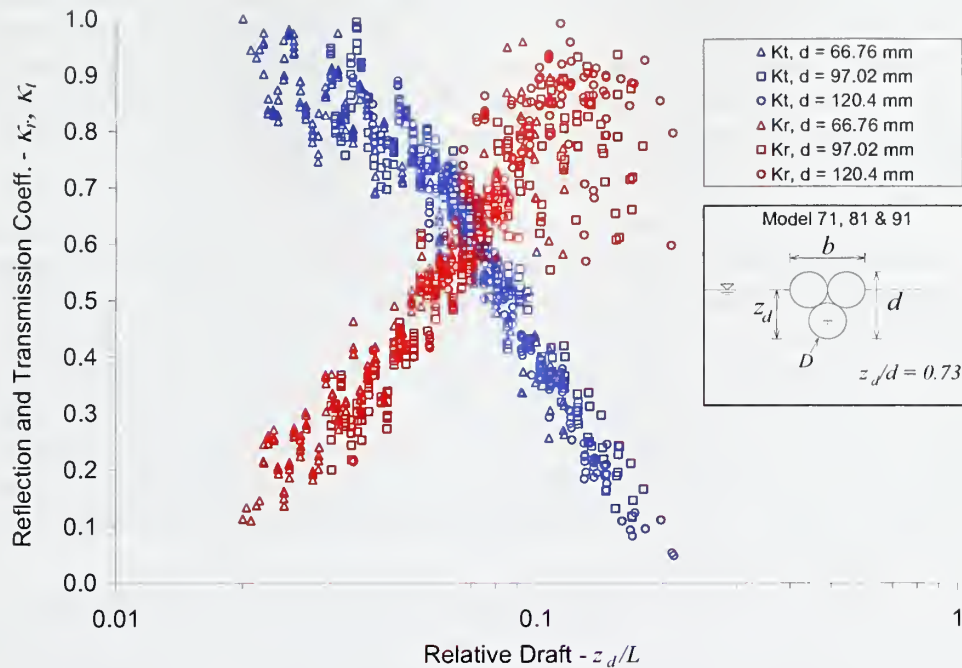
Figure 5.9. Reflection and transmission coefficients of bundle of fixed pipes with different diameters.

5.6.2. Draft Ratio

In Figures 5.10 through 5.17 the transmission and reflection coefficients are plotted against relative depth for the four different configurations discussed earlier. In each plot, the transmission and reflection coefficients are averaged over the range of wave steepness with the same relative depth. The bars represent the range of wave steepnesses for each average point.

Figure 5.10 presents the averaged transmission coefficients for three different submergence ratios of fixed cylindrical pipe sections. The average reflection coefficients are plotted in Figure 5.11 for the same experiments. It can be seen from Figure 5.10 that, on average, longer waves are transmitted more when the cylinder is less submerged. When the waves are shorter, the efficiency of the fully submerged cylinder becomes less dependent on relative depth and the rate of wave attenuation decreases with increasing relative depth.

This can be explained by considering the effect of draft together with the energy transmission by overtopping. It was shown that for a fixed barrier extending downward from the free surface, the transmission coefficient reduces with increasing draft below the mean water level (Ursell, 1947, and Dean and Ursell, 1959). For a fully submerged circular cylinder with no interaction with the free surface, subjected to irrotational flow, the amplitudes of incident and transmitted waves are the same (Dean 1947). Hence, for the same cylinder, if the submergence is increased the transmission coefficient reduces

85

due to the increasing draft but at the same time the amount of energy transmitted by overtopping increases. For shorter waves, the energy concentration gets closer to the surface and the energy transmission due to overtopping becomes significant. But, for longer waves, the energy is spread along the depth of the fluid, and the draft becomes more important in controlling the transmission coefficient. Therefore, the fully submerged cylinder (Model 62) is less efficient for shorter waves.

In Figure 5.11 for the fully submerged cylinder the reflection coefficient is low when compared with the partially submerged cylinders. Although the transmission coefficient for the fully-submerged pipe (model 62) is higher than the others, when relative depth is greater than three, the reflection coefficient is almost one-third of the other configurations. This indicates that most of the energy is dissipated by overtopping, but for partially submerged pipe sections, the attenuation is primarily by reflection. It can also be seen from Figures 5.10 and 5.11 the fully submerged cylinder has more dependency on wave steepness than others. The energy transmission by overtopping is more pronounced in the case of a fully submerged cylinder and as relative depth increases the spread also increases.

In Figure 5.13 and 5.14 two different configurations of bottom-moored pipes, half-submerged (model 64) and fully-submerged (model 65) are compared. For the same size of pipe fully-submerged, moored models are superior to the half-submerged models in terms of attenuation efficiency. Yet, the reflection coefficients are almost the same for the two configurations. The transmission coefficient difference between the two models in Figure 5.13 is by dissipation. As the relative depth increases, the difference between the transmission and reflection coefficients also increases. The transmission coefficients of the two models become closer when the relative depth is larger than 5.
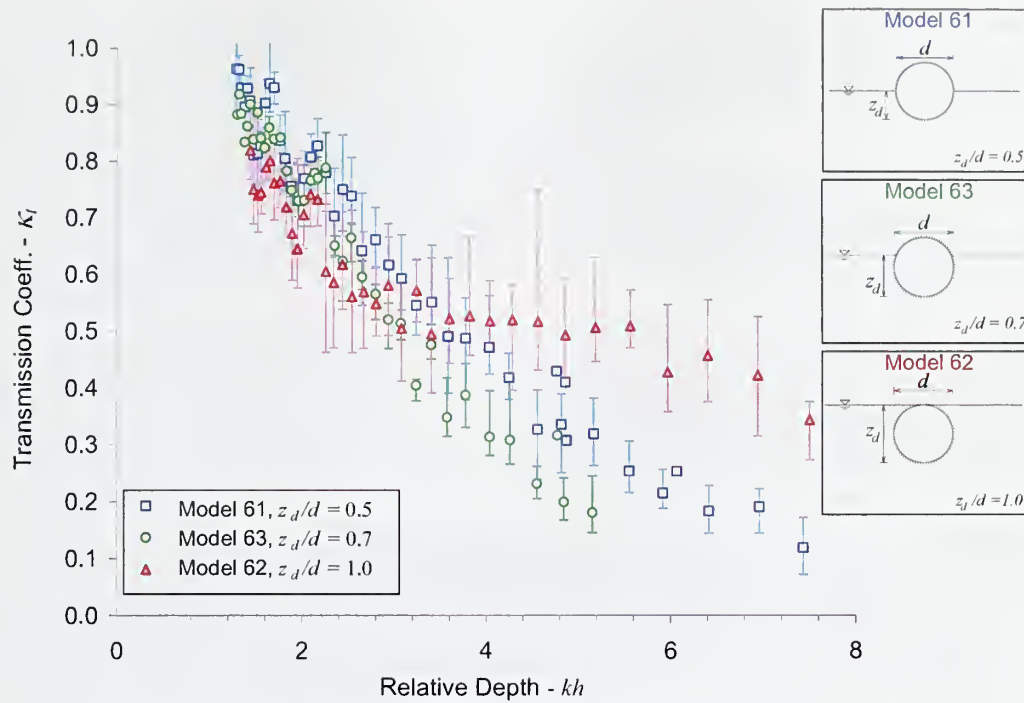
Figure 5.10. Effect of draft ratio on transmission coefficient for fixed pipe with $d = 114.6$ mm. Bars represent the range of wave steepness.
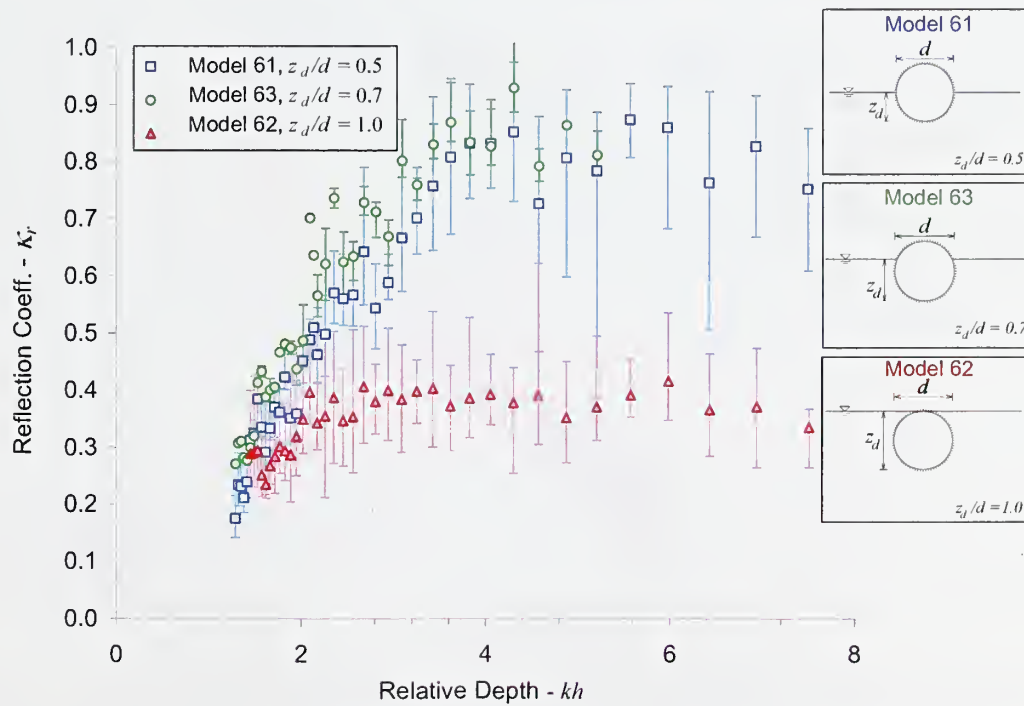
Figure. 5.11. Effect of submergence ratio (aspect ratio) on reflection coefficient for fixed pipe with $d = 114.6$ mm. Bars represent the range of wave steepness.
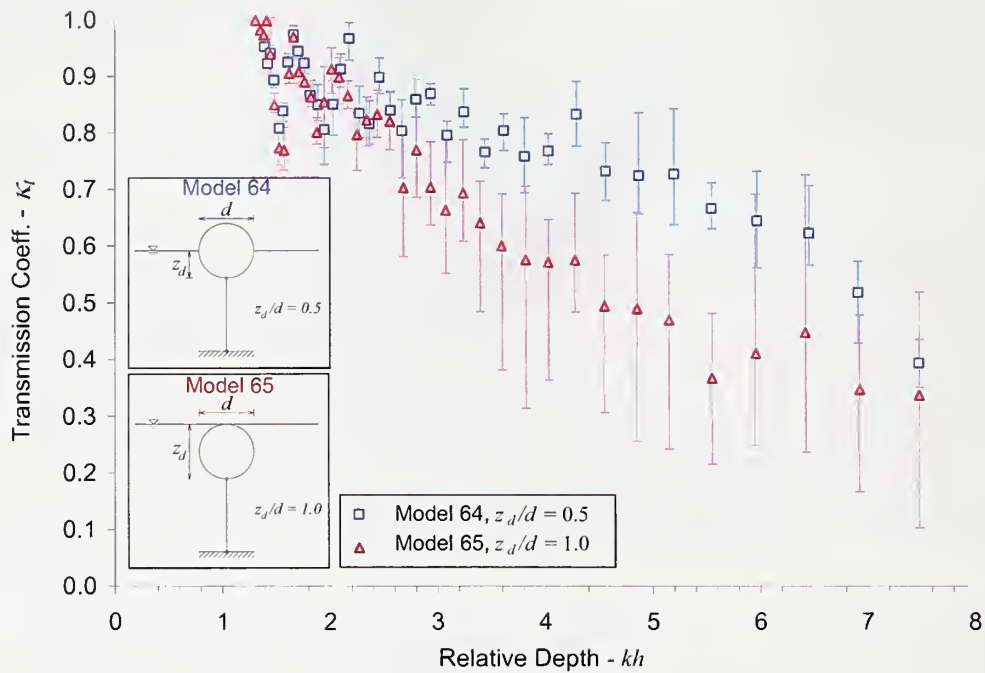
Figure 5.12. Effect of submergence ratio on transmission coefficient for moored pipe with $d = 114.6$ mm. Bars represent the range of wave steepness.
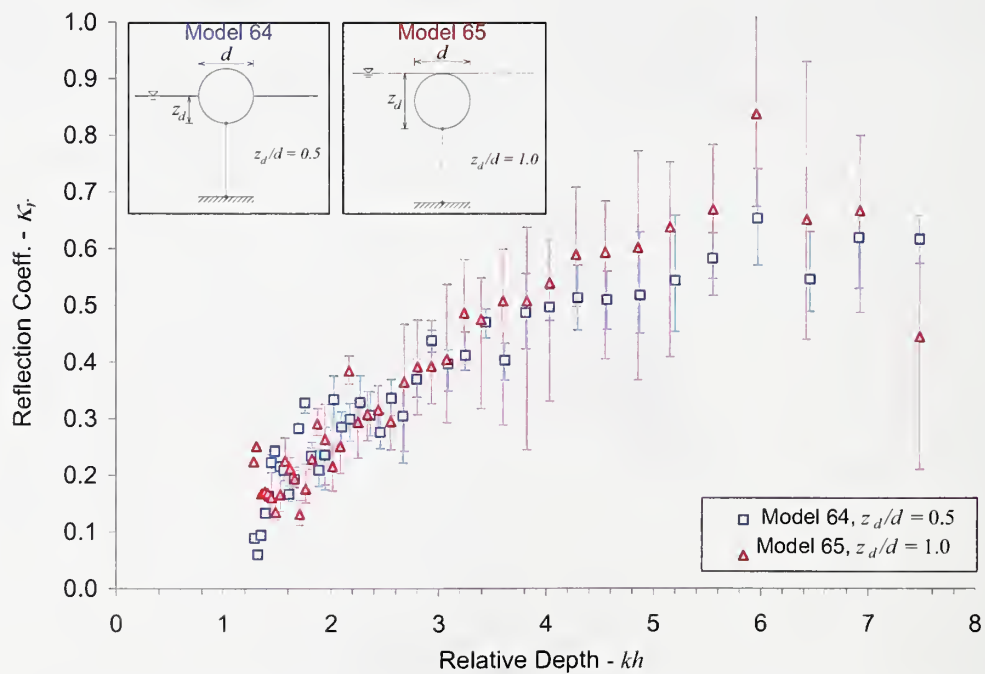
Figure 5.13. Effect of submergence ratio on reflection coefficient for moored pipe with $d = 114.6$ mm. Bars represent the range of wave steepness.

Results for the fully submerged cylinder show wider spread compared to the half-submerged cylinder indicating that the reflection and transmission coefficients depend more on wave steepness for this configuration. The results has a peak at around $kh = 6$ in both transmission and reflection coefficient plots.

The half-submerged and the fully submerged arm-restrained breakwater models are compared in Figure 5.14 and Figure 5.15. Similar to the previous figures, the transmission coefficient is reduced noticeably by increase relative draft and inertia with the added weight.

Since the arm-restrained configuration is free to move around fixed axes it has one-degree of freedom. The holding arm was long enough to allow the assumption that it only moved up and down along the vertical axis with the waves. Therefore, compared to the bottom moored configuration, the arm-restrained model is more likely to block the overtopping waves.

In Figure 5.14, the transmission coefficient is reduced considerably for a wide range of relative depths because of the increased draft and inertia. Unlike the bottom moored configuration, the reflection coefficient is also increased considerably by increasing the relative draft. This indicates that the majority of the wave energy is reflected back.
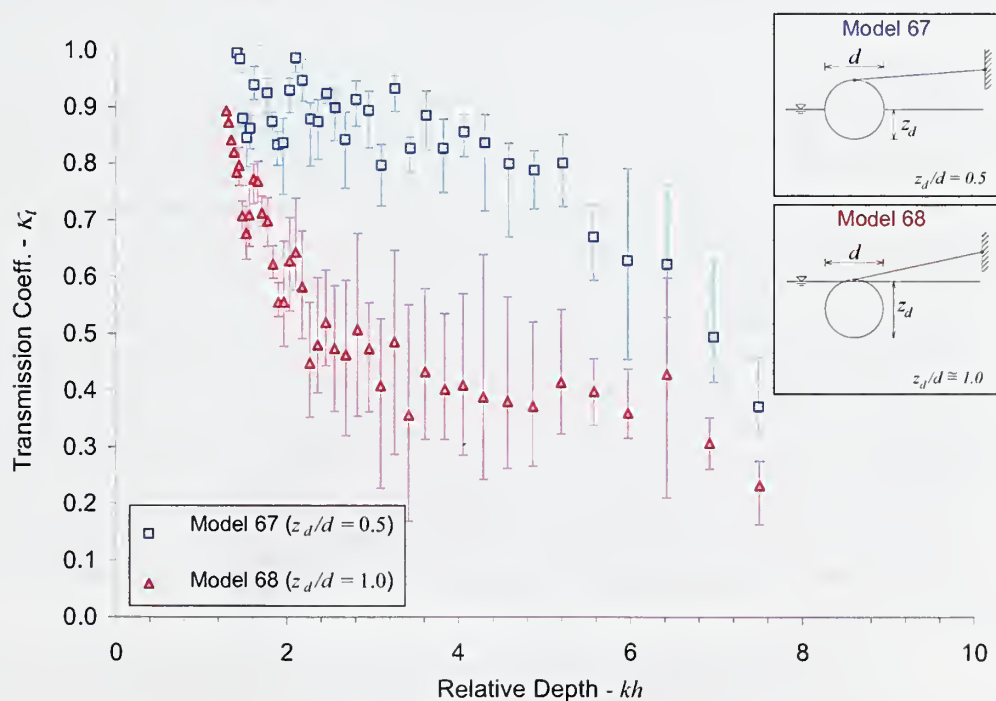
Figure 5.14. Effect of draft ratio on transmission coefficient for arm-restrained pipe with $d = 114.6$ mm. Bars represent the range of wave steepness.
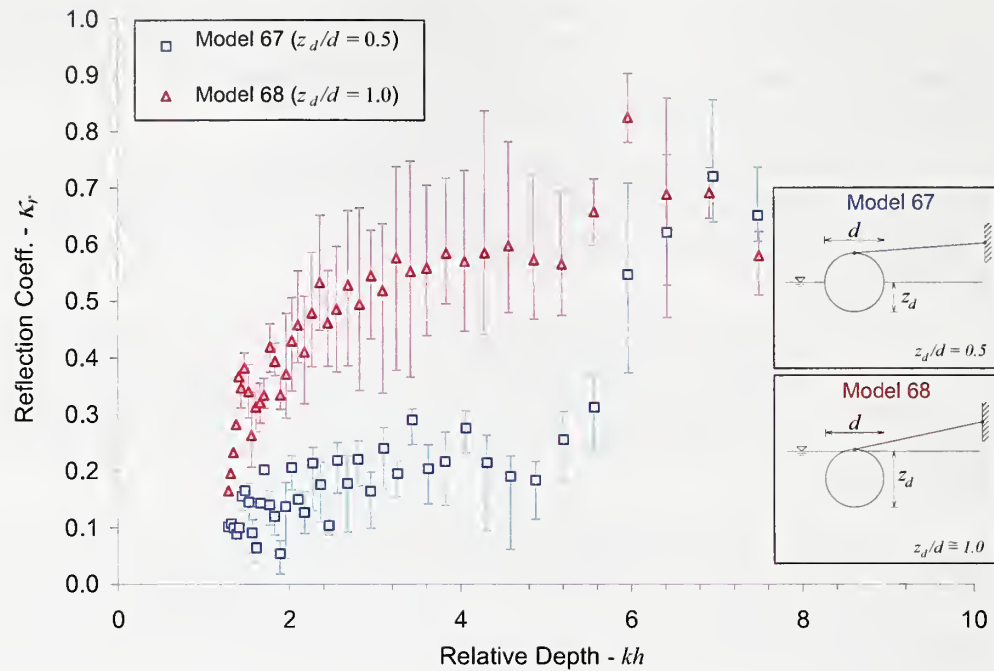
Figure 5.15. Effect of draft ratio on reflection coefficient for arm-restrained pipe with $d = 114.6$ mm. Bars represent the range of wave steepness.

In Figures 5.16 and 5.17 the breakwater models of the same diameter with different amounts of submergences are compared for pile-restrained models. Similar to the other dynamic configurations, pile-restrained models are also relatively less efficient when the draft ratio, z_d/d is 0.5. It can be seen from the figures that for half-submerged configuration, most of the waves are transmitted through the breakwater and there is relatively less reflection. When the pipe is mostly submerged into the water ($z_d/d = 0.96$), the transmission coefficient is considerably reduced and the reflection coefficient is increased. The wider bars indicate that the transmission and reflection coefficients strongly depend on wave height at this draft. Since this model is heavier than the half submerged model, the inertia is also increased significantly. Hence, the cylinder moves less with waves and the majority of the transmission is either over or under the breakwater. As the waves get shorter (kh increases), the wave energy concentration gets closer to the surface and for the same draft less energy passes underneath the breakwater, yet the amount of overtopping also increases giving rise to the transmission coefficient. For this reason, the transmission coefficient stays nearly constant when relative depth, kh is greater than 3.

The highest efficiency of the pile-restrained model is achieved at a submergence ratio, z_d/d of 0.7 which provides optimum draft, inertia and minimum wave overtopping. Figure 5.16 shows that for relative depth kh between 1 and 5 the trend of the averaged transmission coefficient is almost linear but the reflection coefficient in Figure 5.17 first increases and then stays almost constant and finally starts increasing again. In this constant region the reduction in transmission coefficient is mainly due to dissipation.
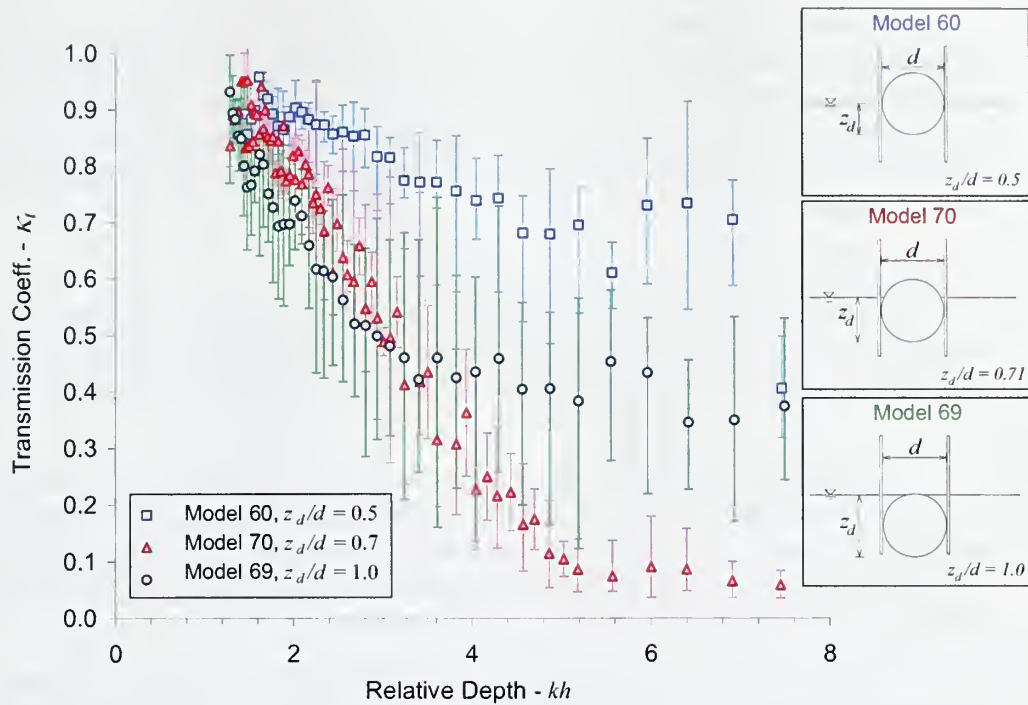
Figure 5.16. Effect of submergence ratio (aspect ratio) on transmission coefficient for pile-restrained pipe with $d = 114.6$ mm. Bars represent the range of wave steepness.
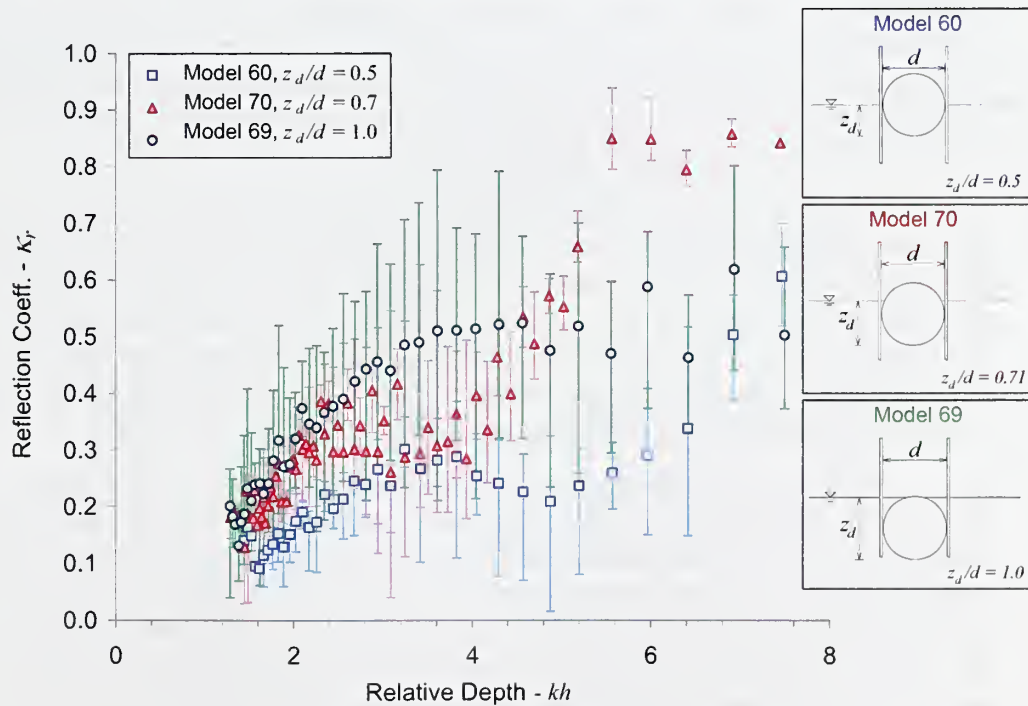
Figure 5.17. Effect of submergence ratio (aspect ratio) on reflection coefficient for pile-restrained pipe with $d = 114.6$ mm. Bars represent the range of wave steepness.

91

It is also seen from Figure 5.16 that model 70 (z_d/d = 0.7) is less efficient compared to model 69 (z_d/d = 0.96) when kh is less than 3 and becomes more efficient when kh is greater than 3. The trends of reflection coefficients for the two configurations intersect at around kh = 4.5. This shows that for longer waves the breakwater motion is important in wave transmission but, as the waves get shorter overtopping dominates in transmitting the waves.

5.6.3. Wave Steepness

A more detailed comparison is made by plotting the transmission and reflection coefficients against relative depth for a range of wave steepness. Only some selected models will be presented in this section. The remaining plots can be found in Appendix C.

In Figure 5.18, the relative depth kh, is plotted against the transmission coefficient for different wave steepness H/L and for half-submerged (z_d/d = 0.5) single pipe section with d=114.6 mm. The subscript of the incident wave height H_i is not shown for simplicity in these figures. The same comparison is made for z_d/d = 0.7 in Figure 5.19 and for z_d/d = 1.0 in Figure 5.20.

The transmission coefficient reduces as the relative depth, kh, increases. Given that the cylinder is fixed in place the only way that energy can be transmitted to the other side is either under or over the cylinder. During the experiments for z_d/d = 0.5, the wave height was always less than the freeboard of the pipe section above the mean water level. Thus, it can be assumed that no energy was transmitted over the breakwater. Considering a constant draft and water depth the transmitted wave energy strongly depends on the velocity distribution along the depth. As the waves get shorter the energy concentration of the waves gets closer to the surface. Therefore, less energy is transmitted at higher relative depth. The same conclusion was made in the previous section.

There is no significant dependency of the transmission coefficient on wave steepness within the range covered during the experiments when z_d/d = 0.5. Therefore, Figure 5.18 shows that the transmission coefficient does not depend on the wave height when there is no overtopping. Likewise, the transmission coefficient does not depend on wave steepness for a longer wave but there is a slight separation between the individual steepness plots as the wavelength increases. Yet, it is not clear enough to find a systematic dependency on wave steepness due to the scatter of the data.

When the same pipe section is fully submerged, (z_d/d = 1.0) in Figure 5.20, the separation between the individual steepness plots increases, and the data become scattered due to experimental uncertainties. It can be seen from Figure 5.20 that for longer and steeper waves, the transmission coefficient is higher. For shorter waves the data become more scattered and no such generalization can be made. This is because for the same wavelength, more energy is transmitted over the cylinder. Similarly, for the same wave steepness, the wave height increases with increasing wavelength and transmission by overtopping becomes more pronounced.
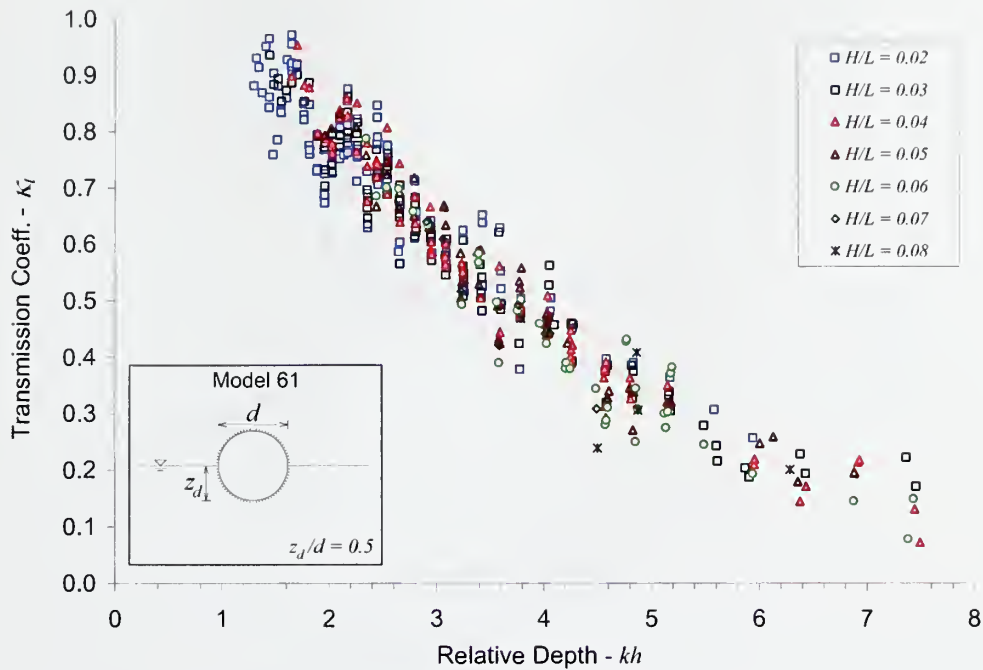
Figure 5.18. Effect of wave steepness, H_i/L, on transmission coefficient for half-submerged fixed pipe with $d = 114.6$ mm.
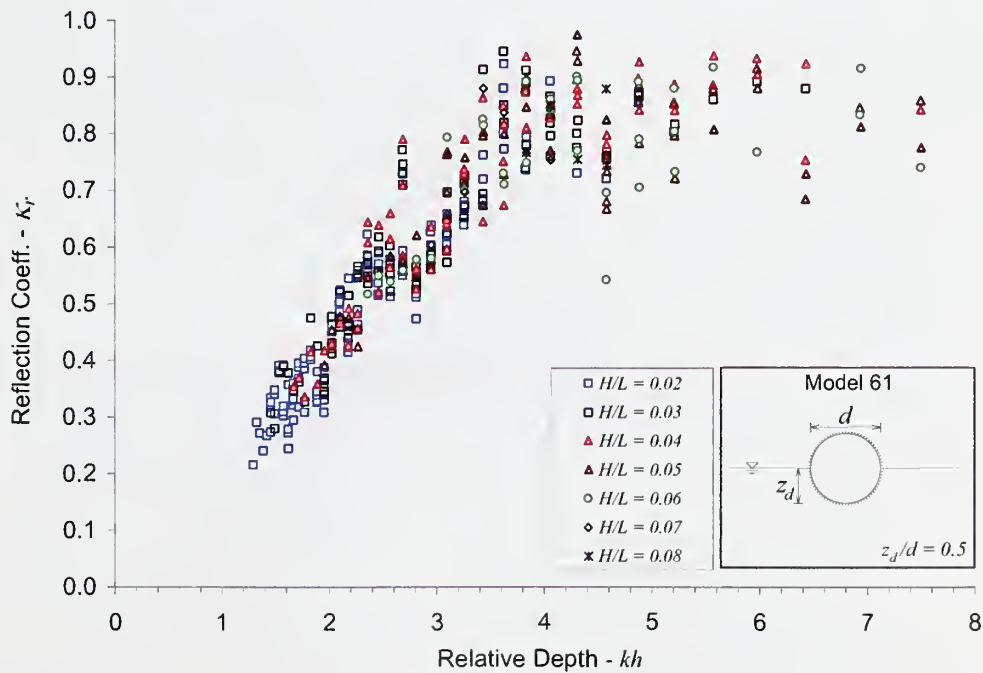
Figure 5.19. Effect of wave steepness, H_i/L, on reflection coefficient for half-submerged fixed pipe with $d = 114.6$ mm.

93
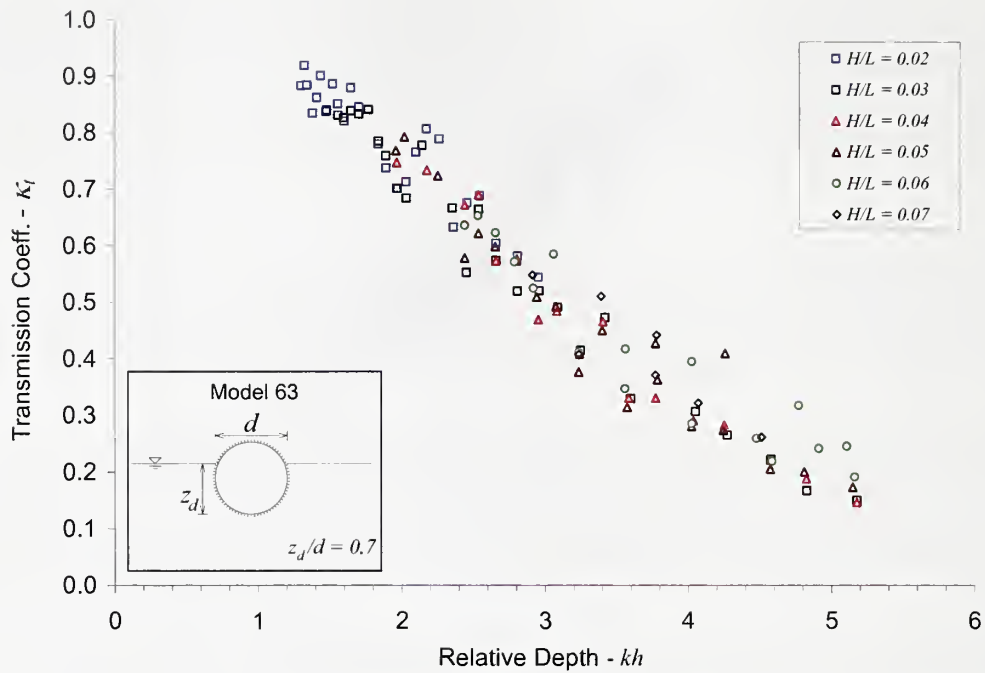
Figure 5.20. Effect of wave steepness on transmission coefficient for partially submerged fixed pipe with $d = 114.6$ mm.
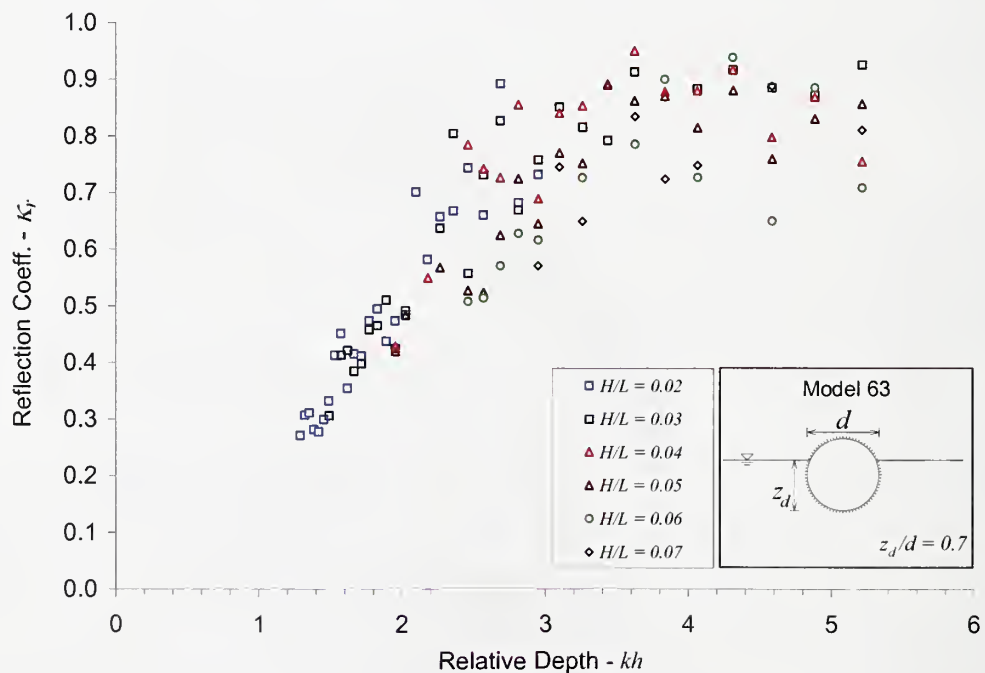
Figure 5.21. Effect of wave steepness on transmission coefficient for partially submerged fixed pipe with $d = 114.6$ mm.
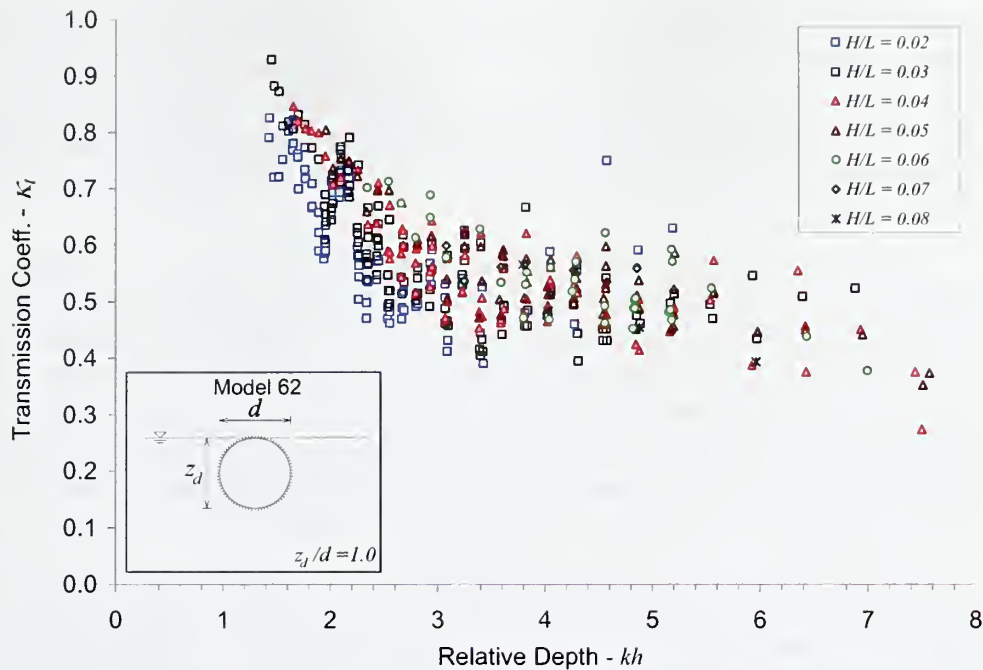
Figure 5.22. Effect of wave steepness on transmission coefficient for fully submerged fixed pipe with $d = 114.6$ mm.
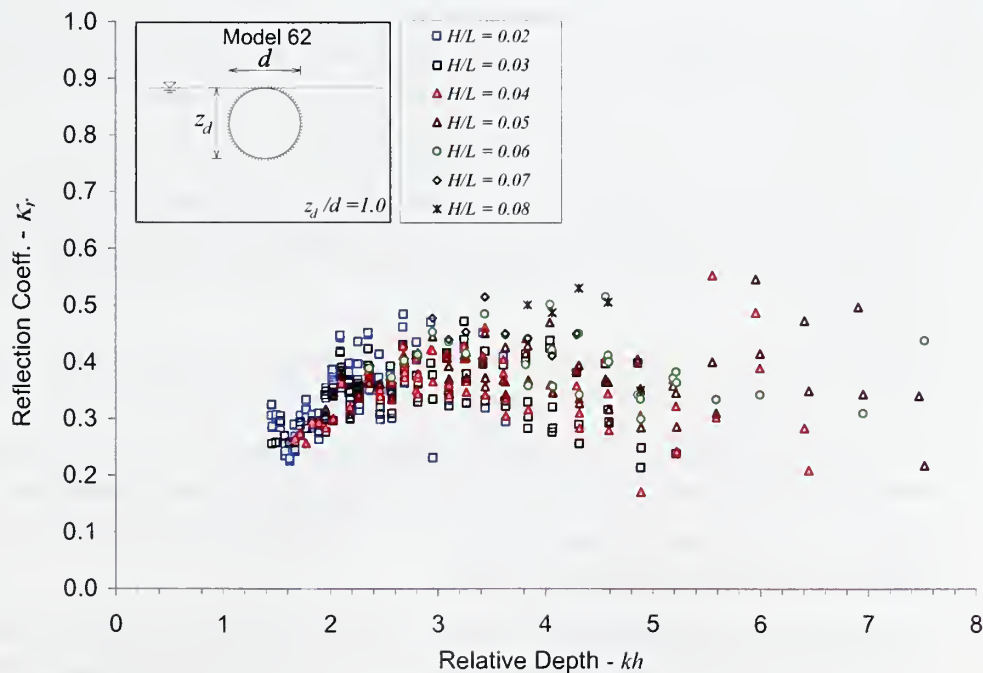
Figure 5.23. Effect of wave steepness on transmission coefficient for fully submerged fixed pipe with $d = 114.6$ mm.

Unlike the fixed pipe sections, the partially restrained pipes have some degrees of freedom. The amplitude of the generated waves with the harmonic oscillation of the cylinder depends on the incoming wave height Therefore, the transmission coefficient depends more on wave height (or wave steepness) than fixed models. The reflection and transmission coefficients of half, 70% and fully submerged pile-restrained single pipes are plotted against the relative depth, *kh,* for different wave steepness, *H/L,* in Figures 5.22 to 5.29

In Figure 5.24, there is a slight separation between the trends of the data with different wave steepness. The transmission coefficient is higher for higher waves, although there is no overtopping. The transmission is higher for relative depths between 6 and 7 as noted before. It was observed during the experiments that the half submerged model has the highest amplitudes of heave motion compared to other pile-restrained arrangements. For the fully submerged circular cylinder, in Figure 5.28, the trends of the data for different wave steepness separate significantly. The transmission coefficient is considerably higher for steeper waves just like the fixed case.

When the model is immersed up to 70% of its diameter, the transmission coefficient is still less dependent on wave steepness (Figure 5.26). The waves with $H/L = 0.02$ and 0.03 are transmitted and reflected more compared to the steeper waves which is not in agreement with the other two drafts. This can be explained as follows: The wave generation by the plunging motion of the breakwater is less compared to $z_d/d = 0.5$ due to the increased inertia. The freeboard of the breakwater restricts overtopping for most of the waves within the range of the experiments. Lower steepness waves were transmitted slightly more for longer waves since wave breaking induced by the moving cylinder was less at lower wave heights. Yet, above a certain range of wave steepness, the trends are not organized and the data with lower steepness are more scattered.

Other conclusions of the partially submerged models are listed as follows:

- For the same relative depth, the wave steepness does not have a significant influence on transmission coefficient if there is no overtopping. When the model is fully submerged, the wave height becomes important, just as it did in the fixed pipe experiments.

- Steeper waves are transmitted more for the same relative depth. For the same steepness, the breakwater is more efficient for shorter waves.

- The wave height dependency decreases with increasing relative depth. For deepwater waves, the transmission coefficient depends more on the wave steepness.

- There is no significant influence of the wave steepness in terms of breakwater efficiencies for pipes bundled together.

- The transmission coefficients of higher steepness waves are reduced when the second pipe is added to the arm-restrained and pile-restrained configurations. Data are still separated according to the wave height, but it is observed that there is a reasonable improvement in terms of wave transmission at wave steepness higher then 0.06.
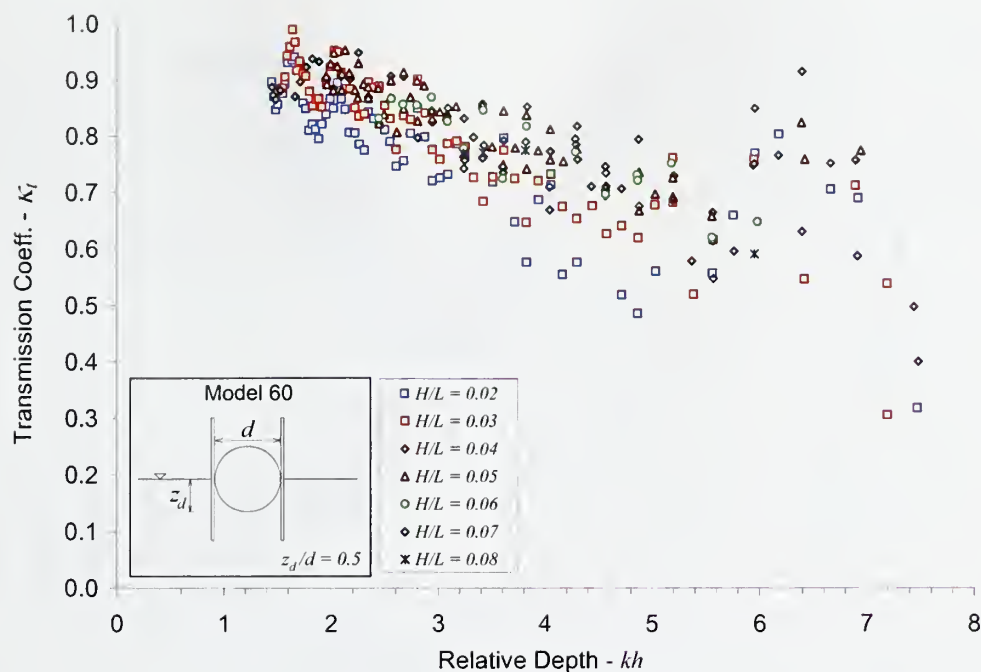
Figure 5.24. Effect of wave steepness, H_i/L on transmission coefficient for half-submerged pile-restrained breakwater with $d = 114.6$ mm.
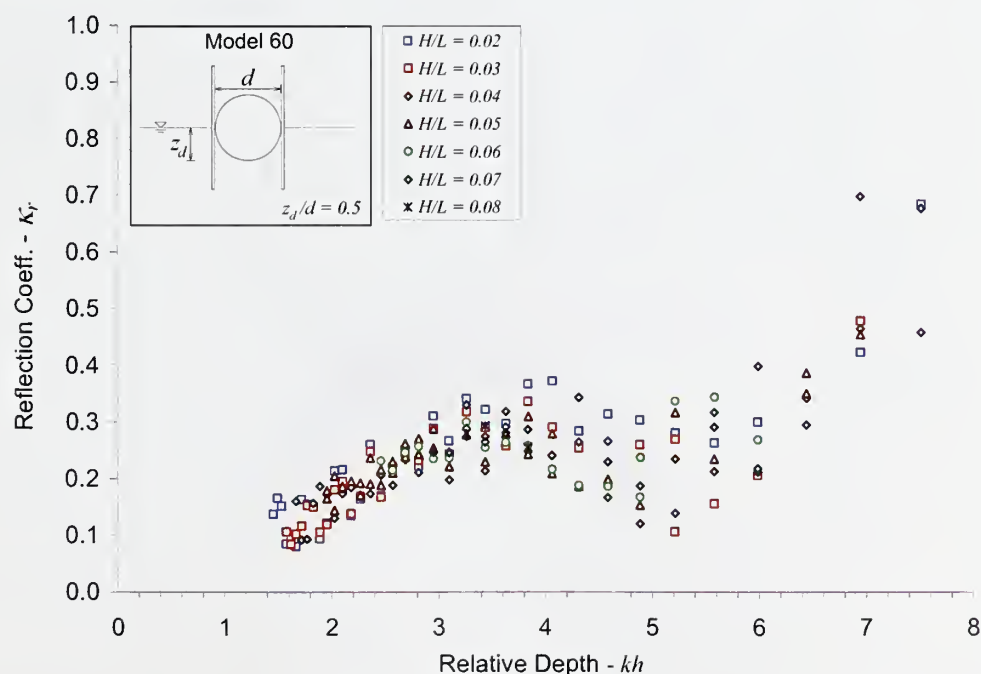
Figure 5.25. Effect of wave steepness, H_i/L on reflection coefficient for half-submerged pile-restrained breakwater with $d = 114.6$ mm.
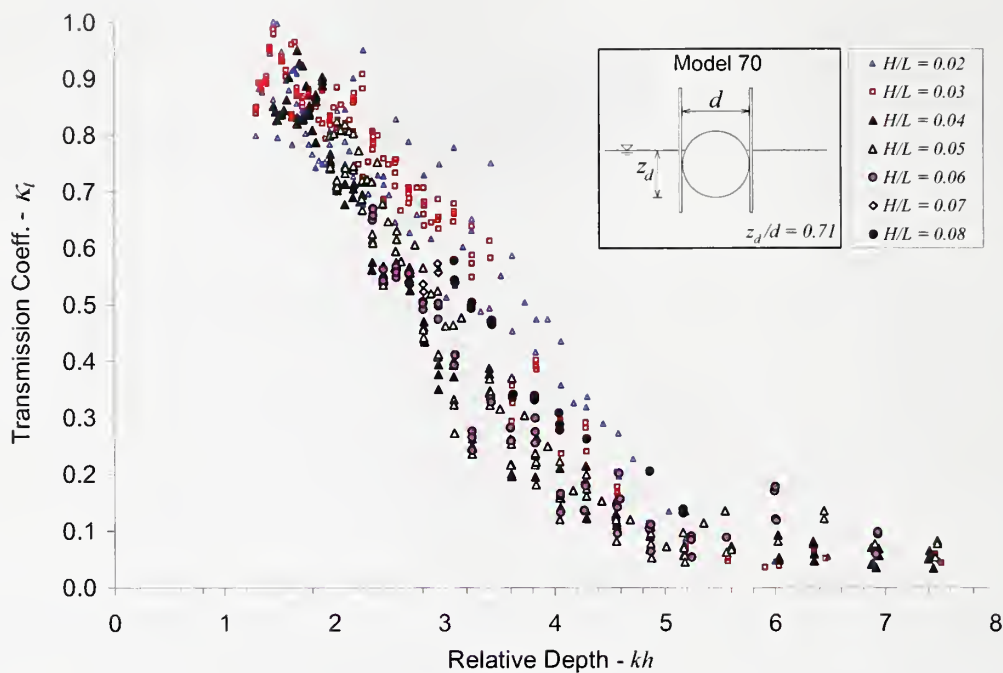
Figure 5.26. Effect of wave steepness, H_i/L on transmission coefficient for partially submerged ($z_d/d = 0.71$) pile-restrained breakwater with $d = 114.6$ mm.
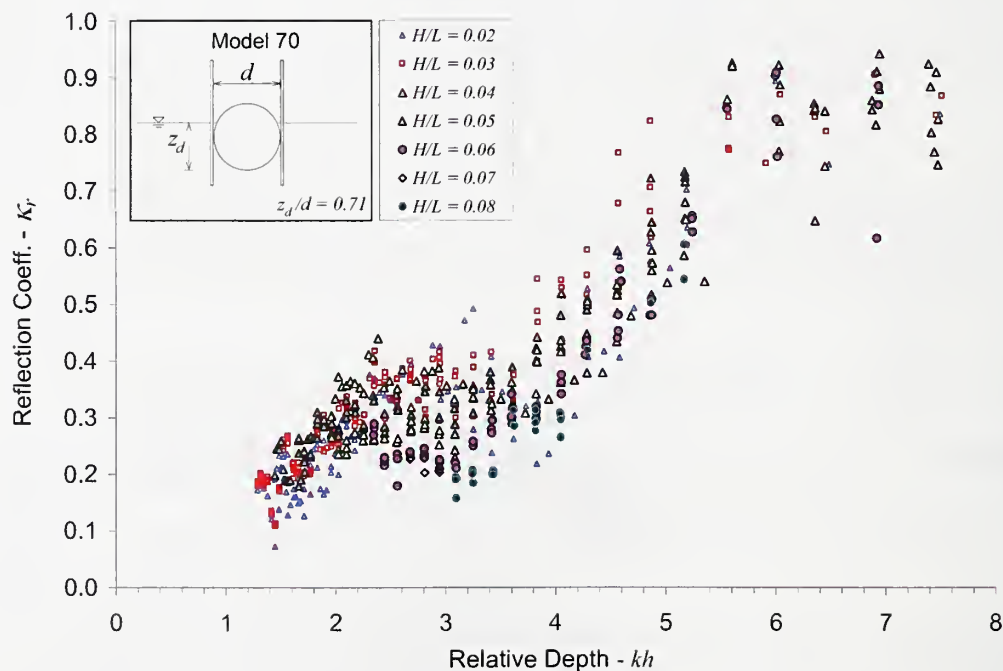
Figure 5.27. Effect of wave steepness, H_i/L on reflection coefficient for partially submerged ($z_d/d = 0.71$) pile-restrained breakwater with $d = 114.6$ mm.
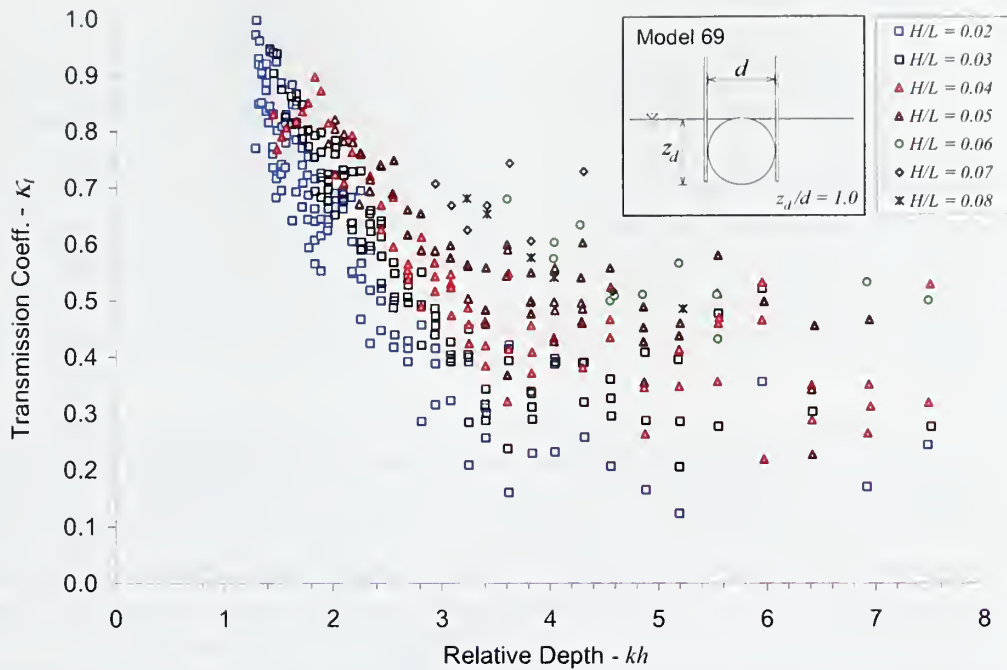
Figure 5.28. Effect of wave steepness, H_i/L on transmission coefficient for fully submerged pile-restrained breakwater with $d = 114.6$ mm.
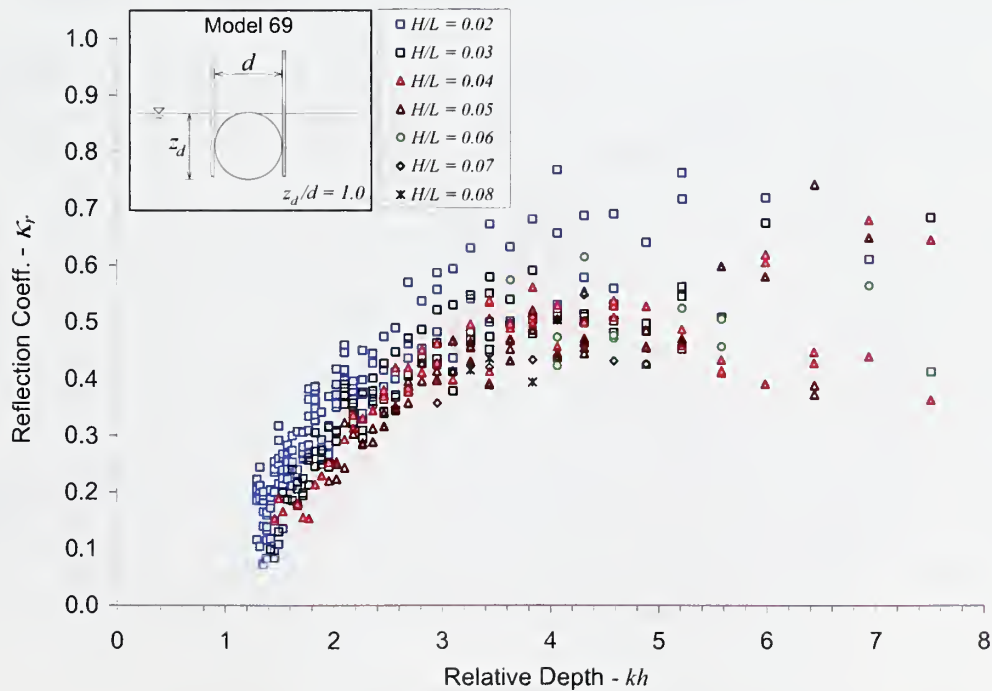
Figure 5.29. Effect of wave steepness, H_i/L on reflection coefficient for fully submerged pile-restrained breakwater with $d = 114.6$ mm.

99

5.6.4. Geometry and Restraint Type

As noted earlier, a group of pipes can be bundled together instead of using a single pipe section as a floating breakwater, to have the same submergence depth with smaller pipe diameters. This alternative mode of construction may increase the durability of the breakwater and can reduce the cost depending on the size. In Figure 5.30, the transmission coefficient of the single pipe with aspect ratio, $z_d/d = 0.7$ (model 63) and the bundle of pipes with $z_d/d = 0.68$ (model 91) are compared for varying relative draft. It is seen that there is not a considerable difference between transmission and reflection coefficients of the two models indicating that, for the tested shapes, the shape of the cylinder has little influence on the efficiency of the wave absorber for the same aspect ratio.

In Figure 5.31, the half submerged single pipe breakwater models of diameter $d = 114.6$ mm with different constraints are compared. Each data point represents the average transmission coefficient for each relative depth, kh, over the range of wave steepness, H/L. The pile-restrained configuration has the highest efficiency among the partially constrained configurations and the bottom-moored breakwater is relatively less efficient compared to any other model. This indicates that, for the range of wave parameters considered here, horizontal restraint is superior to vertical restraint. Yet, none of the models have results as good as the fully restrained breakwater in terms of transmission coefficient. The major difference between the arm-restrained and pile-restrained models is that the pile-restrained model is free to roll. Yet, there is no significant difference between the two models in terms of transmission and reflection coefficients.
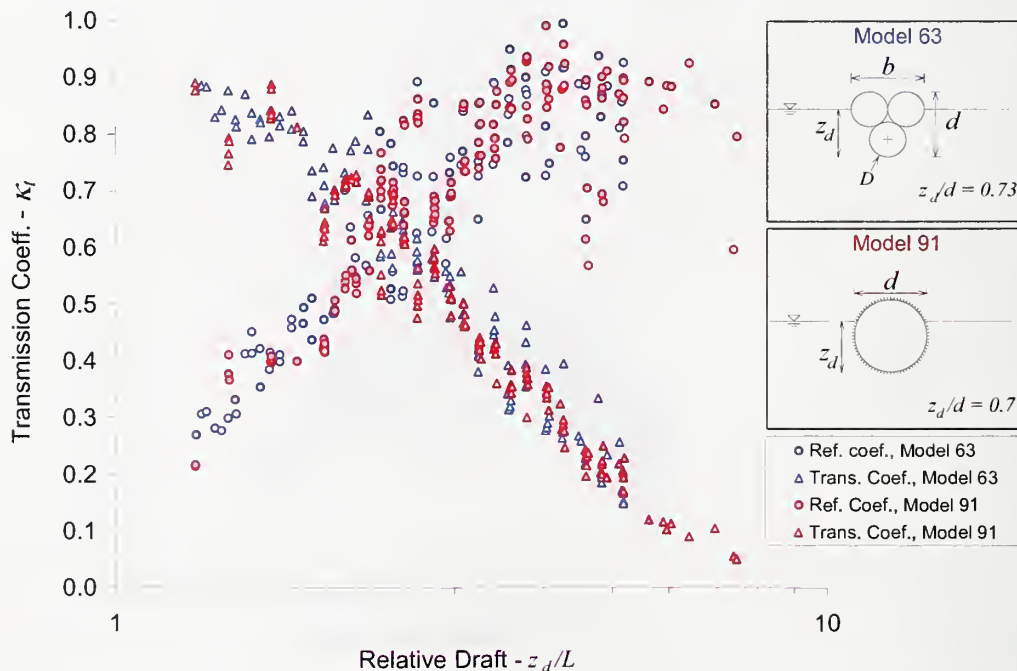
Figure 5.30. Comparison of transmission coefficients of fixed single pipe and bundle of three pipes.
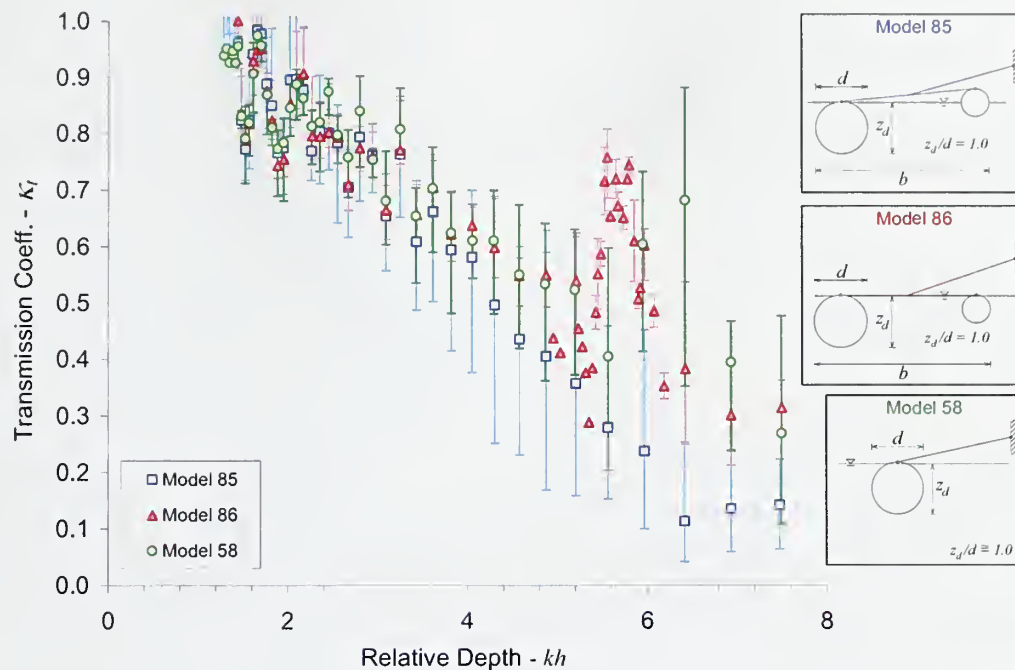
Figure 5.31. Effect of second pipe submergence on transmission coefficient for arm-restrained double pipe model. Bars represent the range of wave steepness.

It can be seen from Figure 5.32 that arm and pile-restrained breakwater models have relatively low reflection coefficients compare to the others. The reflection coefficient drops with increasing relative depth between 4 and 5. This indicates that in this region, the wave transmission is reduced primarily by damping rather then reflection.

When the pipe section is submerged completely (Figures 5.34 and 5.35), the arm and pile retrained models become the most efficient. The transmission coefficients for these two models are lower than the fully constrained breakwater for longer waves. For the fully submerged circular cylinder, the energy transmission with overtopping becomes significant and the dynamic properties of the partially restrained models improve the transmission characteristics of the breakwater. Note that the data points are averaged over the steepness range and for milder waves the transmission coefficients of arm-restrained and pile-restrained breakwaters are even lower than average while the transmission coefficients of the fixed model do not change significantly with wave steepness. The reflection coefficients of the fully submerged models are compared in Figure 5.51. The reflection coefficients for all the configurations are not as high as the half submerged pipes showing that the dissipation is higher for fully submerged models.

101
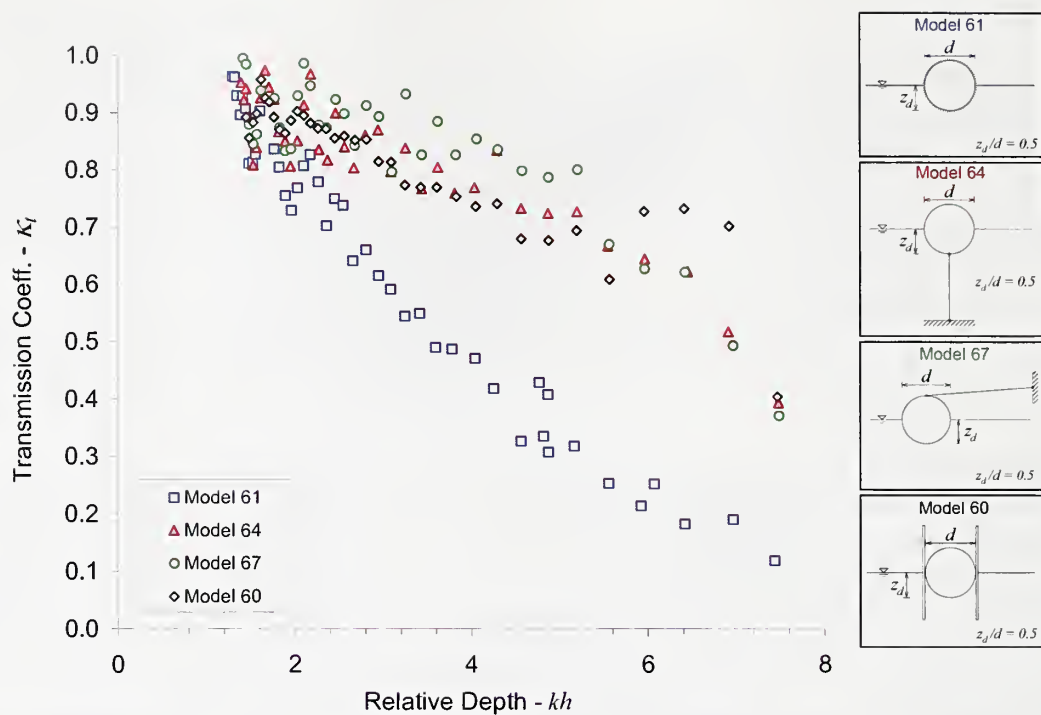
Figure 5.32. Comparison of the transmission coefficients of half-submerged ($z_d/d = 0.5$) fixed, moored, arm-restrained and pile-restrained breakwater models with $d = 114.6$ mm.
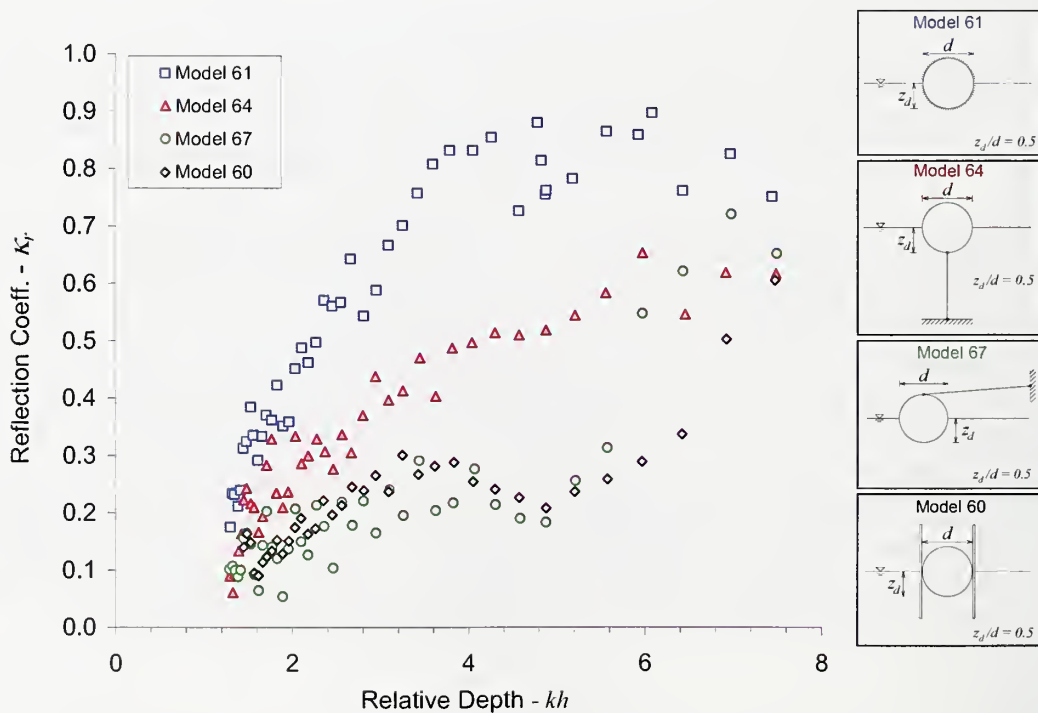
Figure 5.33. Comparison of the reflection coefficients of half-submerged ($z_d/d = 0.5$) fixed, moored, arm-restrained and pile-restrained breakwater models with $d = 114.6$ mm.
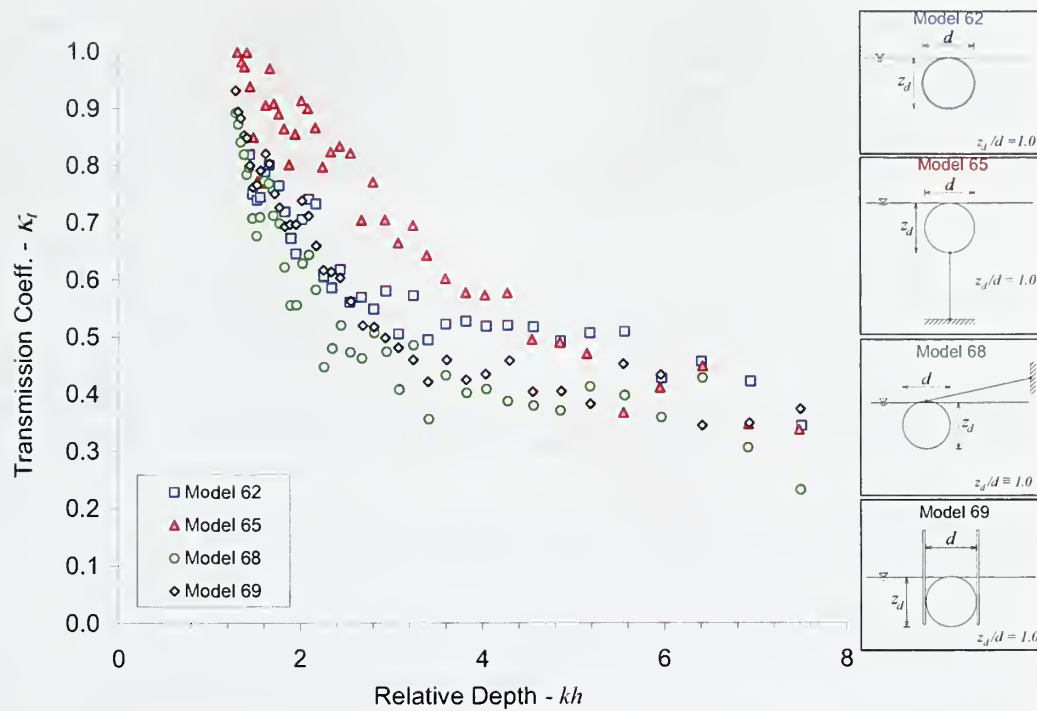
Figure 5.34. Comparison of the transmission coefficients of fully submerged (z_d/d = 1.0) fixed, moored, arm-restrained and pile-restrained breakwater models with d = 114.6 mm.
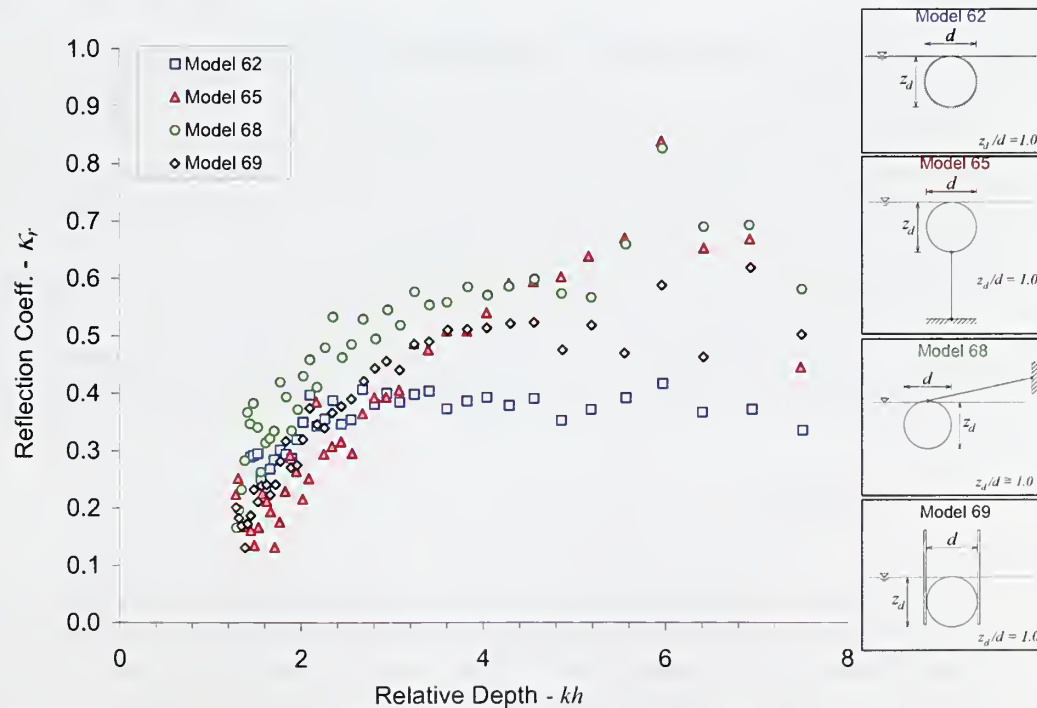
Figure 5.35. Comparison of the reflection coefficients of fully submerged (z_d/d = 1.0) fixed, moored, arm-restrained and pile-restrained breakwater models with d = 114.6 mm.

103
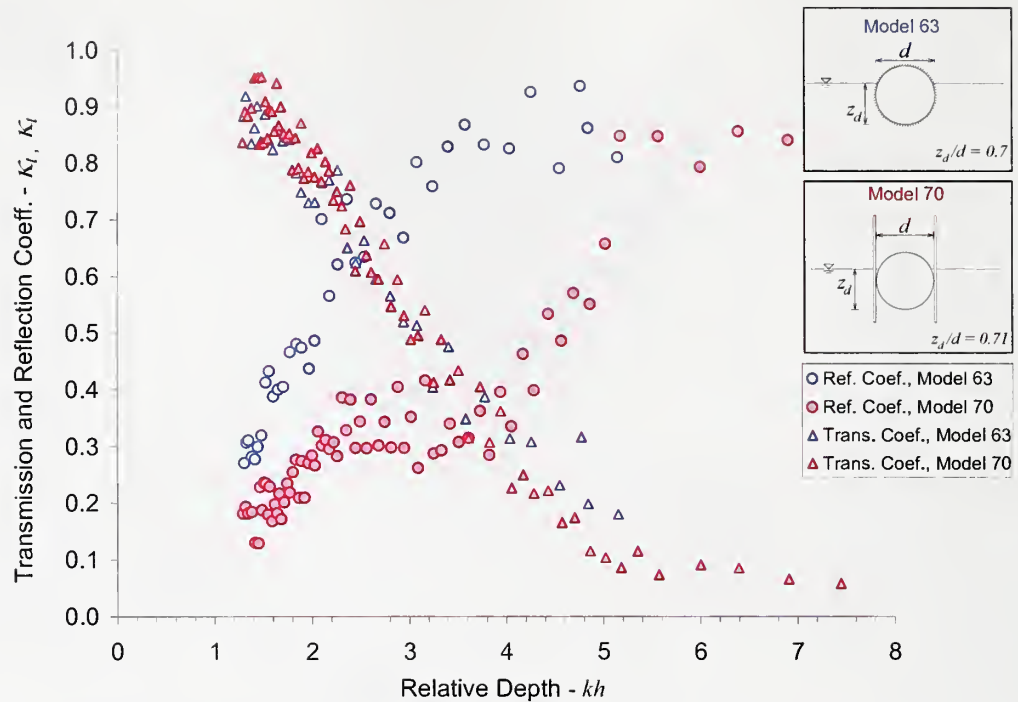
Figure 5.36. Comparison of the transmission and reflection coefficients of partially submerged ($z_d/d = 0.7$) fixed, and pile-restrained breakwater models with $d = 114.6$ mm.

In Figure 5.36 the transmission and reflection coefficients of fixed and pile-restrained partially submerged breakwater models ($z_d/d = 0.7$) are compared. It is seen that the pile-restrained configuration has transmission coefficients as low as the fully restrained pipes. The reflection coefficients of the pile-restrained breakwater are less than the fully constrained configuration even though their transmission characteristics are the same. For longer waves both of the models have low reflection. When the waves get shorter, the reflection coefficients of the pile-restrained breakwater increase but not as much as of the fixed pipe since some of the energy is damped when they interact with the partially restrained cylinder. When the waves get even shorter, the dynamic response of the pile-restrained breakwater becomes insignificant and it acts like the fixed pipe.

5.7.   Conclusion

A series of experiments were conducted in the wave tank at USDA-ARS National Sedimentation Laboratory and used to test a variety of circular cylindrical models with several diameters for combinations of dimensionless parameters described in the previous Chapter. The results compared favorably with the closed form solution and experimental results of Dean and Ursell (1959) for the fixed models.

104

As would be expected, for both fixed and floating cases, larger diameter breakwaters had better performance than smaller ones. There is an optimal relative submergence that maximizes the efficiency of a given breakwater design. This value varies based on the type of restraint. For example, fully submerged pile-restrained breakwaters performed better than fully submerged fixed breakwaters for a range of wave parameters.

Other specific conclusions follow:

- Of the restraint types tested here, the pile-restrained model was the most effective at attenuating waves.

- The bottom moored arrangement was less effective than pile-restrained. The moored design also has the disadvantage of a strong dependence on water level.

- For low-amplitude waves like those considered in the current study, a relative submergence of z_d/d=0.7 was found to be optimal for the pile-restrained model.

- Bundles of smaller pipes were found to perform in a manner comparable to a single pipe of the same diameter.

- Generally, steeper waves are transmitted more when overtopping is allowed and most of the reduction of wave transmission is by breaking rather then reflection.

- Dynamic properties of the breakwater structure can be important for short and steep waves.

VI. FIELD APPLICATION

6.1.   Introduction

Approximately 700 miles of earthen levees are currently being used for commercial aquaculture and irrigation storage in the United States. More than half of these levees experience significant embankment erosion due to wind-driven waves (Carman, 2003). In irrigation reservoirs, water is stored in the winter and pumped onto crops in the summer, resulting in water levels that fluctuate over several feet, making vegetative bank protection impractical. Tires, construction debris, and riprap have been successfully used for bank protection, but these are not acceptable methods because of ecological and economical concerns (Carman, 2003). Some of the current protection techniques are presented in Figure 6.1.
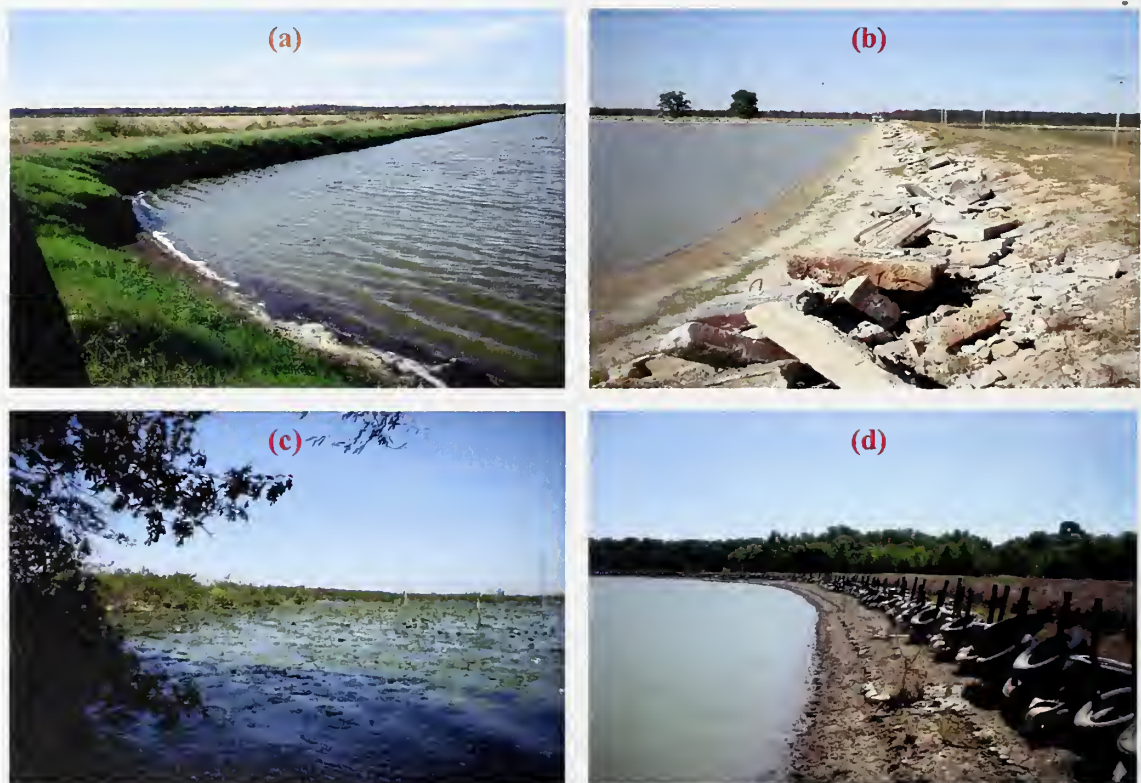
Figure 6.1.Protection techniques currently under use: (a) vegetation, (b) construction debris, (c) lily pads, (d) tires (Carlisle, AR, 2004)

Levee erosion by waves is controlled by wave properties and bank materials. Because of the wide range of soil types in levee embankments, the current study focused on reducing wave energy, which, for any soil type should decrease erosion. Lower amplitude, waves have been shown to cause less erosion than higher amplitude waves (CERC, 2006). Even though low-amplitude waves often occur over longer time periods than larger waves, there will be little or no levee damage until some critical shear stress is exceeded. This is one reason why some levees may stand with little damage for years but then sustain substantial damage from one strong storm (USDA-SCS, 1974).

One objective of the present work is to design and test the effectiveness of floating breakwaters for protection against levee erosion. The final design of the breakwaters will be implemented by landowners using commonly available materials. For this reason, the breakwaters were constructed out of inexpensive polyethylene irrigation tubing. The results of the laboratory experiments with cylindrical pipe sections show that floating breakwaters are a viable option for low cost protection of earth levees.

The description of the work will be broken into three sections. First, preliminary field data collection in 2005 on wind and wave characteristics is described. Next, a brief description of the results from a short-term prototype-scale field study in 2007 and 2008 is presented. The work also focused, in collaboration with Dennis Carman of the White River Irrigation district, on the logistics of purchasing and handling the irrigation tubing, connecting it together, and deploying it in the reservoir. Finally the results will be compared with the available laboratory data.

6.2.   Data Collection

The actual water waves are rather complex due to their random and mathematically nonlinear behavior. Linear wave theory described in Chapter II is applicable to a large range of the wave situations (CERC, 2006). Yet, the characteristics of the waves in nature have to be understood in order to validate the applicability of the theory and correctly scale the problem.

With this motivation, three field studies were carried out in Schafer Lake, an irrigation reservoir approximately 10 km east of Carlisle, Arkansas. Figure 6.2 shows the layout of the measuring stations and prototype testing sites in Schafer Lake between 2005 and 2008. Each solid represents average wind direction and effective fetch lengths (F_{eff}) for the set of data collected at that station. The effective fetch lengths were calculated by averaging the fetch lengths measured at $3°$ intervals over a range of $12°$ above and below the bearing of the average wind direction. As an example, the fetch lengths were shown with dashed lines for the March, 2005 field study. The dots are the locations of the measuring gauges.

Figure 6.2 (a) A satellite image of the Schafer Lake with the surrounding area, (b) The layout of the measuring stations on Schafer Lake and corresponding fetch lengths. Dashed lines are the 12° range of fetch lengths on both sides with 3° interval that has been averaged to calculate the effective fetch length.

In March, 2005, a temporary wind and wave monitoring station was deployed in Schafer Lake so that wind-driven wave characteristics could be measured for use in scaling the laboratory model study (Figure 6.2). The prevalent wind direction was observed to be from the northeast, so the measurement tower was positioned in the southwest corner of the reservoir in order to maximize the fetch length. The water depth at the installation point was 2.5 m. The embankments are constructed from soil pushed outward from the reservoir side, leaving deeper water near the banks. Based on the lack of relief in the surrounding area, bathymetric variations can be neglected far from the banks. Approximately 110 minutes of concurrent wind direction, wind speed, and wave height data were collected. The wind averaged 13 m/s during the data collection period. Thus, it was appropriate to use the measured wind and wave conditions as a basis for designing the model-scale experiments.

Water level measurements were made using 2 ultrasonic distance sensors separated by a fixed distance of 30 cm, aligned roughly parallel to the observed wind direction, and mounted approximately 35 cm above the mean water level. The ultrasonic distance sensors collected data at a rate of 10 Hz. Wind speed was measured by a Wind Sentry Anemometer located 2 meters above the mean water level mounted on the same instrument platform used for the wave measurements Figure 6.3. The accuracy of the wind speed sensor was 0.5 m/s in a range of 0 to 50 m/s. The wind direction is obtained by recording the voltage produced by potentiometer connected to a wind vane. The instruments were connected to a computer placed on one of the levees close to the measurement station.
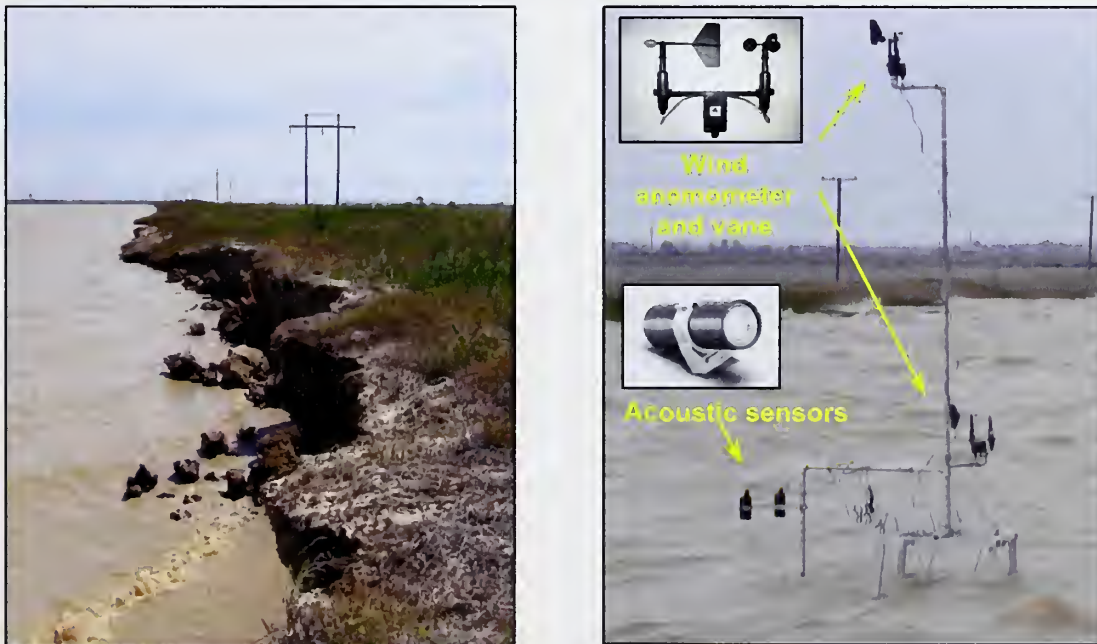
Figure 6.3 Left: South shore of the Shafer Lake illustrating extensive erosion damage. Right: The temporary wind and wave monitoring station constructed and used in March 2005.

In April, 2007, a wind and wave measurement station was constructed to test the efficiencies of pile-restrained breakwaters near the south shore of the Shafer Lake (Figures 6.2 and 6.4). Based on the results of the model study, two breakwater configurations were chosen for prototype scale field testing in Schafer Lake. Approximately 25 meters of each of demonstration breakwater was deployed. One utilized a single 29 cm polyethylene drainage tube, and the second was a composite design made up of one standard 24 cm outside diameter drainage pipe connected at the top to a 12 cm outside diameter smooth walled pipe. Two polyethylene drainage tubes were connected with PVC pipes to secure the distance between them, and they were held in place by two piles. The piles were constructed out of 2" by 4" (5 cm x 10 cm) timber planks. The piles were connected to each other at the top on one side and supported by diagonal planks to ensure structural rigidity. The details of the prototype breakwater are given in Figure 6.5.

Three capacitance type water level sensors were used to record the water level at various stations around the breakwater. One of the sensors with 50 cm staff length was used to estimate the incident wave height at a station far from the breakwater (wave gauge 1 in Figure 6.4). The transmitted wave height was measured with a 50 cm staff length sensor which was connected to the wind tower, 7.5 away from the breakwater (wave gauge 2 in Figure 6.4). The third sensor with 100 cm staff length was connected to monitor the offshore side of the breakwater to (wave gauge 3 in Figure 6.4). The sensors recorded analog data at a rate of 30 Hz with ±1mm resolution.

Two wind speed and direction sensors were mounted on the wind tower at elevations 1.7 m and 6 m above the mean water level (Figure 6.4). The wind speed sensor generated an analog voltage signal which was recorded at a rate of 512 Hz. This signal was converted to actual wind speed before being stored with a data rate of 30 Hz and ±0.5m/s resolution. A data acquisition box was also connected to the wind tower which included two 12V batteries to supply the power to the instruments and a portable computer to acquire and store the data. The water depth was between 1.7 m and 1.8 m at the two measuring stations during the data recording for 13 hours.

In June 2008, a second field test was conducted in the same reservoir to assess the effectiveness of floating breakwaters at full scale. This time the North-east corner of the lake was selected to yield the maximum fetch length for the prevailing wind direction (Figures 6.2 and 6.6). For this test, a stack of three 10 cm tile drain (perforated) pipes were connected to another 10 cm pipe as in Figure 6.7. Once again, PVC pipes were used to keep the pipes together and maintain the distance between them. The breakwater was held in place by ropes attached to the ends of the pipes and held in tension by rods secured to the shore. Two measuring towers were constructed approximately 4 m away from the breakwater on both sides to set the instruments. The wave height was measured at these two locations with capacitance type level sensors with 50 cm staff length. The water depth was 2.1 m at the offshore gauge and 1.9 m at the onshore gauge. Two wind sensors were connected to the tower closer to the shore at elevation of 1.2 and 3.6 m above the mean water level.
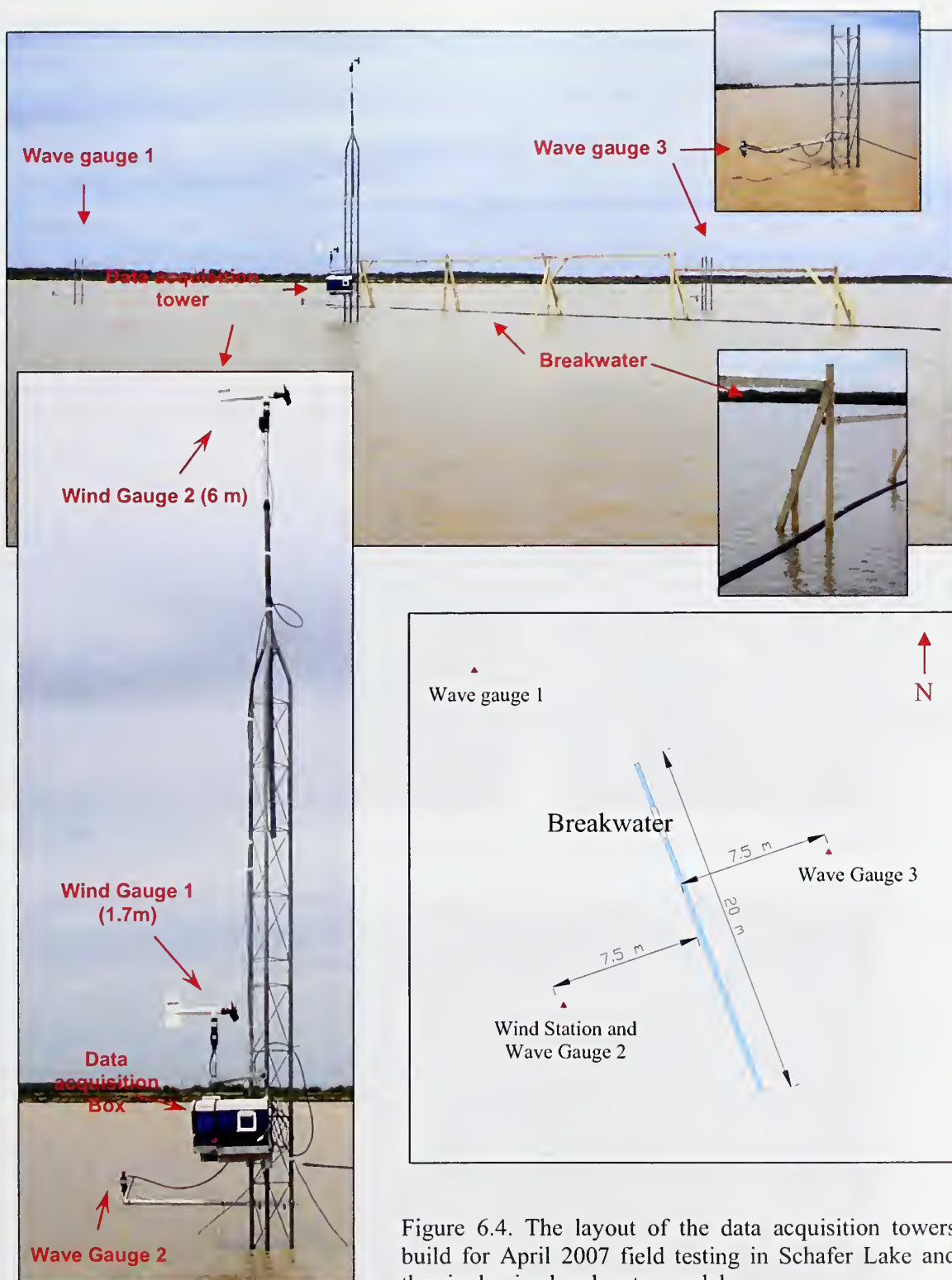
Figure 6.4. The layout of the data acquisition towers build for April 2007 field testing in Schafer Lake and the single pipe breakwater model.

111
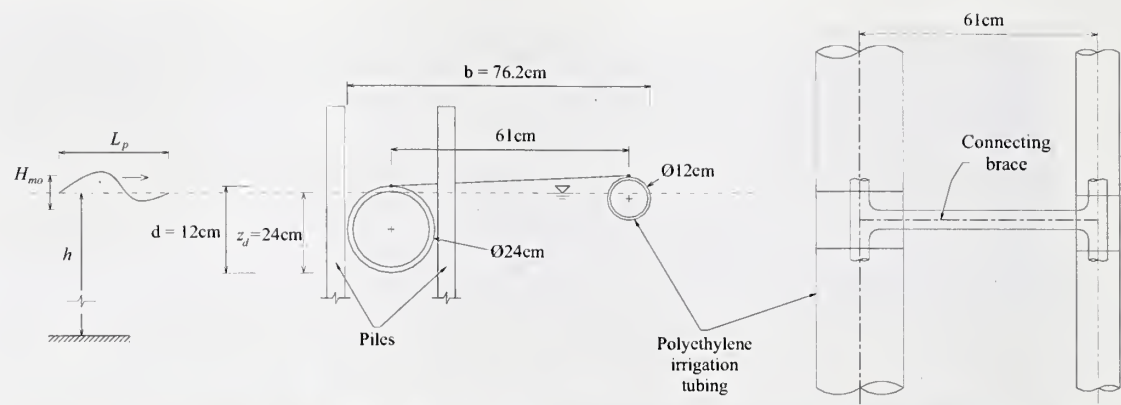
Figure 6.5. Details of the prototype scale field tests with two pipe arrangement in April 2007.
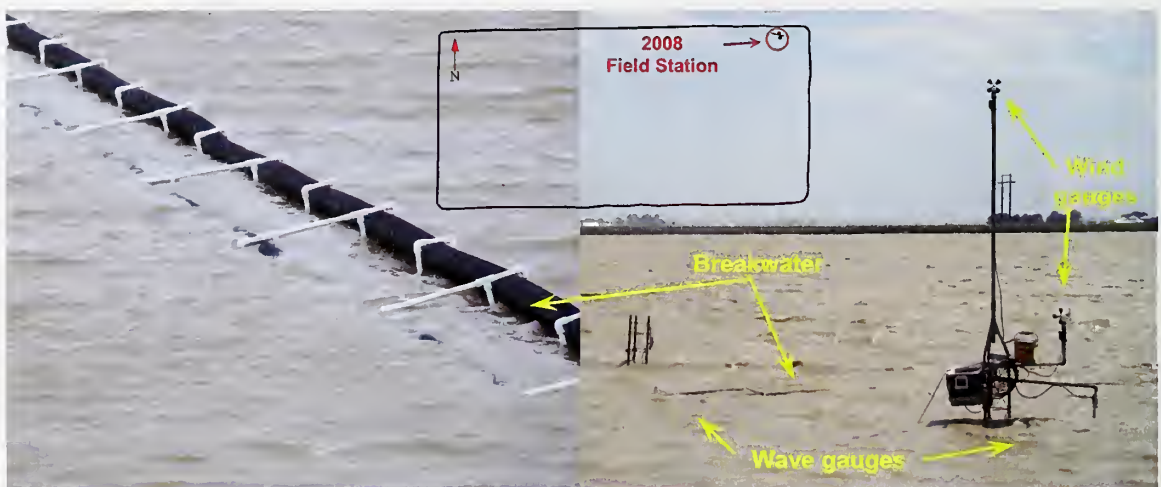
Figure 6.6 The layout of the 2008 field station.
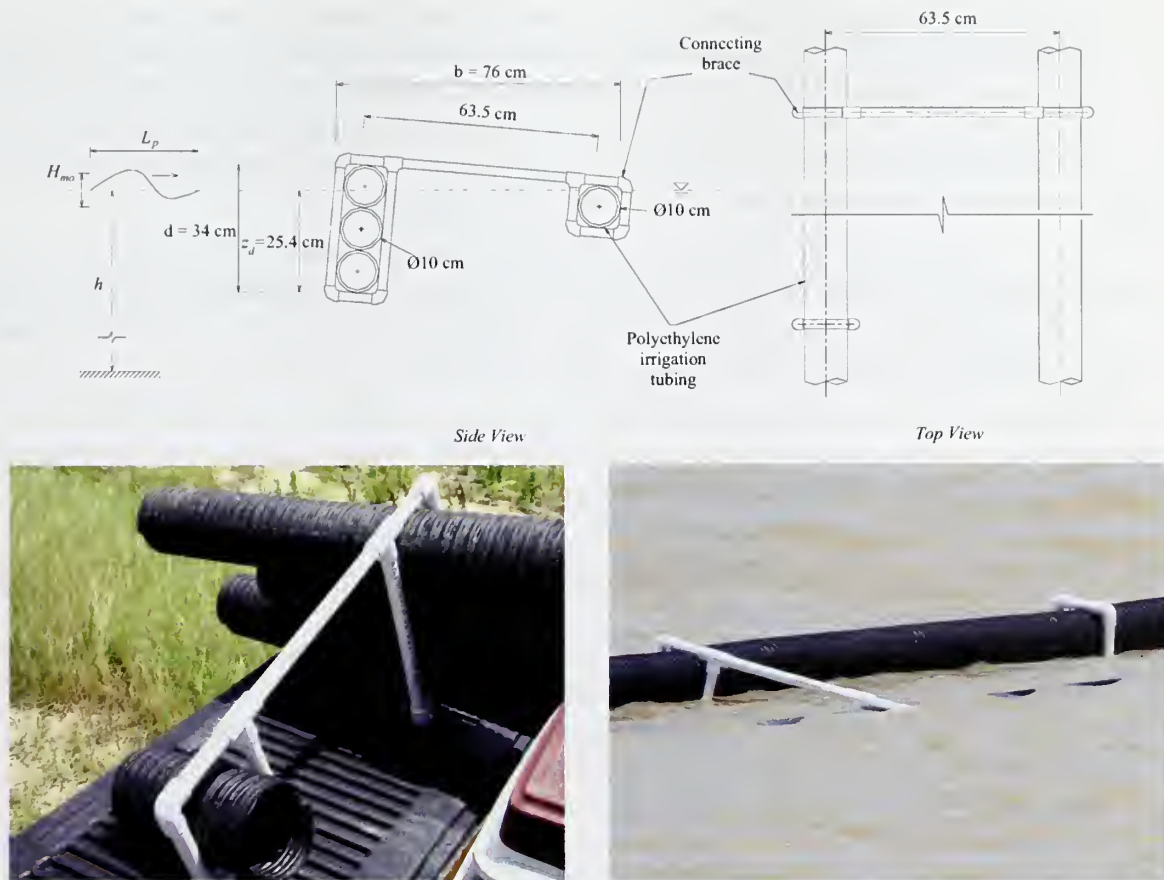
Figure 6.7.Details of the prototype breakwater installed in June 2008.

6.3.   Data Analysis

For the analysis of the data a computer program was developed which interpreted the theory of random waves discussed in Section 2.4. A Butterworth low pass filter passes relatively low frequency components in the signal but blocks the high frequency components. A 4th order Butterworth low pass filter with a cutoff frequency of 4 Hz was applied to the data to remove spurious high frequency noise. The time series of surface elevations was analyzed by both time-domain (wave train) and frequency domain (spectral) analysis.

The water surface elevation signal was divided into segments of sizes depending on the minimum duration for the wind to travel the fetch length (Appendix G). For example, the segment length for 2005 data was 4096 data points which corresponds to 6.83 minutes for 10 Hz data recording. The averaging intervals are given in Table 6.1. Each of these segments was divided into 512 (51.2 s) point sub-segments for spectral analysis. 50% data overlapping gives better statistical results to reduce the statistical uncertainties (NDBC, 1996). Therefore both the main and sub-segments were overlapped

113

by 50%. Then, 8 wave spectra within each segment were averaged for each frequency band to get the average spectrum for the 6.83 minute interval. The data segmenting is illustrated in Figure 6.8. The data sets given in Table 6.1 were also evaluated by time domain analysis using the zero down-crossing method (CERC, 2006). The details of the time domain analysis were described in Section 3.3.1. Each data segment described above was analyzed separately with 50% overlapping.

The wind speed data were averaged in time at intervals of the minimum duration given in Table 6.1. For the March 2005 field data set, the power law given by Equation 6.1 was used to estimate the wind speed at the 10 m elevation, U_{10}, using the measured wind speed values, U_z, at the $z = 2$ m elevation.

$$U_{10} = U_z \left(\frac{10}{z} \right)^{1/7}$$

(6.1)

Table 6.1 Summary of collected data. Effective duration is the interval during which a sustained wind speed and direction assumed.

Data set	Total Duration of Data Rec. (min)	Effective Duration (min)	Wind Direction (deg. cw from north)	Wind Speed U_{10} (m/s)	Effective Fetch F (m)	Minimum Duration t_{min} (min)	Averaging Interval Δt (min)
Mar-05	96	96	310±14	10.3±1.3	586	18	146
Apr-07, 7b	173	15	316±23	3.1±0.5	355	21	15.9
Apr-07, 7c		63	3±11	3.1±0.5	355	16	15.9
Apr-07, 8a	278	64	352±9	5.4±0.3	273	12	15.9
Apr-07, 8b		90	327±6	6.3±0.8	327	14	15.9
May-08	55	55	185±5	5.4±0.3	315	14	13.7
Jun-08	2,591 (43hrs)	2,591 (43hrs)	153±7	9.5±1	450	16	15.9
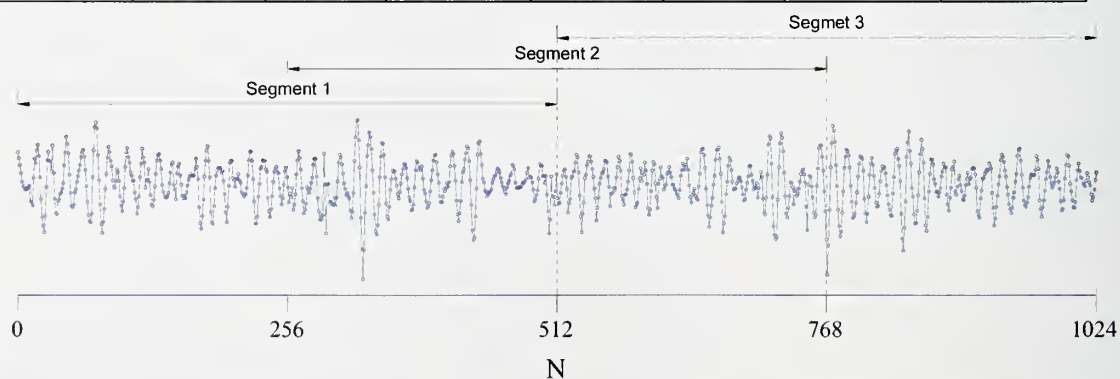
Figure 6.8. Illustration of data segmenting with 50 percent overlapping. N is the datum index.

This formula is verified with 24 hours of wind speed data collected at the same pond in May, 2007. For data from 2007 and 2008, wind speed at 10 m was estimated using data recorded at two different elevations and by assuming a logarithmic wind profile. The logarithmic wind profile is expressed by

$$U_z = \frac{u_*}{k} \ln\left(\frac{z}{z_o}\right) \tag{6.2}$$

where k is the von Kármán constant ($k = 0.41$), z_o is the surface roughness height, and u_* is the shear velocity. u_* and z_0 are estimated by substituting the measured wind speed at two elevations into Equation 6.2. Then, the wind at 10 m is estimated by using the calculated values of u_* and z_0. It is suggested to use Equation 6.2 in an elevation range of 8-12 m (CERC, 2006). The data from 2007 were used to compare the estimated wind velocity at the 10 m elevation using Equations 6.1 and 6.2 (Figure 6.9). As would be expected, the data recorded at 6 m provided a better estimation of U_{10} than the data recorded at 1.7 m. However, Figure 6.9 shows that power law can be used to estimate U_{10}.

The wind direction was correlated with the wave direction for 2005 data set (Figure 6.10). The wavelength was computed from both linear wave theory using Equation 3.13 and measured wave propagation speeds. If the linear wave theory is valid the dispersion relation is given by Equation 3.13. The wavelength can also be estimated using the discrete implementation of the cross-correlation function which is defined by:

$$R_{xy}(n) = \sum_{k=1}^{N} x(k) y(k+n) \tag{6.3}$$

where N is the sample interval and x and y are the time series data from each sensor.

The waves with the highest spectral energy have more influence on the correlation between two recorded signals. Hence, the wavelength corresponding to the peak frequency has to be rather closer to the measured celerity then the wavelengths corresponding to other frequencies. Therefore, the theoretical wavelength L_p was obtained from Equation 3.13 by iterations using the peak frequency f_p.

115
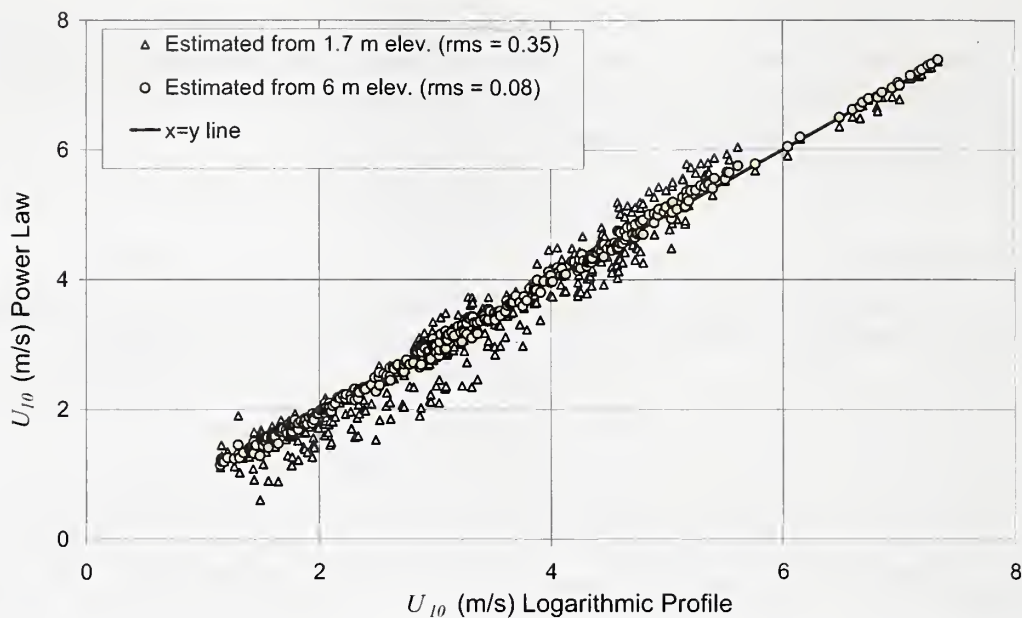
Figure 6.9 Comparison of wind speeds at 10 m elevation extrapolated using the logarithmic wind profile and power law.
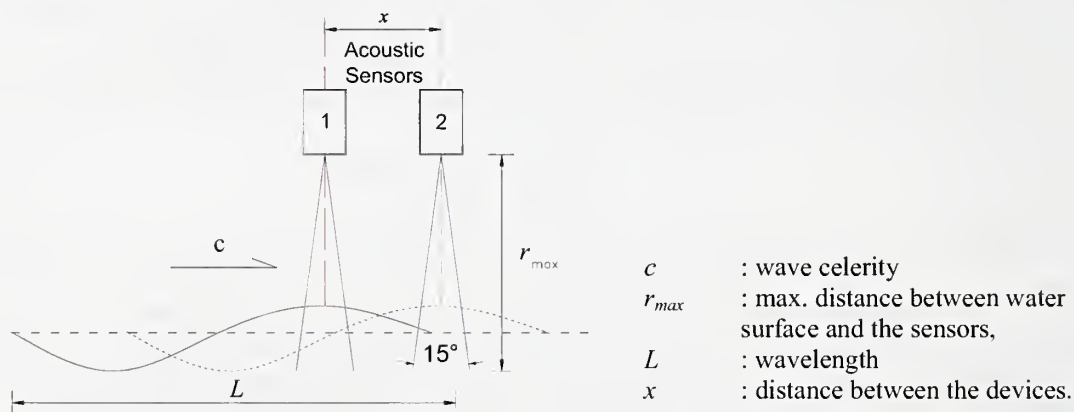
Figure 6.10 Wavelength measurements in March, 2005.

6.4. Results and Discussion

The wind speed and direction variation during the 2005 data recording is presented in Figure 6.11. There are 3 significant wind direction changes during the recording. These are later combined with the map of the pond for estimating an average fetch length. The systematic difference between wind directions from two instruments is due to the alignment error between two wind vanes.

116

The spectral estimates for wave height and wave period are given in Figures Figure 6.12 and 6.13. Figure 6.13 shows the statistical estimates for wave heights H_s, H_{max} and H_{rms}. The results from both level sensors are consistent in all the comparative figures. Note that peak period T_p is rather larger then mean period T_m and spectral mean period T_z showing that the spectrum is skewed with a longer tail on the right side (higher frequency). It can also be seen from the figures that the wave properties follow the changes in wind speed fairly fast which indicates the averaging interval for these values are reasonable.

The ranges of the characteristic wave parameters obtained from both spectral analysis and time domain analysis are summarized in Table 6.2. Longuet-Higgins (1952) developed a theoretical relationship for the ratios of different characteristic wave heights assuming that the spectrum is narrow banded and the energy is received from a large number of sources with random phases between them. A comparison of the theoretical results of Longuet-Higgins (1952) with the current field data is made in Table 6.3.

Table 6.2. The ranges of predicted wave parameters from the frequency and time domain analysis.

	Characteristic wave parameters	Level sensor I	Level sensor II
Spectral Analysis	Wave height, H_{mo} (m)	0.10 – 0.25	0.10 – 0.25
	Peak period, T_p (s)	1.1 – 1.7	1.0 – 1.8
	Mean spectral period, $\overline{T}$ (s)	0.8 - 1.3	0.8 – 1.2
	Mean period, T_m (s)	0.9 – 1.4	0.9 – 1.3
Zero Crossing Analysis	Significant wave height, H_s (m)	0.09 – 0.23	0.09 – 0.23
	Maximum wave height, H_{max} (m)	0.20 – 0.38	0.20 – 0.35
	Root-Mean-square wave height, H_{rms} (m)	0.07 – 0.17	0.07 – 0.17
	Mean wave height, $\overline{H}$ (m)	0.06 – 0.15	0.06 – 0.14
	$H_{1/10}$ (m)	0.12 – 0.29	0.12 – 0.26
	Mean period, $\overline{T}$ (s)	0.9 – 1.4	0.9 – 1.4
	Significant period, T_s (s)	0.9 – 1.7	0.5 – 2.2

Table 6.3. Relation between significant wave height and other wave height statistics.

	H_{max}/H_s	H_{rms}/H_s	$\overline{H}/H_s$	$H_{1/10}/H_s$
Theoretical predictions under narrow-banded conditions (Longuet-Higgins, 1952)	1.86	0.71	0.64	1.27
Current data (March, 2005)	1.76	0.72	0.64	1.25
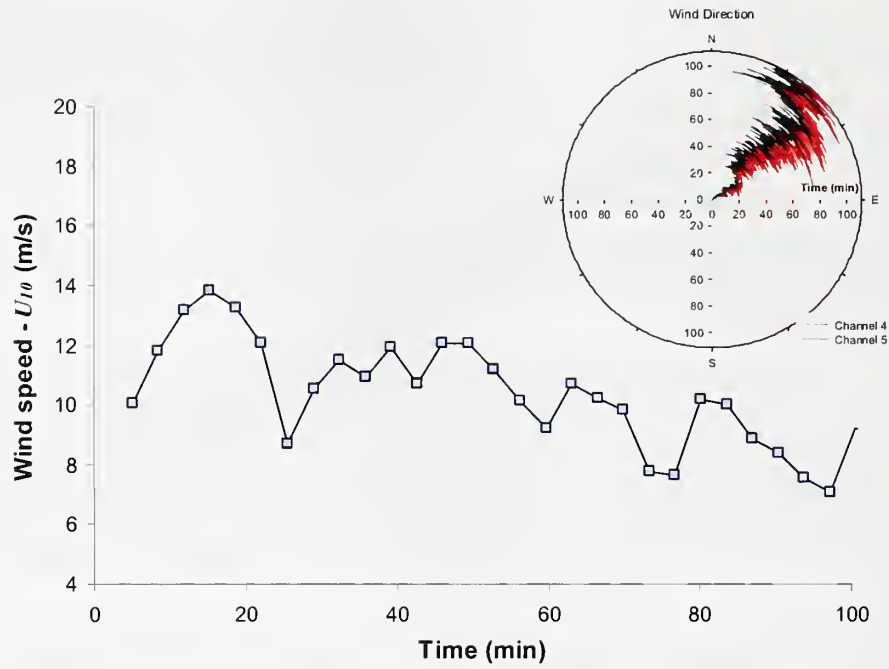
Figure 6.11 Wind speed and direction for the 2005 data set estimated by Power Law.
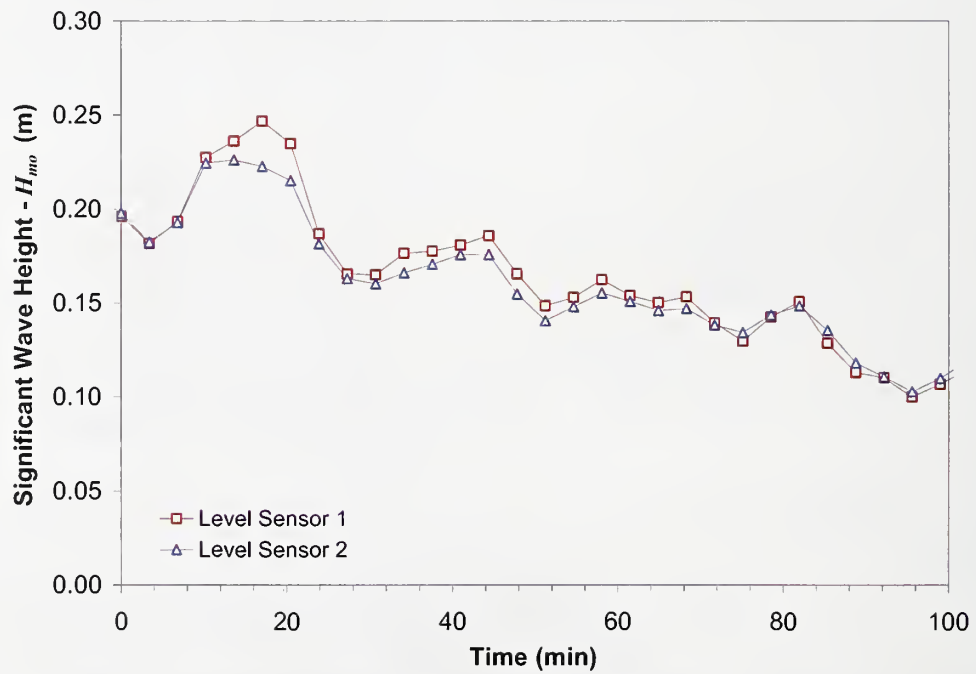
Figure 6.12 Energy-based significant wave height for 2005 data set.
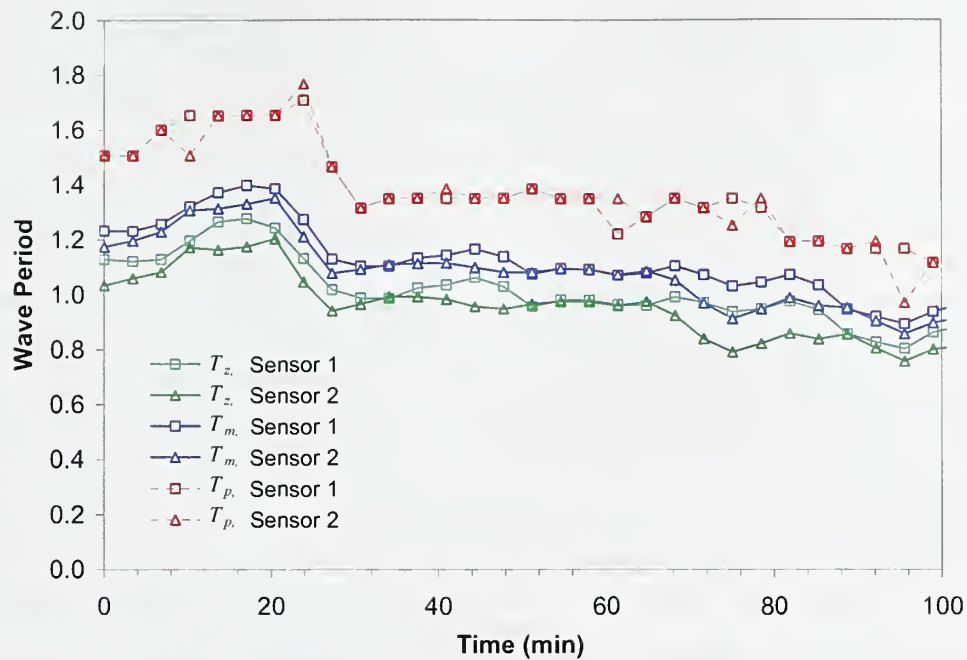
Figure 6.13 Peak mean and mean spectral periods for 2005 data set
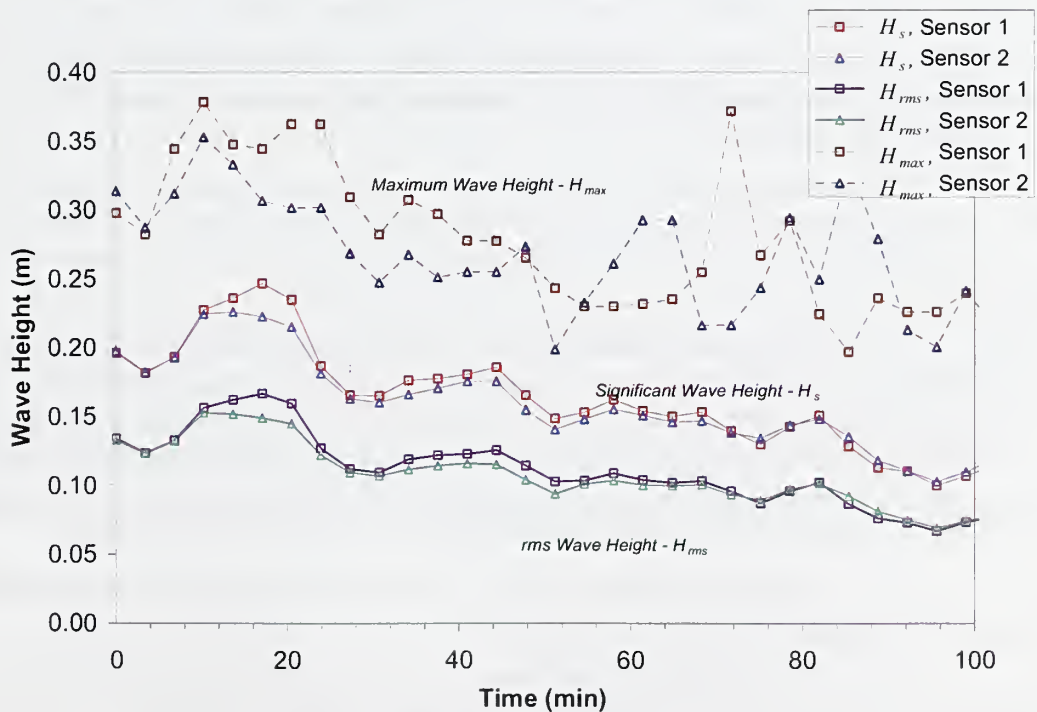
Figure 6.14 Wave heights by time domain analysis for 2005 data set.
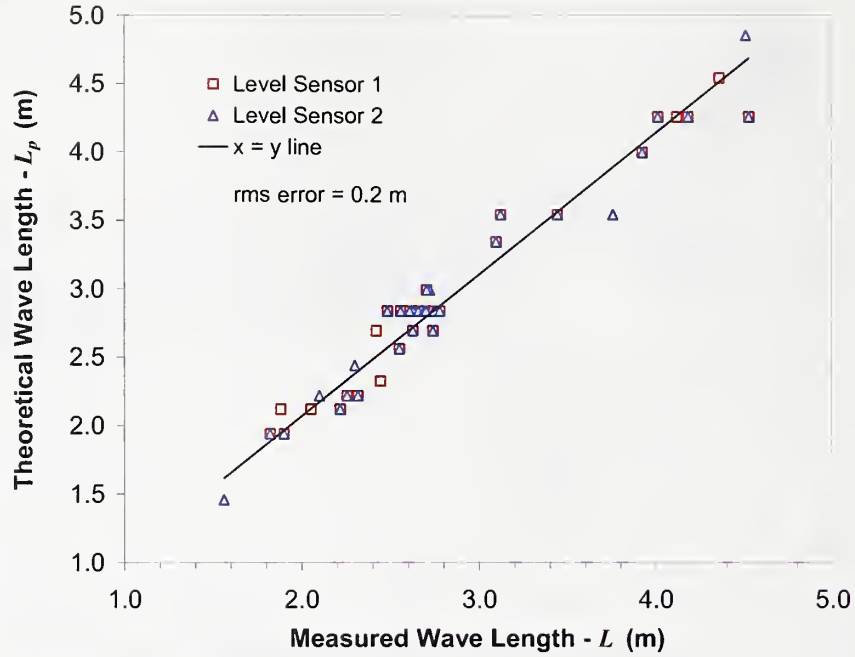
Figure 6.15. The comparison of measured and computed wavelengths.

It can be seen that there is a good agreement with the field data except for H_{max}/H_s. The H_{max}/H_s ratio is small for the experimental data than the theory predicts. This is mainly because the length of the data record is not sufficient to see extreme wave heights.

The measured and theoretical wavelengths are compared in Figure 6.15. The wavelengths are in reasonably good agreement with the theory showing that the waves in the field propagate according to the linear wave theory dispersion relationship (Equation 3.13).

The results of the 2007 field study are presented in Figures 6.15-6.17. The first plot in these figures shows the wind vectors along the breakwater. Note that x-axis (time) is aligned with the breakwater in these feather plots which means, if the wind vector is perpendicular to x-axis, it is also perpendicular to the breakwater. Second plot is the wind speed at 10 m elevation which is calculated by assuming logarithmic wind profile. The next two plots show H_{mo} and T_p during the entire data recording period.

The last plot in Figures 6.16, 6.17 and 6.18 is transmission coefficient for H_{mo} which is defined by:

$$K_t = \frac{(H_{mo})_2}{(H_{mo})_1} \quad \text{and} \quad K_t' = \frac{(H_{mo})_2}{(H_{mo})_3} \tag{6.4}$$

where the subscripts on H_{mo} indicates the wave gauge number (see Figure 6.4). Figure 6.15 shows the results for the single pipe with d=29 cm breakwaters while Figures 6.16 and 6.17 are the results for double pipe breakwater shown in Figure 6.5. The wind speed went up to 8 m/s and its direction ranged between east and north throughout the study (about 20° relative to the normal of the breakwater).

In Figures 6.16-6.18, several things should be noted. The changing wind direction caused the waves to impact the absorber at different directions, resulting in sensor I and sensor II encountering, at times, either incident or transmitted waves. The algorithms used to analyze the data took this into account, and swapped the treatment of data from the sensors so that κ_t could be correctly calculated. Both early and late in the record, values of κ_t greater than 1 are seen. These result from low amplitude waves whose direction was nearly parallel to the wave absorber causing the level sensors to measure nearly identical wave heights. This, combined with measurement error from the sensors, resulted in time periods where the transmission coefficient was greater than one. In Figure 6.18, for winds that were approximately normal to the floating breakwater (from about 11:00 a.m. to 12:45 p.m.), the reduction in transmitted wave amplitudes (1-κ_t) ranged from 40%-55%. Similar reductions were achieved in Figure 6.16 for the single pipe between around 3:00 am and 5:00 am but the wind speed was relatively low.

Figure 6.19 shows the wind speed data collected over an approximately 43 hour period in June, 2008. The wind speeds were relatively high with sustained speeds over12 m/s for several hours. The wind direction was primarily from the south (40° relative to the to the normal of the breakwater) throughout the period of data collection.

Figure 6.20 shows the wave height, H_{mo} and, peak period T_p and mean period, T_m, over the data recording at the offshore gauge. In Figure 6.21 the wave height data form two gauges is compared with the transmission coefficient, K_t which is defined as:

$$K_t = \frac{\left(H_{mo}\right)_{Sensor 1}}{\left(H_{mo}\right)_{Sensor 2}} \tag{6.5}$$

In Figure 6.22 the time domain analysis estimates for wave height are plotted for the data recorded at the offshore gauge (Level sensor 2). The kh values in Figure 6.23 were always greater then π which implies that deepwater conditions were predominant during the recording period. Another important dimensionless parameter is the wave steepness which is defined as the ratio of the wave height to the wavelength. Wave steepness, $\dfrac{H_{mo}}{L_p}$ was estimated to be between 0.05 and 0.06 most of the time as shown in Figure 6.24.

As shown in Figure 6.20, the wave amplitude was only decreased by an average amount of approximately 20%. Several factors contributed to the high wave transmission coefficients. The measurements were taken about 60 m from the end of the flaoting breakwater, so waves that came in all angles did not have to pass through the absorber.

121
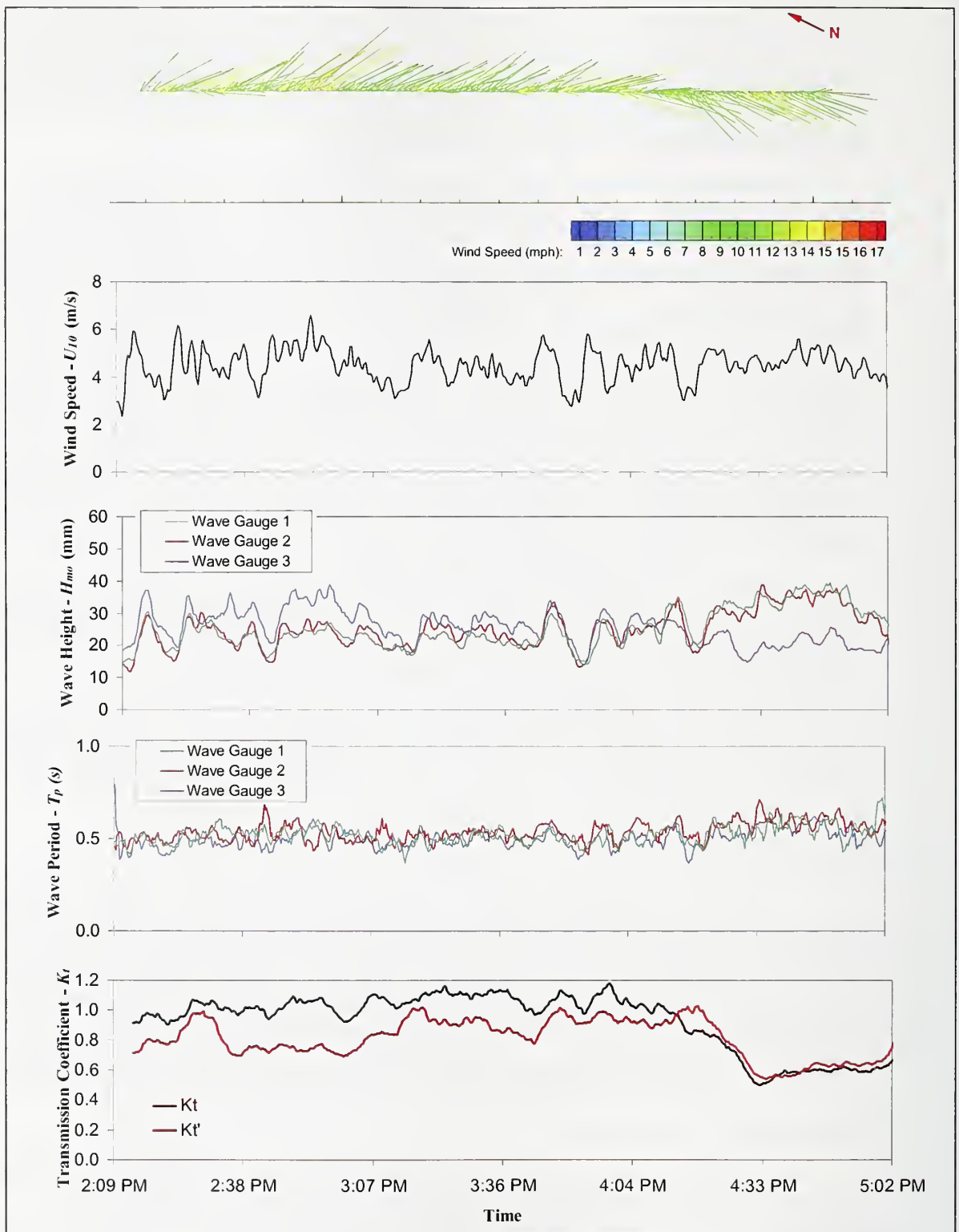
Figure 6.16 Wind and wave data from April 17, 2007 prototype scale field study with single pipe breakwaters. K_t and K_t' are defined in Equation 6.4.
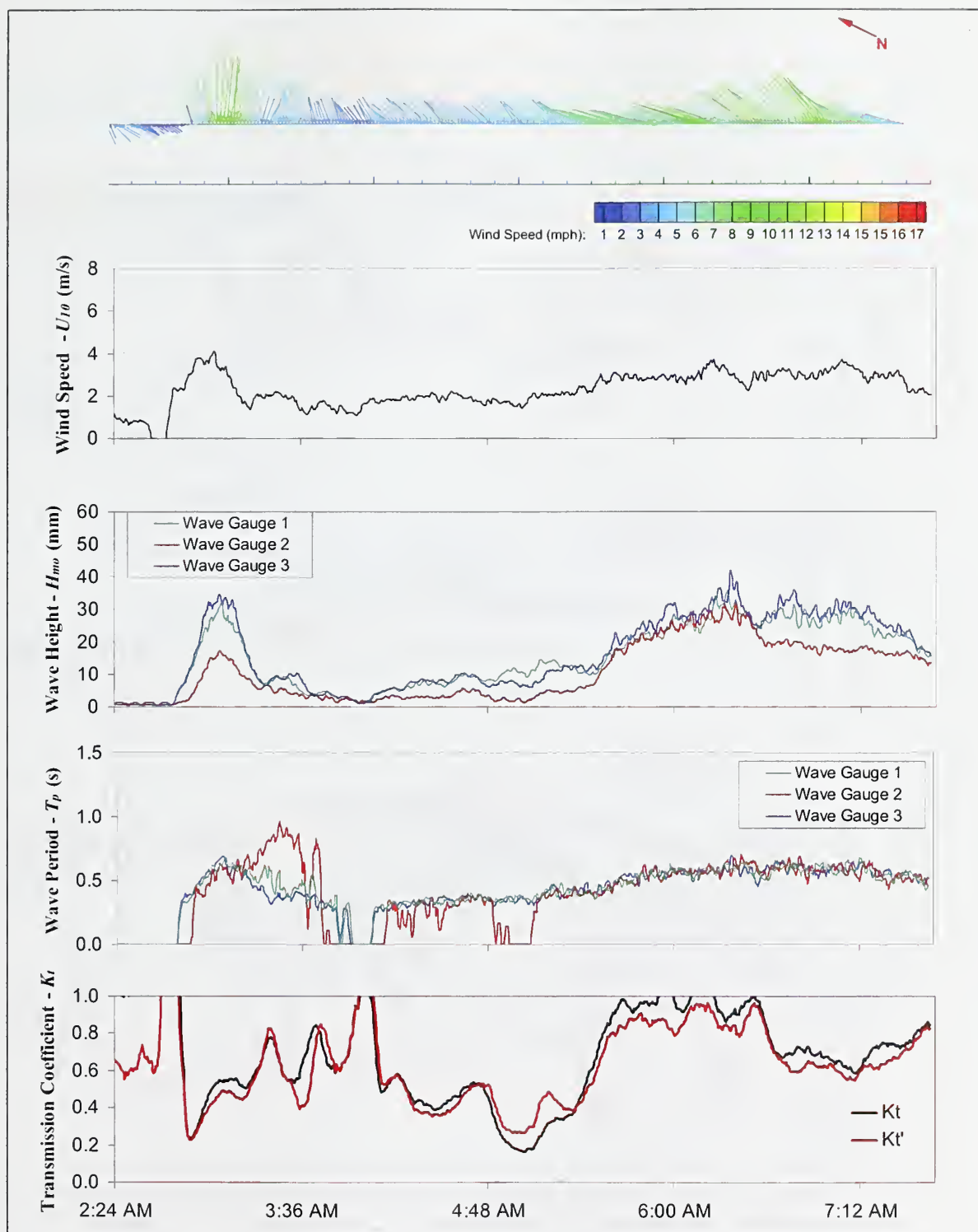
Figure 6.17. The recorded wind and wave data with double pipe breakwater in April 18, 2007. K_t and K_t' are defined in Equation 6.4.
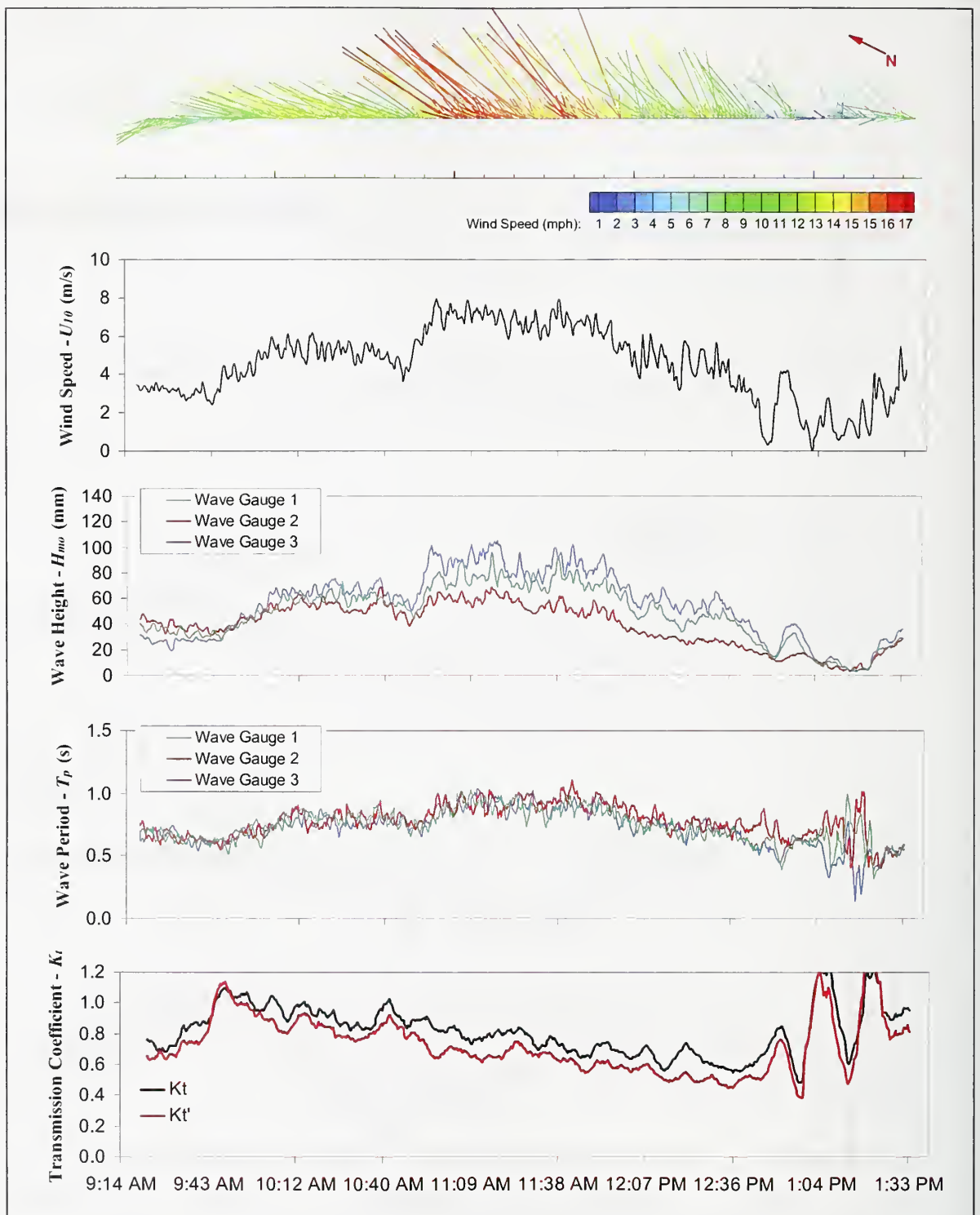
Figure 6.18. . The recorded wind and wave data with double pipe breakwater in April 18, 2007 (continued). K_t and K_t' are defined in Equation 6.4.
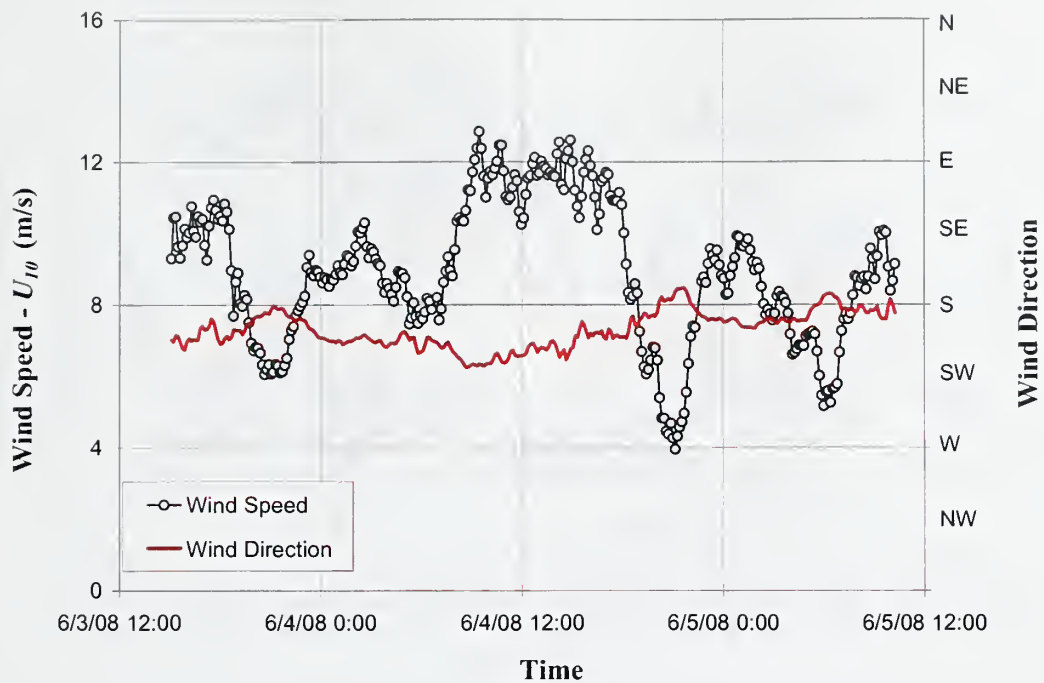
Figure 6.19. Wind speed and direction for June-08 data.
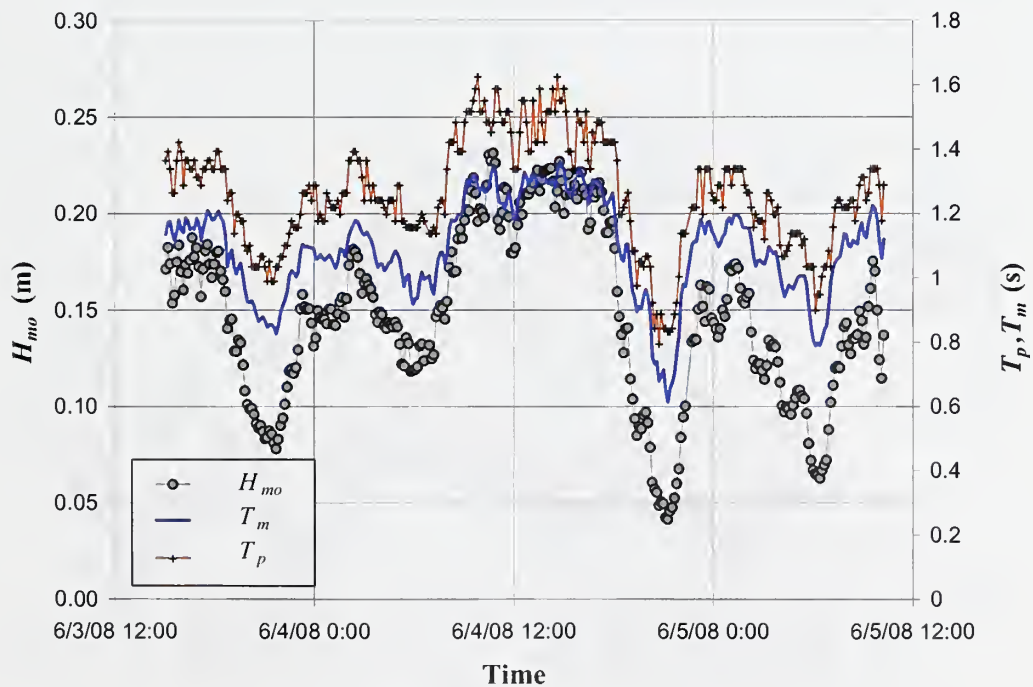
Figure 6.20 Significant wave height, peak period and mean period for June-08 data.
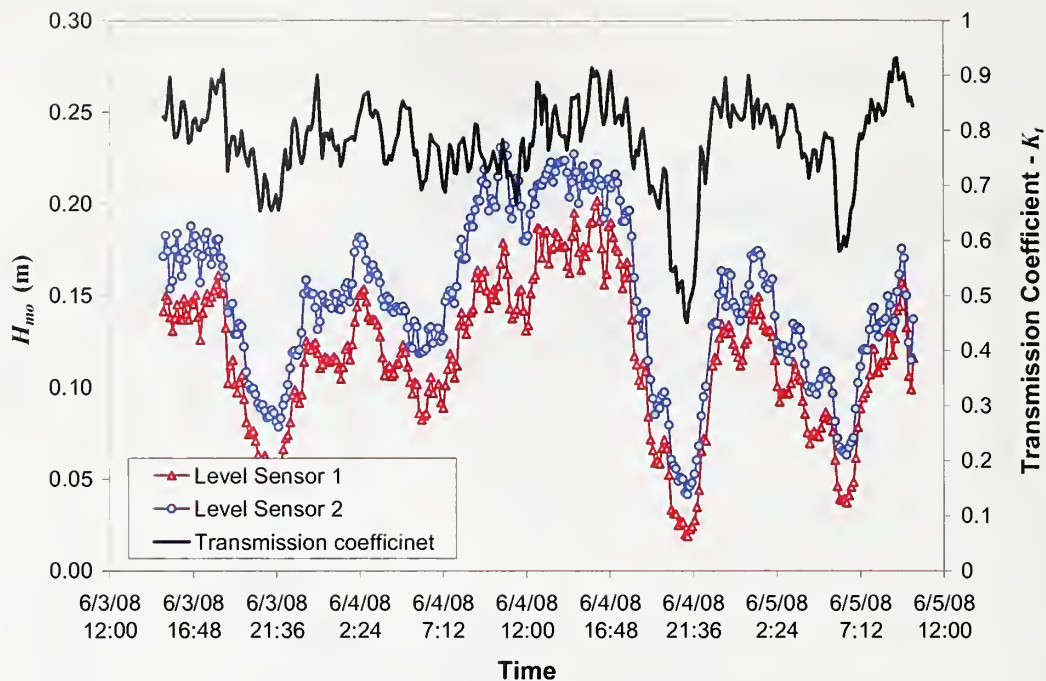
Figure 6.21 Significant wave height on both sides if the absorber and transmission coefficient for June -08 data.
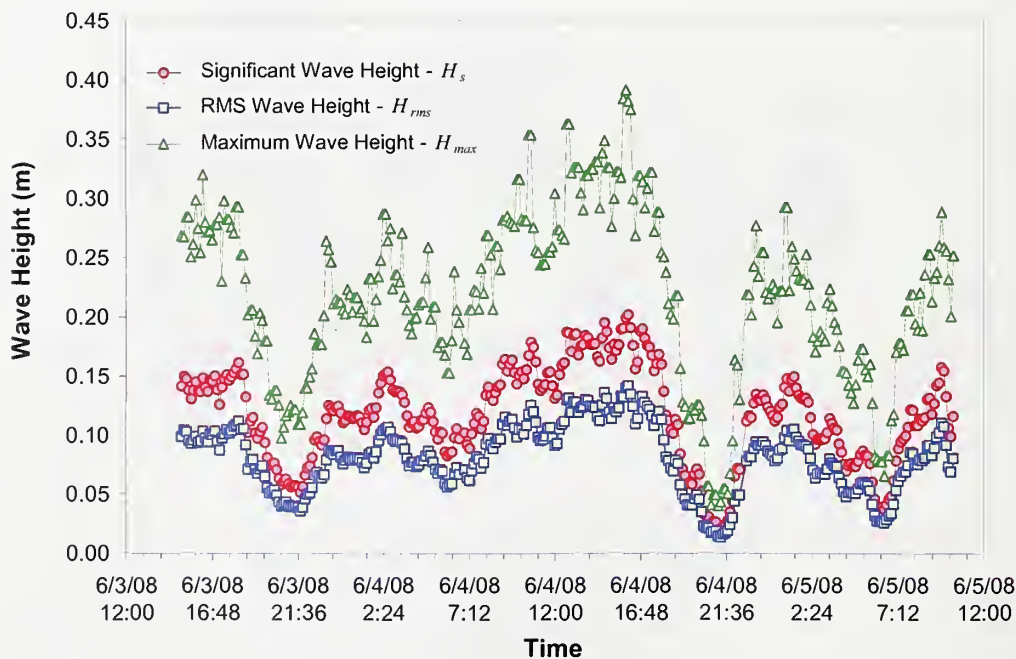
Figure 6.22 Wave heights statistics for June-08 data.
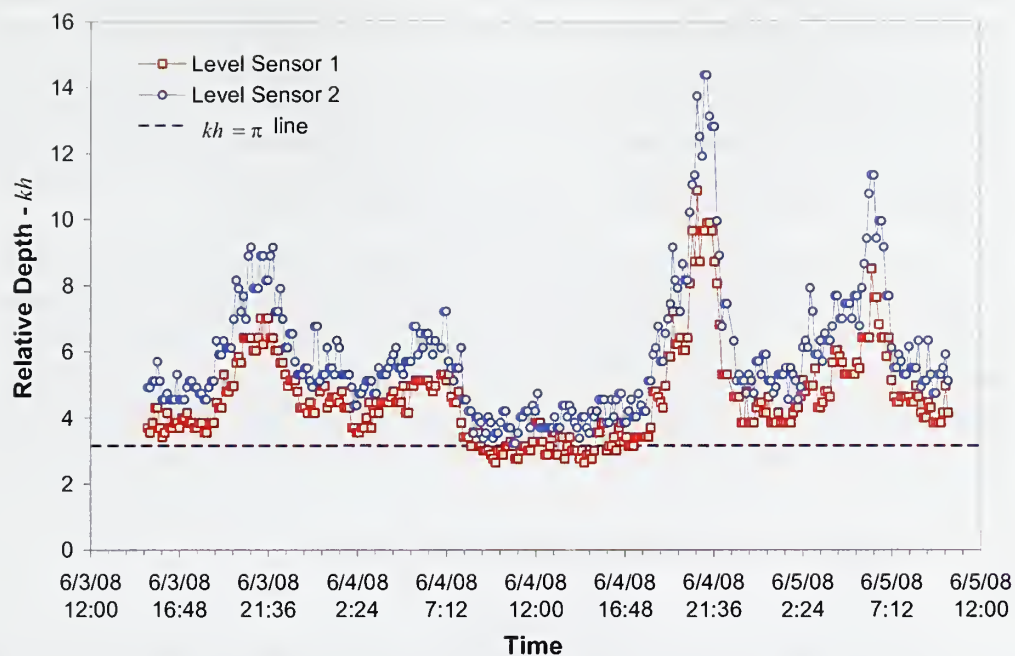
Figure 6.23. Relative depth variation of June 2008 data recording.
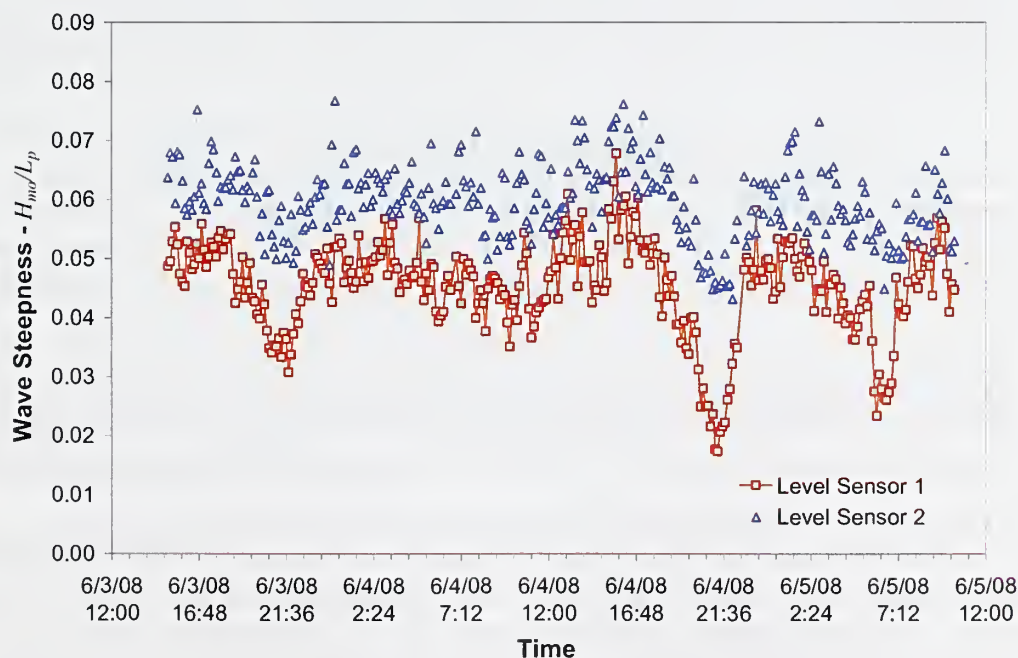
Figure 6.24. Wave steepness variation of June 2008 data recording.

The rope restraint allowed greater freedom of motion than the piles used in the laboratory experiments. The short lengths of model breakwaters tested in the laboratory resulted in stiff sections with no deflection on wave impact, whereas in the field, the flexibility of the tile drains might have increased the wave transmission. Another important weakness is that, although the draft, z_d of the new configuration was the same as of the two pipe configuration in 2007, the cross-sectional area was significantly less. It was proven during model studies that the inertia of the breakwater has an important role in reducing wave transmission in addition to breakwater draft.

The waves measured in the current field test were the largest measured during the project. Based on the laboratory and field results from this project, an absorber with a 60-75 cm diameter absorber will be necessary to adequately attenuate waves that were measured in 2008. Due to the high winds and large waves, there was damage to the absorber during the course of data collection. Several joints separated which both allowed waves to pass through and further reduced the rigidity of the floating breakwater.

6.5.   Comparison of the Laboratory and Field Tests

The field work to date has shown that laboratory work under predicts the scale of wave absorber necessary for effective use in the field. Some of the reasons for this include: higher rigidity of short sections used in the laboratory, more complete restraint of motion in the laboratory, the randomness of natural waves, and the large range in angle of attack of waves in the field. Based on these findings, the optimal absorber in the laboratory does not scale linearly with the dimensionless parameters. By combining field and laboratory data, an estimate of the needed difference in scale can be evaluated.

Model 96 is a pile breakwater design composed of two PVC pipes of different diameters attached at the top with a gap between the sections. In the laboratory experiments, the pipes were restrained by two piles on both sides of the larger pipe (Figure 6.25). In order to provide sufficient buoyancy to achieve the desired draft, Styrofoam caps were used. The remaining gap inside was filled with water and air.

The transmission coefficient as a function of breakwater size and wave steepness for Model 96 is shown in Figure 6.25. A two-parameter function can be fitted to the data in Figure 6.25 considering all the other parameters as constant. The trend of the data has an asymptotic behavior around $K_t = 0.2$ for wave steepness, $\dfrac{H_{mo}}{L_p}$ less than 0.03. For constant relative size, d/L, the transmission coefficient increases with increasing wave steepness at a decreasing rate. Therefore, a logistic curve is fitted to the data on the $K_t - \dfrac{d}{L_p}$ plane while a logarithmic curve is fitted on the $K_t - \dfrac{H_{mo}}{L_p}$ plane.
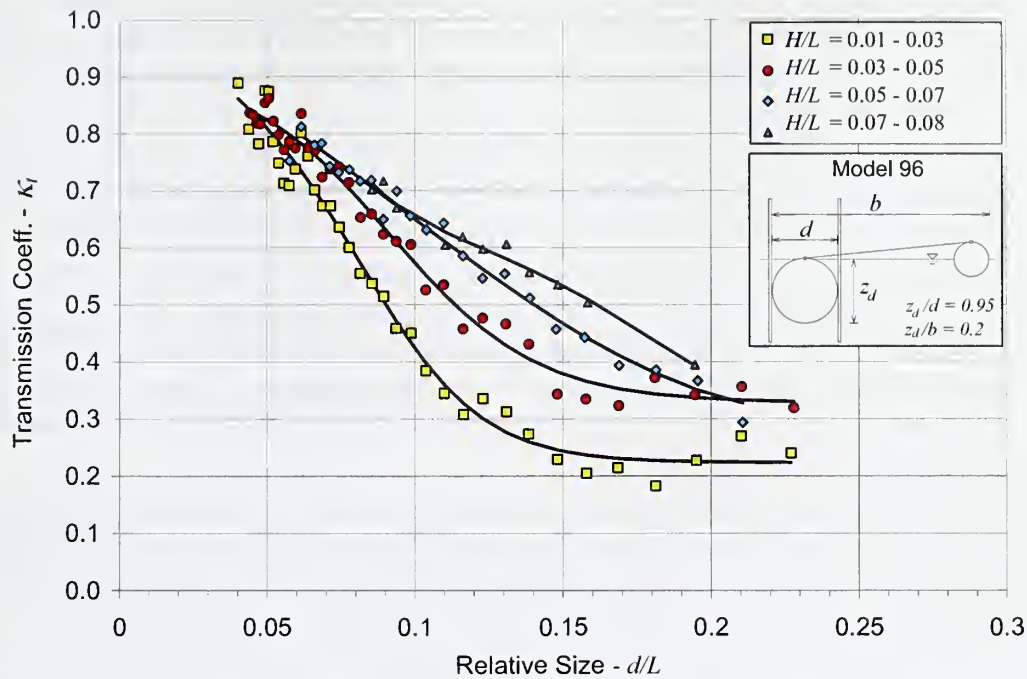
Figure 6.25 Effect of breakwater size on transmission coefficient for model 96.

The following equation was obtained by fitting the surface described above to the measured data:

$$K_t = \left[\frac{-0.147 - 1.87 \cdot e^{-14.7\left(\frac{d}{L_p}\right) + 1.66}}{1.57 + 0.81 \cdot e^{-0.46\left(\frac{d}{L_p}\right) + 0.796}} \right] \times \log\left[0.243\left(\frac{H_{mo}}{L_p}\right) + 1.03 \right] \tag{6.4}$$

$0.01 < \dfrac{H_{mo}}{L_p} < 0.08$ and $0.04 < \dfrac{d}{L_p} < 0.23$ ($R^2 = 0.97$ and rms error $= 0.033$).

The dimensionless breakwater size can be estimated from the curves or by trial and error solution of the empirical relation (Equation 6.4) below for a given transmission coefficient and wave steepness.

A comparison of laboratory results for Model 96 and the two field tests is shown in Figure 6.26. The wave steepness (H_{mo}/L_p) for the field tests was 0.05-0.06, so only the data in that range of wave steepness were included for Model 96 in Figure 6.25. The relative depth was greater than π as shown in Figure 6.24, indicating that the deepwater assumption can be used in calculations. Another parameter affecting the transmission coefficient is the wave approach angle, which was not considered in the model studies. In reality, the wave energy travels in the direction of the wave ray, the line along which the

wave number vector is always tangent (Dean and Dalrymple, 1991). Therefore, the energy associated with the wave also travels in the direction of the wave ray. For the waves travelling on the x-y plane the wave number vector is defined as:

$$\mathbf{k} = k_x \mathbf{i} + k_y \mathbf{j} \qquad (6.5)$$

where $\mathbf{i}$ and $\mathbf{j}$ are the unit vectors in the x an y directions respectively. It can be assumed that the energy associated with the component of the wave number parallel to the breakwater does not contribute to the transmission coefficient. Since the wavelength normal to the breakwater ($L_x = \dfrac{k_x}{2\pi}$) is greater than the incident wavelength, the relative sizes d/L will be less and therefore the data corresponding to the April 2007 and June 2008 field studies in Figure 6.26 will be shifted to the left if directional effects also included.

The 2008 field configuration was moored only at the ends letting the pipes move horizontally. Therefore, it has similar dynamics to model 65, the half-submerged bottom moored configuration. Model 65 is also plotted in 6.26 for comparison.
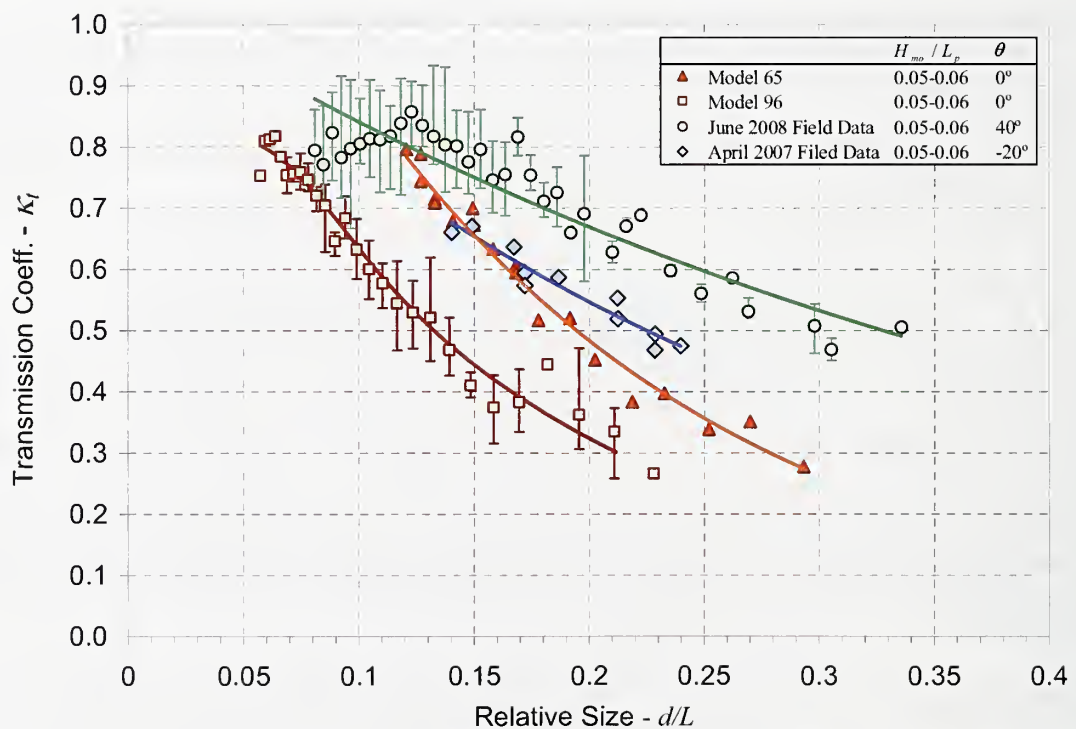
Figure 6.26 The transmission coefficients of the field and experimental study for models 96 and experimental study for model 65.

Ideally, the mooring method should result in the highest degree of restraint possible. In the laboratory tests, pile restraints were the most effective. Due to problems with obtaining relatively inexpensive pile restraints, these were not tested in the field. Ropes tied to posts driven into the levee were used. This method is simple and inexpensive, but does not limit the motion of the breakwater as well as piles. A combination of widely spaced piles and rope/wire restraint may be necessary. Long term field studies should result in more specific guidance.

This result above is based on laboratory data and should be scaled up for field deployment. The breakwater design used during the April, 2007, field data collection is the closest to the Model 96 laboratory results, making it the most reasonable point of comparison. For a given transmission coefficient and a wavelength (L), a larger breakwater will be needed in the field.

The key parameter needed for properly sizing a breakwater is the amplitude of the waves that will impact it. Since wave measurements for small reservoirs are seldom available, wind speeds and directions can be used to predict wave characteristics. Such predictions are common for coastal and marine environments, but there is much less data on the relationship between winds and waves for smaller water bodies. This deficiency is addressed in Appendix G based on the field data collected during the course of the current project.

In the absence of local wind speed/direction measurements, generic design criteria should be used. However, this may result in gross over or under sizing of the breakwater. USDA-SCS Technical Release 56 (TR56) (USDA-SCS, 1974) recommends using a 50 mph (22 m/s) wind over the longest fetch available for designing vegetative bank protection. The cost of breakwaters makes this recommendation generally infeasible. Based on the limited data available from the current work, a 9 m/s wind over the longest fetch in a given reservoir is a reasonable design parameter. Regarding wind direction, the authors of TR56 could find no justification for expecting an increased probability for high wind from a specific direction. The limited field data collection described in this report supports the claim; therefore, in the absence of local wind data or observations indicating greater levee damage from waves in given direction, the use of maximum fetch length as a design parameter is recommended.

After determining the size of the breakwater, the logistics of installing and restraining it must be addressed. The main focus of the work described here was in determining the feasibility of using floating breakwaters and in establishing sizing guidance. However, the limited amount of field work does allow some suggestions for deployment.

The method for joining together the sections of a composite absorber should take into account the buoyancy of the pipe. Using too many braces or braces that are too heavy may result in a breakwater that will not float. Drainage pipe has a density only slightly lower than water, thus, it cannot support a large mass of braces. If sections of breakwater are joined end-to-end, a rugged fastening method should be used to ensure

131

that the floating breakwater can withstand the tension resulting from wind and wave loads.

The current study focused on the reduction of wave energy before the waves reach the levees. Transport of sediment in small reservoirs and lakes is primarily due to the waves and their associated currents, currents related to the wind stress, and density distribution. The breaking of the waves result in erosion along the breaking line and the material is carried offshore until bed shear drops lower than the critical shear stress. The wave breaking in the surf zone is controlled by the beach-profile shape, water depth, wind direction and wind speed and soil properties. It was observed throughout the field studies that the main damage is due to the strong waves undercutting and resulting in bank failure during an extreme event. The undercutting rate is directly related with wave breaking and depends on energy and direction of the waves and fluctuations in water depth. Therefore, restoration of the reservoir morphology and beach profiles can contribute reducing the erosion.

6.6.   Estimation of Wave Barrier Size

The size of breakwater to reduce the wave height to a desired level can be estimated based on wind data using the wind-wave relations and transmission properties of the experimental model for those wave conditions. The step by step procedure and an example calculation follow:

1. Calculate the wind speed at 10 m, U_{10} using Equation G.3a,
2. Calculate the wind stress factor U_A from Equation G.2,
3. Calculate the dimensionless number $\dfrac{gF}{U_A^2}$ using the fetch length and U_A,
4. Check the minimum duration with Equation G.8 using the calculated $\dfrac{gF}{U_A^2}$.
5. Calculate T_p and H_{mo} either using Figures G.3 and G.4 (use "Fitted line") or equations G.7a and G.7b
6. Calculate the wave length using G.9b.
7. Check if deepwater condition is satisfied using relative depth h/L_p. If $h/L_p < 0.5$ then waves are in deepwater range.
8. Calculate the wave steepness, H_{mo}/L_p. The wave steepness is usually around 0.05-0.06 for the available field data but a range of steepnesses between 0.02 and 0.08 are available for experimental data.
9. Find the corresponding d/L_p from Figure 6.25 for the desired transmission coefficient, K_t and the calculated wave steepness, H_{mo}/L_p or, insert the wave steepness into the Equation 6.4 and iterate for d/L_p to get the desired transmission coefficient.

10. Calculate the breakwater dimension, *d*, by using wave length, L_p. Other dimensions can be adjusted according to Figure 6.25.
11. Multiply the dimensions obtained above by 1.5-2.0 in order to achieve similar wave reduction to that observed in the laboratory (see explanation below).

This result above is based on laboratory data and should be scaled up for field deployment. The wave barrier design used during the April, 2007, field data collection is the closest to the Model 96 laboratory results, making it the most reasonable point of comparison. For a given transmission coefficient and a constant value of wavelength (*L*), a larger wave barrier will be needed in the field. For high values of the transmission coefficient, the two values become similar. For a 50% transmission coefficient, the ratio between field and laboratory barrier size is approximately 2, meaning that the dimension of a wave barrier in the field would have to be doubled to equal the performance seen in the laboratory. For lower transmission coefficients, the ratio will be larger than 2, resulting in wave barrier sizes that are impractical due to size and cost. Doubling the size for a wave barrier in the field relative to the laboratory measurements is a conservative estimate, since the April 2007 data were collected with winds that were 20^0 off of the normal angle of attack. For practicality, it is recommended that the size of barrier predicted by laboratory results be increased by 1.5-2 times, with the understanding that the smaller wave barriers will transmit more wave energy than desired. This scaling factor is also supported by the work of Jackson (1964) discussed in the literature review section.

6.6.1. Example Application

Consider the wind is recorded as 17 mph at an elevation of 9 ft above the mean water surface at a location with 1,500 ft fetch length and 8 ft water depth. Calculate the breakwater size *d* which yields transmission coefficient, $K_t = 0.5$.

1. Calculate wind speed, U_{10} at 32.8 ft (10 m),

$$U_{10} = U_z \left(\frac{32.8}{z} \right)^{1/7} = 17 \left(\frac{32.8}{9} \right)^{1/7} = 20.4 \text{ mph}$$

2. Calculate wind stress factor, U_A,

$$U_A = 0.59 U_{10}^{1.23} = 0.59 \times 20.4^{1.23} = 24.1 \text{ mph (35.4 ft/s)}$$

3. Calculate $\dfrac{gF}{U_A^2} = \dfrac{32.17 \times 1500}{(35.4)^2} = 38.6$

4. Check minimum duration,

$$\frac{gt_{min}}{U_A} = 108.2\left(\frac{gF}{U_A^2}\right)^{0.28} \quad \text{or} \quad t_{min} = 108.2\frac{U_A^{0.44}F^{0.28}}{g^{0.72}}$$

$$t_{min} = 108.2\frac{U_A^{0.44}F^{0.28}}{g^{0.72}} = 108.2\frac{35.4^{0.44}1500^{0.28}}{32.17^{0.72}} = 326 \text{ s} = 5.43 \text{ min}$$

This is the averaging duration for wind speed.

5. Calculate T_p and H_{mo} from equations G.7a and G.7b,

$$T_p = 0.4147\frac{U_A^{0.44}F^{0.28}}{g^{0.72}} = 0.4147\frac{35.4^{0.44}1500^{0.28}}{32.17^{0.72}} = 1.27 \text{ s}$$

$$H_{mo} = 0.0025\frac{U_A^{1.12}F^{0.44}}{g^{0.56}} = 0.0025\frac{35.4^{1.12} \times 1500^{0.44}}{32.17^{0.56}} = 0.49 \text{ ft}$$

6. Calculate the wave length from equation G.9b,

$$L_p = 5.12T_p^2 = 5.12 \times 1.27^2 = 8.26 \text{ ft}$$

7. Check deep water condition,

$h/L_p = 8 / 8.26 = 0.97 > 0.5$, deep water.

8. Calculate the wave steepness,

$H_{mo}/L_p = 0.49 / 8.26 = 0.060$

9. Calculate the breakwater dimension D_1,
   From Figure 6.25 for a transmission coefficient of 0.5 one reads $d/L_p = 0.13$.
   $K_t = 0.5$ and $H_{mo}/L_p = 0.060$.

10. $D_1 = 0.13 \times 8.28 = 1.08$ ft ($\cong 13''$)

   From Figure 7.7, $D_1/b = 0.3$, $b = 13/0.3 = 43''$
   and $D_2/D_1 = 0.43$, $D_2 = 13 \times 0.43 = 5\frac{5}{8}''$

The closest available pipe size can be selected to satisfy the desired attenuation needs. Based on the discussion of laboratory vs. field sizing, each dimension should be multiplied by 1.5-2.0. The choice of multiplier will be based on available funds and the value of the levee being protected.

6.6.2. Wave Barrier Restraint

After determining the size of wave barrier, the logistics of installing and restraining it must be addressed. The main focus of the work described here was in determining the feasibility of using floating wave barriers and in establishing sizing guidance. However, the limited amount of field work does allow some suggestions for deployment.

- The mooring method should result in the highest degree of restraint possible. In the laboratory tests, pile restraints were the most effective. Due to problems with obtaining relatively inexpensive pile restraints, these were not tested in the field. Ropes tied to posts driven in to the levee were used. This method is simple and inexpensive, but likely does not limit the motion of the wave barrier as well as piles. A combination of widely spaced piles and rope/wire restraint may be necessary. Long term field studies should result in more specific guidance.

- The method for joining together the sections of a composite absorber should take into account the buoyancy of the pipe. Using too many braces or braces that are too heavy may result in a wave barrier that will not float. Drainage pipe has a density only slightly lower than water, so it cannot support a large mass of braces.

If sections of wave barrier are joined end-to-end, a rugged fastening method should be used to ensure that the barrier can withstand the tension resulting from wind and wave loads.

VII.   NUMERICAL MODEL

7.1.   Introduction

It was shown in the physical model studies that the transmission of wave energy through a floating breakwater is controlled by various mechanisms. For a partially submerged and partially restrained floating body wave energy is transmitted under, over and possibly through the structure. The separate contribution of each mechanism depends on the design of the breakwater as well as the wave characteristics. The flow around a floating object is complex and transient due to its coupled motions with the fluid. A numerical model is necessary to solve the governing equation of this complex flow and to understand the individual contribution of each phenomenon.

In this study, a commercially available software package, FLOW-3D, was utilized for simulating the flow field around a cylindrical breakwater under various combinations of wave characteristics and breakwater configurations by solving the governing equations of flow and rigid body motion with the appropriate initial and boundary conditions. The standard code was customized to be able to generate regular and irregular waves at a source region. The customized version also improved the data input/output for wave data analysis.

The procedure followed to set-up the numerical model and to carry out the simulations is outlined in Figure 7.1. The current text is organized parallel to the outline plotted in Figure 7.1. The mathematical model is built by making reasonable simplifications and assumptions to derive a set of partial differential equations and boundary conditions to mimic the constructed physical model. The details of the physical problem in connection with the numerical simulation will be described in the next chapter in more detail. The governing equations and the associated boundary conditions are presented in Section 7.2. These partial differential equations are converted to simple algebraic equations by some approximations. In relation with the discretization of the equations the problem domain is also divided into discrete components which will be referred as the computational mesh. The numerical solutions algorithm utilized for the solution of the current problem with mesh generation and implementation of the boundary conditions is introduced in Section 7.3. The verification and validation of the problem with the numerical simulations and processing the output data is also left to the next chapter.
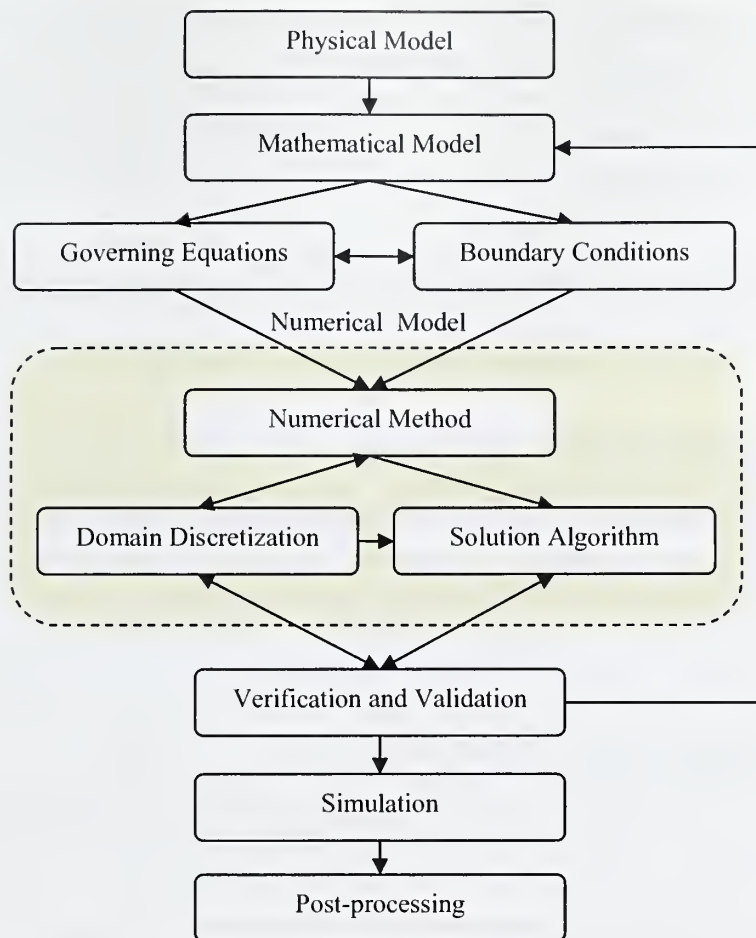
Figure 7.1 Procedure for numerical simulations.

7.2. Governing Equations

The floating breakwater models considered here are essentially single or multiple circular cylindrical elements. Each circular section is either solid or hollow with a finite wall thickness. The breakwater material is assumed to be rigid and homogenous. The density of the hollow cylinder and the inner fluid region elevation are adjusted to ensure that it floats on the surface with a predefined draft.

7.2.1. Average Flow Field

For a fluid continuum governing equations are derived from the conservation laws for mass, momentum and energy. The mass conservation equation is

$$\frac{\partial}{\partial t}\rho + \nabla \cdot (\rho \mathbf{v}) = S \tag{7.1}$$

where ρ is the mass density of the fluid, $\mathbf{v}$ is the velocity vector and ∇ is the gradient operator. Note that the bold letters define vector variables and the dot (.) denotes the scalar product of two vectors. S on the right hand side the equation represents the sources and sinks. In the absence of mass sources and for incompressible flows the mass conservation equation reduces to the divergence of the velocity which is written as:

$$\nabla \cdot \mathbf{v} = 0 \tag{7.2}$$

The momentum transport equation for the average flow field is

$$\rho \left(\frac{\partial \mathbf{v}}{\partial t} + \mathbf{v} \cdot \nabla \mathbf{v} \right) = -\nabla p - \nabla \cdot \boldsymbol{\tau} + \mathbf{B} \tag{7.3}$$

Here, $\mathbf{B}$ is the body force vector, $\boldsymbol{\tau}$ is the viscous stress tensor, p is the pressure and ρ represents the mass density of the fluid. The momentum transport equation for the fluid continuum reduces to the Navier-Stokes equations for Newtonian fluids for which stress is linearly proportional to strain. For an incompressible fluid with constant viscosity, the Navier-Stokes equations can be written as

$$\rho \left(\frac{\partial \mathbf{v}}{\partial t} + \mathbf{v} \cdot \nabla \mathbf{v} \right) = -\nabla p + \mu \nabla^2 \mathbf{v} + \mathbf{B} \tag{7.4}$$

7.2.2. Dynamics of the Floating Body

The rigid body motion of the object is coupled with the fluid motion. The dynamics of the floating object can be calculated if the pressure field around it is known. The flow field is affected by the motion of the object as well.

Velocity at any point on the rigid body can be calculated by adding the velocity of an arbitrary base point and the velocity due to the rotation around this point. It is convenient to select the center of mass as the base point for an unconstrained object. If the object is free to rotate around a fixed point or axis the base point can be selected as the point of rotation.

$$\mathbf{v}_P = \mathbf{v}_G + \boldsymbol{\omega} \times \mathbf{r}_{P/G} \tag{7.5}$$

Where p is a point on the object $\mathbf{v}_G$ is the velocity of the center of mass $\boldsymbol{\omega}$ is the angular velocity of the object $\mathbf{r}_{P/G}$ is the position vector from G to P. From Newton's Second Law the equation of motion for the rigid body translation is

$$\sum \mathbf{F} = m\mathbf{a} \text{ or } \sum \mathbf{F} = m\frac{d\mathbf{v}_G}{dt} \tag{7.6}$$

where $\sum \mathbf{F}$ is the total force acting on the object and m is the mass of the object. Likewise the equation of rigid body rotation is

$$\sum \mathbf{T} = \mathbf{I} \cdot \boldsymbol{\alpha} + \boldsymbol{\omega} \times (\mathbf{I} \cdot \boldsymbol{\omega}) \text{ or } \sum \mathbf{T} = \mathbf{I} \cdot \frac{d\boldsymbol{\omega}}{dt} + \boldsymbol{\omega} \times (\mathbf{I} \cdot \boldsymbol{\omega}) \tag{7.7}$$

where $\sum \mathbf{T}$ is the total torque around G, α is the angular acceleration and I is the inertia tensor around G.

The total force is expressed as;

$$\sum \mathbf{F} = \mathbf{F}_b + \mathbf{F}_s \qquad (7.8)$$

where $\mathbf{F}_b$ represent the body forces which is the gravity force in our case and $\mathbf{F}_s$ represent the surface forces like hydraulic pressure forces, shear forces and other external forces restricting the motion of the object. Likewise, the total torque is a combination of body forces and surface forces defined above. The gravity torque is equal to zero by definition if the center of mass is selected as the base point.

In some cases it is required to simulate rigid body collisions. The model of Stronge (2000) for collision with six degrees of freedom was adopted in FLOW-3D. The model was modified by Wei (2006b) to account for bodies with fixed axis point and prescribed motion. In this model the collision can be perfectly elastic, partially plastic and completely plastic. The model allows simulating the friction at the point of contact between the colliding objects and during sliding. The friction between rough surfaces is based on Coulomb's Law of friction. The speed and the direction of the objects can vary during the collision. It is assumed that all the objects are rigid and their velocities change instantaneously during collusion. Stronge's energetic coefficient of restitution is utilized to determine the computation of the collision integration (Stronge, 2000). Details of the collision model can be found in Wei (2006b).

7.2.3. Turbulence

At large Reynolds numbers the flow field becomes complex and unsteady, resulting in chaotic and random variations of the flow variables in time and space. The turbulent flow field is always unsteady, three-dimensional, and random. It is composed of three-dimensional, random vorticity fluctuations called eddies. It is not possible to model all the scales of turbulent flow with the current computer capabilities. Therefore, instead of resolving the individual eddies, their effects on average flow are taken into account by means of a turbulence model. The time averaging of the turbulent fluctuations in velocity and pressure introduce additional unknowns into the governing equations. Thus, additional equations are required for the closure of the problem. Various turbulence models are developed including the zero equation, one equation, two equation, and Reynolds-stress models. Mathematical closure of these equations requires empirical constants which are mostly problem specific and hence selection of a turbulence model requires special care (Tennekes and Lumley, 1972, Versteeg and Malalasekera, 1995)

In the current study, high Reynolds numbers are expected close to the boundaries and during wave breaking. Turbulence models have been successfully applied to flows with wave breaking in some recent studies (Liu and Lin, 1997, Clauss et al, 2005, Greaves, 2007). A suitable turbulence model with proper boundary conditions is required to correctly model the problem.

139

There are five turbulence models available in FLOW-3D. These are the Prandtl mixing length model, the one-equation, the two-equation k-ε and Renormalization-Group (RNG) models, and large eddy simulation (LES) model. These models include the influence of fractional areas/volumes and turbulence generation and decay associated with buoyancy forces. RNG model is utilized for turbulent simulations.

7.2.4. Boundary Conditions

If an interface is represented by a function $f(x,y,z,t)$ the kinematic boundary condition along any impermeable interface is

$$\frac{Df}{Dt} = 0 \text{ along the interface.} \tag{7.9}$$

Impermeable and no-slip boundary conditions are applied to the solid walls. Since the fluid cannot pass though the wall which may be moving, the normal velocities relative to the wall are set to be equal to zero. The no-slip condition requires that the tangential velocity component to also equal zero with respect to the wall. Tangential and normal stresses are specified along the free surface. Dynamic free-surface boundary conditions are applied by neglecting the pressure variations along the free surface. Hence, the tangential stress is set to zero and the normal stress is assumed to be the sum of the air pressure and surface tension pressure.

7.3.   Numerical Method

The equations of motion for the fluid continuum given in Section 7.2 are highly nonlinear and transient. Therefore, a numerical scheme has to be adopted to approximate the solution. The discrete approximations of the governing partial differential equations are derived in various ways depending on the selected numerical algorithm. FLOW-3D solves these equations using Finite Difference and Finite Volume approximations. In the Finite Difference Method the value of a continuous function at a location can be approximately represented by a linear combination of its derivatives at another location with Taylor series expansion. The quality of the approximation depends on the distance between two points and the highest order of the derivatives included. In the Finite Volume Method (FVM), the computational domain is divided into a finite number of control volumes. The integral forms of the governing equations are satisfied in these non-overlapping control volumes. These two methods are derived using the Eulerian descriptions of the conservation equations and are more suitable for fluid flow. The numerical methods discussed above are well developed and widely used in various applications in mechanics and the details of the solutions algorithms will not be given here (Versteeg and Malalasekera, 1995)

The continuous partial differential equations are replaced by approximate algebraic equations which are valid at discrete locations in time and space. The computational domain is divided into finite number of control volumes (cells). These

cells subdivide the physical space into small portions with several nodes associated with each cell. Each fluid parameter is represented in a mesh by an array of values at these discrete nodes. The approach used in FLOW-3D is also based on a structural Eulerian mesh which divides the computational domain into well-ordered rectangular cells. The Eulerian grid is fixed in space, allowing the material to move through the boundary. Therefore, the shape and the volumes of the cells do not change during computation. The mass, momentum and energy fluxes across the fixed mesh cells are computed to redistribute the flow variables.

An Eulerian grid has some advantages in fluid flow problems but it is difficult to represent irregular geometries accurately (Liu and Liu, 2003). In case of Cartesian grid, reducing the grid spacing increases the number of the cells and, thus, the computational cost. Therefore, special methods are developed to deal with irregular geometries. In FLOW-3D the geometry is constructed by components (objects) which define the flow region for a simulation. The flow geometry is then embedded into the computational mesh by computing fractional areas of the cell faces and fractional volumes open to the flow. This method will be explained in section 7.3.6. The free surface is tracked by the Volume of Fluid (VOF) method in FLOW-3D this is discussed in section 7.3.5.

7.3.1. Numerical Discretization

To solve the governing equations numerically, the computational domain is divided into a Cartesian mesh of uniform size. The mesh is composed on rectangular cells of width, δx depth, δy and height, δz in the x, y and z directions, respectively. Fluid velocities and pressures are located at staggered mesh locations. The active mesh region is surrounded by boundary cells used to set the boundary conditions. The cells in the x-direction are labeled with i, the cells y-direction are labeled with j and those in the z-direction are labeled with k. Fluid velocities u, v and, w and the fractional areas A_x, A_y and A_z are at the center of the cell-faces normal to x, y and z directions, respectively. Scalar quantities such as pressure, p, fluid fraction value, F, fluid density, ρ, and molecular viscosity, μ are defined at the cell centers (Figure 7.2).

The time discretization of the continuity Equation 7.2 and momentum Equation 7.4 for incompressible flows and Newtonian fluids can be written as:

$$\frac{\mathbf{v}^{n+1} - \mathbf{v}^n}{\delta t} = -\left(\mathbf{v} \cdot \nabla \mathbf{v}\right)^n - \frac{1}{\rho}\nabla p^{n+1} + \frac{\mu}{\rho}\nabla^2 \mathbf{v}^{n+1} + \frac{1}{\rho}\mathbf{B}^n \qquad (7.10)$$

$$\nabla \cdot \mathbf{v}^{n+1} = 0 \qquad (7.11)$$

A superscript n refers to a quantity evaluated at the current time step. Therefore, the terms written for the $(n+1)^{th}$ time step on the right hand side of the equations are evaluated implicitly at time

$$t^{n+1} = t^n + \delta t \qquad (7.12)$$
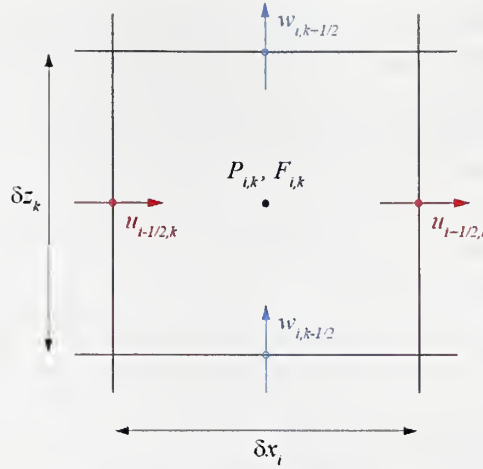
Figure 7.2 The locations of the variables in a computational cell. The velocities are defined at the center of the cell faces whereas the scalar variables are located at the cell center.

Equations 7.10 and 7.11 are highly coupled and can only be solved with an iterative procedure. The basic solution procedure through one increment in time δt can be summarized as follows:

1- The momentum Equation 7.10 is solved explicitly to compute the first guess velocities using the initial conditions or previous time step values.

2- The pressures are iteratively adjusted to satisfy the continuity Equation 7.11 and the velocities in Step 1 are updated according to the pressure change (Section 7.3.4).

3- The free surface is updated to give the new fluid configuration according to the new velocity field. Turbulence quantities are also updated at this step.

7.3.2. Momentum Advection

There are four explicit algorithms in FLOW-3D to solve the advective fluxes. These are the first-order upwind differencing method, a second-order method based on central differencing, a second-order monotonicity-preserving upwind differencing method and third-order upwind differencing. Only the first order upwind differencing will be presented here.

For the momentum control volume shown in Figure 7.3 the advection term in Equation 7.4 in non-conservative form for x-momentum becomes

$$u(\mathbf{v} \cdot \nabla) = u_{i+\frac{1}{2},k}\left(\frac{\partial u}{\partial x}\right)_{i+\frac{1}{2},k} + \overline{w}_{i+\frac{1}{2},k}\left(\frac{\partial u}{\partial z}\right)_{i+\frac{1}{2},k} \tag{7.13}$$

and for z-momentum:

$$w(\mathbf{v} \cdot \nabla) = \overline{u}_{i,k+\frac{1}{2}}\left(\frac{\partial w}{\partial x}\right)_{i,k+\frac{1}{2}} + w_{i,k+\frac{1}{2}}\left(\frac{\partial w}{\partial z}\right)_{i,k+\frac{1}{2}} \tag{7.14}$$

142

where $\bar{u}$ and $\bar{w}$ are obtained by interpolating neighboring fluid velocities as

$$\bar{u}_{i,k+\frac{1}{2}} = \frac{u_{i-\frac{1}{2},k} + u_{i+\frac{1}{2},k} + u_{i-\frac{1}{2},k+1} + u_{i+\frac{1}{2},k+1}}{4} \tag{7.15}$$

$$\bar{w}_{i+\frac{1}{2},k} = \frac{w_{i,k-\frac{1}{2}} + w_{i,k+\frac{1}{2}} + w_{i+1,k-\frac{1}{2}} + w_{i+1,k+\frac{1}{2}}}{4} \tag{7.16}$$

The velocity gradients in Equations 7.13 and 7.14 are obtained using an interpolated donor cell approximation method.

$$\left(\frac{\partial u}{\partial x}\right)_{i+\frac{1}{2},k} = \frac{(1+\alpha s_u)}{2}\left(\frac{\partial u}{\partial x}\right)_{i,k} + \frac{(1-\alpha s_u)}{2}\left(\frac{\partial u}{\partial x}\right)_{i+1,k} , \quad s_u = sign\left(u_{i+\frac{1}{2},k}\right) \tag{7.17}$$

$$\left(\frac{\partial u}{\partial z}\right)_{i+\frac{1}{2},k} = \frac{(1+\alpha s_w)}{2}\left(\frac{\partial u}{\partial z}\right)_{i+\frac{1}{2},k-\frac{1}{2}} + \frac{(1-\alpha s_w)}{2}\left(\frac{\partial u}{\partial z}\right)_{i+\frac{1}{2},k+\frac{1}{2}} , \quad s_w = sign\left(w_{i+\frac{1}{2},k}\right) \tag{7.18}$$

where $0 < \alpha < 1$. Similar relations hold for the gradient of w. The velocity gradients in the above equations are evaluated at the cell-centers or cell-vertices using central difference approximations.

The first-order upwind method can be adjusted between central differencing and the donor cell method by a parameter α. Although it is robust and sufficiently accurate it introduces numerical diffusion due to the nature of the method.
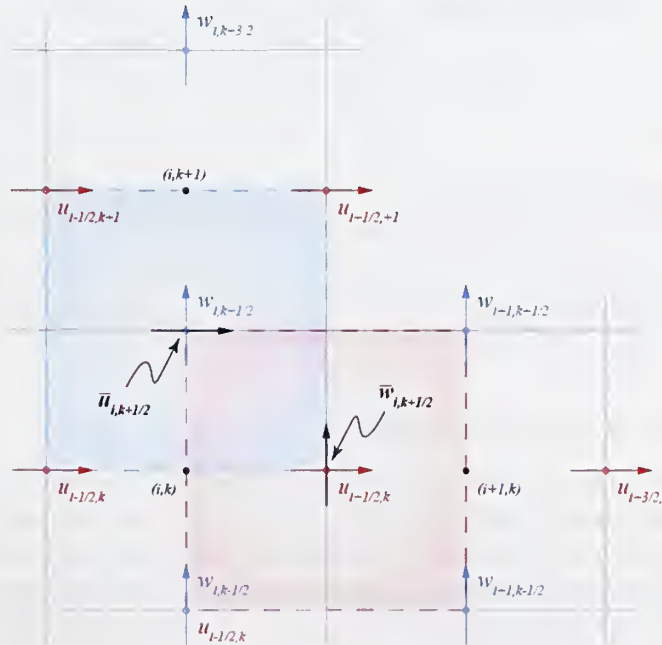
Figure 7.3 The u and w control volumes and interpolated velocity components.

143

The second-order method is the less diffusive, but is not always stable for free surface problems. In this method the advection and viscous terms are first calculated using the first-order scheme with the unwind parameter α set to 1. Then, the first-order calculations are repeated by setting α to -1 using the calculated velocities in the previous step. The results of the two calculations are averaged to get the second-order approximation for the new time level velocities. The second-order, monotonicity preserving method is derived by using the second-order polynomial approximations for the advected variables in each coordinate direction. According to this method, a second-order term is added to the regular first-order upwind approximation. To ensure monotonic behavior of the method, the second-order approximation to the first derivative of the advected variable is restricted.

An implicit method is available for the treatment of the advective terms. But the implicit advection option is not compatible with the Lagrangian VOF methods. Hence the implicit treatment of the advective terms is selectively applied to the cells with no free surface. Also, only the first-order advection options can be used in combination with the implicit advection.

7.3.3. Viscous Stresses

The viscous term $\dfrac{\mu}{\rho}\nabla^2\mathbf{v}^{n+1}$ in Equation 7.10 is written as:

$$\left[\nabla^2\mathbf{v}\right]^{n+1}\cdot\mathbf{i} = \frac{u^{n+1}_{i+\frac{3}{2},k} - 2u^{n+1}_{i+\frac{1}{2},k} + u^{n+1}_{i-\frac{1}{2},k}}{\delta x^2} + \frac{u^{n+1}_{i+\frac{1}{2},k+1} - 2u^{n+1}_{i+\frac{1}{2},k} + u^{n+1}_{i+\frac{1}{2},k-1}}{\delta z^2} \qquad (7.19)$$

for x-momentum and

$$\left[\nabla^2\mathbf{v}\right]^{n+1}\cdot\mathbf{k} = \frac{w^{n+1}_{i+1,k+\frac{1}{2}} - 2w^{n+1}_{i,k+\frac{1}{2}} + w^{n+1}_{i-1,k+\frac{1}{2}}}{\delta x^2} + \frac{w^{n+1}_{i,k+\frac{3}{2}} - 2w^{n+1}_{i,k+\frac{1}{2}} + w^{n+1}_{i,k-\frac{1}{2}}}{\delta z^2} \qquad (7.20)$$

for z-momentum. Equations (7.19) and (7.20) can be treated either explicitly or implicitly. In case of explicit treatment the time step size limitation can be an important control over the efficiency of the numerical solution. There are three implicit methods to solve viscous stresses in FLOW-3D: Successive Under-Relaxation (SUR) method, Alternating Direction Implicit (ADI) method and Generalized Conjugate Gradient (GCG) method.

7.3.4. Pressure Solution Algorithm

The numerical treatment of the continuity equation leads to an algorithm for determining pressures and updating velocities. For incompressible flows the continuity Equation 7.11 can be directly interpreted as an elliptic condition on pressure and velocities. The available implicit pressure solvers in FLOW-3D are Incompressible Successive Over-Relaxation (SOR) method, Incompressible line implicit method which is

a modified Alternating-Direction-Implicit (SADI) and General-Minimum-Residual (GMRES).

Equations 7.10 and 7.11 are recast in the following forms in the FLOW-3D implicit solution procedures.

$$
\frac{u^*_{i+\frac{1}{2},k} - u^n_{i+\frac{1}{2},k}}{\delta t} = -\frac{1}{\rho}\frac{p^n_{i+1,k} - p^n_{i,k}}{\delta x} - \frac{\mu}{\rho}\left[\frac{u^*_{i+\frac{3}{2},k} - 2u^*_{i+\frac{1}{2},k} + u^*_{i-\frac{1}{2},k}}{\delta x^2} + \frac{u^*_{i+\frac{1}{2},k+1} - 2u^*_{i+\frac{1}{2},k} + u^*_{i+\frac{1}{2},k-1}}{\delta z^2}\right] \tag{7.21}
$$

$$
-\left(u\cdot\nabla\mathbf{v}\right)^n_{i+\frac{1}{2},k} + \left(f_x\right)^n_{i,k}
$$

$$
\frac{w^*_{i,k+\frac{1}{2}} - w^n_{i,k+\frac{1}{2}}}{\delta t} = -\frac{1}{\rho}\frac{p^n_{i,k+1} - p^n_{i,k}}{\delta z} - \frac{\mu}{\rho}\left[\frac{w^*_{i+1,k+\frac{1}{2}} - 2w^*_{i,k+\frac{1}{2}} + w^*_{i-1,k+\frac{1}{2}}}{\delta x^2} + \frac{w^*_{i,k+\frac{3}{2}} - 2w^*_{i,k+\frac{1}{2}} + w^*_{i,k-\frac{1}{2}}}{\delta z^2}\right]
$$

$$
-\left(v\cdot\nabla\mathbf{v}\right)^n_{i,k+\frac{1}{2}} + \left(f_z\right)^n_{i,k}
$$

$$
\tag{7.22}
$$

$$
\frac{u^{n+1}_{i+\frac{1}{2},k} - u^*_{i+\frac{1}{2},k}}{\delta t} = -\frac{1}{\rho}\frac{p'_{i+1,k} - p'_{i,k}}{\delta x} \tag{7.23}
$$

$$
\frac{w^{n+1}_{i,k+\frac{1}{2}} - w^*_{i,k+\frac{1}{2}}}{\delta t} = -\frac{1}{\rho}\frac{p'_{i,k+1} - p'_{i,k}}{\delta z} \tag{7.24}
$$

where,

$$
p' = p^{n+1} - p^n \tag{7.25}
$$

is the pressure change in each cell and

$$
\mathbf{u}^* = u^*\mathbf{i} + w^*\mathbf{k} \tag{7.26}
$$

is the intermediate velocity vector. Substituting the Equations 7.25 and 7.26 into Equation 7.11

$$
\nabla\cdot\mathbf{u}^* - \frac{\delta t}{\rho}\nabla^2 p' = 0 \tag{7.27}
$$

GMRES is designed to solve non-symmetric linear systems. Since it is robust and easily parallelizable, it has been widely used in CFD codes (Yao , 2004). GMRES solver uses either Alternating Direction Implicit (ADI) or the generalized conjugate gradient (GCG) method to solve the viscous terms. The GMRES solver does not use any over- or under-relaxation. Details of this algorithm and implementation to FLOW-3D can be

145

found in Yao (2004). The maximum number of iteration per time step can be adjusted for these solvers. The time step size for the implicit solvers is adjusted so that the number of iterations does not exceed the limiting value.

a. The implicit Equations 7.21 and 7.22 are solved for the intermediate velocity vector $\mathbf{u}^*$ either by the ADI or GCG algorithm. If the viscous terms are treated explicitly the intermediate velocities are obtained with no iterations.

b. The pressure change p' is obtained by solving the Equation 7.27 using GMRS algorithm.

c. The new velocities at time level $n+1$ are obtained by solving Equations 7.23 and 7.24 with the calculated pressure change in step b.

7.3.5. Free Surface Tracking

The Volume of Fluid (VOF) method is employed to handle the free surface boundary. The VOF method, developed by Hirt and Nichols (1981), is a powerful tool that enables a finite difference representation of free surfaces and interfaces that are arbitrary oriented with respect to the computational grid. The VOF method has been extensively used for free surface tracking since it requires minimum storage and it follows regions rather than boundaries (Kothe and Mjolsness, 1992, Kawasaki, 1999, Hur and Mizutani, 2004 and Lara et. al. 2006). It is robust enough to handle the breaking and merging fluid regions.

In the VOF method the free surfaces are tracked by a step function, $F(x,y,z,t)$. The function F is assigned the value 1 in a cell filled with fluid, 0 for a cell with no fluid and some value between 0 and 1 in a surface cell (Figure 7.4). The solution algorithms using the VOF method consist of three major steps: 1) The transport of the VOF function within the fluid, 2) reconstruction of the free surface and 3) computation of the volumetric fluxes according to the new orientation of the free surface.

The transport equation for the VOF function is governed by,

$$\frac{\partial F}{\partial t} + \mathbf{v} \cdot \nabla F = 0 \tag{7.28}$$
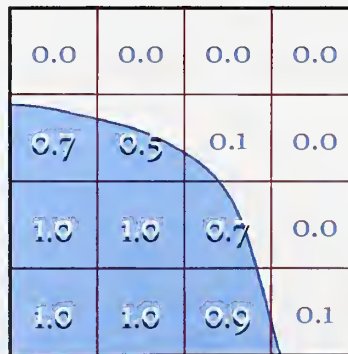
Figure 7.4 Illustration of the typical values of the VOF function, F near the free surface.

The free surface is approximated from the VOF function, F, which stores the fraction of the fluid in a given control volume. The location and the orientation of the free surface within the cell are reconstructed by using the values of VOF function in and around the control volume. The normal direction of the surface is approximated as the direction with the highest gradient of the function F.

The VOF function is advected as a Lagrangian invariant in an Eulerian mesh. The average value of F over a surface cell gives the volume fraction of fluid within the cell. The convective flux calculation in Eulerian methods requires averaging of the flow properties which results in smoothing of the discontinuities. Since F is a step function special methods are used for the flux approximation during the numerical simulations that preserves the discontinuous nature. The original VOF method created by Hirt and Nichols (1981) has a fluxing scheme that uses a donor-acceptor cell approach depending on the local orientation of the interface. This method is stable but may result in diffusion of the interface or overfilling and over-emptying the computational cells when the volume fluxes are significant in all directions and the time step size is close to the stability limit (Barkhudarof, 2004). Various enhancements have been made to the original algorithm to improve its accuracy and stability in complex one and two fluid flows (Kothe and Mjolsness, 1992).

The Lagrangian VOF advection method is based on 3D reconstruction of the fluid interface with piecewise linear representation where the free surface is assumed to be planar in each control volume containing the interface. The fluid volume bounded by the cell faces and the interface is moved according to the local velocity field in a Lagrangian manner. Then the advected volume is overlaid onto the Eulerian grid to obtain the new values of the VOF function, F.

The steps of this method are summarized as follows (Figure 7.5):

1. The interface in a donor cell is approximated with the planar surface defined by

$$\mathbf{n} \cdot \mathbf{p} = c \qquad (7.29)$$

where $\mathbf{n}$ is the unit normal vector, $\mathbf{p}$ is the position vector of a point on the surface of the plane and c is a constant.

2. The VOF function, F is linearized around point the center by

$$F - F_0 = (\mathbf{p} - \mathbf{p}_0) \cdot \nabla F \qquad (7.30)$$

where $\mathbf{p}_0$ is the position vector of the cell center. The least squares method is used to compute the gradient of F and the constant c is computed iteratively to match the volume of fluid in the cell to the amount bounded by the plane.

3. Then, the fluid is translated by moving each face of the cell using the velocity component at that face. The velocity component is assumed to be constant along the face to preserve the orientation of the face. The volume of the cell after the translation may be different that the original volume allowing compression and stretching during translation.

147
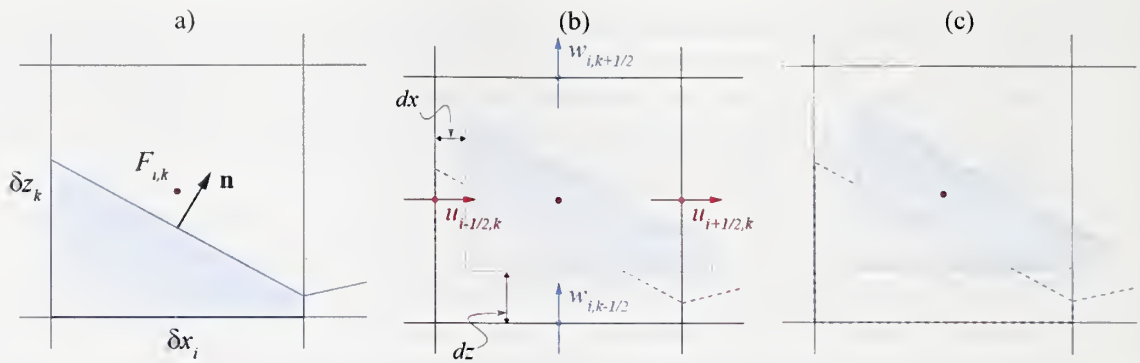
Figure 7.5 Three steps of Lagrangian interface tracking method. (a) Piecewise linear interface reconstruction with the normal **n**, (b) moving the control volume and (c) overlaying the advected volume on the grid (Adopted from Barkhudarof, 2004).

4. Finally, the advected volume is distributed to the new acceptor cells by using the difference between the original and final cell volume.

The method conserves the fluid volume in a local sense such that, the volume leaving a donor cell is equal to the volume placed into the acceptor cells. Each cell can be a donor once during the procedure but a cell can accept from more then one donor cells. If the total fluid in an acceptor cell exceeds the volume of the cell then the excess volume is discarded and added to the total volume error. Therefore, the total volume error depends on the time step size.

The advection equation for the VOF function is solved at the end of each time step like the other scalar advections. Therefore, updated velocities are used for the computation of F. A closure mechanism is added to fill up partial voids in interior fluid regions. When surface tension forces are required it is surface normal has to be more accurate. For this purpose the boundary is represented with a single valued function. Another correction is made when the calculated F values are slightly more than one or less than zero at the end of scalar advection calculations. A cell with a fluid fraction value, F less than unity but with no empty neighbor cells is considered a full cell in one fluid problem in FLOW-3D.

7.3.6. Floating Body

The Fractional Area-Volume Obstacle Representation method (Hirt and Sicilian, 1985) is used in FLOW-3D to represent solid objects. In this method the solid objects within the rectangular mesh are defined by fractional cell areas and the volumes of the cells partially occupied by the solid object. When the volume fraction, V_f is zero in a cell, then the cell is entirely allocated to the object. These dry cells are skipped during computation. The fractional areas/volumes of the mesh are initially set to one. The formulation of the viscous stresses requires free-slip condition along all the internal boundaries. No-slip effects have been added separately through the wall shear-stress algorithm. The fixed mesh method in FLOW-3D also allows the user to simulate general

moving objects (GMO) in fluid flow. At each time step, area and volume fractions in a fixed-rectangular mesh are re-calculated according to the new location of the object. Surface and body, forces are calculated for the moving object dynamically coupled with water. The area fraction, A_f and volume fraction, V_f are defined as:

$$V_f = \frac{V_{open}}{V_{cell}} \text{ and } A_f = \frac{A_{open}}{A_{face}} \tag{7.31}$$

where V_{open} is the volume of the cell open to the flow, V_{cell} is the total volume of the cell, A_{open} is the area of the face open to the flow and A_{face} is the total area the face as illustrated in Figure 7.7.

For moving object problems, the continuity equation (7.1) and the momentum equation (7.4) for fluid flow and the transport equation for the volume of fluid (VOF) (7.28) function are modified to account for the effect of moving objects to displace the fluid. The translational and rotational velocities are added as a source term into the fluid continuity equation and free surface advection equation. The momentum equation is modified with the additional shear terms due to the moving wall.

The modified equations governing the flow field are as follows

Continuity equation:

$$\frac{\partial}{\partial t}\left(\rho V_f\right) + \nabla \cdot \left(\rho \mathbf{v} A_f\right) = 0 \tag{7.32}$$

or,

$$\frac{V_f}{\rho}\frac{\partial \rho}{\partial t} + \frac{1}{\rho}\nabla \cdot \left(\rho \mathbf{v} A_f\right) = -\frac{\partial V_f}{\partial t} \tag{7.33}$$
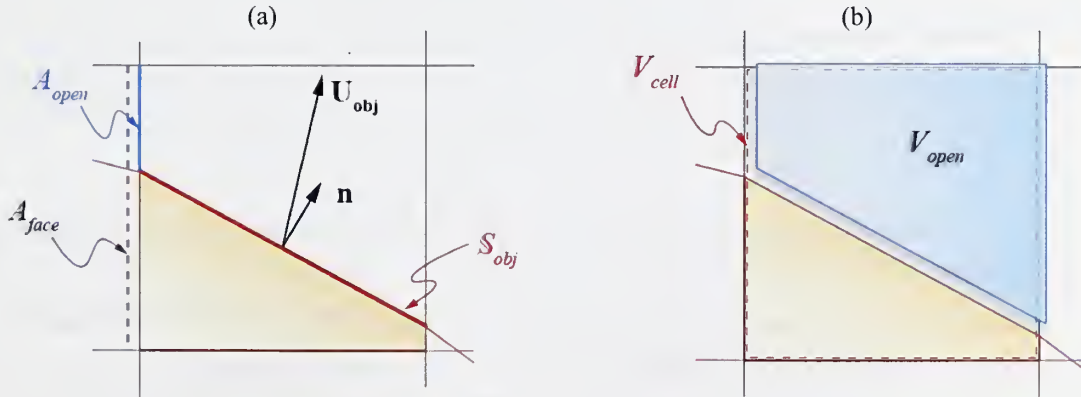
Figure 7.6 The definition sketch of the variables in fractional area/volume obstacle representation.

149

Momentum equation:

$$\frac{\partial \mathbf{v}}{\partial t} + V_f \left(\mathbf{v} A_f \cdot \nabla \mathbf{v} \right) = -\frac{1}{\rho} \left[\nabla p + \nabla \cdot \left(A_f \tau \right) \right] + \mathbf{B} \tag{7.34}$$

Free surface advection (VOF):

$$\frac{\partial F}{\partial t} + \nabla \cdot \left(F \mathbf{v} A_f \right) = -\frac{F}{V_f} \frac{\partial V_f}{\partial t} \tag{7.35}$$

The source term due to the change in volume fraction in equations (7.33) and (7.35) is calculated from;

$$\frac{\delta V_f}{\delta t} = \mathbf{U}_{obj} \cdot \mathbf{n} \frac{S_{obj}}{V_{cell}} \tag{7.36}$$

where $\mathbf{U}_{obj}$ is the velocity of the moving object in a mesh cell, $\mathbf{n}$ is the unit normal vector, S_{obj} is the surface area of the object in that cell and V_{cell} is the total volume of the cell.

To solve the equations of motion of a floating rigid body explicitly the gravitational, hydraulic and other external forces are computed using the previous time step velocities and the new location of the object is calculated at each time step. But the explicit solution of the motion equations for the fluid and solid coupling can result in stability problems when the density of the object is less than the fluid density (Wei, 2006a). An implicit scheme is also available to overcome this problem in which the forces and moment adding on the object are calculated iteratively using the current flow field instead of the obtained at the previous time step. This requires solution of fluid and rigid body equation together through iteration (Wei, 2006a). The equations of motion for the floating body (7.6) and (7.7) are approximated as:

$$\mathbf{F}_h^{n+1} + \sum \mathbf{F}_i = m \left(\frac{\mathbf{V}_G^{n+1} - \mathbf{V}_G^n}{\Delta t} \right) \tag{7.37}$$

$$\mathbf{T}_h^{n+1} + \sum \mathbf{T}_i = \mathbf{I} \cdot \left(\frac{\omega^{n+1} - \omega^n}{\Delta t} \right) + \omega^n \times \left(\mathbf{I} \cdot \omega^n \right) \tag{7.38}$$

The computational procedure of FLOW-3D GMO model is summarized as follows:

1. Calculate the forces on the moving object using fluid pressure and velocities from the previous time step.

2. Calculate the mass center velocity and angular velocity explicitly using the previous time step forces (and torques).

3. Calculate the new position and the orientation of the object.

4. Update the volume and area fractions, V_f and A_f.

5. Calculate the added mass by solving Equation 7.36

6. Solve the fluid equations for pressure and velocity by one predictor – correction iteration. If the iteration converges go to step 10.

7. Update the forces once again using the updated fluid pressure and velocities. Apply under-relaxation if necessary.

8. Update the mass center and angular velocity of the object using implicit equations (7.37) and (7.38).

9. Go to step 5.

10. Proceed with the next time step.

7.3.7. Boundary Conditions

For the closure of the numerical solution the conditions along all the mesh boundaries and internal obstacle surfaces must be defined. A layer of fictitious cells are added along all the mesh boundaries to set some of the conditions. The scalar qualities are defined at the centers of the boundary cells.

7.3.7.1. Wall Boundary

A no-slip condition is applied along the wall boundaries. In practice the velocity distribution close to the boundary is controlled by surface forces, wall roughness and turbulence. However, it is not efficient to resolve all the details of the multilayer structure of the boundary layer. Therefore, a wall function is necessary to estimate the tangential velocities along the boundary cells. It is also assumed that velocities are small enough so that cavitation does not occur.

The normal component of the velocity is zero at the rigid wall boundary cell. A no-slip condition is imposed through the wall shear stress. An additional term in the momentum equation accounts for the wall shear stress at the cells with area fraction less than unity. The wall shear stress is included in an implicit way to avoid possible numerical instabilities in cells with large wall areas and small flow volumes. The acceleration term to account for wall shear-stress in the x-momentum equation is:

$$aw_x = -\frac{2\mu\Lambda}{A_x \, \delta z^2}(1 - A_z)(u - u_0)$$ (7.39)

The area fraction A_x is estimated at the cell face which w is located. The area fraction, A_z is the average of the area fractions of the cells on both sides of u. u_0 is the x-velocity of the boundary for moving objects. The factor Λ accounts for the turbulent boundary stresses. For laminar flow $\Lambda = 1$. For turbulent flows, a law-of-the-wall velocity profile is assumed near the wall, which modifies the wall shear stress magnitude.

7.3.7.2. Free Surface

In the VOF method the interface is located somewhere else within a surface cell. The normal pressure at the cells including an interface is set equal to the neighboring normal void region pressure and surface tension pressure (if surface tension model is used). When the interface is the free surface this pressure becomes the absolute pressure. This value is then extrapolated to the center of the surface cell assuming hydrostatic distribution within the cell. The hydrostatic variation depends on the net acceleration in the direction normal to the surface. The surface pressure is treated as a fixed boundary value during pressure iterations. Tangential stress at the free surface is zero. The velocity components at surface cell boundaries outside the interface are extrapolated to satisfy zero velocity-divergence at the surface.

7.3.7.3. Open Boundary

As in model studies the wave reflection has to be eliminated from the boundary at the downstream end of the numerical wave tank. In a physical model, a wave absorber was designed and installed to minimize the reflected waves. This is analogous to a wave tank with an open end (or infinite length). Similarly, for the numerical model any disturbance should leave the computational domain with minimum reflection. Numerous methods have been used to handle the open boundary.

One way of eliminating reflected waves is to extend the computational domain to have enough time before the reflected waves reach back to the test region (Clauss et al 2005). The extended zone can be discretized with a coarse grid to minimize computational time and increase numerical dissipation. A numerical damping zone can also be used to dissipate the outgoing waves by introducing artificial friction terms (Lin and Liu 2004).

The open boundary condition can be mathematically imposed by a radiation boundary condition. The Sommerfeld radiation boundary condition is written as;

$$\frac{\partial Q}{\partial t} + C \frac{\partial Q}{\partial x} = 0 \qquad (7.40)$$

Here Q is any flow variable, x is the outward direction with respect to the boundary and C is the local phase speed. The above statement simply forces any quantity Q at the boundary to propagate across the boundary with speed C. The waves don't have to be directed normal to the boundary or be linear (Hirt, 1999). Note that the flow variables propagate with different celerity and cross the boundary at different phases. Hence, the radiation condition is applied to a region rather than just at the boundary. It was shown that this boundary condition works well with non-linear free surface waves as well as shock waves and it absorbs the waves in a wide range of selected C values (Lin and Liu, 1999). A detailed review about the application of radiation boundary condition can be found in Orlanski (1976).

7.3.8. Mesh Refinement and Multi-Block Mesh

A fine grid is necessary to increase the accuracy of the solution around the object boundary. Also the grid has to be capable of representing the geometry of the objects with complex shapes correctly. Local grid refinement is required to save computational time. In FLOW-3D multiple mesh blocks are used to provide different resolution in different parts of the computational domain. This method is called the multi-block gridding technique (Figure 7.7).

According to this method each mesh block is formed by a standard rectangular mesh and spans a certain region of the computational domain. The mesh blocks can be either nested or linked but they cannot partially overlap each other. Data transfer in between the blocks is thorough the ghost (boundary) cells along the boundaries of each block.The flow variables are interpolated from the real cells of the donor block to the boundary cells of the acceptor block. Conserved quantities and the fluid fraction are interpolated using a piecewise constant method. Pressure and velocities are linearly interpolated to preserve the gradients.

A mixture of Neuman and Dirichlet type boundary conditions are used for the solution of the pressure Poisson equation. The contribution of each boundary condition type is controlled by a weighting factor to ensure the continuity of velocities and pressure as well as local conservation of mass. The interpolation procedure introduces additional truncation errors into the solution. The errors may be significant when the spatial and temporal variation near the inter-block boundaries. The cell size ratio between any adjacent mesh block in any coordinate direction is suggested to be greater then 0.5 to avoid significant loss in accuracy. Details of the mesh block technique can be found in Flow Science, 2004.

For multi-block problems, pressure and velocities are computed in each block and mass and momentum conservations are satisfied during mesh block iteration. The solution procedure is illustrated in Figure 7.8.
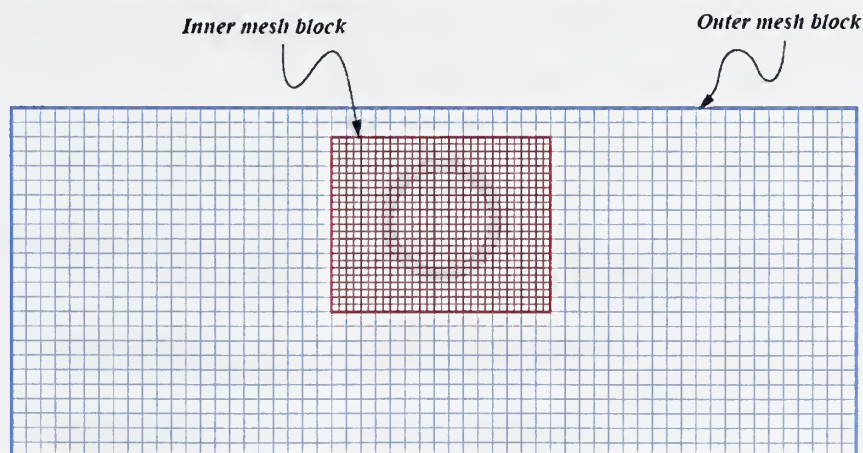
Figure 7.7 Definition sketch of the mesh multi-block mesh in FLOW-3D (the drawing is just for demonstration, it is not to the scale).
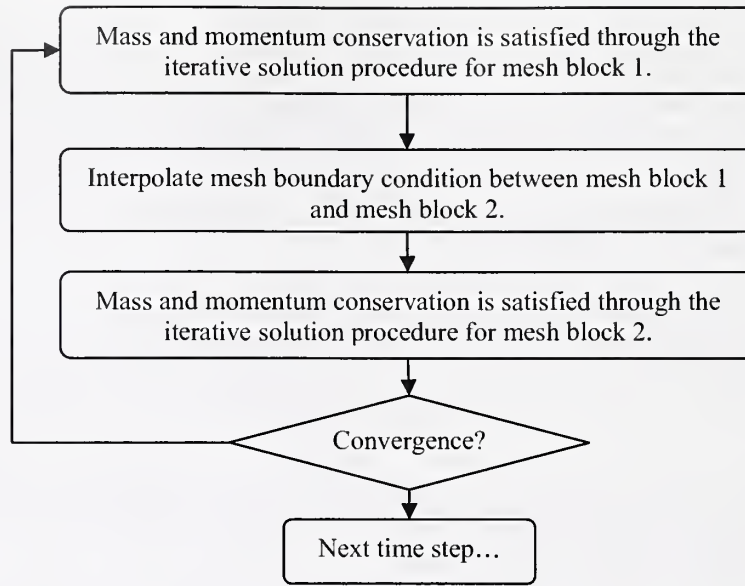
Figure 7.8 An illustration of the multi-block iteration.

7.3.9. Stability Considerations

When the time step size is selected to be set automatically, FLOW-3D adjusts the time step size according to the stability conditions. The first condition requires the mesh velocity (the velocity required to cross one cell in one time step) to be less the fluid velocity in that cell. This condition also depends on the fractional area/volume open to the flow.

$$\delta t < 0.45 \cdot \min\left(\frac{V_f \delta x_i}{A_x u}, \frac{V_f \delta y_j}{A_y v}, \frac{V_f \delta z_k}{A_z w}\right) \tag{7.41}$$

Another condition is that the propagation speed of the surface waves should be less than the mesh velocity in all directions. This condition is imposed in FLOW-3D in z-direction as according to the following relation:

$$\delta t < 0.5 \cdot \frac{\min\left[\delta x_i, \delta y_j\right]}{\sqrt{\delta z_k \cdot a_z}} \tag{7.42}$$

where a_z is the acceleration in z-direction. The condition is multiplied by an extra factor of 0.5 to ensure convergence.

The diffusion of any quantity should not be faster than mesh velocity. This condition is written as:

$$\delta t < \frac{0.25}{\max\left[r_m \dfrac{\mu}{\rho}\left(\dfrac{1}{\delta x_i^{\,2}} + \dfrac{1}{\delta y_j^{\,2}} + \dfrac{1}{\delta z_k^{\,2}} \right)\right]} \tag{7.43}$$

Finally, the parameter α that controls the amount of upwinding that is used for the momentum advection terms (Equations 7.17 and 7.18) is limited for stability as follows;

$$\delta t < \left(\frac{|u|}{\delta x_i} + \frac{|v|}{\delta y_j} + \frac{|w|}{\delta z_k} \right) < \alpha \le 1.0 \tag{7.44}$$

Additionally, the time step size is controlled by an algorithm that checks the area/volume ratios of the cells. This ratio can be restricted in favor of making small errors in volumes.

7.4.   Mass Source Wave Generation

Different methods have been employed to generate desired waves in numerical wave tanks. The simplest way is to define time-varying free surface displacement and velocity distributions at the mesh boundary. Linear or higher order wave theories can be used to calculate the boundary values for velocities and water level (Chapter III). This boundary condition is available in FLOW-3D and can be assigned using the user interface. But only linear monochromatic waves can be generated with the available tool in FLOW-3D. The version 9.3 of FLOW-3D allows superposition of 10 linear waves to generate pseudo random wave conditions. To generate irregular or higher order waves custom made subroutines should be developed.

The waves can also be generated by a moving boundary like a flap-type wave generator which is a planar rigid wall hinged at the bottom of the tank. The plate oscillates around the pivot at a prescribed frequency and stroke to generate regular waves or follow a prescribed trajectory for the paddle motion to generate random waves. In this method the motion of the paddle is defined by a time series for the angular velocity of an object sigle-degree of freedom. The angular velocities are computed by a custom code and added into the FLOW-3D input file. Wave generation with a moving paddle is a better way to reflect the physical model conditions but the computational cost is much higher than a regular mesh boundary condition. Since the paddle motions can be arbitrary, irregular waves can also be generated with this method. However, the linear wave theory velocity distribution is not satisfied with this method due to the secondary wave modes with amplitudes that decay exponentially.

The re-reflection of reflected waves from the wave paddle is a common problem in both physical and numerical wave tanks (Lin and Liu, 1999). A sufficiently long channel can be used to have enough waves for the tests as in model studies but increasing the size of the domain not only requires more computational time to but also increases the

155

time required for the waves to reach the test section, thus the duration of the simulation. The numerical errors and instabilities also become more significant when a larger mesh is used for the simulations. These problems are discussed in more detail in the next Chapter.

One method for wave generation in a numerical wave tank is to use a mass source generation function inside the computational domain (Lin and Liu, 1999). This method is advantageous because it is possible to absorb the reflected waves without influencing the wave generation. Waves from the obstacle can pass through the mass generation source and leave the domain through an open boundary without influencing the computations.

The general form of the continuity equation is modified according to the following relation considering a mass source inside the 2D domain Ω,

$$\frac{\partial}{\partial t}\left(\rho V_f\right)+\nabla \cdot \left(\rho \mathbf{v} A_f\right)= S_m \quad \text{in} \quad \Omega \tag{7.45}$$

where S_m is the mass source term A_f and V_f are the area and volume fractions based on the fractional area/volume method (Section 7.3.6). Note that if the object is moving then A_f and V_f vary in time. For incompressible flows the continuity equation reduces to

$$\nabla \cdot \left(\mathbf{v} A_f\right)= -\frac{\partial V_f}{\partial t}+\frac{S_m}{\rho} \quad \text{in} \quad \Omega \tag{7.46}$$

The term $\dfrac{S_m}{\rho}$ on the right hand side of the equation represents the mass sources which is nonzero only within the source region Ω and can be defined by a mass source functions as:

$$s(x,z,t) = \frac{S_m}{\rho} \tag{7.47}$$

$s(x,z,t)$ may be a point source or a line source. If it is a point source then s is simply the Dirac delta function. If it is assumed that all the mass change generated by the source function contributes to the wave generation one can write

$$\int_0^t \int_\Omega s(x,z,t)d\Omega dt = 2\int_0^t C\eta(t)dt \tag{7.48}$$

where C is wave celerity, $\eta(t)$ is the free surface displacement and the multiplier 2 is introduced since the waves are generated on both sides of the source (Lin and Liu, 1999). Recalling from Chapter III for a linear monochromatic wave the water surface is defend by

$$\eta = \frac{H}{2}\sin\left(kx - \omega t\right) \tag{7.49}$$
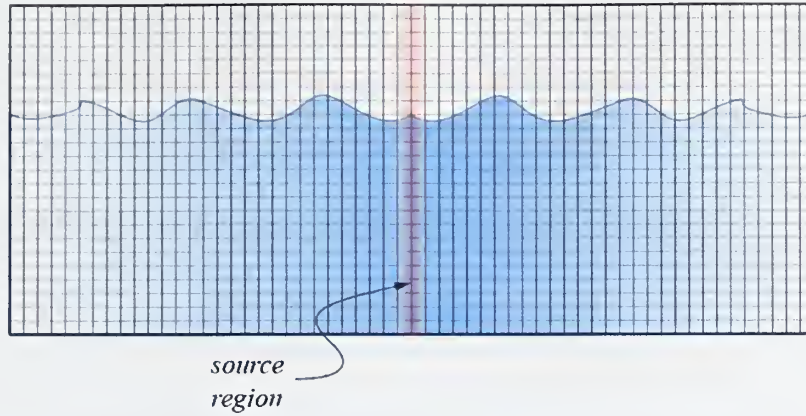
source
region

Figure 7.9 The wave generation source region on a regular mesh.

Note that the Equation 7.49 is modified by a $\dfrac{\pi}{2}$ phase shift to ensure that the source function has an initial value of zero ($s_{t=0} = \eta_{t=0} = 0$, Lin and Liu, 1999). Substituting η for linear monochromatic waves and assuming the source is at $x = 0$ yields a source function

$$s(t) = \frac{CH}{A}\sin(\omega t) \tag{7.50}$$

where ω is the angular frequency of the waves, H is the wave height, and A is the area of the source region in a 2D domain. Point source wave generation requires the source region to be at a certain depth below the mean water level. Lin and Liu (1999) suggest the height of the source region to be between 1/10-1/2 of the water depth. It is also recommended to use locate the center of the region 1/3-1/2 of water depth below the surface. This method gives reasonable results within a certain range of waves within shallow and transitional range. However, as the waves get shorter the vertical gradient of the velocities become larger and the generated waves deviate from the desired waves.

One solution to this problem is to move the source region closer to the surface of the water for shorter waves. Another limitation of this method is that the velocity distribution in the vicinity of the source region deviates significantly from the wave distribution of the target wave. Therefore, the source region has to be far enough from the test section to have steady-state wave conditions.

A solution to these problems is to distribute the mass generation according to the mass flux variation along a vertical line. The mass generated along the region illustrated in Figure 7.10 has to be equal to the mass flux though faces of the region to satisfy continuity, as follows:

$$\int_0^t \int_\Omega s(x,z,t)\,d\Omega\,dt = 2\int_0^t \int_{-h}^{\eta(t)} u(x,z,t)\,dz\,dt \tag{7.51}$$

157

Note that the $z = 0$ at the still water level. If the amplitude of the waves is small the right-hand-side of Equation 7.51 can be linearized yielding:

$$\int_0^t \int_\Omega s(x,z,t)d\Omega dt = 2\int_0^t \int_{-h}^0 u(x,z,t)dzdt \tag{7.52}$$

Recalling from Chapter III the horizontal component of the velocity under a linear wave is given by:

$$u(x,z,t) = \frac{H}{2}\omega\frac{\cosh[k(h+z)]}{\sinh(kh)}\sin(kx - \omega t) \tag{7.53}$$

Again the periodic term in Equation 7.53 is replaces with $\sin(kx - \omega t)$ to ensure stability. Substituting 7.53 into 7.52 and using the dispersion relationship (Equation 3.13) the new source function can be calculated as

$$s(z,t) = \frac{H}{x_s}\frac{g}{C}\frac{\cosh[k(h+z)]}{\cosh(kh)}\sin(\omega t) \tag{7.54}$$

where x_s is the horizontal span of the mass generation region. According to the above equation the mass is generated in a rectangular region of length x_s and height h and, its magnitude is a continuous function of time and vertical space, z.

Equation 7.54 is incorporated into the FLOW-3D solver by a FORTRAN subroutine after some adjustment. In FLOW-3D a mass source is associated with a geometry component. The source term given in Eq (7.54) appears only at the cell centers enclosed by the component and enters the domain through the component's open surface. Therefore, the mass source object has to be completely porous in order to alter the flow. The intensity of the source at every obstacle cell is calculated according to the z-coordinate of the cell center at every time step. During computations, if some part of the mass source is out of the water mass is still generated at times when the source is positive. Yet, no mass is removed when the source becomes negative (sink). This imbalance leads to accumulation of mass within the wave tank. To avoid this problem the source component is extended sufficiently above the water level and the source function is multiplied by the VOF function at each cell. If a cell is full then the mass is generated, if a cell is empty no mass is generated and at a surface cell only a fractional portion of the mass is generated. Note that with this new approach the height of the mass source region is equal to the current water depth. Hence, the source function is further modified to account for the non-linear effects. This final adjustment ensures the total mass generated in the region Ω_t at time t is equal to that of the initial linear region Ω. The nonlinear correction factor is given as:

$$a_{corr} = \frac{\sinh(kh)}{\sinh(kh_t)} \tag{7.55}$$

where h_t is the water depth at time t and h is still water depth.

With these corrections the wave generator source function reads

$$s(x,z,t) = a_{corr}F(x,z,t)\frac{H}{x_s}\frac{g}{C}\frac{\cosh[k(h+z)]}{\cosh(kh)}\sin(\omega t) \qquad (7.56)$$

Irregular waves can be approximated by superposing a series of monochromatic waves with a know distribution of wave heights and period. If the energy spectrum of the waves is know the wave train can be constructed by inverse Fourier transform as explained in Section 3.3.3. Each of these modes can be generated with the source function given by the equation 7.5 and superimposed with some random phase difference (Equation 3.48). This is formulated as follows:

$$s(x,z,t) = \frac{gF(x,z,t)}{x_s}\sum_{i=1}^{N}(a_{corr})_i\frac{H_i}{C_i}\frac{\cosh[k_i(h+z)]}{\cosh(k_ih)}\sin(\omega_i t + \delta_i) \qquad (7.57)$$

where

$$(a_{corr})_i = \frac{\sinh(k_ih)}{\sinh(k_ih_t)} \qquad (7.58)$$

The source functions presented above are tested for a wide range of regular and irregular waves and compared with linear wave theory and laboratory experiments. The verification and validation of the wave generation is discussed in the next chapter.

VIII.   NUMERICAL SIMULATIONS

8.1.   Introduction

The objectives of the numerical simulations are to validate the numerical model described in Chapter VII with the available experimental and field data, and to investigate the performance characteristics of floating breakwater models with and without overtopping in regular and irregular wave conditions.

A commercially available software package, FLOW-3D, is modified to solve the interaction of regular and irregular waves with breakwater models. The governing equations and the solution procedure of FLOW-3D were described in Chapter VII. The simulations were carried out in a two-dimensional vertical computational domain discretized with a regular mesh of square cells. The domain was divided into three regions: left and right numerical dissipation zones and the numerical wave tank of interest. Numerical dissipation zones were added at both ends of the tank to prevent wave reflection form the boundaries. At these regions, the computational mesh was varied form finer to coarser along horizontal axis to induce numerical dissipation and reduce computational cost. Sommerfeld radiation condition was applied at the end of each numerical dissipation zones (Figure 8.3). The treatment of the open boundary is discussed in Appendix E.

The sensitivity of the numerical model to computational grid size was tested within the proposed range of waves. Sensitivity of results to the computational mesh is discussed in Appendix D.

The waves were generated in a mass source region inside the numerical wave tank. The performance of the new method described in Section 7.4 for generating regular and irregular waves with a mass source was tested. The results were compared both with linear wave theory and the laboratory experiments. The verification of the mass source wave generation is presented in Appendix F.

For the verification and validation of the numerical model, some of the laboratory experiments were simulated in the numerical wave tank. Hollow and solid circular cylinders with different drafts and wave conditions corresponding to the laboratory experiments were simulated numerically. The numerical simulations were broadly classified according to degrees of freedom of these cylinders. This includes (a) models with zero degrees of freedom, (b) a single degree of freedom and (c) multiple degrees of freedom. For each type of constraint, the cylinders were tested with various drafts and wave conditions to compare with the experiments. The validation and verification of the numerical model with the experimental results is discussed in Section 8.5.

In the second part of the study, the numerical wave tank was adapted to match the field conditions to investigate its performance with irregular waves. The double-pipe pile-restrained model (Model 96) was simulated in the new wave tank. In Section 8.7, the details of prototype scale simulations are presented.

8.2.   Simulation Procedure

The standard FLOW-3D solver includes a preprocessor and a solver. To run a simulation, the user has to provide an ASCII input file that includes all the input and control parameters. The input file is prepared by using the FLOW-3D GUI. After each simulation the solver generates a binary output file, including the flow variables at all nodes and specified times. The postprocessor program retrieves data from both written by the solver, and an ASCII input file, which instructs the postprocessor how to extract and present the data

In addition to the standard code, additional routines were developed and integrated with FLOW-3D to run the simulations. These routines include wave generation, data acquisition and analysis. Additional input data for the modified code is provided to the solver by an ASCII input file, "wave.inp". This file includes the wave parameters and the instructions for the additional output files. A GUI was developed in Labview which serves an easier way to prepare wave.inp. The input file has to be saved in the same folder as the FLOW-3D input file. The complete procedure for a single run is summarized in Figure 8.1.

The preprocessor reads both of the input files and prepares to be used by the solver. The data is transferred from the preprocessor to the solver through some temporary intermediate files. The custom subroutines are called explicitly at each time step by the solver.

The original solver outputs data at specified intervals for all the nodes. The modified version allows the user to store high frequency data at selected locations avoiding excessive output files. The time series data such as, water surface profile, breakwater displacements and forces, etc. are stored in the memory at each time step but written into a file, "pr_dlss_*.dat" at specified intervals. The spatial data is stored at user defined times into the file "stp_dlss_*.dat".

Time series and spatial output data were analyzed by two computer programs. One of these programs is for linear monochromatic wave analysis and the other one is for random wave analysis. The regular wave numerical data is analyzed in a similar way as the experimental data. Likewise, the random wave numerical data is analyzed using the same methods in field data analysis.

Another tool is created using Matlab for preparing necessary plots and tables. This additional Matlab code can read both the new output files and processed data files and create the necessary plot that will be presented here.
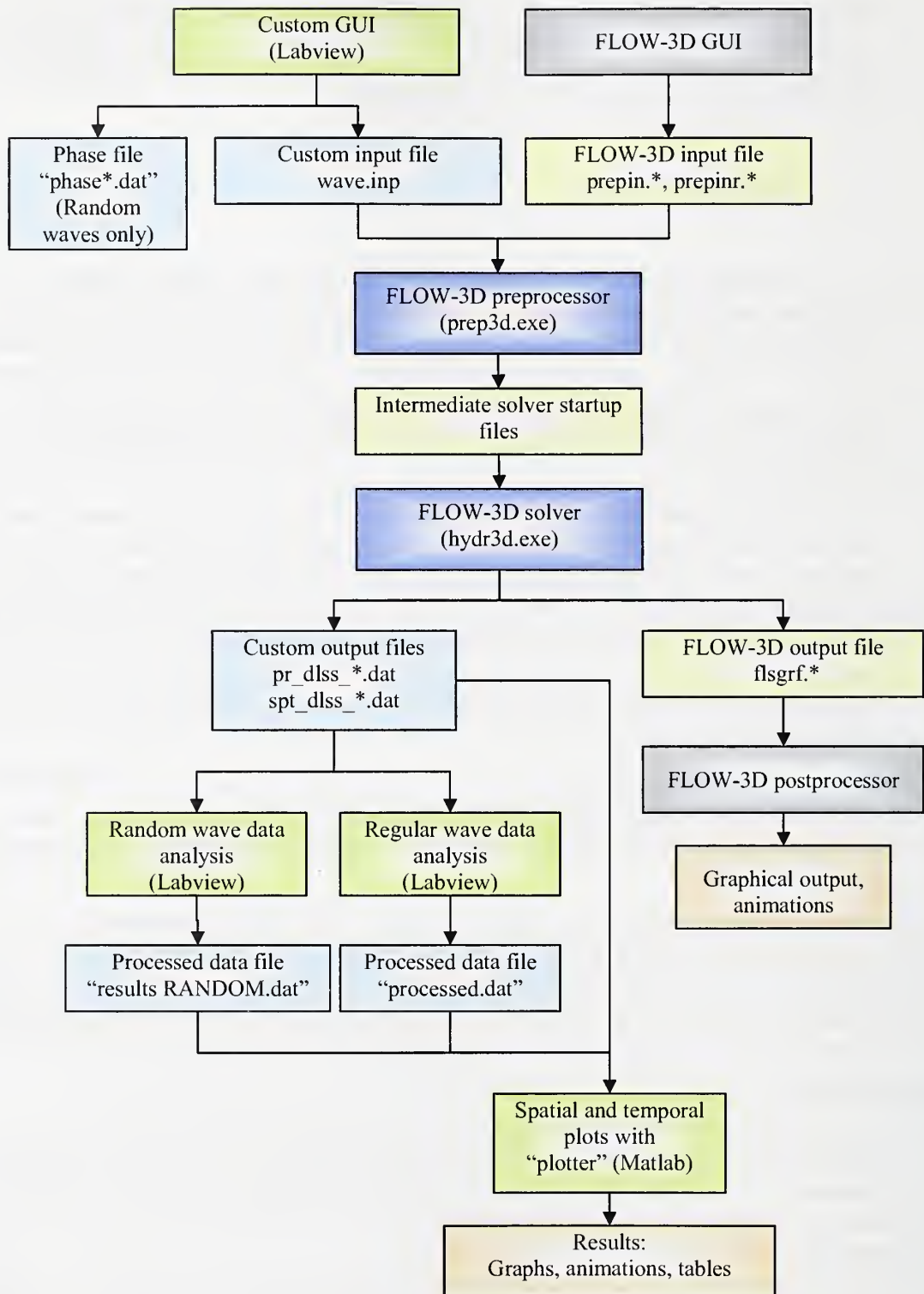
Figure 8.1 Flowchart for numerical computations.

8.3. Considerations for Model Setup

The major difficulties associated with the solution of the nonlinear equations governing the flow around a floating object can be summarized as follows:

- The numerical complexities due to the hyperbolic nature of the governing equations,

- The nonlinear free surface boundary that is unknown at the solution time step,

- Solution of the nonlinear interaction between the floating object and the flow field around it,

- An efficient wave generation method which does not block the flow,

- Treatment of the open boundary condition to avoid unwanted wave reflection form the boundaries

Some of these complications, such as free surface evaluation and rigid body motion can be resolved by using the available handles in the existing numerical model. But the others require development of new procedures. The characteristics of the selected models and their validation are described in the following sections.

8.4. Numerical Model Options

As discussed earlier, numerical solution of the governing equations given in Chapter VII involves various approximations which usually require special procedures. There are several options in FLOW-3D to handle different parts of the solution. Some of these options were tested prior to the design of the numerical wave tank. The final simulations including the mesh sensitivity and the validation of the wave generation were run using the methods that are described in Appendices D, E and F. Only the results of these preliminary tests are given here. The comparisons of different methods are excluded for the sake of brevity.

The implicit GMRES algorithm (Section 7.3.4) is selected for the solution of the continuity equation. During the preliminary tests it was observed that this method has better mass conservation and accuracy compared to the other available methods, SOP and SADI. The multiple dynamically adjusted convergence criteria is set to 1.0 for pressure iterations. In the GMRES implicit solver the viscous stresses are solved implicitly using the generalized conjugate gradient (GCG) method.

There are four explicit solution options in the existing numerical model for momentum advection; first order, second-order, second-order monotonicity preserving, and third order methods. The amount of upwinding is controlled by the parameter, α for the first-order method. Setting α to 1 leads to a fully unwinding scheme while $\alpha = 0$ results in a central differences scheme. The first order method with $\alpha = 1$, were

compared during the preliminary tests. It was observed that the first order method was stable and reasonably accurate but introduced unrealistic numerical diffusion. The excessive dissipation was slightly reduced by using the second-order monotonicity preserving method but it was observed that the water surface profiles had excessive fluctuations. In Figure 8.2 the three methods are compared for a regular monochromatic wave at four wave cycles away from the wave generator. As it is demonstrated in this figure, although higher order methods are less dissipative the mean water level starts fluctuating after 20 wave periods. Also, using the first order method saved considerably CPU time compared to the higher order methods. The first-order method was chosen for the remainder of the simulations.

It was noted in Section 7.3.6 that the coupling between the rigid body motion and the fluid flow can be implicit or explicit. The floating object considered in the current study typically had specific gravity less than unity. It was observed that the explicit method led to stability problems for those breakwater modes with specific densities less than unity. Therefore, implicit scheme is used for rigid body-fluid coupling for the floating breakwater models considered here.

A number of free surface tracking methods are available in the numerical model. The standard, unsplit and split Lagrangian methods for one fluid flows are tested for the current study. The Split Lagrangian method gave the best results among the three methods.
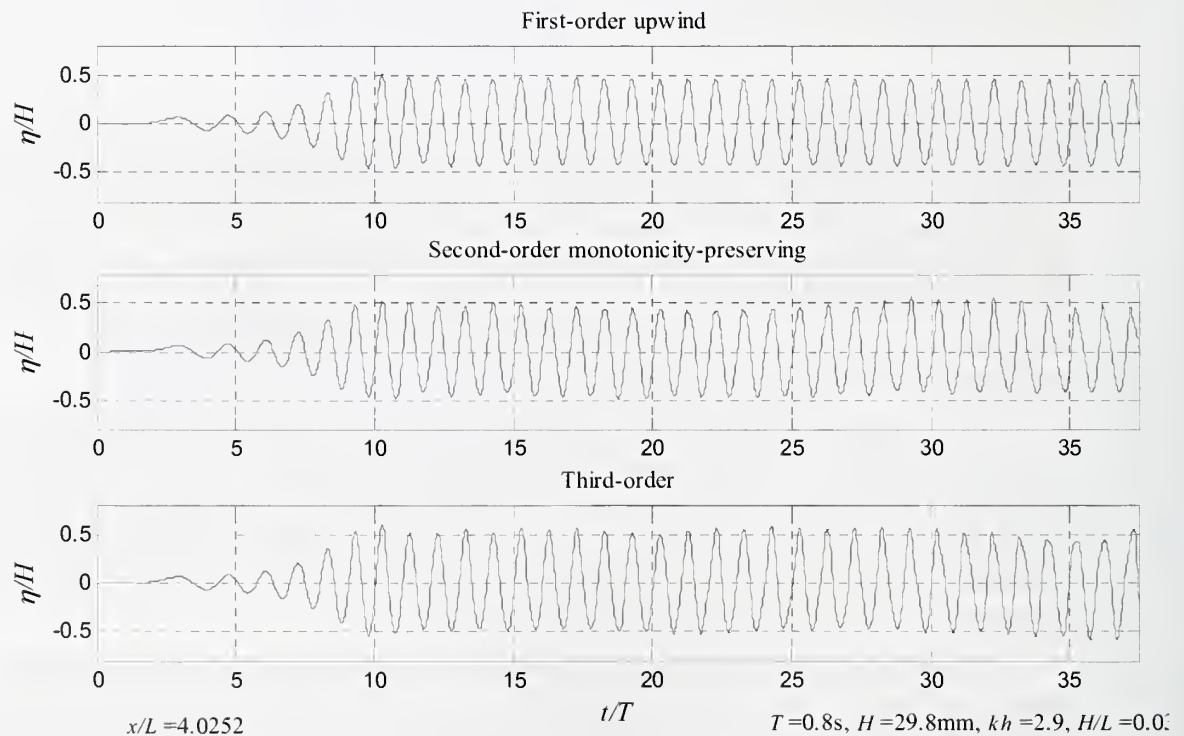
Figure 8.2 The comparison of momentum advection methods in 5 m long numerical wave tank.

In some cases, the free surface stability limit can be manually set to control the time step size. The safety factor for free surface stability given in Equation 7.42 was tested for different values between 0.5 and 1, but no significant improvement was observed. The default value, 1 was used for the rest of the study. The time step size can be excessively small if a cell has a large open face area compared to its volume. If the area/volume ratio of the cell exceeds a limiting parameter defined by the user, then those cells are readjusted in the preprocessor. The default value, -3.1 was used for the current study. Other parameters to control the time step size (Section 7.3.9) were kept as default during the runs. The adequacy of time step size was verified by setting it to a constant value smaller than that controlled automatically by the stability and convergence criteria. No significant improvement was observed for the test cases considered.

8.5.   Numerical Modeling of the Laboratory Experiments

The numerical wave tank must reflect the physical wave tank as closely as possible. Ideally, this includes some of the anomalies that were inevitable in laboratory conditions. For example, the wave absorber in the physical wave tank was reflecting up to 10% of the wave energy back into the test section. The wave paddle inevitably generates higher-order wave modes together with the defined waves. The laboratory wave tank is three-dimensional but considered as two-dimensional by neglecting the irregularities, side wall affects, alignment problems, etc. However, it is hardly possible to model all of these minor effects and in most of the cases the computational cost is drastically increased. Therefore, the possible sources of uncertainties are avoided during modeling of the numerical setup such as direct modeling of the wave paddle or wave absorber. In addition to the simplifications that have been explained in the previous sections, the numerical experiments were confined to a shorter wave tank. It is assumed that, once the waves reach a steady state, the spatial variation can be ignored. Hence, the wave interaction with a floating breakwater 12.5 away from the wave generator, can be assumed identical to a case where the waves are radiated from a source 2.5 m away form the breakwater. To validate this assumption, some of the simulations were carried out in a full length (15 m) numerical wave tank and compared with the corresponding experiments in the shorter tank. One of these simulations will be discussed in Section 8.5.4.

Figure 8.3 illustrates the details of the 2D rectangular domain created to carry out the numerical simulations. The main section of the computational domain was 5 m long and 0.6 m high extending from $x = 0$ to 5m. This part of the domain is divided into a regular mesh of 1×1 cm square cells. To avoid reflection form the left and right boundaries, additional 40 m long numerical dissipation zones were added at both ends. Similar to the previous simulations the mesh was stretched along x-axis to introduce numerical dissipation. An open boundary condition was at the end of each dissipation zones. A no-slip boundary condition was applied along the bottom boundary. The water depth was kept constant in all the runs at $h = 0.466$ m.
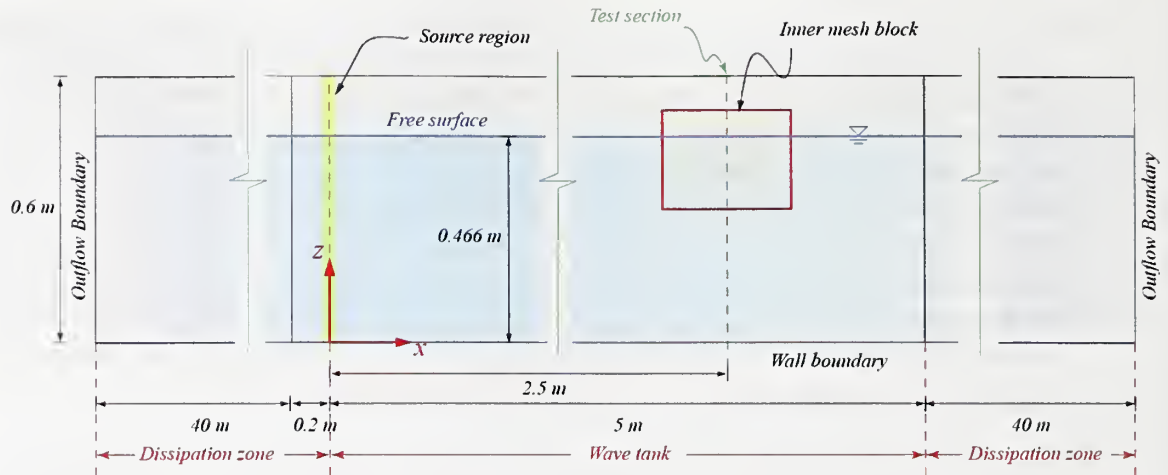
Figure 8.3 The description of the computational domain for breakwater model simulations

The waves were generated with the mass source wave generator at section $x = 0$ as described in Section 7.4. The source region was 3 cm long and 60 cm high. The breakwater models ware placed at $x = 2.5$ m in the numerical wave tank. Total simulation time was 30 s in all of the runs.

A finer mesh block was generated around the models to better resolve the round geometries and sharp gradients of the flow variables (Section 7.3.8). Wall thickness, t_w, of the pipes at model scale was on the order of 5-10 mm and at prototype scale it was on the order of 10 to 15 mm. A finer mesh was also necessary to avoid cells containing both the inner and outer fluid domains as illustrated in Figure 8.4.

To avoid this problem, the diagonal length of the cell should be less than the thickness of the hollow cylinders which can be written as:

$$t_w > \delta x \sqrt{2} = \delta z \sqrt{2} \tag{8.1}$$

The solid regions violating the condition given in 8.1 are ignored by the preprocessor.

The size of the inner mesh block was varied for each model, but remained constant at all wave conditions. For the partially constrained models, the inner mesh area was large enough to ensure that the breakwater did not cross the boundaries.
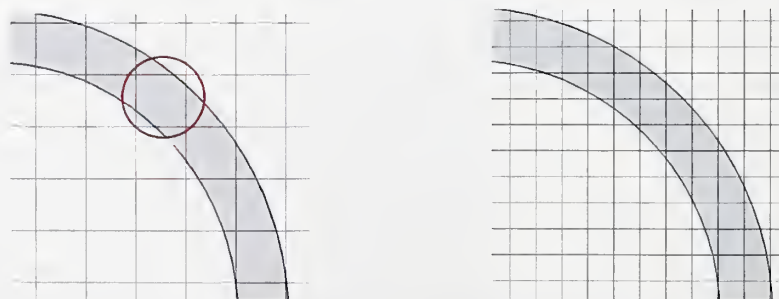
Figure 8.4 The representation of solid objects by fractional area method in a coarse and fine mesh

8.5.1. Description of Models

The simulated models consist of (a) fully restrained (fixed), (b) vertically restrained with a single mooring line (bottom moored), and (c) horizontally restrained with piles at both sides of the breakwater (pile-restrained). The two-cylinder pile-restrained model was also tested during the numerical study. The same numbering system which was developed for physical models was also used in numerical test for consistency. The breakwater models and the wave conditions are summarized in Table 8.1.

The fixed-pipe models were simulated as 114 mm diameter solid circular cylinders with zero degrees of freedom. Two different drafts, $z_d/d = 0.5$ and 1.0, were tested to replicate the models 61 and 62. The centers of the cylinders were fixed at $x = 2.5$ m and $z = 0.466$ m for model 61. The fully submerged fixed model, model 62, was placed in the numerical wave tank, its center being at $x = 2.5$ m and $z = 0.409$ m (Figure 8.5).
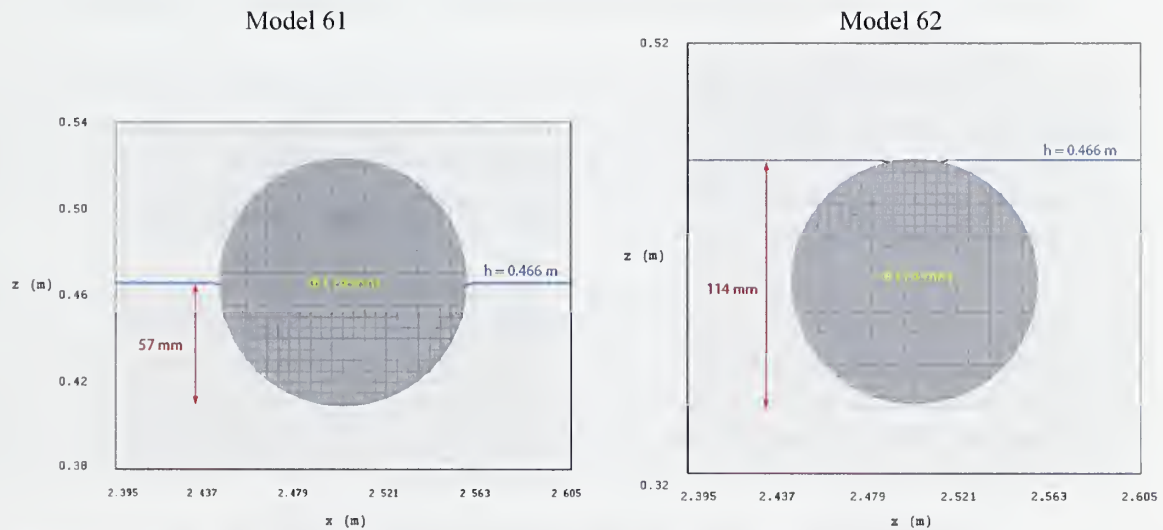
Figure 8.5 Fixed breakwater models and the inner mesh block with $\delta x = \delta z = 0.5$ cm
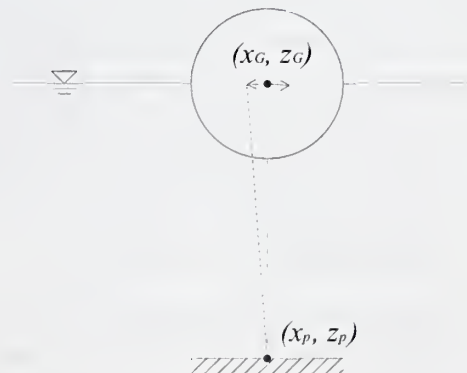
Figure 8.6 Moored breakwater configuration for the numerical simulations.

167
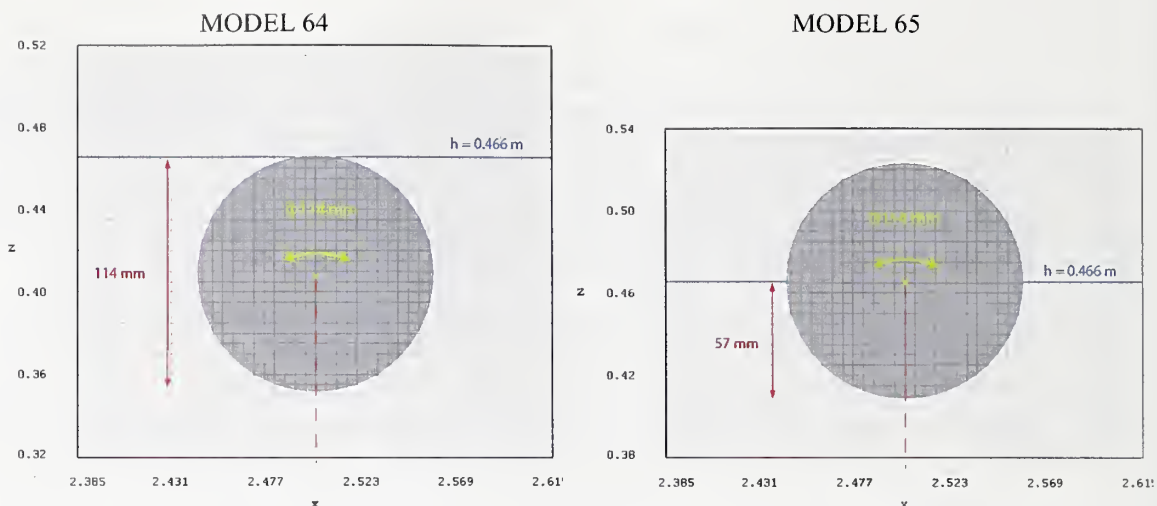
Figure 8.7 Bottom moored breakwater models and the inner mesh block with $\delta x = \delta z = 0.5$ cm.

The moored breakwaters were simulated by circular cylinders with diameter of 114 mm. In order to imitate the influence of the mooring line the cylinder was fixed in the x and z directions but was left free to rotate around a fixed point. The origin for the y-axis rotation was set as the point where the mooring line is attached to the bottom of the wave tank as illustrated in Figure 8.6.

By this simple approximation, it was assumed that the mooring line is always in tension and attached at the center of the circle. Two of the physical models, Model 64 and model 65 were selected for these runs. Model 64 was positioned, its center being at $z = 0.466$ m and model 65 was centered at $z = 0.409$ m just as the fixed cylinders. The scaled drawings of the bottom moored models and the inner mesh block geometries are shown in Figure 8.7.

The pile-restrained models 60, 70, 69 and 96 were simulated in the numerical wave tank. The single pipe models 60 and 69, with $z_d/d = 0.5$ and 0.96 are represented both by solid and hollow cylinders (Figures 8.8 through 8.11). The inner diameter of the hollow cylinder was 96 mm and the outer diameter was 114 mm leaving a thickness of 9 mm. The pipe material was defined as impervious and the density was set equal to the PVC pipe density (~ 1.2 gr/cm^3). The necessary draft was provided by adjusting the fluid level inside the pipe to match the bulk density of the physical model. The density of the solid cylinder model 69 ($z_d/d = 0.96$) was 0.981 kg/m^3 and the model 60 ($z_d/d = 0.5$) was 0.5kg/m^3. In order to distinguish between a hollow and a solid cylinder a suffix "-h" is added at the end of the model number (e.g. model 60-h).

The effects of the piles were approximated by two different methods. In the first method, the x-axis translation of the breakwater model was restricted while the z-axis translation and y-axis rotation were set free. As an improved approach, the piles were simulated directly by additional solid components. Two vertical solid blocks were added at distances 59 mm away from center of the breakwater model on both sides. The gap

168

between the piles and the breakwater model was initially 2 mm on each side. The porosities of these piles were 1.0 in order to make them invisible to the flow. The collusion model was activated to correctly model the rigid body dynamics. The energy loss during collusions and the friction between the piles and the breakwater was neglected (Coulomb's friction coefficient = 0 and Strong's energetic restitution coefficient = 1). These models were named with a suffix "-p" added to the model number (e.g. model 60-p).

The experiments with model 70, the single cylinder model with draft z_d/d=0.7, were simulated with solid cylinders. The density of the solid cylinder was adjusted to 0.7477 kg/m^3/m to provide the necessary draft. The restraining of the model was modeled by restricting x-axis displacements.

MODEL 60   MODEL 60 – h

Figure 8.8 Pile-restrained breakwater models and the inner mesh block with $\delta x = \delta z = 0.5$ cm.

MODEL 70   MODEL 60 - h - p
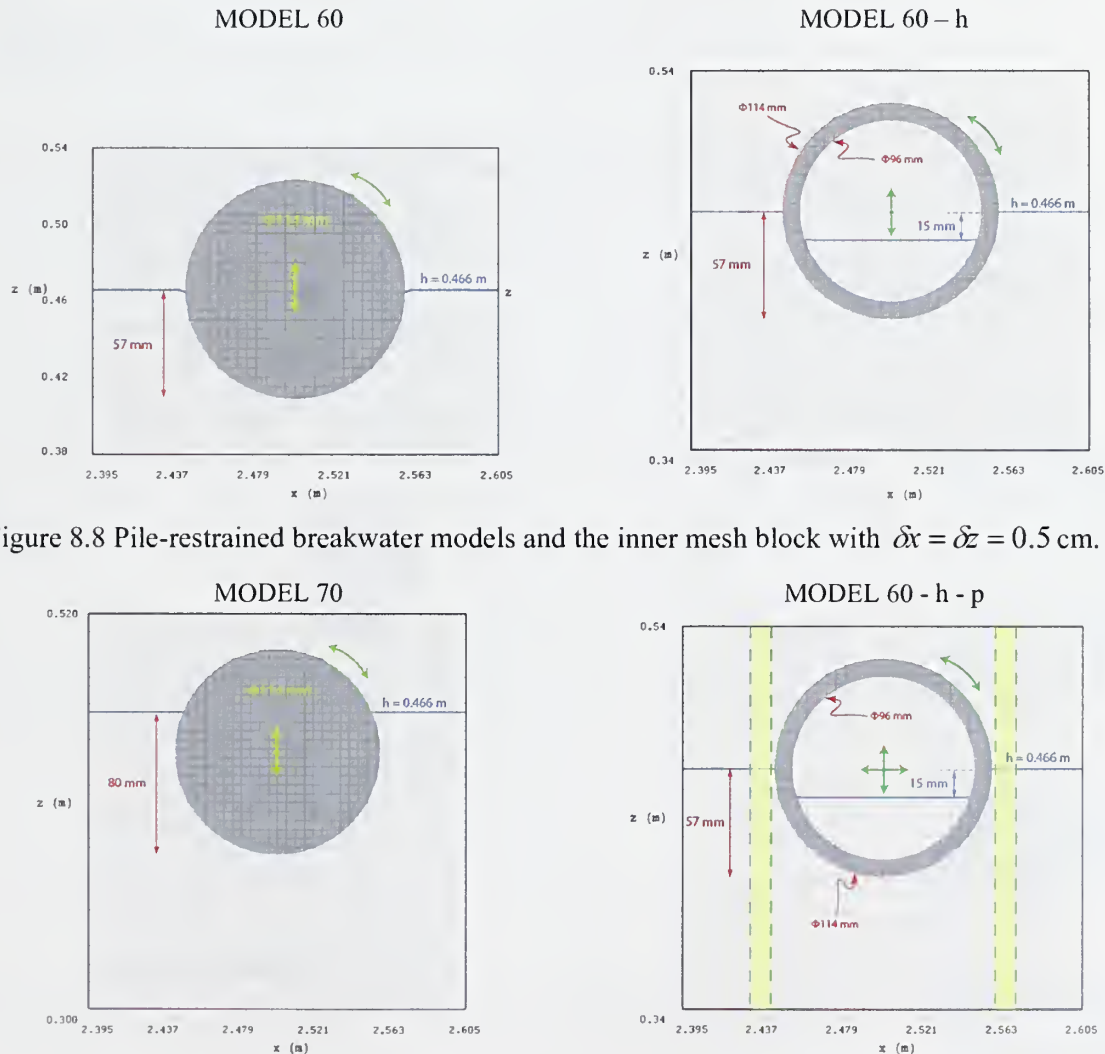
Figure 8.9 Pile-restrained breakwater models and the inner mesh block with $\delta x = \delta z = 0.5$ cm.

169
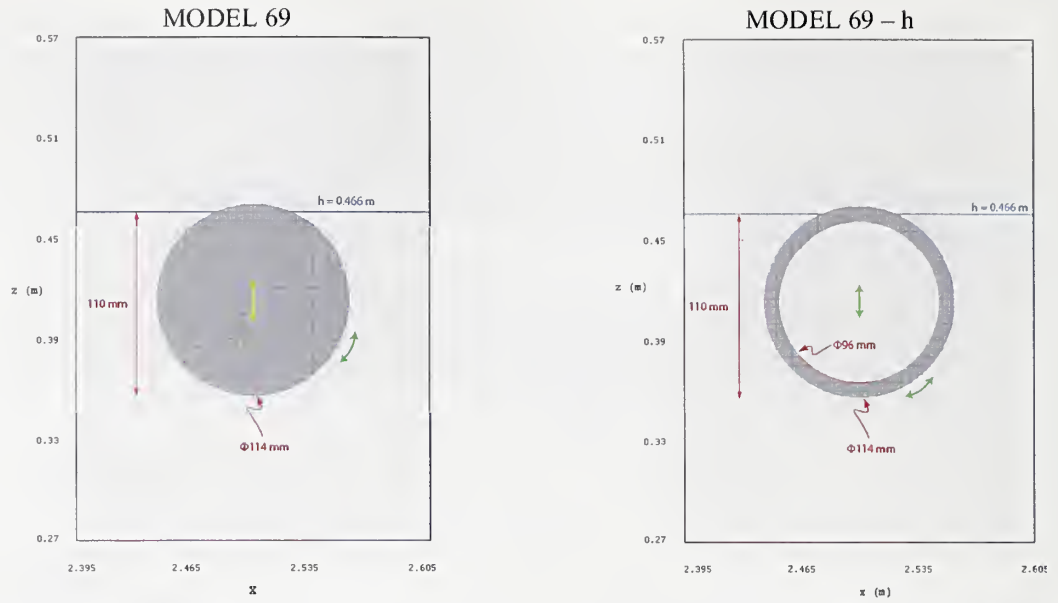
Figure 8.10 Pile-restrained breakwater models 69 and 69 - h and the inner mesh block with $\delta x = \delta z = 0.5$ cm
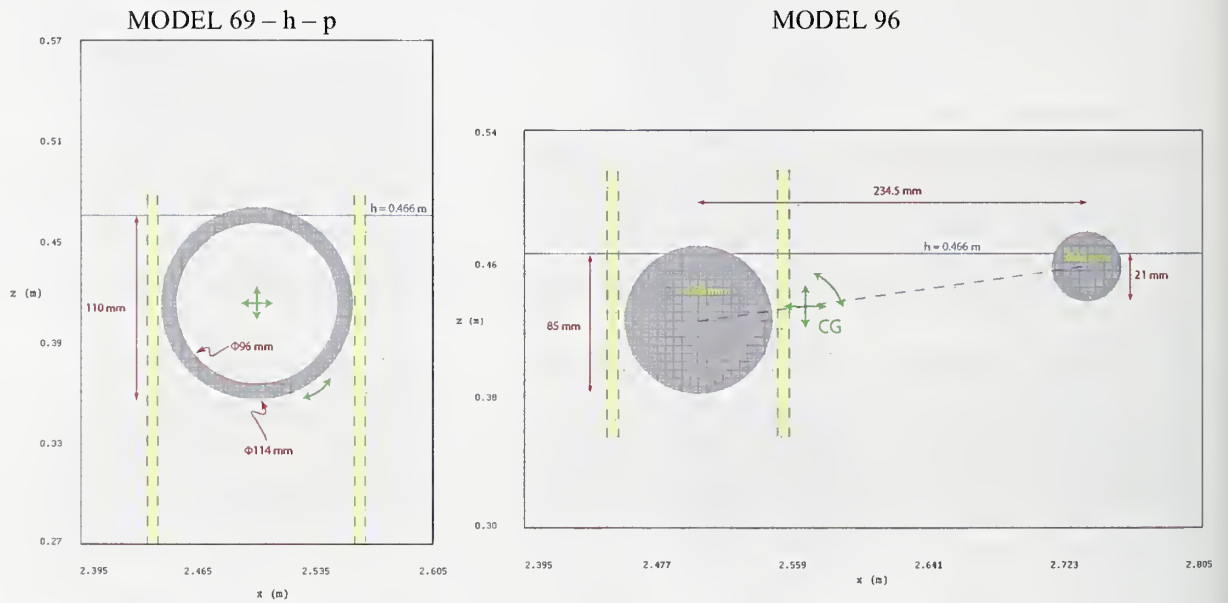
Figure 8.11 Pile-restrained breakwater model 69-h-p and 96 and the inner mesh block with $\delta x = \delta z = 0.5$ cm

Model 96 was simulated by two solid cylinders of diameters 89 mm and 42 mm separated by a center-to-center distance of 234.5 mm (Figure 8.11). The density of the first cylinder was 0.9841 kg/m^3/m and the second cylinder was 0.7477 km/m^3/m, providing the necessary buoyancies for drafts, $z_d/d = 0.96$ and 0.7, respectively. The rigid connection between two pipes was replicated by defining the cylinders as subcomponents

170

of the same object. The piles were modeled by means of two vertical solid blocks, 46.5 mm away from the center of the first cylinder on both sides. The clearance between the piles and the cylinder was 2 mm on each side, initially. The piles were 100% porous and the collusion model was activated with zero friction and zero energy loss similar to the model 60-p.

8.5.2. List of Numerical Simulations

The ranges of wave parameters are based on the conditions of the laboratory experiments and field conditions. The properties of the breakwater configuration, ranges of wave conditions and the dimensionless variables for each model are summarized in Table 8.1. All of the simulations are carried at a constant depth of 0.466 m. The wave conditions were controlled by changing the wave period T_p and wave steepness H/L. In Table 8.2 the lists of conducted simulations are presented.

Table 8.1 The list of parameters for the simulated models in the numerical wave tank. Red arrows in the figures indicate the degrees of freedom for each model.

Restraining	Model No.	Vertical length scale d (mm)	Draft z_d (mm)	Water depth h (m)	Wave height H (mm)	Wave period T (s)	Subm. ratio $\frac{z_d}{d}$	Incident wave steepness $\frac{H}{L}$	Relative depth kh	Definition sketch of breakwater configuration
Fixed	41	48.5	24.3	0.446	14-62	0.5-0.9	0.5	0.03 0.05	2.4 – 7.5	
	51	60.2	30.1							
	61	114	57		8-80	0.5-1.2		0.02-0.08	1.4 – 7.5	
	62	114	110	0.466	8-80	0.5-1.2	1.0	0.02-0.08	1.4 – 7.5	
Bottom moored	64	114	57	0.466	10-75	0.5-1.0	0.5	0.03 0.05	2.0 – 7.5	
	65	114	110	0.466	10-75	0.5-1.0	0.96	0.03 0.05	2.0 – 7.5	

171

Table 8.1 The list of parameters for the simulated models in the numerical wave tank (continued).
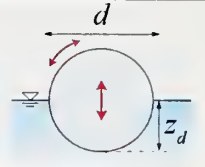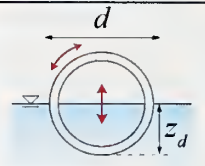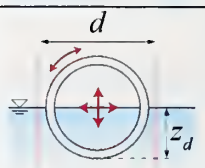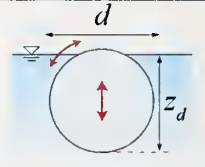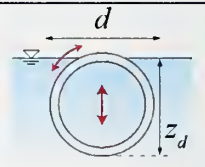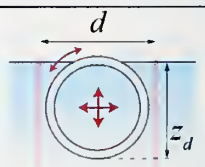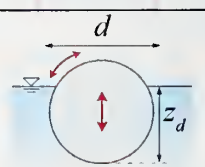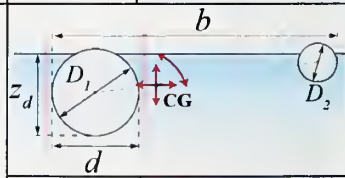
Restraining	Model No.	Vertical length scale d (mm)	Draft z_d (mm)	Water depth h (m)	Wave height H (mm)	Wave period T (s)	Subm. ratio $\frac{z_d}{d}$	Incident wave steepness $\frac{H}{L}$	Relative depth kh	Definition sketch of breakwater configuration
Pile-restrained	60	114	57	0.446	10-80	0.5-1.2	0.5	0.02-0.08	1.4 – 7.5	
	60 - h	114	57	0.446	10-75	0.5-1.2	0.5	0.02 0.03 0.05	1.4 – 7.5	
	60 – h - p	114	57	0.446	10-75	0.5-1.2	0.5	0.03 0.05	1.4 – 7.5	
Pile-restrained	69	114	110	0.446	10-80	0.5-1.2	0.96	0.02-0.08	1.4 – 7.5	
	69 - h	114	110	0.446	10-75	0.5-1.2	0.96	0.03 0.05	1.4 – 7.5	
	69 - h- p	114	110	0.446	10-75	0.5-1.2	0.96	0.03 0.05	1.4 – 7.5	
	70	114	80	0.446	10-80	0.5-1.2	0.7	0.02-0.08	1.4 – 7.5	
	96	89 ($D_1 = 89$ $D_2 = 42$)	85	0.446	10-80	0.5-1.2	0.96	0.03 0.05	1.4 – 7.5	$b = 300$mm

172

Table 8.2 The list of conducted simulations in the numerical wave tank. The check marks denote the completed runs and the crosses stand for skipped conditions. The letter 'T' is added to the simulations with RNG turbulence model. High wave period and steepness values result in extreme wave amplitudes (e.g. T= 1.2, H/L = 0.08 corresponds to H = 161 mm). On the lower end, small wave period and steepness are also excluded.

Model No.		$\dfrac{H_i}{L}$	T (s)							
			0.5	0.55	0.6	0.7	0.8	0.9	1.0	1.2
Fixed	41	0.03	×	✓	✓	✓	✓	✓	×	×
		0.05	✓	✓	✓	✓	✓	✓	×	×
	51	0.03	×	✓	✓	✓	✓	✓	×	×
		0.05	✓	✓	✓	✓	✓	✓	×	×
	61	0.02	×	✓	✓	✓	✓	✓	✓	✓
		0.03	✓T	✓T	✓T	✓T	✓T	✓T	✓	✓
		0.05	✓T	✓T	✓T	✓T	✓T	✓T	✓T	×
		0.08	✓	✓	✓	✓	✓	×	×	×
	62	0.02	✓	✓	✓	✓	✓	✓	✓	✓
		0.03	✓T	✓T	✓T	✓T	✓T	✓T	✓	✓
		0.05	✓T	✓T	✓T	✓T	✓T	✓T	✓T	×
		0.08	✓	✓	✓	✓	✓	×	×	×
Bottom moored	64	0.03	×	✓	✓	✓	✓	✓	✓	×
		0.05	✓	✓	✓	✓	✓	✓	✓	×
	65	0.03	×	✓	✓	✓	✓	✓	✓	×
		0.05	✓	✓	✓	✓	✓	✓	✓	×
Pile-restrained	60	0.02	×	×	✓	✓	✓	✓	✓	✓
		0.03	✓	✓	✓	✓	✓	✓	✓	✓
		0.05	✓	✓	✓	✓	✓	✓	✓	×
		0.08	✓	✓	✓	✓	✓	×	×	×
	60-h	0.02	×	×	✓	✓	✓	✓	✓	✓
		0.03	✓T	✓T	✓T	✓T	✓T	✓T	✓T	×
		0.05	✓T	✓T	✓T	✓T	✓T	✓T	✓T	×
	60-h-p	0.03	✓	✓	✓	✓	✓	✓	✓	×
		0.05	✓	✓	✓	✓	✓	✓	✓	✓
	69	0.02	×	✓	✓	✓	✓	✓	✓	✓
		0.03	✓	✓	✓	✓	✓	✓	✓	✓
		0.05	✓	✓	✓	✓	✓	✓	✓	×
		0.08	✓	✓	✓	✓	✓	×	×	×
	69-h	0.03	✓T	✓T	✓T	✓T	✓T	✓T	✓T	✓T
		0.05	✓T	✓T	✓T	✓T	✓T	✓T	✓T	×
	69-h-p	0.03	✓	✓	✓	✓	✓	✓	✓	✓
		0.05	✓	✓	✓	✓	✓	✓	✓	×
	70	0.02	×	✓	✓	✓	✓	✓	✓	✓
		0.03	✓	✓	✓	✓	✓	✓	✓	✓
		0.05	✓	✓	✓	✓	✓	✓	✓	×
		0.08	✓	✓	✓	✓	✓	×	×	×
	96	0.03	✓	×	✓	✓	✓	✓	✓	✓
		0.05	✓	×	✓	✓	✓	✓	✓	✓

8.5.3. Data Collection and Analysis

The breakwater was placed at x= 2.5 m of the numerical wave tank. The time series of water surface displacements was recorded at the source region ($x = 0.0$) and on both sides of the breakwater, at 0.6 m and 3.9 m. The time series data was recorded at every computational time step. Therefore the frequency of the recorded data varied depending on the model geometry and wave conditions. Nevertheless, an upper limit of 0.05 s was set to avoid too large time steps.

Normally, the water surface displacements were calculated at sections that correspond to the x-coordinates of the cell centers. The water surface elevations at the intermediate sections were linearly interpolated using the two cell center values on both sides.

The time series data was analyzed in the same fashion with the experimental data. The portion of the transmitted wave signal after the waves reach a steady state was trimmed to be used in the analysis. First wave crests and troughs were located using a "peak finder" anlgorithm. Then, the wave heights were calculated as the distances between the consequent wave crests and troughs. The wave period was calculated by frequency domain analysis.

Reflected wave height was estimated in two ways during the numerical data analysis. The first method required a moving probe similar to the physical wave tank. The probe was moved at a distance Δx away from the previous position at each time step, δt. This was formulated as follows:

$$x^n = x^{n-1} + \Delta x^n \text{ and,} \tag{8.1}$$

$$\Delta x^n = \delta t^n v_p \tag{8.2}$$

where v_p is the moving probe speed and n is the time index.

The probe speed and the time to begin moving were calculated with the same method as in the laboratory model (Appendix A). This method required longer simulation time in order to have fully developed standing waves before the probe starts moving. The time series water surface displacements η/H is shown in Figure 8.31 for model 61 (fixed single cylinder, $z_d/d = 0.5$). The probes at $x/L = 0$ and 3.9 are fixed. The moving probe traveled from $x/L = 0.6$ to 1.57 at a speed 0.042 s starting at 6.86 s of the 30 s simulation time. The speed was calculated according to the wave conditions to ensure that there were enough number of wave crests and troughs within the envelope so that the nodes and antinodes could be located correctly. To be able to scan the distance between x/L = 0.6 and 1.57 with this speed the simulation time should be over 56 s which almost doubles the computational cost. Therefore, the spatial profiles are used instead of moving probe for comparison with the physical experiments.

In the second method, the water surface profile behind the model, between $x = 0$ and 2.5 m, was recorded at consecutive times during 30th wave cycle. During post processing, these profiles were overlaid on each in order to form a stationary wave

envelope along the channel length that connects the wave crests and troughs. The nodes and anti-nodes of this envelope were used to estimate the reflected wave height by using Equation 3.65. In Figure 8.32 a sample spatial profile of water surface displacement is plotted for the same simulation with model 61 given in Figure 8.12. The stationary envelopes are clearly seen on the offshore side of the breakwater which is fixed at $x/L = 2.5$. The dashed red lines indicate the locations of the fixed and moving probes that were referred in Figure 8.13.

$T = 0.8$s, $H = 29.8$mm, $kh = 2.9$, $H/L = 0.03$
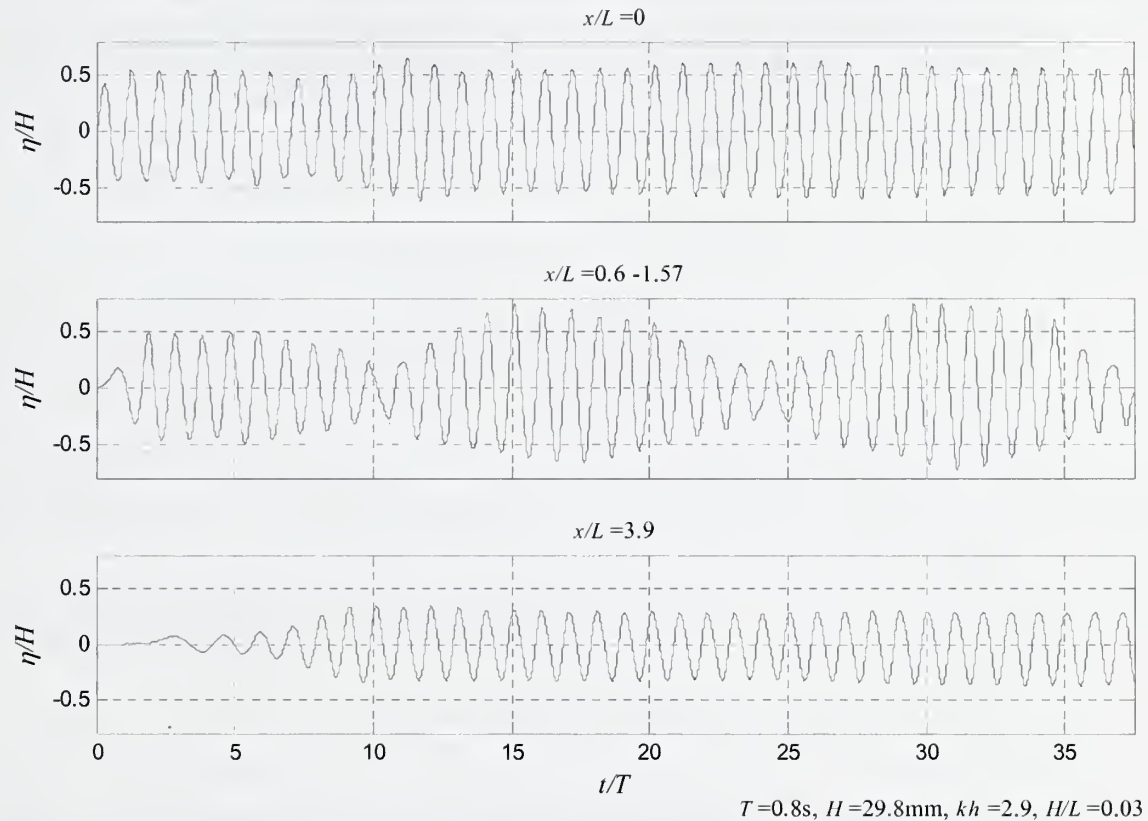
Figure 8.12 Time variation of water surface displacements.

$T = 0.8$s, $H = 29.8$mm, $kh = 2.9$, $H/L = 0.03$
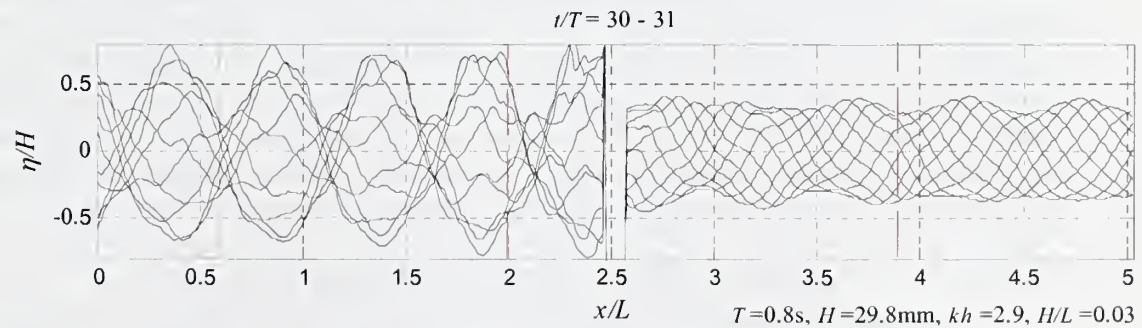
Figure 8.13 Spatial variation of water surface displacements in 30th wave cycle.

175

8.5.4. Presentation of Results

Prior to the test in the 5 m long numerical wave tank, the full length (15 m) of the physical wave tank was simulated for some of the wave parameters. In Figure 8.33 time series water surface displacements recorded at the laboratory are compared with the numerical simulation results for the wave conditions, $T = 0.8$ s, $H/L = 0.03$ and $h = 0.466$ m. The first gauge started moving form x = 9.6 m to 11.1 m at a speed 42.56 mm/s about 21 s after the paddle was initiated. In the numerical wave tank the same condition was imposed by moving the virtual probe at the same speed as the moving gauge. Figure 8.14 shows that the wave fronts arrive to the first gauge at the same time with no phase difference. During laboratory experiments it was observed that there was a slight delay in the communication between computer and the indexer that controls the wave paddle. Therefore, there is a shift between the two signals after the gauge starts moving.
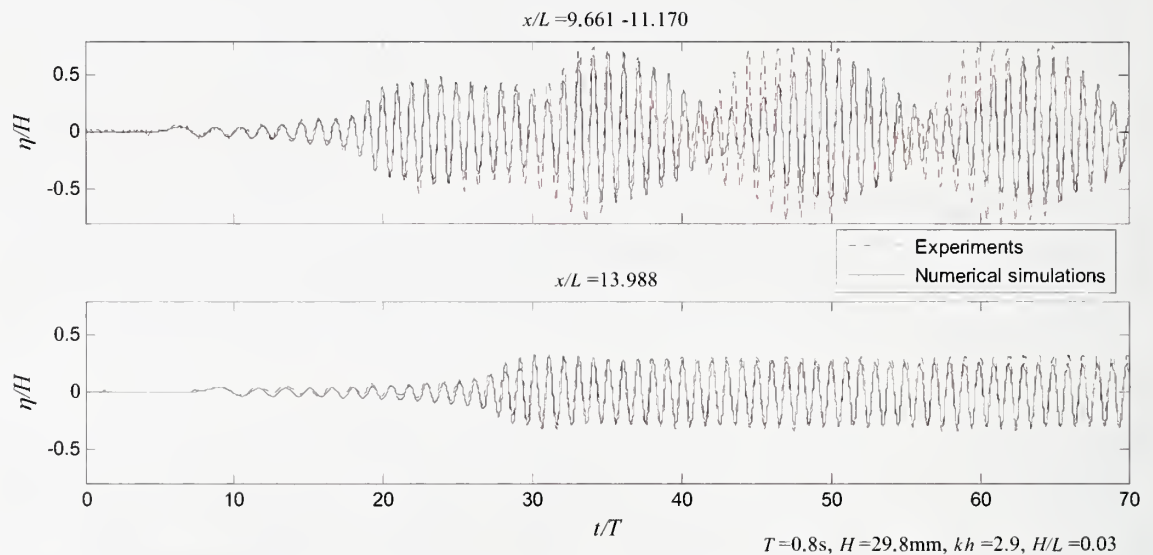
Figure 8.14 Comparison of numerical simulations with physical experiments of the model 61.

The computed wave amplitudes closer to the nodes of the standing wave are less than those measured the laboratory. There is a good agreement in terms of wave period and phase. The fixed gauge recording at x = 13. 9 m matches fairly well with the experiments. The average water surface elevation slightly drops after 50 wave periods. This is due to the loss of mass at the boundaries. The remaining simulations are carried out in the 5 m domain. It is also shown in Figure 8.14 that the antinodes of the standing wave are less for the numerical simulations compared to the experiments.

8.5.4.1. Comparison of Water Surface Profiles with Experiments

The time variations of transmitted wave water surface displacements for the experimental and numerical models are compared between Figure 8.15 and 8.17. Figures 8.15 and 8.16 include the plots for the solid cylinder models (models 61, 62, 60, 70, 69 and 96) and Figure 8.17 presents hollow and pile-restrained models 60 – h (- p) and 69 -

h (- p). The wave conditions were, $T = 0.6$ s, $H = 0.03$ m ($H/L = 0.03$) at $h = 0.466$ m. Only 20 wave periods in the steady portion of the wave data are plotted in these figures. Since the waves arrive at the test section at different times in numerical and physical wave tanks, the compared wave trains are shifted to mach the phases.

In general, laboratory measurements and numerical simulations match very well for models 61, 64, 65, 60 and 96. The transmitted wave height is slightly over estimated in the simulation with model 70 ($z_d / d \cong 0.7$). Although, there is fairly good agreement between wave amplitudes of the transmitted wave trains for models 62 and 69 ($z_d / d \cong 1$), there is small lag between the secondary wave modes.
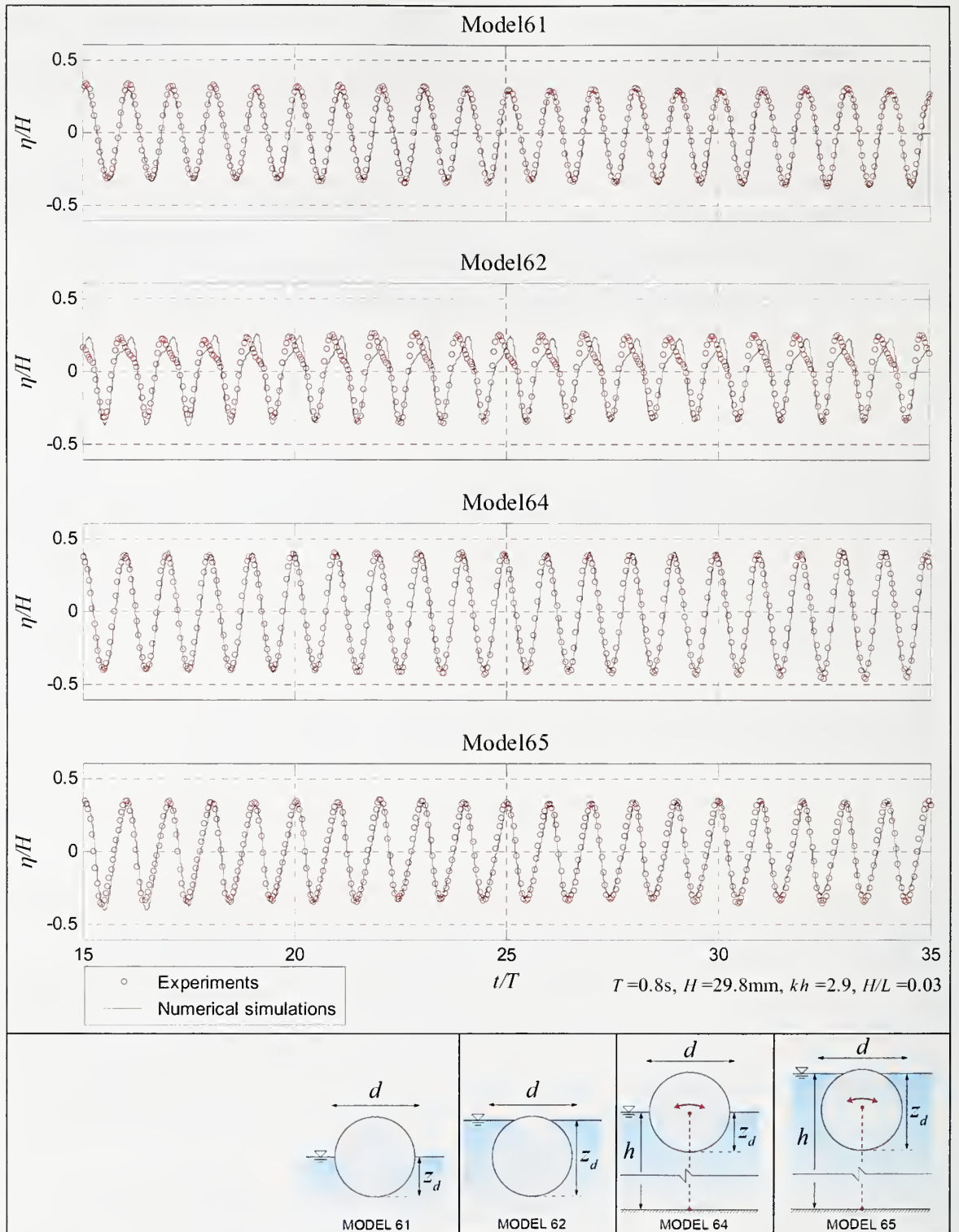
Figure 8.15 The comparison of experimental and numerical transmitted waves.
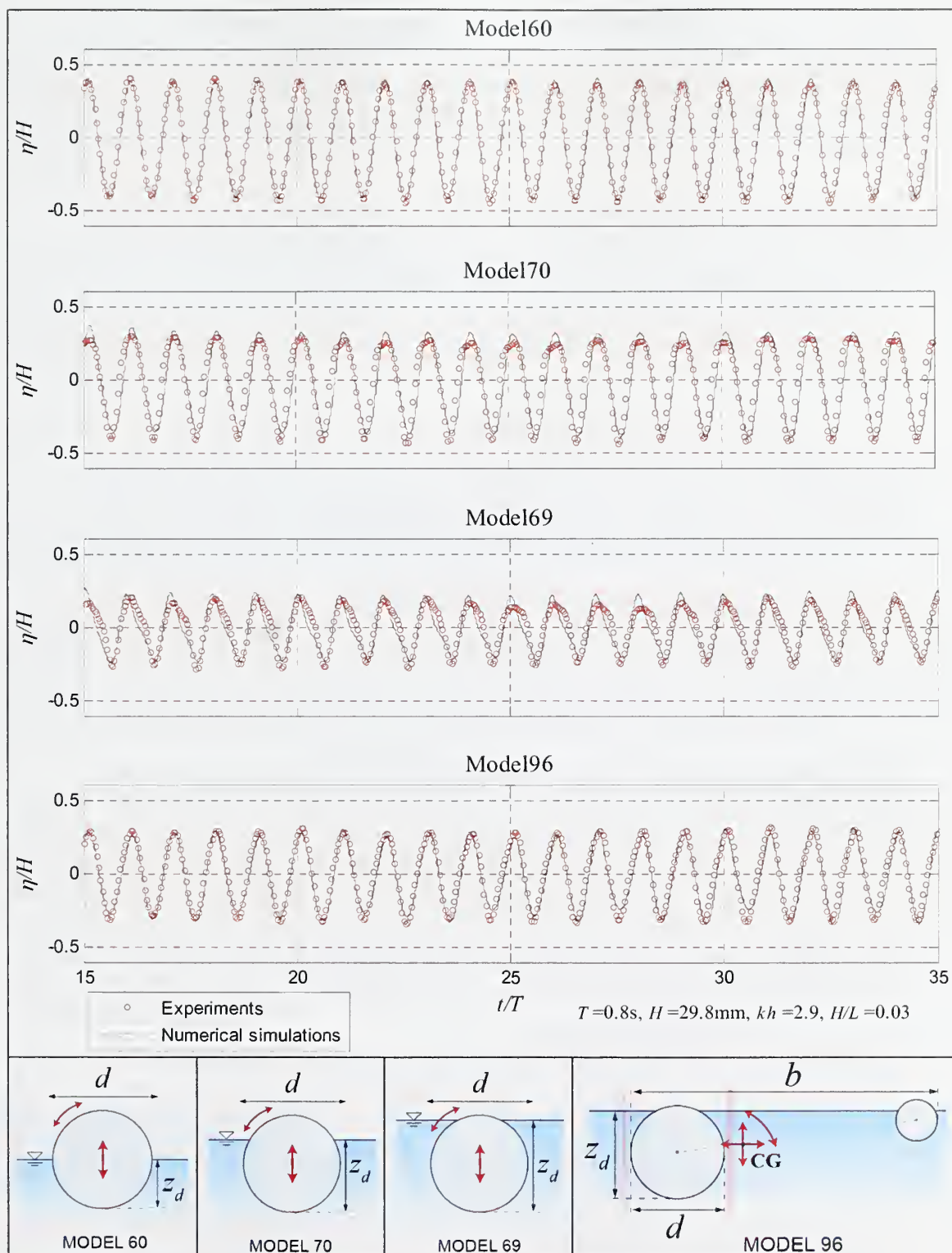
Figure 8.16 The comparison of experimental and numerical transmitted waves.
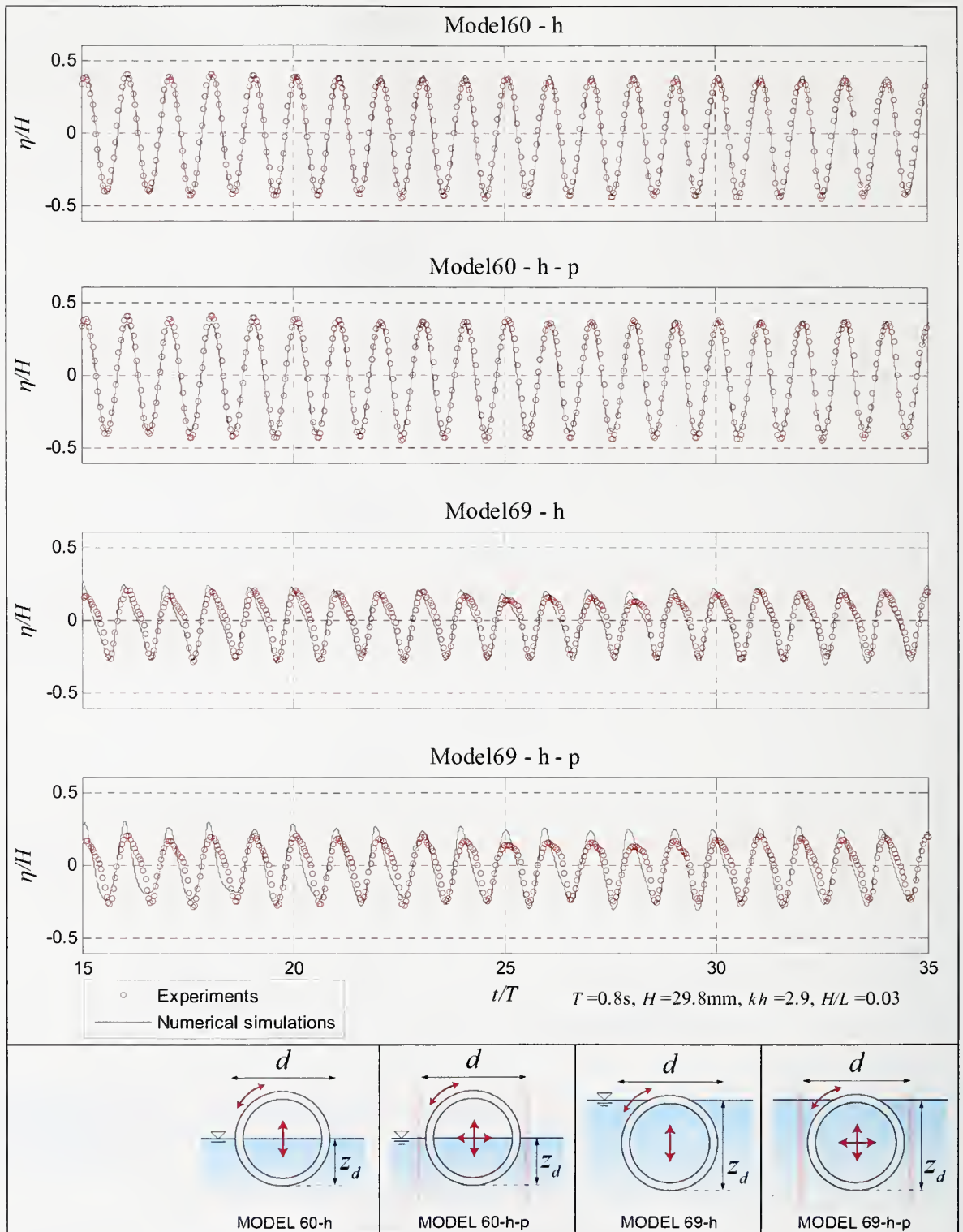
Figure 8.17 The comparison of experimental and numerical transmitted waves.

The fully immersed hollow cylinder, model 96 - h in Figure 8.17 matches better compared to the solid cylinder. But the model 69 - h - p does not compare as good as the model 60 - h indicating that the main reason for the difference is the mass distribution of the breakwater model rather then x-restraint. Moreover, there is no significant difference between models 60, 60-h and 60-h-p in terms of temporal variation of the transmitted wave.

It was shown in Chapter 5 that in these models, the amount of wave transmission is primarily controlled by the relative draft and inertia. When the models are completely immersed ($z_d / d \cong 1$), overtopping considerably influence the transmitted wave characteristics. Figures 8.16 and 8.17 show that, the numerical model reproduces temporal properties of the transmitted wave reasonably well even when there is overtopping.

8.5.4.2. Comparison of κ_t and κ_r Coefficients with the Experiments

The transmission coefficient, κ_t is the ratio of the incident wave height H_i to the transmitted wave height, H_t where H_i is the wave height is considered to be the input wave height for both numerical and experimental data. The reflected wave height H_r is calculated from the spatial envelopes as explained in the previous section.

Numerically calculated transmission and reflection coefficients of the fixed models 41, 51 and 61 with z_d/d=0.5 are compared with the experimental results and their variation with relative draft, z_d/L, is shown Figure 8.18. Figures 8.19 through 8.25 presents the comparison of transmission and reflection coefficients of the fixed, bottom moored and pile-restrained breakwater models with changing relative depth kh.

Figure 8.18 show that the numerical wave tank can replicate the experimental conditions for different pipe diameters. Similar to the experimental results, the trends of the data corresponding to different pipe diameters separate as the relative draft decrease at $H/L = 0.05$. This is because, as the breakwater size gets smaller compared to the wave size, waves start overtopping the breakwater. Hence, the transmission coefficient is also a function overtopping in addition to draft. The reflection coefficients of the numerical models are also in reasonably good agreement with the experiments for smaller relative drafts. However, at higher relative drafts, the numerical solution underestimates the reflection coefficients.

In all of the figures, the calculated transmission coefficients are in good agreement with the experimental results for $H/L = 0.03$ and 0.05 within the range of tested relative depths. When $H/L = 0.02$, the numerical simulations, in general, overestimate the transmission coefficient. On the other hand, at $H/L = 0.08$, the numerical predictions of transmission coefficients are higher then the measured ones.

The half submerged pile-restrained breakwater, model 60 (- h), has a peak around $kh = 4$. This value is closer to the natural period of this model (T = 0.5 - 0.6). There is a slight increase of the κ_t transmission coefficient at other steepness values around the same kh. The experimental values of κ_t around this value are less than that of the

181

numerical estimates. The heave motion of the breakwater is amplified at wave periods closer to its natural period. Therefore, wave damping is reduced which increase to both transmitted and reflected wave heights. In laboratory conditions the friction between the piles could be one of the reasons of the difference between the two transmission coefficients.

In general, the reflection coefficients, κ_r, are also in reasonably good agreement with the experimental results. κ_r, Simulations with Model 61 estimates lower κ_r values when the reflection is high in Figure 3.19. One reason for the mismatch is the method used for reflection coefficient estimation. As κ_r approaches to unity the amount the amplitudes at the nodes of the standing wave gets closer to zero and hence, the calculated κ_r values become more sensitive to minor fluctuations.

In all of the comparative figures, the physical model is best replicated between H/L = 0.03 and 0.05. At this range, the pile-restrained models 60 and 69 are also compared for three different representations of their geometric configuration. It is shown in Figures 8.22 and 8.23 that the trends of κ_t and κ_r does not change considerably by improving the geometric representation of these models at lower kh. Models 60-h-p and 69-h-p transmits the waves less and reflects them more, then the other two geometric arrangements of the same models as kh increases in Figure 8.22.
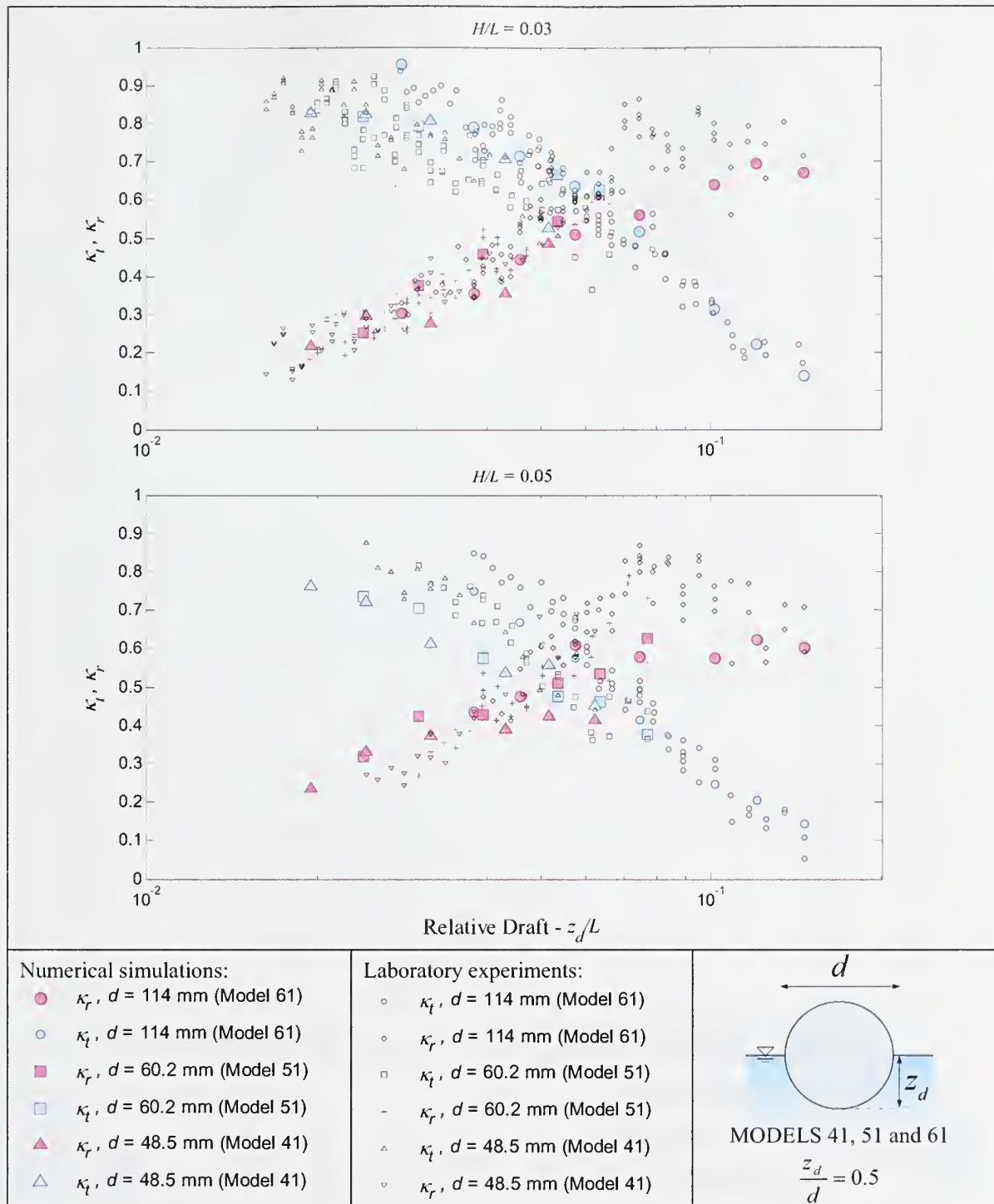
Figure 8.18 Comparison of numerical simulations with laboratory experiments for half submerged fixed pipe arrangement.
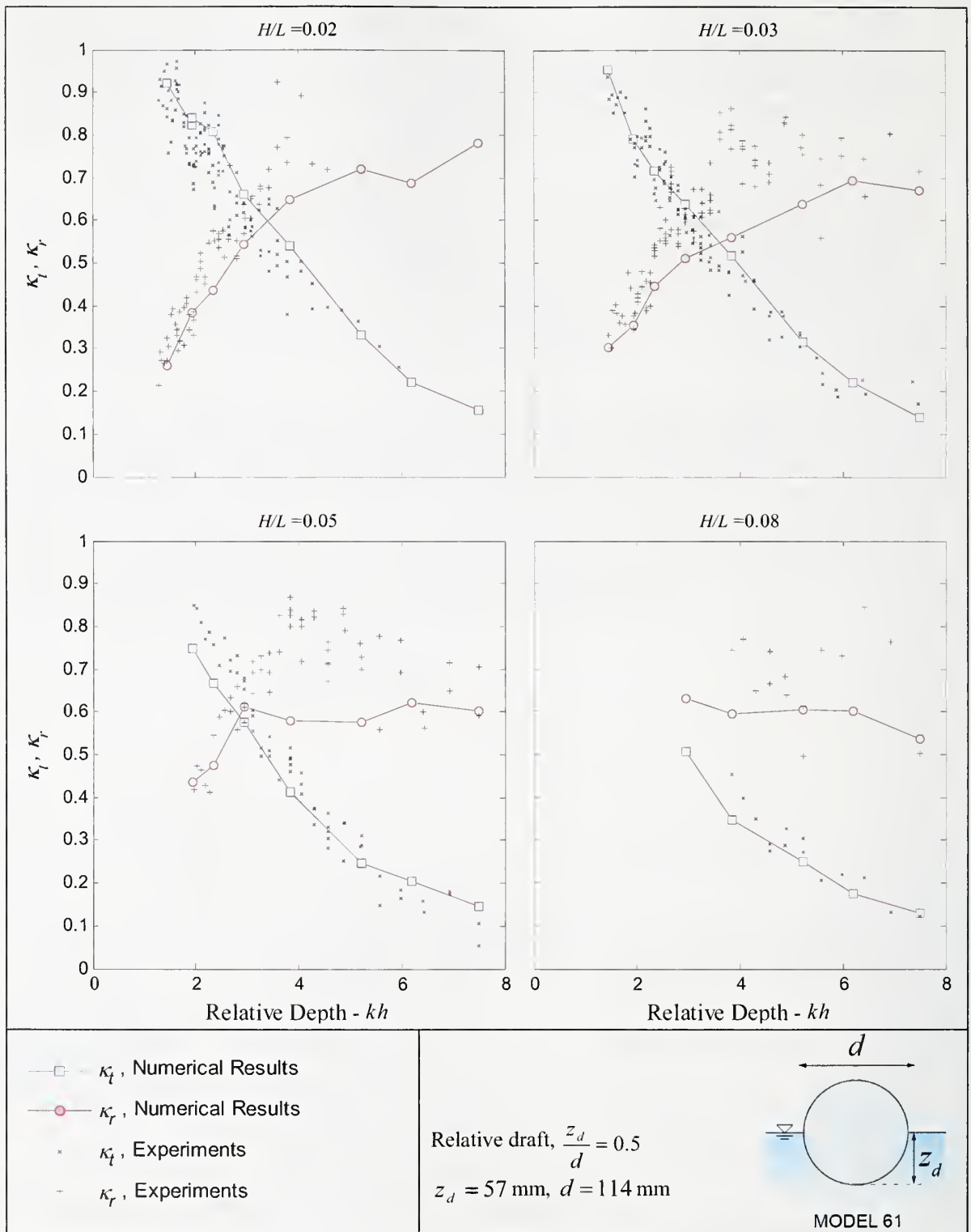
Figure 8.19 Comparison of numerical simulations with laboratory experiments for half-submerged fixed pipe arrangement.

184
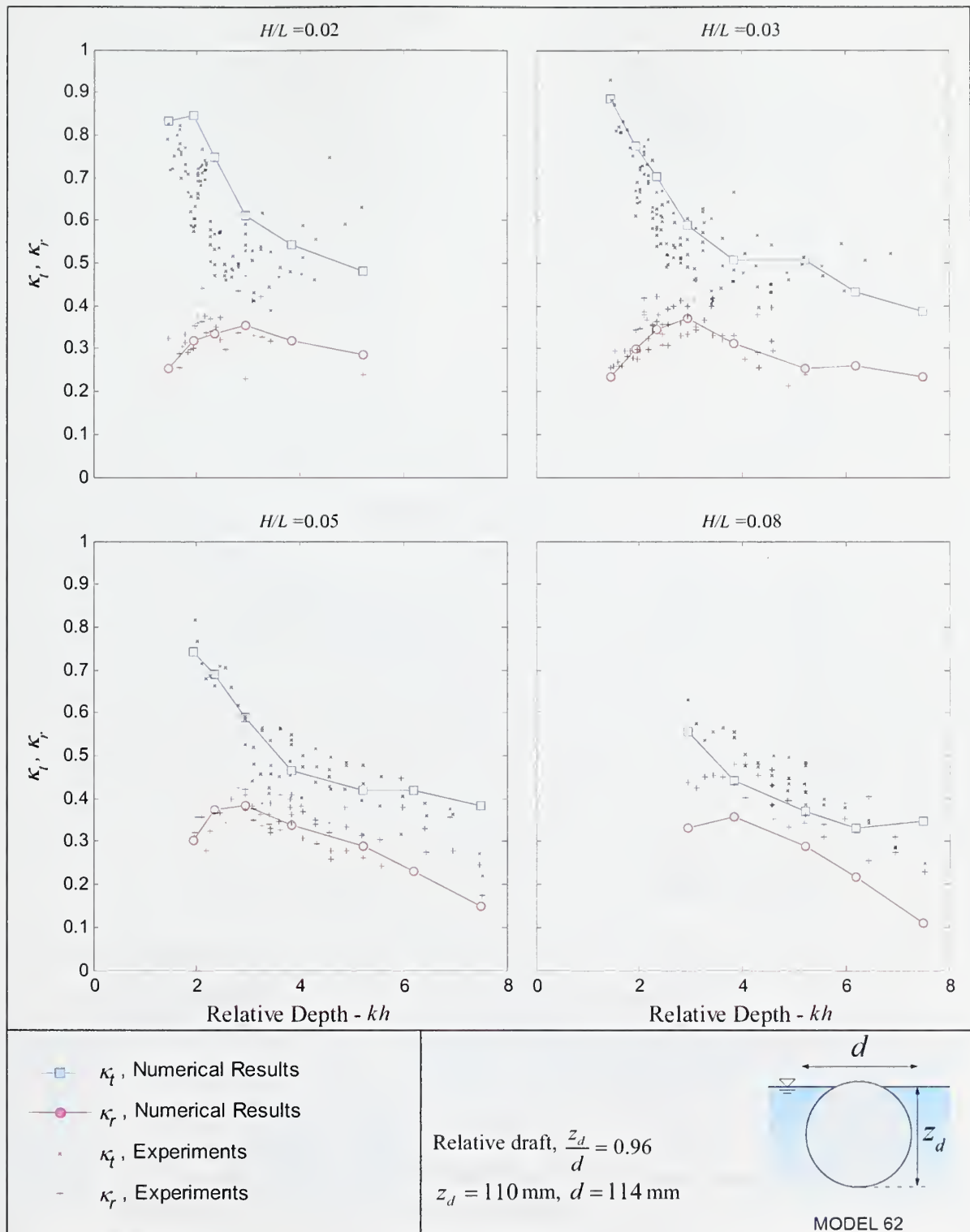
Figure 8.20 Comparison of numerical simulations with laboratory experiments for fully-submerged fixed pipe arrangement.

185
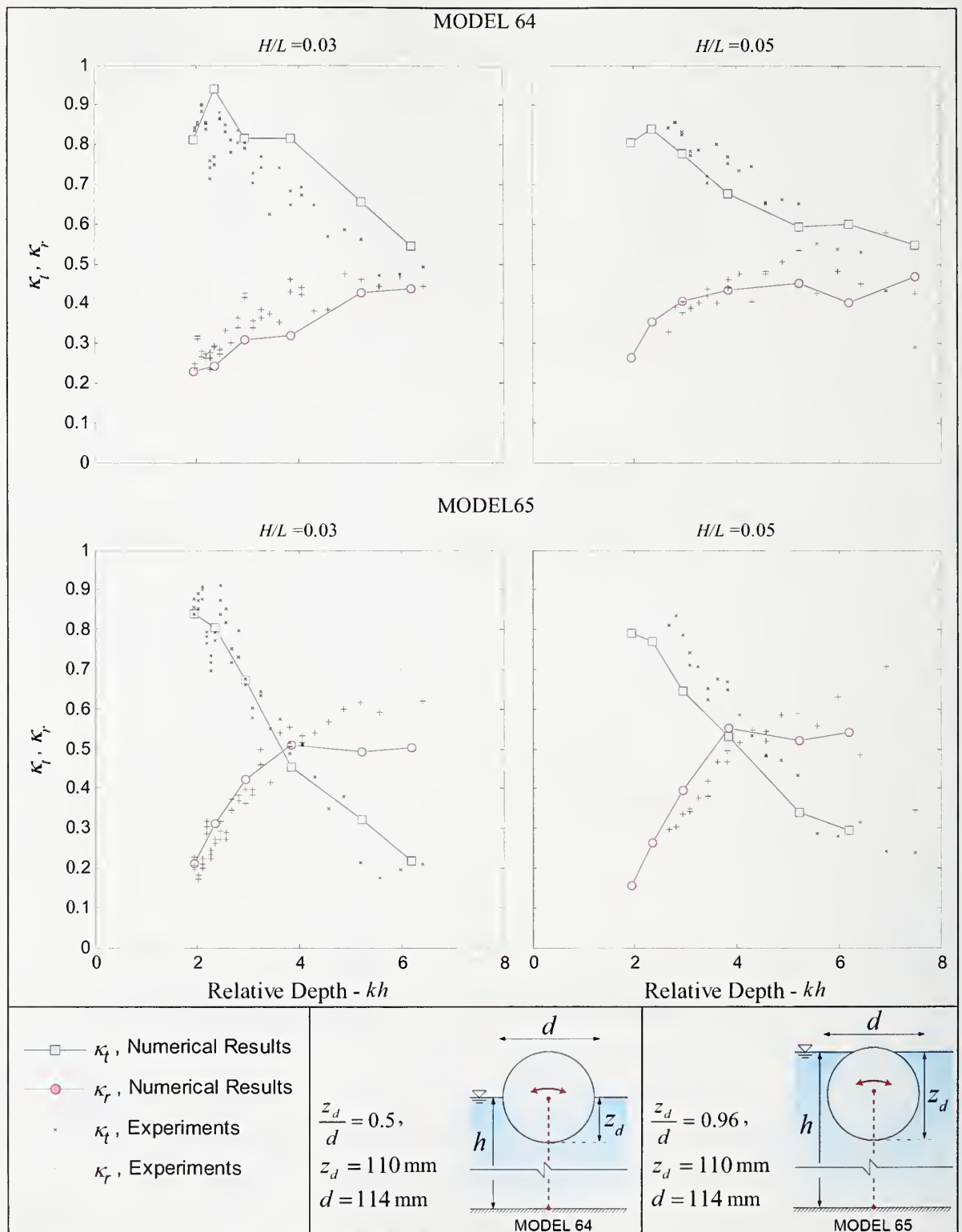
Figure 8.21 Comparison of numerical simulations with laboratory experiments for bottom moored pipe arrangement.
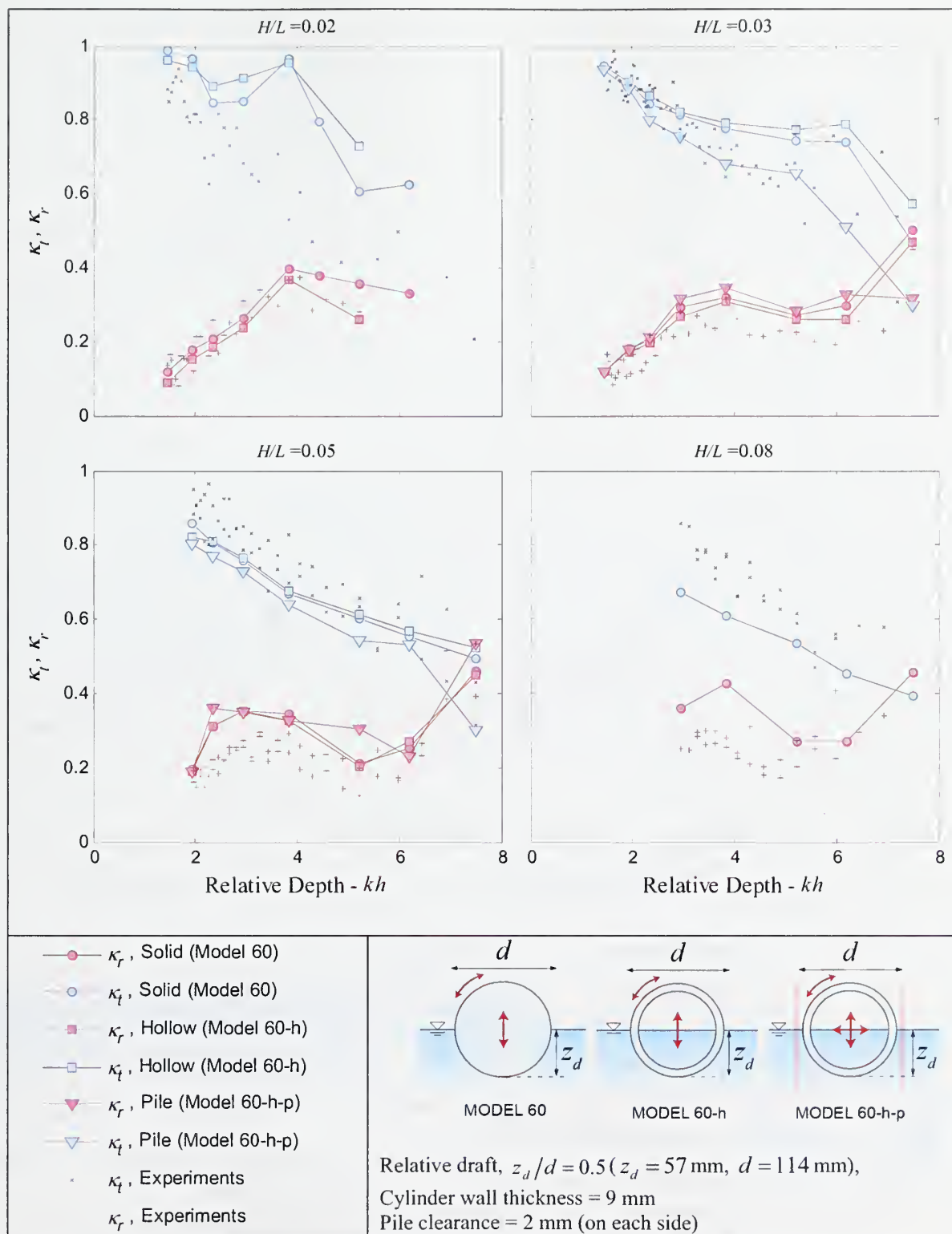
Figure 8.22 Comparison of numerical simulations with laboratory experiments for half-submerged pile-restrained pipe arrangement.
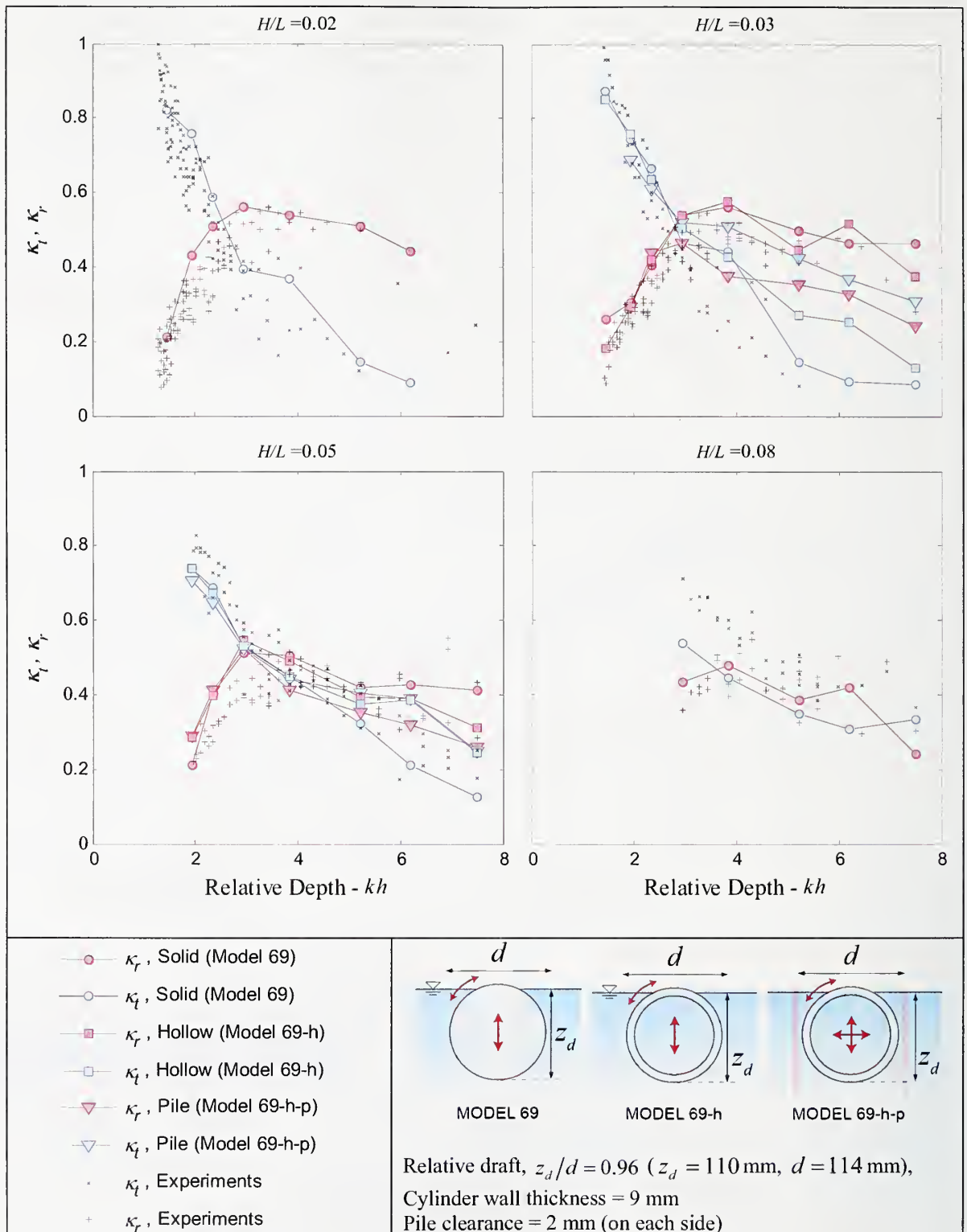
Figure 8.23 Comparison of numerical simulations with laboratory experiments for fully-submerged pile-restrained pipe arrangement.
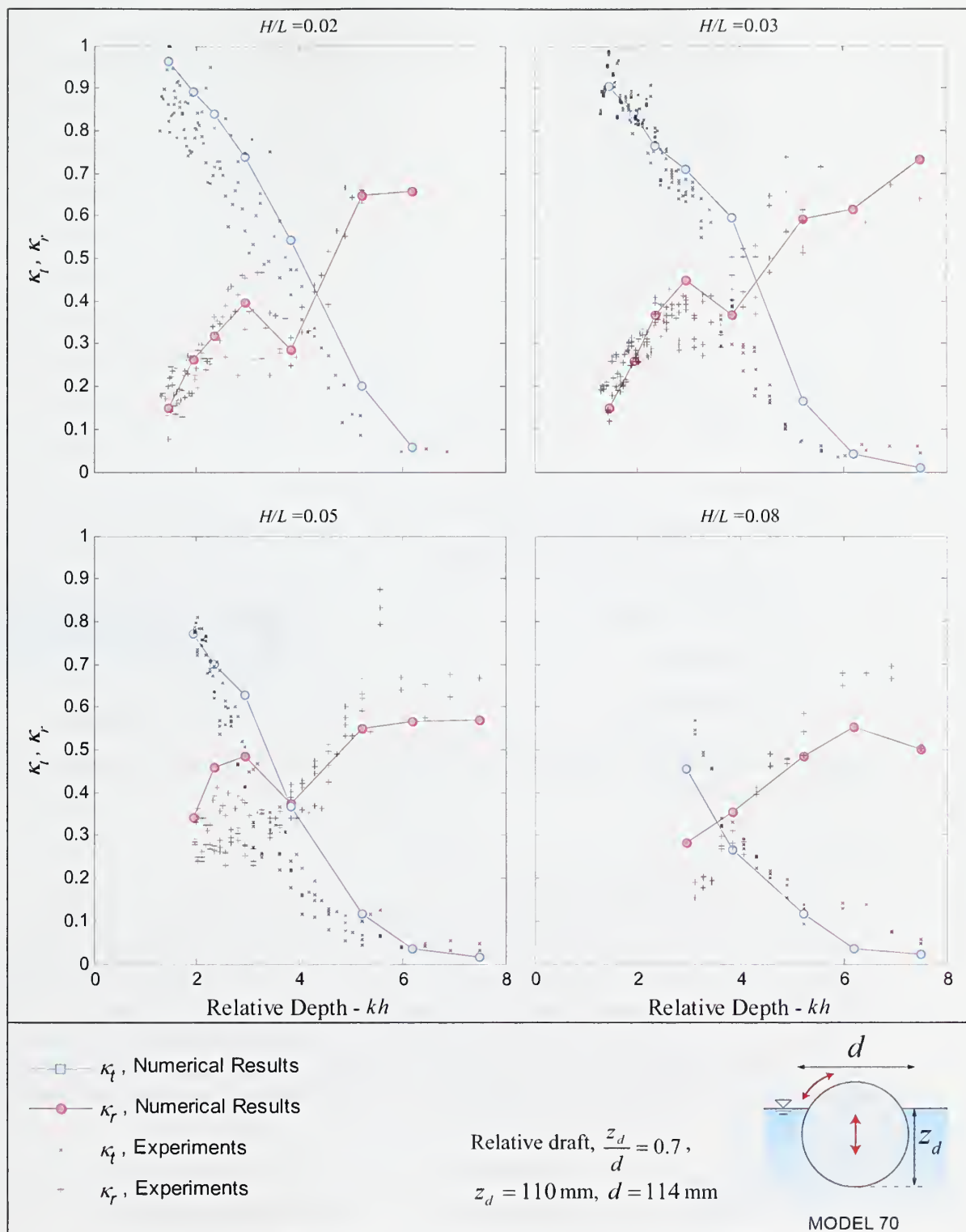
Figure 8.24 Comparison of numerical simulations with laboratory experiments for partially-submerged pile-restrained pipe arrangement.
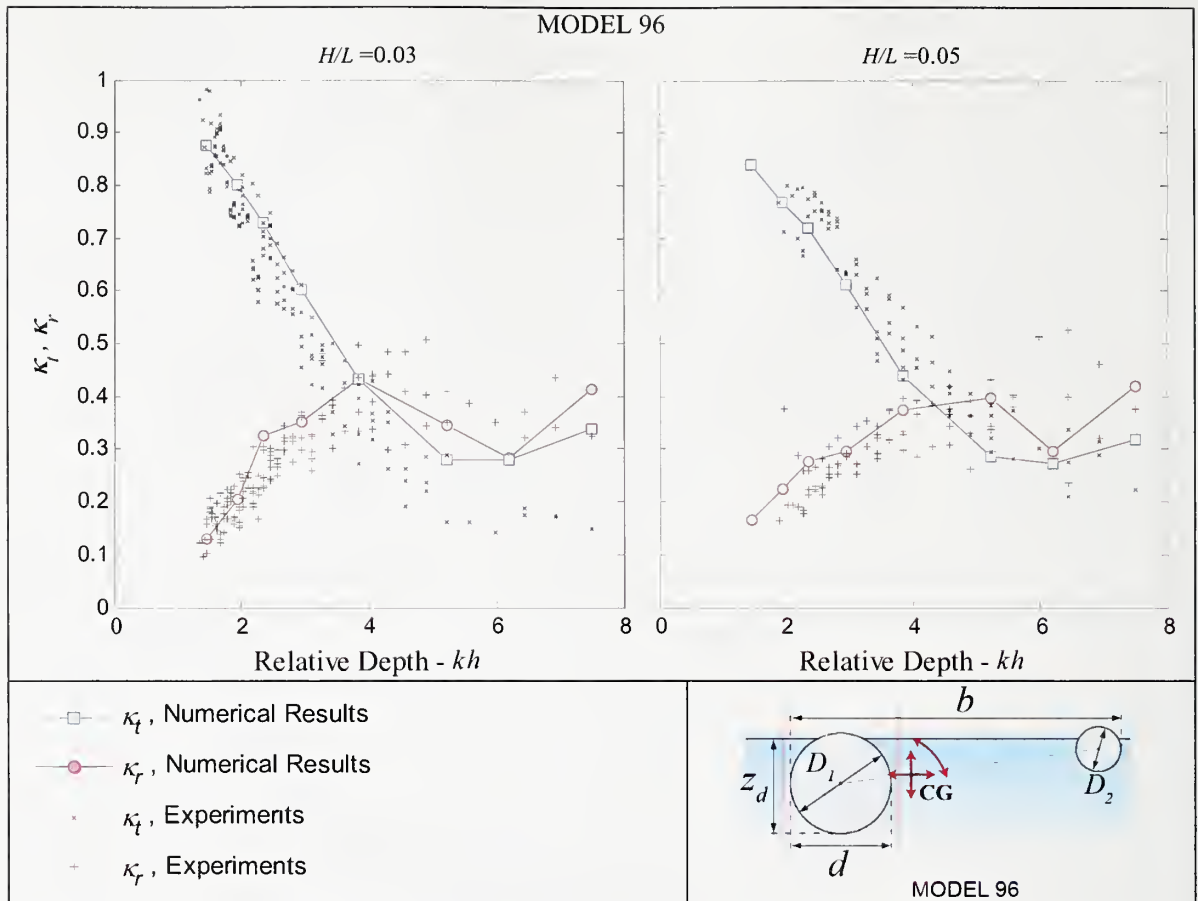
Figure 8.25 Comparison of numerical simulations with laboratory experiments for pile-restrained two-pipe arrangement.

8.5.4.3. Turbulent Simulations

Some of the simulations are repeated with the RNG turbulence model. The momentum advection is selected as second-order monotonicity preserving to avoid excessive dissipation in these simulations. The results of these simulations are compared with the experimental results and corresponding laminar solutions in Figures 8.26 and 8.27 for models 61, 62, 60-h and 69-h. There is no significant change in the transmissions and reflections coefficients when turbulence is included. This shows that the transmission is primarily controlled by wave reflection and viscous dissipation rather then turbulence.
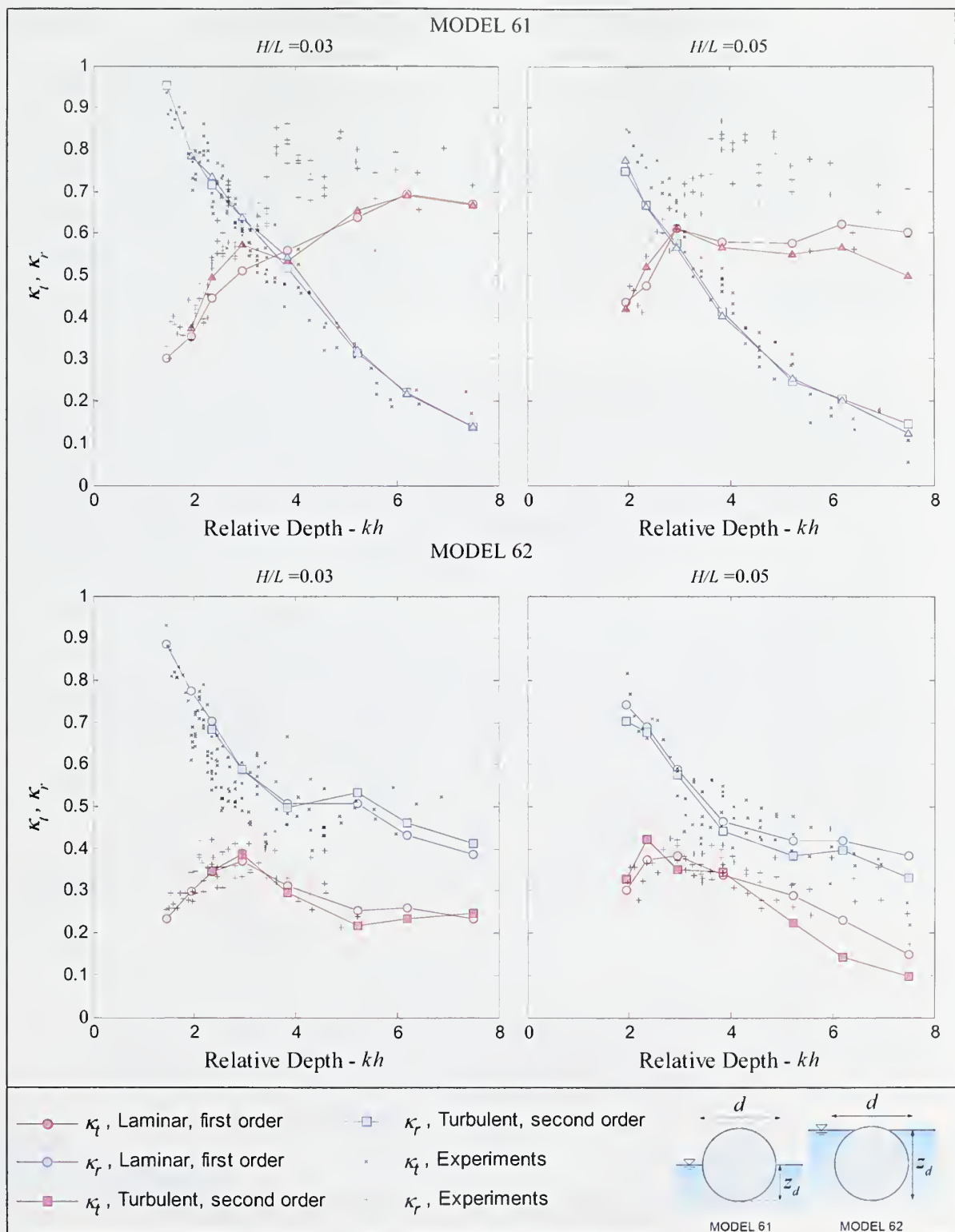
Figure 8.26 Comparison of laminar and turbulent numerical simulations with laboratory experiments for fixed pipe arrangement.
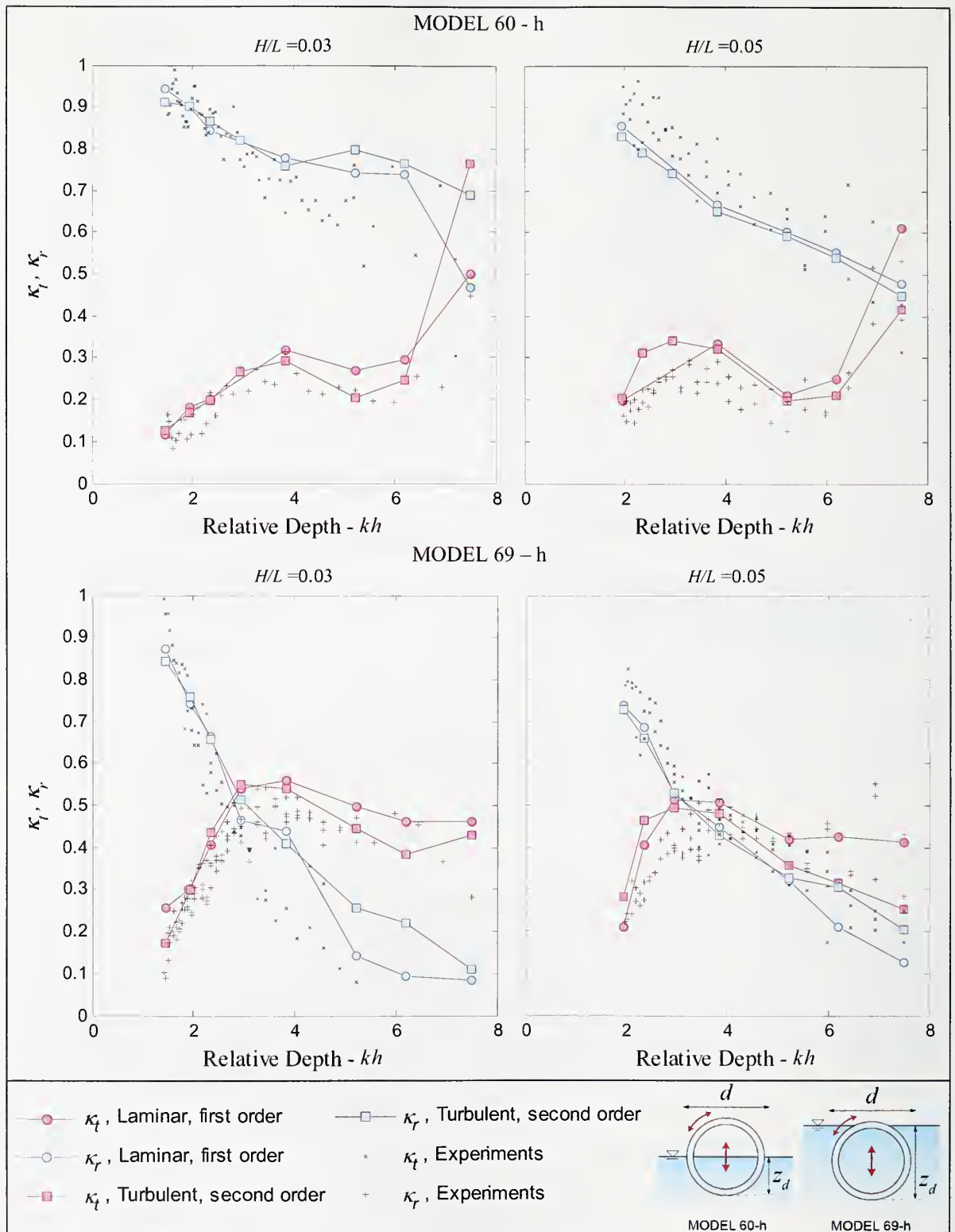
Figure 8.27 Comparison of laminar and turbulent numerical simulations with laboratory experiments for pile-restrained pipe arrangement.

8.5.4.4. Comparison of Motion Response with Experiments

The motion response of the half submerged pile-restrained breakwater model 60 is compared with the numerical simulations at two wave heights, $H = 17$ mm and 28 mm ($H/L = 0.03$ and 0.05) and T = 0.6 s. The heave (x-axis translation) and roll (y-axis rotation) response of the laboratory modes were estimated from the video recordings at 15 frames per second with a resolution of 320x240 pixels. The "*.avi" files were first converted into separate frames and then, the positions of the breakwater models were digitized manually on these frames. The angular velocities are calculated by following the relative position of a fixed point on the PVC pipe. The water surface displacement at a fixed point on the onshore side of the breakwater was also tracked. The digitized data is calibrated with the pipe diameter.

In Figure 8.28 and 8.29, the temporal variations of the water surface displacements at $x = 3.1$ m estimated form the video recording are compared with the wave gauge recording at x = 13.9 m during the same experiment. The wave trains are shifted to eliminate the phase difference between them. The results show that for both of the experiments, the analysis of the video recordings gives good estimates for the water surface displacements. The motion of the cylinder can be obtained using the same analysis.
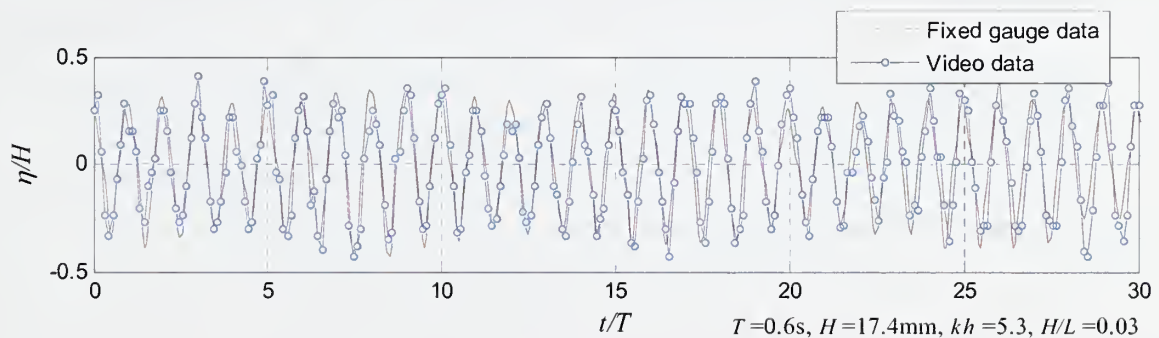
Figure 8.28 The comparison of video and experimental data. (Hexp=16.86)
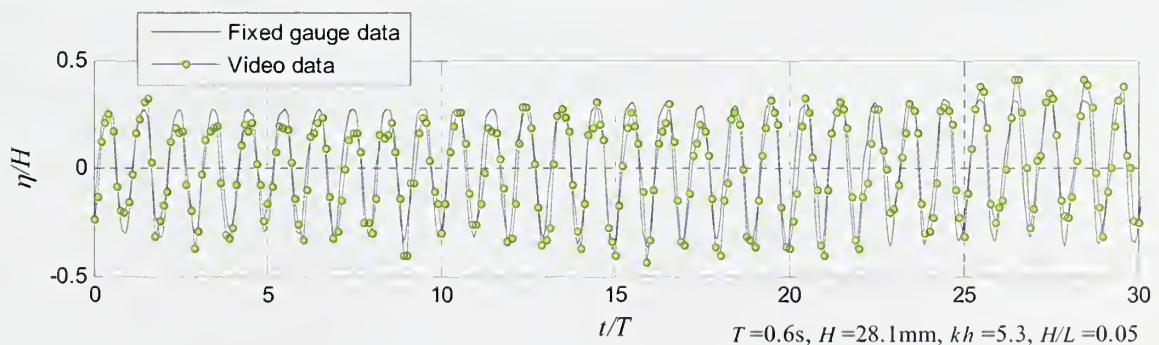
Figure 8.29 The comparison of video and experimental data. (Hexp=28.25)

193

In Figures 30 and 31, the time series water surface displacement, η/H, and the heave response, ξ_z/H, of model 60 are plotted in time for both video recording analysis and numerical simulations. Recall that the numerical and physical wave tanks had different lengths. This required the wave trains to be shifted in time to match the phases. Once the water surface elevations were correlated, the time history of the breakwater motion in heave was also shifted with the same phase and compared with the numerically calculated signals.
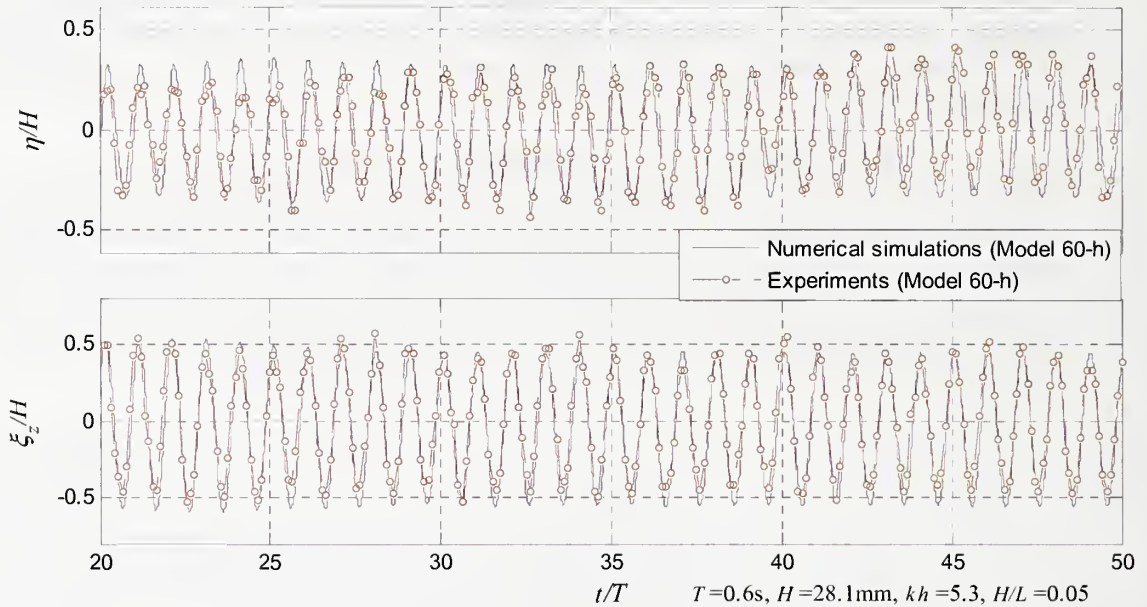
Figure 8.30 Motion response comparison.
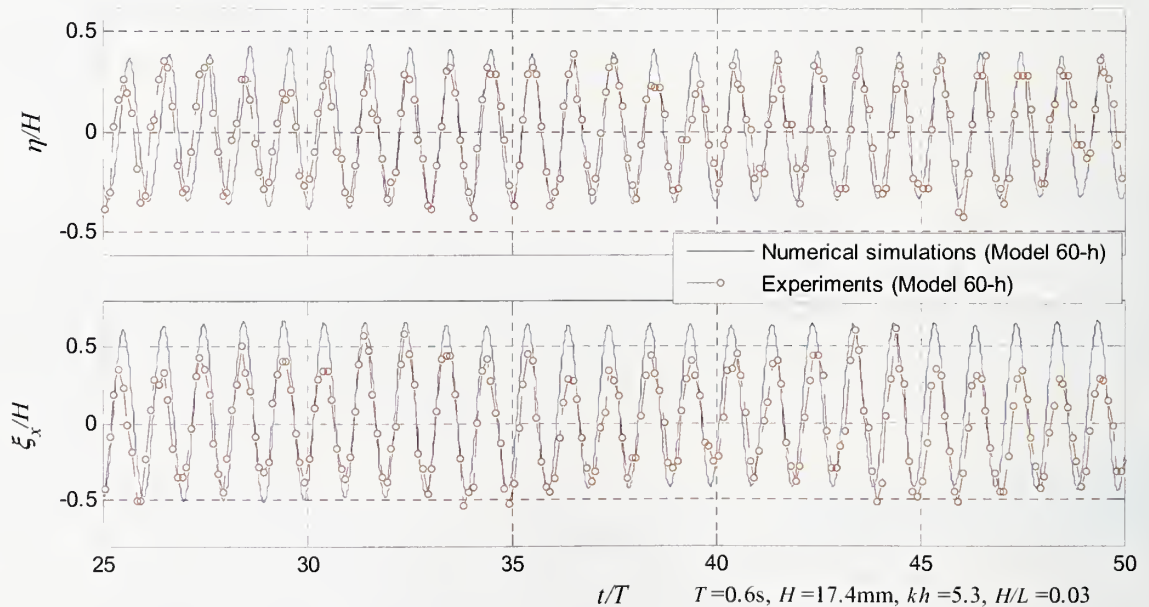
Figure 8.31 Motion response comparison

194

Between two simulations the one with the higher wave amplitude agree better with the video recording analysis. The numerically estimated wave amplitudes are slightly less than the measured ones in both of the cases. The dimensionless amplitude of the heave motion, ξ/H, is higher then the measured ones but there is no phase shift between the numerical simulation and video recoding analysis results.

The dimensionless angular velocities of the analyzed models are compared with the numerical simulation results in Figure 8.32 and 8.33. Two additional simulations were carried out to investigate the effect of friction between the pipe and the piles. Two new configurations, model 60-p and model 60-h-p are also included for comparison. In these Figures, ω is the wave angular velocity and ω_y is the angular velocity of the cylinder around y-axis. The noise in the video recording data is due to the low resolution of the captured frames. It was shown before that the wave transmission characteristics of the models 60, 60-h and 60-h-p are slightly different at kh. The roll response of model 60-h-p varies considerably among the three ways of representations. In Figure 8.32, there is a good agreement between the simulated recorded pile-restrained breakwater models (model 60-h-p). However, the models 60 and 60-h rotate in the reverse direction. In Figure 8.33, the numerically simulated models rotate in counter clockwise direction (waves propagating in positive-x direction) whereas the physical model rolls in clockwise direction.
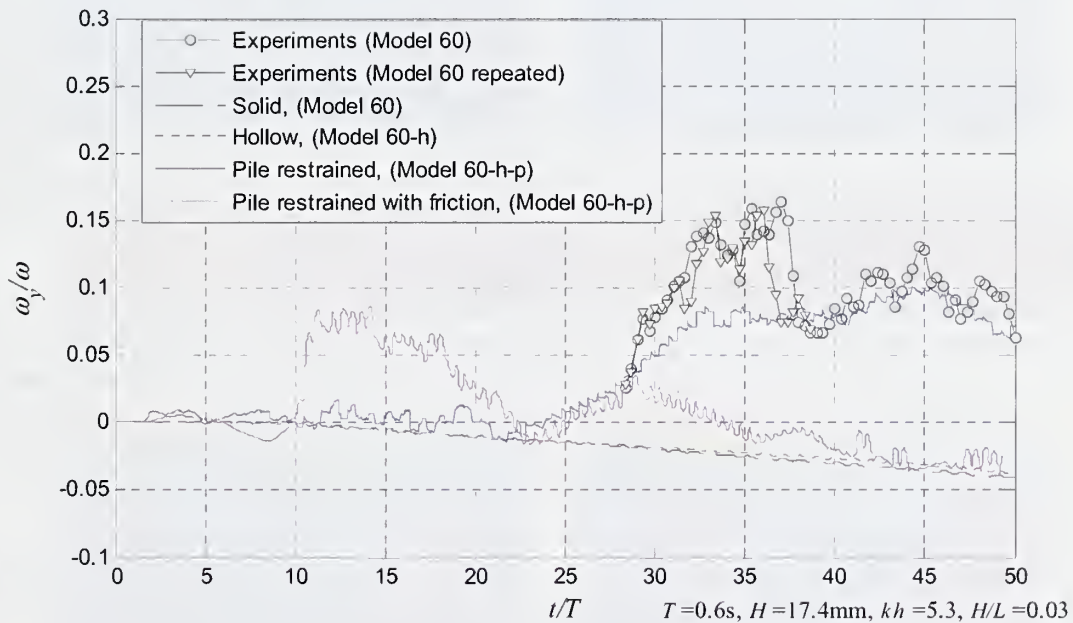
Figure 8.32 Angular velocities of the model 60 at H/L = 0.03 calculated form the numerical data and video recording analysis.

Figure 8.33 Angular velocities of the model 60 at $H/L = 0.05$ calculated from the numerical data and video recording analysis.

The rotation is driven by the tangential and the normal components of the force applied by the fluid on the surface of the cylinder. x-component of the net normal force does not contribute to the rotation since it is always collinear with the contact point between the cylinder and the pile. y-component of the normal force forms couple with the friction force at the contact point and rotates the cylinder. If the friction at the contact point is neglected, the main driving force is the shear stress which rotates the cylinder in counter clockwise direction as in Figure 8.32 and 8.33 models 60 and 60-h.

The impact during the collusions with the piles alters the net moment on the cylinder by disturbing the inner fluid region and the flow around the cylinder. This is the reason why the angular velocity of the models 60-p and 60-h-p is different than the other two models. The moment of inertia of a hollow cylinder is less than that of a solid cylinder of the same density. But, the water inside increases the drag and therefore, the hollow cylinder rolls slightly slower then the solid cylinder.

The purple lines in Figures 8.31 and 8.32 represent the Models 60-h-p with Coulombs friction factor, 1 which is equivalent to the friction between concrete and rubber. The angular velocity of the cylinder was reproduced well after the roll motion become steady. Comparing Figures 8.31 and 8.32, it is concluded that the friction between the pipe and the cylinder has an important impact on the direction and magnitude of the roll. After the wave front reaches to the cylinder, at the early stages, its angular velocity is unstable. Once the motion is stabilized, the rotation is sustained at a constant angular speed.

In Figures 8.34, 8.35 and 8.37, the free surface profiles and velocity magnitude contours during a wave cycle are plotted for the numerical model and compared with the corresponding frames of the video recording for models 60 (-h-p), 69 (-h-p) and 96. Note that the phases of some of the frames are not exactly the same as the numerical simulations. This is due to the variable time step size of the numerical simulations. The contour plots below each frame of the video recoding corresponds to the same phase indicated on the frames.

The water surface profiles were traced on the images shown in Figures 8.35 and 8.37 and, compared with the numerical simulation results in Figures 8.36 and 8.38. In all of the figures, numerical and laboratory results are found to agree favorably in terms of spatial variation of the water surface profile except some local variations close to the pipes.
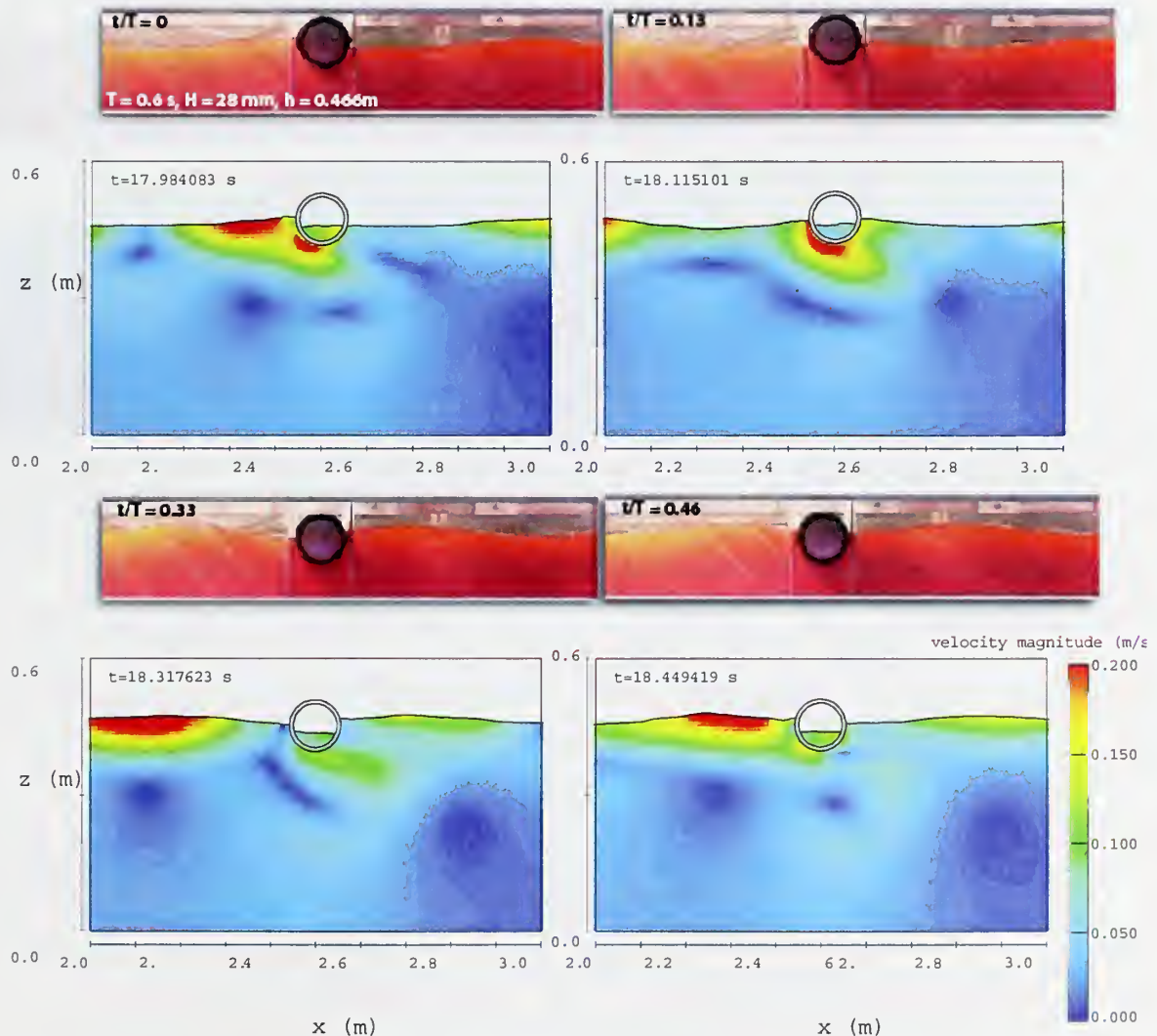
Figure 8.34. The velocity magnitude contours and the free surface displacements compared for a wave cycle with the video recording of laboratory experiments for model 60 (-h-p).
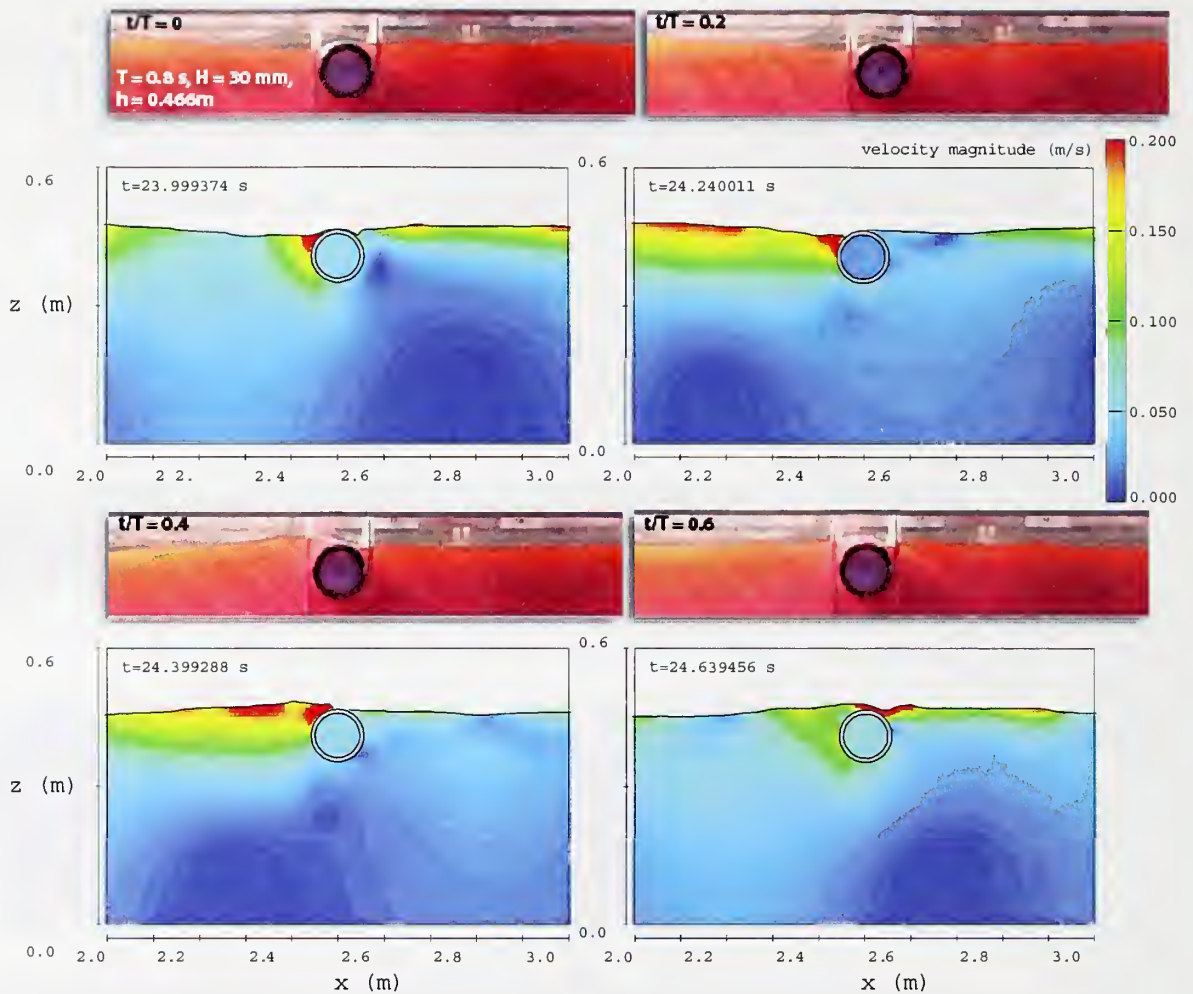
Figure 8.35 The velocity magnitude contours and the free surface displacements compared for a wave cycle with the video recording of laboratory experiments for model 69 (-h-p).
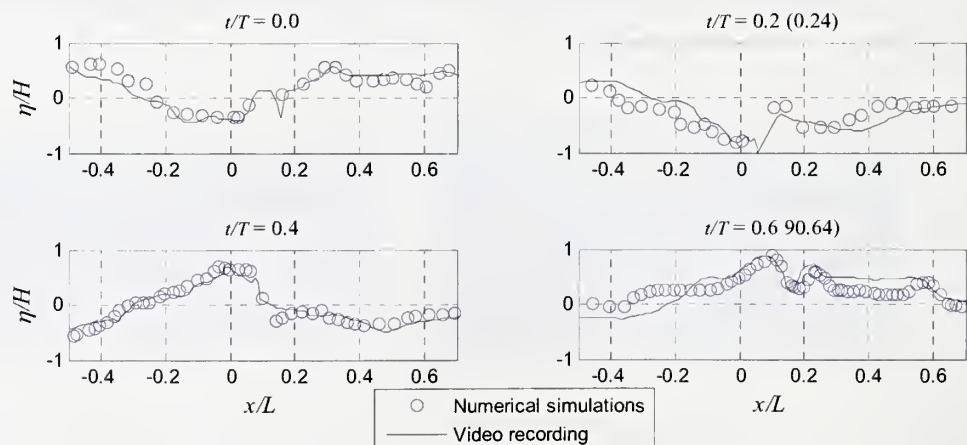
Figure 8.36 The spatial variation of the water surface profiles for model 96 at $T = 0.8$ s, $H = 30$ mm and $h = 0.466$ m.
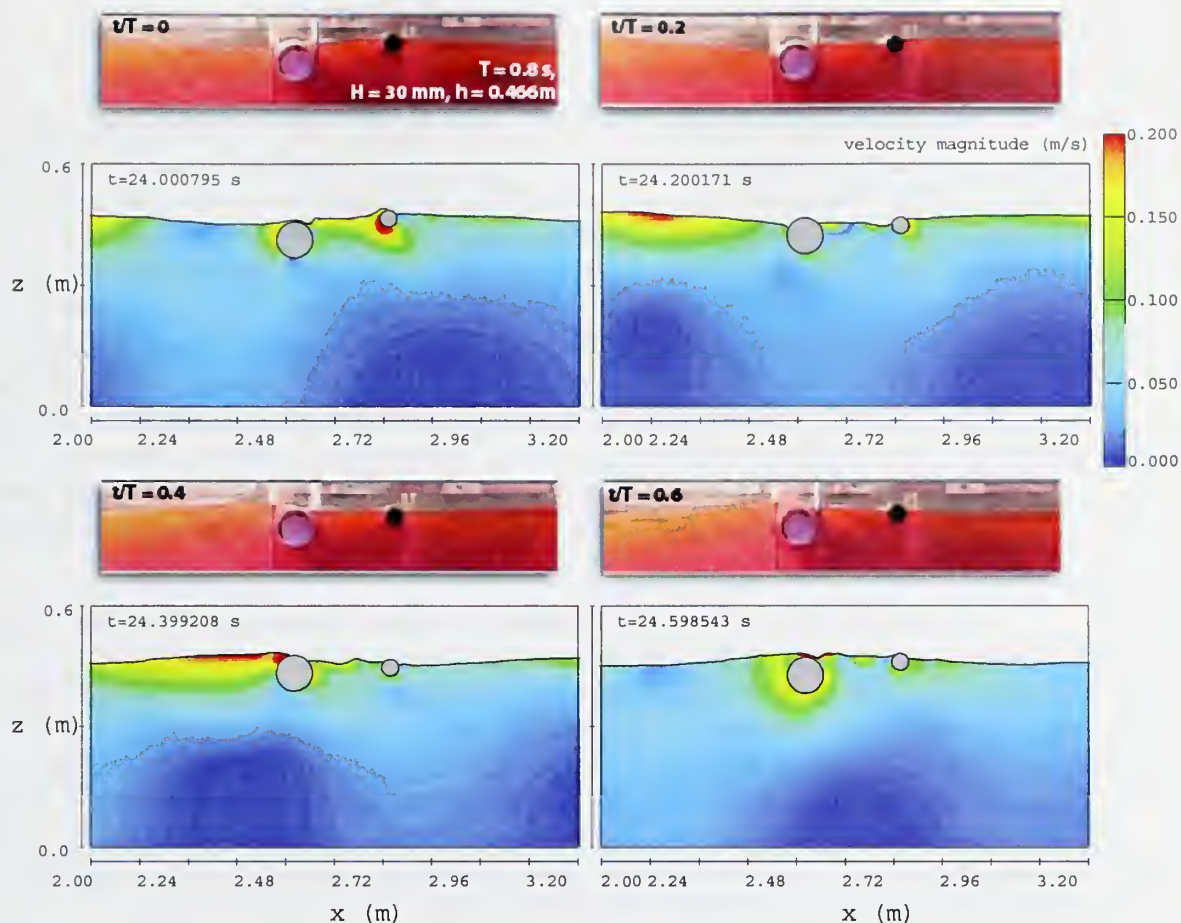
Figure 8.37. The velocity magnitude contours and the free surface displacements compared for a wave cycle with the video recording of laboratory experiments for model 96.
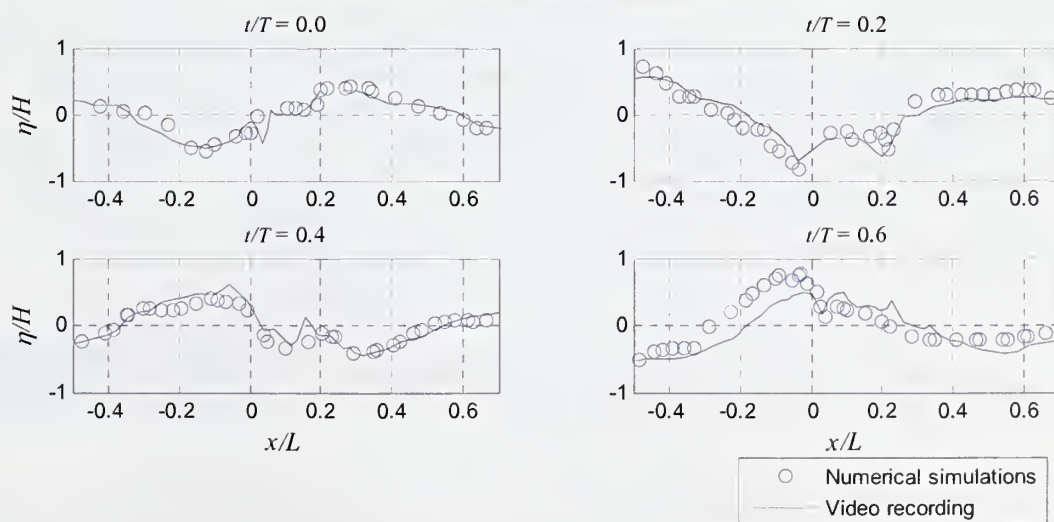
Figure 8.38 The spatial variation of the water surface profiles for model 96 at $T = 0.8$ s, $H = 30$ mm and $h = 0.466$ m.
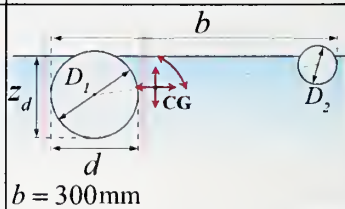
8.6. Random wave Simulation at Laboratory Scale

Three simulations were carried out with irregular waves at laboratory scale. The same computational domain described in Figure 8.3 was used for these simulations. The purpose of these simulations was to identify the differences with monochromatic and irregular wave conditions on the breakwater performance. These simulations are summarized in Table 8.3. Figure 8.39 shows the spectral density distributions of the time series water surface elevation data at $x = 0$ (the wave generation source) and at $x = 3.9$ m without any breakwater model installed and, at $x = 3.9$ m, model 96 being installed at $x = 2.5$ m. The dashed line for each test is the input JONSWAP spectrum. Evidently, after installing the breakwater the wave energy at $x = 3.9$ is reduced considerably. The spectral peaks are shifted slightly to the left which indicates that the absorber attenuates the high frequency components (shorter waves) more than low frequency bands (longer waves). The spectral shift is highest at $T_p = 1$ s. The transmitted wave spectrum has a second peak around 1.4 Hz.

Given in Equation 6.4, the amount of wave-height transmission of the irregular waves is characterized by the transmission coefficient similar to that of the monochromatic waves. In Figure 8.40 the transmission coefficients of model 96 in regular and irregular waves are compared for the numerical simulations and the laboratory experiments with regular waves. There is not a significant difference between regular and irregular waves in terms of wave attenuation. For higher kh values, irregular wave transmission is slightly less than the regular wave transmission. Figure 8.40 reveals that the laboratory result with regular waves can provide adequate information about the performance characteristics of the floating breakwaters subjected to irregular wave conditions. These results can be improved by running longer simulations for a wider range of wave conditions.

Table 8.3 The list of parameters for the simulated models in the numerical wave tank.

Model No.	Vertical length scale d (mm)	Draft z_d (mm)	Water depth h (m)	Wave height H_{mo} (mm)	Wave period T_p (s)	Subm. ratio $\dfrac{z_d}{d}$	Incident wave steepness $\dfrac{H_{mo}}{L_p}$	Definition sketch of breakwater configuration
96	89 ($D_1 = 89$, $D_2 = 42$)	85	0.446	16.9 29.8 45.0	0.6 0.8 1.0	0.96	0.03	$b = 300$mm
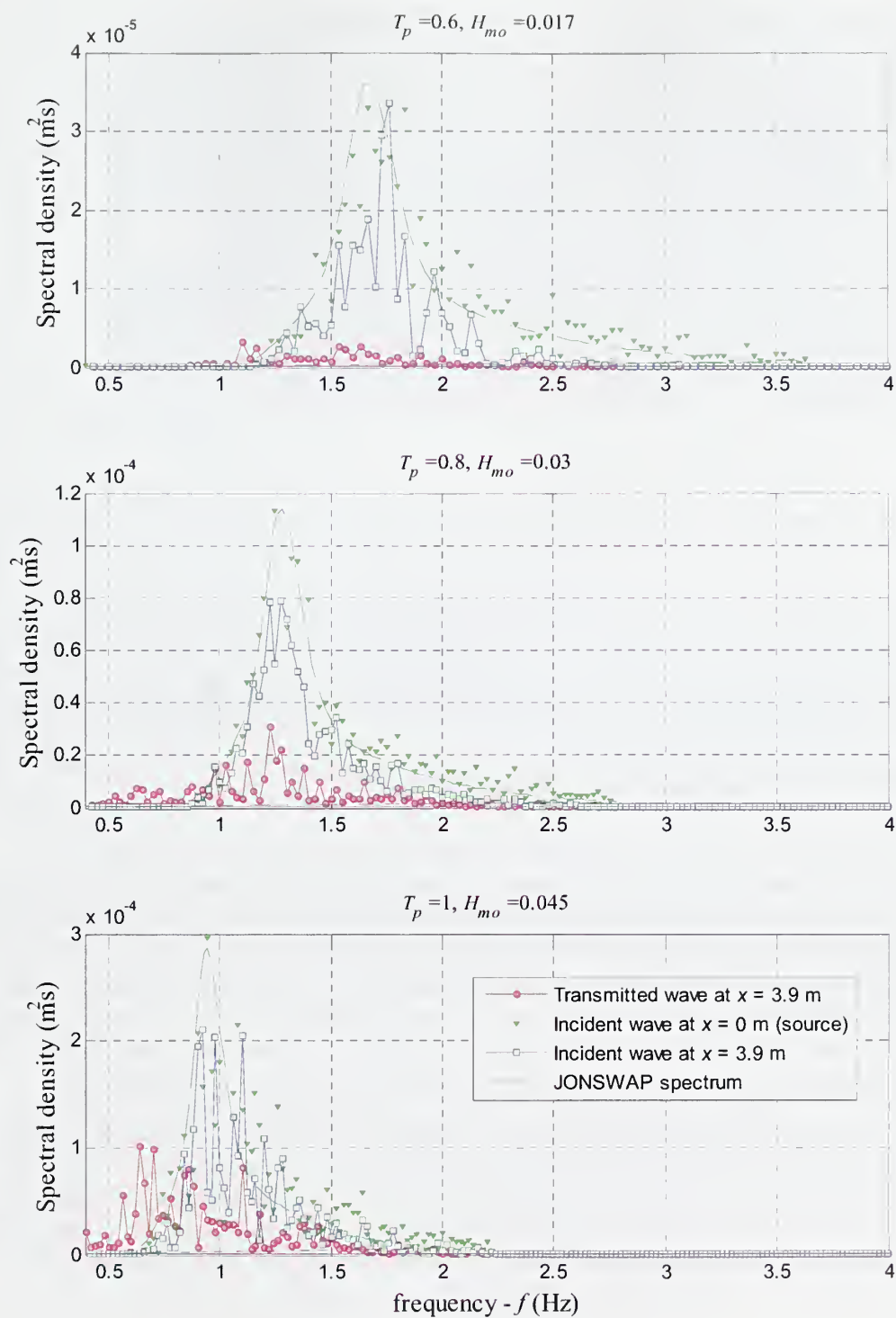
Figure 8.39. The spectral densities of the incident and transmitted waves for the simulation of model 96 with irregular waves at laboratory scale.
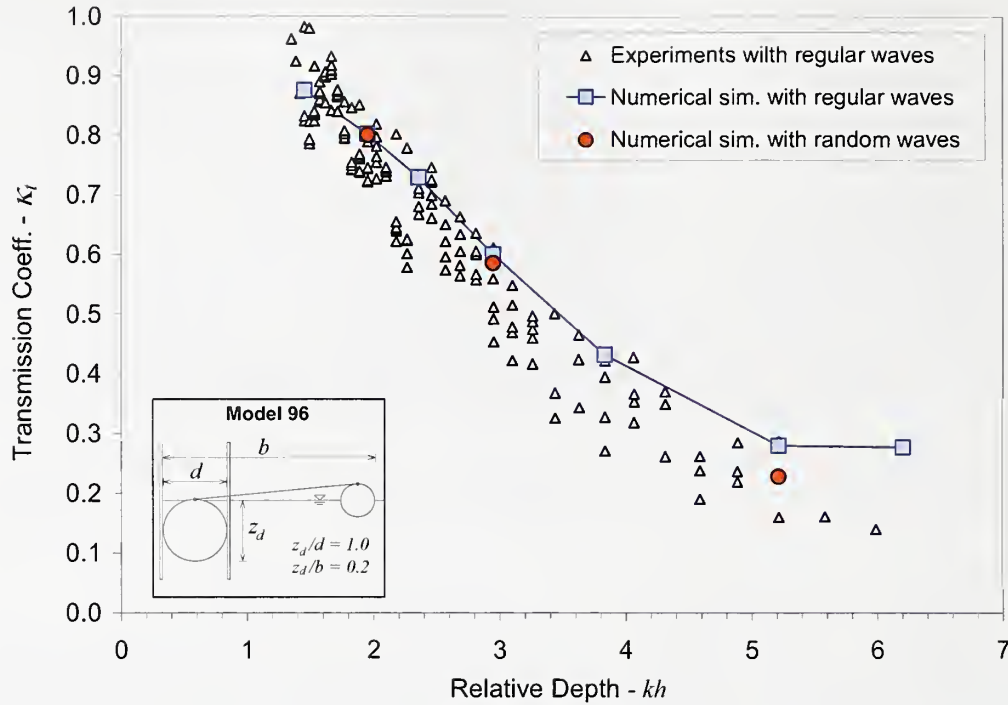
Figure 8.40 Regular and random wave simulations for model 96 at laboratory scale.

8.7. The Simulation of Field Implementation

The two-dimensional domain given in Figure 8.3 was modified to simulate model 96 in prototype scale. The wave tank of interest was 6 m long and 2 m high with $\delta x = \delta z = 1$ cm. The numerical dissipation zones were extended to 60 m on each side of the main part and the grid was stretched from $\delta x = 1$ cm to 25 cm along x-direction. A 46 cm x 100 cm mesh block was nested into the primary mesh as in model scale simulations. The same pipe sizes and configuration in 2007 field study were used in the simulations. The details of the model within the nested grid are given in Figure 8.41.

The wave spectrum between 11:00am and 12:00am in April 28th 2007 was used as a reference for full scale numerical simulation. The wave height H_{mo}= 7.18 cm and wave period, T_p= 1 s were used as input for the numerical simulations. The total CPU time was about 40 hours to carry out 80 s of simulation on a 2GHz Intel Core 2 Duo processor. Similar to the simulations at laboratory scale, simulation was repeated with the same irregular wave signal without the breakwater installed.
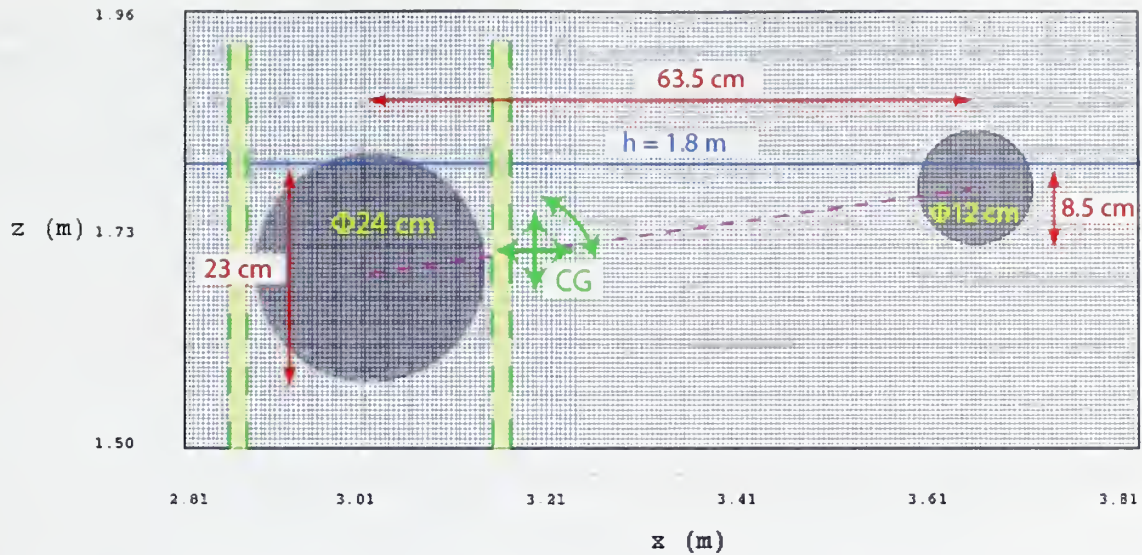
Figure 8.41 The scaled drawing of the prototype scale breakwater model with the nested grid.

In Figure 8.42 simulated water surface displacements are shown both with and without the breakwater installed. The recorded water surface at $x = 4$ m for two cases are overlaid in the last plot in Figure 8.42. The parameters are non-dimensionalized by the spectral wave parameters, H_{mo} and T_p. The wavelength, $L_p = 1.56$ m was calculated trough dispersion relationship using T_p. In Figure 8.43, the spectral densities of the water surface displacements are compared with that of the field data. The input JONSWAP spectrum is shown by dashed lines in this figure.

The incident wave spectrum in Figure 8.61 shows that the transmitted wave characteristics are represented correctly during the numerical simulations. However, the transmitted wave spectrum does not agree well with the recoded spectrum in the field. Most of the high frequency components are absorbed by the breakwater in the numerical simulations whereas the spectral transformation in the field is rather uniform. The scattering of the data corresponding to the numerical results is due to short simulation time.

There are several reasons for the difference between transmitted wave spectra. In the field study, flexible polyethylene pipes were used as floating breakwaters and most of the time they were subjected to oblique wave attack. Whereas, the numerical simulations were carried out on a two-dimensional domain and rigid circular cylinders were used as breakwaters.
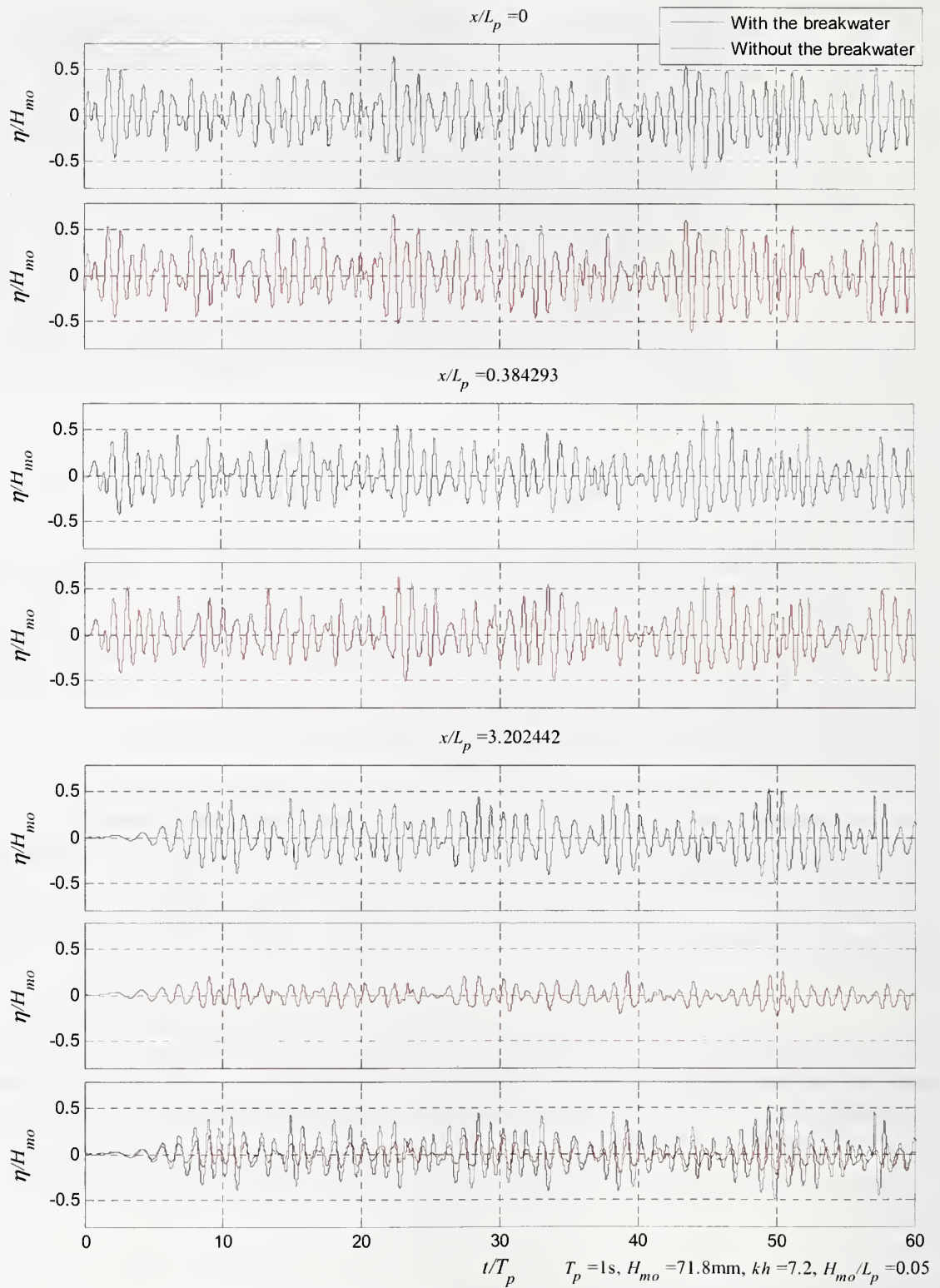
Figure 8.42 The simulated water surface elevations with and without the prototype breakwater installed. The control simulation without the breakwater is designated by red lines.

204
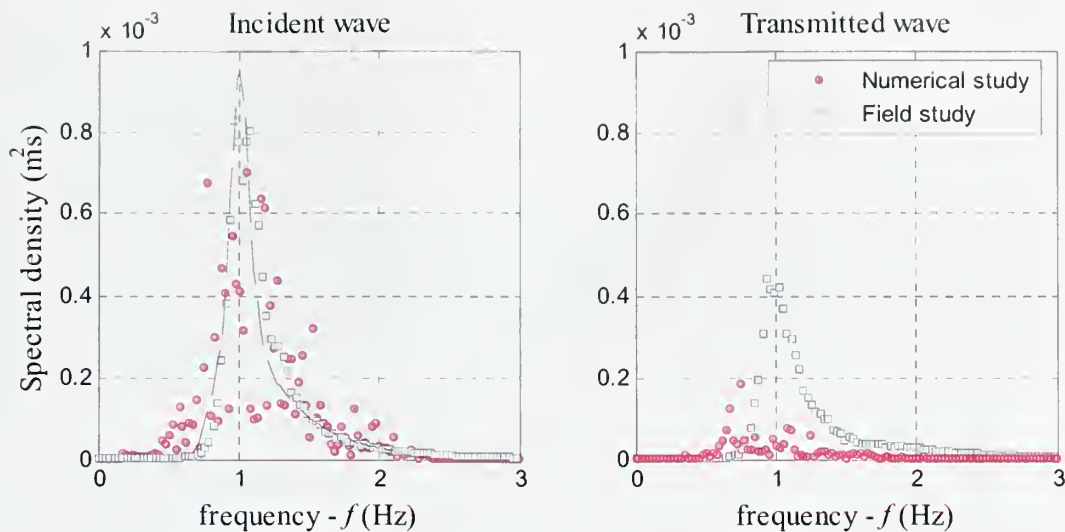
Figure 8.43 The spectral densities of the prototype scale simulations compared with the field data. The dashed line is the input spectrum for the numerical simulations.

The laboratory scale and prototype scale simulations are compared with the laboratory experiments with monochromatic waves and field experiments in Figure 8.44. Logistic curves are fitted to both laboratory and field data as described in Section 6.5. The bars represent the range of data at steepness values, $H/L = 0.03$ and 0.05. The numerical simulations are with irregular waves of steepness $H_{mo}/L_p = 0.03$ at laboratory scale and $H_{mo}/L_p = 0.05$ at prototype scale. Results of both simulations agree well with the laboratory experiments. Previously discussed in Section 6.5, the field data separate from all other data sets. One reason for this is that, waves approach with an angle of 20° (the angle between the normal to the breakwater line and the wave direction on horizontal plane). This leads to smaller wave numbers in the normal direction, k_n and larger transmission coefficients for the same wavelength. Another reason is that, both laboratory and numerical experiments were carried out for idealized conditions with rigid pipes and restraining; which was not completely satisfied in the field experiments.

However, the results of the prototype scale simulations show that idealized conditions can be generated by the numerical model. Moreover, the predictive capabilities of the breakwater do not seem to be significantly sensitive to scale shift between model and prototype scales. The current numerical procedure can be used to provide qualitative and quantitative information for the design of floating breakwaters.

Future work is necessary, with the objectives of better representation of the material properties in three dimensions, such as longitudinal flexibility, corrugation and porosity. Additional laboratory experiments with random waves will improve the numerical model.
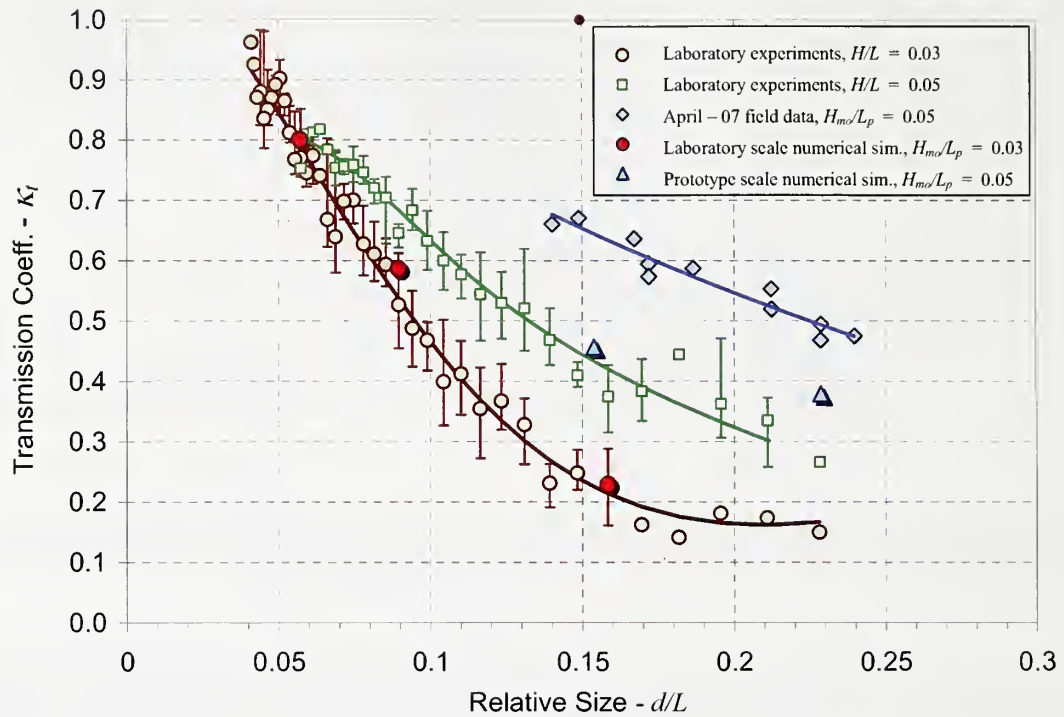
Figure 8.44 The laboratory and field experiments are compared with the numerical simulation with random waves in model and prototype scale. The laboratory experiments are with monochromatic waves and the error bars represent the ranges of data for the steepness.

IX. CONCLUSIONS

The use of floating breakwaters for wave energy reduction was investigated in laboratory and filed settings. An existing CFD software package was modified in order to simulate the interaction of regular and irregular waves with the floating breakwater models. The details and the specific conclusions of these studies are summarized in the following sections.

9.1.   Laboratory Experiments

For the laboratory experiments a wave flume was constructed at the USDA-ARS National Sedimentation Laboratory. The experiments were specifically designed to investigate floating breakwaters for the protection of levees in small reservoirs, like those used to store irrigation water in the Arkansas prairie region. Preliminary field measurements of wave characteristics allowed the model breakwater and waves to be scaled so that the results could be applied in a meaningful way. The laboratory experiments included the testing of cylindrical floating breakwater models with different diameters and combinations of dimensionless parameters described in the text.

The conclusions of the laboratory experiments follow:

— The experimental results compared favorably with the closed form solution and experimental results of Dean and Ursell (1959) for the fixed models.

— For the fixed models, the transmission coefficient strongly depends on relative draft.

— The breakwater performance can be improved by partially restraining its motions. Pile restrained model was the most effective in reducing wave energy transmission compared to the other restraint types tested here. The best combination of performance and cost was obtained using a pile-restrained floating breakwater with parallel pipes submerged at $z_d/d=1.0$ on the upwind side and $z_d/d=0.6$ on the downwind side.

— The bottom-moored arrangement was less effective than pile-restrained in terms of wave energy reduction. The moored design also has the disadvantage of strong dependence on water level.

— There is an optimal relative submergence, z_d/d, that maximizes the reflection and dissipation characteristics of a given breakwater design. For relatively small waves like those considered in the current study, a relative submergence of $z_d/d=0.7$ was found to be optimal for the pile-restrained model. Reflection

coefficients were also reduced considerably compared to the fixed model with z_d/d=0.7.

— The optimal relative submergence value varies based on the type of restraint. For example, fully submerged pile-restrained floating breakwaters performed better than fully-submerged fixed floating breakwaters for a range of wave parameters.

— Bundles of smaller pipes were found to perform in a manner comparable to a single pipe of the same diameter.

9.2.   Field Implementation

A subsequent field test validated the conclusion from the laboratory testing that this design can be used to reduce wave energy impacting levees. In the first field test the double-pipe pile-restrained breakwaters were implemented in an irrigation pond. In the second field study, a bundle of irrigation pipes was tested. The pipes were fixed at both ends by ropes tied to posts driven into the levee. The conclusions of these studies can be summarized as follows:

— The field tests validated that floating breakwaters are viable option for levee protection. Wave amplitudes were reduced by up to 60% during the field testing.

— Mooring method is should result in highest horizontal restraining. The rope restraining in the second field test was simple and inexpensive but the results were not as good as the previous study due to lack of restraining.

— As expected, larger diameter breakwaters performed better than smaller ones. However, the material and transportation costs of the pipe increase rapidly with diameter. The use of bundled smaller pipes to arrive at larger diameters appears to be a better option than one single large diameter pipe. Yet, this brings the issue of fastening the small pipes together to withstand the wave conditions.

— The method for joining together the sections of a composite absorber should take into account the buoyancy of the pipe. Using too many braces or braces that are too heavy may result in a breakwater that will not float. The drainage pipe that was used in the field has a density only slightly lower than water, so it cannot support a large mass of braces.

9.3.   Numerical Study

The numerical simulations were carried out in a 5 m long and 0.6 m high two-dimensional numerical wave tank. A new wave generation procedure using a mass source function was developed, and validated for regular and irregular waves with the available

laboratory data. The new wave generation function distributed mass correctly over the entire water depth by taking in the account the variation of the water surface elevation.

The numerical simulations were compared both with some of the experimental results in the laboratory wave tank and field study results. The validation of the numerical model was performed based on the recorded free surface displacement measurements and analysis of the video recordings. Some of the numerical results were also compared with the spatial and temporal variations of the water surface displacement and the heave and roll motions of the breakwater models. The capability of the numerical model to reproduce field observations was tested at irregular wave conditions. A steady portion of the 2007 data was used as an input for the prototype scale simulation. The numerical results compared reasonably well with the experiments in all three mooring configurations.

The results of the numerical simulations can be summarized as follows:

— The spatial and temporal variations of the free surface displacements are correctly captured.

— The transmission coefficient of the simulated models compared very well with the physical model experiments. The measured and numerically computed reflection coefficients were also in good agreement within the range of wave parameters studied here.

— The simulations with RNG turbulence model indicated that turbulence plays a minor role in breakwater efficiency within the parameter range of experiments.

— The first order approximation of the momentum advection resulted in a faster solution and smoothened the waves but also introduced additional dissipation into the solution. However, the additional dissipation was negligible, except at higher wave steepness values.

— It was observed that the numerical simulations can replicate the laboratory model if the dynamic and material properties of the model are correctly defined. It was shown that the friction and the gap between the pile and the pipe play an important role in the roll response of the pile-restrained single pipe breakwater models. The heave response of the breakwater also compared well with the video results.

9.4.   Future Work

The laboratory experiments were conducted with unidirectional monochromatic waves whereas the waves observed in the field were random and three-dimensional. Future laboratory work may include experiments with random waves to better represent the field conditions.

It was shown in the laboratory and field studies that floating breakwater performance can be increased by increasing the relative draft and inertial which leads the bulk densities of the breakwater to be close to the density of water. Long term field tests are necessary to investigate the density changes due to accumulation of sediments and biological activity.

The current study focused on the reduction of wave energy before the waves reach the levees. The rate of erosion relative to the wave size was not investigated in the here. Transport of sediment in small reservoirs and lakes is primarily due to the currents related to the waves, wind stress, and density distribution. It was observed throughout the field studies that the main damage is due to the strong waves undercutting and resulting in bank failure during an extreme event. Therefore, restoration of the reservoir morphology and beach profiles can contribute reducing the erosion. The layout of the breakwater in the reservoir has to be optimized to have the highest possible reduction in the total wave power along the banks. Partitioning the reservoirs into smaller areas with the floating breakwaters can be more feasible compared to breakwaters close to the banks. More work is necessary for the logistics of floating breakwater installations and restraining.

Wave overtopping significantly changes the shape of the transmitted waves. Some part of the mass is transported over the breakwater which should influence the mean flow underneath the structure. The numerical model can be used to estimate the currents underneath the breakwater induced by overtopping.

In the field study, flexible polyethylene pipes were used as floating breakwaters and they were subjected to oblique wave attack. Future work is necessary with the objectives of improving the numerical model by extending the computational domain into three-dimensions to test the influence of the angle of wave attack and better representation of the material properties in three dimensions, such as longitudinal flexibility and corrugation. The multi-directional wave can be simulated by using mass source wave generator at multiple locations.

REFERENCES

Adee, B. H. and Martin, W., Theoretical analysis of the Floating Breakwater Performance, *Proceedings of the Floating Breakwater Conference,,* University of Rhode Island, Kingston, Rhode Island, 21-40, 1974.

Adee, B. H. and Richey, E. P. *Proceedings* of the 2nd Conference on Floating Breakwaters. Seattle, Washington: University of Washington, 1981.

Akari, T. Development of IHI Floating Breakwater, *IHI Engineering Review,* English edition, 11(3), 1978.

B. Van Leer, "Towards the Ultimate Conservative Difference Scheme. IV. A New Approach to Numerical Convection," J. Comput. Phys., 23, 276, 1977.

Barkhudarov, M. R., Lagrangian VOF Advection Method for Flow-3D, *Flow Science, Inc.*, 2004.

Bishop, C. T., Field Assessment of a Floating Tire Breakwater, *Canadian Journal of Civil Engineering*, 12(4): 782-795, 1985.

Booij N., Ris, R.C. and Holthuijsen, L.H., (1999). A third-generation wave model for coastal regions, Part 1, Model description and validation. *Journal of Geophysical Research*, C4, 104, 7649-7666.

Bretschneider C. L. (1952). The Generation and Decay of Wind Waves in Deep Water, Transactions of American Geophysical Union, 33, 381-389.

Carman, D. 2003. Personal Communication with Dennis Carman, Agricultural Engineer at the NRCS National Water Resource Management Center, Little Rock, AR, August 12, 2003.

Carr J. H., Mobile Breakwaters, *Proceeding of the Second Conference on Coastal Engineering*, 281-295, 1951.

CERC, U.S. Army Corps of Engineers, *Coastal Engineering Manual*, U.S. Army Corps of Engineers, Washington, D.C., 2006.

Chen, Q., Wang, L., Zhao, H. and Dougless, S.L., Prediction of Storm Surges and Wind Waves on Coastal Highways in Hurricane-Prone Areas, Journal of Coastal Research, 23(5): 1304,1317

Clauss, G. F., Schimittner, C. E. and Stuck, R. Numerical Wave Tank – Simulation of Extreme Waves for the Investigation of Structural Responses, *Proceedings of OMAE2005*, 24th International Conference on Offshore mechanics and Arctic Engineering, 2005.

Davidson, D. D., Wave Transmission and Mooring Force Tests of Floating Breakwater, Oak Harbor, *Washington Hydraulic Model Investigation* n, Technical Report H-71-3, U.S. Army Corps of Engineers Waterways Experimental Station, Vicksburg, Mississippi, 1971.

Dean, G. D. and Dalrymple, R. A., *Water Wave Mechanics for Engineers and Scientists*, World Scientific, 1991.

Dean, R. G., and Ursell, F. *Interaction of a Fixed, Semi-Immersed Circular Cylinder with a Train of Surface Waves*, M.I.T. Hydrodynamics Laboratory Technical Report No. 37, 1959.

Dean, W. R., On the Reflection of Surface Waves by a Submerged Circular Cylinder, *Proceedings of the Cambridge Philosophical Society* 44:483–491, 1948.

Dean, W. R., On the Reflection of Surface Waves by a Submerged Plane Barrier, *Proceedings of the Cambridge Philosophical Society*, 41:231–236, 1945.

Dimmer, N., Agnon, Y. and Stiassnie, M., A Simplified Analytical Model for a Floating Breakwater in Water of Finite Depth, *Applied Ocean Research* 14:33-41, 1992.

Ding, Y., Wang, S. S. Y., and Jia, Y. (2006). Development and validation of a quasi three-dimensional coastal area morphological model, Journal of Waterway, Port, Coastal, and Ocean Engineering, ASCE, Vol.132, No.6, pp. 462-476.

Flow Science, Inc. Multi-Block Gridding Technique for FLOW-3D, 2004.

Goda Y.and Ippen A. T., *Theoretical and Experimental Investigations of Wave Energy Dissipators Composed of Wire Mesh Screens* Hydrodynamics Laboratory Report, Dept. of Civil Engineering, Massachusetts Institute of Technology, Cambridge, Massachusetts, 1963.

Greaves, D. M., Viscous Waves and Wave-Structure Interaction in a Tank Using Adapting Quadtree Grids, *Journal of Fluids and Structures*, 23(8):1149-1167, 2007.

Hales, L. Z. *Floating Breakwaters State-of-the-Art Literature Review*, U.S. Army, Corps of Engineers, Coastal Engineering Research Center, 1981.

Harleman, D. R. F. and Shapiro, W. C., Investigation on the Dynamics of Moored Structures in Waves, MIT Hydrodynamics Laboratory, TR No. 24, 1958.

Harms, V. W., Design Criteria for Floating Tire Breakwaters, *Journal of the Waterway, Port, Coastal, and Ocean Division*, 105(2):149-170, 1979.

Hegde, A. V., Kamath, K. and S. Magadum, A. S., Performance Characteristics of Horizontal Interlaced Multilayer Moored Floating Pipe Breakwater, *Journal of Waterway, Port, Coastal, and Ocean Engineering*, 133(4): 275-285, 2007.

Hirt C. W., Addition of Wave Transmitting Boundary Conditions to the FLOW-3D Program, *FLOW-3D Documentation*, Vol. FSI-99-TN49, 1999.

Hirt, C. W. and Nichols, B. D. Volume of Fluid (VOF) Method for the Dynamics of Free Boundaries, *Journal of Computational Physics*, 39:201-225, 1981.

Hirt, C. W. and Sicilian, J. M., A Porosity Technique for the Definition of Obstacles in Rectangular Cell Meshes, *Proceedings Fourth International Conf. Ship Hydro., National Academy of Science*, Washington, DC, September 1985.

Hughes, S. A. *Physical Models and Laboratory Techniques in Coastal Engineering*, World Scientific, 1993.

Hur, D.-S. and Mizutani, N., Numerical Estimation of the Wave Forces Acting on a Three Dimensional Body on Submerged Breakwater *Coastal Engineering*, 47(3):329-345, 2003.

IAHR/PIANC, List of Sea State Parameters, *Supplement to Bulletin No. 52 of the Permanent International Association of Navigation Congresses*, Brussels, 1986.

Ippen, A. T. (Ed.), *Estuary and Coastline Hydrodynamics*, McGraw-Hill Book Company, 1966.

Isaacson, M., Baldwin, J. and Bhat, S., Wave Propagation Past a Pile-restrained Floating Breakwater, *International Journal of Offshore and Polar Engineering*, 8(4):265-269, 1998.

Isaacson, M., Wave Effects on Floating Breakwaters, *Proceeding of the 1993 Canadian Coastal Conference*, Vancouver, BC., 1:53-65, 1993.

Jackson, R., A Twin-Log Floating Breakwater, Small Boat Basin No. 2., Juneau, Alaska, Miscellaneous Paper No. 2-648, U.S. Army Engineer Waterways Experiment Station, Vicksburg, MS, 1964.

Kawasaki, K., Numerical Simulation of Breaking and Post-Breaking Wave Deformation Process around a Submerged Breakwater, *Coastal Engineering Journal*, 41(3-4):201-223, 1999.

Keulegan, Garbis H., *Wave Damping Effects of Fibrous Screens: Hydraulic Model Investigation*, US Army Engineering Waterways Experiments Station, Research Report, September 1972.

Kim, H. T., Sawaragi, T., and Aoki, S. I., Wave Control by Pile-Supported Floating Breakwaters, *Proceedings of the Fourth International Offshore and Polar Engineering Conference*, Osaka, ISOPE, 3: 545-549, 1994.

Koftis, T. H., Prinos, P. and Koutandos, E.,2D-V Hydrodynamics of Wave-Floating Breakwater Interaction, *Journal of Hydraulic Research*, 44(4):451-469, 2006.

Komen G. J., Cavaleri, L., Donelan, M., Hasselmann, K., Hasselmann, S., Janssen, P.A.E.M. (eds.) (1994). Dynamics and Modeling of Ocean Waves, Cambridge.

Kothe, D. B. and Mjolsness, R. C., Ripple: A New Model for Incompressible Flows with Free Surfaces, *AIAA Journal*, 30 (11):2694-2700, 1992.

Kowalski, T., *1974 Floating Breakwaters Conference Papers,* Marine Technical Report Series, No. 24. Kingston, Rhode Island: University of Rhode Island, 1974.

Lara, J. L., Garcia, N. and Losada, I. J., RANS Modeling Applied to Random Wave Interaction with Submerged Permeable Structures, *Coastal Engineering*, 53: 395-417, 2006.

Le Mehaute, B., Progressive Wave Absorber, *Journal of Hydraulic Research,* 10(2):153-169, 1972.

Lean, G. H., A Simplified Theory of Permeable Wave Absorbers, *Journal of Hydraulic Research*, 5:15-30, 1967.

Lin, P. and Liu, P. L.-F., Internal Wave-Maker for Navier-Stokes Equations Models *Journal of Waterway, Port, Coastal and Ocean Engineering,* 125(4): 207-217, 1999.

Lin, P. and Liu, P.L.-F., A Numerical Study of Breaking Waves in the Surf Zone. *Journal of Fluid Mechanics* 359:239–264, 1998.

Liu, M. B. and Lui, G. R., *Smoothed particle hydrodynamics: a meshfree particle method*, World Scientific, 2004.

Liu, P. L.-F. and Lin, P., *A Numerical Model for Breaking Wave: The Volume of Fluid Method*, Research Rep. CACR-97-02. Center for Applied Coastal Research, Ocean Eng. Lab., Univ. of Delaware, Newark, Delaware 19716, 1997.

Lochner R. Feber, O. and Penny, W., The Bombardon Floating Breakwater, *The Civil Engineer in War*, Docks and Harbors, The Institution of Civil Engineers, London, England, 2:256, 1948.

Longuet-Higgins, M. S., A Non-Linear Mechanism for the Generation of Sea Waves, *Proceeding of the Royal Society of London*, Series A, 311, 371-389, 1969.

Longuet-Higgins, M. S., On the Distribution of the Heights of Sea Waves: Some Effects of Nonlinearity and Finite Band Width, *Journal of Geophysical Research*, 85(C3): 1519-1523, 1980.

Longuet-Higgins, M. S., On the Statistical Distribution of the Heights of Sea Waves, *Journal of* Marine *Research*, 11(3):245-266, 1952.

Macagno, E.O., *Houle dans un canal présentant un passage en charge,* 1953.

Madsen, P. A., Wave Reflection from a Vertical Permeable Wave Absorber, *Coastal Engineering*, 7:381-396, 1983.

Mani, J. S. Reflection Characteristics of Wave Absorber - A Case Study, *Journal of the Institution of Engineers (India)*, 67:63-67, 1986

Mani, J. S., Design of Y-Frame Floating Breakwater, *Journal of Waterway, Port, Coastal, Ocean Engineering*, 117(2): 105-118, 1991.

McCartney, B. L., Floating Breakwater Design, *Journal of Waterway, Port, Coastal and Ocean Engineering*, 111(2):304-318, 1985.

McLaren, R. W., Preparation of Floating Breakwater Manual, *Proceedings of Second Conference on Floating Breakwaters*, Adee and Richey, Eds, Seattle, 1981.

Miche, R., Mouvements ondulatoires des mers en profondeur constante ou décroissante, *Annales des Ponts et Chaussées*, 114:25-78, 131-64, 270-292, 369-406, 1944.

Miles J. W. (1957). On the Generation of Surface Waves by Shear Flows, Journal of Fluid Mechanics, 3, 185-204.

Mizutani, N., Rahman A., Numerical Analysis of Wave *and* Floating Breakwater Interaction Using VOF Method, *Proceedings of the Fourteenth International Offshore* and Polar Engineering Conference, 2004.

Morey, Bradley J., *Floating Breakwaters Predicting Their Performance*, National Library of Canada, Ottawa, Thesis(M. Eng.), Memorial University, 1998.

Murali, K., and Mani, J. S., Performance of cage floating breakwater. *Journal of Waterway, Port, Coastal, Ocean Engineering*, 123(4): 172–179, 1997.

NDBC Technical Document 96-01, Non-directional and Directional Wave Data Analysis Procedures, *Stennis Space Center*, 1996.

Nece, R. E. and Richey E. P., *Wave Transmission Tests on Floating Breakwater for Oak Harbour*, University of Washington Charles W. Harris Hydraulics Laboratory, Technical Report No. 32, 1972.

Ofuya, A. O., *On Floating Breakwaters*, Research Report No. CE-60, Queens University, Kingston, Ontario, Canada, 1968.

Orlanski, J., A simple boundary condition for unbounded hyperbolic flows, *Journal of Computational Physics*, 21: 251-269, 1976.

Ouellet, Y. and Datta, I., A Survey of Wave Absorbers, *Journal of Hydraulic Research*, 24:265-280, 1986.

Ozeren, Y., Wren, D. G. and Alonso, C. V., Development of Floating Wave Barriers for Cost Effective Protection of Irrigation and Catfish Pond Levees, *Transactions of the ASABE*. 51(5):1599-1612, 2008.

Phillips, O. M. (1957). On the Generation of Waves by Turbulent Winds, Journal of Fluid Mechanics 2, 417-445.

Rahman, M., Mizutani, N. and Kawasaki, K., Numerical Modeling of Dynamic Responses and Mooring Forces of Submerged Floating Breakwater, *Coastal Engineering*, 53:799–815, 2006.

Readshaw, J. S., The design of floating breakwater, *Proceedings of Second Conference on Floating Breakwaters*, Adee and Richey, Eds, Seattle, 1981.

Richey, E. P and Nece, R. E, Floating Breakwaters – State of the Art, , Proceedings of the *Floating Breakwater Conference*, University of Rhode Island, Kingston, Rhode Island, 1-19, 1974.

Ris, R.C., Holthuijsen, L.H. and Booij, N., (1999). A third-generation wave model for coastal regions, Part 2, model description and validation. *Journal of Geophysical Research*, C4, 104, 7667-7681.

Sen, D., Numerical Simulation of motions of Two-Dimensional Floating Bodies, *Journal of Ship Research*, 37(4):307-330, 1993.

Seymour R. J., and Isaacs, J. D., Tethered Float Breakwaters, Proceeding of the Floating Breakwater Conference, University of Rhode Island, Rhode Island, 1974.

Shore Protection Manual, 4 ed., 2 Vol, U. S. Army Engineer Waterways Experiment Station, U. S. Government Printing Office, Washington, DC, 1984.

Sobey R. (1986). Wind Wave Prediction, Annual Review of Fluid Mechanics 18: 149-172

Sorensen, R. M. (1993). Basic Wave Mechanics for Coastal and Ocean Engineers, John Wiley and Sons, Inc.

Stiassnie, M., A Simple Mathematical Model of a Floating Breakwater, 1980.

Straub, L. G., Bowers, C. E. and Herbrich, J. B., Laboratory tests of permeable wave absorbers, *Proceedings of Sixth Conference on Coastal Engineering,* Gainesville, Palm Beach, and Miami Beach, 729-742, December 1956.

Stronge, W. J., *Impact Mechanics*, Cambridge University Press, Cambridge, UK, 2000.

Sulisz, W., Numerical modeling of wave absorbers for physical wave tanks, *Journal of Waterway, Port, Coastal and Ocean Engineering* 129(1):5-14, 2003.

Sundar, V., Sundaravadivelu, R., and Purushotham, S., Hydrodynamic characteristics of moored floating pipe breakwater in random waves. *Proc., Institution of Mechanical Engineers, Part M: J. Engrg. Maritime Environment*, 217(M): 95–110, 2003.

Sverdrup, H. U. and Munk W.H. (1947). Wind Sea and Swell: Theory of Relations for Forecasting, Publication 601, U. S. Navy Hydrographic Office, Washington, DC.

Tennekes, H. and Lumley, J. L., *A First Course in Turbulence*, MIT Press, Cambridge, Massachusetts, 1972.

Tsinker, G., *Marine Structures Engineering: Specialized Applications*, Chapman and Hall, New York, 1995.

Twu, S. W. and Lin, D. T., On a highly effective wave absorber, Coastal Engineering, 15:389-405, 1991.

Ursell, F., The Effect of a Fixed Barrier on Surface Waves in Deep Water, *Proceedings of the Cambridge Philosophical Society* 43:374–382, 1947.

USDA-SCS. Technical Release No. 56 "A guide for design and layout of vegetative wave protection for earth dam embankments." 1974.

Versteeg, H. K. and Malalasekera, W., *An Introduction to Computational Fluid Dynamics, The Finite Volume Method*, Pearson, Prentice Hall, 1995.

Vincent, C. L., Demirbilek, Z., and Weggel, J. R. (2002). Estimation of Nearshore waves. In: Vincent, L., and Demirbilek, Z. (editors), Coastal Engineering Manual, Part II, Coastal Hydrodynamics, Chapter II-3, Engineer Manual 1110-2-1100, U.S. Army Corps of Engineers, Washington, DC.

WCHL, Western Canada Hydraulic Laboratories, *Development of a Manual for the Design of Floating Breakwaters.* Canadian manuscript report of Fisheries and Aquatic Sciences, 1629. Ottawa, Ont: Dept. of Fisheries and Oceans, Small Craft Harbors Branch, 1981.

Wei, G., An Implicit Method to Solve Problems of Rigid Body Motion Coupled With Fluid Flow, *Flow Science Inc.,* 2006a.

Wei, G., Three-Dimensional Collusion Modeling for Rigid Bodies and Its Coupling with the Fluid Computation, *Flow Science Inc.*, 2006b.

Werner, G., Experiences with floating breakwaters: A literature review, *P.I.A.N.C-A.I.P.C.N. Bulletin*, 63(2):3-30, 1988.

Wiegel, R. L. Transmission of Waves Past a Rigid Vertical Thin Barrier, *Journal of Waterways Harbors Division*, ASCE 86:1-12, 1960.

Wiegel, R. L., *Oceanographical Engineering*, Prentice-Hall, Inc., 1964.

Williams, A. N., Geiger, P. T. and McDougal, W. G., Flexible Floating Breakwater *Journal of Waterway, Port, Coastal and Ocean Engineering*, 117(5);429-450, 1991.

Yao, G. F., Development of New Pressure-Velocity Solvers in FLOW-3D *Flow Science, Inc.* FSI-04-TN68, 2004.

APPENDICES

A. EXPERIMENTAL PROCEDURE AND DATA ANALYSIS

A.1.   Experimental Procedures

A computer program was developed in Labview to conduct multiple experiments and store the data. The flowchart of the program is given in Figure A.1.
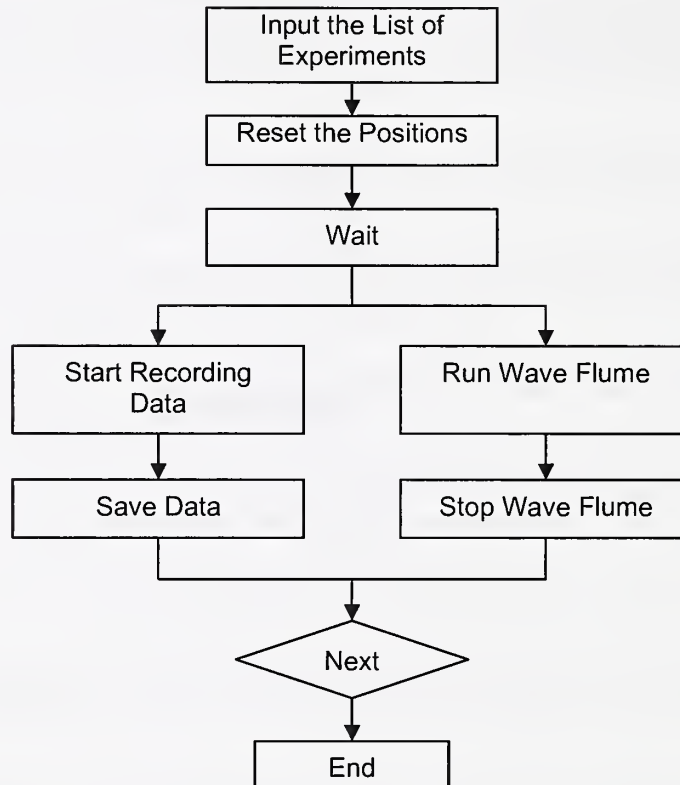
Figure A.1 Flowchart of the experimental procedure and data collection.

The GUI allowed the user to populate the set of experiments to be conducted. The list of experiments were generated with the desired wave parameters of water depth, h, wave period, T and wave height H (or wave steepness H/L). When H/L was used as an input the corresponding wave height was computed iteratively using the dispersion relationship (Equation 3.13). The limiting value for the wave steepness was checked to avoid wave braking with the relation given in Equation 3.30. The draft of the breakwater, z_d, model length scale, d, and the locations of the gauges and the breakwater were also set before starting the experiment. Each breakwater configuration had a distinct two digit model number that was set on the input screen by the user. A reference number was assigned to each experiment which is also given as the name of the data file for that experiment. The first two digits of the reference number was the model number, second

two digits was the water depth in centimeters, the fifth and sixth digit was the wave height in millimeters, the next three digits were the wave period in one hundreds of a second and the last digit was the rank of the repeated experiment with the same parameters within the same run.

The belt drive was connected to the paddle with a rod at a certain height from the bottom of the flume. The length of the moment arm was changed to adjust the applied torque on the paddle by moving the connection point of this rod to the paddle (Figure A.2). The connection point was entered through the GUI. The stroke at the mean water level was computed according to the flap type wavemaker equation (Equation 4.17). The stroke at the water surface was converted to the stroke of the belt drive with the following relation:

$$S_{bi} = S \frac{h_{bi}}{h} \qquad (A.1)$$

where h_{bi} is the distance of the ith connection point of the arm to the paddle from the bottom of the flume and S_{bi} is the corresponding stroke of the belt. The details of this set up are shown in Figure A.2.

Figure A.2 Definition sketch of the Belt drive connection.

Once the generated waves hit the breakwater some portion of the wave energy is reflected. The experiments have to be stopped before the re-reflected waves from the wave generator reach back to the moving gauge. Therefore the total time for the data recording is limited with the distances of the gauges and the model from the paddle and the wave properties. The total operation period was computed by assuming the wave

front travels with the group wave speed, C_G. The group wave speed was calculated assuming deepwater conditions by using Equation 3.25 as follows;

$$C_G = \frac{gT}{4\pi} \tag{A.2}$$

Hence, the required times for the waves to reach the moving gauge, test section and the fixed gauge are given by,

$$t_t = \frac{x_t}{C_G}, \quad t_{g1} = \frac{x_{g1}}{C_G} \quad \text{and} \quad t_{g2} = \frac{x_{f2}}{C_G}, \tag{A.3}$$

where x_{g1}, x_t and x_{g2} are the distances of the moving gauge (Figure A.3), breakwater model and fixed gauge form the wave paddle, t_{g1}, t_t and t_{g2} are the required time for the waves to reach initial position of the moving gauge, breakwater model and fixed gauge, respectively.

The total time for the reflected waves from the model to reach back to the moving gauge for the second time after hitting the paddle is computed according to the following relation;

$$t_{total} = 2t_t + t_{g1} \tag{A.4}$$

The linear actuator started moving when the reflected waves from the model reached to the moving gauge. The travel distance and the speed of the moving gauge was restricted by the location of the moving gauge, location of the test section, linear actuator length and wave train speed. The delay between the beginning of wave generation and the initiation of the gauge motion is given by,

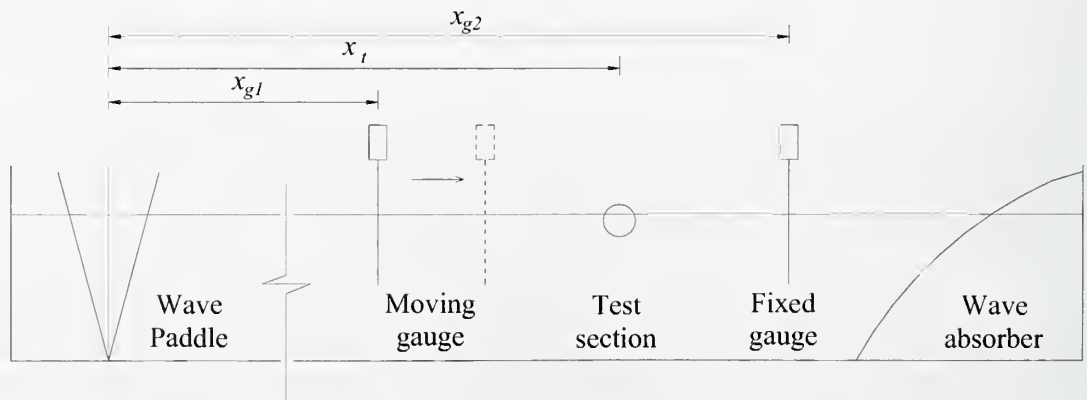$$t_{delay} = 2t_t - t_{g2} \tag{A.5}$$

Figure A.3 Distances of the moving gauge, breakwater model and fixed gauge form the wave paddle.

Moving gauge had a speed that ensured the distance, d_g was scanned before the end of the run. The gauge moved towards the breakwater model at a constant speed, v_g which is defined as;

$$v_g = \frac{d_g}{2t_{g1}} \tag{A.6}$$

where d_g is the distance traveled by the moving gauge. The definition sketch for the actuator is given in Figure A.4. It was observed that four wave envelopes were enough for each experiment to extract the incident and reflected wave information. Therefore, if the length of the actuator was grater then four times the theoretical envelope length then the travel distance was set to this value so that at most four envelopes are scanned.

The length of envelope which is the length between two anti-nodes of the standing wave is calculated from,

$$l_{env} = \frac{L}{2} \tag{A.7}$$

If the length of the actuator is not enough to scan one full envelope then a warning message appears on the screen to notify the user. When the wave length was smaller then half of the actuator length, the travel distance was reduced to have enough the resolution. Ideally, if the scan rate of the moving gauge is low the resolution of the resulting envelope is higher. However, the scan has to be computed before any reflected waves from the paddle reaches back to the moving gauge. This can be formulized as follows:

$$2L > l_a, \qquad d_g = l_a$$
$$2L \le l_a, \qquad d_g = 2L \tag{A.7}$$

where l_a is the full length of the actuator. The wave length is computed using 3.13.
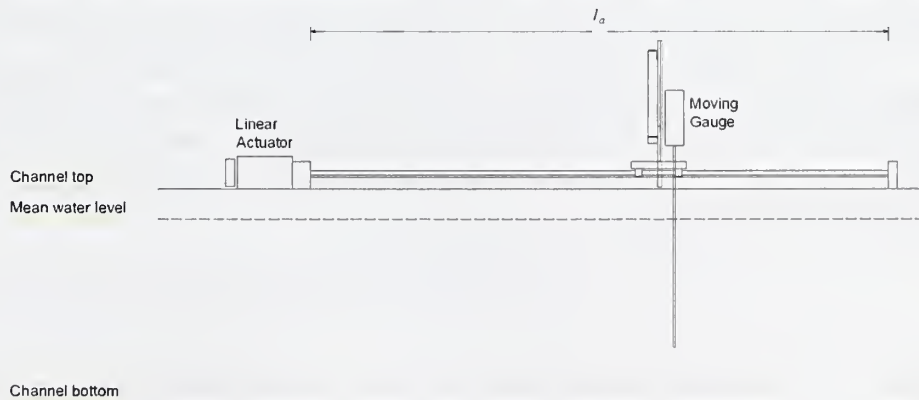

Figure A.4 Definition sketch of the linear actuator.

The experiments were run sequentially immediately after the execution of the input list. The program reset the position of the moving gauge to 9.6 m and paddled position to a phase angle π with stroke, S, that corresponding to a wave period, T and a wave height, H (or steepness, H/L). Then, it waited until the water surface was still by checking the standard deviation (SD) of the water surface elevation signal from two level sensors. If the SD of the water surface for the specified time interval was less then a threshold value the and, the gauge and the paddle are not moving the experiment was executed. The time interval was set to a value in the order of the gravity wave period along the flume (16.5 s for 46 cm water depth). The water surface fluctuation was limited to 1 or 2 mm. The SD of the noise, when the water was still, ranged between 0 and 1 mm. The next experiment was not executed before 3 min and the experiments were executed after 10 minutes regardless of the controls defined above. These values were set by inspection. The paddle started wave generation approximately 5 s after the initiation of the data recording. After the end of each experiment, the recoded time series signal of water surface elevations at two gauges, the motion of the paddle and the gauge and the parameters of the experiment were stored into the computer. The control program waited for the water to become still before the next run. The program allowed the user to skip or stop the experiment at any time. The collected data for each experiment was saved in a file named with the corresponding reference number.

A.2.   Experimental Data Analysis

The data analysis involved the time series analysis and spectral analysis of the time series signal of water surface elevations at both gauges. Time series measurements of wave paddle motion and moving gauge position were also analyzed to verify the executed motions. A computer program was developed in Labview to read and process data files recorded during the experiments. The program allowed the user to select and analyze multiple files. At the end of the analysis the information acquired form each file was stored in a data base. The flowchart of the program is given in Figure A.5.

The periods of wave profile received from two water level sensors were obtained through spectral analysis by using a Fast Fourier Transform routine. Peak period, which is the reciprocal of the spectral frequency with maximum spectral density, was used as the wave period. The wave period computation from the moving gauge recording was corrected with the speed of the gauge with

$$T_{g1} = T_{g1}^r \left(1 - \frac{v_g}{C} \right) \tag{A.8}$$

where T_{g1} is the actual period of the progressive waves passing through the moving gauge, T_{g1}^r is the wave period relative to the moving gauge, v_g is the gauge speed and C is the wave propagation speed.

The wave heights were estimated by time domain analysis. A quadratic equation was fitted to five data points around each peak and the peaks and valleys were found from the zero first derivative of the equation. Wave height was defied by the difference between two successive peak and valley. The transmitted wave height was obtained by simply averaging the estimated wave heights within the transmitted wave signal. Local maximum and minimum water surface elevations along the interval of gauge motion were located by using the same peak detector. The highest and lowest of these wave heights at these quasi-antinodes and quasi-nodes were used to estimate the incident and reflected wave heights by using Equations 3.36 and 3.37. All the dimensional and dimensionless parameters for a run were saved into a file.
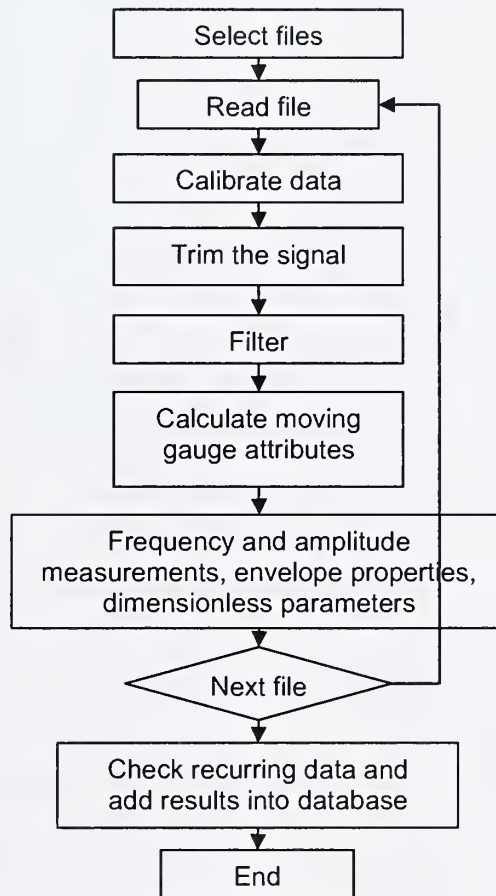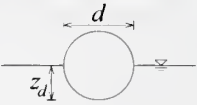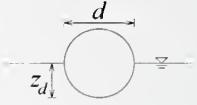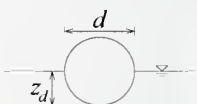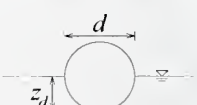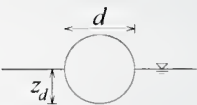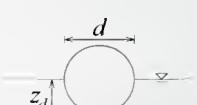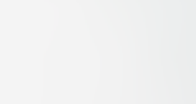
Figure A.5 Flowchart of the experimental data analysis.

225

Table B.1 Ranges of wave parameters for the fixed models ($h = 466$ mm).

Model No.	Vertical Dimension d (mm)	Draft z_d (mm)	Wave Height H (mm)	Wave period T (s)	Wave steepness $\dfrac{H_i}{L}$	Relative depth kh	Relative draft $\dfrac{z_d}{L}$	Aspect ratio $\dfrac{z_d}{d}$	Definition sketch of breakwater configuration
41	48.5	24.3	15	0.50-1.3	0.006-0.08	1.3-7.5	0.01-0.06	0.5	
			20	0.50-1.3					
			25	0.50-1.2					
			30	0.50-1.2					
			35	0.50-1.1					
			40	0.54-1.0					
			45	0.58-1.0					
51	60.2	30.1	15	0.50-1.3	0.006-0.08	1.3-7.5	0.01-0.08	0.5	
			20	0.50-1.3					
			25	0.50-1.2					
			30	0.50-1.2					
			35	0.52-1.1					
			40	0.54-1.0					
			45	0.56-1.0					
61	114.6	57.3	15	0.50-1.3	0.006-0.1	1.3-7.5	0.03-0.15	0.5	
			20	0.50-1.3					
			25	0.50-1.2					
			30	0.50-1.2					
			35	0.50-1.1					
			40	0.52-1.0					
			45	0.58-1.0					
			50	0.60-1.0					
41	48.5	24.3	15	0.50-1.3	0.006-0.08	1.3-7.5	0.01-0.06	0.5	
			20	0.50-1.3					
			25	0.50-1.2					
			30	0.50-1.2					
			35	0.50-1.1					
			40	0.54-1.0					
			45	0.58-1.0					
51	60.2	30.1	15	0.50-1.3	0.006-0.08	1.3-7.5	0.01-0.08	0.5	
			20	0.50-1.3					
			25	0.50-1.2					
			30	0.50-1.2					
			35	0.52-1.1					
			40	0.54-1.0					
			45	0.56-1.0					
61	114.6	57.3	15	0.50-1.3	0.006-0.1	1.3-7.5	0.03-0.15	0.5	
			20	0.50-1.3					
			25	0.50-1.2					
			30	0.50-1.2					
			35	0.50-1.1					
			40	0.52-1.0					
			45	0.58-1.0					
			50	0.60-1.0					

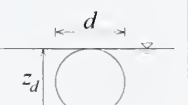| Model No.	Vertical Dimension d (mm)	Draft z_d (mm)	Wave Height H (mm)	Wave period T (s)	Wave steepness $\dfrac{H_i}{L}$	Relative depth kh	Relative draft $\dfrac{z_d}{L}$	Aspect ratio $\dfrac{z_d}{d}$	Definition sketch of breakwater configuration
63	114.6	80.2	17 - 75	0.80-1.3 0.60-1.2 0.60-1.0 0.60-1.0 0.60-0.9 0.60-0.8	0.03 0.04 0.05 0.06 0.07 0.08	1.4-7.5	0.02-0.12	0.7	
42	48.5	48.5	20 25 30 35 40	0.50-1.0 0.50-1.0 0.52-1.0 0.54-1.1 0.52-1.1	0.01-0.08	1.6-7.5	0.03-0.12	1.0	
52	60.2	60.2	15 20 25 30 35 40 45	0.50-1.2 0.50-1.2 0.50-1.2 0.50-1.2 0.50-1.1 0.52-1.0 0.56-1.0	0.006-0.1	1.4-7	0.03-0.15	1.0	
62	114.6	114.6	20 25 30 35 40 45	0.50-1.2 0.50-1.2 0.50-1.2 0.52-1.2 0.54-1.2 0.56-1.2	0.006-0.1	1.4-7.5	0.05-0.3	1.0	
71	$d = 62.3$ mm ($D = 33.4$ mm $b = 66.8$	45.6	15 20 25 30 35	0.50-1.3 0.50-1.2 0.50-1.2 0.50-1.2 0.52-1.1	0.006-0.1	1.4-7.5	0.02-0.12	0.73	
81	$d = 90.5$ mm ($D = 48.5$ mm $b = 97$ mm)	66.26	15 20 25 30 35 40 45 50	0.50-1.2 0.50-1.2 0.50-1.2 0.50-1.2 0.50-1.2 0.54-1.0 0.56-1.0 0.60-0.9	0.006-0.1	1.4-8	0.03-0.18	0.73	
91	$d = 112.3$ mm ($D = 60.2$ mm $b = 120.4$ mm)	82.23	20 25 30 35 40 45	0.50-1.1 0.50-1.1 0.50-1.2 0.50-1.2 0.52-1.3 0.58-1.3	0.009-0.1	1.3-7.5	0.04-0.2	0.73	

Table B.2 Ranges of wave parameters for the bottom moored models ($h = 466$ mm).

Model No.	Vertical Dimension d (mm)	Draft z_d (mm)	Wave Height H (mm)	Wave period T (s)	Wave steepness $\dfrac{H_i}{L}$	Relative depth kh	Relative draft $\dfrac{z_d}{L}$	Aspect ratio $\dfrac{z_d}{d}$	Definition sketch of breakwater configuration
44	48.5	24.3	15 20 25 30 35 40 45	0.50-1.3 0.50-1.2 0.50-1.2 0.50-1.2 0.52-1.1 0.56-1.0 0.58-0.9	0.006-0.08	1.3-7.5	0.01-0.06	0.5	
54	60.2	30.1	15 20 25 30 35 40 45	0.50-1.2 0.50-1.3 0.50-1.2 0.50-1.2 0.52-1.2 0.54-1.0 0.58-1.0	0.006-0.08	1.3-7.5	0.01-0.08	0.5	
64	114.6	57.3	15 20 25 30 35 40 45 50	0.50-1.2 0.50-1.2 0.50-1.2 0.50-1.2 0.52-1.1 0.56-1.0 0.58-1.0 0.60-0.9	0.006-0.08	1.4-7.5	0.03-0.15	0.5	
45	48.5	48.5	15 20 25 30 35 40 45	0.50-1.3 0.50-1.2 0.50-1.2 0.50-1.2 0.54-1.1 0.58-1.0 0.60-0.9	0.006-0.07	1.4-7.5	0.02-0.1	1.0	
55	60.2	60.2	15 20 25 30 35 40 45	0.50-1.2 0.50-1.2 0.50-1.2 0.50-1.2 0.52-1.1 0.54-1.0 0.56-1.0	0.007-0.08	1.4-7.5	0.03-0.15	1.0	
65	114.6	114.6	15 20 25 30 35 40 45 50	0.50-1.3 0.50-1.2 0.50-1.2 0.50-1.2 0.52-1.2 0.54-1.0 0.56-1.0 0.60-1.0	0.006-0.08	1.3-7.5	0.05-0.3	1.0	
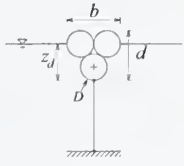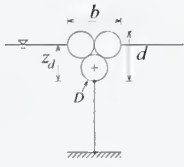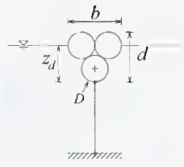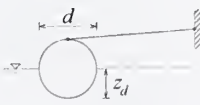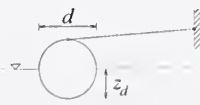
Model No.	Vertical Dimension d (mm)	Draft z_d (mm)	Wave Height H (mm)	Wave period T (s)	Wave steepness $\dfrac{H_i}{L}$	Relative depth kh	Relative draft $\dfrac{z_d}{L}$	Aspect ratio $\dfrac{z_d}{d}$	Definition sketch of breakwater configuration
74	d = 62.3 mm (D = 33.4 mm b = 66.8 mm)	45.6	15 20 25 30 35 40 45	0.50-1.3 0.50-1.2 0.50-1.2 0.50-1.2 0.52-1.1 0.54-1.0 0.56-1.0	0.006-0.09	1.3-7.5	0.02-0.1	0.73	
84	d = 90.5 mm (D = 48.5 mm b = 97 mm)	66.26	15 20 25 30 35 40 45	0.50-1.3 0.50-1.2 0.50-1.2 0.50-1.2 0.52-1.1 0.54-1.0 0.56-1.0	0.006-0.08	1.4-7.5	0.03-0.2	0.73	
94	d = 112.3 mm (D = 60.2 mm b = 120.4 mm)	82.23	15 20 25 30 35 40 45	0.50-1.3 0.50-1.2 0.50-1.2 0.50-1.2 0.52-1.1 0.54-1.0 0.56-1.0	0.006-0.09	1.4-7.5	0.04-0.2	0.73	

Table B.3 Ranges of wave parameters for the arm restrained models (h = 466 mm).

Model No.	Vertical Dimension d (mm)	Draft z_d (mm)	Wave Height H (mm)	Wave period T (s)	Wave steepness $\dfrac{H_i}{L}$	Relative depth kh	Relative draft $\dfrac{z_d}{L}$	Aspect ratio $\dfrac{z_d}{d}$	Definition sketch of breakwater configuration
57	60.2	30.1	15 20 25 30 35 40 45	0.50-1.3 0.50-1.2 0.50-1.2 0.50-1.2 0.54-1.1 0.56-1.0 0.58-1.0	0.006-0.08	1.3-7.5	0.01-0.08	0.5	
67	114.6	57.3	15 20 25 30 35 40 45	0.50-1.3 0.50-1.2 0.50-1.2 0.50-1.2 0.54-1.1 0.56-1.0 0.58-1.0	0.006-0.08	1.3-7.5	0.03-0.15	0.5	

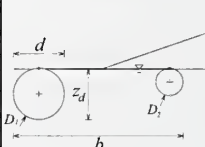| Model No.	Vertical Dimension d (mm)	Draft z_d (mm)	Wave Height H (mm)	Wave period T (s)	Wave steepness $\dfrac{H_i}{L}$	Relative depth kh	Relative draft $\dfrac{z_d}{L}$	Aspect ratio $\dfrac{z_d}{d}$	Definition sketch of breakwater configuration
58	60.2	30.1	15 20 25 30 35 40 45	0.50-1.3 0.50-1.2 0.50-1.2 0.50-1.2 0.52-1.1 0.56-1.0 0.58-1.0	0.006-0.07	1.3-7.5	0.03-0.15	1.0	
68	114.6	57.3	15 20 25 30 35 40 45	0.50-1.3 0.50-1.2 0.50-1.2 0.50-1.2 0.54-1.2 0.58-1.0 0.58-0.9	0.006-0.07	1.3-7.5	0.05-0.3	1.0	
85	60.2 ($D_1 = 60.2$ $D_2 = 37.3$ $b = 301$)	60.2	15 20 25 30 35 40 45	0.50-1.3 0.50-1.2 0.50-1.2 0.50-1.2 0.56-1.1 0.58-1.0 0.60-1.0	0.005-0.08	1.3-7.5	0.02-0.15	0.2	
86	60.2 ($D_1 = 60.2$ $D_2 = 37.3$ $b = 301$)	60.2	15 20 25 30 35 40 45	0.50-1.3 0.50-1.2 0.50-1.2 0.50-1.2 0.56-1.1 0.58-1.0 0.60-1.0	0.006-0.08	1.3-7.5	0.01-0.08	0.2	

Table B.4 Ranges of wave parameters for the pile restrained models ($h = 466$ mm).

Model No.	Vertical Dimension d (mm)	Draft z_d (mm)	Wave Height H (mm)	Wave period T (s)	Wave steepness $\dfrac{H_i}{L}$	Relative depth kh	Relative draft $\dfrac{z_d}{L}$	Aspect ratio $\dfrac{z_d}{d}$	Definition sketch of breakwater configuration
60	114.6	s57.3	10 - 78	0.60-1.2 0.50-1.2 0.50-1.1 0.50-1.0 0.54-0.9 0.52-0.8 0.56-0.76	0.02 0.03 0.04 0.05 0.06 0.07 0.08	1.4-7.5	0.03-0.15	0.5	

Model No.	Vertical Dimension d (mm)	Draft z_d (mm)	Wave Height H (mm)	Wave period T (s)	Wave steepness $\dfrac{H_i}{L}$	Relative depth kh	Relative draft $\dfrac{z_d}{L}$	Aspect ratio $\dfrac{z_d}{d}$	Definition sketch of breakwater configuration
70	114.6	81.6	10 - 78	0.60-1.3 0.50-1.3 0.50-1.1 0.50-1.0 0.50-0.9 0.50-0.84 0.50-0.78	0.02 0.03 0.04 0.05 0.06 0.07 0.08	1.4-7.5	0.04-0.2	0.71	
59	89	83.4	12-78	0.60-1.3 0.50-1.2 0.50-1.0 0.50-1.0 0.60-0.86 0.50-0.8 0.64-0.74	0.02 0.03 0.04 0.05 0.06 0.07 0.08	1.3-7.5	0.04– 0.2	0.94	
69	114.6	110.0	12-78	0.60-1.3 0.50-1.2 0.50-1.1 0.50-1.0 0.50-0.9 0.60-0.84 0.60-0.76	0.02 0.03 0.04 0.05 0.06 0.07 0.08	1.3-7.5	0.05– 0.3	0.96	
69	114.6	110.0	12-78	0.60-1.3 0.50-1.2 0.50-1.1 0.50-1.0 0.50-0.9 0.60-0.84 0.60-0.76	0.02 0.03 0.04 0.05 0.06 0.07 0.08	1.3-7.5	0.05– 0.3	0.96	
			20 25 30 35 40 45	0.50-1.3 0.50-1.3 0.50-1.3 0.54-1.3 0.58-1.3 0.60-1.3	0.009-0.07				
96	89	85	12-78	0.60-1.3 0.50-1.2 0.50-1.1 0.50-1.0 0.50-0.9 0.50-0.8 0.60-0.7	0.02 0.03 0.04 0.05 0.06 0.07 0.08	1.3-7.5	0.04– 0.2	0.96	b= 300 mm D_1 = 89 mm D_2 = 42 mm
			20 25 30 35 40 45	0.50-1.3 0.50-1.3 0.50-1.3 0.54-1.3 0.58-1.3 0.60-1.3	0.009-0.08				

231

Figure C.1 Effect of wave steepness on transmission coefficient for half-submerged moored pipe with $d = 114.6$ mm.

Figure C.2. Effect of wave steepness on reflection coefficient for half-submerged moored pipe with $d = 114.6$ mm.

Figure C.3 Effect of wave steepness on transmission coefficient for fully submerged moored pipe with d = 114.6 mm.

Figure C.4 Effect of wave steepness on reflection coefficient for fully submerged moored pipe with d = 114.6 mm.
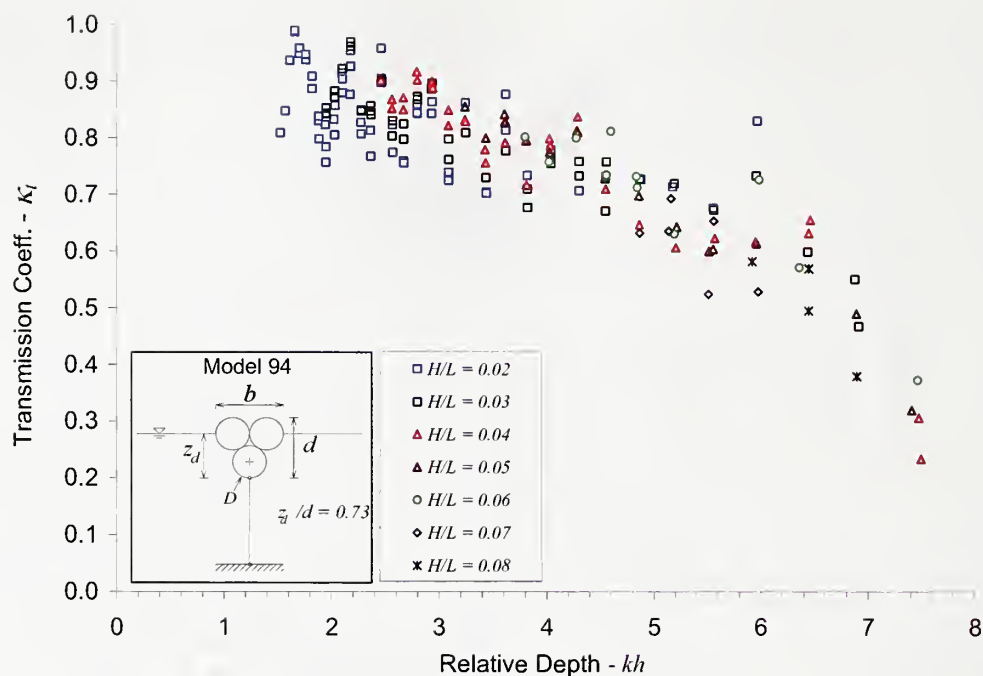
Figure C.5 Effect of wave steepness on transmission coefficient for fully submerged moored bundle of pipes with d = 120.4 mm.
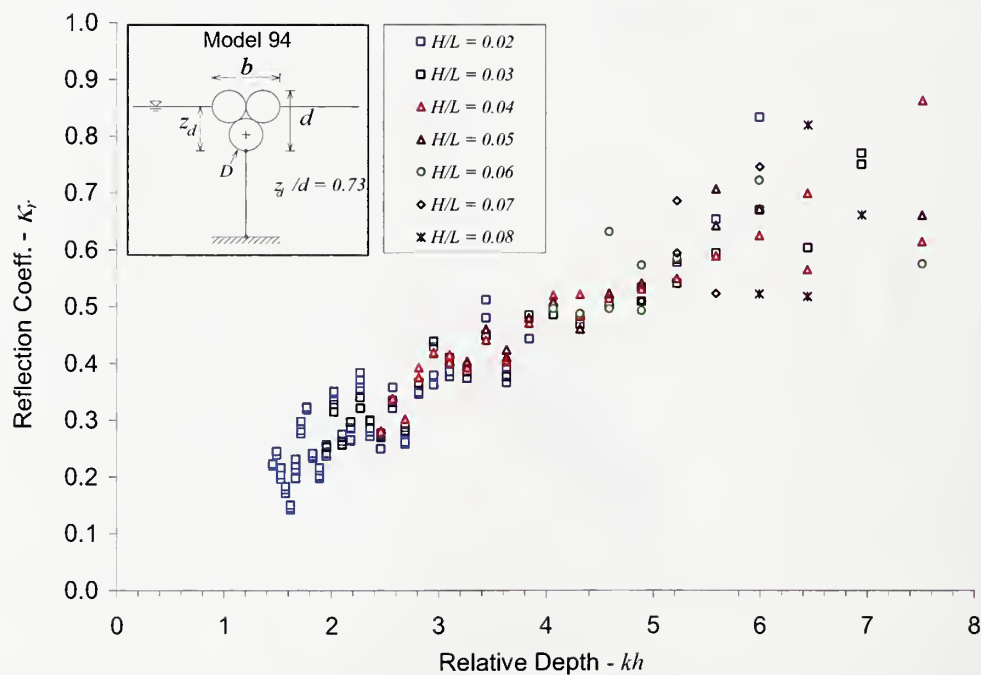
Figure C.6 Effect of wave steepness on reflection coefficient for fully submerged moored bundle of pipes with d = 120.4 mm.
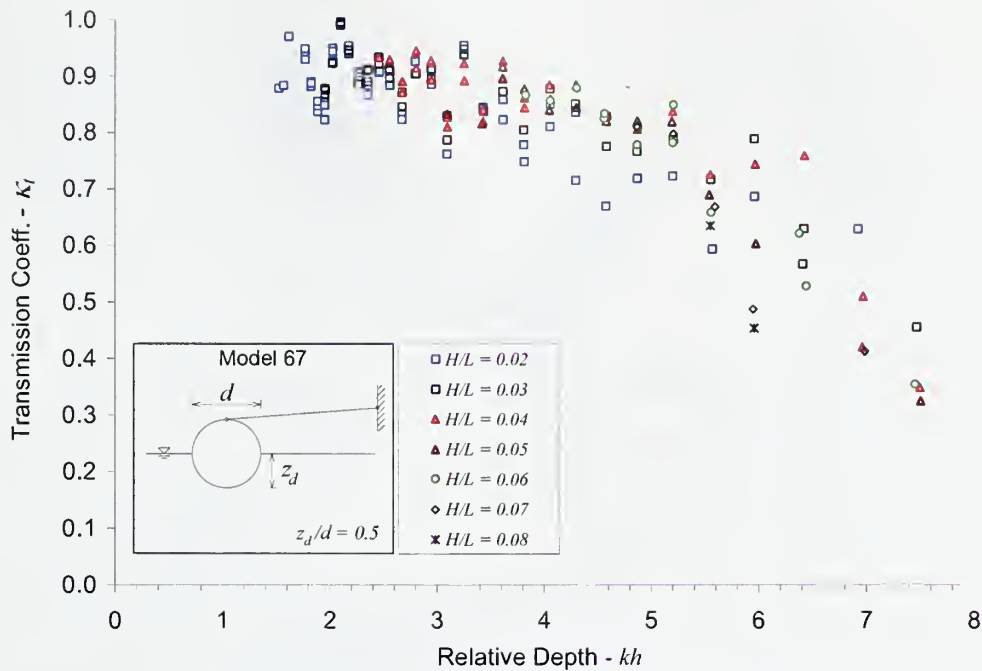
Figure C.7 Effect of wave steepness, H_i/L on transmission coefficient for half-submerged arm restrained pipe with $d = 114.6$ mm.
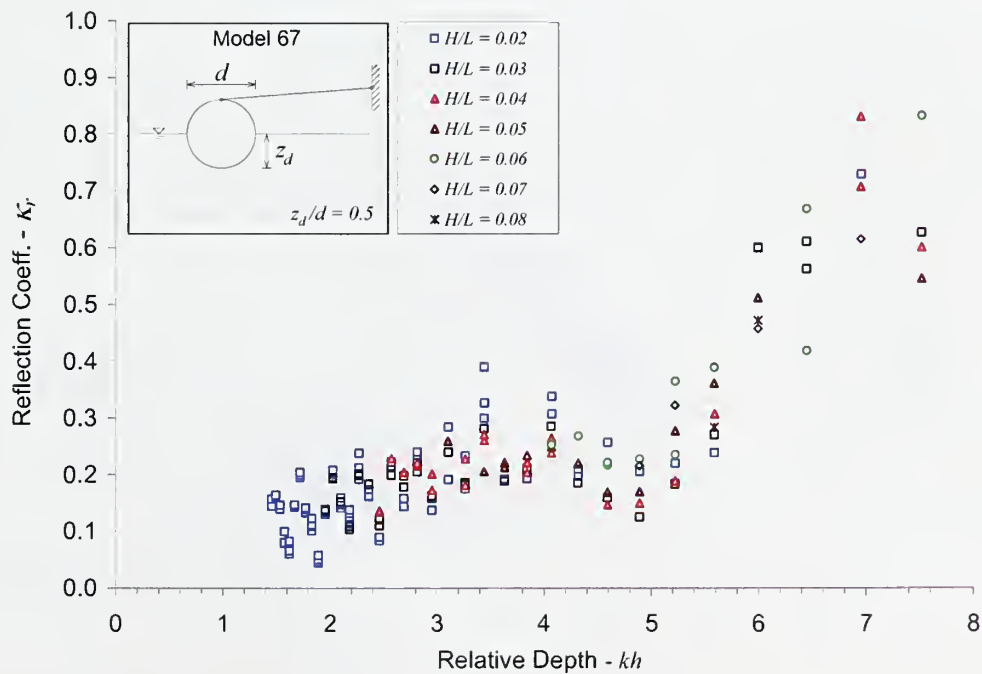
Figure C.8 Effect of wave steepness, H_i/L on reflection coefficient for half-submerged arm restrained pipe with $d = 114.6$ mm.
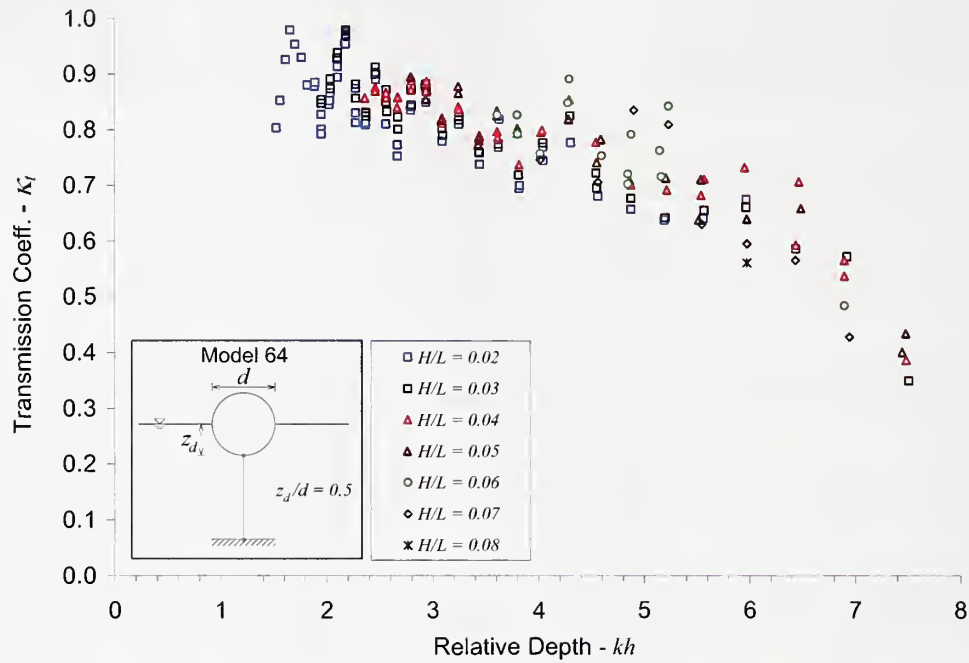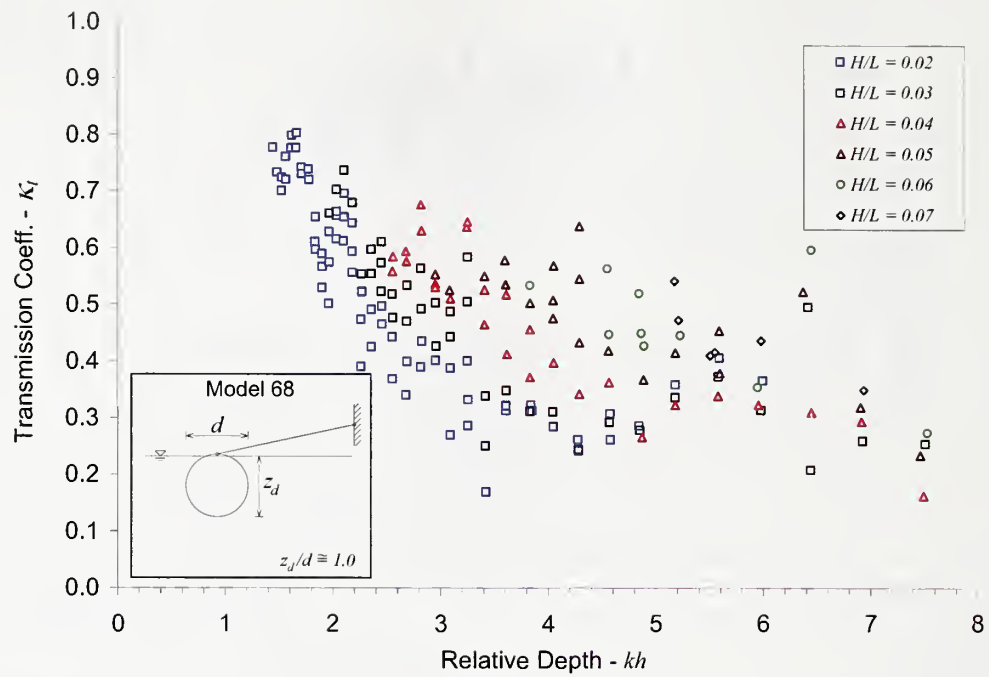
Figure C.9 Effect of wave steepness, H_i/L on transmission coefficient for fully-submerged fixed pipe with $d = 114.6$ mm.
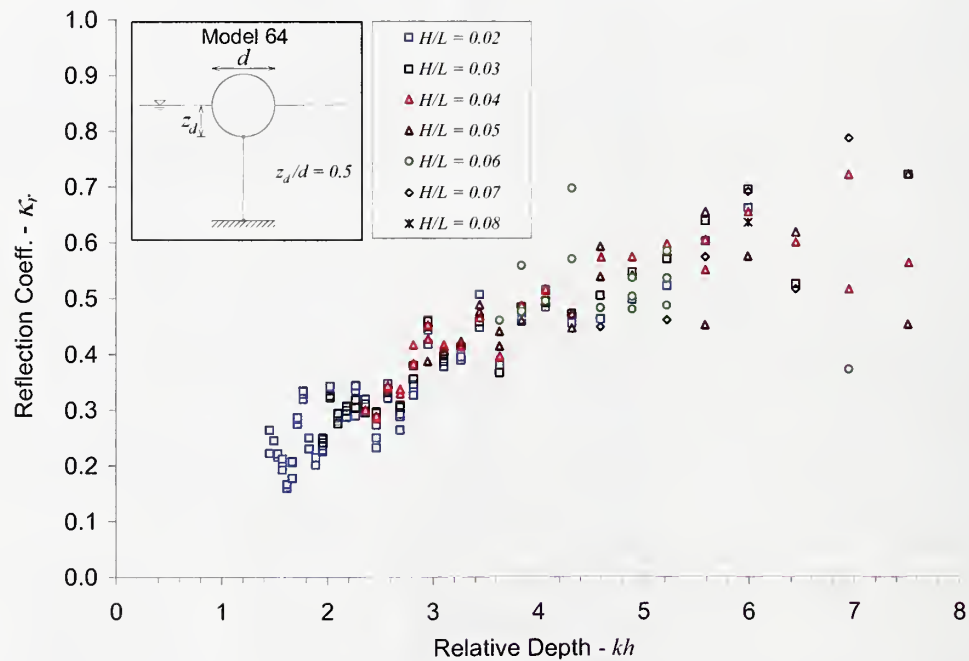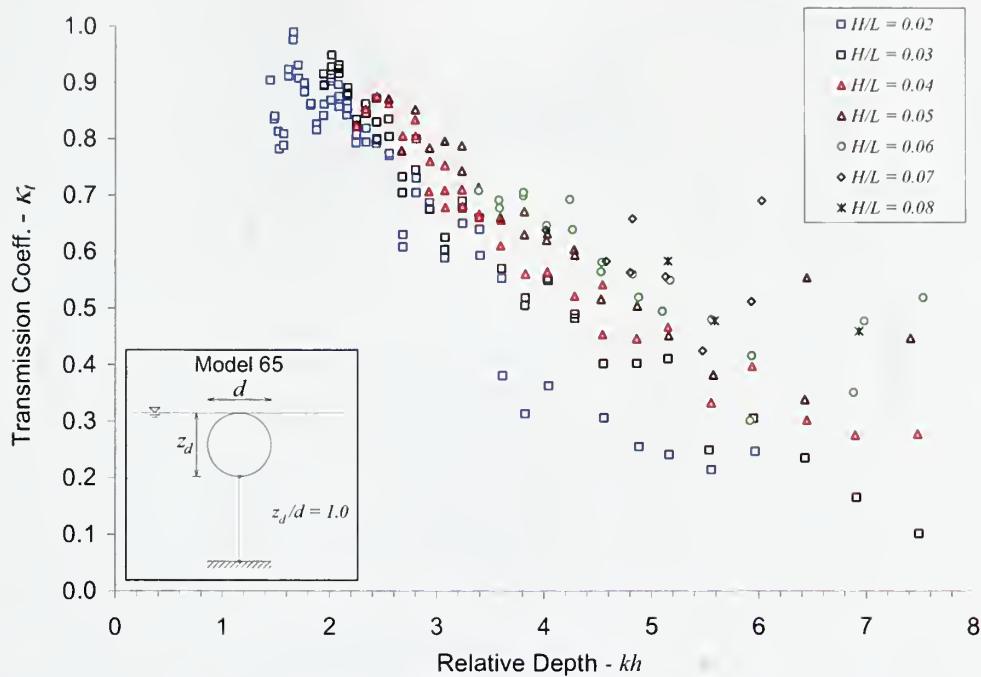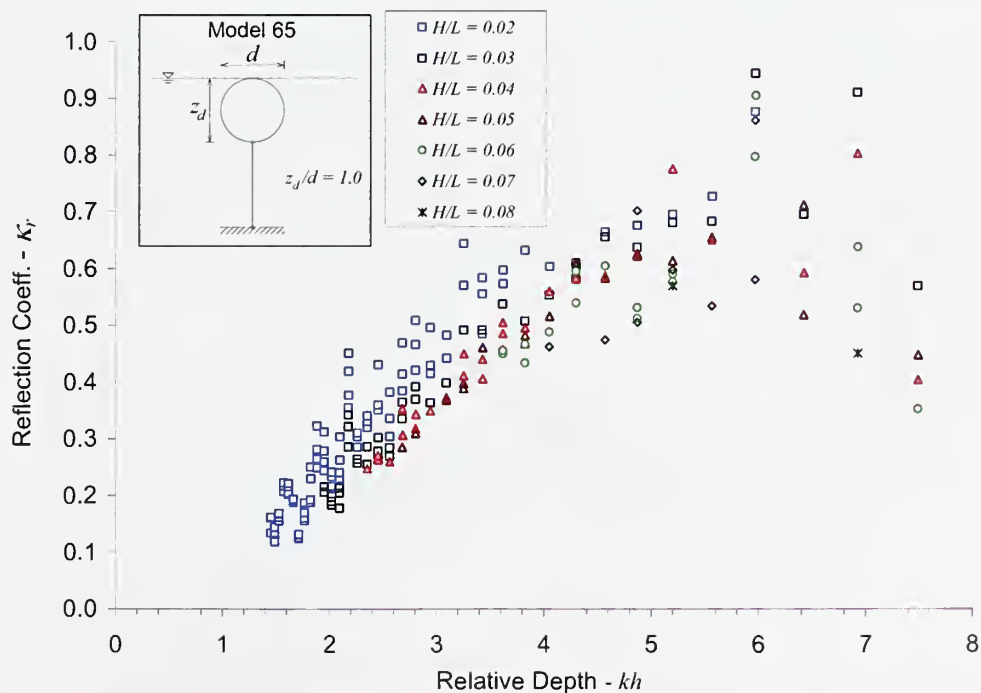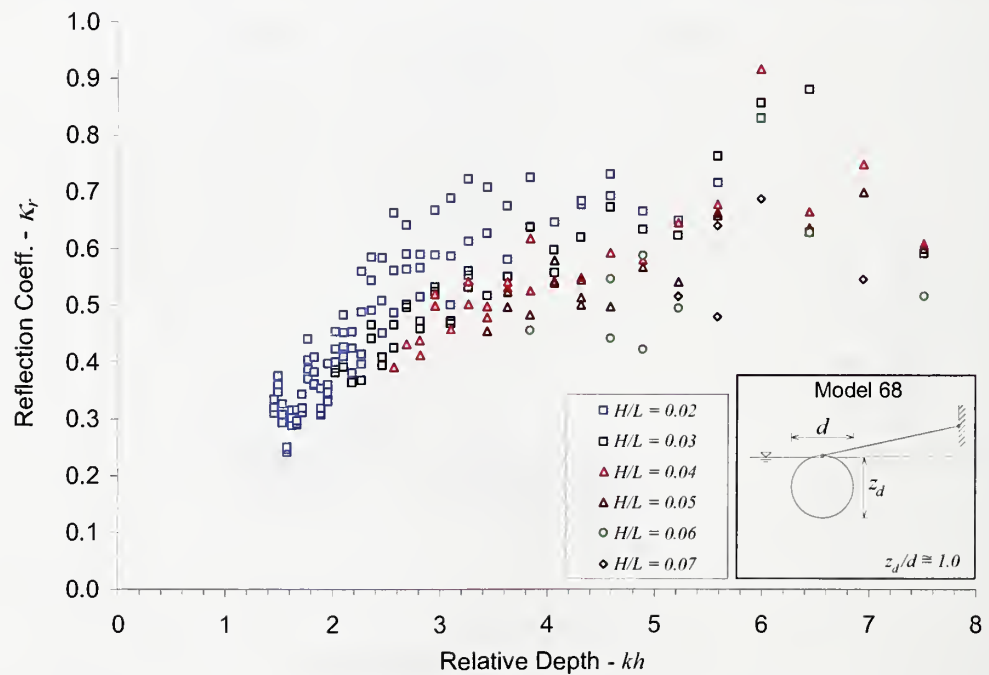

Figure C.10 Effect of wave steepness, H_i/L on reflection coefficient for fully-submerged fixed pipe with $d = 114.6$ mm.
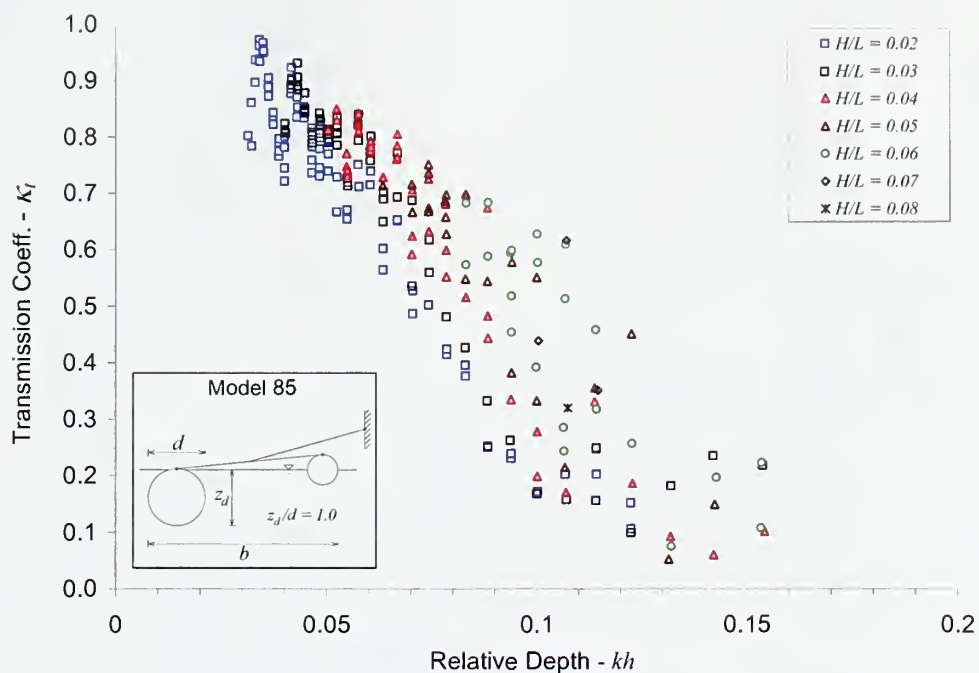
Figure C.11 Effect of wave steepness, H_i/L on transmission coefficient for arm restrained double pipe model (First pipe is fully submerged and second pipe is half submerged).
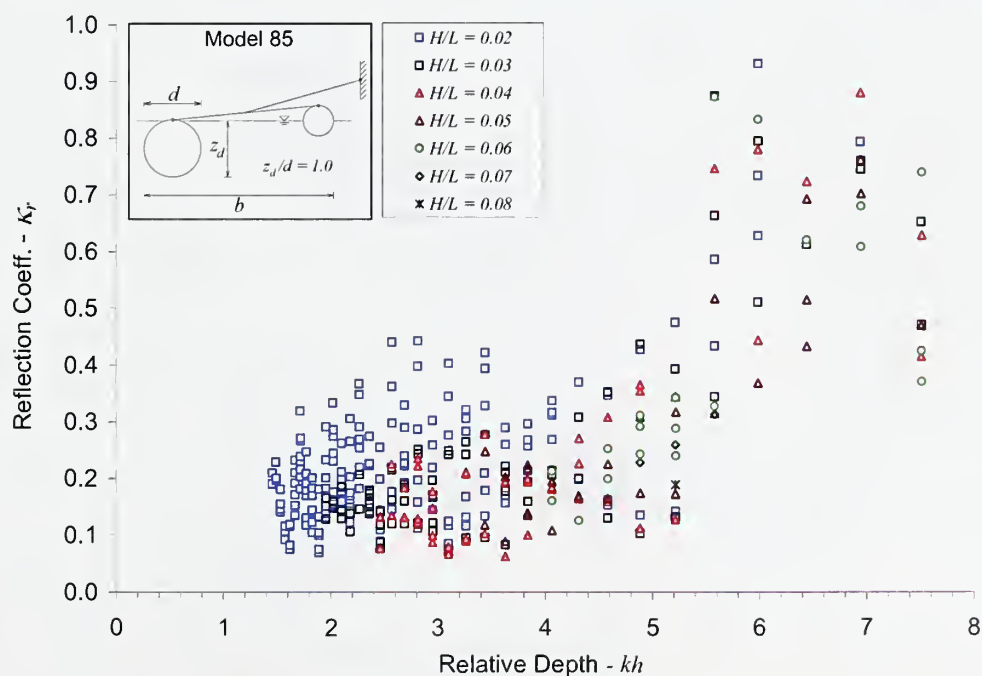
Figure C.12 Effect of wave steepness, H_i/L on reflection coefficient for arm restrained double pipe model (First pipe is fully submerged and second pipe is half submerged).

237
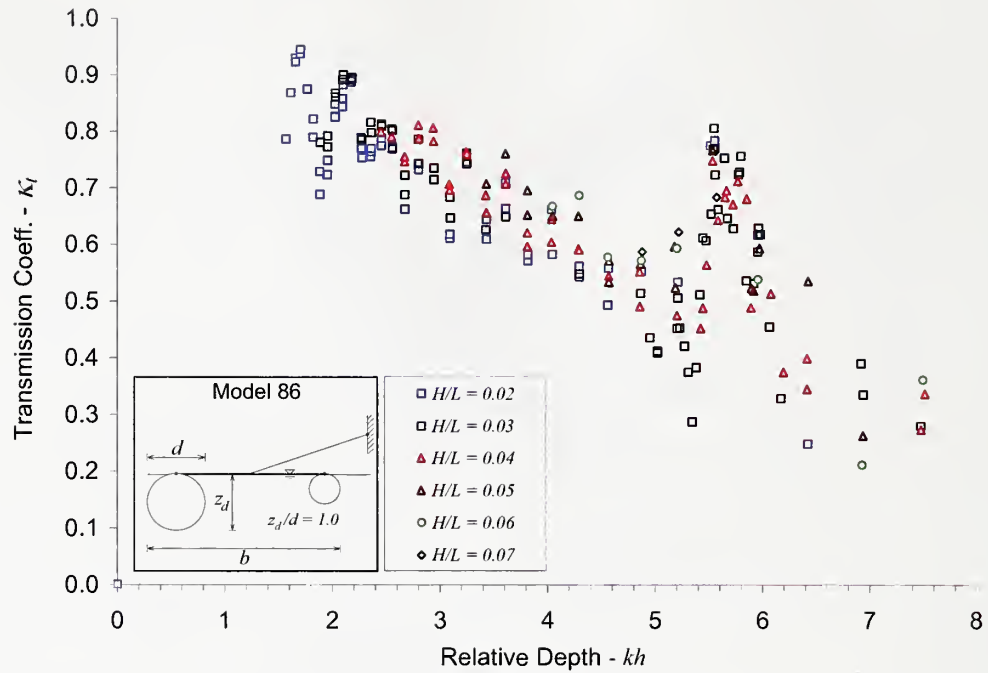
Figure C.13 Effect of wave steepness, H_i/L on transmission coefficient for arm restrained double pipe model (Both pipes are fully submerged).
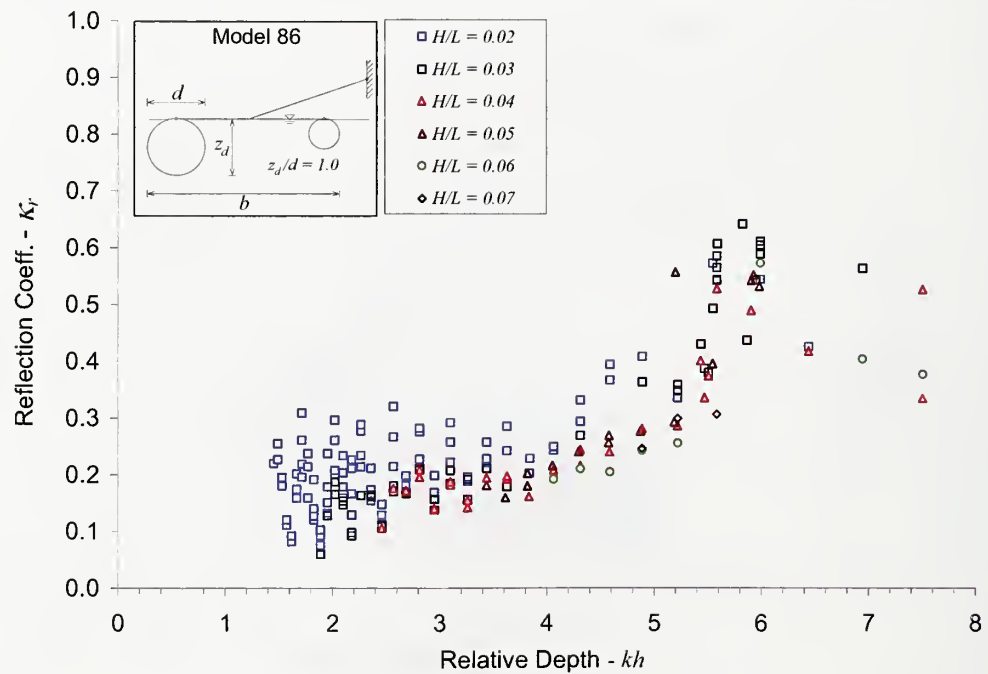
Figure C.14 Effect of wave steepness, H_i/L on reflection coefficient for arm restrained double pipe model (Both pipes are fully submerged).
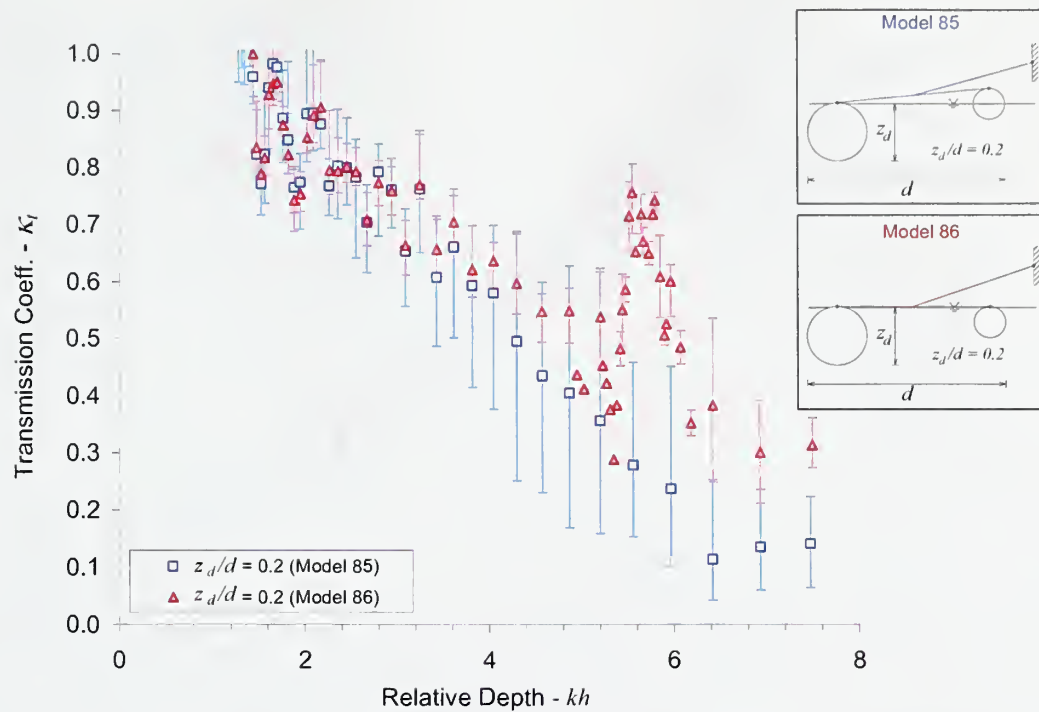
Figure C.15 Effect of second pipe submergence on transmission coefficient for arm restrained double pipe model. Bars represent the range of wave steepness.
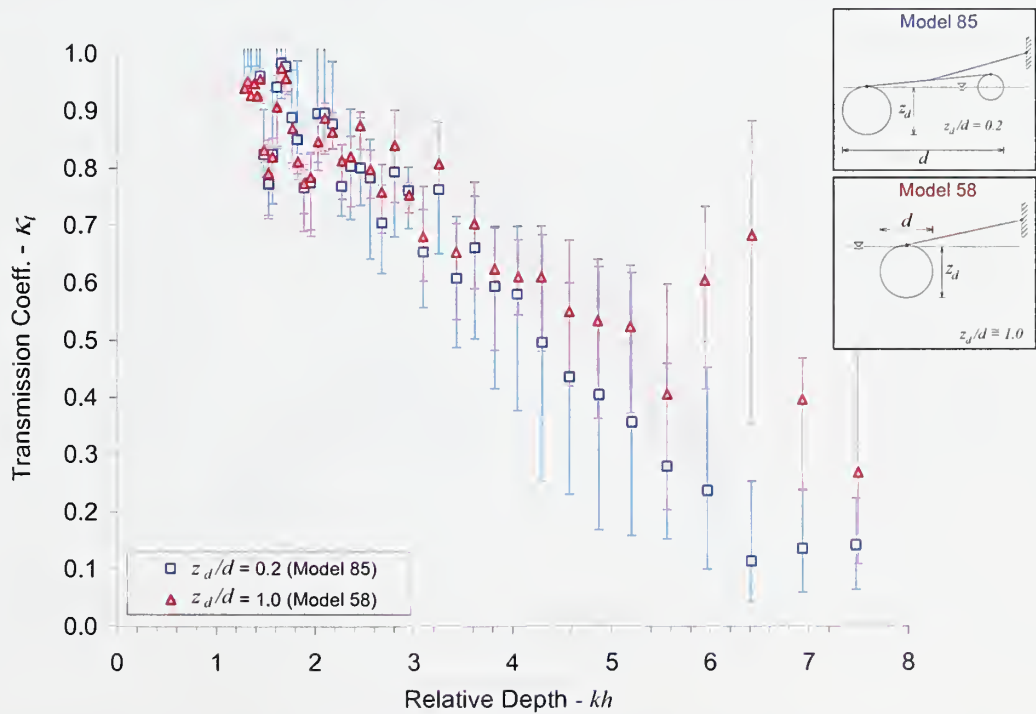
Figure C.16 Comparison of transmission coefficients of single and double pipe arm restrained breakwater models.
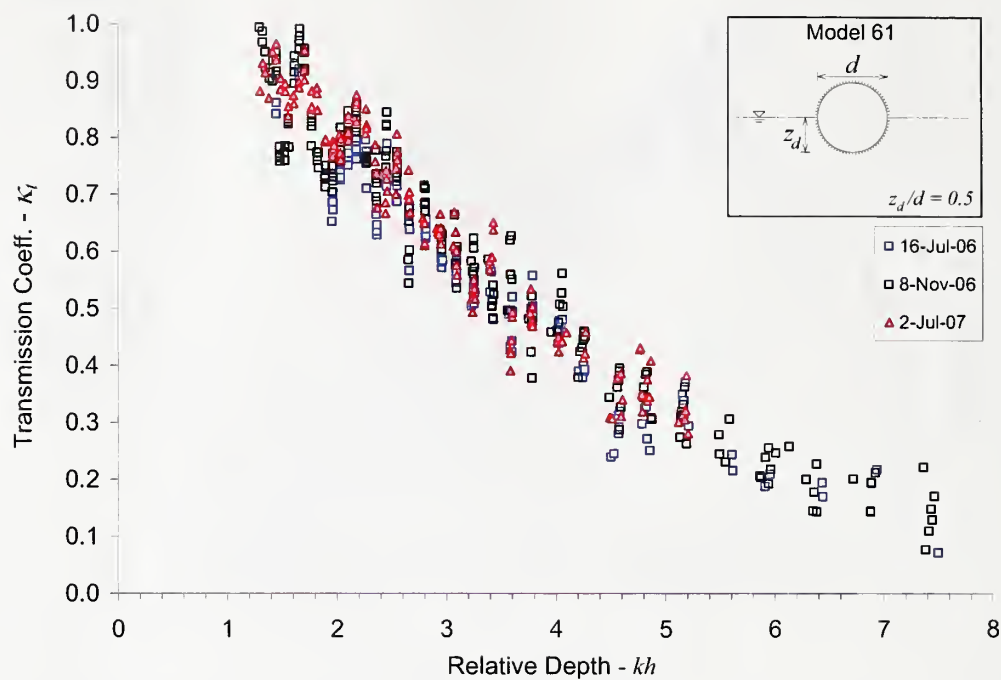
Figure C.17 The comparison the transmission coefficient data for the fixed half submerged single pipe breakwater model recorded at different dates.
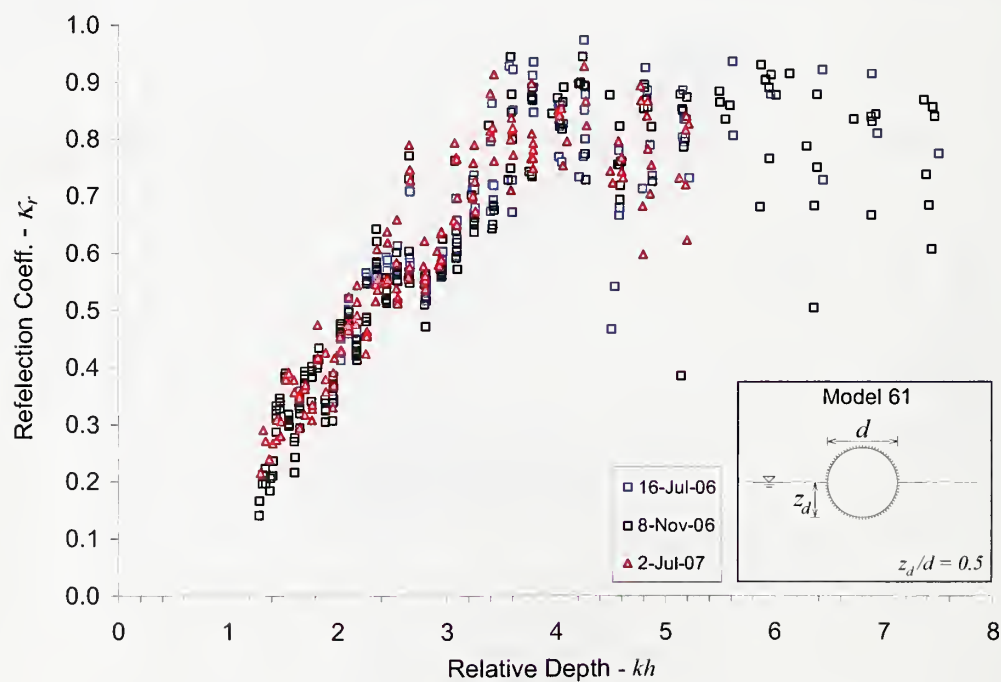
Figure C.18 The comparison the reflection coefficient data for the fixed half submerged single pipe breakwater model recorded at different dates.
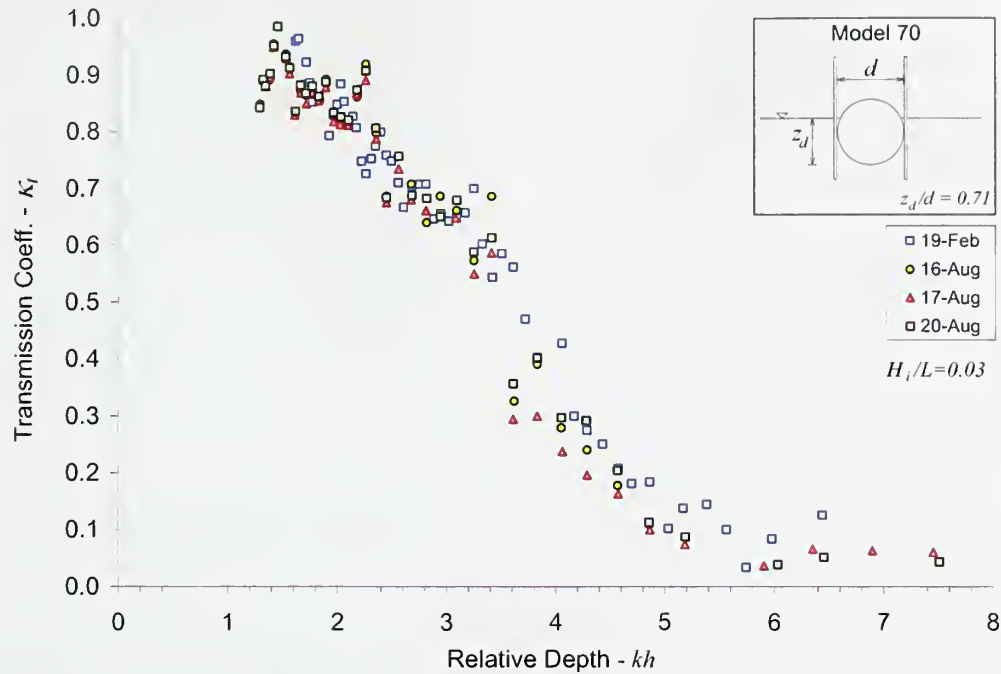
Figure C.19 The comparison the transmission coefficient data for the pile restrained partially submerged (z_d/d = 0.071) single pipe breakwater model recorded at different dates (H_i/L = 0.03).
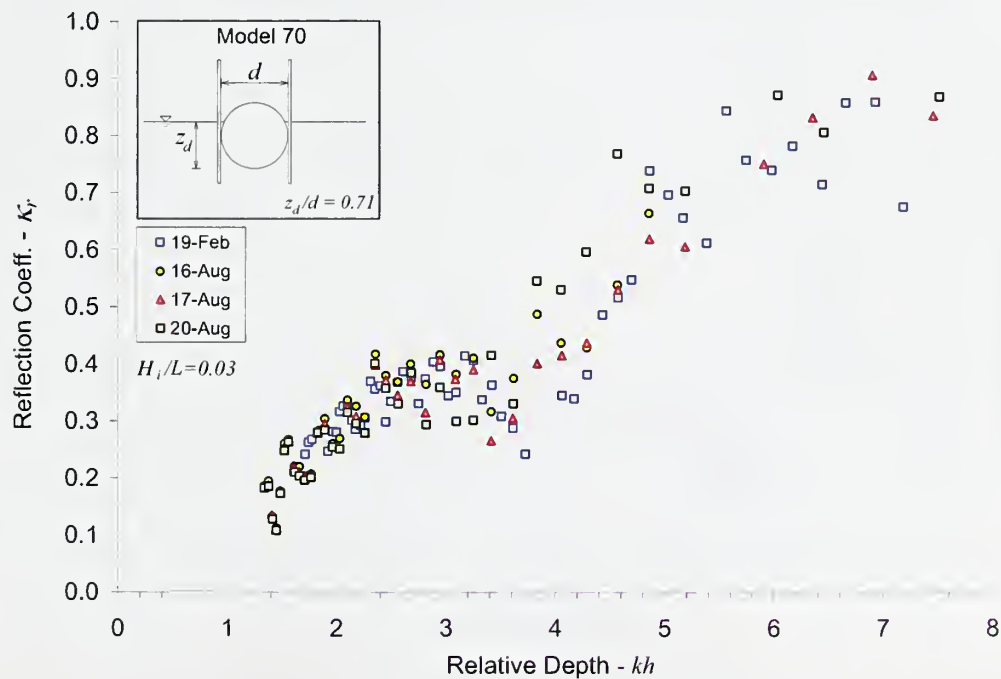
Figure C.20 The comparison the reflection coefficient data for the pile restrained partially submerged (z_d/d = 0.071) single pipe breakwater model recorded at different dates (H_i/L = 0.03).
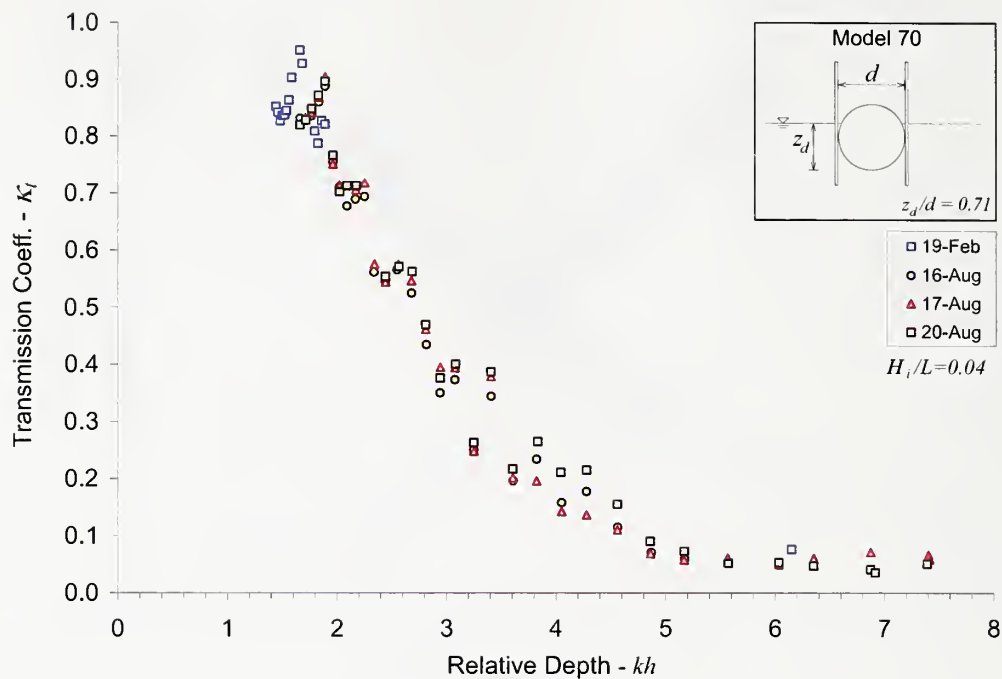
Figure C.21 The comparison the transmission coefficient data for the pile restrained partially submerged (z_d/d = 0.071) single pipe breakwater model recorded at different dates (H_i/L = 0.04).
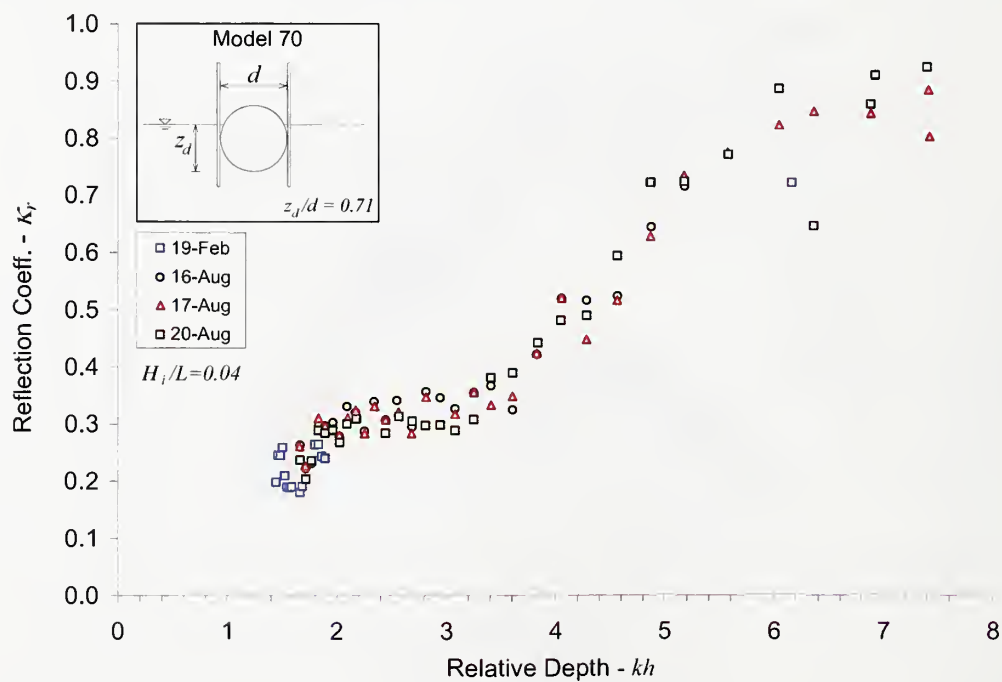
Figure C.22 The comparison the reflection coefficient data for the pile restrained partially submerged (z_d/d = 0.071) single pipe breakwater model recorded at different dates (H_i/L = 0.04).
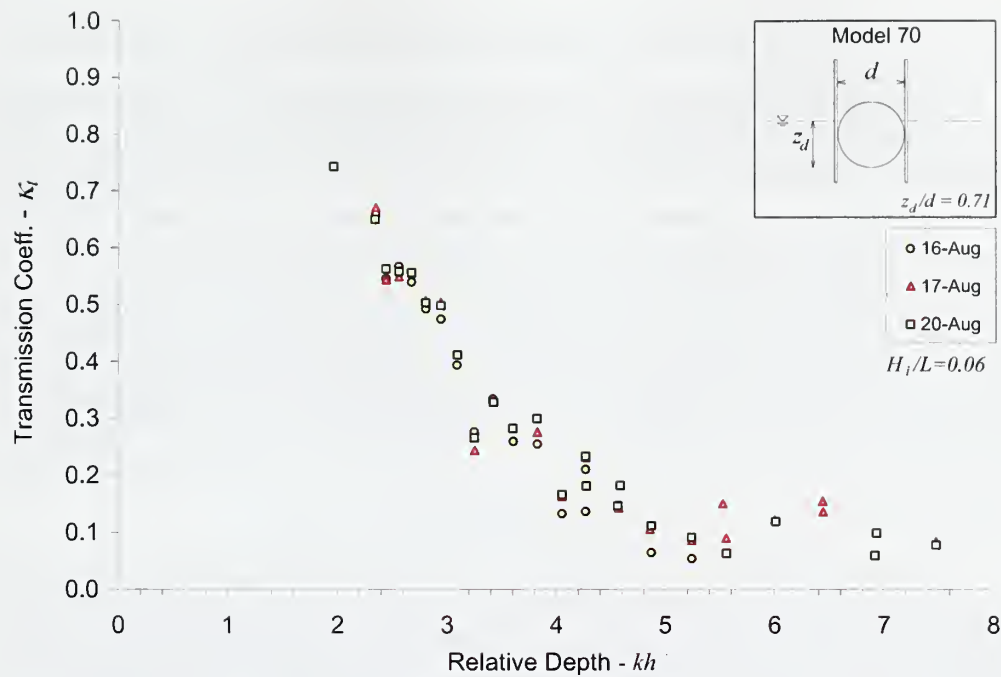
Figure C.23 The comparison the transmission coefficient data for the pile restrained partially submerged ($z_d/d = 0.071$) single pipe breakwater model recorded at different dates ($H_i/L = 0.06$).
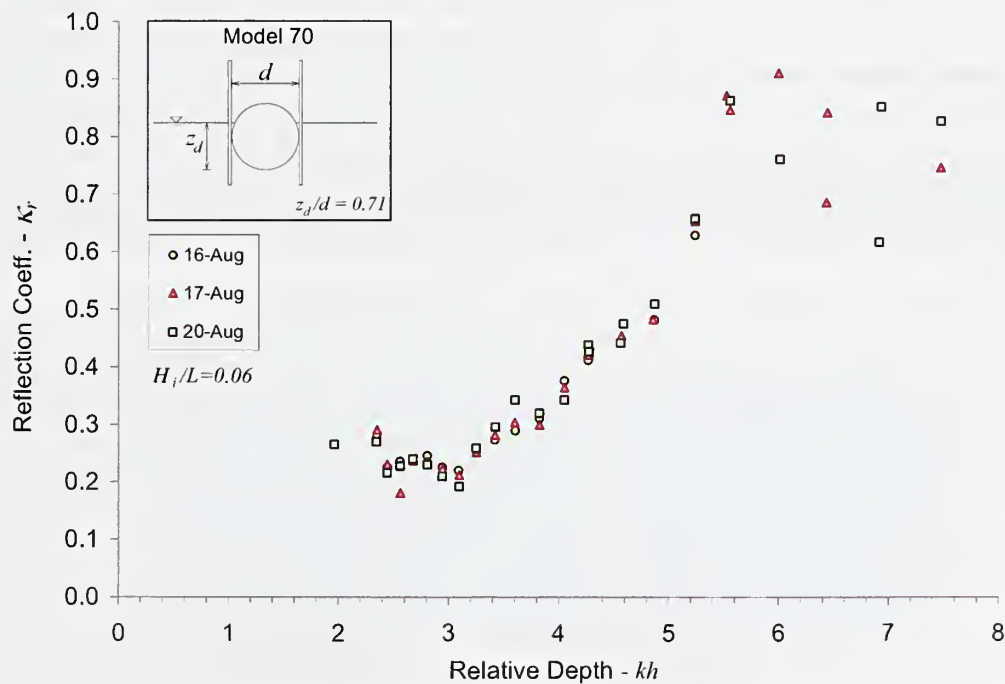
Figure C.24 The comparison the reflection coefficient data for the pile restrained partially submerged ($z_d/d = 0.071$) single pipe breakwater model recorded at different dates ($H_i/L = 0.06$)

D. SENSITIVITY ANALYSIS AND SELECTION OF MESH

The selection of a proper computational mesh is vital in numerical simulations for the solution accuracy and efficiency. Thus, a set of initial numerical simulations were carried out to test the sensitivity of the numerical solutions to the mesh size and an optimum mesh size was obtained. For these simulations a 5 m long and 0.6 m deep 2D numerical domain was created in Flow3D. At the left boundary of the computational domain, a numerical wavemaker was established by prescribing the velocities and the free surface elevation according to the linear monochromatic wave. This boundary condition is readily available in FLOW-3D. The numerical domain is shown in Figure D.1. No-slip condition was applied at the bottom boundary. To introduce numerical dissipation, the mesh was stretched in x direction between 15 m to 40 m linearly increasing the length of the cells from δx to $12\delta x$ (Figure D.2). Sommerfeld radiation condition was applied at the right boundary (Section 7.3.7.3).

The simulations were carried out with a water depth of 46.6 cm, wave height 3 cm and wave period 0.8 s, corresponding to a wavelength of 1 m. The total computation time was 30 seconds for each simulation. The output variables were stored at every time step. The time step size was controlled by stability and convergence conditions and was on the order of 0.01s throughout the simulation. The simulations were carried out with various different mesh sizes. The results of the simulations with cell sizes, $\delta x = \delta y = 5$ cm, 4 cm, 3 cm, 2 cm, and 1 cm will be presented here.

In Figure D.2 the time averaged, dimensionless wave heights are plotted at different distances from the left boundary, x/L and for the different mesh sizes. The wave fronts in Figure D.2 also differ for different mesh sizes such that; as the mesh is refined steady state is achieved faster compared to the courser mesh. This indicates that the radiation speed differs according to the mesh that the waves travel. To better demonstrate this phenomenon, the wave tank is extended to 15 m and the simulation time is increased to 48 s.
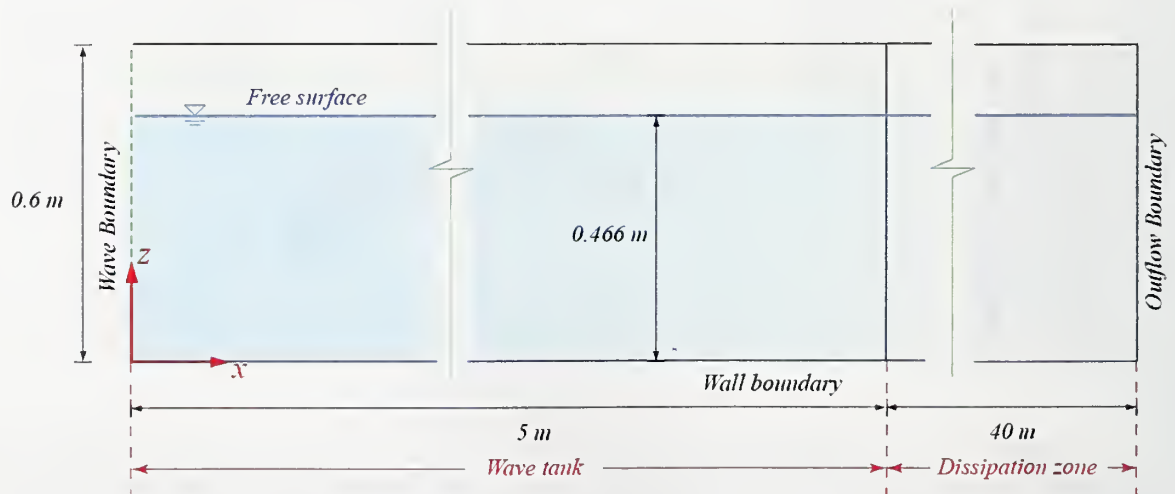
Figure D.1 Definition sketch of the numerical wave tank for sensitivity analysis.

Figure D.3 shows the water surface profile along the numerical wave tank at the end of 60 wave periods. It is clearly seen that, as the waves propagate, the wavelengths increase. The wave period, however, stay constant regardless of the mesh size at all section as expected. This indicates that the propagation speed increases in coarser mesh. In fact, the phases of the waves change with the mesh size at the end of 37 wave periods in Figure D.2.

In Figure D.4 the dimensionless water surface displacements η / H, at 4L away from the left boundary are compared for the five different mesh sizes. Also the theoretical wave height attenuation for deep water waves and measured wave heights at three different sections of the physical wave tank are included in Figure D.4 for comparison (Ippen, 1966). The relations for deep water wave attenuation due to viscous damping is given by

$$\frac{H}{H_o} = \exp\left[\frac{-16\nu\pi^2}{CL}\left(\frac{x}{L}\right)\right] \qquad (D.1)$$

where, ν is the kinematic viscosity of water, C is the waves celerity. Throughout the simulations with different cell sizes it was observed that steady waves were obtained when size of the square cells were 5 cm. However, over 10% of the wave height was lost at the end of the wave tank (5 m or the left boundary). As the mesh was refined, the wave height attenuation was reduced but waves become unsteady Figure D.4 shows that the results are considerably improved when the mesh is refined to 1 cm cells. The wave attenuation is reduced to less than 10% at 4L and steady waves are obtained along 30 wave periods. Yet, the wave heights are still less than the ones measures at the same stations of the physical wave tank.

In Figure D.5a the phase diagrams of numerical simulations with two mesh sizes with 5 cm cells and 1 cm cells are compared with the experimental results and analytical solution. The plots are generated by overlaying 20 waves after steady state is reached.

The numerical simulations with 1 cm mesh size compare better with the experimental results. It is also seen from the figure that wave crests are flatter in both laboratory and numerical waves. This is because of the nonlinear effects which are ignored in linear wave theory. In Figure D.5b the phase diagrams at sections $x/L = 0$, 1 and 4 are compared with the linear wave theory for the mesh with 2 cm cell size. The wave pattern does not change significantly after they leave the source region. There is a slight difference between the troughs of the waves at $x/L = 1$ and 4 but the wave crests remain the same after they become steady. It can be concluded that steady waves can only be generated with relatively coarse grid but this causes the waves to be dissipated with excessive numerical damping. Refining the mesh up to 1 cm square cells reduces the numerical wave attenuation and the generated waves match the real waves better.
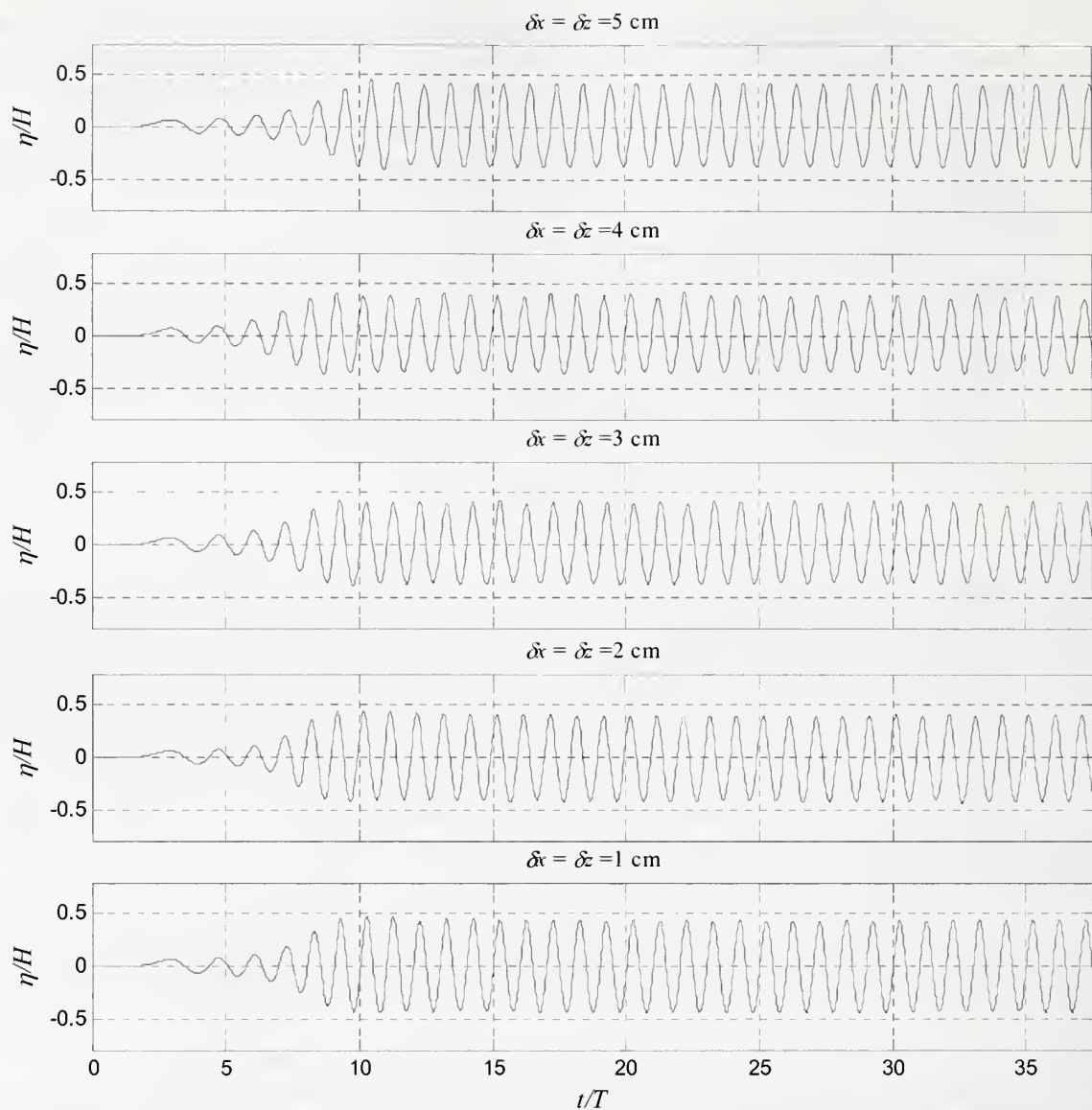
Figure D.2 The comparison of water surface profiles at 4*L* downwave of the wave generator for different grid sizes.
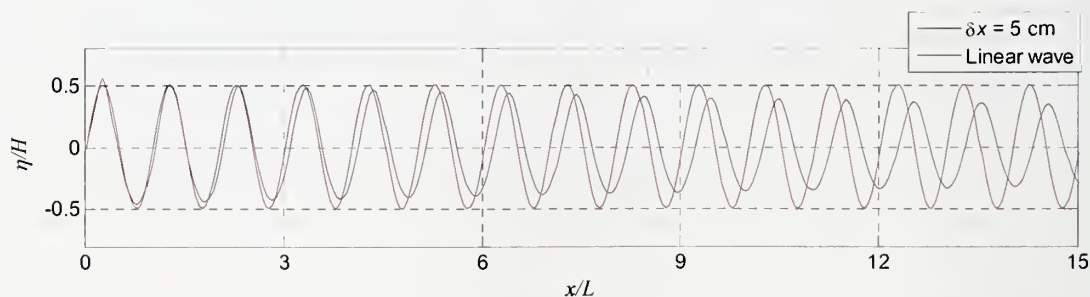
Figure D.3 Phase comparison of the numerical simulations with linear wave theory and experiments ($T = 0.8$s, $H = 30.0$ mm, $kh = 2.9$, $H/L = 0.03$).
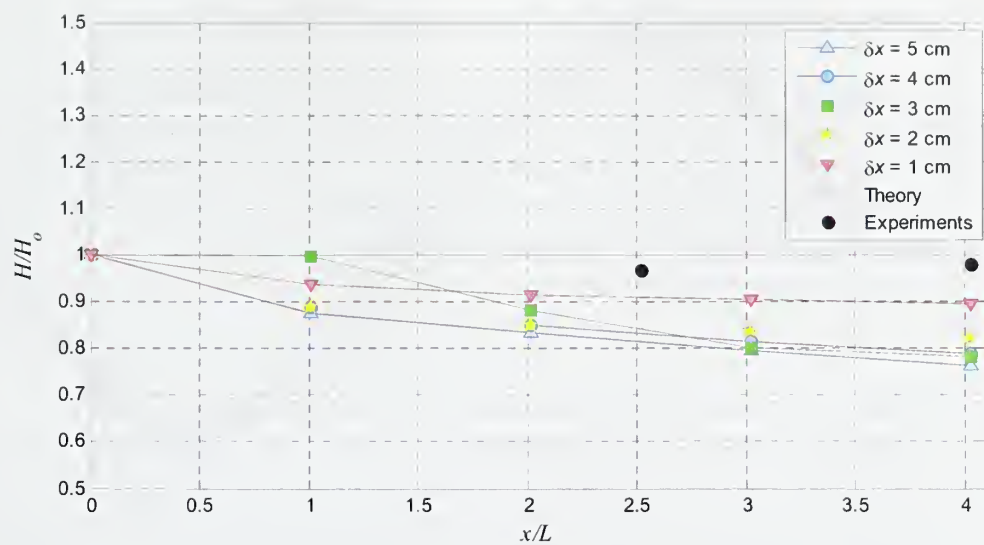
Figure D.4 The wave height attenuation for different computational cell sizes. H_i is the wave height at the source.

(a)

(b)
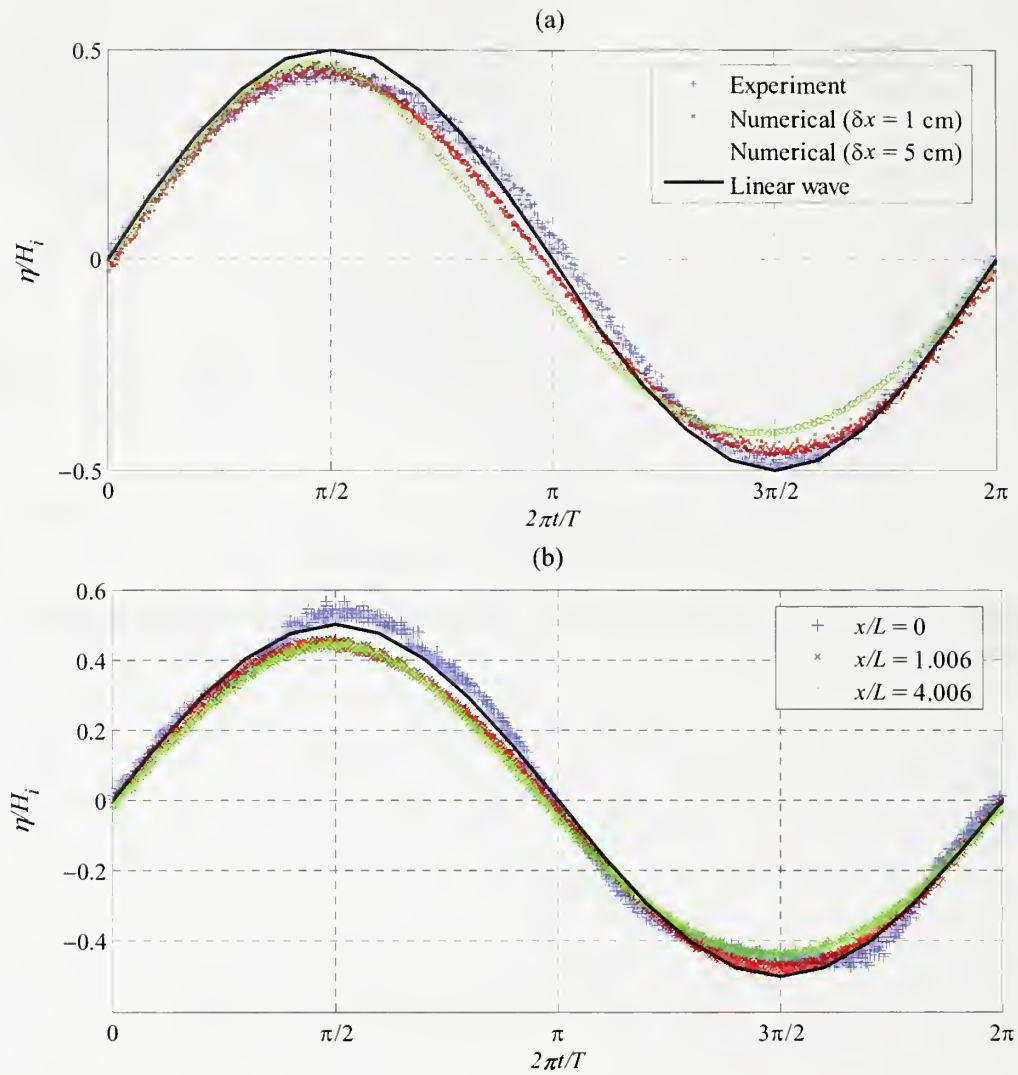
$T = 0.8$s, $H = 30.0$ mm, $kh = 2.9$, $H/L = 0.03$

Figure D.5 (a) Phase comparison of the numerical simulations with linear wave theory and experiments at $x/L = 4$, (b) Comparison of waves at three different section of the numerical wave tank.

E. OPEN BOUNDARY TREATMENT IN THE NUMERICAL WAVE TANK

To test the outflow boundary condition a rectangular regular mesh was generated in the computational domain described above. The sizes of the rectangular cells used for the simulations were $\delta x = \delta z = 1$ cm. As a control, the computational domain was extended to 40 m and the outflow boundary condition was applied along the right boundary at the end of the domain. The structured mesh with square elements was kept the same between 0 and 5 m as in the previous case. For both cases the wave height was 3 cm, wave period 0.8 s and the water depth was 46.6 cm corresponding to a wavelength of 1 m. The total computation time was 30 seconds.

In Figure E.1 the water level variation at the left boundary (x=0) is compared for 5 cm cells between 0 to 15 m in case of extended domain (a) and outflow boundary at 5 m (b). It was observed that when the outflow boundary condition is applied at the right boundary, although the generated waves inside the domain were steady, the mass conservation was not satisfied during the simulation time. As shown in Figure 2a, the mean water level dropped considerably after 40 periods. The results were similar at other sections within the numerical domain. Therefore, the extended numerical domain was utilized for rest of the simulations.
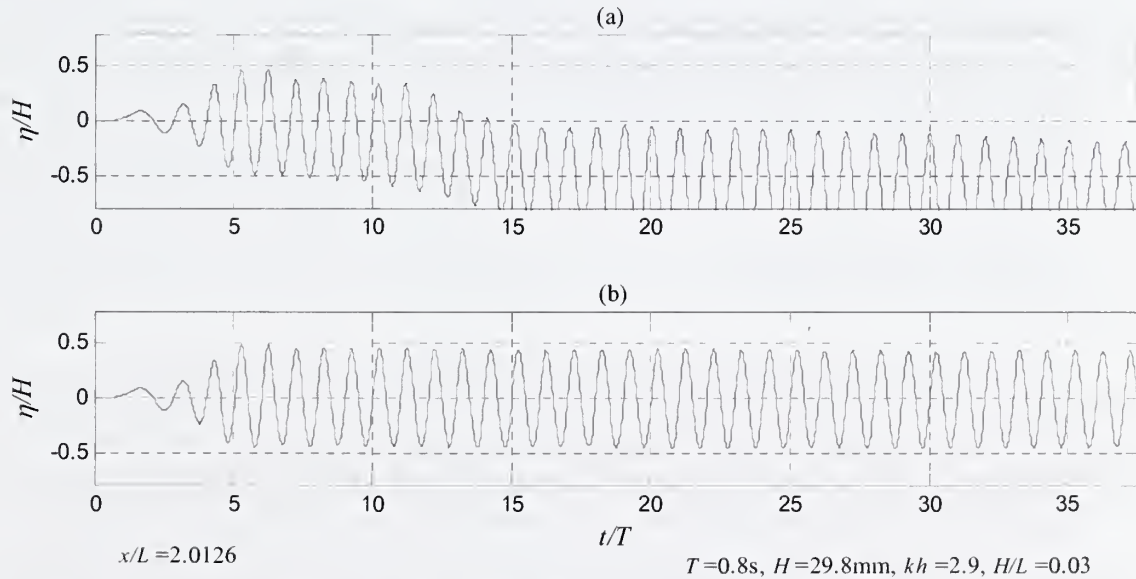
Figure E.1 The time history of the water surface elevation at x=0 compared for (a) outflow boundary condition at x=15 m and (b) 40 m long domain with stretched grid between 5 m and 40 m. The cell sizes $\delta x = \delta y = 1$ cm.

F. VALIDATION OF NUMERICAL WAVE GENERATION METHOD

A mass source was used to generate regular and irregular waves. It is possible to define mass sources inside the computational domain with the existing solver. But, an unsteady mass generation can only be defined by tabular data with limited number bands. Therefore, instead of using the standard software, the time dependent mass source function was directly coded into the existing solver. The custom developed FORTRAN subroutines allowed to update the amount of mass generation and data input/output at user defined locations and times. The user has to prepare an ASCII, "wave.inp", that contains the necessary information for wave generation and data output. A GUI is designed in Labview to set the wave conditions and to create the input file. The computational domain layout is shown in Figure F.1.

The amount of mass generation was controlled with the new method which was presented in Section 7.4. The amount of the mass generated per unit time should be equal to the horizontal component of the velocity to satisfy the continuity. The required velocity distribution along a vertical line can be approximated using the linear wave theory or Stokes 2nd order wave theory. Only linear wave theory was considered in the current study. In FLOW-3D the mass is generation region is defined by inserting a solid component. The porosity of the component is set to be equal to 1.0 to avoid blocking the the flow field. The width of the source region is equal to the width of the component. The source field extends all the way from the top of the domain to the bottom. The total mass generated per unit time is multiplied by the initial value of the VOF function to limit the mass generation to only wetted cells. The total mass to be generated is redistributed along the source region at each time step according to the water depth at the current time step.

F.1.   Regular Waves

A series of tests were carried out with the source wave generator to demonstrate the suitability for the generation of regular and irregular waves. The results are compared with the linear wave theory. The first set of tests was performed with linear monochromatic waves in numerical wave tanks with a source region at the center. The main part of the domain, the numerical wave tank was 10 m long and 0.6 m deep divided in a uniform Cartesian grid with δx = 1 cm and δz 1cm square cells. Numerical dissipation zones were added at both ends of the numerical wave tank to avoid reflection of the outgoing waves. The length of each dissipation zone was 40 m and the computational grid was stretched from δx =1 cm to 25 cm x-axis along these regions (Figure F.1). The Sommerfeld radiation condition was applied along the left and right boundaries at the end of each dissipation zone. The time step size was controlled by the stability and convergence conditions described in Section 7.3.9. The rectangular source region was between x = -1.5 to 1.5 cm and z = 0 to 60 cm. The 3 cm span covered 3 columns of cells along x-axis. The total simulation time was 20 s.
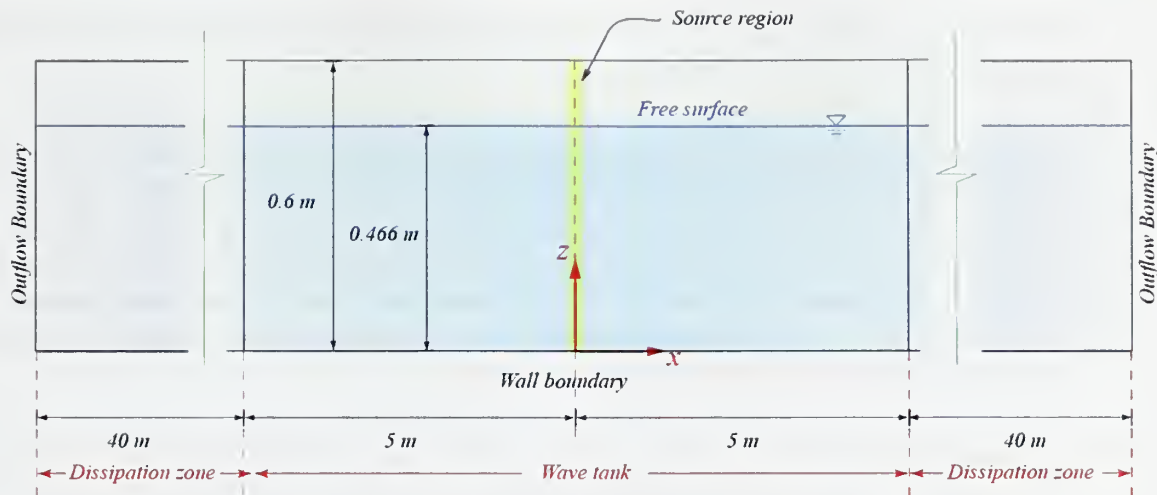
Figure F.1 Definition sketch of the numerical wave tank for wave generation verification.

Several numerical simulations were carried out using the same domain and source function described above. Figure F.2 shows the water surface profiles at different times of a typical simulation with wave period $T = 0.8$ s, wave height $H = 3$ cm and at a constant water depth, $h=0.466$ m. This corresponds to a wave steepness, $H/L = 0.03$ and relative depth, $kh = 2.9$. Two waves are formed progressing in opposite directions. It was observed that for this particular case, after 15 wave periods the waves become quasi-steady. The water surface matches with the linear wave theory even at the source region. It is also observed that the waves gradually get smaller as they progress away from the generation zone. As noted in the previous section, this is due to the dissipative nature of the first order approximation of the advective terms. Nevertheless, the numerically generated waves compare well with the linear theory throughout the computational domain.

It was observed that at higher values of wave steepness the waves slightly degenerate as they move away from the source region. This is mainly caused by the lower order approximation of linear wave theory in which the wave height is not considered in dispersion relation. A similar result is also noted in Lin and Liu (1999). But it should be noted that although there is a slight shift in comparison with the analytic solution the same nonlinear effects should be expected in the real waves. Moreover, the transfer function that controls wave paddle motion in the physical wave tank is based on linear wave theory. It will be shown later in this section that the numerically generated waves compare fairly well with the physical waves.

In Figure F.3 the fixed point water surface elevations are compared at several sections of the numerical wave tank. It was observed those steady waves are generated at all sections after the 14th wave period. At the source region ($x/L = 0$) the wave crests are above $H/2$ and the wave the troughs are below $-H/2$, which indicates a deviation from

linear theory. As they propagate they become sinusoidal a short distance away form the wave generator.

The velocity profiles under the wave crests and troughs corresponding to horizontal and vertical velocity components are plotted at different locations and times and compared with linear wave theory in Figure F.4. The numerical tests confirmed well with the theory after the wave propagation reached a quasi-steady state throughout the domain. It is also shown that both of the velocity components are almost identical to the velocity components computed using linear wave theory at the generation region and in the vicinity of it. The waves can be considered as linear practically everywhere within the wave tank after a quasi-steady state is reached.

$T = 0.8s$, $H = 30.0mm$, $kh = 2.9$, $H/L = 0.03$
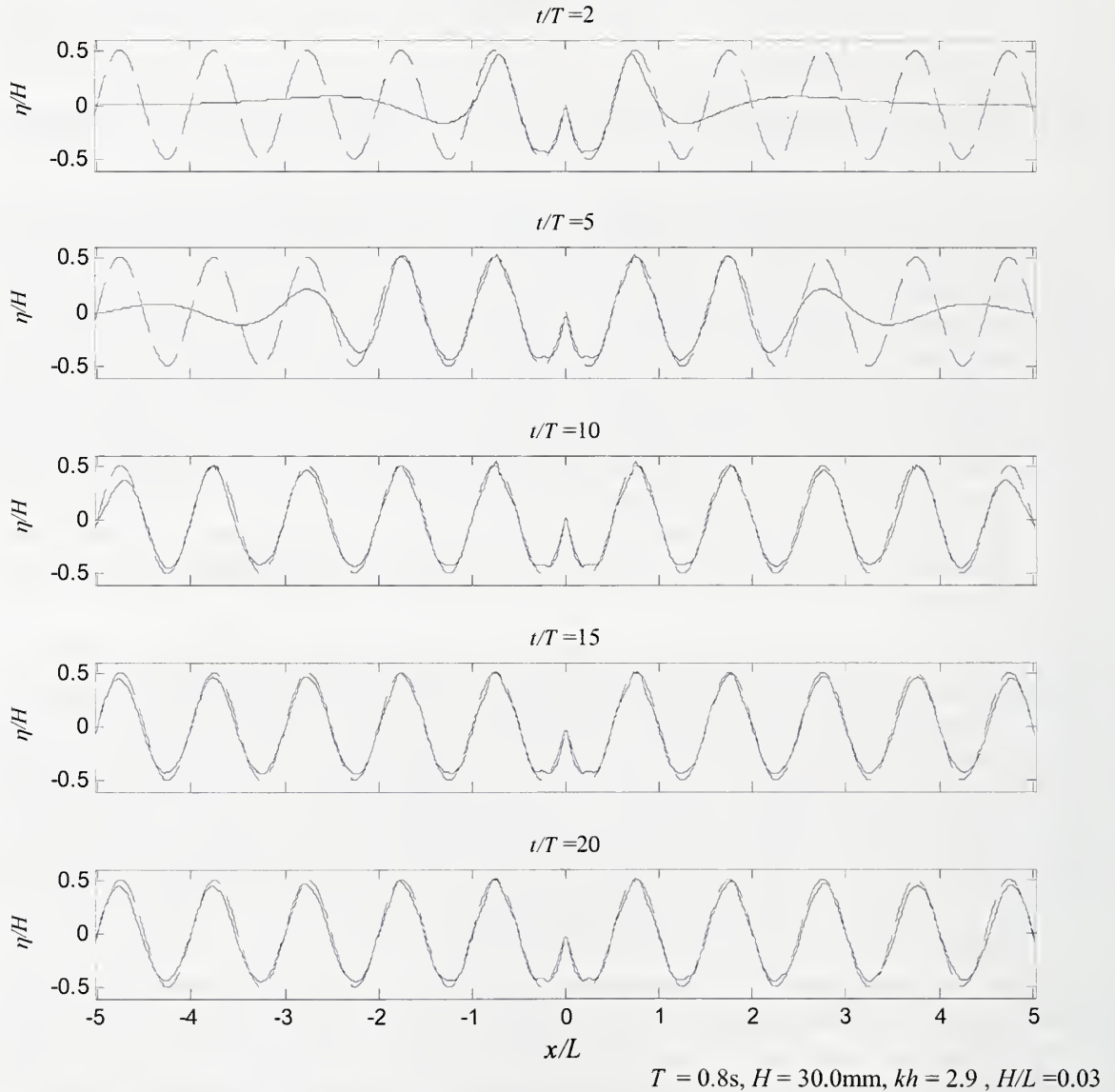
Figure F.2 Comparison of numerical results (solid line) with linear wave theory (dashed line) of two progressive waves. The source region is at $x/L = 0$.

$x/L = 0$

$x/L = 1.0063$

$x/L = 2.0126$

$x/L = 3.0189$

$x/L = 4.0252$
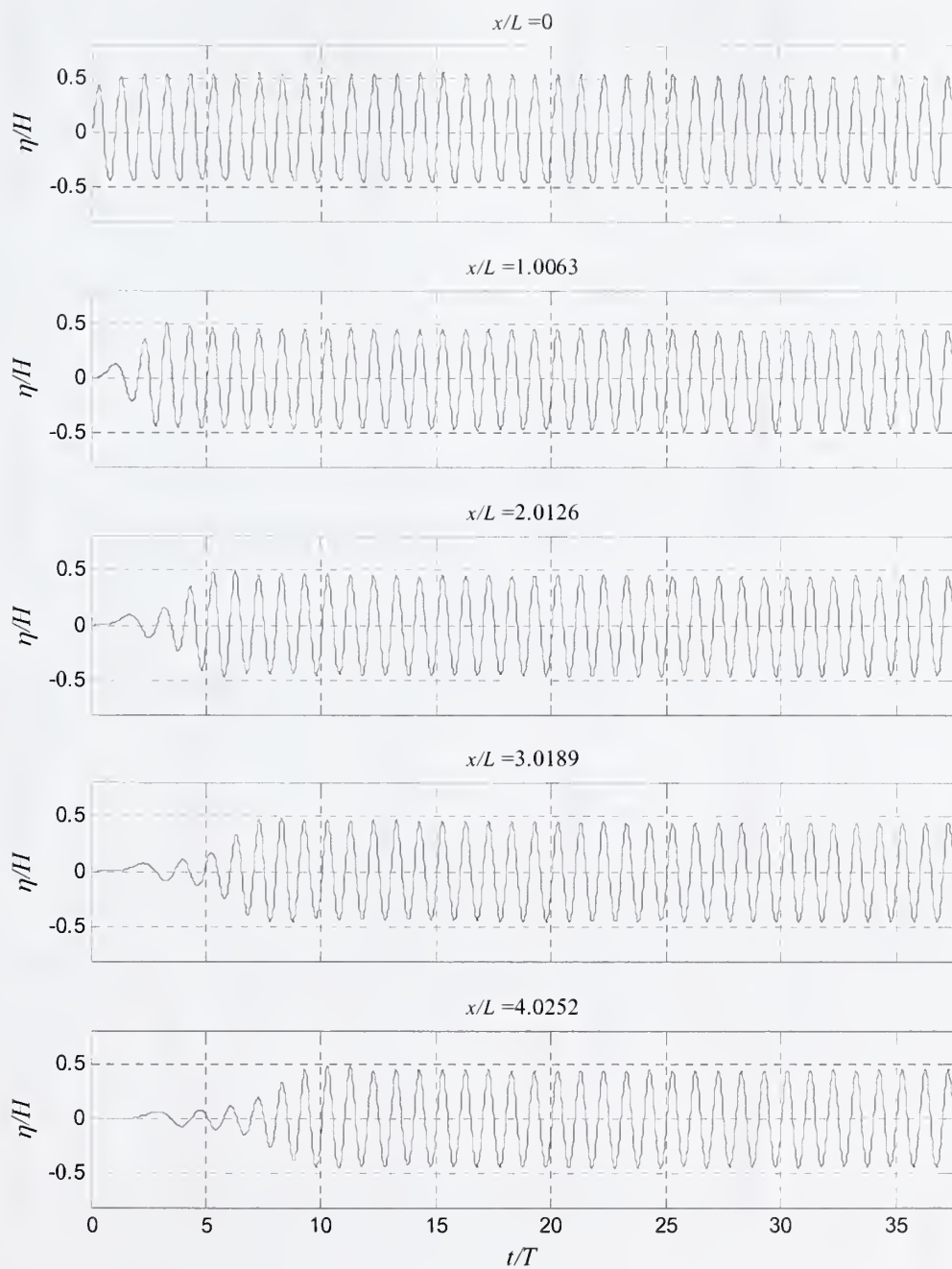
$T = 0.8$s, $H = 29.8$mm, $kh = 2.9$, $H/L = 0.03$

Figure F.3 The change of water surface elevation at 6 sections along the numerical wave tank throughout the simulation period.
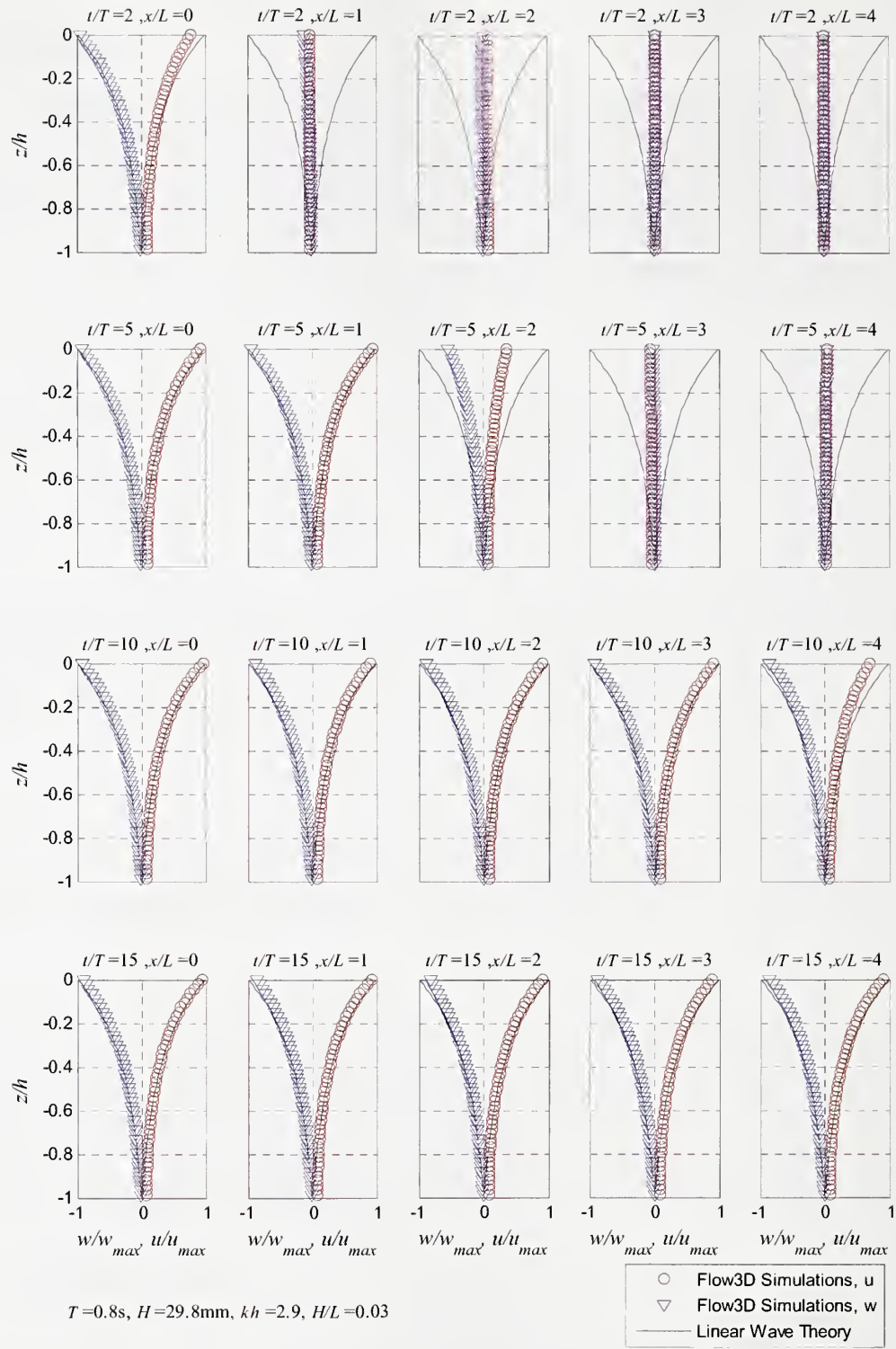
Figure F.4 Comparison of the vertical and horizontal velocity (u and w) distributions between the numerical wave tank and the analytical solution with linear wave theory. Note that v/v_{max} is at $x/L+3/4L$ and w/w_{max} is at $x/L+1/2L$.

In Figure F.5, ten water surface profiles with a delay of $t/T = 0.1$ between them are overlaid on each other after 40 wave periods. The wave steepness is kept small ($H/L = 0.01$) to avoid wave breaking and to minimize nonlinearities. As seen in Figure F.5, the reflected waves from the wall form pure standing waves in the region between the wave generation and the wall. In the region between the open boundary and the wave generation source, a wave group composed of two monochromatic wave trains of the same wave height and period propagate in the same direction and with some phase difference between them. The nodes of the standing waves are close to 1 ($|\eta|_{max} / H \cong 0.5$), which indicates perfect reflection from the wall. Moreover, the reflected waves pass through the source region without being affected which indicates that there is no significant reflection from the source region. Another implication is that the amplitude of the wave group on the left is almost constant, which shows that the waves leave the computational domain freely through the open boundary.

It is shown that the new wave generation method can be effective for the simulation of floating breakwaters where there will be some reflections from the model. Instead of using a very long domain to minimized the influence of these reflected waves on the results, a smaller domain can be safely used which significantly reduces the computational cost by reducing both the number of cells and the computational time.

The internal wave generation techniques described in several studies are suitable only in intermediate or shallow water depths. Using the new procedure described here, it is possible to generate waves in deepwater conditions as well as shallow and transitional ranges.
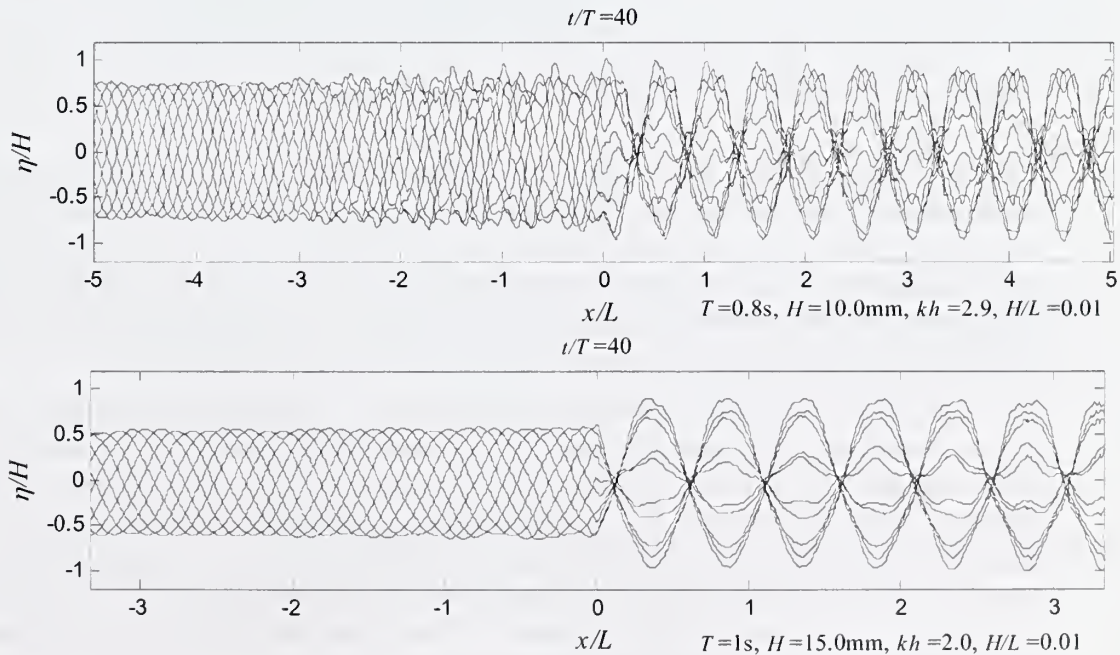
Figure F.5 The envelope of reflected waves from a rigid wall for two different wave conditions at t/T=40. The left boundary is open and right boundary is a wall.

255

To compare the numerical wave generation with the laboratory experiments, the mass source region is moved to the right boundary of the numerical wave tank. The length of the wave tank is reduced to 5 m keeping the two 40 m long dissipation zones at both ends. A second mesh block is also inserted at the section ($x = 2.395$ m - 2.605 m and $z = 0.27$ m -0.57 m) were the breakwater models will be tested as shown in Figure F.6. The cell sizes in this nested mesh block were $\delta x = \delta z = 0.5$ cm. This way, the influence of the inner mesh on the transmitted waves was also tested. The list of wave parameters for these simulations is given in Table F.1. The wave period, T, and the wave steepness, H/L, were used to change the wav conditions. The wave height was calculated from the wave steepness according to the dispersion relationship. The water depth was kept constant at 0.466 m for all of the simulations.
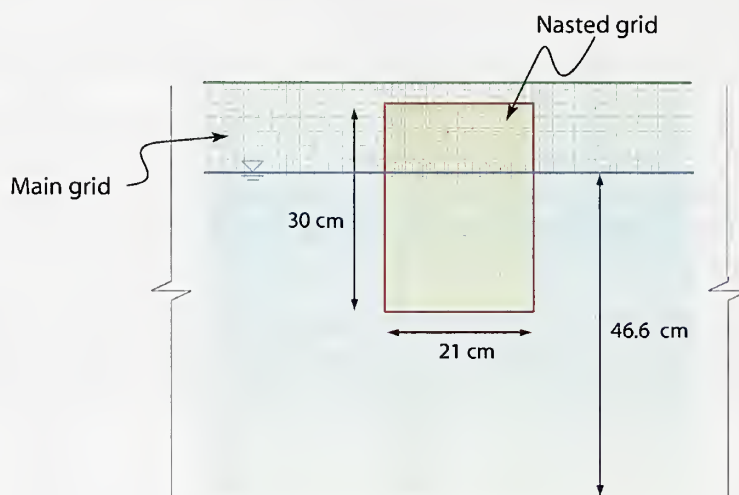
Figure F.6 A typical mesh block 60 cm high 5 m wide numerical wave tank.

In Figure F.7 the water surface elevations recorded in the numerical wave tank are compared with the experiments for three different wave conditions. The first two figures are at a distance of 4 m away and the third one is 2.5 m away from the wave generator. It can be seen from these plots that the numerical waves were in good agreement with the actual waves for the presented wave parameters. There is no significant phase difference between the two wave trains and the energy fronts match reasonably well.

In Figure F.8 the dimensionless wave heights calculated in the numerical wave tank are compared with measurements for four wave steepnesses. The wave heights were measured at $x = 3.9$ m in the numerical wave tank and 13.9 m in the physical wave tank. The wave height attenuation increases as the waves get steeper in the numerical wave tank. It is shown that up to $H/L = 0.05$ the numerical results are in reasonably good agreement but when the steepness increased to 0.08, the simulations do not reflect the real case correctly. These plots were used to identify the amount of numerical dissipation in the simulations with the breakwater models.

Table F.1 The list of simulations without the models installed. Check marks indicate the conducted runs and crosses stand for the skipped runs.

| $\dfrac{H}{L}$	T (s)							
	0.5	0.55	0.6	0.7	0.8	0.9	1.0	1.2
0.02	✗	✗	✓	✓	✓	✓	✓	✓
0.03	✓	✓	✓	✓	✓	✓	✓	✓
0.05	✓	✓	✓	✓	✓	✓	✓	✗
0.08	✓	✓	✓	✓	✓	✗	✗	✗
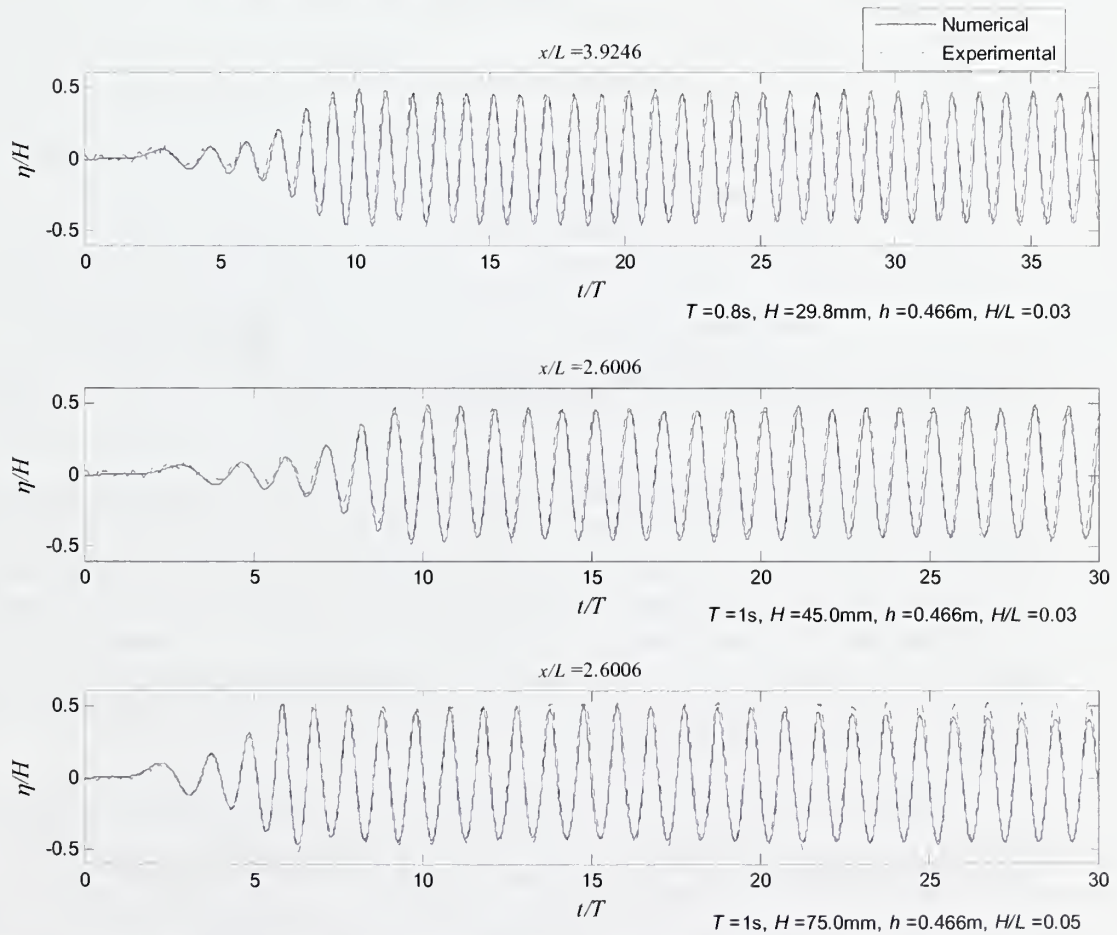
Figure F.7 The envelope of reflected waves from a rigid wall at two different wave conditions at t/T=40. The left boundary is open boundary.

257
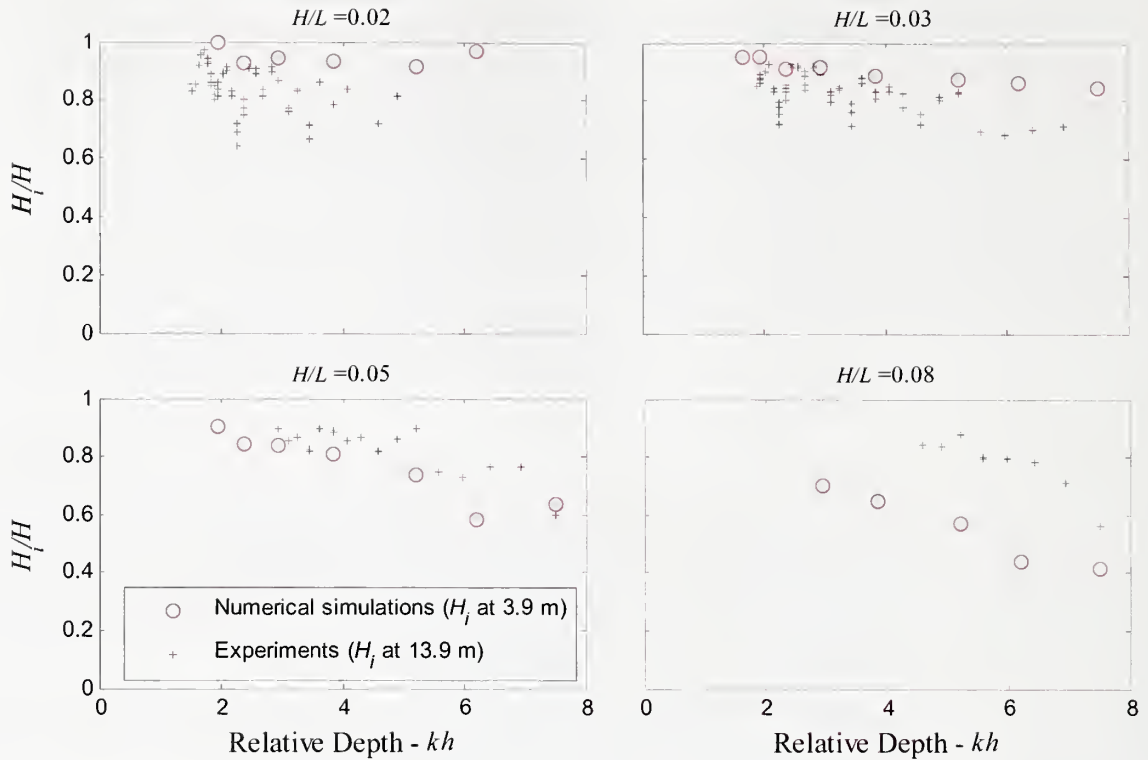
Figure F.8 The wave height readings of numerical and experimental wave tank for the range of simulated wave parameters. H_i is the input wave height.

Additional tests were made to compare the new method with the mass source function given in Lin and Liu (1999). The source function given by Lin and Liu (1999) is coded into FLOW-3D to compare the results. It is observed that the new method which considers the velocity distribution over the depth is more efficient for deep water waves and steeper waves. It was observed that the source region has to be moved closer to the surface to be able to generate steeper waves as noted in Lin and Liu (1999). The new method solves these problems since the rate of mass generation is automatically adjusted according to the velocity distribution.

Another aspect that has to be considered is the horizontal span of the source region. The horizontal variations of the velocity under the wave are not included into the model. The horizontal span has to be small compared to the wavelength for this assumption to be valid. On the other hand if the span is too small, the amount of mass generation per unit length at certain times becomes too large leading to numerical errors. After a series of test with various wave conditions it is suggested to set the source width greater then 1 cm to avoid these errors. It is not required to have the source region match the boundaries of the computational cells. It was observed that using a smaller time step reduced the noise but leads to excessive damping. The free surface stability limit is also a good way to limit the time step size. When the time step size is reduced the profile becomes smoother but the waves are over damped and get longer.

F.2. Irregular Waves

Irregular waves can be approximated by a discrete wave energy spectrum with a finite number of frequencies. The details of irregular wave generation were explained in Section 3.3.3 and the implementation for the current method was presented in Section 7.4. Irregular wave generation with the current method was tested through a series of simulations (Table F.2). The JONSWAP spectrum corresponding to a wave height, H_{mo} and peak wave period, T_p. The portion of the wave spectrum within 2% of the peak frequency energy level was divided into 100 frequencies to generate the random wave signal.

Table F.2 List of simulations with irregular waves.

$\dfrac{H_{mo}}{L_p}$	T_p (s)					
	0.6	0.7	0.8	0.9	1.0	1.2
	H_{mo} (mm)					
0.03	16.9	22.9	29.8	37.2	45.0	60.5
0.05	28.1	38.2	49.7	62.1	75.0	×

Table F.3 Random wave experiments in the laboratory wave tank.

Water depth	Peak period	Wave steepness	Relative depth
h (mm)	T_p (s)	$\dfrac{H_{mo}}{L_p}$	kh
446	0.6 – 1.2 0.6 – 1.2 0.6 – 1.0 0.6 – 1.0	0.02 0.03 0.04 0.05	1.3 – 6

The numerical results are also compared with the experimental results that were obtained in the physical wave tank. Waves were generated with a flap-type wave generator which was driven by a belt drive (Figures 4.13 and 4.14). Another computer program was developed to move the wave paddle with a given random wave signal. The list of experiments is given in Table F.3. Each experiment was 100 s long and repeated three times with a separated set of random phases. The data were collected at 9.6 m and 13.9 m away from the wave paddle with 30 Hz sampling frequency. The collected data were processed via both spectral and time domain analysis with the same procedures used as with the numerical model. Each experiment was analyzed in three overlapping windows.

In Figure F.9 the analytically calculated free surface profiles are compared with the numerical solutions at the source region ($x = 0$) for three different wave periods, T_p

and the corresponding wave heights, H_{mo}. It is seen form these figures that except for some local and minor fluctuations there is a good agreement between the numerical simulations and analytical solution. Also there is no significant phase difference between the waves indicating that current method can safely be used for irregular wave generation. In Figure F.10 and F.11 the spectral densities of each irregular wave train at three sections along the numerical wave tank is plotted. The data is also compared with the input JONSWAP spectrum for each run. As the waves propagate away from the source region the energy corresponding to high frequency components slightly degrease. The simulation with $T_p = 0.6$ s has the most noticeable separation compared to the other. As the peak wave period increase (hence the H_{mo} increase) the energy of the at the peak frequency is less that of the input spectrum. When the wave steepness H_{mo}/T_p is increased to 0.05 in Figure 8.11 the spectra become more scattered.

The frequency and time domain analysis of the waves are performed using a computer program developed in Labview. The each random wave signal recorded at three different section of the numerical wave tank are analyzed to obtained wave parameters including peak wave period, T_p, mean wave period, Tm, energy-based significant wave height, H_{mo} and time series significant wave height H_s. Each run is divided into three overlapping windows of 50 peak waves. The number of data points varied according to the time step size. The frequency of the data was between 60 Hz and 70 Hz (time step size, δt, 0.014 s-0.017 s) corresponding to window sizes for spectral analysis at least 2000 points.

In Figures F.12 and F.13 some of the selected spectral parameters are compared with the input values for both laboratory experiments and numerical simulations. Figure F.12 presents the plots for waves with $H_{mo}/L_p = 0.03$ and Figure F.13 includes the plots for $H_{mo}/L_p = 0.05$. The mean periods, T_m, are in good agreement with the experiments and the input waves. The peak period, T_p, shows larger scatter in both experiments and simulation. When the waves are steeper, the scatter of the peak periods increased even more (Figure F.13). This is due to the short simulation time which limits the number of samples for the frequency domain analysis. Since the mean period integral value the resulting tend is smoother compared to the peak period. The most significant difference between the expected and measured quantities in these plots is the wave height, H_{mo}, in the numerical wave tank. At 6 cm wave height the difference between the input and measured values goes up to 20%. At $H_{mo}/L_p = 0.03$ the waves do not attenuate much after they leave the source region. But, when the $H_{mo}/L_p = 0.05$, the waves attenuate as they propagate.

It is shown in Figures F.10 and F.11 that the major gap between the spectral densities of the generated and measured waves is around the peaks. The nonlinearities for these larger waves are more pronounced and therefore, these waves are not generated correctly. A higher order theory can be more accurate for those cases. The simulation can be run longer to increase the number of samples for the analysis and therefore the accuracy of the wave generation can be increased. It should be noted that after the waves leave the generation region, they yield the required wave height and peak wave period

within reasonable limits. Each simulation was run twice, one with and the other without the breakwater installed. The same random wave signal was used for these two consecutive runs.
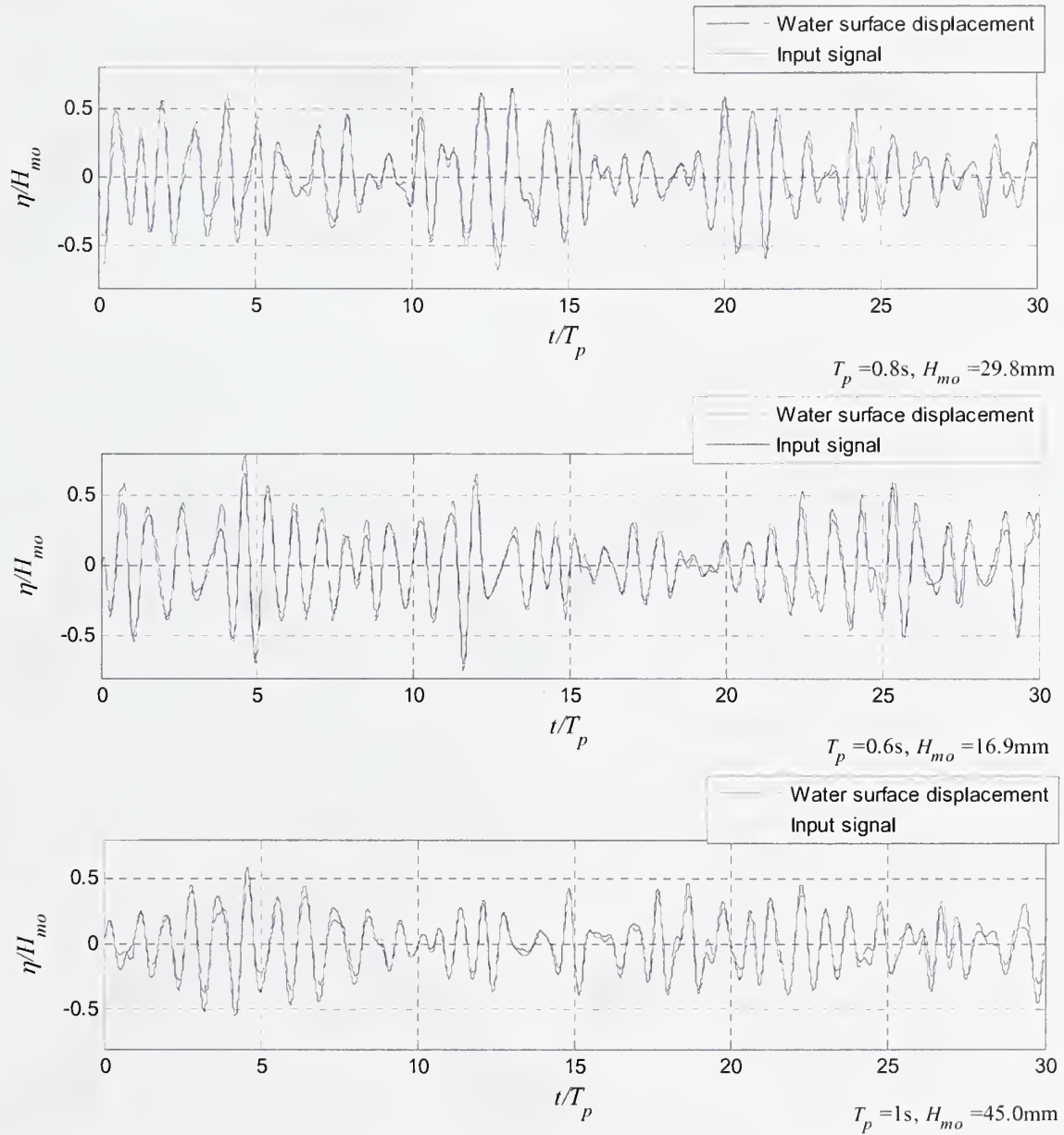
Figure F.9 The comparison of the input signal with the water surface displacement at the wave generation source.

261
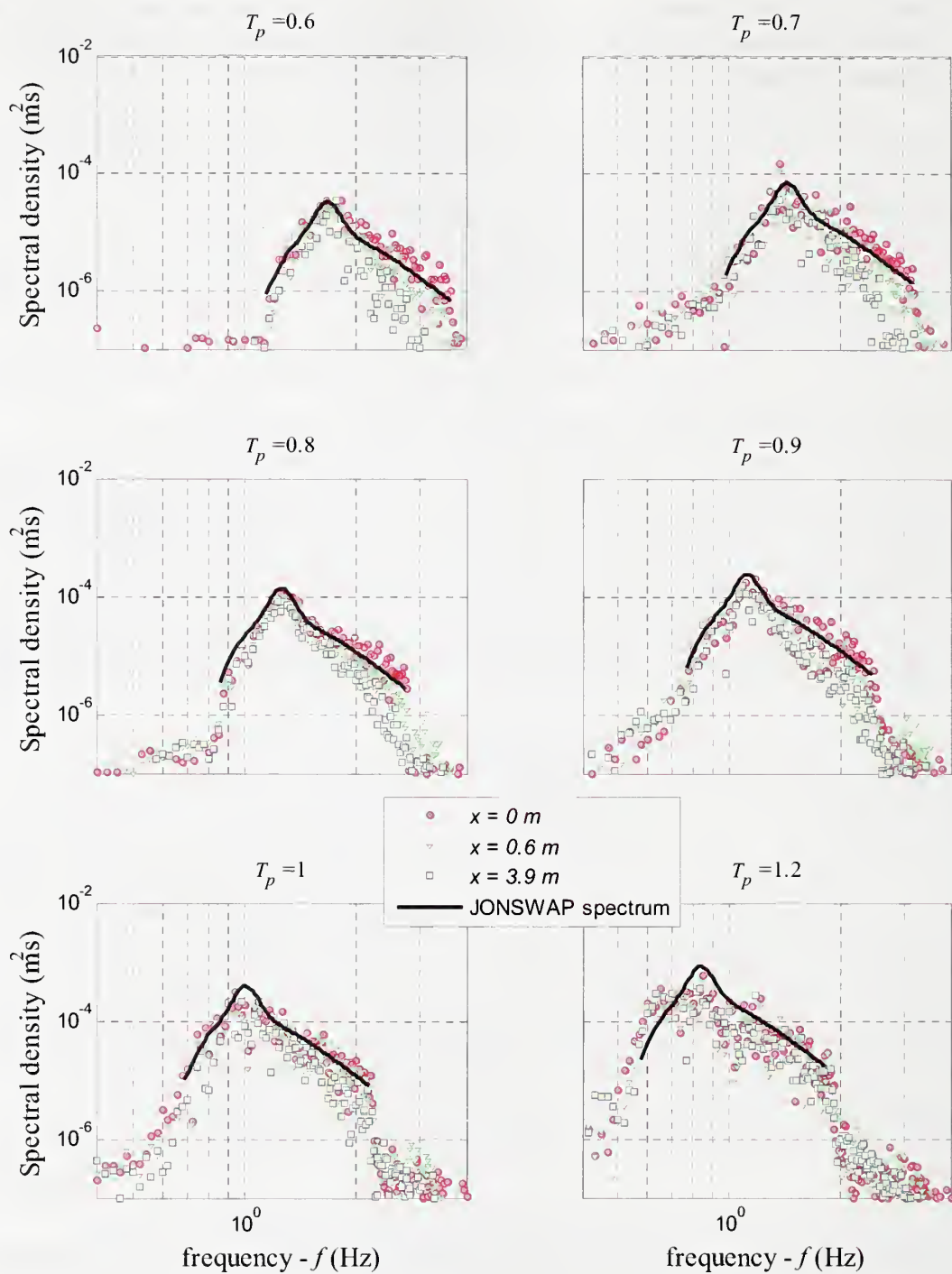
Figure F.10 The recorded wave spectra at stations x = 0, 0.6 and 3.9 m of the numerical wave tank for 100 wave periods compared with the JONSWAP spectrum with the same H_{mo} and T_p (H_{mo}/L_p, = 0.03).
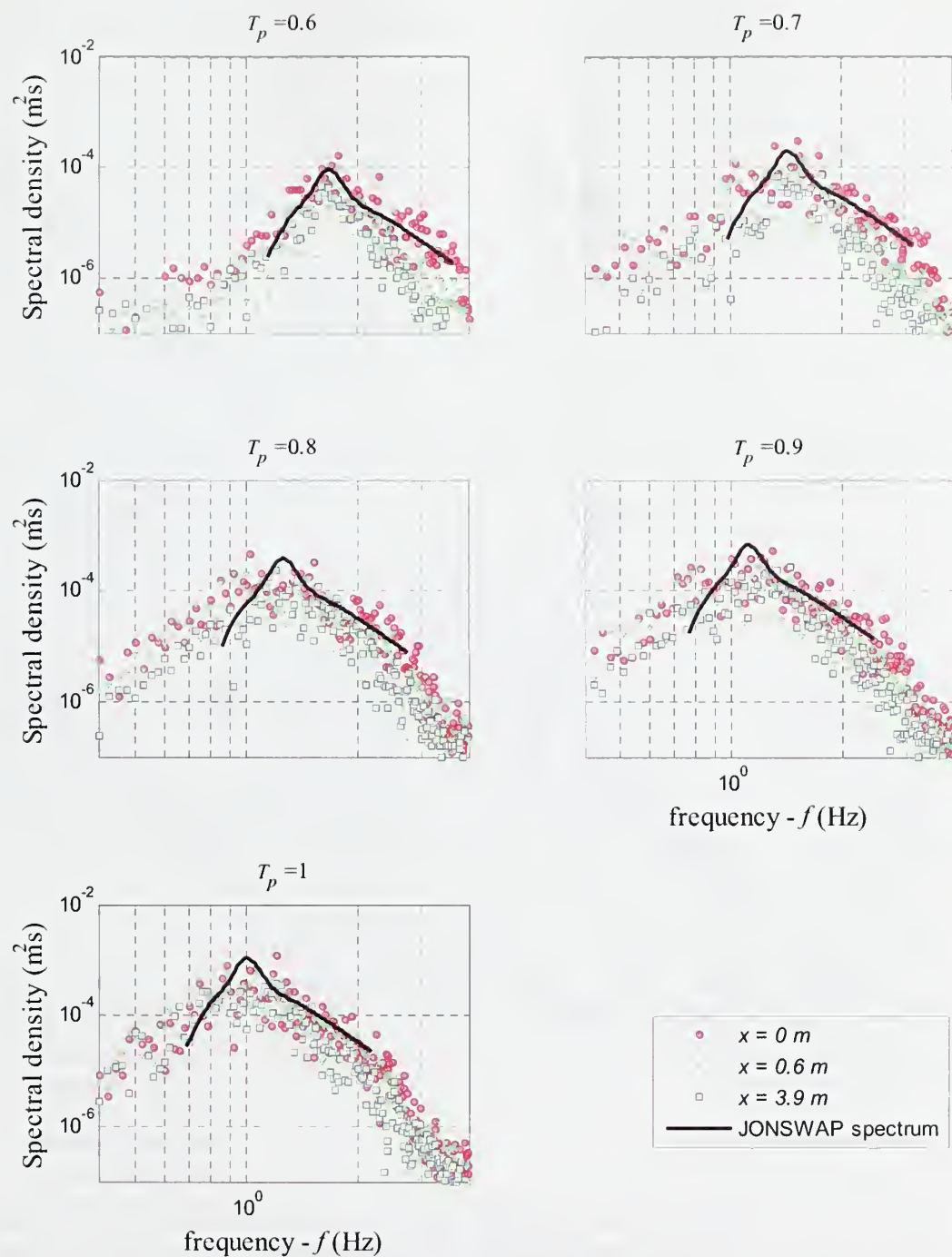
Figure F.11 The recorded wave spectra at stations x = 0, 0.6 and 3.9 m of the numerical wave tank for 100 wave periods compared with the JONSWAP spectrum with the same H_{mo} and T_p (H_{mo}/L_p, = 0.05).

263
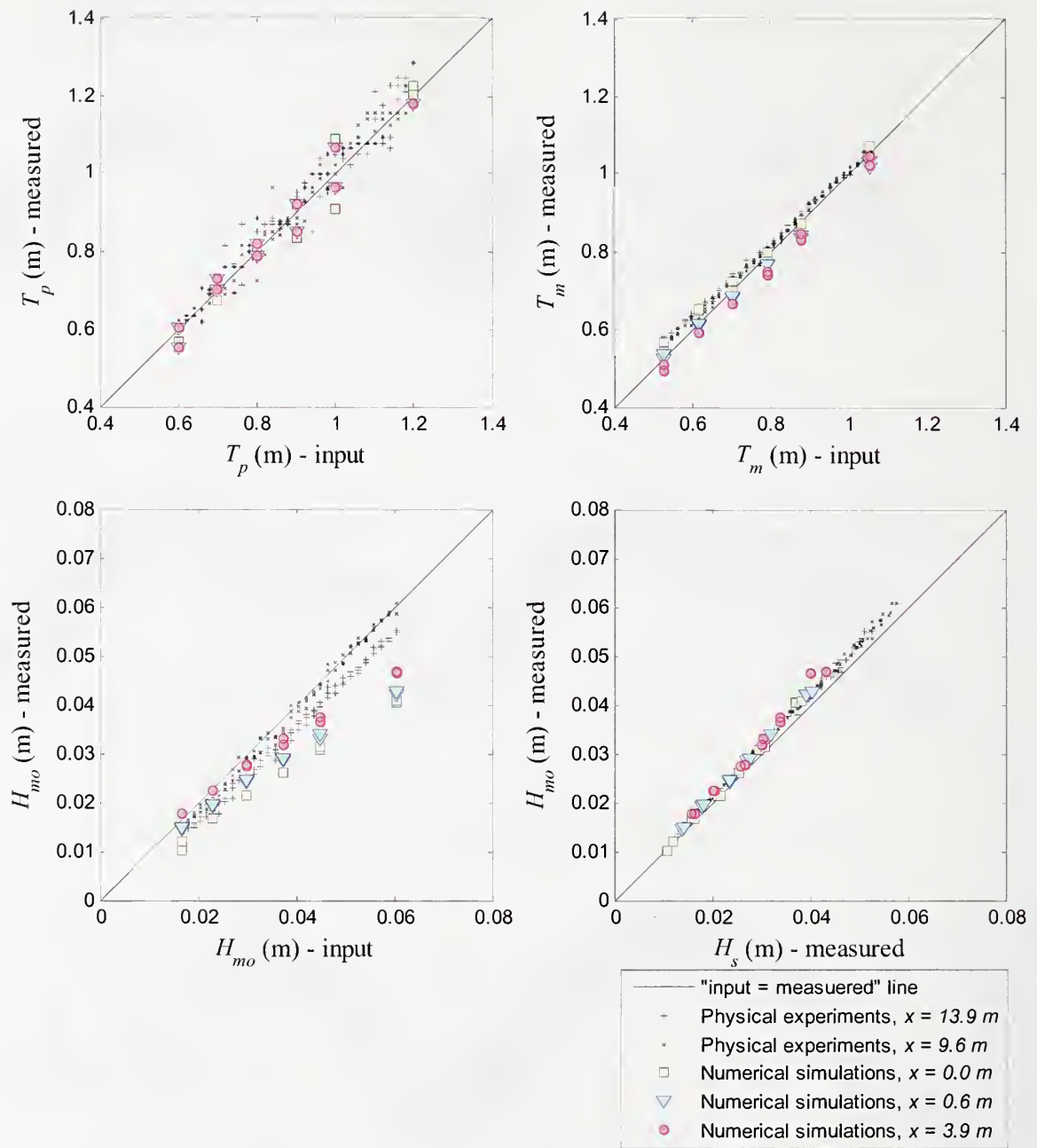
Figure F.12 The bulk properties of the irregular waves generated in the numerical and experimental wave tank are compared with the input wave parameters, peak period, T_p, mean period, T_m and significant wave height, H_{mo}. The last figure compares the spectral estimate of the wave height, H_{mo} and time series evaluation of the significant wave height, H_s. (see Chapter III). $H_{mo}/L_p = 0.03$ for all runs.
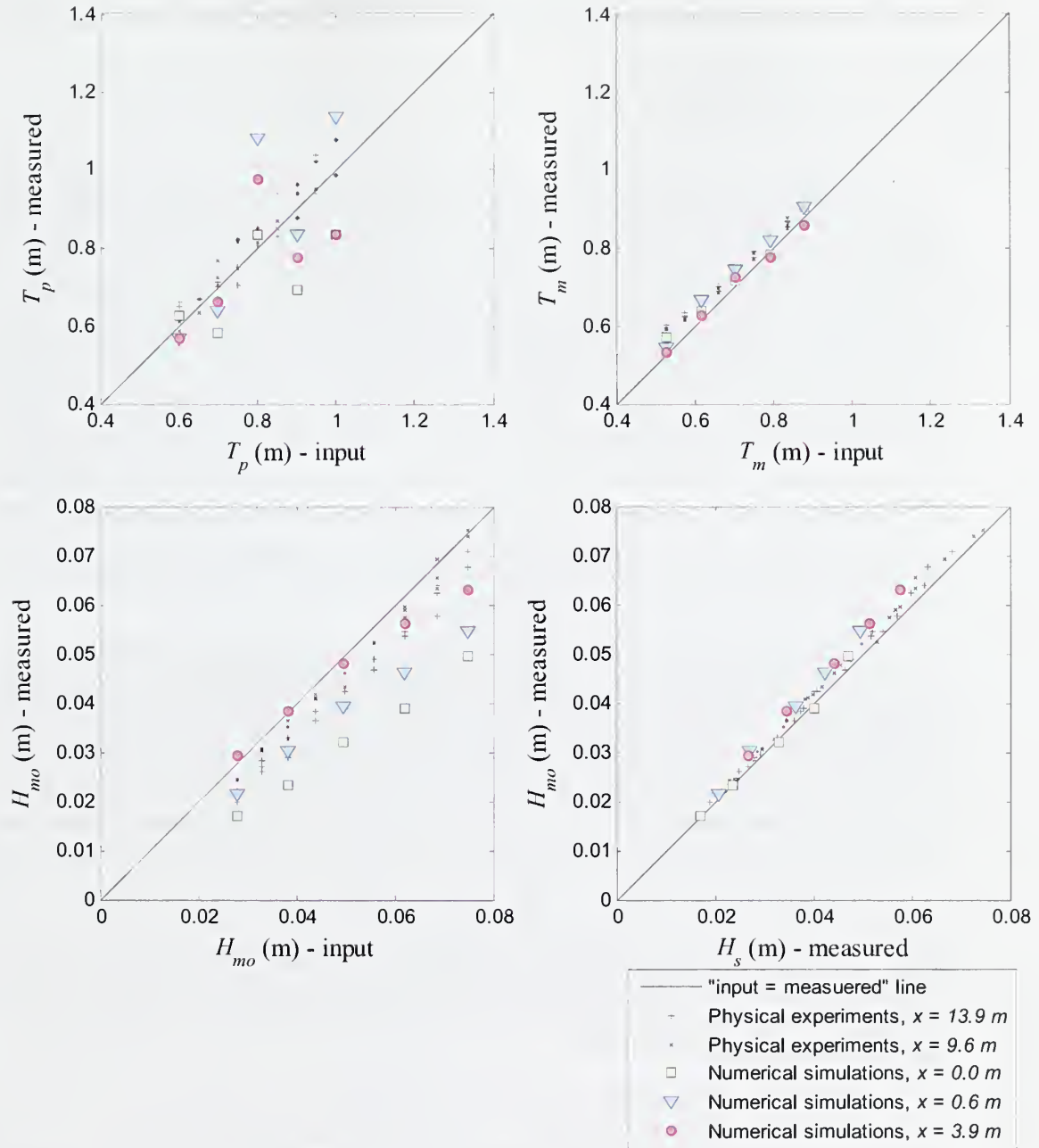
Figure F.13 The bulk properties of the irregular wave generated in the numerical and experimental wave tank are compared with the input wave parameters, peak period, T_p, mean period, T_m and significant wave height, H_{mo}. Last figure compares the spectral estimate of the wave height, H_{mo} and time series evaluation of the significant wave height, H_s. (see Chapter III). $H_{mo}/L_p = 0.05$ for all runs.

G. WIND WAVE PREDICTION

G.1.   Introduction

The energy transferred to the water surface by wind generates a range of wave sizes that increase in height and period as the waves travel across the available fetch length. The process of wave generation by wind can be explained by combining the resonance model developed by Philips (1957) and the shear flow model by Miles (1957). Pressure fluctuations within the wind field disturb the still water and cause water surface undulations. These pressure fluctuations moving in the direction of the wind resonate with the free wave speed and amplify the undulations. As the size of these undulations increase, they begin to affect the pressure distribution within the wind field, resulting in a pressure difference between two wave crests. The net force created by the higher pressure on the windward face of the wave results in wave growth. Another explanation for the energy transfer between wind and waves was developed by Longuet-Higgins (1969). As the wave heights increase, shorter waves steepen and break on the crests of faster travelling, longer waves. Therefore, as the velocity, fetch, or duration of the wind increases, wave height and period also increase.

If the wind blows with a constant speed and direction over a certain fetch for sufficient time for the waves to travel the entire fetch length, wave characteristics will only depend on the fetch length and wind velocity. This is known as the fetch-limited condition, and it is assumed that steady state wave conditions are achieved for that fetch (Shore Protection Manual, 2003). If the wind duration is less than the required time for the waves to travel the fetch, then wave growth will be time dependent and the wave generation is described as duration limited. Ideally, the wind speed increases suddenly in an area far enough from the boundaries for the duration-limited condition to be satisfied. This condition is rarely met in confined areas. Wind blowing for an unlimited duration over an unlimited distance will have a limiting fetch length beyond which the waves do not continue to grow. This limiting condition is called a fully developed sea, and the rate of energy input to the waves from the wind is balanced with dissipation by wave breaking and turbulence (Sorensen, 1993).

Due to the complexity of the physical phenomena, methods for wave prediction are based on semi-empirical relations. The methods have been modified as wind and wave data were accumulated over time, resulting in better predictions. The significant wave method (SMB method) was developed by Sverdrup and Munk (1947) and improved by Bretschneider (1952). The SMB method combined a simple energy growth concept with empirical calibrations using field data. The random behavior of the waves in nature is characterized by their spectra which provide a measure of the energy traveling at each frequency. Therefore, recent efforts seek to predict the wave energy spectrum given wind conditions (Sorensen, 1993). There are several numerical models currently available for predicting wave fields under complex wind conditions and bathymetries (Ding et al.,

2006; Lin et al., 2006; SWAN, 2007). However, the current work is intended for use by field practitioners and will be confined to a relatively simple semi-empirical model.

A parametric model to predict deep water wave characteristics is recommended in the 1984 Shore Protection Manual (SPM). The Coastal Engineering Manual (CEM), an updated version of the SPM released in 2003, contains a modified method for predicting wind-driven waves. Both the SPM and CEM methods will be considered; however, due to its better performance for the current application, only the SPM method will be modified for use in small reservoirs. New coefficients necessary for using the SPM (1984) method in small reservoirs are calculated based on wind and wave characteristics measured in Schafer Lake, an irrigation pond near Carlisle, Arkansas. The results should be applicable to inland reservoirs of similar shape and size to Schafer Lake. There were no trees or surface relief (other than the levee) nearby, so the results given here can be generalized to other lakes. If vegetation or topography creates locally reduced wind speeds in a subject lake, the method given here can yield results that may serve as an upper limit for wave size.

G.2. Brief Development of SPM (1984) Method of Wave Prediction

In the SPM (1984) method, deep water wave predictions are made using a parametric model based on the JONSWAP spectrum. The JONSWAP spectrum is a standard wave energy spectrum created for fetch limited, deepwater conditions from a large number of marine wave data sets. The SPM (1984) method yields the significant wave height, H_{mo}, and peak period, T_p, based on wind velocity. The significant wave height and the peak period can be expressed in terms of the most significant parameters as:

$$H_{mo}, T_p = f(U_A, F, t_d, h)$$ (G.1)

where U_A is the wind stress factor, F is the fetch length, t_d is the wind duration, and h is the water depth. The wind stress factor accounts for the nonlinear relationship between wind speed and shear stress and is mainly dependent on the temperature difference between air and water and the surface roughness.

$$U_A = 0.71 U_{10}^{1.23}$$ (G.2)

where U_{10} is the average wind speed at 10 meters above the mean water level.

The SPM (1984) recommends the equivalent fetch to be calculated based on the narrow spread of the energy in the wave spectrum. This procedure uses the mean of fetch lengths measured at 3° intervals over a range of 12° above and below the bearing of the average wind direction. The CEM (2003) version on the other hand suggests a straight line fetch with no correction to be used in calculations. The mean fetch defined in the SPM (1984) is used to account for the wind direction variation. This becomes more

important for small water bodies since wind at angles not normal to a shoreline will result in a range of possible fetch lengths. For example, for the field data collected in the current study a wide range of fetch lengths are within the ±12 degree range and are better represented by the average fetch length than the straight line distance from the instruments to the shoreline in the direction of the prevailing wind.

Wave prediction requires knowledge of the wind velocity near the water surface over an appropriate averaging interval. The time interval should be equal to the time needed for the waves to travel the available fetch and allow the assumption of fetch limited conditions. The averaging interval for the current data is adjusted for each data set according to the minimum duration for the waves to travel the fetch length (Table 7.1). For the March 2005 field data set, the power law given by Equation G.3a was used to estimate the wind speed at 10 m using the measured wind speed values at $z=2$ m above the mean water level.

$$U_{10} = U_z \left(\frac{10}{z} \right)^{1/7}$$
(G.3a)

For data from 2007 and 2008, the wind speed at 10 m was estimated using the data at two elevations and by assuming a logarithmic wind profile. The logarithmic wind profile is expressed for neutral conditions by

$$U_z = \frac{u_*}{k} \ln \left(\frac{z}{z_o} \right)$$
(G.3b)

where k is the von Kármán constant ($k = 0.41$), z_o is the surface roughness height, and u_* is the shear velocity. u_* and z are estimated by substituting the measured wind speed at two elevations into Equation (G.3b). Then, the wind at 10 m is estimated by using the calculated values of u_* and z. The SPM (1984) suggests the use of equation 3a in an elevation range of 8-12 m. The data from 2007 was used to compare the estimated wind velocity at 10 meters using equation 3a and 3b (Figure G.1). As would be expected, the data recorded at 6 m provided a better estimation of U_{10} than the data recorded at 1.7 m. However, Figure G.1 shows that the use of the power law to estimate U_{10} based on the 2005 data set was valid.

Table G.1 Summary of collected data.

|	Duration (min)	Wind Direction (deg. ccw from north)	Wind Speed U_{10} (mph)	Effective Fetch F (m)	Minimum duration t_{min} (min)	Averaging interval Δt (min)
Mar-05	96	309.6±14	23±3	586	17.9	13.6
Apr-07, 6b	50	182±12	10±0.6	102	7.0	9.1
Apr-07, 7b	15	316±23	7±1.2	355	21.0	15.9
Apr-07, 7c	63	3±11	6.6±0.6	355	16.1	15.9
Apr-07, 8a	64	352±9	12.1±1.8	273	12.4	15.9
Apr-07, 8b	90	327±6	13.7±12.6	327	14.4	15.9
May-08	55	185±5	12±1	315	13.7	13.7
Jun-08	2,591 (43hrs)	153±7	21.4±2	450	16	15.9
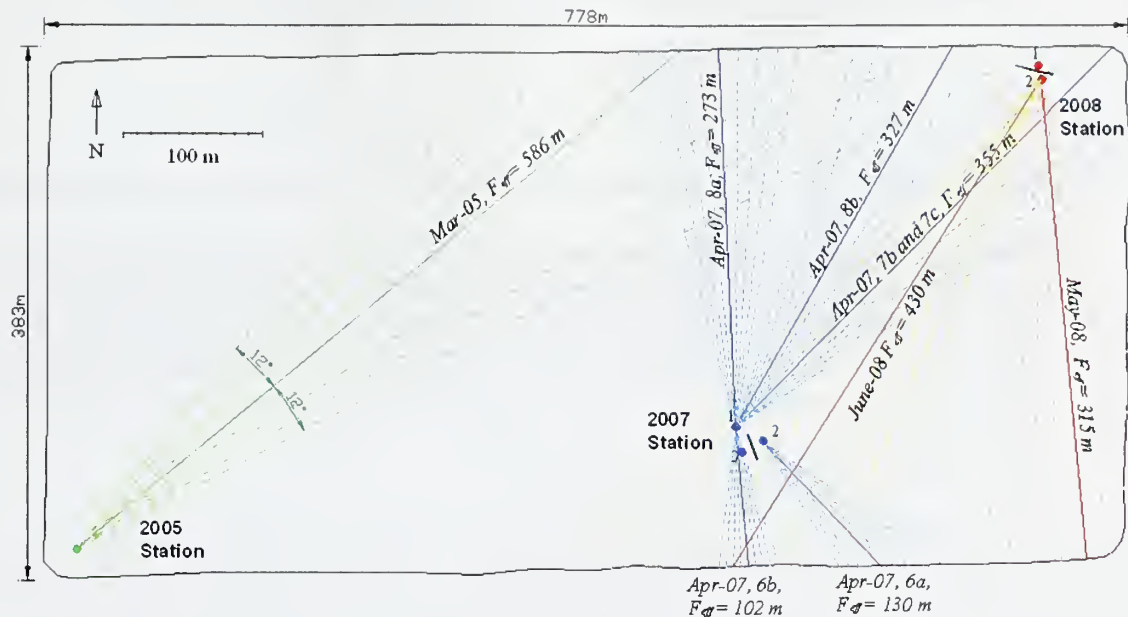
Figure G.1. The layout of the measuring stations on Schafer Lake and corresponding fetch lengths. Dashed lines are the 12° range of fetch lengths on both sides with 3° interval that has been averaged to calculate the effective fetch length.
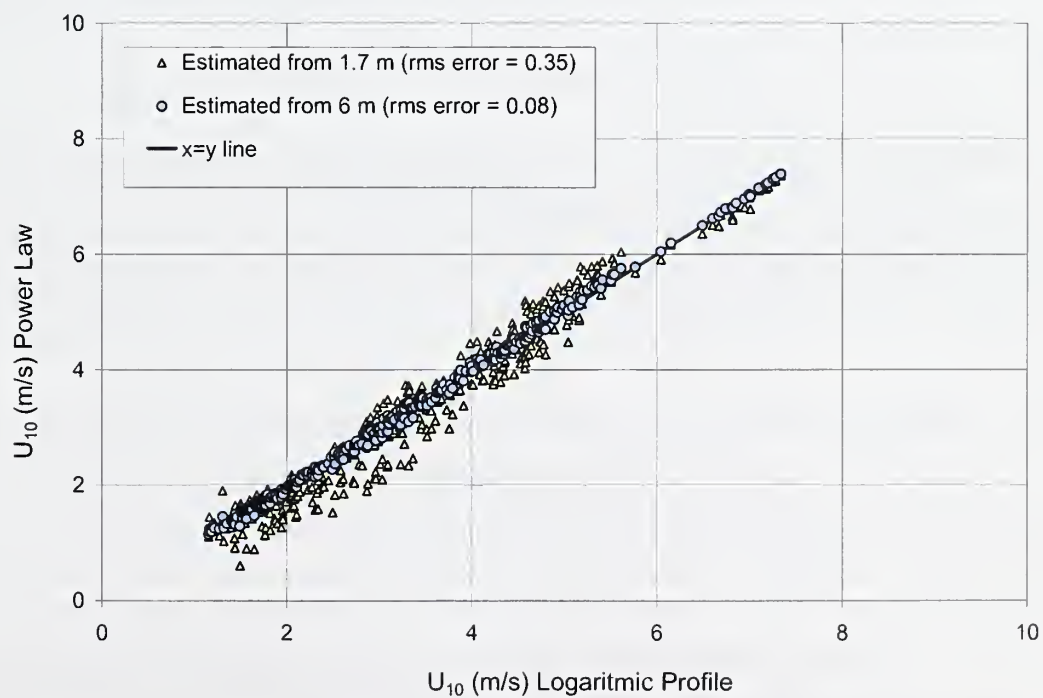

Figure G.2. Comparison of wind speeds at 10 m extrapolated by logarithmic wind profile and power law.

269

Dimensional analysis of the basic wave generation relationship yields:

$$\frac{gH_{mo}}{U_A^2}, \frac{gT_p}{U_A} = f\left(\frac{gF}{U_A^2}, \frac{gt_d}{U_A}, \frac{gh}{U_A^2}\right) \tag{G.4}$$

The last term, $\dfrac{gh}{U_A^2}$, is not considered for deepwater (wavelength is less than half the water depth) conditions. The minimum duration, t_{min}, is the time for significant waves to travel the fetch length. If the wind duration is less than the minimum duration for a fetch, the waves are defined as duration-limited. After this duration has been reached, the waves are defined as fetch-limited. If the wind persists long enough in magnitude and direction for the waves to become fetch-limited, then the wave parameters no longer depend on $\dfrac{gt_d}{U_A}$, and Equation 5 reduces to:

$$\frac{gH_{mo}}{U_A^2}, \frac{gT_p}{U_A} = f\left(\frac{gF}{U_A^2}\right) \tag{G.5}$$

The functional relationship in Equation G.5 states that significant wave height, H_{mo}, and peak wave period, T_p, are both a function of the fetch length and wind speed. The SPM(1984) gives the following parametric model for predicting deepwater waves from wind properties:

$$\frac{gH_{mo}}{U_A^2} = 0.0016\left(\frac{gF}{U_A^2}\right)^{1/2} \tag{G.6a}$$

$$\frac{gT_p}{U_A} = 0.286\left(\frac{gF}{U_A^2}\right)^{1/3} \tag{G.6b}$$

$$\frac{gt_{min}}{U_A} = 68.8\left(\frac{gF}{U_A^2}\right)^{2/3} \tag{G.6c}$$

If the actual duration is less than the limiting value given in Equation G.6b, then a new fetch is calculated using Equation 6c and the actual duration.

G.3.   Results

The relationships given in Equation G.6a-G.6c are plotted for the data acquired in Schafer Lake in 2005, 2007, and 2008 in Figures G.3 and G.4. The equations of the fitted lines are:

$$\frac{gH_{mo}}{U_A{}^2} = 0.0025 \left(\frac{gF}{U_A{}^2} \right)^{0.44}$$

(G.7a)

$$\frac{gT_p}{U_A} = 0.4147 \left(\frac{gF}{U_A{}^2} \right)^{0.28}$$

(G.7b)

In order to assume that the wave generation is fetch limited, the wind must maintain a velocity for a sufficient time period. If the waves are assumed to be traveling at group wave speed, the minimum duration for the waves to be fetch limited can be calculated by integrating Equation 7b over the fetch which yields

$$\frac{gt_{min}}{U_A} = 108.2 \left(\frac{gF}{U_A{}^2} \right)^{0.28}$$

(G.8)

The wave parameters H_{mo} and T_p can be predicted for a given wind speed and direction using Equations G.2, G.3, and G.7. The empirical relationship above is derived only with the data collected in Schafer Late, but it should hold for ponds with similar properties. Schafer Lake is well suited for establishing a general relation, since there are no trees nearby and the only appreciable topographic relief is the reservoir levee.

According to linear wave theory, the wave length, L, as a function of the wave period, T, for deepwater conditions is given by the following relation.

$$L = \frac{gT^2}{2\pi}$$

(G.9a)

If the relative depth $\frac{h}{L}$ is greater than 0.5 (or $kh > \pi$ where $k = \frac{2\pi}{L}$), the waves are classified as deep water, and, for most practical purposes, this is sufficient justification for the assumption of the explicit relationship between wave length and period. The same relation can be used for random waves to obtain a representative wave length from peak wave period:

$$L_p = \frac{gT_p{}^2}{2\pi} \text{ or } L_p = 5.12T_p{}^2$$

(G.9b)

It can be seen from Figures G.3 and G.4 that the model provides a good fit to the wave data, which cover a wide range of amplitude and period. Dashed lines in Figure G.3 and G.4 were calculated using the SPM (1984) formulations given in Equations G.6a and G.6b. Dotted lines are from the CEM (2003) method. The *rms* error relative to the unmodified SPM (1984) method for significant wave height was reduced by 67% and for peak wave period the error was reduced by 71%.
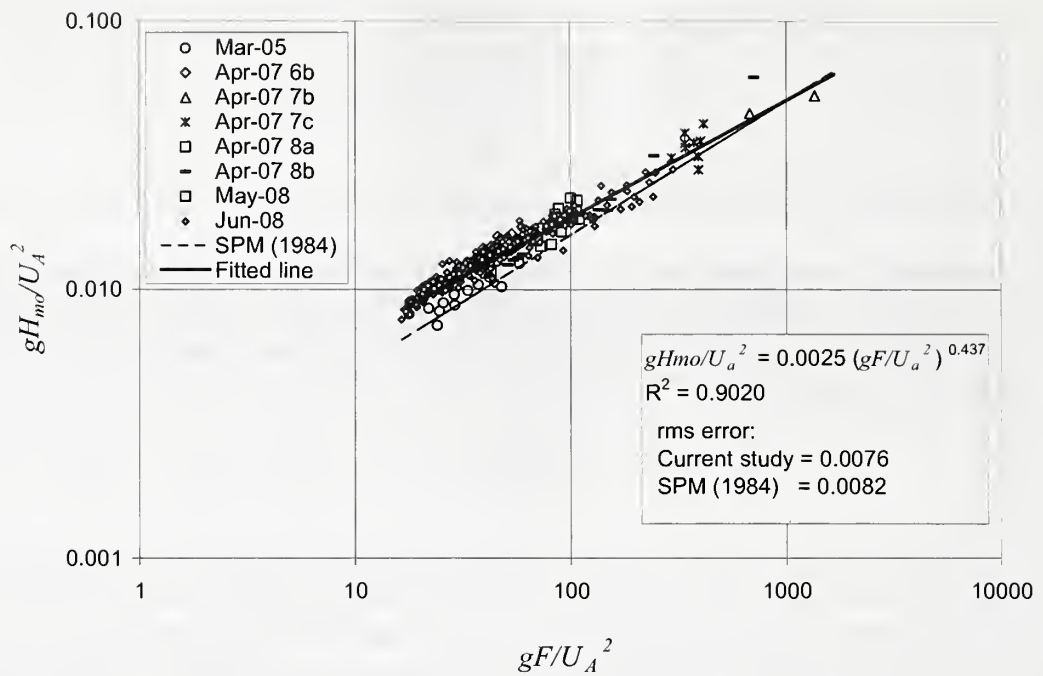
Figure G.3. Wave prediction relationship for significant wave height estimations.
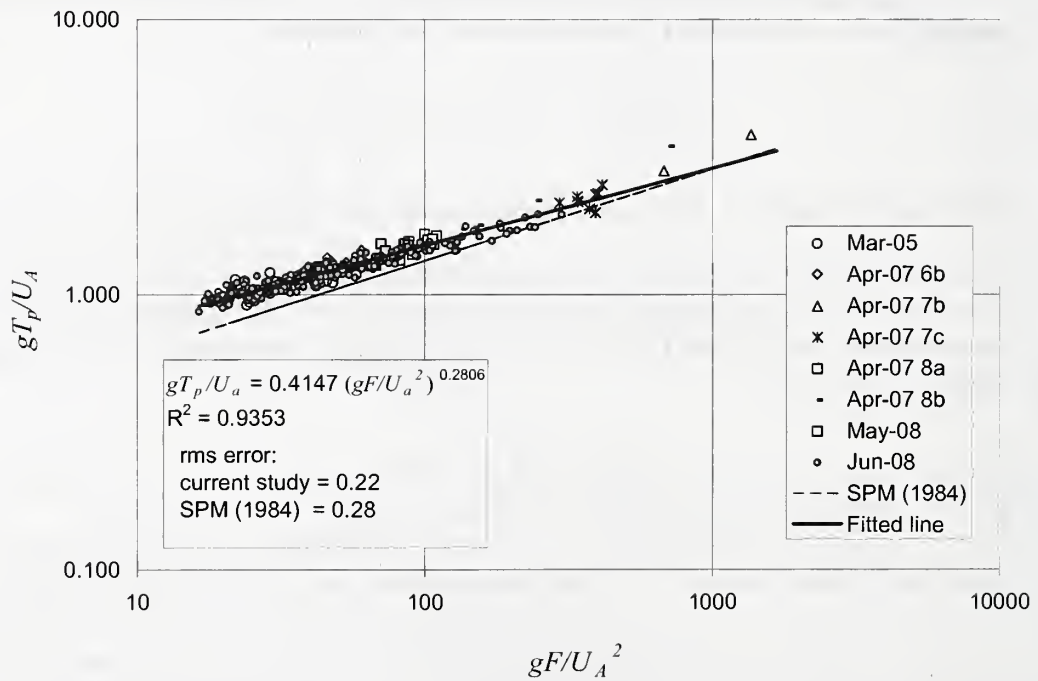

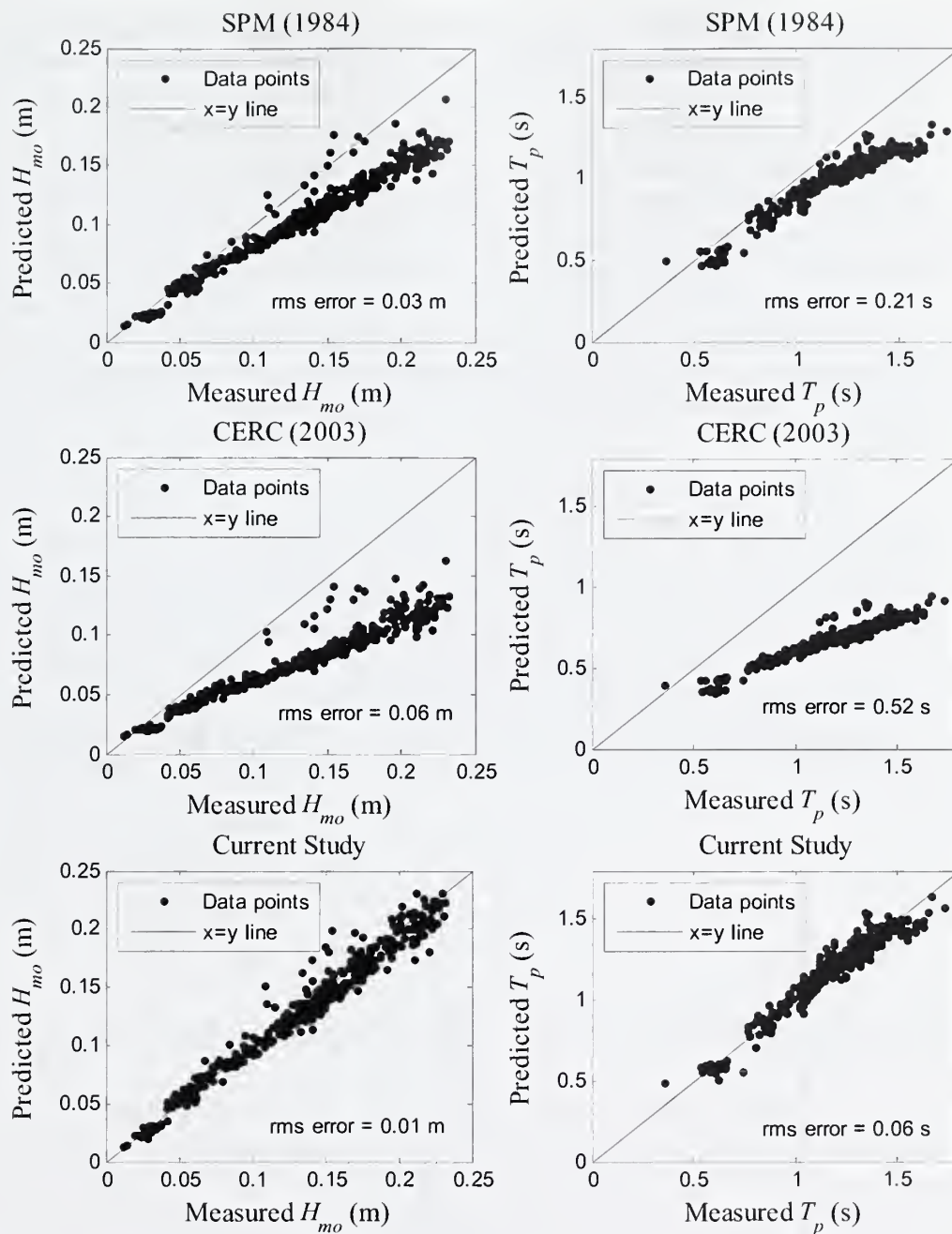Figure G.4. Wave prediction relationship for peak wave period estimations.

Figure G.5.Comparison between SPM(1984) and CERC(2003) prediction of waves and prediction with coefficients determined in the current work.

The wave periods predicted by SPM (1984) method in Figure G.3 were smaller than the measured values at lower wave periods. This may be due to reflected waves from the shore in the opposite direction of the wave propagation. During the initial growth of the waves, energy is transferred from the high frequency waves to lower frequencies due

to breaking, shifting the energy spectrum to a lower frequency range. The reflected waves interact with the incoming waves and increase turbulent dissipation, reducing the energy transferred to the longer waves. Similarly, the measured wave heights are larger than those predicted with the SPM (1984) method for smaller waves. Figure G.5 shows the measured values of significant wave height H_{mo} and peak wave period, T_p are compared with the predicted values with the original SPM (1984) method, the CEM (2003) method, and the current approach. For the higher values of both H_{mo}, and T_p, the current procedure gives better estimates compared to SPM (1984). The shift in the energy density spectrum is illustrated in Figure 7.6 where the average spectrum of a 6 hour portion of June 2008 data is compared with the JONSWAP spectrum for the same H_{mo} and T_p. The waves with higher frequencies, which correspond to shorter waves, have more energy compared to the JONSWAP spectrum and the total wave energy is larger than the predicted wave energy.

Although wave generation by wind is complex, it is possible to predict wave properties from the wind data at a steady-state when wind speed and direction data are available. Even though these data may not be available at a given field site, long term estimates of wave characteristics should be valid if the prediction is made based on wind data from the same region as long as the topography near the weather station is similar to that of the irrigation reservoir. The flat topography of the land surrounding the reservoir combined with the lack of trees or other impediments to the wind should allow this data to be generalized to other areas. In locations where there is more shielding of the wind, the predictions found here will provide an estimate of the upper limits of expected wave size.
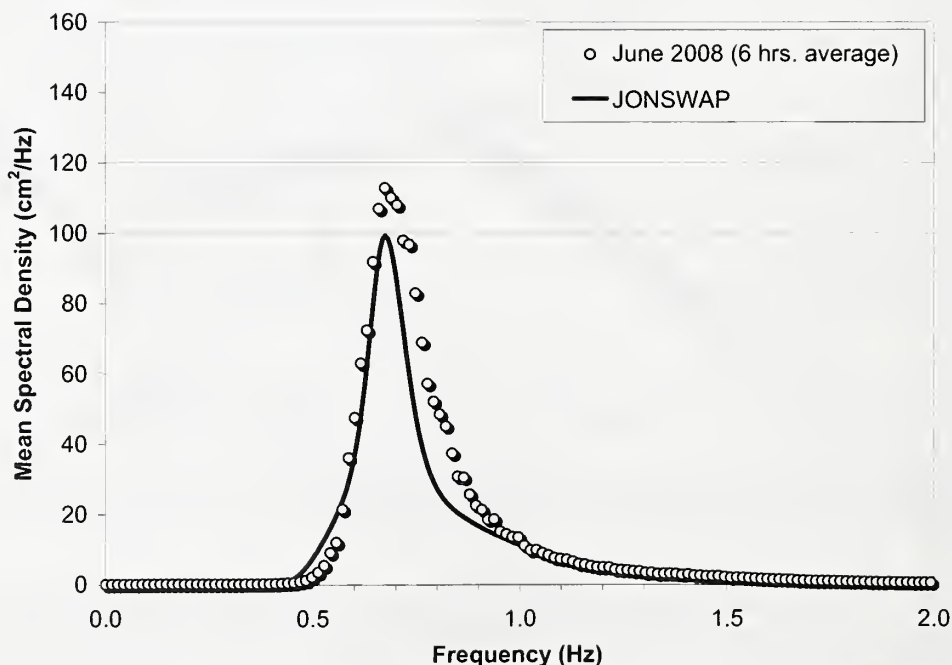

Figure G.6.Comparison of the JONSWAP spectrum with 6 hours of June 2008 data wave data.

H. EFFECT OF REFLECTED WAVES FROM THE WAVE ABSORBER ON FIXED GAUGE READINGS

For an ideal wave flume, the test section should be as far as possible from the wave generator in order maximize time available for data recording. Besides, the reflection from the end opposite the generator should be minimized. For the current experimental setup the test section was 11.1 m from the wave generator and 1.6 m from the toe of the wave absorber. These distances were necessitated by the available flume length and resulted in waves reflected from the wave absorber effecting the measurements of transmitted waves made by the fixed gauge. Regardless of the shape, size, or configuration of the model, the results are affected by minor oscillations. This was especially true for lower frequency waves. In Figure H.1 the average transmission coefficient of all the available experiential data is plotted.
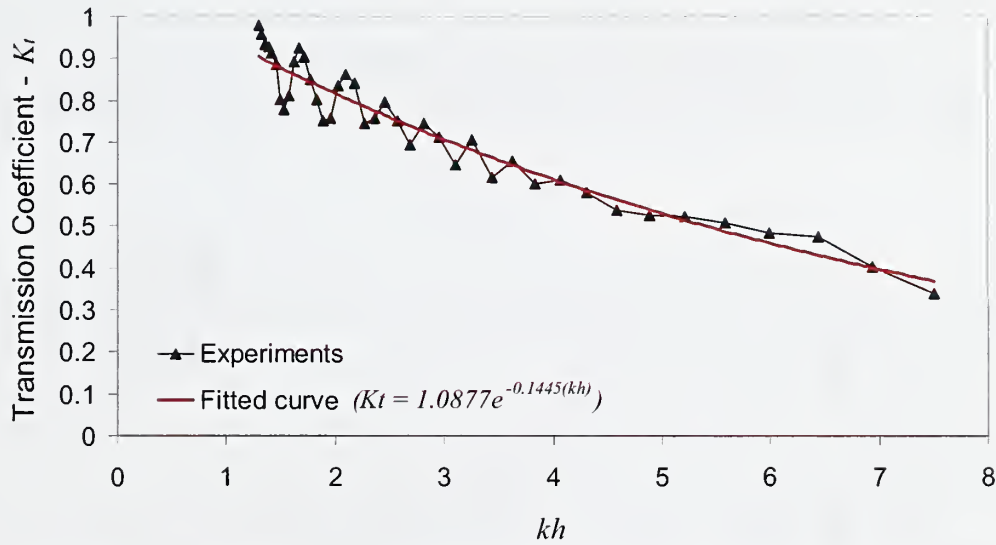

Figure H.7. The average transmission coefficient of all the experiments with changing relative depth, *kh*.

A computer program was created to aid in understanding the reason for the deviations shown in Figure H.2. The program simulated partial reflections of linear waves from an obstacle at a certain distance. For a progressive wave with zero initial phase and partially reflected from an obstacle, the amplitude η for the composite wave is:

$$\eta = \frac{H}{2}\left(\sin(kx - \sigma t)\right) + K_r \frac{H}{2}\left(\sin(kx + \sigma t + \delta)\right), \qquad \text{H.1}$$

where H is the wave height of the original wave, k is the wave number, σ is the wave angular frequency, K_r is the reflection coefficient and δ is the phase angle between the incoming and reflected waves. The phase angle depends on the boundary condition and it is constant at a distance, X_g, from the obstacle.
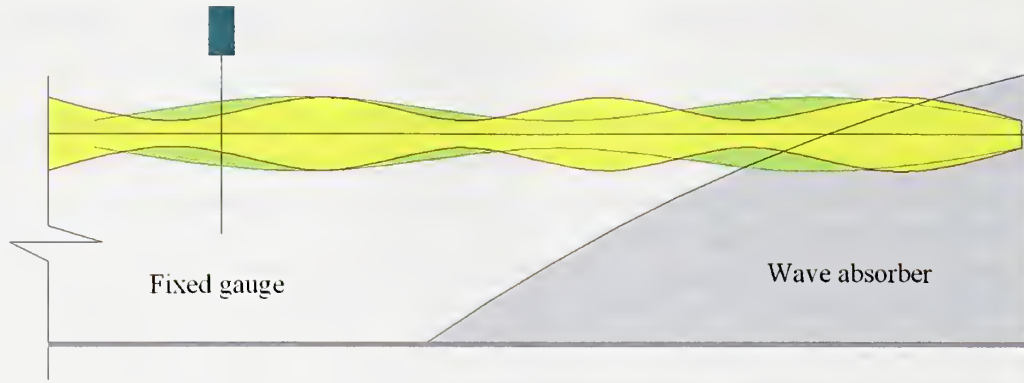
275

Figure H.8. The schematic representation of standing waves for two different wave periods (green and yellow) for the same wave height.

The wave absorber at the end of the flume has less than 10% reflection for most of the experiments. The average reflection coefficient is given in Figure H.3 with a fitted curve.
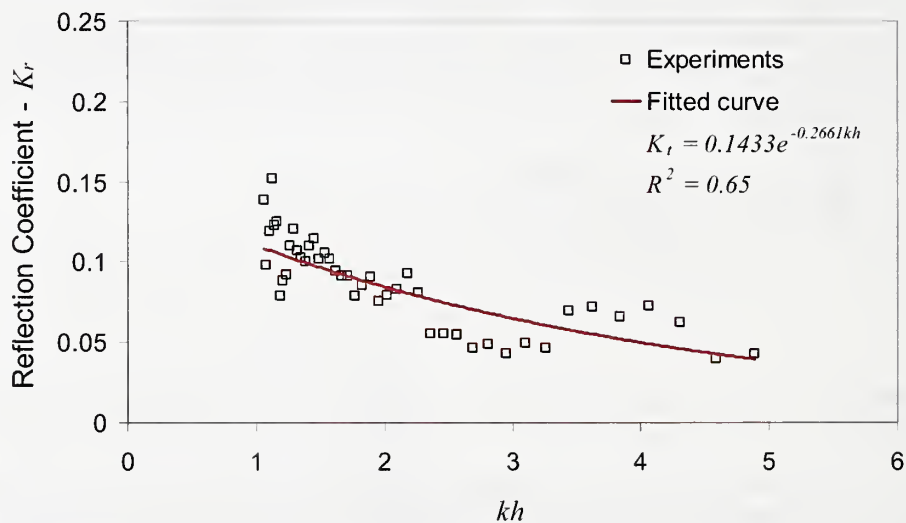

Figure H.3. Average values of the reflection coefficient from the wave absorber.

The recorded signal at a fixed gauge at x_g can be obtained with the dimensionless form of the equation H.1 as

$$\frac{\eta}{H} = \sin(kx_g - \sigma t) + K_r(kh)\sin(kx_g + \sigma t + \delta(kX_g))$$ H.2

Note that the reflection coefficient is a function of kh and the phase angle is a function of kX_g. By imposing some more simplifications it can be proven that Equation H.2 is a standing wave and the resulting envelope is stationary. Therefore, the measured

wave height, H_{env}, at a location x_g corresponding to the generated wave height H, will depend on the phase and the distance between the gauge and the obstacle. If the gauge moves with a velocity of v_g in x-direction then the equation becomes:

$$\frac{2\eta}{H} = \sin\left(kx_g + (kv_g - \sigma)t\right) + K_r(kh)\sin\left(kx_g + (kv_g + \sigma)t + \delta(kX_g)\right).$$ H.3

For a fixed reflection coefficient, K_r, the fixed gauge reads a different wave height for each wave period ranging between H_{min} and H_{max}. This effect causes oscillations around the actual wave height when the wave period varied. The amplitude of these oscillations depends on the reflection coefficient.

Since the reflection coefficient reduces with increasing relative depth, kh the amplitude of the oscillations decay with increasing kh. The experiments were conducted at a limited number of wave periods. Therefore, the program was also run for those wave periods to see the effect on the results. The plot in Figure H.5 for those discrete values is irregular and aliasing occurs at higher values of kh. If the mean curve in Figure H.1 is subtracted from the data points and divided by transmission coefficient, the same dimensionless parameter can be obtained for the experimental data (Equation H.4).

$$\frac{K_{t(env.)} - K_t}{K_t} = \frac{H_{t(env.)} - H_t}{H_t}$$

In Figure H.5, the normalized difference between the generated and measured wave height is plotted for different relative depths including the effect of the wave absorber on the reflection coefficient. It can be seen from Figure H.5 that the simulation and the experiments yielded similar results (X_g=3.5 m). The slight difference in oscillation frequencies may be due to the irregular shape and nonlinear response of the wave absorber. There is also some difference between the amplitudes of the two signals since the decay of the reflection coefficient is irregular. Nevertheless, the oscillations are less than 10% of the mean and have negligible influence on the general trend of the experimental data. Therefore, no corrections were made to the reported results.

This also shows that the incident and reflected wave heights can be estimated by varying the wave period instead of moving the gauge.
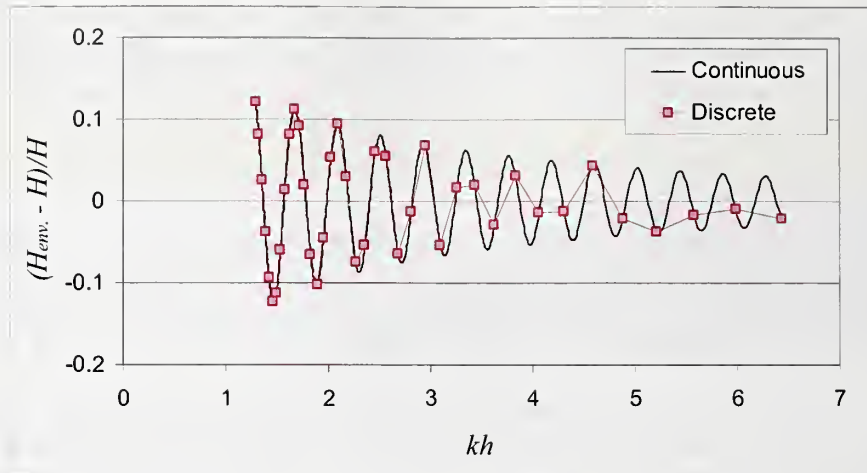
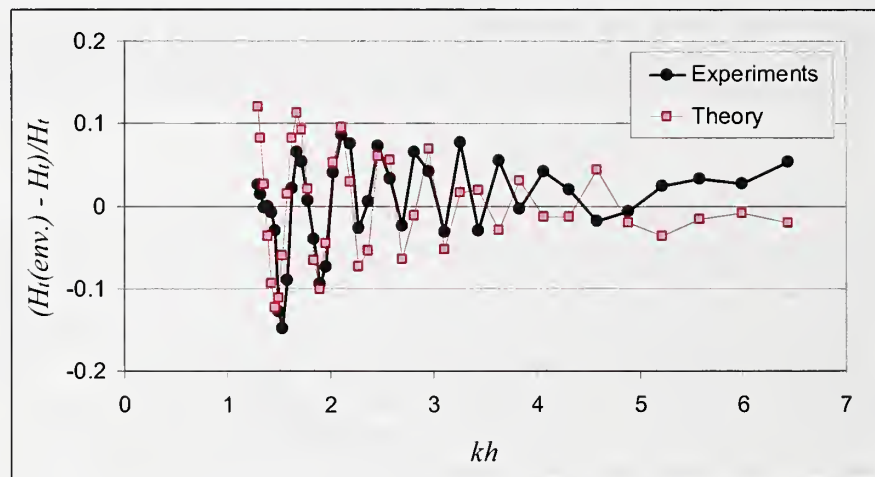Figure H.4. Continuous and discrete plots of the wave height variation with relative depth, *kh*.

Figure H.5. Comparison of the simulations of wave height variation with the experiments.